Vol. 65 ■ No. 7 ■ July 2024

JNM
The Journal of Nuclear Medicine

JNM Podcasts
jnm.snmjournals.org/podcasts

SOC for Metastatic Prostate Cancer

FEATURED ARTICLE

Deescalated ^{225}Ac-PSMA-617 Versus ^{177}Lu/^{225}Ac-PSMA-617 Cocktail Therapy: A Single-Center Retrospective Analysis of 233 Patients. Hendrik Rathke et al. See page 1057.

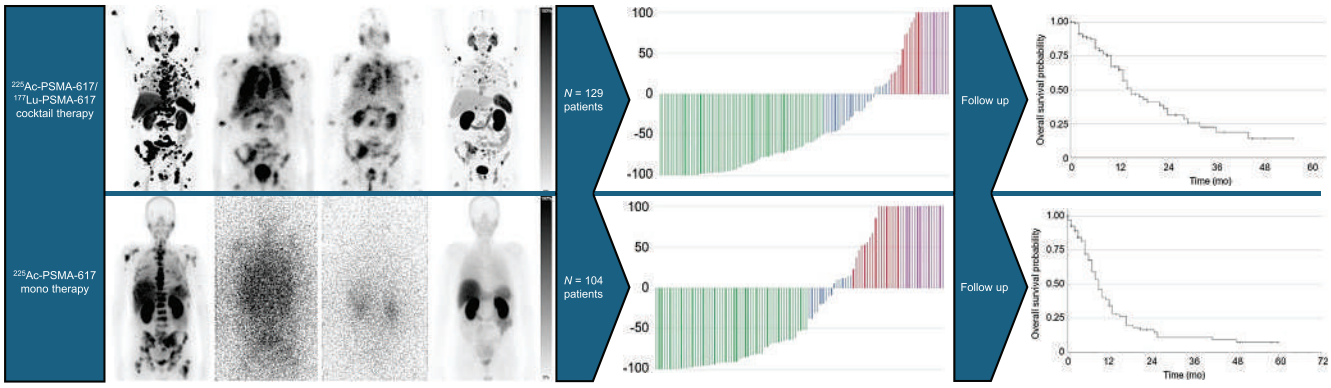

Early identification of IBD: Granzyme B–targeted PET for detection and treatment monitoring in inflammatory bowel disease. Pedram Heidari et al. See page 1137.

SNMMI SOCIETY OF NUCLEAR MEDICINE & MOLECULAR IMAGING

SNMMI would like to thank our Value Initiative Industry Alliance member companies for their support. Together we have made incredible progress advancing patient care and precision medicine.

Leadership Circle

BLUE EARTH DIAGNOSTICS
A Bracco Company

SIEMENS Healthineers

CardinalHealth
Essential to care™

CURIUM™
LIFE FORWARD

Eisai

GE HealthCare

itm
PASSION FOR PRECISION

LANTHEUS

Lilly

NOVARTIS

UNITED IMAGING

Visionary Member

mim SOFTWARE

RayzeBio

Principal Member

BAYER

BRACCO
LIFE FROM INSIDE

CAPINTEC
A MIRION MEDICAL COMPANY

CELLECTAR BIOSCIENCES

cyclomedica

DAXOR
THE BLOOD VOLUME COMPANY

EVERGREEN THERAGNOSTICS

Innervate Radiopharmaceuticals

isotopia
Nuclear Medicine

JUBILANT RADIOPHARMA

Life Molecular Imaging
HEALTH CARE

monrol

SHINE

SPECTRUM
DYNAMICS MEDICAL

Telix

TTg
Imaging Solutions

Corporate Member

Debiopharm
WE DEVELOP FOR PATIENTS

HERMES MEDICAL SOLUTIONS

MEDTRACE

NorthStar
MEDICAL RADIOISOTOPES, LLC

SOFIE
From start to clinic

Voximetry
PATIENT SPECIFIC RADIATION DOSIMETRY

SNMMI SOCIETY OF NUCLEAR MEDICINE & MOLECULAR IMAGING
VALUE INITIATIVE

Learn more about becoming a Value Initiative Member Company:
valueinitiative.snmmi.org

SNMMI MARS SHOT

Funding Innovation for the Future of Nuclear Medicine

The SNMMI Mars Shot initiative ignites the focus, determination, and resources needed to unlock long-sought answers to using nuclear medicine to combat human illnesses. Be a part of this transformative journey, turning groundbreaking nuclear medicine research into the treatments of tomorrow, and redefining healing on a global scale.

DONATE TODAY

SNMMI Qualified Systems Personnel Training Program (QSPTP)

ENHANCE YOUR EXPERTISE IN RADIOPHARMACEUTICAL SCIENCES

Defining the competencies in the release of manufactured radiopharmaceuticals

THROUGH DIDACTIC AND HANDS-ON LEARNING, THIS COURSE IS DESIGNED TO MEET THE FOLLOWING LEARNING OBJECTIVES:

- Provide theoretical knowledge and practical experience needed to assume responsibility for small scale manufacture, quality control, and release of radiopharmaceuticals
- Provide cross-training for chemists and nuclear pharmacists:
  - in manufacturing and quality assurance
  - in synthesis and pharmaceutical formulation of radiopharmaceuticals
- Educate learners on regulatory compliance requirements associated with radiopharmaceutical manufacturing
- Understand application of radiopharmaceuticals
- Understand the components of research applications, including IND and RDRC processes

The didactic course may be taken independently of the hands-on component. The hands-on component requires the completion of the didactic course prior to participation.

The program is designed for students with the following educational background: PharmD, B.S. or M.S. Pharmacists or B.S. or M.S. in Chemistry (or other science related degree).

For more information, visit ***snmmi.org/qsptp***

JNM
Volume 65 • Number 7 • July 2024

IS IT REALLY HAPPENING?

995 **Is Automatic Tumor Segmentation on Whole-Body ^{18}F-FDG PET Images a Clinical Reality?**
Lalith Kumar Shiyam Sundar and Thomas Beyer

FOCUS ON MOLECULAR IMAGING

998 **Molecular Imaging in Gynecology: Beyond Cancer**
Joni Sebastiano, Cindy Rodriguez, Zachary V. Samuels, Kristen Pepin, and Brian M. Zeglis

ONCOLOGY

Clinical

1004 ■ BRIEF COMMUNICATION. **Frequent Amplification and Overexpression of PSMA in Basallike Breast Cancer from Analysis of The Cancer Genome Atlas**
Wenhui Zhou, Sumit Halder, Sanna Herwald, Michael Ghijsen, Gowhar Shafi, Mohan Uttarwar, Eric Rosen, Benjamin Franc, and Sirish Kishore

1007 **Utility of PSMA PET/CT in Staging and Restaging of Renal Cell Carcinoma: A Systematic Review and Metaanalysis**
Moe S. Sadaghiani, Saradha Baskaran, Michael A. Gorin, Steven P. Rowe, Jean-Claude Provost, Iryna Teslenko, Roman Bilyk, Hong An, and Sara Sheikhbahaei

1013 **A Prospective Randomized Multicenter Study on the Impact of [^{18}F]F-Choline PET/CT Versus Conventional Imaging for Staging Intermediate- to High-Risk Prostate Cancer**
Laura Evangelista, Fabio Zattoni, Marta Burei, Daniele Bertin, Eugenio Borsatti, Tanja Baresic, Mohsen Farsad, Emanuela Trenti, Mirco Bartolomei, Stefano Panareo, et al.

1021 **Diagnostic Performance of [^{18}F]AlF-Thretide PET/CT in Patients with Newly Diagnosed Prostate Cancer Using Histopathology as Reference Standard**
Jie Zang, Yun Yang, Shaoming Chen, Chao Wang, Shaohao Chen, Shun Hu, Hai Cai, Xiaodong Li, Ning Xu, Xiaoyuan Chen, et al.

1027 **Prognostic Implications of ^{68}Ga-FAPI-46 PET/CT–Derived Parameters on Overall Survival in Various Types of Solid Tumors**
Masao Watanabe, Wolfgang P. Fendler, Hong Grafe, Nader Hirmas, Rainer Hamacher, Helena Lanzafame, Kim M. Pabst, Hubertus Hautzel, Clemens Aigner, Stefan Kasper, et al.

Basic

1035 **In Vivo PET Imaging of ^{89}Zr-Labeled Natural Killer Cells and the Modulating Effects of a Therapeutic Antibody**
Truc T. Pham, Alicia Chenoweth, Natasha Patel, Arshiya Banu, Gabriel Osborn, Philip J. Blower, Sophia N. Karagiannis, and Michelle T. Ma

1043 **CEACAM5-Targeted Immuno-PET in Androgen Receptor–Negative Prostate Cancer**
Cinzia Imberti, Roberto De Gregorio, Joshua A. Korsen, Tran T. Hoang, Samantha Khitrov, Teja Kalidindi, Subhiksha Nandakumar, Jooyoung Park, Samir Zaidi, Naga Vara Kishore Pillarsetty, et al.

THERANOSTICS

Clinical

1051 **A Phase 0 Study to Assess the Biodistribution and Pharmacokinetics of a Radiolabeled Antibody Targeting Human Kallikrein 2 in Participants with Metastatic Castration-Resistant Prostate Cancer**
Neeta Pandit-Taskar, Joseph A. O'Donoghue, Dushen Chetty, Steven Max, Danielle Wanik, Ohad Ilovich, Michael Russell, Tenzin Nyima, Chaitanya R. Divgi, Margaret Yu, et al.

1057 ■ FEATURED ARTICLE OF THE MONTH. **Deescalated ^{225}Ac-PSMA-617 Versus ^{177}Lu/^{225}Ac-PSMA-617 Cocktail Therapy: A Single-Center Retrospective Analysis of 233 Patients**
Hendrik Rathke, Erik Winter, Frank Bruchertseifer, Manuel Röhrich, Frederik Lars Giesel, Uwe Haberkorn, Alfred Morgenstern, and Clemens Kratochwil

1064 **Assessing Response to PSMA Radiopharmaceutical Therapies with Single SPECT Imaging at 24 Hours After Injection**
Surekha Yadav, Fei Jiang, Sara Kurkowska, Rachelle Saelee, Amanda Morley, Felix Feng, Rahul Aggarwal, Courtney Lawhn-Heath, Carlos Uribe, and Thomas A. Hope

1070 **Relationship Between Absorbed Dose and Response in Neuroendocrine Tumors Treated with [^{177}Lu]Lu-DOTATATE**
Carl Fredrik Warfvinge, Johan Gustafsson, Daniel Roth, Jan Tennvall, Johanna Svensson, Peter Bernhardt, Anna Åkesson, Elinore Wieslander, Anna Sundlöv, and Katarina Sjögreen Gleisner

1076 ■ BRIEF COMMUNICATION. **Randomized Trial of Prostate-Specific Membrane Antigen PET/CT Before Definitive Radiotherapy for Unfavorable Intermediate- and High-Risk Prostate Cancer (PSMA-dRT Trial)**
John Nikitas, Ethan Lam, Kiara Adame Booker, Wolfgang P. Fendler, Matthias Eiber, Boris Hadaschik, Ken Herrmann, Nader Hirmas, Helena Lanzafame, Martin Stuschke, et al.

1080 **True-Positive ^{18}F-Flotufolastat Lesions in Patients with Prostate Cancer Recurrence with Baseline-Negative Conventional Imaging: Results from the Prospective, Phase 3, Multicenter SPOTLIGHT Study**
Mark T. Fleming, Rick Hermsen, Andrei S. Purysko, Albert Chau, Phillip Davis, Brian F. Chapin, David M. Schuster, Mohamad Allaf, Ryan J. Avery, Norbert Avril, et al.

Basic

1087 **Receptor-Targeted Peptide Conjugates Based on Diphosphines Enable Preparation of ^{99m}Tc and ^{188}Re Theranostic Agents for Prostate Cancer**
Truc T. Pham, Ingebjørg N. Hungnes, Charlotte Rivas, Julie Cleaver, George Firth, Philip J. Blower, Jane Sosabowski, Gary J.R. Cook, Lefteris Livieratos, Jennifer D. Young, et al.

RADIONUCLIDE THERAPY

Clinical

1095 **Safety and Efficacy of Radiosynoviorthesis: A Prospective Canadian Multicenter Study**
Mélanie Desaulniers, Michel Paquette, Stéphanie Dubreuil, Helena Senta, Éric Lavallée, J. Carter Thorne, and Éric Turcotte

RADIOBIOLOGY/DOSIMETRY

Clinical

1101 **Dose Reduction in Pediatric Oncology Patients with Delayed Total-Body [^{18}F]FDG PET/CT**
Clemens Mingels, Benjamin A. Spencer, Hande Nalbant, Negar Omidvari, Mehrad Rokni, Axel Rominger, Fatma Sen, Simon R. Cherry, Ramsey D. Badawi, Yasser G. Abdelhafez, et al.

CARDIOVASCULAR

Clinical

1107 **Natural History of Myocardial $\alpha_v\beta_3$ Integrin Expression After Acute Myocardial Infarction: Correlation with Changes in Myocardial Blood Flow**
Matthieu Dietz, Christel H. Kamani, Colin Bousige, Vincent Dunet, Judith Delage, Vladimir Rubimbura, Marie Nicod Lalonde, Giorgio Treglia, Niklaus Schaefer, Wail Nammas, et al.

1113 **Determining Hemodynamically Significant Coronary Artery Disease: Patient-Specific Cutoffs in Quantitative Myocardial Blood Flow Using [^{15}O]H_2O PET Imaging**
Roel Hoek, Pepijn A. van Diemen, Pieter G. Raijmakers, Roel S. Driessen, Yvemarie B.O. Somsen, Ruben W. de Winter, Ruurt A. Jukema, Jos W.R. Twisk, Lourens F.H.J. Robbers, Pim van der Harst, et al.

NEUROLOGY

Clinical

1122 **Patterns of Early Neocortical Amyloid-β Accumulation: A PET Population-Based Study**
Emily E. Lecy, Hoon-Ki Min, Christopher J. Apgar, Daniela D. Maltais, Emily S. Lundt, Sabrina M. Albertson, Matthew L. Senjem, Christopher G. Schwarz, Hugo Botha, Jonathan Graff-Radford, et al.

1129 **Cerebral ^{18}F-FDG PET/CT Metabolism as Diagnostic Signature for Central Nervous System Toxicity After Immune Checkpoint Blockade Cancer Treatment**
Yifei Ma, Jiling Zeng, Fadian Ding, Yiwei Xu, Youlong Wang, Guanqing Zhong, Nianqi Liu, Yanqi Wang, Yiming Li, Shuqin Chen, et al.

GASTROENTEROLOGY

Basic

1137 ■ FEATURED BASIC SCIENCE ARTICLE. **Granzyme B PET Imaging for Assessment of Disease Activity in Inflammatory Bowel Disease**
Pedram Heidari, Arvin Haj-Mirzaian, Suma Prabhu, Bahar Ataeinia, Shadi A. Esfahani, and Umar Mahmood

AI/ADVANCED IMAGE ANALYSIS

Clinical

1144 **Deep Learning–Enabled Quantification of ^{99m}Tc-Pyrophosphate SPECT/CT for Cardiac Amyloidosis**
Robert J.H. Miller, Aakash Shanbhag, Anna M. Michalowska, Paul Kavanagh, Joanna X. Liang, Valerie Builoff, Nowell M. Fine, Damini Dey, Daniel S. Berman, and Piotr J. Slomka

1151 **Histology-Based Radiomics for [^{18}F]FDG PET Identifies Tissue Heterogeneity in Pancreatic Cancer**
Esther M.M. Smeets, Marija Trajkovic-Arsic, Daan Geijs, Sinan Karakaya, Monica van Zanten, Lodewijk A.A. Brosens, Benedikt Feuerecker, Martin Gotthardt, Jens T. Siveke, Rickmer Braren, et al.

THE ILLUSTRATED POST

1160 **Example of Artificial Intelligence–Based Decision Support for Amino Acid PET: Early Prediction of Suspected Brain Tumor Foci for Patient Management**
Philipp Lohmann, Robin Gutsche, Jan-Michael Werner, N. Jon Shah, Karl-Josef Langen, and Norbert Galldiks

1161 **Case Report: Pulmonary Actinomyces Infection Mimics Lung Cancer on [^{68}Ga]Ga-FAPI PET/CT**
Giulia Cuzzani, Emilia Fortunati, Lucia Zanoni, Cristina Nanni, Filippo Antonacci, Francesca Giunchi, Gian Piero Bandelli, Irene Brusa, Piergiorgio Solli, and Stefano Fanti

DEPARTMENT

8A **This Month in JNM**

JNM The Journal of NUCLEAR MEDICINE

The Official Publication of **SNMMI**

MISSION STATEMENT: *The Journal of Nuclear Medicine* advances the knowledge and practice of molecular imaging and therapy and nuclear medicine to improve patient care through publication of original basic science and clinical research.

JNM (ISSN 0161-5505 [print]; ISSN 2159-662X [online]) is published monthly by SNMMI, 1850 Samuel Morse Drive, Reston, VA 20190-5316. Periodicals postage is paid at Herndon, VA, and additional mailing offices. Postmaster, send address changes to *The Journal of Nuclear Medicine,* 1850 Samuel Morse Drive, Reston, VA 20190-5316. The costs of publication of all nonsolicited articles in *JNM* were defrayed in part by the payment of page charges. Therefore, and solely to indicate this fact, these articles are hereby designated "advertisements" in accordance with 18 USC section 1734.

DISCLOSURE OF COMMERCIAL INTEREST: Johannes Czernin, MD, editor-in-chief of *The Journal of Nuclear Medicine,* has indicated that he is a founder of Sofie Biosciences and holds equity in the company and in intellectual property invented by him, patented by the University of California, and licensed to Sofie Biosciences. He is also a founder and board member of Trethera Therapeutics and holds equity in the company and in intellectual property invented by him, patented by the University of California, and licensed to Trethera Therapeutics. He also serves on the scientific advisory boards of RayzeBio and Aktis Oncology. No other potential conflicts of interest were reported. Manuscripts submitted to *JNM* with potential conflicts are handled by a guest editor.

EDITORIAL COMMUNICATIONS should be sent to: Editor-in-Chief, Johannes Czernin, MD, *JNM* Office, SNMMI, 1850 Samuel Morse Drive, Reston, VA 20190-5316. Phone: (703) 326-1185; Fax: (703) 708-9018. To submit a manuscript, go to https://submit-jnm.snmjournals.org.

BUSINESS COMMUNICATIONS concerning permission requests should be sent to the publisher, SNMMI, 1850 Samuel Morse Drive, Reston, VA 20190-5316; (703) 708-9000; home page address: jnm.snmjournals.org. Subscription requests and address changes should be sent to Membership Department, SNMMI at the address above. Notify the Society of change of address and telephone number at least 30 days before date of issue by sending both the old and new addresses. Claims for copies lost in the mail are allowed within 90 days of the date of issue. Claims are not allowed for issues lost as a result of insufficient notice of change of address. For information on advertising, contact Team SNMMI (Kevin Dunn, Rich Devanna, and Charlie Meitner; (201) 767-4170; fax: (201) 767-8065; TeamSNMMI@cunnasso.com). Advertisements are subject to editorial approval and are restricted to products or services pertinent to nuclear medicine. Closing date is the first of the month preceding the date of issue.

INDIVIDUAL SUBSCRIPTION RATES for the 2024 calendar year are $665 within the United States and Canada; $714 elsewhere. Make checks payable to the SNMMI. CPC IPM Sales Agreement No. 1415158. Sales of individual back copies from 1999 through the current issue are available for $60 at http://www.snmmi.org/subscribe (subscriptions@snmmi.org; fax: (703) 667-5134). Individual articles are available for sale online at http://jnm.snmjournals.org.

Automated WB tumor segmentation: Shiyam Sundar and Beyer examine the transition toward automation in whole-body tumor segmentation using PET/CT imaging, including innovations in artificial intelligence and the need for collaboration across academia, industry, and clinical users. . . . . ***Page 995***

Molecular imaging in gynecology: Sebastiano and colleagues survey recent advances in PET, SPECT, MRI, and fluorescence imaging for diagnosis and management of benign gynecologic conditions, with emphasis on clinical reports, areas of need, and growth opportunities. . . . . ***Page 998***

Aberrant PSMA expression in BLBC: Zhou and colleagues investigate the molecular basis of the application of PMSA-targeting radiopharmaceuticals in breast cancer subtypes, including basallike breast cancer.. . . . . ***Page 1004***

PSMA PET/CT in RCC: Sadaghiani and colleagues provide a systematic review and metaanalysis of the utility and detection rate of PSMA PET/CT in staging and evaluation of primary renal cell carcinoma and restaging of metastatic or recurrent disease. . . . . ***Page 1007***

[^{18}F]F-choline PET/CT in PCa: Evangelista and colleagues compare the efficacy of [^{18}F]F-choline PET/CT with that of conventional imaging for staging and managing intermediate- to high-risk prostate cancer. . . . . ***Page 1013***

[^{18}F]AlF-thretide PET/CT in PCa: Zang and colleagues assess the diagnostic accuracy and whole-body radiation dosimetry of [^{18}F]AlF-thretide PET/CT in patients with newly diagnosed, treatment-naïve prostate cancer, using histopathology as a reference standard. . . . . ***Page 1021***

^{68}Ga-FAPI-46, ^{18}F-FDG PET/CT, and OS: Watanabe and colleagues look at comparative and complementary prognostic values (including for overall survival) of [^{68}Ga]Ga-fibroblast activation protein inhibitor–46 PET/CT and ^{18}F-FDG PET/CT in a range of tumor entities. . . . . ***Page 1027***

PET imaging of NK cells: Pham and colleagues use PET to trace natural killer cell migration to human epidermal growth factor receptor 2–positive HCC1954 breast tumors, focusing on trastuzumab antibody treatment effects on NK cell tumor accumulation.. . . . . ***Page 1035***

CEACAM5 imaging in AR$^-$ PCa: Imberti and colleagues report on development of an immuno-PET agent targeting the carcinoembryonic antigen–related cell adhesion molecule 5 and evaluate its ability to delineate androgen receptor–negative prostate cancer in preclinical studies.. . . . . ***Page 1043***

[^{111}In]-DOTA-h11B6 in mCRPC: Pandit-Taskar and colleagues detail the results of a first-in-human phase 0 trial with ^{111}In-radiolabeled anti–human kallikrein 2 monoclonal antibody to assess hK2 as a target for treatment of metastatic castration-resistant prostate cancer. . . . . ***Page 1051***

Ac-PSMA therapy vs Lu/Ac cocktail: Rathke and colleagues review clinical experience and published data on ^{225}Ac-PSMA-617 treatment in advanced-stage prostate cancer, both as deescalated monotherapy and as part of a ^{177}Lu-PSMA-617/^{225}Ac-PSMA-617 cocktail regimen. . . . . ***Page 1057***

Lesion-based response to PSMA RPT: Yadav and colleagues ask whether baseline lesion-absorbed dose in ^{177}Lu-PSMA-617 radiopharmaceutical therapies can predict corresponding responses and identify connections between lesion-absorbed dose and prostate-specific antigen response. . . . . ***Page 1064***

[^{177}Lu]Lu-DOTATATE response in NETs: Warfvinge and colleagues explore the relationship between tumor-absorbed dose and tumor response in a cohort of patients with neuroendocrine tumors treated with [^{177}Lu]Lu-DOTATATE, with implications for dosimetry-guided regimen design. . . . . ***Page 1070***

PSMA PET/CT before RT: Nikitas and colleagues report on a multicenter randomized phase III trial evaluating the utility of PSMA PET/CT before definitive radiotherapy in men with unfavorable intermediate- or high-risk prostate cancer. . . . . ***Page 1076***

^{18}F-Flotufolastat vs standard imaging: Fleming and colleagues detail findings from the SPOTLIGHT study, assessing the performance of ^{18}F-flotufolastat PET/CT for identifying PSMA-positive lesions in biochemical recurrence of prostate cancer but negative conventional baseline imaging. . . . . ***Page 1080***

Targeted ^{99m}Tc and ^{188}Re theranostics: Pham and colleagues report on application of a diphosphine platform incorporating ^{99m}Tc into receptor-targeted peptides to label a prostate-PSMA–targeted peptide with ^{99m}Tc and ^{188}Re for imaging and radiotherapy of prostate cancer. . . . . ***Page 1087***

Radiosynoviorthesis in synovitis: Desaulniers and colleagues describe the results of a Health Canada–approved trial on the safety and efficacy of intraarticular radionuclide treatment in patients with synovitis refractory to standard treatments.. . . . . ***Page 1095***

TB pediatric PET/CT dose reduction: Mingels and colleagues define a lower limit of reduced injected activity in delayed [^{18}F]FDG total-body PET/CT in pediatric oncology patients. . . . . ***Page 1101***

$\alpha_v\beta_3$ integrin dynamics after AMI: Dietz and colleagues monitor angiogenesis through myocardial integrin $\alpha_v\beta_3$ expression in patients with ST-segment elevation myocardial infarction and correlate integrin expression levels with subsequent changes in ^{82}Rb PET/CT parameters. . . . . ***Page 1107***

Patient-specific cutoffs in [^{15}O]H_2O PET: Hoek and colleagues assess the influences of prior coronary artery disease, sex, and age on optimal cutoffs of hyperemic myocardial blood flow and coronary flow reserve and whether cutoff optimization enhances diagnostic [^{15}O]H_2O PET. . . . . ***Page 1113***

Patterns of early Aβ deposition: Lecy and colleagues investigate amyloid-β signals in the peri-threshold SUV ratio range using Pittsburgh compound B PET in a population-based study, with implications for diagnosis and understanding of Alzheimer disease phenotypes.. . . . ***Page 1122***

PET/CT and immune-related CNS toxicity: Ma and colleagues analyze ^{18}F-FDG PET/CT images to identify probable biomarkers specific to immune-related central nervous system toxicity in cancer patients treated with immune checkpoint inhibitors. . . . . ***Page 1129***

Granzyme B PET for IBD: Heidari and colleagues use ^{68}Ga-NOTA-GZP PET to target granzyme B, released from cytotoxic T and natural killer cells, and detect early inflammatory bowel disease in murine models of colitis. . . ***Page 1137***

Deep learning amyloidosis quantification: Miller and colleagues evaluate a deep learning approach for fully automated volumetric quantitation of ^{99m}Tc-pyrophosphate using segmentation of coregistered anatomic structures from CT attenuation maps. . . . . ***Page 1144***

MCT4-based radiomics for [^{18}F]FDG PET: Smeets and colleagues investigate correlations between radiomics features extracted from [^{18}F]FDG PET images and histologic expression patterns of monocarboxylate transporter-4, a glycolytic marker in pancreatic cancer. . . ***Page 1151***

AI-based prediction of brain tumor foci: Lohmann and colleagues present a case study in suspected glioma illustrating the potential of artificial intelligence–based decision support for diagnostic and treatment planning based on amino acid PET.. . . . . ***Page 1160***

[^{68}Ga]Ga-FAPI-46 uptake and infection: Cuzzani and colleagues describe a case of actinomycosis in which [^{68}Ga]Ga-FAPI-46 PET findings mimic lung cancer. . . . . ***Page 1161***

Is Automatic Tumor Segmentation on Whole-Body ^{18}F-FDG PET Images a Clinical Reality?

Lalith Kumar Shiyam Sundar and Thomas Beyer

Quantitative Imaging and Medical Physics Team, Medical University of Vienna, Vienna, Austria

The integration of automated whole-body tumor segmentation using ^{18}F-FDG PET/CT images represents a pivotal shift in oncologic diagnostics, enhancing the precision and efficiency of tumor burden assessment. This editorial examines the transition toward automation, propelled by advancements in artificial intelligence, notably through deep learning techniques. We highlight the current availability of commercial tools and the academic efforts that have set the stage for these developments. Further, we comment on the challenges of data diversity, validation needs, and regulatory barriers. The role of metabolic tumor volume and total lesion glycolysis as vital metrics in cancer management underscores the significance of this evaluation. Despite promising progress, we call for increased collaboration across academia, clinical users, and industry to better realize the clinical benefits of automated segmentation, thus helping to streamline workflows and improve patient outcomes in oncology.

Key Words: image processing; research methods; AI; tumor segmentation; whole-body PET

J Nucl Med 2024; 65:995–997
DOI: 10.2967/jnumed.123.267183

In the domain of oncologic imaging, ^{18}F-FDG PET/CT has established itself as an indispensable tool facilitating the detection and management of tumors through the visualization of metabolic activity. By highlighting areas of increased glucose consumption, this imaging technique enables clinicians to discern malignancies from benign tissues, thus providing key information to the diagnosis, staging, and evaluation of therapeutic response in cancer patients.

The quantification of tumor burden through metabolic tumor volume, disease dissemination index, and total lesion glycolysis has further refined the utility of ^{18}F-FDG PET, offering prognostic value and aiding in the stratification of treatment approaches (*1*–*5*). These parameters encapsulate both the volume and the metabolic intensity of tumors and thereby serve as crucial indicators of tumor aggressiveness and response to therapy. However, the manual segmentation of tumor volumes is labor-intensive and subject to interobserver variability, hence limiting its feasibility in routine clinical practice. In response to these challenges, and in view of the ever-increasing workload, there is renewed interest in automatic whole-body tumor ^{18}F-FDG volume segmentation so as to enhance the reproducibility and efficiency of tumor burden assessments.

DIGITAL DISSECTION: ACADEMIA BETS ON AI FOR TUMOR SEGMENTATION

Today, the academic community has shifted attention toward leveraging artificial intelligence (AI) for multiple tasks along the imaging value chain, most notably perhaps toward automated whole-body PET ^{18}F-FDG tumor segmentation. This transition seeks to surmount the limitations inherent in traditional thresholding techniques, which often indiscriminately encapsulate both physiologic and pathologic tissues.

By harnessing the sophistication of AI algorithms—particularly those evolving from the foundational U-Net architecture—there is a concerted effort to precisely target and segment pathologic tissues, without the inclusion of nonpathologic regions. Initiatives such as AutoPET (*6*) and HECKTOR (*7*) have been pivotal, providing open-source datasets that are instrumental for the training and refinement of AI models. Among the array of methodologies used, nnU-Net (*8*) and MONAI's Auto3Dseg (*9*) stand out, by offering robust performance for enhanced accuracy in tumor segmentation building on a wealth of curated training datasets.

Despite the body of academic publications that show success and advocate for AI-driven tumor segmentation methodologies, there is a notable paucity of open-source solutions, a gap that poses significant challenges to the advancement of the imaging field. Moreover, the available open-source datasets are predominantly focused on specific types of cancers—namely lymphoma, lung cancer, and melanoma for AutoPET (*6*) and head and neck cancer for HECKTOR (*7*). This specialization limits their utility for training AI models that are generalizable across a broader spectrum of cancers and centers.

SMART SIMPLICITY: COMMERCIAL TOOLS ARE OFFERING PRACTICAL SOLUTIONS

In response to the market need for automated lesion segmentation tools, leading commercial vendors make significant strides in the development of fully automated and semiautomated methodologies for whole-body tumor volume segmentation from ^{18}F-FDG PET images. These methodologies commence with threshold-based segmentation to highlight hypermetabolic regions, which inherently include both pathologic and physiologic tissues. The challenge then is in distinguishing these tissues accurately, a task that vendors are addressing with distinct strategies.

For example, Auto ID (Siemens Healthineers) uses AI to differentiate between pathologic and physiologic tissues after an initial

Received Feb. 6, 2024; revision accepted May 13, 2024.
For correspondence or reprints, contact Lalith Kumar Shiyam Sundar (lalith.shiyamsundar@meduniwien.ac.at).
Published online Jun. 6, 2024.

threshold-based segmentation (*1*). This technique signifies a step toward full automation, aiming to reduce the need for manual intervention for ensuring segmentation accuracy. In contrast, Hermes Medical Solutions and MIM Medical have embraced a simplified, semiautomatic, one-click methodology. They have introduced Single Click Segmentation (Hermes) and Lesion ID (MIM), which allow medical professionals to easily refine the prethresholded segmentations with just one click, effectively isolating nonpathologic tissues. Essentially, this approach involves users manually identifying and categorizing regions within the prethresholded segmentation as either nonpathologic or pathologic. This user-friendly approach emphasizes simplicity while providing clinicians with straightforward segmented regions for clinical use. By seeking to provide certified tools that balance efficiency with practicality, commercial vendors are playing a pivotal role in the ongoing effort to improve diagnostic processes and, ultimately, patient outcomes in the field of oncology.

FROM BENCH TO BEDSIDE: HAS AUTOMATED VOLUME PARAMETER EXTRACTION PROLIFERATED TO CLINICS?

As discussed earlier, extensive clinical research has underscored the significance of volumetric parameters from ^{18}F-FDG PET/CT, specifically metabolic tumor volume and total lesion glycolysis, in enhancing prognostic evaluations and monitoring therapeutic responses across a diverse spectrum of cancers. Despite the significant potential of both parameters, they are not being used in routine clinical practice or trials. However, on the basis of our personal correspondence with both nuclear medicine clinicians and vendors, there seems to be a growing interest from the clinical community to extract volume-based metabolic parameters for lymphoma patient management (*4*,*5*). There is also an expectation toward fully automated solutions, as manual corrections can be tedious in patients with extensive disease.

THE FINAL FRONTIER: COMPLETE AUTOMATION—POSSIBLE OR PREPOSTEROUS?

Complete automation of target region segmentation might be possible with AI. For example, fully automatic, CT-based organ segmentation is now a reality with strong open-source solutions (*10*,*11*). Both academic and industrial sectors show unanimous interest in harnessing AI methodologies for PET-based tumor segmentation. This convergence of interest, however, encounters notable challenges, particularly with the generalizability of AI models across various cancer types. The capability of an AI algorithm, trained on ^{18}F-FDG PET/CT images for lung cancer segmentation, to perform equally well on colorectal cancer, for instance, remains in question. There is initial evidence suggesting that algorithms designed for lung cancer might be adaptable for breast cancer segmentation when ^{18}F-FDG PET/CT images are used (*12*). Nonetheless, the issue of algorithm generalizability is not confined to cancer types alone; it extends to differing imaging systems and reconstruction protocols across sites, further complicating the model's adaptability (*13*).

The challenges of model generalizability are further amplified when considering the use of different imaging tracers. Nuclear medicine uses a broad spectrum of tracers to detect and quantify tumor characteristics, necessitating the development of distinct AI models for each tracer. This requirement imposes an economic burden, as clinics face escalating costs with the introduction of each new model by vendors (*14*). Such a situation underscores a significant shortcoming in the current methodologic approach, highlighting the urgent need for economically viable and universally applicable AI solutions. Moreover, the extensive and varied nature of these challenges underscores the critical need for comprehensive, large-scale validation studies. These studies are indispensable for affirming the preliminary evidence and for assessing the real-world applicability of AI algorithms across different cancers, imaging tracers, and health care settings.

In light of current trends in AI, the ideal solution appears to be the development of a large, unified foundational tool capable of segmenting various tracer images. However, achieving regulatory approval for such a tool is challenging because of the specificity of intended uses outlined in certification processes. Furthermore, the regulatory landscape for AI applications in health care in general is fraught with seemingly high barriers in the complex process of validation and certification.

In addition, the availability of comprehensive and well-curated PET datasets remains limited, a surprising fact given the modality's long-standing presence. In contrast, the field of radiology has seen significant advancements through the open sourcing of its datasets while effectively addressing privacy concerns (*15*). Therefore, there is a pressing need to create extensive databases of PET images and to secure funding for expert labeling or to engage labeling services. Recent developments in advanced vision foundational models, such as the segment anything model (SAM) (*16*), offer promising solutions by enabling segmentation through points, bounding boxes, or prompts. These models are already being explored in medical imaging, with significant investment from commercial vendors, such as United Imaging Healthcare for clinical applications (*17*,*18*).

Despite many methodologic and regulatory hurdles, the potential benefits of offering the prospect of a single, versatile tool capable of segmenting any tissue of interest are immense. To ensure the seamless integration of these methodologies into clinical workflows, it is imperative that they enhance clinical workflows without adding complexity or significant cost. This approach not only fosters innovation but also encourages a harmonious blend of technology and clinical practice for the betterment of patient care.

STATUS QUO AND STATUS GO

The beginning integration of AI into oncologic imaging, particularly with ^{18}F-FDG PET/CT, marks a significant step forward in the management and treatment of cancer. Although AI promises to streamline diagnostic processes and improve accuracy, hurdles such as model generalizability, economic viability, and legislative barriers pose significant challenges to AI's broader application for automated tumor segmentation in the clinic. The path forward necessitates collaborative research, increased funding, and the creation of extensive PET image databases. These measures are vital to advance AI methodologies to a level where they can be effortlessly integrated into clinical practices without burdening medical professionals. In addition, targeted grant support for labeling services is crucial to enhance the accuracy and effectiveness of AI models across different cancer types.

Current PET-based AI algorithm development for tumor segmentation places a significant emphasis on optimizing metrics such as the Dice similarity coefficient (DSC). For instance, leaderboards such as AUTOPET (*6*) primarily highlight DSC scores, with top reported values of around 0.37. However, initiatives such as HECKTOR (*7*) extend their focus beyond DSC (top DSC, 0.79), incorporating both prediction accuracy and DSC to evaluate algorithms, acknowledging the need for algorithms to predict clinical outcomes such as overall survival, progression-free survival, or treatment response. Although achieving high DSCs is commendable

for technical precision, such as in CT organ segmentation, it may not suffice for the clinical applicability required in PET tumor segmentation. For example, a DSC of 0.70 could offer prognostic accuracy comparable to manual segmentation, suggesting that beyond a certain threshold, further technical advancements might not result in significant clinical improvement. This situation calls for a strategic shift in research priorities, aiming to identify the minimum accuracy threshold that meaningfully enhances clinical endpoints, thereby ensuring that algorithm development aligns with clinical needs and contributes effectively to patient management.

As we go forward, success in overcoming the complex challenge of tumor segmentation relies on collective effort rather than solitary endeavors. The solution extends beyond the capacity of any single entity, requiring a collaborative approach that leverages the strengths of academia, industry, and clinical practitioners. Clinicians, in their unique role, are invited to articulate key requirements for their expertise to be ventilated by technical and methodologic progress; likewise, they are also instrumental in initiating and contributing to large-scale, open-source databases that have high-quality data with appropriate metadata (cancer type, stages, imaging systems, reconstruction protocol, etc.) and annotations, thus laying the groundwork for developing precise AI models. The importance of standardized annotations for generating high-quality datasets cannot be overstated. Therefore, it is imperative that clinicians define and adopt consensus guidelines during the annotation process (*19*).

Academia can contribute through rapid innovation, developing open-source low-click annotation tools (e.g., MedSAM (*18*) and MONAILabel (*20*)) and pioneering segmentation technologies to keep pace with the evolving demands of tumor segmentation. Recent academic efforts have highlighted the role of hyperparameter changes, minor architecture adjustments, and data augmentation in improving the accuracy of the tumor segmentation (*21*,*22*). Finally, industry can augment these efforts by providing essential resources through research funding support and applying business expertise to ensure that the promising innovations are practically and sustainably deployed in real-world scenarios.

We believe there is a significant opportunity for both academic institutions and businesses to collaborate more closely. This collaboration via research agreements could extend beyond data sharing or independently evaluating the solutions offered by industry. For instance, they could work together on creating generic software frameworks that would serve the interests and needs of both the academic and the industrial sectors. An example of such successful collaboration is the MONAI framework (*9*), cocreated by Nvidia and King's College London, which demonstrates how these partnerships can yield durable solutions that serve both research and clinical needs.

The primary issue with academic software is its transient nature and the maintenance challenges it faces, largely due to a lack of incentives for ongoing support. Collaborations with industry not only aim to address this issue but also provide academics with crucial experience in developing sustainable software. This symbiotic relationship fosters an environment for innovation, allowing academia to translate research into practical applications and allowing industry to identify and cultivate technologic advancements that are appropriate for clinical use. However, for these partnerships to thrive, it is imperative to define rules of engagement and roles, intellectual property rights, and monetization strategies from the start. The benefits of such collaborations—ranging from accelerated technologic progress and improved software sustainability to ultimately better patient care—underscore their importance for the future of AI applications in nuclear medicine.

DISCLOSURE

No potential conflict of interest relevant to this article was reported.

REFERENCES

1. Sibille L, Seifert R, Avramovic N, et al. ^{18}F-FDG PET/CT uptake classification in lymphoma and lung cancer by using deep convolutional neural networks. *Radiology.* 2020;294:445–452.
2. Seifert R, Weber M, Kocakavuk E, Rischpler C, Kersting D. Artificial intelligence and machine learning in nuclear medicine: future perspectives. *Semin Nucl Med.* 2021;51:170–177.
3. Froelich JW, Salavati A. Artificial intelligence in PET/CT is about to make whole-body tumor burden measurements a clinical reality. *Radiology.* 2020;294:453–454.
4. Barrington SF, Cottereau A-S, Zijlstra JM. Is ^{18}F-FDG metabolic tumor volume in lymphoma really happening? *J Nucl Med.* 2024;65:510–511.
5. Cottereau A-S, Nioche C, Dirand A-S, et al. ^{18}F-FDG PET dissemination features in diffuse large B-cell lymphoma are predictive of outcome. *J Nucl Med.* 2020;61:40–45.
6. Gatidis S, Hepp T, Früh M, et al. A whole-body FDG-PET/CT dataset with manually annotated tumor lesions. *Sci Data.* 2022;9:601.
7. Andrearczyk V, Oreiller V, Boughdad S, et al. Automatic head and neck tumor segmentation and outcome prediction relying on FDG-PET/CT images: findings from the second edition of the HECKTOR challenge. *Med Image Anal.* 2023;90:102972.
8. Isensee F, Jaeger PF, Kohl SAA, Petersen J, Maier-Hein KH. nnU-Net: a self-configuring method for deep learning-based biomedical image segmentation. *Nat Methods.* 2021;18:203–211.
9. Jorge Cardoso M, Li W, Brown R, et al. MONAI: an open-source framework for deep learning in healthcare. arXiv website. https://arxiv.org/abs/2211.02701. Published November 4, 2022. Accessed May 21, 2024.
10. Shiyam Sundar LK, Yu J, Muzik O, et al. Fully automated, semantic segmentation of whole-body ^{18}F-FDG PET/CT images based on data-centric artificial intelligence. *J Nucl Med.* 2022;63:1941–1948.
11. Wasserthal J, Breit H-C, Meyer MT, et al. TotalSegmentator: robust segmentation of 104 anatomic structures in CT images. *Radiol Artif Intell.* 2023;5:e230024.
12. Weber M, Kersting D, Umutlu L, et al. Just another "Clever Hans"? Neural networks and FDG PET-CT to predict the outcome of patients with breast cancer. *Eur J Nucl Med Mol Imaging.* 2021;48:3141–3150.
13. Jha AK, Bradshaw TJ, Buvat I, et al. Nuclear medicine and artificial intelligence: best practices for evaluation (the RELAINCE guidelines). *J Nucl Med.* 2022;63:1288–1299.
14. Brady AP, Allen B, Chong J, et al. Developing, purchasing, implementing and monitoring AI tools in radiology: practical considerations. A multi-society statement from the ACR, CAR, ESR, RANZCR and RSNA. *Radiol Artif Intell.* 2024;6:e230513.
15. DuMont Schütte A, Hetzel J, Gatidis S, et al. Overcoming barriers to data sharing with medical image generation: a comprehensive evaluation. *NPJ Digit Med.* 2021;4:141.
16. Kirillov A, Mintun E, Ravi N, et al. Segment anything. arXiv website. https://arxiv.org/abs/2304.02643. Published April 5, 2023. Accessed May 21, 2024.
17. Liu Q, Zheng M, Planche B, et al. PseudoClick: interactive image segmentation with click imitation. In: *Computer Vision: ECCV 2022.* Springer; 2022:728–745.
18. Ma J, He Y, Li F, Han L, You C, Wang B. Segment anything in medical images. *Nat Commun.* 2024;15:654.
19. Barrington SF, Meignan M. Time to prepare for risk adaptation in lymphoma by standardizing measurement of metabolic tumor burden. *J Nucl Med.* 2019;60:1096–1102.
20. Diaz-Pinto A, Alle S, Nath V, et al. MONAI label: a framework for AI-assisted interactive labeling of 3D medical images. arXiv website. https://arxiv.org/abs/2203.12362. Published March 23, 2022. Accessed May 21, 2024.
21. Isensee F, Maier-Hein KH. Look Ma, no code: fine tuning nnU-Net for the AutoPET II challenge by only adjusting its JSON plans. arXiv website. https://arxiv.org/abs/2309.13747. Published September 24, 2023. Revised December 12, 2023. Accessed May 21, 2024.
22. Yousefirizi F, Klyuzhin IS, O JH, et al. TMTV-Net: fully automated total metabolic tumor volume segmentation in lymphoma PET/CT images—a multi-center generalizability analysis. *Eur J Nucl Med Mol Imaging.* February 8, 2024 [Epub ahead of print].

Molecular Imaging in Gynecology: Beyond Cancer

Joni Sebastiano[1–3], Cindy Rodriguez[1,2,4], Zachary V. Samuels[1,2,4], Kristen Pepin[5], and Brian M. Zeglis[1–4,6]

[1]Department of Chemistry, Hunter College, City University of New York, New York, New York; [2]Department of Radiology, Memorial Sloan Kettering Cancer Center, New York, New York; [3]Ph.D. Program in Biochemistry, Graduate Center of City University of New York, New York, New York; [4]Ph.D. Program in Chemistry, Graduate Center of City University of New York, New York, New York; [5]Department of Obstetrics and Gynecology, Weill Cornell Medicine, New York, New York; and [6]Department of Radiology, Weill Cornell Medical College, New York, New York

Gynecological pathologies account for approximately 4.5% of the overall global disease burden. Although cancers of the female reproductive system have understandably been the focus of a great deal of research, benign gynecological conditions—such as endometriosis, polycystic ovary syndrome, and uterine fibroids—have remained stubbornly understudied despite their astonishing ubiquity and grave morbidity. This historical inattention has frequently become manifested in flawed diagnostic and treatment paradigms. Molecular imaging could be instrumental in improving patient care on both fronts. In this Focus on Molecular Imaging review, we will examine recent advances in the use of PET, SPECT, MRI, and fluorescence imaging for the diagnosis and management of benign gynecological conditions, with particular emphasis on recent clinical reports, areas of need, and opportunities for growth.

Key Words: molecular imaging; PET; SPECT; fluorescence imaging; intraoperative imaging; MRI

J Nucl Med 2024; 65:998–1003
DOI: 10.2967/jnumed.124.267546

Gynecological diseases represent a tremendous global health burden (*1*). Within this umbrella, cancers have rightly received a great deal of focus, but nonmalignant disorders—such as endometriosis, polycystic ovary syndrome (PCOS), and uterine fibroids—have long been understudied and underaddressed. Although societal factors (i.e., the historically patriarchal nature of science and medicine) certainly play a factor in this neglect, the very low mortality rates associated with these conditions are almost surely responsible as well. Yet what these disorders lack in mortality, they more than make up for in ubiquity and morbidity. For example, it is estimated that up to 21% of women worldwide have PCOS, and endometriosis affects roughly 10% of women of reproductive age globally (*2,3*). Furthermore, these disorders exact a considerable toll on women, with symptoms ranging from menstrual cycle irregularity and gastrointestinal distress to chronic pain and infertility (*4*).

Received Feb. 5, 2024; revision accepted May 13, 2024.
For correspondence or reprints, contact Brian M. Zeglis (bz102@hunter.cuny.edu).
Published online Jun. 13, 2024.

Current strategies for the diagnosis and treatment of benign gynecological disorders are lacking. The clinical gold standard for the detection of endometriosis, for example, is laparoscopic surgery, an invasive procedure whose inherent limitations—that is, expense, pain, and operator bias—contribute to a 5- to 7-y diagnostic delay for the condition (*5*). With respect to treatment, surgical resection remains a common strategy for uterine fibroids and adenomyosis, though less invasive options exist as well (*6*). Molecular imaging has the potential to be instrumental in improving care on both fronts. Noninvasive imaging agents could offer diagnostic options that are safer, cheaper, and more effective. Similarly, theranostic imaging could help monitor the efficacy of emergent molecular therapies (e.g., the use of progesterone receptor modulators for uterine fibroids), whereas intraoperative imaging could help improve accuracy during the resection of benign lesions such as uterine fibroids and endometriomas (*7*).

Recent years have played witness to increasing interest in the use of molecular imaging in patients with benign gynecological disorders. However, the literature is somewhat fragmented, and the intersection of these 2 fields has not yet been collectively reviewed. In this installment of the Focus on Molecular Imaging series, we will examine recent advances in the use of PET, SPECT, MRI, and fluorescence imaging for the diagnosis and management of these conditions (Fig. 1). Although both preclinical and clinical results will be covered, particular emphasis will be placed on recent human trials as well as areas of need and opportunities for growth. It is our sincere hope that this work will not only highlight exciting extant results but also inspire new work by bringing attention to the gaps that can be filled by repurposing old tools or developing new ones.

Before we begin, it is important to recognize that one imaging modality—ultrasonography—has long been commonplace in gynecology. Ultrasonography is easily the most often-used noninvasive diagnostic tool in the field, helping clinicians visualize both normal and aberrant pelvic anatomy. Yet despite its ubiquity, ultrasound is not without problems, as it suffers from suboptimal specificity for some conditions (e.g., endometriosis and adenomyosis) and is susceptible to operator, technique, and interpretation biases (*8*). We have chosen not to cover ultrasound imaging in this review, primarily because its outsized presence in the field threatens to swamp our discussion of other emergent modalities but also because, strictly speaking, it is more of an anatomic than molecular imaging methodology. However, excellent reviews on its present and future role in the management of benign gynecological conditions can be found elsewhere (*8*).

ENDOMETRIOSIS

Endometriosis is a chronic female reproductive disorder characterized by the growth of endometrial tissue outside the uterus (*9*).

Disorder	Modality	Agent	Stage	Notes	Reference no.
Endometriosis	MRI		Clinical	Can detect only deep infiltrating endometriosis and lesions >5 mm beneath peritoneal surface	14
	PET/CT	[^{18}F]fluorocholine	Preclinical	Lesions showed ~0.34 ID/g	15
		[^{64}Cu]Cu-DOTA-bevacizumab	Preclinical	Uptake in lesions but poor target-to-background ratio	16
		[^{18}F]FDG	Clinical	Detected 55% of confirmed lesions	17
		[^{68}Ga]Ga-DOTATATE	Clinical	Successful for detection of deep infiltrating endometriosis, but no uptake in superficial endometriosis	18
		[^{18}F]FES	Clinical	Provided greater agreement with histology than MRI	3
	NIRF	Indocyanine green	Clinical	Positive predicative values of NIRF and WL imaging for endometriosis tissue are 69% and 64%, respectively	20
	NIRF	Indocyanine green	Clinical	Signal in surrounding healthy tissue aided in resection	21, 22
Adenomyosis	MRI		Clinical	Sensitivity and specificity are 29.7% and 85.3%, respectively; accuracy increases during direct evaluations	24
	PET/CT	Incidental uptake with [^{18}F]FDG	Clinical	Uptake can lead to false positives during PET/CT for cancer diagnoses	25, 26
		[^{68}Ga]Ga-DOTATATE	Clinical	Lesions showed uptake of radiotracer	18
	SPECT	[^{67}Ga]Ga^{3+}	Clinical	Uptake observed in pyoadenomyosis (n = 1)	27
Uterine fibroids or leiomyomas	TVS	Saline infusion sonohysterography	Clinical	Sensitivity and specificity of >99% and >91%, respectively	30
	PET/CT	[^{18}F]FDG	Clinical	Uptake can lead to false positive cancer diagnoses	31–33
		[^{18}F]FES	Clinical	When coupled with [^{18}F]FDG, may improve differentiation between malignant and benign lesions	34, 35
		Other radiotracers	Clinical	Incidental uptake occasionally observed during PET/CT for other indications	36–38
PCOS	PET/CT	[^{18}F]FDG	Clinical	Patients with PCOS showed significantly lower brown adipose tissue levels than healthy patients	39, 40
	SPECT	^{99m}Tc-labeled noscapine	Preclinical	Higher uptake in PCOS lesions than control	41
Functional ovarian cysts	TVS		Clinical	Sensitivity and specificity of 93.5% and 91.5%, respectively	42
	PET/CT	[^{18}F]FDG	Clinical	Average sensitivity and specificity are 94% and 86%, respectively, compared with 92% and 85% for MRI	43
	MRI	Amide proton transfer-MRI	Clinical	Can provide early and accurate diagnosis and differentiation between serous cystadenomas, mucinous cystadenomas, and functional cysts	44
	PET/CT	[^{18}F]FDG	Clinical	Inferior to MRI for diagnosis of teratomas and determining maturity and malignancy	45
	SPECT	[^{67}Ga]Ga^{3+}	Clinical	Inferior to MRI for diagnosis of teratomas and determining maturity and malignancy	46
Brenner tumors	MRI		Clinical	More effective than PET/CT at monitoring tumor growth	47
	PET/CT	[^{18}F]FDG	Clinical	Benign tumors less avid than malignant ones	48

FIGURE 1. Studies cited for diagnosis and management of conditions.

Most endometriosis lesions grow on the outer perimetrium, fallopian tubes, and ovaries. However, in some cases—known as deep infiltrating endometriosis—endometrial tissue may grow on the bowels, rectum, and bladder or even within the thoracic cavity (*10*). Approximately 10%–15% of all women of reproductive age have the condition, but it is most common in women with infertility (25%–50%) and chronic pelvic pain (70%–85%) (*5,9*). The most common symptoms include chronic pelvic pain, acute pelvic pain, and infertility, but women with endometriosis are susceptible to a wide variety of other comorbidities, including cancer, lupus, rheumatoid arthritis, and cardiovascular disease (*11*). The societal and economic costs of endometriosis are alarming: those afflicted experience stigma, diminished quality of life, and reduced work productivity, and its management is responsible for about $70 billion in yearly health expenditures in the United States alone (*3,11*).

The current standard of care for the diagnosis of endometriosis is exploratory laparoscopy (*12*). This approach is invasive, painful, expensive, and prone to sampling and operator biases, factors that have combined to create long diagnostic delays for the condition (*5,9*). Anatomic imaging also plays an important role in the care of patients with the condition. Ultrasonography is frequently used as a prediagnostic tool to visualize lesions before surgical diagnosis and resection, but it can exhibit suboptimal sensitivity and accuracy in the context of smaller lesions (*13*). MRI has also been used to determine the size, location, and infiltrative stage of large lesions before surgical resection, especially in cases of deep infiltrating endometriosis (*14*). Unfortunately, MRI has proven suboptimal for the detection of small superficial lesions (i.e., <5 mm beneath the surface of the peritoneum) (*14*).

In light of the clear limitations of extant methods for the detection of endometriosis, researchers have begun to explore the possibility of using nuclear imaging—and PET in particular—for the visualization of endometriosis. Silveira et al., for example, used a rat model of the disease to determine the uptake of [^{18}F]fluorocholine in superficial lesions. Although the activity concentration of the tracer in implanted endometriosis tissue was found to be 3-fold higher than that in the muscle and peritoneum, the biodistribution data revealed very high uptake in several healthy tissues, most notably (and problematically) the ovaries (*15*). More recently, Amartuvshin et al. probed the value of a ^{64}Cu-labeled variant of the vascular endothelial growth factor–targeting antibody bevacizumab for the delineation of subcutaneous endometriosis lesions. Unfortunately, in vivo experiments revealed low activity concentrations in the target tissue and high levels of uptake in healthy tissues (*16*).

Shifting to the clinic, a handful of trials have focused on the potential of a trio of commonly used PET tracers—[^{18}F]FDG, 16α-[^{18}F]fluoro-17β-estradiol ([^{18}F]FES), and [^{68}Ga]Ga-DOTATATE—for the detection of endometriosis. Balogova et al., for example, performed [^{18}F]FDG PET/CT on 18 patients with known or suspected endometriosis and found that the radiotracer effectively delineated only 11 of 20 (55%) confirmed lesions (Fig. 2) (*17*). More recently, a team at the Université Libre de Bruxelles in Belgium performed [^{68}Ga]Ga-DOTATATE PET/CT on a cohort of patients (n = 12) scheduled for exploratory laparoscopy for suspected endometriosis. Although the authors ultimately concluded that the radiotracer was effective for the visualization of deep infiltrating endometriosis (i.e., the sensitivity and specificity were 57% and 80%, respectively), no uptake was observed in superficial peritoneal endometriosis or ovarian endometriomas (*18*). Without question, the most promising clinical results have been obtained with [^{18}F]FES. In 2016, Cosma et al. performed [^{18}F]FES PET on a group of patients (n = 4) with suspected endometriosis who also underwent MRI and laparoscopic excision coupled with histology. The data demonstrated that [^{18}F]FES PET/CT fully agreed with histology and showed greater accuracy than MRI for lesions: PET/CT correctly identified 9 of 9 lesions, whereas MRI produced 3 false negatives and 3 false positives (*3*).

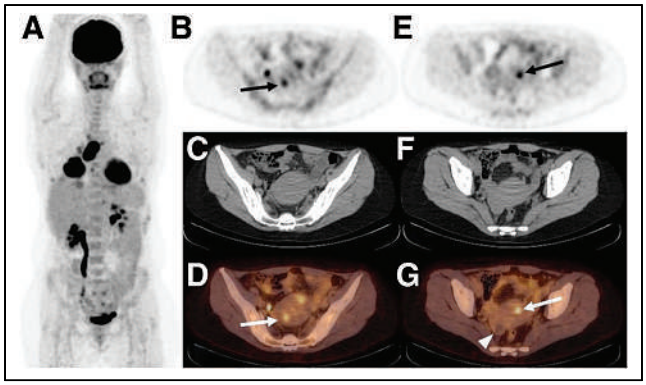

FIGURE 2. [^{18}F]FDG PET/CT of 47-y-old woman with sarcomatous lung cancer and 11-y history of endometriosis at time of imaging. (A) Intense [^{18}F]FDG uptake can be seen in primary lung cancer lesions as well as lymph node and pleural metastases. (B–G) Two foci of increased [^{18}F]FDG avidity can be seen in endometriosis lesions in uterine wall via PET (B and E) and PET/CT (D and G) (arrows) but are not clearly visualized by CT alone (C and F). No [^{18}F]FDG uptake was observed in known right ovarian endometrioma (arrowhead). (Reprinted with permission of (*17*).)

Molecular imaging could also play a key role in surgeries for endometriosis. Indeed, intraoperative imaging tools capable of visualizing endometriosis lesions could reduce operator bias during both laparoscopic diagnoses and surgical resections (*19*). Along these lines, a 2021 study by Al-Taher et al. compared intraoperative near-infrared fluorescence imaging with indocyanine green and conventional white-light laparoscopy for the delineation of endometriosis lesions in a cohort of 15 patients (*20*). The investigators determined that the positive predictive values for near-infrared fluorescence and white-light imaging were 69% and 64%, respectively, suggesting that the former could have modest value in the context of surgical resections. Interestingly, 2 other recent studies have sought to use intraoperative imaging to illuminate healthy tissues and thus differentiate endometriosis lesions. Aleksandrov et al. used indocyanine green to identify healthy rectum tissue when removing deep infiltrating endometriosis from the bowels (*21*), whereas Thigpen et al. used indocyanine green to differentiate between the ureters and endometriosis lesions during surgery (*22*). In both cases, the authors concluded that intraoperative near-infrared fluorescence imaging aided in the safe resection of the diseased tissue while reducing complications; however, the approximate location of the lesions still needs to be known before surgery.

Taken together, the PET and near-infrared fluorescence studies described in this section clearly suggest that molecular imaging could play important roles in the diagnosis and treatment of endometriosis. However, it is impossible to deny that the results have been middling at best, a problem that we suspect is related to the reuse of established imaging agents (i.e., [^{18}F]FDG, [^{18}F]fluorocholine, and indocyanine green). It is likely that novel probes with specificity for endometrial tissue will offer the best chance for the development of clinically effective tools.

ADENOMYOSIS

Adenomyosis is a chronic disease similar to endometriosis that is characterized by the invasion and growth of endometrial tissue within

the myometrium, the muscular middle layer of the uterus. Adenomyosis, although asymptomatic in almost a third of patients, can cause pelvic pain, infertility, and heavy menstrual bleeding (*23*). Ultrasonography and MRI are the primary diagnostic tools for the condition, but these modalities exhibit suboptimal accuracy, especially when adenomyosis is not suspected (*23*). For example, pelvic ultrasound has a sensitivity of 10.9% and a specificity of 98.3%. MRI fares slightly better, with a sensitivity of 29.7% and a specificity of 85.3%, numbers that improve slightly (though not overwhelmingly) during direct evaluations for the condition (*24*). New approaches to the diagnostic imaging of adenomyosis are thus needed, but there have been only a handful of reports on the use of nuclear imaging for the condition. And indeed, most of these have described the incidental uptake of radiopharmaceuticals in lesions. For example, a pair of reports that focused on cervical cancer and carcinomatosis has found that adenomyosis lesions can be [^{18}F]FDG-avid, complicating the identification of intrauterine metastases via [^{18}F]FDG PET (*25,26*). Furthermore, the aforementioned study that focused on the delineation of endometriosis with [^{68}Ga]Ga-DOTATATE also found that adenomyosis lesions exhibited increased accretion of the radiolabeled peptide as well (*18*). Finally, a single case report by Wu et al. from 2014 described the visualization of pyoadenomyosis—a rare complication of adenomyosis—via SPECT with [^{67}Ga]Ga^{3+} (*27*). In sum, the data clearly underscore that the stage is set for new work in this area, particularly the development of dedicated probes specific for adenomyosis.

UTERINE FIBROIDS

Uterine fibroids, or leiomyomas, are benign clonal neoplasms of the uterus that occur in about 70% of women and disproportionately affect Black women (*28*). Though typically asymptomatic, these smooth muscle tumors can cause a wide range of symptoms—including pelvic pain, abnormal menstrual bleeding, and urinary and gastrointestinal issues—and can be associated with infertility and other adverse pregnancy outcomes (*4,29*). A variety of approaches has been used for the treatment of uterine fibroids, including myomectomy, radiofrequency ablation, uterine fibroid embolization, and hormonal birth control. Hysterectomy also remains a common treatment for the condition, with fibroids accounting for over one third of such procedures every year (*4*). Uterine fibroids are typically identified via ultrasonography, with postoperative histology providing a definitive diagnosis. Transvaginal sonography is inexpensive and exhibits high sensitivity (99%) and specificity (91%) that can be improved on even further with the addition of saline infusion sonohysterography for fibroids touching the uterine lining (*30*). MRI can also be used for diagnosis and offers sensitivity and specificity close to 100%, though it is significantly more expensive. That said, MRI can be useful in patients who are unsuitable for transvaginal sonography or saline infusion sonohysterography or who need preoperative mapping for myomectomy (*7*).

Existing methods for the detection of uterine fibroids are clearly sufficient. However, clinical studies on the visualization of leiomyomas with extant and emerging PET tracers are critical, especially in the context of differentiating between fibroids and malignant lesions. For example, a handful of studies has combined to show that leiomyomas of younger and premenopausal women can be especially [^{18}F]FDG-avid, creating the possibility that these fibroids could be misidentified as leiomyosarcomas or endometrial carcinomas (*31–33*). A pair of clinical trials from Japan suggests that [^{18}F]FES and [^{18}F]FDG could play complementary roles in the differentiation of leiomyomas from endometrial carcinomas, leiomyosarcomas, and endometrial hyperplasia (*34,35*). More specifically, a malignant leiomyosarcoma showed positive [^{18}F]FDG accumulation (SUV, 10.5) and negative [^{18}F]FES accumulation (SUV, 1.0) in PET images, whereas a benign leiomyoma showed similarly positive uptake for both PET tracers (Fig. 3) (*35*). Finally, incidental uptake in uterine fibroids has been observed with several other PET tracers—i.e., [^{68}Ga]Ga-DOTATATE, Al[^{18}F]F-NOTA-FAPI, and [^{18}F]NaF—though more comprehensive follow-up studies have yet to be performed (*36–38*). In the end, it is unlikely that molecular imaging will play a key standalone role in the detection of uterine fibroids given the efficacy of existing diagnostic methods. That said, imaging—and PET in particular—could be a valuable tool for differentiating between benign fibroids and more dangerous leiomyosarcomas. More broadly, as the use of a library of radiopharmaceuticals applied in the clinic grows, it will be important to understand the uptake of common radiopharmaceuticals in leiomyomas to prevent false-positive cancer diagnoses.

PCOS

PCOS is an endocrine disorder that affects roughly 5%–15% of reproductive-aged women and can cause excess body hair, acne, weight gain, and infertility. Although the condition can be managed via hormone treatments and weight-loss drugs (as diabetes and insulin resistance are common comorbidities), accurate diagnoses are critical since many of these symptoms can be associated with other etiologies (*4*). Along these lines, PCOS is diagnosed when a patient satisfies 2 of the following 3 criteria: oligomenorrhea or anovulation, often leading to irregular periods; clinical or biochemical signs of hyperandrogenism; and polycystic ovaries on ultrasound. In light of this largely effective diagnostic paradigm, molecular imaging likely has a greater future role to play in understanding the condition rather than delineating it. Several studies have sought to use [^{18}F]FDG to image brown adipose tissue levels in women with PCOS, as brown adipose tissue is a highly energetic tissue that is often functionally abnormal in patients with PCOS. In a 2019 trial, for example, [^{18}F]FDG PET revealed that women with PCOS exhibited lower brown adipose tissue levels

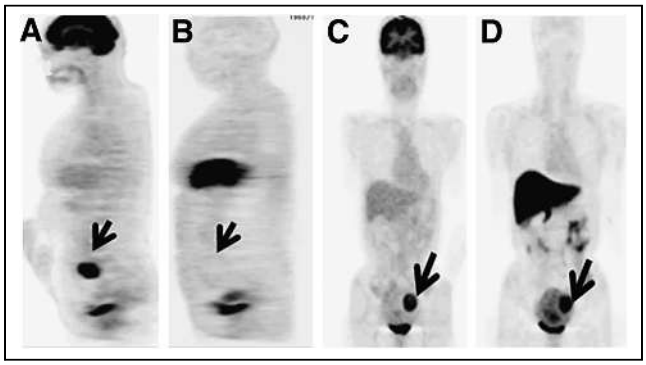

FIGURE 3. [^{3}F]FDG and [^{18}F]FES PET of 75-y-old woman with leiomyosarcoma (A and B, arrows) and 52-y-old woman with uncomplicated benign leiomyoma (C and D, arrows). In former, primary tumor in uterus accumulated [^{18}F]FDG (A) but was negative for [^{18}F]FES (B), and postoperative histopathologic results confirmed leiomyosarcoma. In latter, lesions were avid for both [^{18}F]FDG (C) and [^{18}F]FES (D), and postoperative histopathologic results confirmed uncomplicated leiomyoma and adenomyosis. (Reprinted with permission of (*35*).)

than those without the condition (*39*). A year later, similar results were obtained in a [^{18}F]FDG PET study that compared a cohort of women receiving metformin for PCOS and those without the condition, cementing low levels of brown adipose tissue as a common characteristic of PCOS and opening the door for [^{18}F]FDG as a tool for monitoring the treatment of the condition (*40*). Interestingly, this was not the first attempt at using nuclear imaging in the service of treating PCOS. In 2010, Priyadarshani et al. determined the biodistribution of a ^{99m}Tc-labeled variant of noscapine in a rat model of PCOS, as the alkaloid was (at the time) being explored as a possible therapeutic for the condition (*41*). The results were reasonably promising—the ^{99m}Tc-labeled noscapine produced 0.9 %ID/g in ovarian cysts compared with 0.06 %ID/g for a nonspecific control compound—but no follow-up studies have been published. In the future, it is unlikely that a nuclear imaging agent will be needed as a diagnostic tool for PCOS, but it is almost certain that both established tracers (e.g., [^{18}F]FDG) and novel cyst-specific probes could play important roles in improving our understanding of the disease.

ADNEXAL MASSES AND OVARIAN CYSTS

Adnexal masses are growths found around the ovaries, uterus, or fallopian tubes, including functional ovarian cysts, endometriomas, and teratomas. The accurate detection and identification of these lesions are critical, as they can interfere with cancer diagnoses and, in rare cases, become malignant themselves (*4*). Although most are asymptomatic, adnexal masses can cause pelvic pain on cyst enlargement, cyst rupture, or ovarian torsion (*4*). For patients who do experience symptomatic pain, diagnosis is typically performed via ultrasonography—most efficiently when performed by a sonographer using subjective pattern recognition—but other imaging modalities (e.g., pelvic MRI) may be leveraged for complementary information.

Functional ovarian cysts are a class of adnexal masses that can develop on the ovaries, including follicular, corpus luteum, and theca lutein cysts. The most common approach to diagnosing these cysts is via transvaginal ultrasonography, an approach that offers a sensitivity of 93.5% and a specificity of 91.5% (*42*). Although these values are high, clinicians have nonetheless looked toward molecular imaging for complementary diagnostic tools. In a 2021 metaanalysis of 27 reports on the differentiation between benign and malignant adnexal masses via [^{18}F]FDG PET and MRI, the average sensitivity and specificity were 94% and 86%, respectively, for [^{18}F]FDG PET and 92% and 85%, respectively, for MRI (*43*). In a trial performed in Japan, an emergent type of MRI—amide proton transfer MRI—proved quite useful for the detection and classification of a variety of ovarian cysts. Indeed, amide proton transfer MRI provided correct diagnoses of each type of ovarian cyst, including serous cystadenomas, mucinous cystadenomas, and functional cysts, without additional follow-up studies (Fig. 4) (*44*).

MRI has also been found effective for identifying other benign adnexal masses, such as teratomas. In a 2015 study of 26 patients, for example, MRI proved superior to [^{18}F]FDG PET for distinguishing between benign (mature) and malignant (immature) teratomas (*45*). A previous study with [^{67}Ga]Ga SPECT provided similar results (*46*). The dense and fibrous nature of Brenner tumors—an ovarian lesion that can be benign or malignant—facilitates ready visualization via MRI, making it the current diagnostic gold standard (*47*). There may be room for nuclear imaging, however. To wit, one recent study suggests that malignant Brenner tumors may exhibit higher uptake of [^{18}F]FDG than their benign cousins, aiding in the differentiation between the two (*48*).

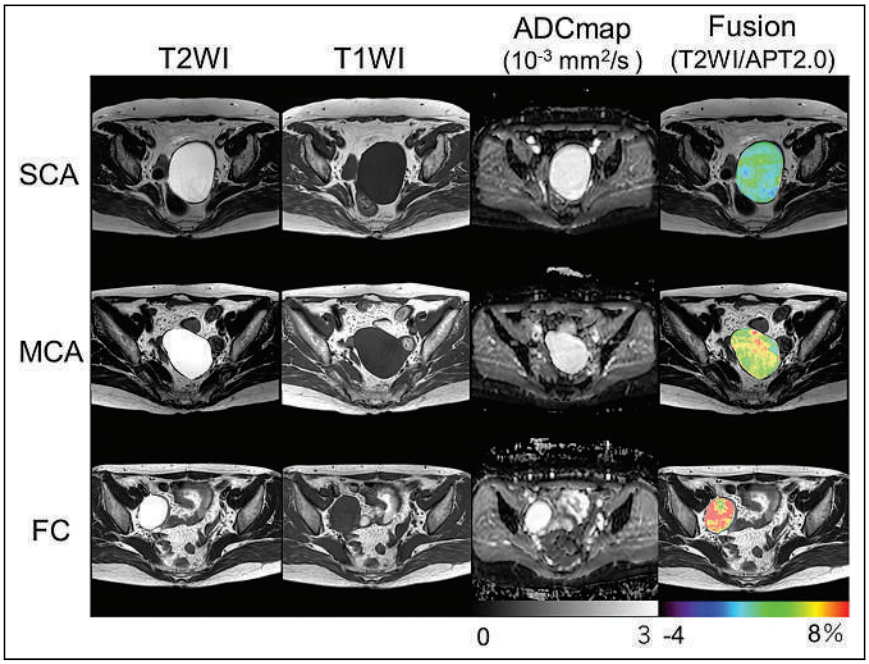

FIGURE 4. Typical T2-weighted images (T2WI), T1-weighted images (T1WI), apparent diffusion coefficient (ADC) maps, and amide proton transfer maps (APT) (overlaid on T2WI) of serous cystadenoma (SCA) (top), mucinous cystadenoma (MCA) (middle), and functional cyst (FC) (bottom). All 3 cystic lesions showed similar signal intensities in T1WI and T2WI as well as similar ADC values. However, amide proton transfer values were clearly different among trio of cysts: low in serous cystadenoma (2.25%), moderate in mucinous cystadenoma (5.03%), and very high in functional cyst (7.38%). Color bar indicates amide proton transfer signal (%). (Reprinted with permission of (*44*).)

CONCLUSION

In assembling this review, we were taken aback (though not entirely surprised) by the degree to which benign gynecological pathologies remain understudied despite their global prevalence (*1,5*). We are heartened, however, to see that molecular imaging research in this area has increased over the last decade, as we believe that molecular imaging has the potential to improve patient outcomes. In conditions for which current diagnostic paradigms are inadequate—such as endometriosis and adenomyosis—molecular imaging could become a pivotal diagnostic tool. Yet molecular imaging could still have a part to play in cases for which standard-of-care diagnostic technologies are sufficient. In PCOS, for example, molecular imaging could help us better understand the syndrome's diverse constellation of symptoms, whereas in the context of benign adnexal masses, it could be deployed to better differentiate between benign and malignant lesions. Going forward, we are eager to see what the next

decade has in store for research at the intersection of these 2 areas. Although there are a plethora of viable paths for work, we believe that the development of novel imaging probes that specifically target these conditions will be especially critical. In the end, details aside, we are simply hopeful that advances in our field can help the millions of women with these conditions.

DISCLOSURE

No potential conflict of interest relevant to this article was reported.

REFERENCES

1. Wijeratne D, Fiander A. Gynaecological disease in the developing world: a silent pandemic. *Obstet Gynaecol.* 2018;20:237–244.
2. Li L, Scotti A, Fang J, et al. Characterization of brown adipose tissue (BAT) in polycystic ovary syndrome (PCOS) patients by Z-spectral imaging (ZSI). *Eur J Radiol.* 2020;123:108777.
3. Cosma S, Salgarello M, Ceccaroni M, et al. Accuracy of a new diagnostic tool in deep infiltrating endometriosis: positron emission tomography–computed tomography with 16α-[^{18}F]fluoro-17β-estradiol. *J Obstet Gynaecol Res.* 2016;42:1724–1733.
4. Boyle KJ, Torrealday S. Benign gynecologic conditions. *Surg Clin North Am.* 2008;88:245–264.
5. As-Sanie S, Black R, Giudice LC, et al. Assessing research gaps and unmet needs in endometriosis. *Am J Obstet Gynecol.* 2019;221:86–94.
6. Critchley HOD, Babayev E, Bulun SE, et al. Menstruation: science and society. *Am J Obstet Gynecol.* 2020;223:624–664.
7. Stewart EA, Laughlin-Tommaso SK, Catherino WH, et al. Uterine fibroids. *Nat Rev Dis Primers.* 2016;2:16043.
8. Abinader R, Warsof SL. Benefits and pitfalls of ultrasound in obstetrics and gynecology. *Obstet Gynecol Clin North Am.* 2019;46:367–378.
9. Bulun SE, Yilmaz BD, Sison C, et al. Endometriosis. *Endocr Rev.* 2019;40:1048–1079.
10. Koninckx PR, Ussia A, Adamyan L, Wattiez A, Donnez J. Deep endometriosis: definition, diagnosis, and treatment. *Fertil Steril.* 2012;98:564–571.
11. Eisenberg VH, Decter DH, Chodick G, Shalev V, Weil C. Burden of endometriosis: infertility, comorbidities, and healthcare resource utilization. *J Clin Med.* 2022;11:1133.
12. Endometriosis research to develop non-invasive treatment and diagnosis. Eunice Kennedy Shriver National Institute of Child Health and Human Development website. https://www.nichd.nih.gov/about/org/od/directors_corner/prev_updates/endometriosis-research. Reviewed April 24, 2020. Accessed May 22, 2024.
13. Chen-Dixon K, Uzuner C, Mak J, Condous G. Effectiveness of ultrasound for endometriosis diagnosis. *Curr Opin Obstet Gynecol.* 2022;34:324–331.
14. Bauşic A, Coroleucă C, Coroleucă C, et al. Transvaginal ultrasound vs. magnetic resonance imaging (MRI) value in endometriosis diagnosis. *Diagnostics (Basel).* 2022;12:1767.
15. Silveira MB, Rodrigues DM, Araújo MR, et al. ^{18}F-fluorocholine uptake and positron emission tomography imaging in rat peritoneal endometriosis. *Reprod Sci.* 2018;25:19–25.
16. Amartuvshin T, Hanaoka H, Yamaguchi A, Tsushima Y. Positron emission tomography imaging of vascular endothelial growth factor with ^{64}Cu-labeled bevacizumab for non-invasive diagnosis of endometriosis. *J Endometr Pelvic Pain Disord.* 2019;11:194–200.
17. Balogova S, Daraï E, Noskovicova L, et al. Interference of known or suspected endometriosis in reporting FDG PET/CT performed in another indication. *Clin Nucl Med.* 2022;47:305–313.
18. Fastrez M, Artigas C, Sirtaine N, et al. Value of the ^{68}Ga-DOTATATE PET-CT in the diagnosis of endometriosis. A pilot study. *Eur J Obstet Gynecol Reprod Biol.* 2017;212:69–74.
19. Simko S, Wright KN. The future of diagnostic laparoscopy. Cons. *Reprod Fertil.* 2022;3:R91–R95.
20. Al-Taher M, van den Bos J, Terink I, et al. Near-infrared fluorescence imaging for the intraoperative detection of endometriosis: a pilot study. *Life (Basel).* 2021;12:15.
21. Aleksandrov A, Meshulam M, Smith AV, et al. Fluorescence-guided management of deep endometriosis. *Fertil Steril.* 2020;114:1116–1118.
22. Thigpen B, Koythong T, Guan X. Robotic-assisted laparoscopic ureterolysis for deep infiltrating endometriosis using indocyanine green under near-infrared fluorescence. *J Minim Invasive Gynecol.* 2022;29:586–587.
23. Schrager S, Yogendran L, Marquez CM, Sadowski EA. Adenomyosis: diagnosis and management. *Am Fam Physician.* 2022;105:33–38.
24. Zanolli NC, Cline BC, Befera NT, Martin JG. Diagnostic accuracy of clinically reported adenomyosis on pelvic ultrasound and MRI compared to surgical pathology. *Clin Imaging.* 2022;82:117–120.
25. Yu JI, Huh SJ, Kim YI, Kim TJ, Park BK. Variable uterine uptake of FDG in adenomyosis during concurrent chemoradiation therapy for cervical cancer. *Radiat Oncol J.* 2011;29:214–217.
26. Liu Y. Multiple distant adenomyosis mimicking carcinomatosis on FDG PET/CT. *Am J Obstet Gynecol.* 2014;210:486.e13.
27. Wu ET, Cheng MF, Jhuang JY, Yang JH. Preoperative diagnosis of pyoadenomyosis with ^{67}Ga SPECT/CT. *Clin Nucl Med.* 2014;39:e276.
28. Cramer SF, Patel A. The frequency of uterine leiomyomas. *Am J Clin Pathol.* 1990;94:435–438.
29. Bonanni V, Reschini M, La Vecchia I, et al. The impact of small and asymptomatic intramural and subserosal fibroids on female fertility: a case-control study. *Hum Reprod Open.* 2023;2023:hoac056.
30. Dueholm M, Lundorf E, Hansen ES, Ledertoug S, Olesen F. Accuracy of magnetic resonance imaging and transvaginal ultrasonography in the diagnosis, mapping, and measurement of uterine myomas. *Am J Obstet Gynecol.* 2002;186:409–415.
31. Kitajima K, Murakami K, Yamasaki E, Kaji Y, Sugimura K. Standardized uptake values of uterine leiomyoma with ^{18}F-FDG PET/CT: variation with age, size, degeneration, and contrast enhancement on MRI. *Ann Nucl Med.* 2008;22:505–512.
32. Nishizawa S, Inubushi M, Kido A, et al. Incidence and characteristics of uterine leiomyomas with FDG uptake. *Ann Nucl Med.* 2008;22:803–810.
33. Ma Y, Shao X, Shao X, Wang X, Wang Y. High metabolic characteristics of uterine fibroids in ^{18}F-FDG PET/CT imaging and the underlying mechanisms. *Nucl Med Commun.* 2016;37:1206–1211.
34. Tsujikawa T, Yoshida Y, Mori T, et al. Uterine tumors: pathophysiologic imaging with 16α-[^{18}F]fluoro-17β-estradiol and ^{18}F fluorodeoxyglucose PET—initial experience. *Radiology.* 2008;248:599–605.
35. Yoshida Y, Kiyono Y, Tsujikawa T, et al. Additional value of 16α-[^{18}F]fluoro-17β-oestradiol PET for differential diagnosis between uterine sarcoma and leiomyoma in patients with positive or equivocal findings on [^{18}F]fluorodeoxyglucose PET. *Eur J Nucl Med Mol Imaging.* 2011;38:1824–1831.
36. Khalaj K, Rowe JH, Thupili CR, Tammisetti VS. False-positive ^{68}Ga-DOTATATE uptake in a uterine subserosal fibroid mimicking mesenteric neuroendocrine tumor: a case study. *Clin Nucl Med.* 2023;48:e452–e454.
37. Kou Y, Jiang X, Yao Y, et al. Physiological tracer distribution and benign lesion incidental uptake of Al^{18}F-NOTA-FAPI-04 on PET/CT imaging. *Nucl Med Commun.* 2022;43:847–854.
38. Kothekar E, Raynor WY, Werner TJ, Alavi A, Baker JF. ^{18}F-NaF uptake in calcified uterine leiomyoma. *Clin Nucl Med.* 2019;44:e620–e621.
39. Oliveira FR, Mamede M, Bizzi MF, et al. Brown adipose tissue activity is reduced in women with polycystic ovary syndrome. *Eur J Endocrinol.* 2019;181:473–480.
40. Oliveira FR, Mamede M, Bizzi MF, et al. Effects of short term metformin treatment on brown adipose tissue activity and plasma irisin levels in women with polycystic ovary syndrome: a randomized controlled trial. *Horm Metab Res.* 2020;52:718–723.
41. Priyadarshani A, Chuttani K, Mittal G, Bhatnagar A. Radiolabeling, biodistribution and gamma scintigraphy of noscapine hydrochloride in normal and polycystic ovary induced rats. *J Ovarian Res.* 2010;3:10.
42. Biggs WS, Marks ST. Diagnosis and management of adnexal masses. *Am Fam Physician.* 2016;93:676–681.
43. Hu X, Li D, Liang Z, et al. Indirect comparison of the diagnostic performance of ^{18}F-FDG PET/CT and MRI in differentiating benign and malignant ovarian or adnexal tumors: a systematic review and meta-analysis. *BMC Cancer.* 2021;21:1080.
44. Ishimatsu K, Nishie A, Takayama Y, et al. Amide proton transfer imaging for differentiating benign ovarian cystic lesions: potential of first time right. *Eur J Radiol.* 2019;120:108656.
45. Yokoyama T, Takehara K, Yamamoto Y, et al. The usefulness of ^{18}F-FDG-PET/CT in discriminating benign from malignant ovarian teratomas. *Int J Clin Oncol.* 2015;20:960–966.
46. Kunieda E, Hara H, Morikawa Y, et al. Accumulation of gallium-67 within mature and immature teratoma in pediatric patients: investigation for the uptake mechanism. *Ann Nucl Med.* 2008;22:207–213.
47. De Sousa Costeira F, Félix A, Cunha TM. Brenner tumors. *Br J Radiol.* 2022;95:20210687.
48. Matsutani H, Nakai G, Yamada T, et al. MRI and FDG PET/CT findings for borderline Brenner tumor of the ovary: a case report and literature review. *Case Rep Obstet Gynecol.* 2020;2020:8878649.

Frequent Amplification and Overexpression of PSMA in Basallike Breast Cancer from Analysis of The Cancer Genome Atlas

Wenhui Zhou[1], Sumit Halder[2], Sanna Herwald[1], Michael Ghijsen[1], Gowhar Shafi[2], Mohan Uttarwar[2], Eric Rosen[1], Benjamin Franc[1], and Sirish Kishore[1,3]

[1]*Department of Radiology, Stanford University Medical Center, Stanford, California;* [2]*iNDX.AI, Cupertino, California; and* [3]*Department of Radiology, Palo Alto Veterans Affairs Healthcare System, Palo Alto, California*

Prostate-specific membrane antigen (PSMA) is frequently overexpressed in nonprostate malignancies. This preclinical study investigated the molecular basis of the application of PMSA-targeting radiopharmaceuticals in breast cancer subtypes. **Methods:** The somatic copy number status and the transcriptomic and protein expressions of *FOLH1* (gene name of PSMA) were analyzed across breast cancer subtypes in 998 patients from The Cancer Genome Atlas dataset. **Results:** *FOLH1* was frequently amplified in basallike breast cancer (BLBC) (32%) compared with luminal and human epidermal growth factor receptor 2–positive subtypes (16% and 17%, respectively; $P < 0.01$). *FOLH1* expression was higher in BLBC ($P < 0.001$) and was negatively correlated with estrogen-receptor and progesterone-receptor expressions. Consistently, the PSMA protein level was higher in BLBC ($P < 0.05$). Interestingly, *FOLH1* expression was associated with relapse-free and distant metastasis–free survival in patients with BLBC. **Conclusion:** The BLBC subtype exhibited frequent amplification and overexpression of PSMA, supporting the exploration of PSMA-targeting radiopharmaceuticals in this aggressive breast cancer subtype.

Key Words: prostate-specific membrane antigen; basallike breast cancer; genomic alteration; cancer genome

J Nucl Med 2024; 65:1004–1006
DOI: 10.2967/jnumed.123.266659

Prostate-specific membrane antigen (PSMA) is a membrane-anchored glycoprotein that was initially identified as overexpressed in prostate cancer (*1*). Subsequent advances in PSMA-targeting imaging and radioligand therapy have improved the detection and treatment of metastatic prostate cancer (*2–4*). Because PSMA overexpression is commonly observed in other solid tumor types apart from prostate adenocarcinoma (*5*,*6*), PSMA-based radiopharmaceuticals may potentially find broader utility in other cancer types lacking actionable targets. Breast cancer is frequently associated with PSMA overexpression (*5*,*7*). Several studies have reported the feasibility of using ^{68}Ga-PSMA PET imaging to identify primary and metastatic lesions in breast cancer patients, and preclinical research has demonstrated that PSMA-directed radioligand therapy can impede the growth of breast cancer cells (*7–13*). However, considerable heterogeneity of PSMA expression was detected in both histopathology and imaging among breast cancer patients (*7–12*). To address this knowledge gap, this study interrogates the genomic alteration and expression pattern of PSMA across breast cancer subtypes.

MATERIALS AND METHODS

Breast cancer is a heterogeneous disease that can be broadly classified on the basis of its gene expression patterns known as intrinsic molecular subtypes (*14*). The main molecular subtypes (luminal A, luminal B, human epidermal growth factor receptor 2 [HER2]–positive, and basallike) were defined by a 50-gene signature (*14*). The Cancer Genome Atlas is a publicly available dataset that provides comprehensive genomic data and molecular features for approximately 33 cancer types (*15*). Using The Cancer Genome Atlas dataset, we examined the genetic alteration and expression pattern of *FOLH1* (gene name of PSMA) from 998 breast cancer patients on the basis of the intrinsic molecular subtypes of the patients' cancer. The following files were extracted from the public portal: for microarray DNA copy-number aberration data, "brca_scna_all_thresholded.by_genes.txt"; for microarray gene expression data, "BRCA.exp.547.med.txt"; and for reverse-phase protein array expression data, "rppaData-403Samp-171Ab-Trimmed.txt." This study was exempted from the institutional review board as it exclusively used data from the public database.

In this work, we compared the somatic copy number status and the transcriptomic and protein expressions of *FOLH1* among luminal A, luminal B, HER2-positive, and basallike breast cancer (BLBC). Putative copy-number alteration of *FOLH1* based on the Genomic Identification of Significant Targets in Cancer 2.0 values (−2, homozygous deletion; −1, heterozygous deletion; 0, neutral or no change; 1, gain; 2, high-level amplification) (*16*) was extracted, and data were analyzed using 2-tailed unpaired Student *t* tests among the molecular subtypes of breast cancer. Relative *FOLH1* messenger RNA expression values and PSMA protein expression values based on *z* scores using the default threshold of 2 SDs from the mean (*17*) were extracted, and data were analyzed using 1-way ANOVA across multiple intrinsic molecular subtypes of breast cancer. Patient survival data from the pooled Gene Expression Omnibus datasets were obtained from the Kaplan–Meier plot (*18*,*19*). Patients were divided into 2 groups according to the upper and lower quartiles of normalized *FOLH1* expression. The Kaplan–Meier method was used to compute overall survival, relapse-free survival, and distant metastasis–free survival.

RESULTS

Molecular subtype classification revealed that *FOLH1* is more frequently amplified in BLBC (32%) than in HER2-positive (17%), luminal A (12%), and luminal B (23%) molecular subtypes ($P < 0.01$) (Fig. 1A). Consistent with these observations, *FOLH1* gene expression was highly expressed in BLBC compared with that

Received Sep. 14, 2023; revision accepted Feb. 26, 2024.
For correspondence or reprints, contact Wenhui Zhou (wzhou02@stanford.edu).
Published online Apr. 25, 2024.

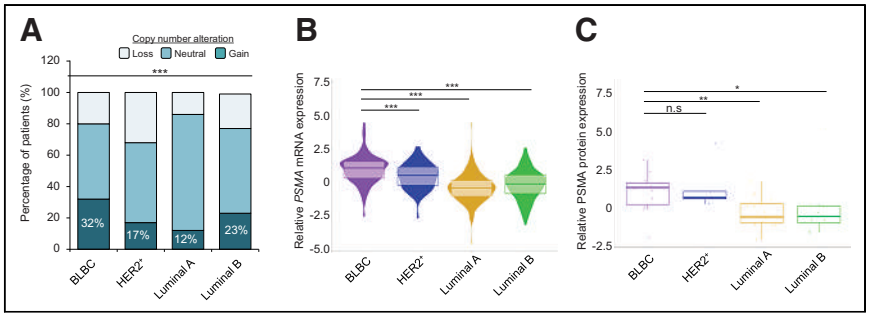

FIGURE 1. Preferential expression of PSMA in BLBC. According to The Cancer Genome Atlas dataset, shown are *FOLH1* somatic copy number analysis (A), *FOLH1* gene expression (B), and PSMA protein expression (C) across breast cancer subtypes. Data were analyzed using 1-way ANOVA and 2-tailed unpaired Student *t* test. Data shown are mean ± SEM. $*P < 0.05$. $**P < 0.01$. $***P < 0.001$. $HER2^+$ = HER2-positive; mRNA = messenger RNA; n.s = not significant.

in other molecular subtypes ($P < 0.001$) (Fig. 1B). Concordantly, *FOLH1* expression was negatively correlated with *ESR1* (gene name of estrogen receptor; $r = -0.36$) and *PR* (gene name of progesterone receptor; $r = -0.26$) but not with *ERBB2* (gene name of HER2; $r = 0.041$) and *AR* (gene name of androgen receptor; $r = -0.16$) (false discovery rate, 0%) (Fig. 2). PSMA protein expression was also assessed to corroborate our results. Concordant with gene expression analysis, the level of PSMA protein was significantly higher in BLBC than it was in other subtypes of breast cancer ($P = 0.03$) (Fig. 1C).

To further assess the clinical relevance, we evaluated the relationship between *FOLH1* expression and cancer survival outcome in breast cancer patients. Interestingly, high *FOLH1* expression was associated with favorable relapse-free survival and distant metastasis–free survival in patients with BLBC subtypes ($P < 0.0001$ and $P = 0.03$, respectively) (Fig. 3). In contrast, no significant association was observed in the luminal and HER2-positive breast cancer subtypes (Supplemental Fig. 1; supplemental materials are available at http://jnm.snmjournals.org). There is no significant association between *FOLH1* expression and overall survival across all breast cancer subtypes (Supplemental Fig. 1).

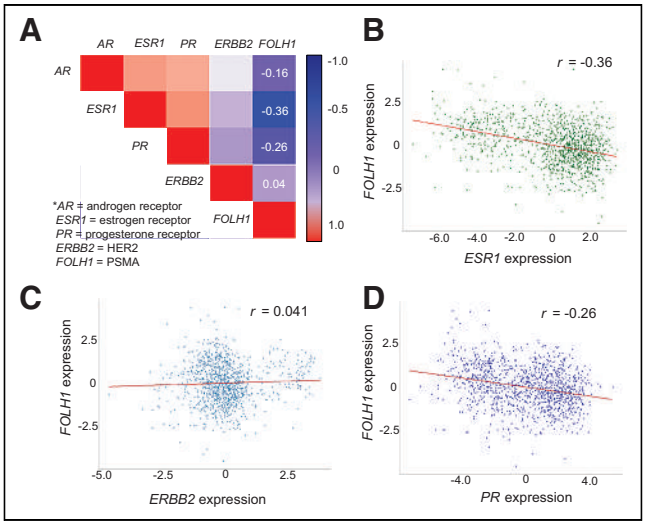

FIGURE 2. PSMA expression negatively correlates with hormone receptor expression. According to The Cancer Genome Atlas dataset, shown are correlation matrix between *FOLH1* expression and selected biomarkers (A), correlation between *FOLH1* gene expression and *ESR1* (B), correlation between *FOLH1* gene expression and *ERBB2* (C), and correlation between *FOLH1* gene expression and *PGR* (D). Pearson *r* statistics are shown.

DISCUSSION

Over the past decade, advances in molecularly targeted PSMA radionuclide-based imaging and therapy have led to remarkable improvement in the diagnosis and treatment of prostate cancer (*2–4*). Despite its name, PSMA is frequently overexpressed in many cancer types and thus presents a targeting opportunity for those cancer types currently without a known biologic target (*5,6*). In this preclinical study, we characterized the genomic alteration and expression pattern of PSMA across breast cancer subtypes. Our findings highlight that the BLBC subtype harbors frequent *FOLH1* amplification, which is linked to overexpression of RNA transcripts and protein of PSMA. Genomic upregulation of PSMA provides a molecular basis for the exploration of PSMA-targeting imaging and therapeutic radiopharmaceuticals in these cancer subtypes.

PSMA overexpression in breast cancer has been reported, though to a lesser degree than with prostate cancer (*5*). Histopathologic evaluation of PSMA expression by Kasoha et al. showed PSMA overexpression in cancer cells and tumor-associated neovasculature of both primary and metastatic breast cancers (*13*). Similarly, Sathekge et al. presented the earliest study that demonstrated in vivo PSMA-expressing tumor targeting in both primary and metastatic breast cancer using ^{68}Ga-PSMA PET/CT (*11*). Our study further expands on this knowledge by examining the expression pattern of PSMA across breast cancer subtypes. We observe substantial heterogeneity of PSMA expression among breast cancer patients. When stratified by molecular subtype status, PSMA overexpression is preferentially observed in the BLBC subtype. Importantly, our result further demonstrates that *FOLH1* amplification is a potential mechanistic underpinning of PSMA overexpression in these subtypes. Consistent with these data, Medina-Ornelas et al. showed that PSMA tumoral uptake is more pronounced in triple-negative breast cancer and HER2 subtypes than in hormonal receptor–positive subtypes (*12*).

The pivotal VISION trial demonstrated a compelling survival benefit of ^{177}Lu-PSMA-617 for PSMA-positive metastatic castration-resistant prostate cancer (*2*). In principle, PSMA represents a biologic target in all cancer types exhibiting PSMA positivity, regardless of tissue of origin. Our results raise the possibility that PSMA-targeting radiopharmaceuticals could offer unique imaging and treatment options for BLBC. Sharing an identical immunophenotype with triple-negative breast cancer, BLBC represents the most aggressive breast cancer subtype without an actionable target. We suspect that PSMA-targeting radiopharmaceuticals may be particularly effective as imaging and therapeutic agents in BLBC given preferential PSMA overexpression and amplification in this cancer subtype. Consistent with this notion, preliminary results from the European PRISMA trial have shown significant in vivo ^{68}Ga-PSMA uptake in patients with metastatic triple-negative breast cancer (*20*). Furthermore, a preclinical study by Morgenroth et al. showed that ^{177}Lu-PSMA-617 specifically localized to triple-negative breast cancer cells and significantly impeded the cells' vitality and angiogenic potential (*10*). Taken together, these findings incentivize future trials to validate the therapeutic efficacy of ^{177}Lu-PSMA-617 for PSMA-positive BLBC.

This study has several important limitations. Most notably, a validation study in human subjects was not performed to confirm the clinical applicability of our analysis of The Cancer Genome Atlas.

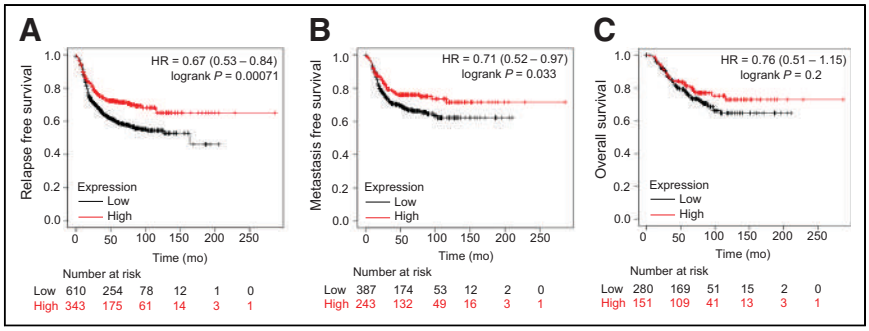

FIGURE 3. High PSMA expression is associated with improved cancer survival outcome in BLBC. Kaplan–Meier curves show relapse-free survival probability of BLBC patients with high or low *FOLH1* gene expression (A), metastasis-free survival probability of BLBC patients with high or low *FOLH1* gene expression (B), and overall survival probability of BLBC patients with high or low *FOLH1* gene expression (C). Number of patients at risk and log-rank *P* values are shown. HR = hazard ratio.

Larger-scale in vivo data of PSMA uptake in breast cancer are limited because ^{68}Ga-PSMA PET/CT is not routinely performed in female patients. Moreover, the biologic significance of PSMA amplification and overexpression was not addressed. Future bioinformatic and mechanistic studies could be useful for elucidating specific molecular pathways, such as cancer-cell metabolism and invasion, which have been implicated in prostate cancer.

CONCLUSION

This study revealed significant overexpression of the gene copies, RNA transcripts, and protein of PMSA in the BLBC subtype compared with expression in other breast cancer subtypes. These findings may help to inform patient selection for future prospective PSMA-targeting radiopharmaceutical imaging and therapeutic trials in breast cancer.

KEY POINTS

QUESTION: Is PSMA preferentially amplified and overexpressed in certain subtypes of breast cancer?

PERTINENT FINDINGS: Analyses from The Cancer Genome Atlas revealed frequent amplification of PSMA copy number, which was associated with the preferential overexpression of messenger RNA and protein of PSMA in the BLBC subtype. Cancer survival analyses showed that PSMA expression levels correlated with relapse-free and distant metastasis–free survival in patients with BLBC.

IMPLICATIONS FOR PATIENT CARE: PSMA represents a promising biologic target for BLBC, a breast cancer subtype currently lacking tailored imaging and therapeutic options. The application of PSMA-targeting imaging and therapeutic radiopharmaceuticals in BLBC holds the potential to address this gap and improve its poor disease prospects.

REFERENCES

1. Israeli RS, Powell CT, Corr JG, Fair WR, Heston WD. Expression of the prostate-specific membrane antigen. *Cancer Res.* 1994;54:1807–1811.
2. Sartor O, de Bono J, Chi KN, et al. Lutetium-177-PSMA-617 for metastatic castration-resistant prostate cancer. *N Engl J Med.* 2021;385:1091–1103.
3. Roberts MJ, Maurer T, Perera M, et al. Using PSMA imaging for prognostication in localized and advanced prostate cancer. *Nat Rev Urol.* 2023;20:23–47.
4. Siva S, Udovicich C, Tran B, Zargar H, Murphy DG, Hofman MS. Expanding the role of small-molecule PSMA ligands beyond PET staging of prostate cancer. *Nat Rev Urol.* 2020;17:107–118.
5. Uijen MJM, Derks YHW, Merkx RIJ, et al. PSMA radioligand therapy for solid tumors other than prostate cancer: background, opportunities, challenges, and first clinical reports. *Eur J Nucl Med Mol Imaging.* 2021;48:4350–4368.
6. Evans JC, Malhotra M, Cryan JF, O'Driscoll CM. The therapeutic and diagnostic potential of the prostate specific membrane antigen/glutamate carboxypeptidase II (PSMA/GCPII) in cancer and neurological disease. *Br J Pharmacol.* 2016;173:3041–3079.
7. Tolkach Y, Gevensleben H, Bundschuh R, et al. Prostate-specific membrane antigen in breast cancer: a comprehensive evaluation of expression and a case report of radionuclide therapy. *Breast Cancer Res Treat.* 2018;169:447–455.
8. Wernicke AG, Varma S, Greenwood EA, et al. Prostate-specific membrane antigen expression in tumor-associated vasculature of breast cancers. *APMIS.* 2014;122:482–489.
9. Bertagna F, Albano D, Cerudelli E, et al. Radiolabelled PSMA PET/CT in breast cancer: a systematic review. *Nucl Med Rev Cent East Eur.* 2020;23:32–35.
10. Morgenroth A, Tinkir E, Vogg ATJ, Sankaranarayanan RA, Baazaoui F, Mottaghy FM. Targeting of prostate-specific membrane antigen for radio-ligand therapy of triple-negative breast cancer. *Breast Cancer Res.* 2019;21:116.
11. Sathekge M, Lengana T, Modiselle M, et al. ^{68}Ga-PSMA-HBED-CC PET imaging in breast carcinoma patients. *Eur J Nucl Med Mol Imaging.* 2017;44:689–694.
12. Medina-Ornelas S, García-Perez F, Estrada-Lobato E, Ochoa-Carrillo F. ^{68}Ga-PSMA PET/CT in the evaluation of locally advanced and metastatic breast cancer, a single center experience. *Am J Nucl Med Mol Imaging.* 2020;10:135–142.
13. Kasoha M, Unger C, Solomayer E-F, et al. Prostate-specific membrane antigen (PSMA) expression in breast cancer and its metastases. *Clin Exp Metastasis.* 2017;34:479–490.
14. Parker JS, Mullins M, Cheang MCU, et al. Supervised risk predictor of breast cancer based on intrinsic subtypes. *J Clin Oncol.* 2009;27:1160–1167.
15. Weinstein JN, Collisson EA, Mill GB, et al. The Cancer Genome Atlas Pan-Cancer analysis project. *Nat Genet.* 2013;45:1113–1120.
16. Cerami E, Gao J, Dogrusoz U, et al. The cBio cancer genomics portal: an open platform for exploring multidimensional cancer genomics data. *Cancer Discov.* 2012;2:401–404.
17. Gao J, Aksoy BA, Dogrusoz U, et al. Integrative analysis of complex cancer genomics and clinical profiles using the cBioPortal. *Sci Signal.* 2013;6:pl1.
18. Győrffy B. Discovery and ranking of the most robust prognostic biomarkers in serous ovarian cancer. *Geroscience.* 2023;45:1889–1898.
19. Lánczky A, Győrffy B. Web-based survival analysis tool tailored for medical research (KMplot): development and implementation. *J Med Internet Res.* 2021;23:e27633.
20. Marta G, Wilmana Z, Taraji L, et al. Prostate-specific membrane antigen (PSMA) expression in patients with metastatic triple negative breast cancer: initial results of the PRISMA study. *J Clin Oncol.* 2023;41(suppl 16):1025.

Utility of PSMA PET/CT in Staging and Restaging of Renal Cell Carcinoma: A Systematic Review and Metaanalysis

Moe S. Sadaghiani[1], Saradha Baskaran[2], Michael A. Gorin[3], Steven P. Rowe[4], Jean-Claude Provost[2], Iryna Teslenko[2], Roman Bilyk[2], Hong An[2], and Sara Sheikhbahaei[1]

[1]Russell H. Morgan Department of Radiology and Radiological Science, Johns Hopkins University School of Medicine, Baltimore, Maryland; [2]Lantheus, Bedford, Massachusetts; [3]Milton and Carroll Petrie Department of Urology, Icahn School of Medicine at Mount Sinai, New York, New York; and [4]Department of Radiology, University of North Carolina School of Medicine, Chapel Hill, North Carolina

Prostate-specific membrane antigen (PSMA) is expressed in the neovasculature of multiple solid tumors, including renal cell carcinoma (RCC). Studies have demonstrated promising results on the utility of PSMA-targeted PET/CT imaging in RCC. This report aims to provide a systematic review and metaanalysis on the utility and detection rate of PSMA PET/CT imaging in staging or evaluation of primary RCC and restaging of metastatic or recurrent RCC. **Methods:** Searches were performed in PubMed, Embase, and abstract proceedings (last updated, August 2023). Studies that provided a lesion-level detection rate of PSMA radiotracers in staging or restaging of RCC were included in the metaanalysis. The overall pooled detection rate with a 95% CI was estimated, and subgroup analysis was performed when feasible. **Results:** Nine studies comprising 152 patients (133 clear cell RCC [ccRCC], 19 other RCC subtypes) were included in the metaanalysis. The pooled detection rate of PSMA PET/CT in evaluation of primary or metastatic RCC was estimated to be 0.83 (95% CI, 0.67–0.92). Subgroup analysis showed a pooled PSMA detection rate of 0.74 (95% CI, 0.57–0.86) in staging or evaluation of primary RCC lesions and 0.87 (95% CI, 0.73–0.95) in restaging of metastatic or recurrent RCC. Analysis based on the type of radiotracer showed a pooled detection rate of 0.85 (95% CI, 0.62–0.95) for ^{68}Ga-based PSMA tracers and 0.92 (95% CI, 0.76–0.97) for ^{18}F-DCFPyL PET/CT. Furthermore, in metastatic ccRCC, the available data support a significantly higher detection rate for ^{18}F-DCFPyL PET/CT than for conventional imaging modalities (2 studies). **Conclusion:** Our preliminary results show that PSMA PET/CT could be a promising alternative imaging modality for evaluating RCC, particularly metastatic ccRCC. Large prospective studies are warranted to confirm clinical utility in the staging and restaging of RCC.

Key Words: renal cell carcinoma; prostate-specific membrane antigen; PSMA PET/CT; metaanalysis

J Nucl Med 2024; 65:1007–1012
DOI: 10.2967/jnumed.124.267417

Renal cell carcinoma (RCC) accounts for 4% of the global cancer burden and 90% of all primary renal malignancies (*1,2*). RCC is the most lethal genitourinary cancer, as it often remains undetected during its early stages because of a lack of specific symptoms. Approximately 20%–30% of the patients present with metastases at initial diagnosis (*2*). Accurate staging and characterization of metastases are crucial for planning the treatment of patients with RCC. Conventional imaging techniques such as ultrasound, contrast-enhanced CT, MRI, and bone scintigraphy have been used for the diagnosis and staging of RCC (*3,4*). The current gold standard modality for evaluating metastatic disease in patients with inconclusive radiologic findings or for surveillance is contrast-enhanced CT using ^{18}F-FDG PET/CT. However, this technique is not sensitive or comprehensive enough to detect early metastatic lesions and is associated with false-negative results, particularly in small lesions (e.g., $<$1 cm) or low-grade tumors (*5*). Approximately 25% of patients experience metastases after undergoing surgery for a seemingly resectable condition (*6*). Therefore, there is a need for a more sensitive modality for early detection and timely management of patients with metastatic RCC. Recent reports on the superiority of prostate-specific membrane antigen (PSMA)–targeted PET imaging over the conventional modalities for prostate cancer at initial staging and recurrence have increased interest in exploring its utility for RCC (*7–9*).

PSMA is a type II transmembrane glycoprotein highly expressed in prostate cancer cells, as well as in the endothelial cells within the neovasculature of multiple solid tumors, including RCC (*10,11*). Clear cell RCC (ccRCC) is the most common RCC subtype and is generally the most aggressive, although there are numerous other subtypes with varying aggressiveness, including chromophobe RCC and papillary RCC (*12*). PSMA expression varies greatly across RCC subtypes. PSMA is strongly expressed in ccRCC (76.2%–88%) compared with chromophobe RCC (31.2%–60%) and is rarely detectable in papillary RCC (*13–15*). With high levels of neovascularity and increased PSMA expression, patients with ccRCC are potential candidates for PSMA PET/CT.

The most widely used PSMA-targeted PET imaging probes are ^{68}Ga- and ^{18}F-labeled. Compared with ^{68}Ga,^{18}F has a longer half-life and higher target-to-background resolution (*16*). Multiple preliminary studies have investigated the clinical utility of PSMA PET/CT in RCC using different PSMA-directed radiotracers and shown promising results (*17–21*). Reviews on the role of PSMA PET/CT in the evaluation and management of RCC have also been published (*22–24*). However, there is a lack of metaanalysis in the available literature that would give better insight into the role of PSMA PET/CT in assessing RCC. In this report, we have

Received Jan. 9, 2024; revision accepted Apr. 29, 2024.
For correspondence or reprints, contact Sara Sheikhbahaei (ssheikh6@jhmi.edu).
Published online May 23, 2024.

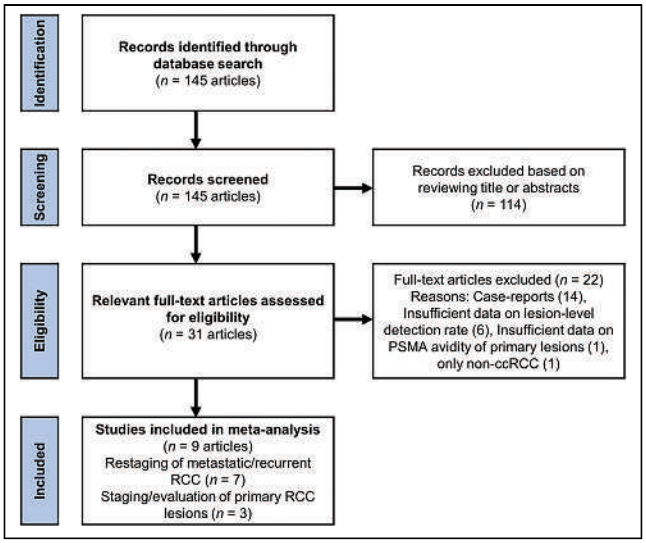

FIGURE 1. Flowchart of systematic review.

provided a systematic review on the utility of PSMA PET/CT in staging and restaging of RCC and performed a metaanalysis on the detection rate of PSMA PET/CT in staging or evaluation of primary RCC and restaging of metastatic or recurrent RCC.

MATERIALS AND METHODS

Search Strategy

A systematic literature review was conducted on August 25, 2023, according to the Preferred Reporting Items for Systematic Review and Meta-Analyses (PRISMA) guidelines (*25*). The search was performed in PubMed, Embase, and abstract proceedings of major scientific meetings (Society of Nuclear Medicine and Molecular Imaging, European Association of Nuclear Medicine) to identify relevant published studies without any restrictions on language, publication date, or publication status. The search strategy was based on the following combination of keywords: (A) "renal cell carcinoma" OR "RCC" AND (B) "PSMA" OR "prostate-specific membrane antigen." Institutional review board approval was not required since it was a retrospective analysis of previously published studies.

Criteria for Study Consideration

Clinical studies investigating the utility of PSMA PET/CT imaging in staging or restaging of patients with RCC (ccRCC or non-ccRCC) were included. Index tests included ^{18}F-DCFPyL, ^{18}F-PSMA-1007, ^{68}Ga-PSMA-11, or ^{68}Ga-P16–093 PET/CT scans. The inclusion criteria included all studies that provided the lesion-based detection rate for any PSMA radiotracers in patients with RCC.

Selection of Studies, Data Extraction, and Study Outcome

All records identified through the electronic search were initially screened for eligibility based on the title and abstract. Two of the authors performed this screening, which excluded review articles, editorials, and irrelevant citations. The full texts of the potentially relevant publications were retrieved and independently checked by the 2 authors for predefined inclusion criteria.

The 2 authors independently extracted the following data from each included study: bibliographic details, patient demographics and disease characteristics, index tests, number of patients, tumor histopathology, and detection rates. The overall pooled detection rate with 95% CIs was estimated among all included studies. In addition, subgroup analysis was performed to estimate the detection rate of ^{18}F-DCFPyL and ^{68}Ga-PSMA PET/CT in patients with metastatic RCC and to compare the performance of PSMA PET/CT relative to other conventional imaging modalities, when feasible (only 2 studies).

Statistical Analysis and Data Synthesis

A lesion-based metaanalysis of single proportions was performed to calculate the pooled detection rate of PSMA PET/CT in patients with RCC using meta package (version 6.5-0) in R version 4.3.1. Forest plots of detection rates were created to display variations in the results of the individual studies. Logit transformation with the inverse variance method was used to perform a metaanalysis of proportions. The I^2 index was calculated to quantify heterogeneity. I^2 lies between 0% and 100%, with respective values of approximately 25%, 50%, and 75% indicating low, moderate, and high heterogeneity. To deal with heterogeneity, random-effect assumptions were used for synthesizing metaanalytic data (*26*). Funnel plots were used to assess publication bias.

RESULTS

Search Results and Study Characteristics

Using the comprehensive search strategy outlined in the methods section, we identified 145 articles, of which 114 were excluded by initial screening of title and abstract. The full texts of the remaining 31 studies were reviewed, and 22 studies were excluded. In total, 9 articles were included in the final metaanalysis and quantitative synthesis (Fig. 1).

Supplemental Tables 1 and 2 (*16–21,27–51*) summarize the published literature on the utility of PET/CT imaging using different PSMA-directed radiotracers, including 12 articles on ^{18}F-based tracers (^{18}F-DCFPyL, ^{18}F-PSMA-1007) and 19 articles on ^{68}Ga-based tracers (^{68}Ga-PSMA-11, ^{68}Ga-P16–093), in patients with RCC (31 studies, including case reports and case series) (supplemental materials are available at http://jnm.snmjournals.org). In these studies, PSMA PET/CT was performed for staging and restaging of RCC, evaluation of primary RCC lesions, or other purposes (e.g., prostate cancer restaging) with incidental detection of RCC metastases.

Detection Rate of PSMA PET/CT in Staging or Restaging of RCC (Lesion-Level Analysis)

All Studies. Nine articles, including 152 patients (133 ccRCC, 19 other RCC subtypes), provided information on the lesion-level detection rate of PSMA PET/CT performed for either staging and evaluation of primary RCC lesions or restaging of metastatic or recurrent RCC. The forest plot representing the pooled data from all included studies is depicted in Figure 2. The estimated pooled

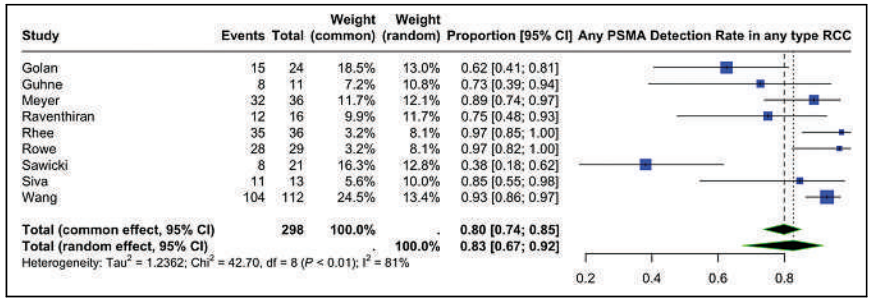

FIGURE 2. Lesion-based detection rate of PSMA PET/CT in staging and restaging of RCC (all included studies).

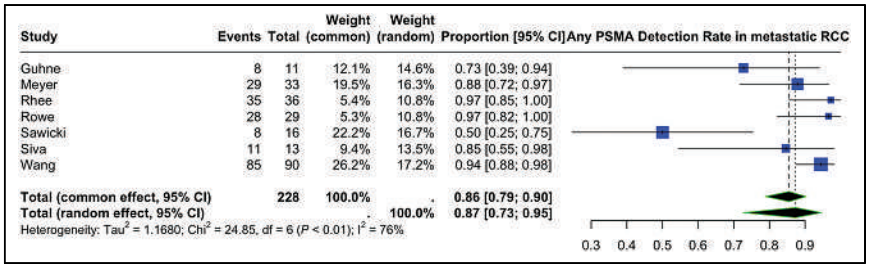

FIGURE 3. Lesion-based detection rate of PSMA PET/CT in restaging of patients with metastatic or recurrent RCC.

lesion-level detection rate of PET/CT with any PSMA radiotracer was 0.83 (95% CI, 0.67–0.92). There was high heterogeneity among the included studies (I^2 = 81%).

Subgroup analysis was based on the clinical indication (restaging of metastatic RCC vs. staging or evaluation of primary RCC), histopathology (all subtypes of RCC vs. studies that included solely ccRCC), and type of radiotracer (^{18}F- vs. ^{68}Ga-based PSMA radiotracers), when feasible.

Restaging of Metastatic or Recurrent RCC. Seven articles, including 90 patients (87 ccRCC, 3 other RCC subtypes), provided information on the lesion-level detection rate of PSMA PET/CT in restaging of metastatic or recurrent RCC (Fig. 3). The estimated pooled lesion-level detection rate of any type of PSMA radiotracer was 0.87 (95% CI, 0.73–0.95). Limiting the cases to studies that included solely ccRCC pathology resulted in a pooled detection rate of 0.85 (95% CI, 0.64–0.95). There was substantial heterogeneity among the included studies, with an I^2 of 76%.

The lowest detection rate has been reported by Sawicki et al. (50%), with all PET-negative metastases being subcentimeter pulmonary nodules in 1 patient (*39*). This study was identified as a possible source contributing to the high heterogeneity. Exclusion of this study from the analysis significantly improved the study heterogeneity (leave-one-out method), with a pooled detection rate of 0.91 (95% CI, 0.83–0.95; I^2 = 42%) (Supplemental Fig. 1).

Staging or Evaluation of Primary RCC Lesions. Three studies, including 62 patients (48 ccRCC, 14 other subtypes), reported the lesion-level detection rate of ^{68}Ga-PSMA PET/CT in the staging or evaluation of primary RCC lesions. Only malignant lesions and their PSMA PET positivity data were included in the analysis. The pooled detection rate of PSMA PET/CT for primary RCC was 0.74 (95% CI, 0.57–0.86), with an I^2 of 38%. In other words, approximately 74% (46/62) of primary RCC lesions were PSMA-positive (Fig. 4).

^{68}Ga-Based Versus ^{18}F-Based PSMA Radiotracer. Among the included studies on patients with metastatic RCC, ^{68}Ga-based PSMA radiotracers were used in 5 studies including 75 patients (72 ccRCC, 3 non-ccRCC). The pooled detection rate in these studies was estimated to be 0.85 (95% CI, 0.62–0.95; I^2 = 82%) (Fig. 5). Limiting the analysis to studies that included solely ccRCC pathology resulted in a pooled detection rate of 0.80 (95% CI, 0.53–0.93).

Two of the included studies on 19 patients with metastatic RCC (all ccRCC subtype) evaluated the utility of an ^{18}F-based PSMA radiotracer (^{18}F-DCFPyL) and provided a direct comparison with conventional imaging (*17,19*). Our analysis revealed that ^{18}F-DCFPyL PET/CT provides a significantly higher detection rate in metastatic RCC than conventional imaging modalities such as CT and MRI, with pooled estimates of 0.92 (95% CI, 0.76–0.97) versus 0.63 (95% CI, 0.50–0.74), respectively (Fig. 6). There was low heterogeneity in this subgroup analysis (I^2 = 28% and 0%, respectively).

Publication Bias

Qualitative evaluation using funnel plots revealed relatively symmetric plots suggestive of a low probability of publication bias (Fig. 7).

DISCUSSION

In this study, we systematically reviewed all the available literature on the utility of PSMA PET/CT imaging in staging or restaging of RCC (supplemental tables) and performed a metaanalysis on the eligible relevant studies when feasible. To our knowledge, this was the first metaanalysis assessing the detection rate of PSMA PET/CT in this patient population. Our results revealed the potential role of PSMA PET/CT in the staging or evaluation of primary RCC lesions and in the restaging of metastatic or recurrent RCC, with a pooled detection rate of 0.74 (95% CI, 0.57–0.86) and 0.87 (95% CI, 0.73–0.95), respectively. Our subgroup analysis revealed that both ^{68}Ga-based (7 studies) and ^{18}F-based (2 studies) PSMA radiotracers have a high detection rate for evaluation of metastatic RCC (*17–21,36,37,39,41*).

We found high heterogeneity among the included studies (I^2 > 75%). The heterogeneous study types, differences in the radiotracers used across studies, and mixed patient populations, including both ccRCC and non-ccRCC and different stages of the disease, could have contributed to the high heterogeneity. In Sawicki et al. (detection rate, 50%), all PET-negative metastases were subcentimeter pulmonary nodules in 1 patient (*39*). This study was identified as a source of heterogeneity. Pulmonary nodules are prone to have decreased tracer activity, which at least partially is explained by breathing-related motion degradation. Furthermore, the subcentimeter size of nodules limits PET resolution because of partial-volume effects, although with targeted radiotracers, it is possible to drive contrast resolution to overcome spatial resolution limitations. Redoing the metaanalysis after exclusion of this study resulted in improved heterogeneity (I^2 = 42%). Primary versus metastatic disease status was identified as another source of heterogeneity, and subgroup analysis on this population improved the heterogeneity (I^2 = 38%). In addition, most of those studies were conducted retrospectively and

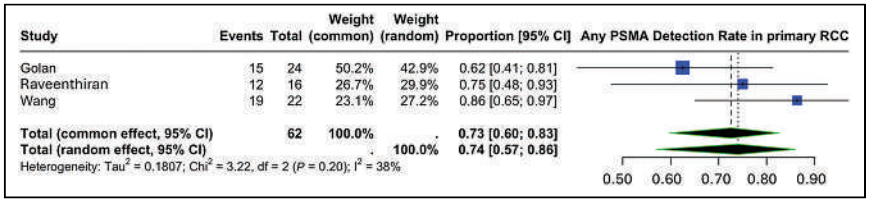

FIGURE 4. Detection rate of PSMA PET/CT in staging or evaluation of primary RCC.

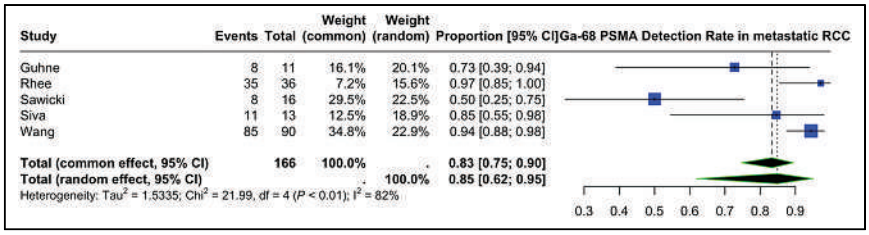

FIGURE 5. Lesion-based detection rate of ^{68}Ga-based PSMA radiotracers in restaging of patients with metastatic RCC.

lacked pathologic proof of disease at the site of radiotracer uptake; this factor could have contributed to heterogeneity.

Demirci et al. (*50*) and Rowe et al. (*17*) were the first to report the utility of PSMA-targeted radiotracers for imaging patients with ccRCC using ^{68}Ga-PSMA-11 and ^{18}F-DCFPyL, respectively. Subsequently, multiple small-scale preliminary studies demonstrated promising results for PSMA PET/CT in staging and restaging of RCC, with the main advantage being the possibility of detecting distant metastasis (*23*). Patients with metastatic RCC have a poor prognosis, with a 5-y survival rate of only 12% (*12*). Therefore, accurate staging and assessment of metastases are crucial for managing patients and determining the treatment strategy. Siva et al. (*41*), Raveenthiran et al. (*20*), and Guhne et al. (*37*) examined the diagnostic utility of ^{68}Ga-PSMA PET/CT for evaluating disease extent in patients with metastatic RCC. In a retrospective series of 8 patients with oligometastatic RCC, Siva et al. demonstrated higher uptake on ^{68}Ga-PSMA than on ^{18}F-FDG PET, suggesting ^{68}Ga-PSMA PET to be a more sensitive modality than ^{18}F-FDG PET for diagnostic evaluation of metastatic RCC (*41*). Raveenthiran et al. examined the effectiveness of ^{68}Ga-PSMA PET/CT, compared with conventional imaging, in guiding management decisions (*20*).

ccRCC accounts for over 75% of RCC diagnoses (*12*) and has strong PSMA expression relative to other RCC subtypes (*13*). A retrospective case series of 38 patients with ^{68}Ga-PSMA PET/CT for staging or restaging of RCC revealed the strongest detection rate in patients with ccRCC and a clinical management change in 43.8% of primary staging cases and 40.9% of restaging cases (*20*). Guhne et al. demonstrated molecular PSMA expression in all PET-positive lesions, with no correlation between histopathologic findings (extent and intensity of PSMA expression) and PET/CT parameters (SUV_{max}, SUV_{mean}, lesion-to-muscle ratio) in patients with metastatic ccRCC; however, this lack of correlation was because most lung metastases showed low tracer uptake (*37*). Seven of our included studies evaluated the role of PSMA PET/CT in patients with metastatic or recurrent RCC, with a pooled detection rate of 87%. Most included patients in these studies had ccRCC pathology (87 ccRCC, 3 other subtypes). In addition, our subgroup analysis on studies that included only ccRCC patients did not show a significant change in the detection rate of PSMA PET/CT. Thus, the presence of a different tumor histopathology is not likely to significantly affect our results in this analysis.

Two of the included studies provided a direct comparison of PSMA PET/CT (^{18}F-DCFPyL) and conventional imaging in metastatic ccRCC and support a higher detection rate of PSMA PET/CT, with a pooled detection rate of 0.92 (95% CI, 0.76–0.97) versus 0.63 (95% CI, 0.50–0.74), respectively (*17,19*). Rowe et al. prospectively analyzed 5 patients with metastatic ccRCC and identified 29 lesions on at least one modality. Of these, 18 metastatic lesions were identified on conventional imaging, whereas 28 sites were identified on ^{18}F-DCFPyL PET/CT, 17 of which corresponded to the disease site seen on conventional imaging. The study reported a higher detection rate (97% vs. 62%) and higher sensitivity (94.7% vs. 78.9%) for ^{18}F-DCFPyL PET/CT than for conventional imaging in the detection of metastatic lesions (*17*). Meyer et al. conducted a prospective study to evaluate the clinical utility of ^{18}F-DCFPyL PET/CT in patients with presumed oligometastatic ccRCC based on conventional imaging. In total, 33 metastatic sites of disease were identified in 17 oligometastatic ccRCC patients, of which 29 sites were detected on ^{18}F-DCFPyL PET/CT and 21 metastatic lesions were identified on conventional imaging. Seventeen of 21 (81%) metastatic lesions detected on conventional imaging had radiotracer uptake. In 4 patients (28.6%), 12 lesions not detected on conventional imaging were identified on ^{18}F-DCFPyL PET/CT, and 3 of these patients were no longer considered oligometastatic. The detection rates of ^{18}F-DCFPyL PET/CT and conventional imaging for identifying sites of metastatic disease were reported as 87.9% and 63.4%, respectively (*19*). Rhee et al. reported a sensitivity of 92% for ^{68}Ga-PSMA PET/CT in detecting RCC metastatic lesions, compared with 68.6% for conventional CT (*18*). A recent study compared the utility of ^{68}Ga-PSMA PET/CT in ccRCC and non-ccRCC and reported that ^{68}Ga-PSMA PET/CT had accuracy and sensitivity superior to conventional imaging in the detection of metastatic lesions in ccRCC (*40*).

The major limitations of the current analysis are high heterogeneity among the studies, lack of definitive indications for the application of PSMA PET/CT in RCC patients, the small number of patients analyzed, lack of data on the location and size of RCC lesions, and the retrospective nature of most of the studies included in the analysis. Despite these limitations, our preliminary results shed light on the potential role of PSMA PET/CT in the detection and characterization of metastatic RCC. Large prospective trials with robust inclusion criteria and pathologic confirmation of lesions would be of value to validate the diagnostic efficiency of

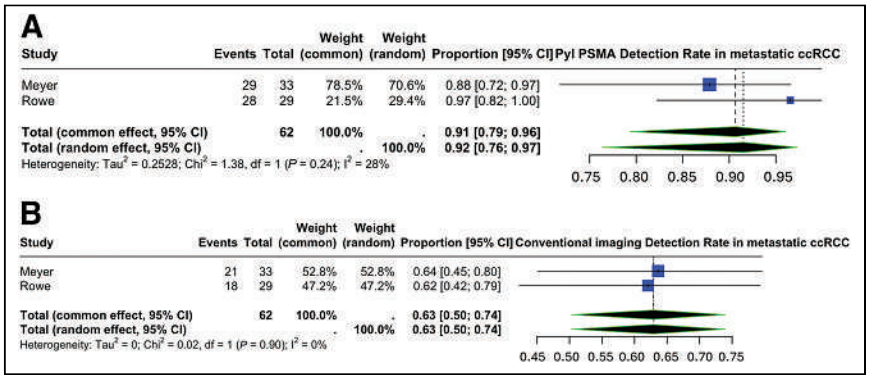

FIGURE 6. Lesion-based detection rate of ^{18}F-DCFPyL PSMA in restaging of metastatic RCC (A), in comparison with conventional imaging modalities (B).

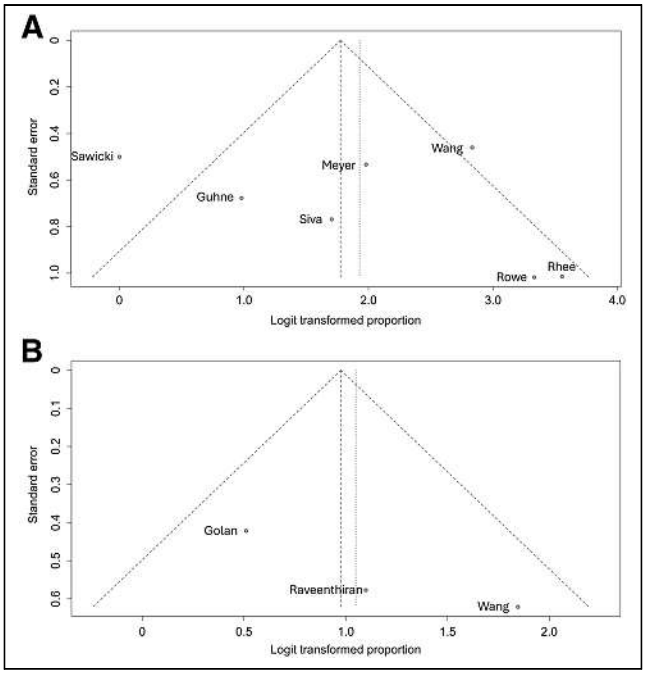

FIGURE 7. Funnel plot of publication bias on detection rate of PSMA PET/CT in restaging of metastatic RCC (A) and evaluation of primary lesions (B).

PSMA PET/CT in RCC, particularly in patients at high risk for metastatic disease at initial staging, response assessment, or surveillance monitoring; in patients with oligometastatic disease; and in patients who can potentially be considered for future radioligand PSMA-targeted therapy.

CONCLUSION

Our metaanalysis showed the detection potential of PSMA PET/CT in staging primary RCC lesions and restaging metastatic or recurrent RCC. Although our findings are based on small-scale studies with high heterogeneity, the preliminary results suggest merit in the use of PSMA PET/CT in RCC, particularly when performed for restaging of metastatic or recurrent disease.

DISCLOSURE

Research funding was provided by Lantheus. No other potential conflict of interest relevant to this article was reported.

ACKNOWLEDGMENTS

We thank Vincent A. DiPippo, Victoria Love, and Neda Huseinovic of Lantheus for providing medical writing support.

KEY POINTS

QUESTION: Does PSMA PET/CT have the potential to be an effective alternative imaging modality for patients with RCC?

PERTINENT FINDINGS: This metaanalysis demonstrated high detection rates for PSMA-targeted imaging of RCC using both ^{18}F- and ^{68}Ga-labeled agents.

IMPLICATIONS FOR PATIENT CARE: These findings suggest a new opportunity for improved detection of metastatic RCC using PSMA-targeted imaging agents.

REFERENCES

1. Siegel RL, Miller KD, Fuchs HE, Jemal A. Cancer statistics, 2021. *CA Cancer J Clin.* 2021;71:7–33.
2. Ljungberg B, Campbell SC, Choi HY, et al. The epidemiology of renal cell carcinoma. *Eur Urol.* 2011;60:615–621.
3. Leveridge MJ, Bostrom PJ, Koulouris G, Finelli A, Lawrentschuk N. Imaging renal cell carcinoma with ultrasonography, CT and MRI. *Nat Rev Urol.* 2010;7:311–325.
4. Rossi SH, Prezzi D, Kelly-Morland C, Goh V. Imaging for the diagnosis and response assessment of renal tumours. *World J Urol.* 2018;36:1927–1942.
5. Brufau BP, Cerqueda CS, Villalba LB, Izquierdo RS, Gonzalez BM, Molina CN. Metastatic renal cell carcinoma: radiologic findings and assessment of response to targeted antiangiogenic therapy by using multidetector CT. *Radiographics.* 2013; 33:1691–1716.
6. Psutka SP, Master VA. Role of metastasis-directed treatment in kidney cancer. *Cancer.* 2018;124:3641–3655.
7. Tanaka T, Yang M, Froemming AT, et al. Current imaging techniques for and imaging spectrum of prostate cancer recurrence and metastasis: a pictorial review. *Radiographics.* 2020;40:709–726.
8. Pienta KJ, Gorin MA, Rowe SP, et al. A phase 2/3 prospective multicenter study of the diagnostic accuracy of prostate specific membrane antigen PET/CT with ^{18}F-DCFPyL in prostate cancer patients (OSPREY). *J Urol.* 2021;206:52–61.
9. Morris MJ, Rowe SP, Gorin MA, et al. Diagnostic performance of ^{18}F-DCFPyL-PET/CT in men with biochemically recurrent prostate cancer: results from the CONDOR phase III, multicenter study. *Clin Cancer Res.* 2021;27:3674–3682.
10. Van de Wiele C, Sathekge M, de Spiegeleer B, et al. PSMA expression on neovasculature of solid tumors. *Histol Histopathol.* 2020;35:919–927.
11. Chang SS, Reuter VE, Heston WD, Gaudin PB. Metastatic renal cell carcinoma neovasculature expresses prostate-specific membrane antigen. *Urology.* 2001;57:801–805.
12. Tung I, Sahu A. Immune checkpoint inhibitor in first-line treatment of metastatic renal cell carcinoma: a review of current evidence and future directions. *Front Oncol.* 2021;11:707214.
13. Baccala A, Sercia L, Li J, Heston W, Zhou M. Expression of prostate-specific membrane antigen in tumor-associated neovasculature of renal neoplasms. *Urology.* 2007;70:385–390.
14. Al-Ahmadie HA, Olgac S, Gregor PD, et al. Expression of prostate-specific membrane antigen in renal cortical tumors. *Mod Pathol.* 2008;21:727–732.
15. Baraban EG, Ged Y, Singla N, et al. Vascular expression of prostate-specific membrane antigen (PSMA) in MiTF family translocation renal cell carcinoma and related neoplasms. *Appl Immunohistochem Mol Morphol.* 2023;31:544–549.
16. Gorin MA, Rowe SP, Hooper JE, et al. PSMA-targeted ^{18}F-DCFPyL PET/CT imaging of clear cell renal cell carcinoma: results from a rapid autopsy. *Eur Urol.* 2017;71:145–146.
17. Rowe SP, Gorin MA, Hammers HJ, et al. Imaging of metastatic clear cell renal cell carcinoma with PSMA-targeted ^{18}F-DCFPyL PET/CT. *Ann Nucl Med.* 2015; 29:877–882.
18. Rhee H, Blazak J, Tham CM, et al. Pilot study: use of gallium-68 PSMA PET for detection of metastatic lesions in patients with renal tumour. *EJNMMI Res.* 2016;6:76.
19. Meyer AR, Carducci MA, Denmeade SR, et al. Improved identification of patients with oligometastatic clear cell renal cell carcinoma with PSMA-targeted ^{18}F-DCFPyL PET/CT. *Ann Nucl Med.* 2019;33:617–623.
20. Raveenthiran S, Esler R, Yaxley J, Kyle S. The use of ^{68}Ga-PET/CT PSMA in the staging of primary and suspected recurrent renal cell carcinoma. *Eur J Nucl Med Mol Imaging.* 2019;46:2280–2288.
21. Wang G, Li L, Wang J, et al. Head-to-head comparison of [^{68}Ga]Ga-P16-093 and 2-[^{18}F]FDG PET/CT in patients with clear cell renal cell carcinoma: a pilot study. *Eur J Nucl Med Mol Imaging.* 2023;50:1499–1509.
22. Ahn T, Roberts MJ, Abduljabar A, et al. A review of prostate-specific membrane antigen (PSMA) positron emission tomography (PET) in renal cell carcinoma (RCC). *Mol Imaging Biol.* 2019;21:799–807.
23. Evangelista L, Basso U, Maruzzo M, Novara G. The role of radiolabeled prostate-specific membrane antigen positron emission tomography/computed tomography for the evaluation of renal cancer. *Eur Urol Focus.* 2020;6:146–150.
24. Urso L, Castello A, Rocca GC, et al. Role of PSMA-ligands imaging in renal cell carcinoma management: current status and future perspectives. *J Cancer Res Clin Oncol.* 2022;148:1299–1311.
25. Page MJ, McKenzie JE, Bossuyt PM, et al. The PRISMA 2020 statement: an updated guideline for reporting systematic reviews. *BMJ.* 2021;372:n71.
26. DerSimonian R, Laird N. Meta-analysis in clinical trials. *Control Clin Trials.* 1986;7:177–188.
27. Rowe SP, Gorin MA, Hammers HJ, Pomper MG, Allaf ME, Javadi MS. Detection of ^{18}F-FDG PET/CT occult lesions with ^{18}F-DCFPyL PET/CT in a patient with metastatic renal cell carcinoma. *Clin Nucl Med.* 2016;41:83–85.

28. Yin Y, Campbell SP, Markowski MC, et al. Inconsistent detection of sites of metastatic non-clear cell renal cell carcinoma with PSMA-targeted [^{18}F]DCFPyL PET/CT. *Mol Imaging Biol.* 2019;21:567–573.
29. Currie GM, Trifunovic M, Liu J, Kim S, Gurney H. ^{18}F-DCFPyL PET/CT in metastatic renal cell carcinoma. *J Nucl Med Technol.* 2022;50:282–285.
30. Perry E, Talwar A, Sharma S, et al. Non-prostate cancer tumours: incidence on ^{18}F-DCFPyL PSMA PET/CT and uptake characteristics in 1445 patients. *Eur J Nucl Med Mol Imaging.* 2022;49:3277–3288.
31. Zeng Y, Luo J, Liao H, Chen P. Utility of ^{18}F-prostate-specific membrane antigen 1007 in imaging of tumor thrombus of renal cell carcinoma. *Clin Nucl Med.* 2021; 46:697–699.
32. Marafi F, Sasikumar A, Al-Terki A, Alfeeli M. ^{18}F-PSMA 1007 in suspected renal cell carcinoma. *Clin Nucl Med.* 2020;45:377–378.
33. Sadeq A, Usmani S, Esmail AA, Fathallah W, Alfeeli MA, Marafi F. Incremental value of ^{18}F-PSMA-1007 PET/CT in detection of metastatic renal cell carcinoma to the brain. *Clin Nucl Med.* 2022;47:627–628.
34. Marafi F, Sasikumar A, Aldaas M, Esmail A. ^{18}F-PSMA-1007 PET/CT for initial staging of renal cell carcinoma in an end-stage renal disease patient. *Clin Nucl Med.* 2021;46:e65–e67.
35. Xiong M, Zhang W, Zhou C, Bao J, Zang S, Lin X. Application of ^{18}F prostate-specific membrane antigen positron emission tomography/computed tomography in monitoring gastric metastasis and cancer thrombi from renal cell carcinoma. *J Oncol.* 2022;2022:5681463.
36. Golan S, Aviv T, Groshar D, et al. Dynamic ^{68}Ga-PSMA-11 PET/CT for the primary evaluation of localized renal mass: a prospective study. *J Nucl Med.* 2021;62: 773–778.
37. Guhne F, Seifert P, Theis B, Steinert M, Freesmeyer M, Drescher R. PSMA-PET/CT in patients with recurrent clear cell renal cell carcinoma: histopathological correlations of imaging findings. *Diagnostics (Basel).* 2021;11:1142.
38. Seront E, Lhommel R, Tombal B. Case report: early ^{68}Ga-PSMA-PET metabolic assessment and response to systemic treatment for first-line metastatic clear cell renal cell carcinoma; about two clinical cases. *Front Oncol.* 2021;11:782166.
39. Sawicki LM, Buchbender C, Boos J, et al. Diagnostic potential of PET/CT using a ^{68}Ga-labelled prostate-specific membrane antigen ligand in whole-body staging of renal cell carcinoma: initial experience. *Eur J Nucl Med Mol Imaging.* 2017;44: 102–107.
40. Li Y, Zheng R, Zhang Y, et al. Special issue "The advance of solid tumor research in China": ^{68}Ga-PSMA-11 PET/CT for evaluating primary and metastatic lesions in different histological subtypes of renal cell carcinoma. *Int J Cancer.* 2023;152: 42–50.
41. Siva S, Callahan J, Pryor D, Martin J, Lawrentschuk N, Hofman MS. Utility of ^{68}Ga prostate specific membrane antigen – positron emission tomography in diagnosis and response assessment of recurrent renal cell carcinoma. *J Med Imaging Radiat Oncol.* 2017;61:372–378.
42. Meng L, Zhang S, Gao J, et al. [^{68}Ga]Ga-PSMA-11 PET/CT has potential application in predicting tumor HIF-2α expression and therapeutic response to HIF-2α antagonists in patients with RCC. *Eur Radiol.* 2022;32:6545–6553.
43. Jha S, Hemrom A, Shamim SA, Barwad A, Batra A. ^{68}Ga-PSMA PET/CT detecting metastatic lesion of RCC: missed on ^{18}F-FDG PET/CT. *Clin Nucl Med.* 2023; 48:e294–e296.
44. Gao J, Meng L, Xu Q, et al. ^{68}Ga-PSMA-11 PET/CT parameter correlates with pathological VEGFR-2/PDGFR-beta expression in renal cell carcinoma patients. *Mol Imaging Biol.* 2022;24:759–768.
45. Tariq A, McGeorge S, Pearce A, et al. Characterization of tumor thrombus in renal cell carcinoma with prostate specific membrane antigen (PSMA) positron emission tomography (PET)/computed tomography (CT). *Urol Oncol.* 2022;40: 276.e1–276.e9.
46. Udovicich C, Callahan J, Bressel M, et al. Impact of prostate-specific membrane antigen positron emission tomography/computed tomography in the management of oligometastatic renal cell carcinoma. *Eur Urol Open Sci.* 2022;44:60–68.
47. Filizoglu N, Cetin IA, Kissa TN, Niftaliyeva K, Ones T. ^{68}Ga-PSMA PET/CT to distinguish brain metastasis of renal cell carcinoma from radiation necrosis after stereotactic radiosurgery. *Clin Nucl Med.* 2021;46:913–914.
48. Zacho HD, Nielsen JB, Dettmann K, Haberkorn U, Petersen LJ. Incidental detection of thyroid metastases from renal cell carcinoma using ^{68}Ga-PSMA PET/CT to assess prostate cancer recurrence. *Clin Nucl Med.* 2017;42:221–222.
49. Saadat S, Tie B, Wood S, Vela I, Rhee H. Imaging tumour thrombus of clear cell renal cell carcinoma: FDG PET or PSMA PET? Direct in vivo comparison of two technologies. *Urol Case Rep.* 2017;16:4–5.
50. Demirci E, Ocak M, Kabasakal L, et al. ^{68}Ga-PSMA PET/CT imaging of metastatic clear cell renal cell carcinoma. *Eur J Nucl Med Mol Imaging.* 2014;41: 1461–1462.
51. Tariq A, Kwok M, Pearce A, et al. The role of dual tracer PSMA and FDG PET/CT in renal cell carcinoma (RCC) compared to conventional imaging: a multi-institutional case series with intra-individual comparison. *Urol Oncol.* 2022; 40:66.e1–66.e9.

A Prospective Randomized Multicenter Study on the Impact of [^{18}F]F-Choline PET/CT Versus Conventional Imaging for Staging Intermediate- to High-Risk Prostate Cancer

Laura Evangelista[1,2], Fabio Zattoni[3,4], Marta Burei[5], Daniele Bertin[5], Eugenio Borsatti[6], Tanja Baresic[6], Mohsen Farsad[7], Emanuela Trenti[8], Mirco Bartolomei[9], Stefano Panareo[9,10], Luca Urso[9,11], Giuseppe Trifirò[12], Elisabetta Brugola[12], Franca Chierichetti[13], Davide Donner[13,14], Lucia Setti[15], Mauro Gallan[16], Paola Del Bianco[17], Giovanna Magni[17], Gian Luca De Salvo[17], Giacomo Novara[3], and the Study Group Coinvestigators

[1]Department of Biomedical Sciences, Humanitas University, Pieve Emanuele, Italy; [2]Nuclear Medicine Unit, IRCCS Humanitas Research Hospital, Rozzano, Italy; [3]Urology Unit, Department of Surgery, Oncology, and Gastroenterology, Urologic Unit, University of Padua, Padua, Italy; [4]Department of Medicine, DIMED, University of Padua, Padua, Italy; [5]Nuclear Medicine Unit, Veneto Institute of Oncology, Padua, Italy; [6]Nuclear Medicine Unit, Department of Radiation Oncology, Centro di Riferimento Oncologico, Aviano, Italy; [7]Department of Nuclear Medicine, Central Hospital of Bolzano, Bozen, Italy; [8]Department of Urology, Central Hospital of Bolzano, Bozen, Italy; [9]Nuclear Medicine Unit, University Hospital, Ferrara, Italy; [10]Nuclear Medicine Unit, Azienda Ospedaliero Universitaria di Modena, Modena, Italy; [11]Department of Environmental and Prevention Sciences, University of Ferrara, Ferrara, Italy; [12]Nuclear Medicine Unit, ICS Maugeri IRCCS Spa SB, Pavia, Italy; [13]Nuclear Medicine Unit, APSS della Provincia Autonoma di Trento, Santa Chiara Hospital, Trento, Italy; [14]Department of Medical and Surgical Sciences, Alma Mater Studiorum Università di Bologna, Bologna, Italy; [15]Nuclear Medicine Unit, Humanitas Gavazzeni, Bergamo, Italy; [16]Nuclear Medicine Unit, Dell'Angelo Hospital, Mestre-Venezia, Italy; and [17]Clinical Research Unit, Veneto Institute of Oncology, Padua, Italy

This study aimed to compare the efficacy of [^{18}F]F-choline PET/CT with conventional imaging for staging and managing intermediate- to high-risk prostate cancer (PCa). The primary objective was to assess the ability of PET/CT with [^{18}F]F-choline to identify lymph node and systemic involvement during initial staging. Secondary objectives included evaluating the impact of [^{18}F]F-choline PET/CT on unnecessary local treatments and assessing the safety of [^{18}F]F-choline agents. Additionally, the study aimed to analyze recurrence-free survival and overall survival 5 y after randomization. **Methods:** A prospective controlled, open, randomized multicenter phase III trial involving 7 Italian centers was conducted. Eligible patients with intermediate- to high-risk PCa were randomized in a 1:1 ratio. Two groups were formed: one undergoing conventional imaging (abdominopelvic contrast-enhanced CT and bone scanning) and the other receiving conventional imaging plus [^{18}F]F-choline PET/CT. The study was terminated prematurely; however, all the endpoints were thoroughly analyzed and enriched. **Results:** Between February 2016 and December 2020, 256 patients were randomly assigned. In total, 236 patients (117 in the control arm and 119 in the experimental arm) were considered for the final assessment. In the experimental arm, the sensitivity for lymph node metastases, determined by final pathology and serial prostate-specific antigen evaluations, was higher than in the control arm (77.78% vs. 28.57% and 65.62% vs. 17.65%, respectively). The [^{18}F]F-choline was tolerated well. The use of [^{18}F]F-choline PET/CT resulted in an approximately 8% reduction in unnecessary extended lymphadenectomy compared with contrast-enhanced CT. Additionally, [^{18}F]F-choline PET/CT had a marginal impact on 5-y overall survival, contributing to a 4% increase in survival rates. **Conclusion:** In the initial staging of PCa, [^{18}F]F-choline PET/CT exhibited diagnostic performance superior to that of conventional imaging for detecting metastases. [^{18}F]F-choline PET/CT reduced the rate of unnecessary extensive lymphadenectomy by up to 8%. These findings support the consideration of discontinuing conventional imaging for staging PCa.

Key Words: fluorocholine; prostate cancer; diagnostic imaging; disease management; prognosis

J Nucl Med 2024; 65:1013–1020
DOI: 10.2967/jnumed.123.267355

Prostate cancer (PCa) remains the most prevalent malignancy among men, with metastatic progression contributing significantly to patient mortality (*1*). Current therapeutic decision-making regarding primary-tumor treatment depends on parameters such as prostate-specific antigen (PSA) value, clinical tumor stage, and biopsy Gleason score (*2*). However, the existing imaging tools and nomograms fall short in accurately staging early pelvic lymph node, bone, and distant metastases.

CT and MRI exhibit limited sensitivity and specificity in detecting small-volume metastatic disease, whereas whole-body bone scans may overlook early bone marrow metastases (*3*). Nonetheless, contrast-enhanced CT (ceCT) and whole-body bone scans are widely used as the standard initial diagnostic imaging modalities for staging localized PCa. Retrospective data suggest that PET imaging using [^{11}C]choline, [^{18}F]F-choline, or [^{18}F]fluoride is more accurate than conventional methods in detecting lymph node and bone metastases, both for staging and for restaging purposes (*4–7*). However, the promising accuracy of radiolabeled choline PET/CT in identifying lymph node involvement during primary staging is tempered by several limitations. These include low sensitivity for micrometastases, inherent nonspecificity of choline uptake, retrospective study designs, limited comparative data with conventional imaging, absence of cost-effectiveness evaluations,

Received Jan. 3, 2024; revision accepted May 7, 2024.
For correspondence or reprints, contact Laura Evangelista (laura.evangelista@hunimed.eu).
Published online Jun. 6, 2024.

and an uncertain impact on patient management. Consequently, current European and American guidelines do not recommend radiolabeled choline PET/CT in the initial staging of newly diagnosed PCa.

Recent advancements, notably radiolabeled prostate-specific membrane antigen (PSMA), have revolutionized PCa imaging, including the initial staging process, as evidenced by the proPSMA trial (*8*). Nonetheless, standardization efforts are under way to enhance the reproducibility and applicability of PSMA PET across different centers. Despite PSMA PET's superior accuracy in detecting metastatic spread and high-risk PCa, its ability to improve clinically relevant outcomes in advanced PCa remains unproven, and it cannot yet replace extended pelvic lymph node dissection (*2*). Currently, only preliminary data are available, from Djaïleb et al. (*9*).

Radiolabeled choline PET/CT remains of interest and is still used worldwide in the diagnostic management of PCa patients. In light of this, a prospective randomized multicenter study was conceived at a time when PSMA imaging was not widespread. This study aimed to compare PET/CT using [^{18}F]F-choline with conventional imaging for staging and managing intermediate- to high-risk PCa. The primary objective was to assess the efficacy of [^{18}F]F-choline PET/CT in identifying lymph node and systemic involvement in these patients at initial staging. Secondary objectives included evaluating the impact of [^{18}F]F-choline PET/CT on unnecessary local treatments and assessing the safety of [^{18}F]F-choline agents. An additional objective was to evaluate recurrence-free survival (RFS) and overall survival (OS) after 5 y from randomization.

MATERIALS AND METHODS

Study Design and Participants

This was a prospective controlled, open, randomized phase III trial involving 7 centers in Italy (Supplemental Table 1; supplemental materials are available at http://jnm.snmjournals.org).

Patients were eligible if they had intermediate- or high-risk PCa according to version 2.2013 of the National Comprehensive Cancer Network–National Comprehensive Cancer Network classification (e.g., PSA $\geq$ 10 ng/mL and Gleason score $\geq$ 7, Gleason score $\geq$ 8 with any PSA value, cT2c-T3 with any PSA value, or PSA $\geq$ 20 ng/mL with any Gleason score), were older than 18 y, were candidates for radical prostatectomy and lymphadenectomy or radiotherapy, and had accessible follow-up information.

Conversely, excluded from the study were patients with a previous history of cancer, metastases to lymph nodes, or metastases to other sites already confirmed by a histopathologic examination; patients who were candidates for hormone therapy as primary treatment because of their general health condition; patients who had already been treated with hormone therapy or previous radiotherapy; and patients who had psychiatric disorders contraindicating PET/CT examination (Supplemental Table 2).

The study protocol was performed in accordance with the Declaration of Helsinki, and all participants provided written informed consent before undergoing any study procedures. The study was approved by the Ethical Committee of the Veneto Institute of Oncology in November 2013 (EudraCT 2013-002511-99; approval 2013/54).

Randomization

Eligible patients were randomized using a 1:1 ratio. The study comprised 2 groups of patients: one was studied by conventional imaging (abdominopelvic ceCT and bone scanning), whereas the other was evaluated by conventional imaging plus [^{18}F]F-choline PET/CT (Supplemental Fig. 1). During the urologic visit, the patient's eligibility for the study was determined by collection of demographic information, medical history, blood serum results, and histopathologic data from the PCa biopsy. A web-based database (REDCap) was used for the randomization and for collecting all data.

Study Procedures

The patients underwent the imaging procedures within 1 mo.

ceCT of Abdomen and Pelvis. ceCT imaging was performed after contrast medium injection. For the lymph node staging, the short axis was measured in all lymph nodes using a cutoff of 10 mm. For distant metastases, any abnormalities in the skeleton, liver, lung, or adrenal gland were considered. Any bone metastases were classified as osteolytic, osteosclerotic, or mixed.

Bone Scanning. Whole-body bone scan images were obtained in anterior and posterior views, 2 or 3 h after ^{99m}Tc-methyldiphosphonate injection. The results were considered positive if there were solitary or multiple asymmetric areas of uptake not considered to be due to recent trauma or an osteoarticular degenerative disease. Conversely, negative findings were defined as no abnormal uptake outside the physiologic distribution of the tracer.

PET/CT. Whole-body PET/CT was performed from the vertex to the proximal femur at 6–7 bed positions (2–3 min per position), 60 min after intravenous administration of the tracer (3 MBq/kg dose of [^{18}F]F-choline). A low-dose whole-body CT scan (with no contrast enhancement; 140 kV, 80–120 mA) was used for attenuation correction and for anatomic localization of the sites of disease. A lymph node metastasis was defined as focal tracer uptake in the abdominopelvic lymph nodes (including nodes with a diameter $<$ 10 mm), subsequently confirmed by equivalent CT images. Weak [^{18}F]F-choline uptake ($<$liver uptake) in inguinal and mediastinal lymph nodes was considered to be reactive lymphadenitis and not pathologic (*10*). A distant metastasis was defined as focal tracer uptake coinciding with bone, liver, lung, or adrenal gland, whether or not it correlated with the morphologic pattern on CT (i.e., bone marrow lesions). The [^{18}F]F-choline PET/CT images were jointly interpreted at each center involved in the trial by 2 specialists trained to perform PET/CT imaging. Intra- and interassay variations were assessed by a masked review of all [^{18}F]F-choline images by an independent nuclear medicine specialist with specific training on [^{18}F]F-choline PET/CT images.

Gold Standard

The standard of reference was the histopathologic data from patients who underwent radical prostatectomy and lymphadenectomy (limited, extended, or superextended). Moreover, in patients who received radiotherapy, chemotherapy, or hormonal therapy, follow-up data were considered, including clinical evaluation, serial biochemistry, and conventional or [^{18}F]F-choline PET/CT imaging for at least 6 mo from the primary treatments. Biochemical recurrence was defined as recurrence after an increase in serum PSA level above 0.2 ng/mL or a serum PSA level above nadir plus 2.0 ng/mL after definitive radiotherapy (*11*).

Outcome Measures

The primary aim was to test the diagnostic performance of [^{18}F]F-choline PET/CT on a per-patient basis by calculating the method's sensitivity, specificity, positive predictive value, negative predictive value, and accuracy. For lymph node metastases, the obturator, external and internal iliac, pararectal, retroperitoneal (lumbar–aortic), and deep inguinal regions were considered. For bone metastases, the following sites were considered separately: pelvis, thoracic and lumbar spinal column, ribs, femurs, humerus, skull, and so on. For distant metastases, the considered sites included the distant lymph nodes (retroperitoneal and deep inguinal), lung, mediastinum, liver, adrenal glands, and soft tissues.

Secondary Endpoints

The proportion of avoidable local treatments was assessed by considering the number of patients who underwent surgery in each study arm. An unnecessary lymphadenectomy was defined as an extended or superextended lymphadenectomy in the case of pathologically confirmed absence of lymph node involvement (pN0) or stage IV disease.

The onset of side effects was examined in patients who were injected with [^{18}F]F-choline. Local tolerance to injection was examined, and cardiac and respiratory rates, as well as arterial blood pressure, were monitored before and after the PET examination. Finally, any symptoms experienced by patients were recorded both at the nuclear medicine department and through a telephone interview within 24 h after the examination. Toxicity was scored as grade 1 (mild adverse event), grade 2 (moderate adverse event), grade 3 (severe adverse event), grade 4 (life-threatening or disabling adverse event), or grade 5 (adverse event–related death), on the basis of the Common Terminology Criteria for Adverse Events.

RFS was defined as biochemical-recurrence–free survival and radiologic-evidence–free survival. Biochemical-recurrence–free survival was defined as the interval from randomization to the onset of biochemical recurrence (*12*,*13*). Radiologic-evidence–free survival was defined as the interval between randomization and the appearance of a PCa recurrence at any radiologic examination (e.g., ceCT, [^{18}F]F-choline PET/CT, or MRI). Finally, OS was defined as the interval between randomization and all-cause mortality.

Statistical Analysis

Eligible patients were randomized with a ratio of 1:1 to one of the two arms for their diagnostic assessment. Each arm included 195 patients, for a total of 390 patients involved in the study. To evaluate the dimension of the simple population, it was assumed that sensitivity for

TABLE 1
Characteristics of Population

Characteristic	Control arm (n = 117, 49.6%)	Experimental arm (n = 119, 50.4%)
Median age (y)	69.7 (51.5–81.2)	69 (43.4–83.7)
Risk of patient		
Intermediate	41 (35%)	46 (38.7%)
High	76 (65%)	73 (61.3%)
Familiarity		
No	74 (94.9%)	52 (86.7%)
Yes	4 (5.1%)	8 (13.3%)
Missing data	39	59
Performance status*		
<100	6 (5.7%)	4 (3.8%)
=100	100 (94.3%)	102 (96.2%)
Missing data	11	13
Initial PSA (ng/mL)	8.36 (1.67–580)	8.35 (2.40–98.31)
PSA category (ng/mL)		
≤4	9 (8.2%)	10 (8.5%)
4–10	56 (50.9%)	57 (48.3%)
10–20	30 (27.3%)	30 (25.4%)
>20	15 (13.6%)	21 (17.8%)
Gleason score		
6	1 (0.9%)	4 (3.4%)
7	49 (42.2%)	53 (44.5%)
8	51 (44%)	42 (35.3%)
9	13 (11.2%)	15 (12.6%)
10	2 (1.7%)	5 (4.2%)
Missing data	1	
Clinical T stage		
T1a-c	13 (11.4%)	18 (15.9%)
T2a-c	87 (76.3%)	80 (70.8%)
T3a-c	14 (12.3%)	15 (13.3%)
Missing data	3	6

*Karnofsky performance status.
Qualitative data are number and percentage; continuous data are median and range.

identifying lymph node metastases in this setting of patients was 18% (*11*). To demonstrate an absolute increase of 20% in the ability of [^{18}F]F-choline PET/CT to identify lymph node metastases, with a significance level (α) of 5% and a power of test of 80%, 137 positive lymph node patients were necessary (2-tailed χ^2 test). If a 35% prevalence of lymph node metastases was supposed, 195 patients for each arm were necessary, for a total of 390 patients. The study arms were compared using the χ^2 test. The results were expressed as percentages with 95% CIs. For the primary endpoint, a conventional methodology was used to evaluate diagnostic performance in terms of sensitivity, specificity, and accuracy for nodal and distant metastatic groups, together and separately. For secondary outcomes, the proportion of patients with a management effect were compared using the Fisher exact test. Safety profiles were compared using the Student unpaired *t* test. Finally, survival analysis was calculated using Kaplan–Meier analysis and log-rank testing.

RESULTS

Patient Population

From February 2016 to December 2020, 256 patients were randomly assigned at 7 sites. Table 1 includes the characteristics of patients for each group. Although the number of patients expected was 390, the accrual was stopped. However, the increase in diagnostic performance by [^{18}F]F-choline PET/CT was enriched, as reported below.

In total, 236 patients were considered for the final assessment: 117 in the control arm and 119 in the experimental arm (Fig. 1). Baseline characteristics were similar in each group. Most of the patients had Gleason scores of either 7 or 8, and roughly 65% of the patients had high-risk PCa. Most patients had the T2b stage (36.8% in the experimental arm and 29.2% in the control arm). The proportion of patients with a stage higher than T2 was 13.3% and 12.4% in the experimental and control groups, respectively. In the control arm versus the experimental arm, 41 (35%) versus 46 (38.7%) and 76 (65%) versus 73 (61.3%) patients had intermediate- and high-risk PCa, respectively.

Diagnostic Accuracy

The detection of lymph node metastases on ceCT was higher in the experimental group (n = 18, 15.1%) than in the control group (n = 9, 7.7%). Additionally, the incidence of bone or distant lymph node or liver metastases on ceCT was slightly higher in the experimental group (n = 12, 10.1%) than in the control group (n = 11, 9.4%). At bone scintigraphy, the experimental group had a slightly higher percentage of positive findings for bone metastases (n = 27, 22.9%) than did the control group (n = 24, 21.1%). PET/CT was positive for local lymph nodes and distant metastases (i.e., distant lymph nodes, bone, lung, or liver) in 41 (35%) and 13 (11%) patients, respectively. In the experimental arm, agreement between ceCT and [^{18}F]F-choline PET/CT for detection of local lymph nodes was 77.8% (n = 91/117).

A histologic reference standard was assessable in 159 patients (n = 73, 62.9%, and n = 86, 72.9%, in the control and experimental arms, respectively). Serial PSA levels within 6 mo from radiotherapy, hormonal therapy, chemotherapy, or a combination of more than one therapy was considered the gold standard in the remaining 77 patients. The most frequently performed surgical procedure was robot-assisted radical prostatectomy (49.3% in the control group and 41.2% in the experimental group), followed by open radical prostatectomy (45.1% in the control group and 48.2% in the experimental group) and laparoscopic radical prostatectomy (5.6% in the control group and 10.6% in the experimental group).

Lymphadenectomy was performed on 69 and 83 patients in the control and experimental groups, respectively. In the control arm, 62 (89.9%) patients were classified as pN0, whereas 7 (10.1%) patients had lymph node metastasis (pN1). Conversely, in the experimental group, 64 (77.1%) patients were pN0 and 18 (21.7%) were pN1. A median of 15 (range, 2–48) and 14 (range, 2–53) lymph nodes was removed in the control and experimental arms, respectively. On the basis of the combination of lymphadenectomy and serial PSA evaluation during follow-up, 66 patients were considered pN1: 34 (29.1%) in the control arm and 32 (27.6%) in the experimental arm. Table 2 presents the diagnostic performance of imaging techniques (ceCT alone vs. [^{18}F]F-choline PET/CT) for detecting lymph node metastases in both arms, with the final pathology finding of the lymphadenectomy serving as the reference standard. On the other hand, Table 3 reports the diagnostic performances for lymph node metastases in both arms by considering the final pathology finding of the lymphadenectomy and serial PSA evaluations as the standard of reference.

On the whole, sensitivities were higher in the experimental arm than in the control one (77.78% vs. 28.57% [P = 0.0661], and 65.62% vs. 17.65% [P = 0.0002], respectively), both in the case of lymphadenectomy as the standard of reference and in the case of histopathology plus serial PSA evaluation as the standard of reference. However, a slight decrease in specificity was reported in both cases ($P < 0.02$). Possibly, some lymph nodes showing signs of inflammation were considered positive during the analysis of the PET images. Nevertheless, although not statistically significant, the negative predictive values were higher in the experimental arms, independently of disease prevalence.

Tables 4 and 5 describe the diagnostic accuracies of imaging techniques in the different risk groups of patients. Because of the limited number of intermediate-risk patients with positive lymph nodes at histopathology, data were missing. However, in the high-risk group, [^{18}F]F-choline PET/CT was more sensitive than ceCT in detecting pathologic lymph nodes (75% vs. 16.67%, respectively). When the combined reference standard was used, the higher value for the sensitivity in the experimental group than in the control one was confirmed in patients with high-risk PCa. Moreover, in intermediate-risk PCa patients, [^{18}F]F-choline PET/CT registered a sensitivity of 50% and a negative predictive value of 87.88%.

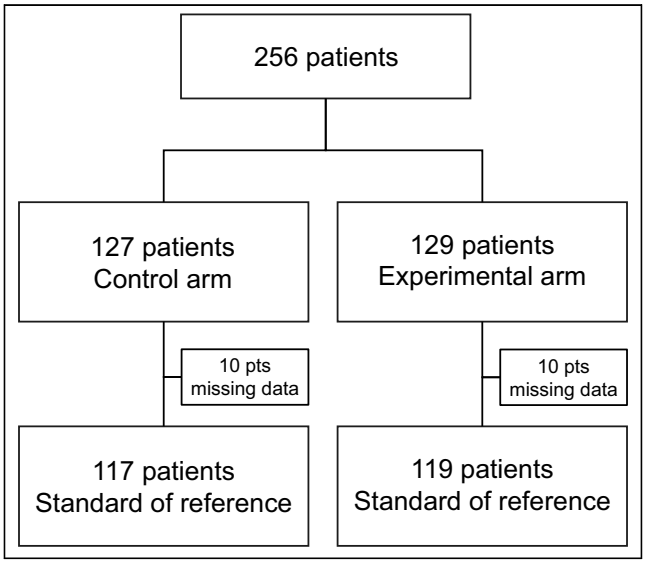

FIGURE 1. Trial profile.

TABLE 2
Diagnostic Performance for Lymph Node Disease in Control and Experimental Arms, Based on Histopathologic Data

Statistic	Control arm	Experimental arm	*P*
Sensitivity	28.6% (3.7%–71%)	77.8% (52.4%–93.6%)	0.0661
Specificity	95.2% (86.5%–99%)	79.7% (67.8%–88.7%)	0.0193
Positive LR	5.9 (1.2–29.5)	3.8 (2.2–6.6)	—
Negative LR	0.8 (0.5–1.2)	0.3 (0.12–0.67)	—
PPV	40% (11.8%–76.9%)*; 76.6% (39.5%–94.2%)†	51.9% (38.6%–65%)‡; 66.5% (53.5%–77.4%)§	1.0000
NPV	92.2% (88%–95%)*; 70.7% (60.1%–79.4%)†	92.7% (84.2%–96.8%)‡; 87.4% (74.3%–94.3%)§	1.0000
Accuracy	88.4% (78.4%–94.9%)*; 71.5% (59.3%–81.7%)†	79.3% (68.9%–87.4%)‡; 79% (68.6%–87.3%)§	—

*Estimated disease prevalence = 10.14%.
†Disease prevalence in population = 35.60%.
‡Estimated disease prevalence = 21.95%.
§Disease prevalence in population = 34.10%.
LR = likelihood ratio; PPV = positive predictive value; NPV = negative predictive value.
Data in parentheses are 95% CIs.

Unnecessary Lymphadenectomy

On the basis of the definition of unnecessary lymphadenectomy, 20 of 117 (17.1%) and 13 of 119 (10.9%) patients received an extended or superextended lymphadenectomy in the case of pathologically confirmed absence of lymph node involvement (pN0) or stage IV disease, respectively, in the control and experimental arms.

Tolerance of [^{18}F]F-Choline Injection

Data about the tolerance of [^{18}F]F-choline injection were available for 63 of 119 (53%) patients. The radiopharmaceutical was well tolerated. No side effects or adverse effects were reported by the patients during the 24 h after the examination (Supplemental Fig. 2).

Survival Analysis

Median follow-up time was 4.43 y (interquartile range, 2.74–5.18 y). At survival analysis, 29 of 117 (24.8%) and 32 of 119 (26.9%) patients in the control and experimental arms experienced recurrence of disease (either biochemical or radiologic recurrence). However, 8 of 117 and 8 of 119 died in the control and experimental arms, respectively, whether related to the cancer or not. Figure 2 reports the Kaplan–Meier analysis for OS and RFS. The 5-y OS was 88.5% versus 92.4% (log-rank test, $P = 0.762$), and the 5-y RFS was 66.4% versus 67.4% (log-rank test, $P = 0.915$), in the control and experimental arms, respectively.

Furthermore, across all patient populations, the detection of positive nodes by histopathology plus serial PSA evaluation correlated with a 5-y OS of 66.7% in the control arm and 90.9% in the experimental arm, as well as a 5-y RFS of 41.7% in the control arm and 62.7% in the experimental arm. However, these differences were not statistically significant (log-rank test, $P = 0.6224$ for OS and $P = 0.6221$ for RFS in the control and experimental arms, respectively) (Figs. 3A and 3C). In contrast, among patients with negative

TABLE 3
Diagnostic Performance for Lymph Node Disease in Control and Experimental Arms, Based on Histopathologic Data and Serial PSA Levels During Follow-up

Statistic	Control arm	Experimental arm	*P*
Sensitivity	17.7 (6.8%–34.5%)	65.6% (46.8%–81.4%)	0.0002
Specificity	96.4% (89.8%–99.3%)	75% (64.4%–83.8%)	0.0002
Positive LR	4.88 (1.29–18.41)	2.62 (1.68–4.11)	—
Negative LR	0.85 (0.73–1.00)	0.46 (0.28–0.75)	—
PPV	66.7% (34.7%–88.3%)*; 74.9% (44.3%–91.9%)†	50% (39%–61%)‡; 60.5% (49.4%–70.5%)§	0.5884
NPV	74.1% (70.9%–77.1%)*; 65.6% (61.9%–69.2%)†	85.1% (77.7%–90.4%)‡; 78.9% (69.6%–86%)§	0.1091
Accuracy	73.5% (64.6%–81.2%)*; 66.5% (57.2%–74.9%)†	72.4% (63.3%–80.3%)‡; 71.6% (62.4%–79.5%)§	—

*Estimated disease prevalence = 29.06%.
†Disease prevalence in population = 38.00%.
‡Estimated disease prevalence = 27.59%.
§Disease prevalence in population = 36.80%.
LR = likelihood ratio; PPV = positive predictive value; NPV = negative predictive value.
Data in parentheses are 95% CIs.

TABLE 4
Diagnostic Performance for Lymph Node Disease in Control and Experimental Arms, Based on Histopathologic Data

Statistic	Control arm		Experimental arm	
	Intermediate	High	Intermediate	High
Sensitivity	—	16.7% (0.4%–64.1%)	—	75% (47.6%–92.7%)
Specificity	—	92.1% (78.6%–98.3%)	—	75% (56.6%–88.5%)
Positive LR	—	2.11 (0.26–17.12)	—	3 (1.55–5.82)
Negative LR	—	0.90 (0.63–1.31)	—	0.33 (0.14–0.80)
PPV	—	25% (60%–80.6%)*	—	60% (36%–80.1%)†
NPV	—	87.5% (73.2%–95.8%)*	—	85.7% (67.3%–96%)†
Accuracy	—	81.8% (67.3%–91.8%)*	—	75% (60.4%–86.4%)†

*Disease prevalence in population = 13.64%.
†Disease prevalence in population = 33.33%.
LR = likelihood ratio; PPV = positive predictive value; NPV = negative predictive value.
Data in parentheses are 95% CIs.

lymph node status at histopathology plus serial PSA evaluation, both 5-y OS and 5-y RFS were comparable between the control and experimental arms, with rates of 90.4% versus 93.0% (log-rank test, $P = 0.4878$) for OS and 68.8% versus 71.0% (log-rank test, $P = 0.6160$), respectively, for RFS (Figs. 3B and 3D).

DISCUSSION

In the present prospective study, we found that in lymph node and bone metastases, [^{18}F]F-choline PET/CT had a per-patient diagnostic accuracy superior to that of conventional imaging alone in men with intermediate- and high-risk PCa. This finding reinforces data from retrospective single-center studies that have suggested potentially higher accuracy for [^{18}F]F-choline PET/CT than for ceCT and bone scanning in the staging of disease (*7*,*14*–*16*). Beheshti et al. (*17*) correlated histopathologic findings after radical prostatectomy and extended lymphadenectomy in 111 patients with intermediate- and high- risk of PCa. Using a patient-based analysis, they reported a sensitivity of 45% and a specificity of 96% for lymph node disease. The authors underlined the failure of [^{18}F]F-choline PET/CT to detect the presence of micrometastatic lymph nodes. Poulsen et al. (*18*) reported, at patient-based analysis, a slightly higher sensitivity of 73.2% and a quite similar specificity of 87.6%. Evangelista et al. (*7*), by a comparison between conventional imaging (i.e., ceCT) and [^{18}F]F-choline PET/CT, demonstrated that the latter is more accurate for the identification of lymph node and distant metastases than are conventional modalities (46.2% vs. 69.2% for CT and PET/CT, respectively). Moreover, [^{18}F]F-choline PET/CT is able to detect bone marrow metastases early, with sensitivity of 79%–100% and specificity of 77.2%–97% (*7*,*19*). In accordance with these latter 2 authors, the present study demonstrated [^{18}F]F-choline PET/CT to be superior to

TABLE 5
Diagnostic Performance for Lymph Node Disease in Control and Experimental Arms, Based on Histopathologic Data and Serial PSA Levels During Follow-up

Statistic	Control arm		Experimental arm	
	Intermediate	High	Intermediate	High
Sensitivity	—	20.8% (7.1%–42.1%)	50% (15.7%–84.3%)	70.9% (48.9%–87.4%)
Specificity	—	94.2% (84.1%–98.8%)	78.4% (61.8%–90.2%)	72.3% (57.4%–84.4%)
Positive LR	—	3.61 (0.94–13.89)	2.31 (0.92–5.83)	2.56 (1.51–4.35)
Negative LR	—	0.84 (0.68–1.04)	0.64 (0.31–1.30)	0.40 (0.21–0.77)
PPV	—	62.5 (24.5%–91.5%)*	33.3% (9.9%–65.1%)†	56.7% (37.4%–74.5%)‡
NPV	—	72.1% (49.9%–82.3%)*	87.9% (71.8%–96.6%)†	82.9% (67.9%–92.9%)‡
Accuracy	—	71.1% (59.5%–80.9%)*	73.3% (58.1%–85.4%)†	71.8% (59.9%–81.9%)‡

*Disease prevalence in population = 31.58%.
†Disease prevalence in population = 17.78%.
‡Disease prevalence in population = 33.80%.
LR = likelihood ratio; PPV = positive predictive value; NPV = negative predictive value.
Data in parentheses are 95% CIs.

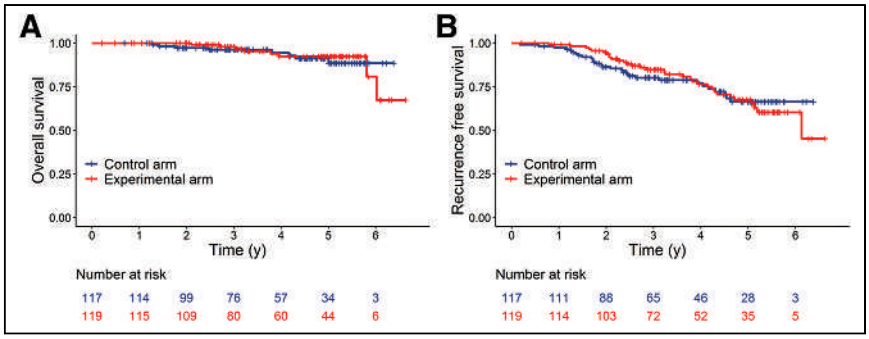

FIGURE 2. Kaplan–Meier curves for OS (A) and RFS (B) stratified according to randomization arm.

ceCT alone for the identification of lymph node disease, with sensitivities of 78% and 66%, respectively, as compared with histopathologic evaluation or the combination of histopathology and serial PSA levels. However, early detection of lymph node disease before surgery can be valuable in reducing the number of aggressive lymphadenectomy procedures or guiding selective lymphadenectomy to avoid unnecessary complications. In the present study, we found about an 8% reduction in unnecessary extended lymphadenectomy with [^{18}F]F-choline PET/CT as compared with ceCT—an interesting finding considering the high incidence of PCa and the complications due to the surgical procedure. However, much effort is ongoing to identify algorithms able to reduce the number of unnecessary extended lymphadenectomy procedures, using PSMA-based PET (*20*).

After radical prostatectomy, approximately 35% of patients will experience biochemical recurrence within 10 y (*21–24*). One reason for this high rate of treatment failure is the limited accuracy of conventional imaging in detecting metastatic disease ab initio. However, to our knowledge, this was the first prospective study that evaluated the effect on the outcome of [^{18}F]F-choline PET/CT versus conventional imaging. Indeed, the 5-y OS was slightly higher in the experimental arm than in the control arm (92.4% vs. 88.5%, respectively), although not statistically significant. However, if the incidence rate range provided by Giona were used (6.3–83.4 per 100,000 people) (*25*), the numbers of individuals affected by intermediate- and high-risk PCa would range from 6.3 to 83,400. Subsequently, approximately 6,552–86,736 individuals could benefit from a 4% increase in survival.

On the other hand, 5-y RFS was similar in both groups. Recently, a study by Urso et al. (*26*) demonstrated that, in real-world experience, [^{18}F]F-choline PET/CT as a tool for the initial management of PCa had a relevant impact in terms of therapy selection and was associated with longer biochemical RFS. Preliminary data about the prognostic value of [^{68}Ga]Ga-PSMA-11 PET–detected nodal involvement in 251 patients without distant metastases, after a follow-up period of 54 mo, were discussed at the last European Congress of Nuclear Medicine (*27*). Patients without lymph node involvement on [^{68}Ga]Ga-PSMA-11 PET imaging were free from treatment failure longer than those with N1M0 disease (hazard ratio, 2.1; range, 1.2–3.17; $P < 0.01$). Conversely, CT- and bone scan–defined N0M0 versus N1M0 were not prognostic (hazard ratio, 0.6; range, 0.1–2.4; $P = 0.45$). In this trial, we confirmed that the presence of positive nodes at histopathologic/PSA evaluation impacted long-term survival outcomes; additionally, [^{18}F]F-choline PET/CT further stratified them, although the observed differences in OS and RFS between the control and experimental arms did not reach statistical significance. Interestingly, among patients with negative lymph node status, there were no notable differences in 5-y OS and RFS rates between the 2 arms. A prolonged follow-up is undoubtedly necessary to comprehensively evaluate the impact of [^{18}F]F-choline PET on long-term outcomes for patients with intermediate- and high-risk PCa.

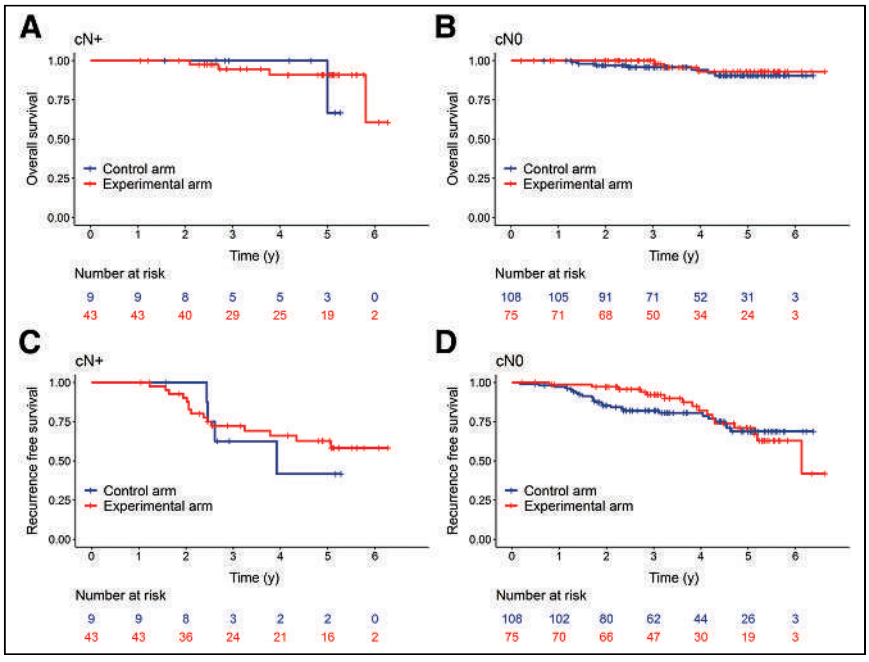

FIGURE 3. Kaplan–Meier curves for OS (A and B) and RFS (C and D) stratified according to positive (A and C) or negative (B and D) lymph nodes at histopathologic and PSA evaluation.

The current trial had some limitations. First, the inability to mask the imaging modality during randomization introduced potential bias. Second, histopathologic assessment was not available in some participants, especially those with local or distant nodal metastases who underwent radiotherapy. However, to overpass this limitation, we used a reference standard incorporating 6 mo of follow-up with serial PSA evaluations and repeated imaging, if needed, which is considered a robust method. Finally, although there has been a large expansion of PSMA-targeted tracers, these agents remain unavailable in certain countries and smaller hospitals. Therefore, the availability of alternative radiopharmaceutical agents for PET imaging could prove invaluable in furthering the expansion of nuclear medicine modalities, particularly in underserved regions and smaller health care facilities.

CONCLUSION

[^{18}F]F-choline PET/CT has demonstrated higher diagnostic performance than conventional imaging in detecting both

lymph node and bone metastases. Moreover, it can reduce the rate of unnecessary extensive lymphadenectomy in more than 8% of patients. Finally, it can slightly affect the 5-y OS, increasing the survival rate to 4%. These results provide additional evidence supporting the discontinuation of conventional imaging for staging PCa.

DISCLOSURE

This clinical trial was supported for a limited number of patients by IASON GmBh (^{18}F-choline supply for 73 patients and a small amount of the insurance payment for patients). IASON GmBh had no role in the study design, data collection, data analysis, data interpretation, or writing of the paper. Prof. Giacomo Novara and Prof. Filiberto Zattoni have additionally supported the clinical trial by a grant from the University of Padua (for the supply of ^{18}F-choline in the remaining enrolled patients and other additional costs). No other potential conflict of interest relevant to this article was reported.

ACKNOWLEDGMENTS

The study group coinvestigators are Luigi Corti, Matteo Sepulcri, Vittorina Zagonel, Umberto Basso, Marco Maruzzo, Luca De Zorzi, Tommaso Silvestri, Enrico Pizzirani, Filiberto Zattoni, Giuseppe Costa, Andrea Guttilla, Andrea Agostini, Angelo Porreca, Paolo Corsi, Massimo Dal Bianco, Mario Gardi, Giovanni Maria Ceresoli, Fabio Matrone, and Roberto Bortolus. We thank all the staff at the Clinical Trials and Biostatistics Unit of the Veneto Institute of Oncology for trial coordination, including Dr. Marina Salomoni (clinical research coordinator) and Drs. Marco Braggion and Beatrice Barbaro (monitoring study coordinators).

KEY POINTS

QUESTION: Is PET/CT with [^{18}F]F-choline able to identify lymph node and systemic involvement during initial staging in intermediate- and high-risk PCa patients?

PERTINENT FINDINGS: A prospective controlled, open, randomized multicenter phase III trial involving 7 Italian centers enrolled 236 patients (117 in the control arm and 119 in the experimental arm). In the experimental arm, the sensitivity for lymph node metastases was higher than in the control arm (77.78% vs. 28.57% and 65.62% vs. 17.65%, respectively).

IMPLICATIONS FOR PATIENT CARE: In the initial staging of PCa, [^{18}F]F-choline PET/CT exhibited superior diagnostic performance to conventional imaging for detecting metastases, thus supporting the consideration of discontinuing conventional imaging in this setting of disease.

REFERENCES

1. Siegel RL, Miller KD, Jemal A. Cancer statistics, 2019. *CA Cancer J Clin.* 2019; 69:7–34.
2. Mottet N, Cornford P, van den Bergh RCN, et al. Prostate cancer. European Association of Urology website. https://uroweb.org/guidelines/prostate-cancer. Accessed May 20, 2024.
3. Wollin DA, Makarov DV. Guideline of guidelines: imaging of localized prostate cancer. *BJU Int.* 2015;116:526–530.
4. Cimitan M, Bortolus R, Morassut S, et al. [^{18}F]fluorocholine PET/CT imaging for the detection of recurrent prostate cancer at PSA relapse: experience in 100 consecutive patients. *Eur J Nucl Med Mol Imaging.* 2006;33:1387–1398.
5. Husarik DB, Miralbell R, Dubs M, et al. Evaluation of [^{18}F]-choline PET/CT for staging and restaging of prostate cancer. *Eur J Nucl Med Mol Imaging.* 2008;35:253–263.
6. DeGrado TR, Coleman RE, Wang S, et al. Synthesis and evaluation of ^{18}F-labeled choline as an oncologic tracer for positron emission tomography: initial findings in prostate cancer. *Cancer Res.* 2001;61:110–117.
7. Evangelista L, Cimitan M, Zattoni F, et al. Comparison between conventional imaging (abdominal-pelvic computed tomography and bone scan) and [^{18}F]choline positron emission tomography/computed tomography imaging for the initial staging of patients with intermediate- to high-risk prostate cancer: a retrospective analysis. *Scand J Urol.* 2015;49:345–353.
8. Hofman MS, Lawrentschuk N, Francis RJ, et al.; proPSMA Study Group Collaborators. Prostate-specific membrane antigen PET-CT in patients with high-risk prostate cancer before curative-intent surgery or radiotherapy (proPSMA): a prospective, randomised, multicentre study. *Lancet.* 2020;395:1208–1216.
9. Djaïleb L, Armstrong WR, Thompson D, et al. Presurgical ^{68}Ga-PSMA-11 positron emission tomography for biochemical recurrence risk assessment: a follow-up analysis of a multicenter prospective phase 3 imaging trial. *Eur Urol.* 2023;84:588–596.
10. Rietbergen DD, van der Hiel B, Vogel W, et al. Mediastinal lymph node uptake in patients with prostate carcinoma on F18-choline PET/CT. *Nucl Med Commun.* 2011;32:1143–1147.
11. Lee SU, Kim JS, Kim YS, et al. Optimal definition of biochemical recurrence in patients who receive salvage radiotherapy following radical prostatectomy for prostate cancer. *Cancer Res Treat.* 2022;54:1191–1199.
12. Cookson MS, Aus G, Burnett AL, et al. Variation in the definition of biochemical recurrence in patients treated for localized prostate cancer: the American Urological Association Prostate Guidelines for Localized Prostate Cancer Update Panel report and recommendations for a standard in the reporting of surgical outcomes. *J Urol.* 2007;177:540–545.
13. Heidenreich A, Aus G, Bolla M, et al. EAU guidelines on prostate cancer. *Eur Urol.* 2008;53:68–80.
14. Nitsch S, Hakenberg OW, Heuschkel M, et al. Evaluation of prostate cancer with ^{11}C- and ^{18}F-choline PET/CT: diagnosis and initial staging. *J Nucl Med.* 2016;57(suppl 3): 38S–42S.
15. Husarik DB, Miralbell R, Dubs M, et al. Evaluation of [^{18}F]-choline PET/CT for staging and restaging of prostate cancer. *Eur J Nucl Med Mol Imaging.* 2008;35:253–263.
16. Gutman F, Aflalo-Hazan V, Kerrou K, et al. ^{18}F-choline PET/CT for initial staging of advanced prostate cancer. *AJR.* 2006;187:W618-W621.
17. Beheshti M, Imamovic L, Broinger G, et al. ^{18}F choline PET/CT in the preoperative staging of prostate cancer in patients with intermediate or high risk of extracapsular disease: a prospective study of 130 patients. *Radiology.* 2010;254:925–933.
18. Poulsen MH, Bouchelouche K, Høilund-Carlsen PF, et al. [^{18}F]fluoromethylcholine (FCH) positron emission tomography/computed tomography (PET/CT) for lymph node staging of prostate cancer: a prospective study of 210 patients. *BJU Int.* 2012;110:1666–1671.
19. Beheshti M, Vali R, Waldenberger P, et al. The use of F-18 choline PET in the assessment of bone metastases in prostate cancer: correlation with morphological changes on CT. *Mol Imaging Biol.* 2009;11:446–454.
20. Gandaglia G, Barletta F, Robesti D, et al. Identification of the optimal candidates for nodal staging with extended pelvic lymph node dissection among prostate cancer patients who underwent preoperative prostate-specific membrane antigen positron emission tomography. external validation of the Memorial Sloan Kettering Cancer Center and Briganti nomograms and development of a novel tool. *Eur Urol Oncol.* 2023;6:543–552.
21. Han M, Partin AW, Pound CR, et al. Long-term biochemical disease-free and cancer-specific survival following anatomic radical retropubic prostatectomy. The 15-year Johns Hopkins experience. *Urol Clin North Am.* 2001;28:555–565.
22. Roehl KA, Han M, Ramos CG, et al. Cancer progression and survival rates following anatomical radical retropubic prostatectomy in 3,478 consecutive patients: long-term results. *J Urol.* 2004;172:910–914.
23. Hull GW, Rabbani F, Abbas F, et al. Cancer control with radical prostatectomy alone in 1,000 consecutive patients. *J Urol.* 2002;167:528–534.
24. Amling CL, Blute ML, Bergstralh EJ, et al. Long-term hazard of progression after radical prostatectomy for clinically localized prostate cancer: continued risk of biochemical failure after 5 years. *J Urol.* 2000;164:101–105.
25. Giona S. The epidemiology of prostate cancer. In: Bott SRJ, Ng KL, eds. *Prostate Cancer.* Exon Publications; 2021:1–15.
26. Urso L, Rocca GC, Borgia F, et al. The role of [^{18}F]F-choline PET/CT in the initial management and outcome prediction of prostate cancer: a real-world experience from a multidisciplinary approach. *Biomedicines.* 2022;10:2463.
27. Kasivisvanathan V, Link E, Lawrentschuk N, et al. Baseline PSMA PET-CT is prognostic for treatment failure in men with intermediate-to-high risk prostate cancer: 54 months follow-up of the proPSMA randomised trial [abstract]. *Eur J Nucl Med Mol Imaging.* 2023;50(suppl 1):037.

Diagnostic Performance of [^{18}F]AlF-Thretide PET/CT in Patients with Newly Diagnosed Prostate Cancer Using Histopathology as Reference Standard

Jie Zang*[1,2], Yun Yang*[1,2], Shaoming Chen*[1,2], Chao Wang[1,2], Shaohao Chen[3], Shun Hu[4], Hai Cai[3], Xiaodong Li[3], Ning Xu[3], Xiaoyuan Chen†[5–9], Jingjing Zhang†[5–7], and Weibing Miao†[1,2,10]

[1]*Department of Nuclear Medicine, First Affiliated Hospital, Fujian Medical University, Fuzhou, China;* [2]*Department of Nuclear Medicine, National Regional Medical Center, Binhai Campus of First Affiliated Hospital, Fujian Medical University, Fuzhou, China;* [3]*Department of Urology, First Affiliated Hospital, Fujian Medical University, Fuzhou, China;* [4]*Department of Pathology, First Affiliated Hospital, Fujian Medical University, Fuzhou, China;* [5]*Department of Diagnostic Radiology, Yong Loo Lin School of Medicine, National University of Singapore, Singapore, Singapore;* [6]*Clinical Imaging Research Centre, Centre for Translational Medicine, Yong Loo Lin School of Medicine, National University of Singapore, Singapore, Singapore;* [7]*Nanomedicine Translational Research Program, NUS Center for Nanomedicine, Yong Loo Lin School of Medicine, National University of Singapore, Singapore, Singapore;* [8]*Department of Chemical and Biomolecular Engineering and Department of Biomedical Engineering, College of Design and Engineering, National University of Singapore, Singapore, Singapore;* [9]*Institute of Molecular and Cell Biology, Agency for Science, Technology, and Research, Proteos, Singapore, Singapore; and* [10]*Fujian Key Laboratory of Precision Medicine for Cancer, First Affiliated Hospital, Fujian Medical University, Fuzhou, China*

This study aimed to assess the diagnostic value of [^{18}F]AlF-thretide PET/CT in patients with newly diagnosed prostate cancer (PCa). **Methods:** In total, 49 patients with biopsy-proven PCa were enrolled in this prospective study. All patients underwent [^{18}F]AlF-thretide PET/CT, and the scoring system of the PRIMARY trial was used for PET image analysis. The dosimetry evaluation of [^{18}F]AlF-thretide was performed on 3 patients. Pathologic examination was used as the reference standard to evaluate the location, number, size, and Gleason score of tumors, for comparison with the [^{18}F]AlF-thretide PET/CT results. PSMA expression was evaluated by immunohistochemical staining. **Results:** All patients tolerated the [^{18}F]AlF-thretide PET/CT well. The total effective dose of [^{18}F]AlF-thretide was 1.16E−02 mSv/MBq. For patient-based analysis of intraprostatic tumors, 46 of 49 (93.9%) patients showed pathologic uptake on [^{18}F]AlF-thretide PET/CT. For lesion-based analysis of intraprostatic tumors, the sensitivity and positive predictive value for [^{18}F]AlF-thretide PET/CT were 58.2% and 90.5%, respectively. Delayed images can detect more lesions than standard images (n = 57 vs. 49, P = 0.005), and the SUV_{max} and tumor-to-background ratio of the former were higher than those of the latter (SUV_{max}: 14.5 ± 16.7 vs. 11.4 ± 13.6, $P < 0.001$; tumor-to-background ratio: 37.1 ± 42.3 vs. 23.1 ± 27.4, $P < 0.001$). The receiver-operating-characteristic curve analysis showed that the areas under the curve for PRIMARY score–predicted true-positive and false-positive lesions were significantly higher than those for the SUV_{max} of standard images (P = 0.015) and seemed higher than those for the SUV_{max} of delayed images (P = 0.257). [^{18}F]AlF-thretide PET/CT showed a higher detection rate than multiparametric MRI for all intraprostatic foci (53.5% vs. 40.8%, P = 0.012) and clinically significant PCa (75.0% vs. 61.4%, P = 0.031). **Conclusion:** [^{18}F]AlF-thretide PET/CT showed high diagnostic value for patients with primary PCa and can be used as an excellent imaging modality for preoperative evaluation of PCa patients.

Key Words: [^{18}F]AlF-thretide; prostate cancer; PRIMARY score; mpMRI

J Nucl Med 2024; 65:1021–1026
DOI: 10.2967/jnumed.123.266940

Prostate cancer (PCa) is one of the most common malignant neoplasms in men (*1*). Because of the advancements in various imaging modalities complementing traditional prostate-specific antigen screening, accurate diagnosis in a larger percentage of affected men has been possible in recent years. Prostate-specific membrane antigen (PSMA) is a transmembrane glycoprotein overexpressed in PCa cells (*2*). The concept of targeting PSMA for imaging and therapy in PCa has been around since the late 1990s and early 2000s, but it was not until the current decade that PSMA-targeted radiopharmaceuticals entered the field of clinical nuclear medicine, such as the most widely used, [^{68}Ga]Ga-PSMA-11 (*3*), and its related derivatives including [^{68}Ga]Ga-PSMA-I&T, [^{18}F]F-DCFPyL, [^{18}F]F-PSMA-1007, and [^{18}F]F-rhPSMA-7.3 (*4*).

For PET imaging, ^{18}F-labeled radiotracers have demonstrated several advantages over ^{68}Ga (half-life, 68 min), including the longer half-life (110 min) and larger-scale radiosynthesis, which may allow transportation to satellite nuclear medicine centers and thus benefit more patients (*5*). In addition, the lower positron emission energy of ^{18}F than of ^{68}Ga (0.65 vs. 1.90 MeV) may also improve the theoretic maximum spatial resolution to obtain higher-quality images (*5*,*6*). Al^{18}F labeling is a method that has been viewed as promising because of its simplicity, short reaction time, and potential for kit preparation (*7*). An Al^{18}F-labeled PSMA ligand (denoted as [^{18}F]AlF-thretide or [^{18}F]AlF-PSMA-BCH) was synthesized using Al^{18}F labeling; this ligand possesses the NOTA structure, strong stability, and the advantages of ^{18}F-labeled

Received Oct. 24, 2023; revision accepted Mar. 25, 2024.
For correspondence or reprints, contact Weibing Miao (miaoweibing@126.com) or Jingjing Zhang (j.zhang@nus.edu.sg).
*Contributed equally to this work.
†Contributed equally to this work.
Published online May 9, 2024.

radiopharmaceuticals. Previous studies have shown that [^{18}F]AlF-thretide has high stability in vitro and in vivo and can accumulate specifically in PCa with high binding affinity, safety, and selectivity, which may result in high diagnostic efficacy (*7*).

Here, we aimed to further investigate the diagnostic accuracy and whole-body radiation dosimetry of [^{18}F]AlF-thretide PET/CT in patients with newly diagnosed, treatment-naïve PCa using histopathology as a reference standard.

MATERIALS AND METHODS

This study was approved by the Ethics Committee of the First Affiliated Hospital, Fujian Medical University (approval [2022]023) and registered at ClinicalTrials.gov (NCT05516329). All participants signed a written informed consent form. Participants who met the inclusion criteria (as stated in the supplemental materials, available at http://jnm.snmjournals.org) underwent [^{18}F]AlF-thretide PET/CT.

The patients were observed for any drug-related adverse events, and the vital parameters of the patients were followed up for 1 wk. The methods are detailed in the supplemental data.

Image Analysis

For each eligible patient, 2 nuclear medicine physicians who were unaware of the prostate multiparametric MRI (mpMRI) and pathologic results evaluated the [^{18}F]AlF-thretide images. SUV_{max} was measured in tumors, and SUV_{mean} was measured in normal organs. The tumor-to-background ratio was defined as the SUV_{max} of tumors divided by the SUV_{mean} of the gluteus maximus. The scoring system of the PRIMARY trial was used to assess the intraprostatic tumors (*8*). Briefly, a 5-level PRIMARY score was assigned on the basis of the most clinically significant patterns and SUV_{max}. Lack of any pattern was given a score of 1; a diffuse transition zone or central zone (not focal), a score of 2; a focal transition zone, a score of 3; a focal peripheral zone, a score of 4; and an SUV_{max} of at least 12, a score of 5. A PRIMARY score of 3–5 was a high-risk pattern (tumor). For extraprostatic lesions, any focal [^{18}F]AlF-thretide uptake above the surrounding background activity that could not be explained by benign or physiologic tracer uptake was considered a tumor. A consensus of imaging, clinical, and follow-up findings was used to determine the distant metastases, which were not verified by histopathology. Dose estimation based on dynamic PET data was analyzed using Hermes software (Hermes Medical Solutions). Details were as described previously (*9*).

All mpMR images were interpreted by 2 independent radiologists (with 10 and 15 y of experience in MRI) while masked to [^{18}F]AlF-thretide PET/CT and pathologic data. Any disagreements between readers were resolved by consensus with a third radiologist. The mpMRI component was scored according to Prostate Imaging Reporting and Data System version 2.1 (*10*). Studies with lesions scored as 3 or above were considered positive.

Histopathology Analysis

A genitourinary pathologist read each section (tissue sections of 4 mm, histologic sections cut at 3 μm, each cross-section divided equally into 4–8 parts) and assessed each lesion for location, area of cancer foci, and International Society of Urological Pathology (ISUP) grade. Then, the histologic samples were digitized using the Motic VM 3.0 digital slice scanning and application system (version 1.0.7.60; Motic China Group Co., Ltd.). The obtained images were arranged and reoriented for comparison between histology and PET imaging. Lesions at the same location on adjacent layers were defined as the same lesion. To define imaging–pathology correspondence on a lesion level, the PET image was rebuilt to a corresponding thickness of 4 mm and a neighboring approach was used (*11*,*12*). This approach allowed the location correspondence to involve the immediately adjacent segments to overcome possible interpretation errors from inaccurate registration. Clinically significant PCa was defined as an ISUP grade group of at least 2.

Outcomes

The primary endpoint was diagnostic accuracy, on both a per-patient and a per-lesion basis. The additional primary endpoint was radiation dosimetry evaluation. The secondary endpoint was safety evaluation based on the Common Toxicity Criteria for Adverse Events 5.0.

The methods for patient inclusion and exclusion criteria, radiopharmaceutical, PET imaging procedures, safety evaluation, mpMRI protocol, immunohistochemistry, and statistical analysis are provided in the supplemental materials (*13*–*15*).

RESULTS

Patient Characteristics and Safety

From August 2022 to March 2023, 49 patients were enrolled in the study. Among them, 4 patients were rated as having low-risk PCa, 15 patients as having intermediate-risk PCa, and 30 patients as having high-risk PCa. Further patient characteristics are listed in Supplemental Table 1.

All patients tolerated the [^{18}F]AlF-thretide PET/CT well. No significant drug-related side effects were reported during follow-up, and vital parameters remained stable. The results are detailed in the supplemental materials.

Biodistribution and Dosimetry

Three patients underwent dynamic PET scans for dosimetry calculations. The representative maximum-intensity projections and biodistribution data assessed by SUV kinetics are shown in Figure 1. The

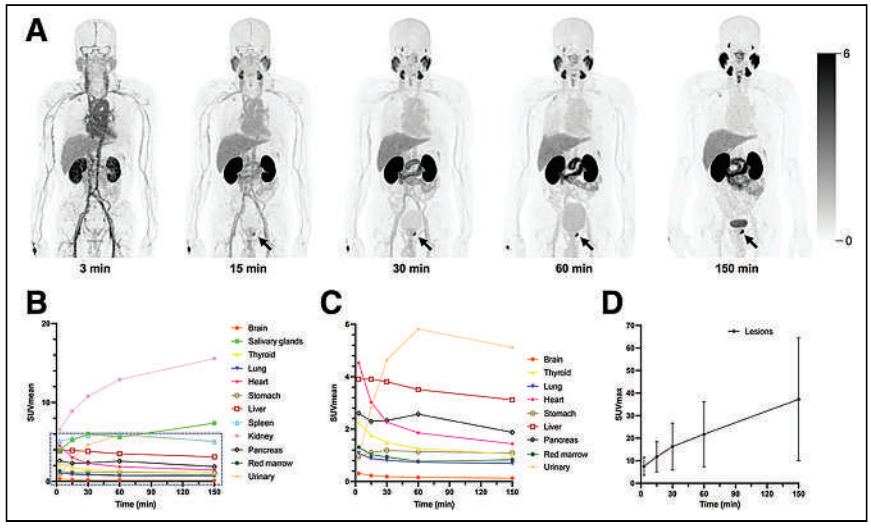

FIGURE 1. (A) Sequential dynamic maximum-intensity projections of [^{18}F]AlF-thretide PET/CT derived from patient with primary PCa (arrows). (B–D) Time–activity curves based on dynamic PET/CT scans from 3 patients.

effective dose of [^{18}F]AlF-thretide was 1.16E−02 mSv/MBq, corresponding to 2.6–3.5 mSv for a target activity of 222–296 MBq. The results for biodistribution and dosimetry are detailed in the supplemental materials, including Supplemental Table 2.

Diagnostic Performance of [^{18}F]AlF-Thretide PET/CT Based on Histopathology

As for the interpretation of lesions, 2 observers revealed substantial agreement at the patient level (Fleiss $\kappa = 0.73$, $P < 0.001$) and moderate agreement at the lesion level (Fleiss $\kappa = 0.67$, $P < 0.001$).

The intraprostatic tumors with the highest PRIMARY score in each patient were selected for patient-based analysis. The numbers of patients with PRIMARY scores of 1, 2, 3, 4, and 5 were 2, 1, 2, 22, and 22, respectively. Among the 49 patients, 46 (93.9%) presented with pathologic uptake on [^{18}F]AlF-thretide PET/CT. The SUV_{max} of the primary tumors on [^{18}F]AlF-thretide PET/CT was 18.7 ± 18.4 at 1 h after injection. There was a weak but significant association between SUV_{max} and baseline total prostate-specific antigen ($r = 0.417$, $P = 0.004$), biopsy Gleason score ($r = 0.342$, $P = 0.031$), and risk stratification ($r = 0.319$, $P = 0.027$). Similarly, there was also a weak but significant correlation between PRIMARY score and baseline total prostate-specific antigen ($r = 0.305$, $P = 0.037$), biopsy Gleason score ($r = 0.426$, $P = 0.006$), and risk stratification ($r = 0.359$, $P = 0.011$).

Among the 49 patients, 41 underwent radical prostatectomy; however, complete tissue specimens could not be obtained from 10 of these patients because suboptimal preservation damaged the pathologic sections or because the patients underwent surgery at other hospitals. Therefore, only 31 samples underwent full histopathologic analysis. For lesion-based analysis, pathologic examination identified 98 malignant foci, and [^{18}F]AlF-thretide PET/CT identified 63 PET-positive lesions, of which 57 were true-positive and 6 were false-positive (2 lesions were pathologically manifested as prostatitis and 4 lesions as cystic dilatation) (Supplemental Fig. 1). The sensitivity and positive predictive value of intraprostatic tumors for [^{18}F]AlF-thretide PET/CT were 58.2% and 90.5%, respectively. It was noteworthy that the delayed images detected 8 more tumors than did the standard images, and the SUV_{max} and tumor-to-background ratio of delayed images were higher than those of standard images ($n = 57$ vs. 49, $P = 0.005$; SUV_{max}: 14.5 ± 16.7 vs. 11.4 ± 13.6, $P < 0.001$; tumor-to-background ratio: 37.1 ± 42.3 vs. 23.1 ± 27.4, $P < 0.001$) (Fig. 2). Among these PET-positive lesions, 9 lesions had a PRIMARY score of 3, of which 2 (22.2%) were false-positive; 36 lesions had a PRIMARY score of 4, of which 4 (11.1%) were false-positive; and 18 lesions had a PRIMARY score of 5 with no false-positive findings (Figs. 3 and 4). The receiver-operating-characteristic (ROC) curve demonstrated that the area under curve (AUC) for PRIMARY score–predicted true-positive and false-positive lesions was 0.909 (95% CI, 0.806–1.011), which was significantly higher than that for the SUV_{max} of standard images (AUC, 0.712; 95% CI, 0.590–0.833; $P = 0.015$) and seemed higher than that for the SUV_{max} of delayed images (AUC, 0.829; 95% CI, 0.729–0.930; $P = 0.257$) (Fig. 4). The optimal diagnostic cutoff for the PRIMARY score according to ROC analysis was 3.5. When the PRIMARY score was greater than 3.5, sensitivity and specificity were 86.5% and 83.8%, respectively. Using an SUV_{max} of 4.8 for standard images as a cutoff, sensitivity and specificity were 63.5% and 91.7%, respectively. Similarly, with an SUV_{max} of 5.0 for delayed images as a cutoff, the values were 69.2% and 91.7%, respectively.

In total, 98 lesions were detected by pathology, and 41 lesions (41.8%) were missed by PET/CT. The pathologic area of true-positive lesions was significantly larger than that of false-negative lesions (139.7 ± 170.6 mm^2 vs. 3.4 ± 4.1 mm^2, $P < 0.001$). The ROC curve analysis showed that the AUC for the pathologic area was 0.957 (95% CI, 0.917–0.996) in distinguishing between true-positive and false-negative lesions. The optimal diagnostic cutoff for area according to the ROC analysis was 9.15 mm^2, and the resulting sensitivity and specificity were 87.0%, and 95.1%, respectively. Among 41 lesions missed by PET/CT, 28 (68.3%) had an ISUP grade group of 1. The AUC for the ISUP grade group–predicted true-positive and false-negative lesions was 0.774 (95% CI, 0.673–0.875). Using the ISUP grade group of 1.5 as a cutoff, sensitivity and specificity were 80.4% and 73.2%, respectively.

Detailed data on diagnosis of lymph node and other metastases for [^{18}F]AlF-thretide PET/CT based on histopathology and comprehensive imaging analysis are in the supplemental materials, including Supplemental Table 3.

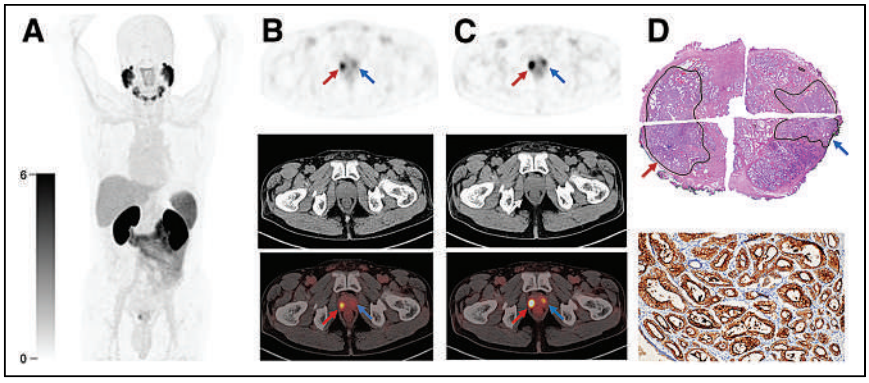

FIGURE 2. A 63-y-old man with biopsy-proven PCa with prostate-specific antigen level of 12.60 ng/mL at time of [^{18}F]AlF-thretide PET/CT. (B) Standard images revealed distinct uptake in right peripheral zone (red arrows) (C) Delayed images demonstrated another focus of activity in left peripheral zone (blue arrows). (D) Hematoxylin–eosin staining confirmed bilateral tumors (right peripheral zone, ISUP grade of 2; left peripheral zone, ISUP grade of 1) (top), and immunohistochemical results showed strong PSMA expression (bottom).

Diagnostic Performance of [^{18}F]AlF-Thretide PET/CT Versus mpMRI

All patients underwent mpMRI examination: 37 patients at our hospital and the other 12 patients at an outside institution. Finally, 24 individuals with full mpMRI, PET/CT, and pathology results were included for comparison and analysis.

For patient-based analysis, the detection rate for intraprostatic tumor was 100% (24/24) and 95.8% (23/24) for [^{18}F]AlF-thretide PET/CT and mpMRI, respectively. For lesion-based analysis, pathologic examination identified 71 malignant foci. [^{18}F]AlF-thretide PET/CT had a higher detection rate than mpMRI (53.5% [38/71] vs. 40.8% [29/71], $P = 0.012$); Specifically, [^{18}F]AlF-thretide PET/CT identified 10 lesions missed by mpMRI, whereas mpMRI identified 1 lesion missed by [^{18}F]AlF-thretide

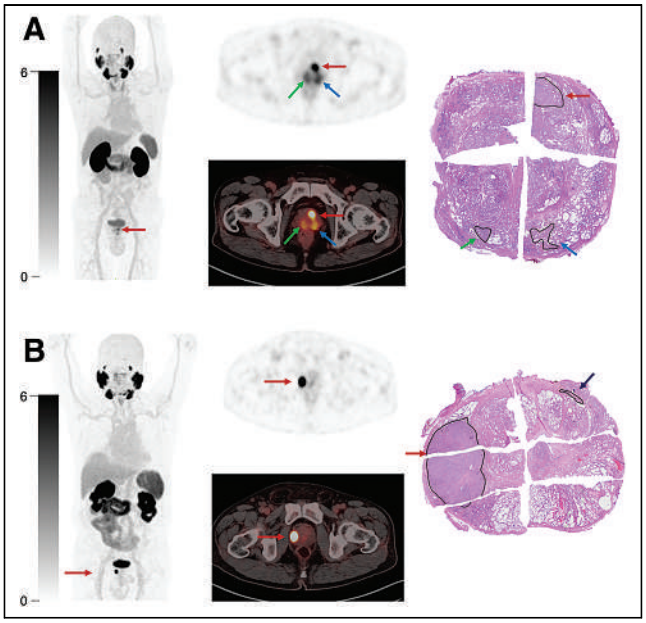

FIGURE 3. (A) [^{18}F]AlF-thretide PET/CT showed multifocal true-positive tumors (PRIMARY scores of 3, 4, and 4, indicated by red, green, and blue arrows, respectively). There was high imaging–pathology correspondence. (B) [^{18}F]AlF-thretide PET/CT revealed true-positive tumors (PRIMARY score of 5, red arrow) and false-negative tumor (PRIMARY score of 1, black arrow).

PET/CT (Supplemental Fig. 2). In addition, 44 of 71 lesions (62.0%) were graded as clinically significant PCa. The detection rate for clinically significant PCa was 75.0% (33/44) and 61.4% (27/44) for [^{18}F]AlF-thretide PET/CT and mpMRI ($P = 0.031$), respectively.

Detailed data on diagnosis of lymph node and bone metastases for [^{18}F]AlF-thretide PET/CT compared with mpMRI are in the supplemental materials.

Immunohistochemistry of PSMA Expression

Thirty-eight surgical specimens of intraprostatic tumors were analyzed with immunohistochemistry. PSMA expression was negative in 2 (5.2%), mild in 3 (7.9%), moderate in 9 (23.7%), and strong in 24 (63.2%). The Spearman correlation coefficient revealed a moderate correlation between SUV_{max} and intensity of staining ($r = 0.449$, $P = 0.005$), percentage of positive cells ($r = 0.490$, $P = 0.002$), and immunoreactive score ($r = 0.540$, $P < 0.001$). Besides, we also found that prostatitis and cystic dilatation had weak to strong PSMA expression, which was consistent with the [^{18}F]AlF-thretide PET images.

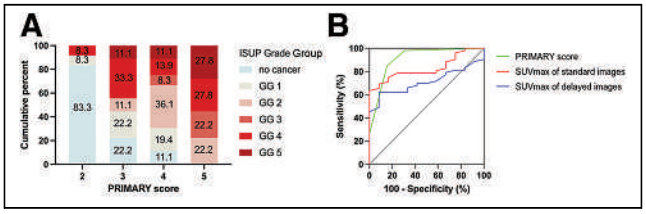

FIGURE 4. (A) Diagnostic sensitivity of [^{18}F]AlF-thretide PET/CT improved with increasing PRIMARY score. (B) ROC curves for PRIMARY score and for SUV_{max} of standard and delayed images.

DISCUSSION

In this single-center, prospective study, we confirmed that [^{18}F]AlF-thretide PET/CT has high accuracy in the detection of PCa, along with satisfactory safety and radiation dosimetry, indicating that [^{18}F]AlF-thretide is a promising radiopharmaceutical and worthy of further research.

In line with previous research (*7*), the biodistribution of [^{18}F]AlF-thretide from 0 to 2.5 h after administration revealed rapid and high tumor uptake, long tumor retention, and urinary excretion, which were similar to the tracers [^{68}Ga]Ga-PSMA-11 and [^{18}F]F-DCFPyL (*16*,*17*). Furthermore, the effective dose of [^{18}F]AlF-thretide (1.16E−02 mSv/MBq) was close to previous findings from 11 PCa patients (*7*). In addition, no clinically significant drug-related adverse events were observed in any of the 49 patients during follow-up, indicating its safety and tolerability.

[^{18}F]AlF-thretide PET/CT showed high diagnostic accuracy in patients with primary PCa. In a per-patient analysis, the total detection rate of intraprostatic tumors for [^{18}F]AlF-thretide PET/CT was 93.9%, which was slightly higher than the reported detectability of [^{68}Ga]Ga-PSMA-11, [^{68}Ga]Ga-PSMA-I&T, and [^{18}F]F-DCFPyL PET/CT (*18*–*20*). In a per-lesion analysis, [^{18}F]AlF-thretide PET/CT also revealed high diagnostic efficiency, with a sensitivity of 58.2% and a positive predictive value of 90.5%, which were also higher than the reported detection rate of [^{18}F]F-PSMA-1007 PET/CT (*21*). In our study, we used a 5-level PRIMARY score to optimize the diagnosis of intraprostatic tumor for [^{18}F]AlF-thretide PET/CT. Through comparative analysis, we found that the PRIMARY score was more accurate than visual SUV analysis, and the detection sensitivity of [^{18}F]AlF-thretide PET/CT also improved with increasing PRIMARY score. Several prospective studies have previously tried to establish the best SUV_{max} cutoff to improve the reliability and reproducibility of PSMA-ligand PET/CT (*22*,*23*); however, this is a method that may lack general applicability in clinical practice because of the strong influence of unharmonized PET cameras, differing reconstruction algorithms, and especially variable PSMA ligands on the semiquantitative calculation of SUV (*8*). The PRIMARY score incorporating intraprostatic pattern and intensity on PSMA PET/CT may achieve high interreader agreement and has the potential to be applied as a standardized PSMA PET/CT reporting method. However, it was noteworthy that CT scans with poor anatomic resolution for the prostate may have difficulty distinguishing the central zone/transition zone from the peripheral zone because of prostatic hyperplasia. As a result, some lesions with a true PRIMARY score of 2–3 may be incorrectly classified as having a score of 4, which may reduce the specificity of the PRIMARY score while guaranteeing the sensitivity (*8*). In the future, clinical trials based on PSMA PET/MRI may be necessary for further analysis of accuracy for the PRIMARY score.

Additionally, delayed [^{18}F]AlF-thretide PET images showed better diagnostic performance than standard images, although extra findings did not alter the overall staging of the patients. Hence, we suggest that 1 h may be the optimal interval between [^{18}F]AlF-thretide injection and PET imaging—similar to most other PSMA-targeting radiotracers (*4*). Of course, a delayed scan at 2.5–3 h after injection also remains necessary for improved contrast and visualization of any indeterminate findings observed on standard images.

On the basis of histopathology analysis, we found that false-negative lesions were smaller and had lower ISUP scores than

true-positive lesions. The area of true-positive tumors on [^{18}F]AlF-thretide PET was much larger than that of false-negative lesions, and the latter showed an average diameter of approximately 3 mm, which was acceptable, considering that most existing PET/CT scanners have an average transverse and axial spatial resolution of 3–5 mm (*24*,*25*). With the advancement of PET scanners and reconstruction algorithms, the ability of [^{18}F]AlF-thretide PET to detect small lesions may improve further in the future. In addition, some studies have illustrated that PSMA PET/CT had lower diagnostic efficacy in low- and intermediate-risk PCa than in high-risk PCa (*26*,*27*). In our study, among the false-negative tumors, 68.3% of lesions had an ISUP grade group of 1, which is generally consistent with the findings of previous studies.

Multiparameter prostate MRI plays an important role in the detection and treatment of primary PCa. Johnson et al. (*28*) showed that mpMRI detected 45% of all lesions and 65% of clinically significant lesions. There is still over a 50% and 30% chance of missing all PCa and clinically significant PCa, respectively, in men with multifocal disease. Therefore, additional methods are needed to better identify PCa foci. In our study, we found that [^{18}F]AlF-thretide PET/CT had a higher detection rate than mpMRI for all intraprostatic foci and clinically significant PCa. However, because of the limited cohort, there was no statistical difference between the 2 imaging modalities in detecting lymph node and bone metastasis.

Furthermore, the immunohistochemistry results confirmed that PSMA was overexpressed in most prostatic tumors. There was a significant positive correlation between the SUV of [^{18}F]AlF-thretide PET/CT and the expression levels of PSMA, which constituted the molecular prerequisite for PSMA imaging. Similar to some previous studies (*3*,*29*), we also found that some benign prostatic lesions had different levels of PSMA expression, which resulted in false-positive findings on the [^{18}F]AlF-thretide PET images. This should be kept in mind as a potential pitfall.

As for the detection of lymph node, bone, and visceral metastases, [^{18}F]AlF-thretide PET/CT showed excellent diagnostic performance, better perhaps than some other compounds in previously reported studies (*20*,*30*–*32*). However, the small sample size of nodal disease in this study may result in bias; further validation of larger cohorts is still needed in the future.

Our study had several limitations, including the relatively small sample size, the lack of pathologic confirmation of suspected bone metastases, and the lack of confirmation of PSMA expression for lymph node metastases.

CONCLUSION

In this prospective study, [^{18}F]AlF-thretide PET/CT demonstrated excellent tumor detection efficacy with favorable tolerability in patients with primary PCa. In particular, the detectability of [^{18}F]AlF-thretide PET/CT for intraprostatic tumors was significantly superior to mpMRI. Our findings suggest that [^{18}F]AlF-thretide may serve as an improved alternative to currently routinely used PSMA-targeted radiopharmaceuticals. Further investigations on larger cohorts are warranted.

DISCLOSURE

This work was supported by the Fujian Provincial Health Technology Project (2021GGA026), the National Natural Science Foundation of China (82202200), the Natural Science Foundation of Fujian Province (2022J05139), Joint Funds for the Innovation of Science and Technology of Fujian Province (2021Y9134), the National University of Singapore (NUHSRO/2021/097/Startup/13; NUHSRO/2020/133/Startup/08; NUHSRO/2023/008/NUSMed/TCE/LOA), an NMRC CS-IRG NIG grant (MOH-001254), the Singapore Ministry of Education (FY2022) a Tier 1 grant (NUHSRO/2022/093/T1/Seed-Sep/06), and the NUS School of Medicine Nanomedicine Translational Research Programme (NUHSRO/2021/034/TRP/09/Nanomedicine). No other potential conflict of interest relevant to this article was reported.

KEY POINTS

QUESTION: What is the diagnostic efficiency of [^{18}F]AlF-thretide PET/CT in patients with newly diagnosed, treatment-naïve PCa using histopathology as a reference standard?

PERTINENT FINDINGS: This histopathologically validated, prospective study showed that 46 of 49 (93.9%) patients showed pathologic [^{18}F]AlF-thretide uptake for intraprostatic tumors based on per-patient analysis. For lesion-based analysis, the sensitivity and positive predictive value for [^{18}F]AlF-thretide PET/CT were 58.2% and 90.5%, respectively.

IMPLICATIONS FOR PATIENT CARE: [^{18}F]AlF-thretide PET/CT showed high diagnostic efficiency for patients with newly diagnosed PCa and can be used as an alternative PSMA imaging agent in the detection of PCa.

REFERENCES

1. Siegel RL, Miller KD, Fuchs HE, Jemal A. Cancer statistics, 2021. *CA Cancer J Clin.* 2021;71:7–33.
2. Leek J, Lench N, Maraj B, et al. Prostate-specific membrane antigen: evidence for the existence of a second related human gene. *Br J Cancer.* 1995;72:583–588.
3. Kuten J, Fahoum I, Savin Z, et al. Head-to-head comparison of ^{68}Ga-PSMA-11 with ^{18}F-PSMA-1007 PET/CT in staging prostate cancer using histopathology and immunohistochemical analysis as a reference standard. *J Nucl Med.* 2020;61:527–532.
4. Fendler WP, Eiber M, Beheshti M, et al. PSMA PET/CT: joint EANM procedure guideline/SNMMI procedure standard for prostate cancer imaging 2.0. *Eur J Nucl Med Mol Imaging.* 2023;50:1466–1486.
5. Kesch C, Vinsensia M, Radtke JP, et al. Intraindividual comparison of ^{18}F-PSMA-1007 PET/CT, multiparametric MRI, and radical prostatectomy specimens in patients with primary prostate cancer: a retrospective, proof-of-concept study. *J Nucl Med.* 2017;58:1805–1810.
6. Grünig H, Maurer A, Thali Y, et al. Focal unspecific bone uptake on [^{18}F]-PSMA-1007 PET: a multicenter retrospective evaluation of the distribution, frequency, and quantitative parameters of a potential pitfall in prostate cancer imaging. *Eur J Nucl Med Mol Imaging.* 2021;48:4483–4494.
7. Liu T, Liu C, Xu X, et al. Preclinical evaluation and pilot clinical study of Al^{18}F-PSMA-BCH for prostate cancer PET imaging. *J Nucl Med.* 2019;60:1284–1292.
8. Emmett L, Papa N, Buteau J, et al. The PRIMARY score: using intraprostatic ^{68}Ga-PSMA PET/CT patterns to optimize prostate cancer diagnosis. *J Nucl Med.* 2022;63:1644–1650.
9. Zang J, Wen X, Lin R, et al. Synthesis, preclinical evaluation and radiation dosimetry of a dual targeting PET tracer [^{68}Ga]Ga-FAPI-RGD. *Theranostics.* 2022;12:7180–7190.
10. Turkbey B, Rosenkrantz AB, Haider MA, et al. Prostate Imaging Reporting and Data System version 2.1: 2019 Update of Prostate Imaging Reporting and Data System version 2. *Eur Urol.* 2019;76:340–351.
11. Turkbey B, Pinto PA, Mani H, et al. Prostate cancer: value of multiparametric MR imaging at 3 T for detection—histopathologic correlation. *Radiology.* 2010;255:89–99.
12. Sonni I, Felker ER, Lenis AT, et al. Head-to-head comparison of ^{68}Ga-PSMA-11 PET/CT and mpMRI with a histopathology gold standard in the detection, intraprostatic localization, and determination of local extension of primary prostate cancer: results from a prospective single-center imaging trial. *J Nucl Med.* 2022;63:847–854.
13. Mohler JL, Antonarakis ES, Armstrong AJ, et al. Prostate cancer, version 2.2019, NCCN clinical practice guidelines in oncology. *J Natl Compr Canc Netw.* 2019;17:479–505.

14. Hale CA, Fleiss JL. Interval estimation under two study designs for kappa with binary classifications. *Biometrics.* 1993;49:523–534.
15. Landis JR, Koch GG. The measurement of observer agreement for categorical data. *Biometrics.* 1977;33:159–174.
16. Prasad V, Steffen IG, Diederichs G, Makowski MR, Wust P, Brenner W. Biodistribution of [^{68}Ga]PSMA-HBED-CC in patients with prostate cancer: characterization of uptake in normal organs and tumour lesions. *Mol Imaging Biol.* 2016;18: 428–436.
17. Szabo Z, Mena E, Rowe SP, et al. Initial evaluation of [^{18}F]DCFPyL for prostate-specific membrane antigen (PSMA)-targeted PET imaging of prostate cancer. *Mol Imaging Biol.* 2015;17:565–574.
18. Hope TA, Goodman JZ, Allen IE, Calais J, Fendler WP, Carroll PR. Metaanalysis of ^{68}Ga-PSMA-11 PET accuracy for the detection of prostate cancer validated by histopathology. *J Nucl Med.* 2019;60:786–793.
19. Pan KH, Wang JF, Wang CY, et al. Evaluation of ^{18}F-DCFPyL PSMA PET/CT for prostate cancer: a meta-analysis. *Front Oncol.* 2021;10:597422.
20. Cytawa W, Seitz AK, Kircher S, et al. ^{68}Ga-PSMA I&T PET/CT for primary staging of prostate cancer. *Eur J Nucl Med Mol Imaging.* 2020;47:168–177.
21. Tragardh E, Simoulis A, Bjartell A, Jogi J. Tumor detection of ^{18}F-PSMA-1007 in the prostate gland in patients with prostate cancer using prostatectomy specimens as reference method. *J Nucl Med.* 2021;62:1735–1740.
22. Fendler WP, Schmidt DF, Wenter V, et al. ^{68}Ga-PSMA PET/CT detects the location and extent of primary prostate cancer. *J Nucl Med.* 2016;57:1720–1725.
23. Wang G, Li L, Zhu M, et al. A prospective head-to-head comparison of [^{68}Ga]Ga-P16-093 and [^{68}Ga]Ga-PSMA-11 PET/CT in patients with primary prostate cancer. *Eur J Nucl Med Mol Imaging.* 2023;50:3126–3136.
24. van Sluis J, de Jong J, Schaar J, et al. Performance characteristics of the digital Biograph Vision PET/CT system. *J Nucl Med.* 2019;60:1031–1036.
25. Sánchez-Crespo A, Andreo P, Larsson SA. Positron flight in human tissues and its influence on PET image spatial resolution. *Eur J Nucl Med Mol Imaging.* 2004;31: 44–51.
26. Uprimny C, Kroiss AS, Decristoforo C, et al. ^{68}Ga-PSMA-11 PET/CT in primary staging of prostate cancer: PSA and Gleason score predict the intensity of tracer accumulation in the primary tumour. *Eur J Nucl Med Mol Imaging.* 2017;44:941–949.
27. Zhou C, Tang Y, Deng Z, et al. Comparison of ^{68}Ga-PSMA PET/CT and multiparametric MRI for the detection of low- and intermediate-risk prostate cancer. *EJNMMI Res.* 2022;12:10.
28. Johnson DC, Raman SS, Mirak SA, et al. Detection of individual prostate cancer foci via multiparametric magnetic resonance imaging. *Eur Urol.* 2019;75:712–720.
29. Rahbar K, Weckesser M, Huss S, et al. Correlation of intraprostatic tumor extent with ^{68}Ga-PSMA distribution in patients with prostate cancer. *J Nucl Med.* 2016; 57:563–567.
30. Klingenberg S, Jochumsen MR, Ulhoi BP, et al. ^{68}Ga-PSMA PET/CT for primary lymph node and distant metastasis NM staging of high-risk prostate cancer. *J Nucl Med.* 2021;62:214–220.
31. Jansen BHE, Bodar YJL, Zwezerijnen GJC, et al. Pelvic lymph-node staging with ^{18}F-DCFPyL PET/CT prior to extended pelvic lymph-node dissection in primary prostate cancer: the SALT trial. *Eur J Nucl Med Mol Imaging.* 2021;48:509–520.
32. Pienta KJ, Gorin MA, Rowe SP, et al. A phase 2/3 prospective multicenter study of the diagnostic accuracy of prostate specific membrane antigen PET/CT with ^{18}F-DCFPyL in prostate cancer patients (OSPREY). *J Urol.* 2021;206:52–61.

Prognostic Implications of ^{68}Ga-FAPI-46 PET/CT–Derived Parameters on Overall Survival in Various Types of Solid Tumors

Masao Watanabe[1,2], Wolfgang P. Fendler[1,2], Hong Grafe[1,2], Nader Hirmas[2], Rainer Hamacher[3], Helena Lanzafame[2], Kim M. Pabst[2], Hubertus Hautzel[1], Clemens Aigner[4], Stefan Kasper[3], Bastian von Tresckow[5], Martin Stuschke[6], Sherko Kümmel[7], Celine Lugnier[8], Boris Hadaschik[9], Viktor Grünwald[3,9], Fadi Zarrad[2], Jens T. Siveke[10,11], Ken Herrmann[1,2], and Manuel Weber[1,2]

[1]Department of Nuclear Medicine, University Clinic Essen, Essen, Germany; [2]Department of Nuclear Medicine, University of Duisburg–Essen and German Cancer Consortium–University Hospital Essen, Essen, Germany; [3]Department of Medical Oncology, West German Cancer Center, University of Duisburg–Essen and German Cancer Consortium–University Hospital Essen, Essen, Germany; [4]Department of Thoracic Surgery and Thoracic Endoscopy, University of Duisburg–Essen and German Cancer Consortium–University Hospital Essen, Essen, Germany; [5]Department of Hematology and Stem Cell Transplantation, West German Cancer Center and German Cancer Consortium (DKTK partner site Essen), University Hospital Essen, University of Duisburg–Essen, Essen, Germany; [6]Department of Radiation Therapy, University of Duisburg–Essen and German Cancer Consortium–University Hospital Essen, Essen, Germany; [7]Department of Gynecology and Gynecologic Oncology, Evang. Kliniken Essen–Mitte, Essen, Germany, and Department of Gynecology with Breast Center, Charité–Universitätsmedizin Berlin, Berlin, Germany; [8]Department of Hematology and Oncology with Palliative Care, Ruhr University Bochum, Bochum, Germany; [9]Department of Urology, University of Duisburg–Essen and German Cancer Consortium–University Hospital Essen, Essen, Germany; [10]Bridge Institute of Experimental Tumor Therapy, West German Cancer Center, University Hospital Essen, Essen, Germany; and [11]Division of Solid Tumor Translational Oncology, German Cancer Center Consortium (DKTK partner site Essen), and German Cancer Research Center, Heidelberg, Germany

Tumoral fibroblast activation protein expression is associated with proliferation and angiogenesis and can be visualized by PET/CT. We examined the prognostic value of [^{68}Ga]Ga-fibroblast activation protein inhibitor (FAPI) (^{68}Ga-FAPI)–46 PET/CT for different tumor entities in patients enrolled in 2 prospective imaging studies (NCT05160051, $n = 30$; NCT04571086, $n = 115$). **Methods:** Within 4 wk, 145 patients underwent ^{68}Ga-FAPI-46 and [^{18}F]FDG (^{18}F-FDG) PET/CT. The association between overall survival (OS) and sex, age, tumor entity, total lesion number, highest SUV_{max}, and the presence of each nodal, visceral, and bone metastasis was tested using univariate Cox regression analysis. Multivariate analyses were performed for prognostic factors with P values of less than 0.05. **Results:** In the univariate analysis, shorter OS was associated with total lesion number and the presence of nodal, visceral, and bone metastases on ^{68}Ga-FAPI-46 PET/CT (hazard ratio [HR], 1.06, 2.18, 1.69, and 2.05; $P < 0.01$, < 0.01, $= 0.04$, and $= 0.02$, respectively) and ^{18}F-FDG PET/CT (HR, 1.05, 2.31, 1.76, and 2.30; $P < 0.01$, < 0.01, $= 0.03$, and < 0.01, respectively) and with SUV_{max} on ^{68}Ga-FAPI-46 PET/CT (HR, 1.03; $P = 0.03$). In the multivariate analysis, total lesion number on ^{68}Ga-FAPI-46 PET/CT was an independent risk factor for shorter OS (HR, 1.05; $P = 0.02$). In patients with pancreatic cancer, shorter OS was associated with total lesion number on ^{68}Ga-FAPI-46 PET/CT (HR, 1.09; $P < 0.01$) and bone metastases on ^{18}F-FDG PET/CT (HR, 31.39; $P < 0.01$) in the univariate analysis and with total lesion number on ^{68}Ga-FAPI-46 PET/CT (HR, 1.07; $P = 0.04$) in the multivariate analyses. In breast cancer, total lesion number on ^{68}Ga-FAPI-46 PET/CT (HR, 1.07; $P = 0.02$), as well as bone metastases on ^{18}F-FDG PET/CT (HR, 9.64; $P = 0.04$), was associated with shorter OS in the univariate analysis. The multivariate analysis did not reveal significant prognostic factors. In thoracic cancer (lung cancer and pleural mesothelioma), the univariate and multivariate analyses did not reveal significant prognostic factors. **Conclusion:** Disease extent on ^{68}Ga-FAPI-46 PET/CT is a predictor of short OS and may aid in future risk stratification by playing a supplemental role alongside ^{18}F-FDG PET/CT.

Key Words: ^{68}Ga-FAPI-46; PET/CT; ^{18}F-FDG; overall survival; total lesion number

J Nucl Med 2024; 65:1027–1034
DOI: 10.2967/jnumed.123.266981

In vivo visualization of fibroblast activation protein (FAP) by means of [^{68}Ga]Ga-FAP inhibitor (FAPI) (^{68}Ga-FAPI) PET/CT imaging is characterized by high tumor uptake and low background accumulation of radioligands (*1*). This results in high detection rates in a multitude of solid tumors in comparison with [^{18}F]FDG (^{18}F-FDG) PET/CT (*2–4*).

FAP expression has been confirmed in many cancers (90% of carcinomas), especially in the stroma in the tumor tissue, and thus may become a universal marker of cancer-associated fibroblasts (*5*). This expression has been associated with proliferation, invasion, angiogenesis, and drug resistance (*5*), leading to a poor prognosis in several malignancies, including gastric (*5*), colorectal (*6*), pancreatic (*7*), and non–small cell lung (*8*) cancer. However, only a few studies, mostly on small cohorts, have examined the prognostic value of ^{68}Ga-FAPI PET/CT in this context (*9–11*).

To address this gap in knowledge, we compared the prognostic implications of ^{68}Ga-FAPI-46 PET/CT and ^{18}F-FDG PET/CT in a large population of patients with various tumors.

Received Oct. 31, 2023; revision accepted May 7, 2024.
For correspondence or reprints, contact Masao Watanabe (d7he4ng@gmail.com).
Published online May 23, 2024.

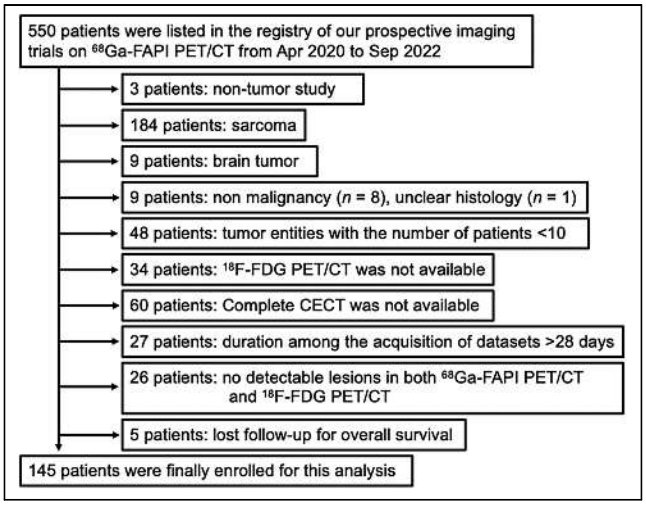

FIGURE 1. Consolidated Standards of Reporting Trials (CONSORT) diagram illustrating enrollment process. CECT = contrast-enhanced CT.

MATERIALS AND METHODS

Patients

We screened our institutional database of prospective imaging studies for consecutive patients who underwent ^{68}Ga-FAPI-46 PET/CT and ^{18}F-FDG PET/CT within 4 wk from April 2020 to September 2022 for imaging of tumors other than sarcoma (because of another ongoing project focused on sarcoma). The patient selection process is shown in Figure 1.

All patients gave written informed consent. Of these, 145 patients were included in 2 prospective imaging studies (NCT05160051, 30 interventional; NCT04571086, 115 observational). Data analysis was approved by the ethics committee of the University of Duisburg–Essen (20-9485-BO and 19-8991-BO). The patient subgroups have previously been reported (*12–16*). We obtained the precursor of ^{68}Ga-FAPI-46 from SOFIE Biosciences.

Image Acquisition

At 23.3 ± 20.2 min (range, 9–102 min) after the injection of 123.9 ± 31.0 MBq (range, 60–199 MBq) of ^{68}Ga-FAPI-46, PET/CT was performed on a Siemens 128-slice Biograph mCT (26/145 patients, 17.9%), Siemens Biograph Vision (115/145 patients, 79.3%), or Philips Vereos (4/145 patients, 2.8%). Acquisition times were based on a prior publication by our group (*13*).

^{18}F-FDG PET/CT was performed 71.8 ± 18.2 min (range, 43–147 min) after the injection of 267.1 ± 84.6 MBq (range, 94–458 MBq) of ^{18}F-FDG. Images were acquired on a Biograph mCT (27/145 patients, 18.6%), Biograph Vision (109/145 patients, 75.2%), or Vereos (9/145 patients, 6.2%). All PET images were iteratively reconstructed with time of flight (Biograph mCT: 3 iterations and 21 subsets, gaussian filtering of 4 mm; Biograph Vision: 4 iterations and 5 subsets, gaussian filtering of 2 mm; Vereos: 2 iterations and 10 subsets, gaussian filtering of 4 mm).

Image Interpretation and Quantitative Analysis

Images were interpreted by a board-certified nuclear medicine physician and radiologist with 14 y of experience, who had completed institutional reader training on 50 ^{68}Ga-FAPI-46 PET/CT datasets including common pitfalls. The reader was not aware of the clinical information. Masked interpretation was chosen to avoid biases due to knowledge of clinical information and to measure the standalone impact of the imaging modalities, even though lack of clinical information may trigger faulty image interpretation at times.

Lesions were classified as malignant if they exhibited focal tracer accumulation incongruent with physiologic or nonneoplastic uptake (*17*) and were categorized into the following anatomic regions: primary, cervicothoracic nodal metastases, abdominopelvic nodal metastases, pulmonary metastases, hepatic metastases, other visceral metastases, and bone metastases. Lesion number (≤10 per region to avoid individual bias, from larger to smaller lesions), and SUV_{max} was assessed visually on Syngo.via software (Siemens Healthineers). Representative diagnosis cases are shown in Figures 2 and 3.

Statistical Analysis

Overall survival (OS) was defined as the interval from the day of the PET/CT scans (^{68}Ga-FAPI-46 PET/CT and ^{18}F-FDG PET/CT) until death or the end of the study (censored in June 2023). For OS, we performed univariate Cox proportional hazards regression analysis using the following variables: sex, age, restaging (vs. initial staging), tumor entity, total lesion number, the presence of nodal metastases, the presence of visceral metastases, the presence of bone metastases, and the highest SUV_{max} of all lesions. Prognostic factors with a P value of less than 0.05 in the univariate analysis, as well as the tumor entity as a categoric parameter (considering the heterogeneity of tumor characteristics), were considered statistically significant and tested in multivariate analyses. We also performed subanalyses for the patients with pancreatic cancer, breast cancer, and thoracic cancer (lung cancer and pleural mesothelioma). Separate Cox analyses for each tumor entity (pancreatic cancer, breast cancer, and thoracic cancer) are susceptible to multiple-comparison problems due to small sample sizes. To resolve this issue, we entered into the multivariate Cox analysis only the prognostic parameters that were significant predictors of OS in the multivariate analysis on the entire cohort. We performed Kaplan–Meier analysis using log-rank testing to determine the statistical association between OS and findings on ^{18}F-FDG PET/CT and ^{68}Ga-FAPI-46 PET/CT. For statistical analysis, we used MedCalc version 22.007, 32-bit (MedCalc Software), and Prism 8 (GraphPad Software). Numeric values are provided as mean ± SD.

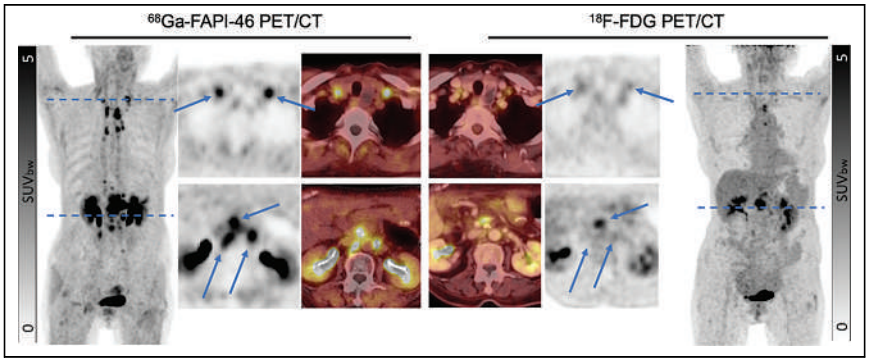

FIGURE 2. Intraindividual comparison between ^{68}Ga-FAPI-46 PET/CT and ^{18}F-FDG PET/CT for restaging in patient with postoperative pancreatic head cancer (73-y-old woman with extensive nodal metastases). Bilateral nodal metastases in supraclavicular region were detectable only on ^{68}Ga-FAPI-46 PET/CT (SUV_{max}, 5.74 on right side and 10.19 on left side; arrows); findings on ^{18}F-FDG PET/CT were nonspecific (SUV_{max}, 2.93 on right side and 3.58 on left side; arrows). At level of bilateral renal pelvis, there were 3 and only 1 detectable paraaortic nodal metastases on ^{68}Ga-FAPI-46 PET/CT (SUV_{max}, 6.75, 11.37, and 11.75 from right to left) and ^{18}F-FDG PET/CT (SUV_{max}, 7.94; other 2 lymph nodes not measurable), respectively (arrows). SUV_{bw} = SUV based on body weight.

RESULTS

Patient Cohort

The final cohort included 145 patients, of whom 85 were male and 60 were female (mean ± SD, 61.6 ± 11.8 y old; range, 30–85 y old). We enrolled 53 patients (36.6%) for staging and 92 patients (63.4%) for restaging. The most common tumor entities were pancreatic cancer (n = 40), mesothelioma (pleural, n = 18; peritoneal, n = 2), and breast cancer (n = 17). Sixty-four of 145 (44.1%) patients died during the mean follow-up period of 13.8 mo (range, 1–30 mo). Patient characteristics are provided in Table 1. Because we enrolled patients requiring either staging or restaging, we classified only the patients with T(positive)/N0/M0, T(any)/N(positive)/M0, and T(any)/N(any)/M(positive), by referring to the ^{68}Ga-FAPI-46 PET/CT, ^{18}F-FDG PET/CT, and contrast-enhanced CT, all of which were performed within 4 wk. The median total lesion number was 4 on ^{68}Ga-FAPI-46 PET/CT (range, 0–53; 1 with no lesions; 44 with 1 lesion; 27 with 2 or 3 lesions; 8 with 4 or 5 lesions; 20 with 6–10 lesions; 45 with >10 lesions) and 3 on ^{18}F-FDG PET/CT (range, 0–57; 8 with no lesions; 47 with 1 lesion; 26 with 2 or 3 lesions; 7 with 4 or 5 lesions; 20 with 6–10 lesions; 37 with >10 lesions).

The treatment records were available for 133 of 145 patients (91.7%). Ninety-four of 145 patients (64.8%) underwent surgery. In 93 cases (93/145, 64.1%), the primary was resected, and in 22 cases (22/145, 15.2%), metastases were resected; in 21 of those, both the primary and metastases were resected (21/145, 14.5%).

Of the 94 patients who underwent surgery, 79 (79/145, 54.5%) received systemic therapy (chemotherapy or immunotherapy). Of the remaining 39 recorded patients without surgery (39/145, 26.9%), 31 (31/145, 21.4%) received systemic therapy. Systemic therapy was used in 110 of 145 (75.9%) patients, of whom 14 had breast cancer, 5 had lung cancer, 14 had pleural mesothelioma, 2 had peritoneal mesothelioma, 13 had cholangiocellular cancer, 33 had pancreatic cancer, 13 had colorectal cancer, 9 had renal cell cancer, and 7 had

TABLE 1
Patient Characteristics (n = 145)

Clinical variable	Value
Mean age (y)	61.6 (range, 30–85)
Male/female	85 (58.6%)/60 (41.4%)
Staging/restaging	53 (36.6%)/92 (63.4%)
Primary tumor	
Breast cancer	17 (11.7%)
T+N0M0/T(any)N+M0/T(any)N(any)M1	5 (3.4%)/4 (2.8%)/8 (5.5%)
Lung cancer	12 (8.3%)
T+N0M0/T(any)N+M0/T(any)N(any)M1	6 (4.1%)/1 (0.7%)/5 (3.4%)
Mesothelioma (pleural/peritoneal)	18 (12.4%)/2 (1.4%)
T+N0M0/T(any)N+M0/T(any)N(any)M1	6 (4.1%)/7 (4.8%)/7 (4.8%)
Cholangiocellular cancer	15 (10.3%)
T+N0M0/T(any)N+M0/T(any)N(any)M1	3 (2.1%)/2 (1.4%)/10 (6.9%)
Pancreatic cancer	40 (27.6%)
T+N0M0/T(any)N+M0/T(any)N(any)M1	11 (7.6%)/7 (4.8%)/22 (15.2%)
Colorectal cancer	15 (10.3%)
T+N0M0/T(any)N+M0/T(any)N(any)M1	3 (2.1%)/0 (0%)/12 (8.3%)
Renal cell cancer	15 (10.3%)
T+N0M0/T(any)N+M0/T(any)N(any)M1	5 (3.4%)/1 (0.7%)/9 (6.2%)
Prostate cancer	11 (7.6%)
T+N0M0/T(any)N+M0/T(any)N(any)M1	4 (2.8%)/0 (0%)/7 (4.8%)
Treatment data, available/not available	133 (91.7%)/12 (8.3%)
Surgery for primary site/metastases	93 (64.1%)/22 (15.2%)
Chemo- or immunotherapy, surgical cases	79 (54.5%)
Neoadjuvant/adjuvant/salvage/unspecified	21 (14.5%)/46 (31.7%)/53 (36.6%)/5 (3.4%)
Chemo- or immunotherapy, no surgery	31 (21.4%)
Other therapy	
RPT/radioembolization/^{223}Ra	4 (2.8%)/3 (2.1%)/1 (0.7%)
Hormone/RFA/radiation therapy	11 (7.6%)/2 (1.4%)/38 (26.2%)

RPT = radiopharmaceutical therapy; RFA = radiofrequency ablation.
Values are number and percentage, except for age.

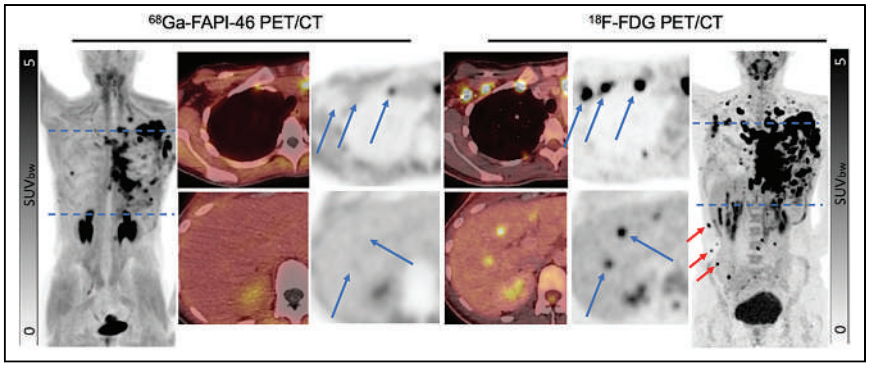

FIGURE 3. Intraindividual comparison between ^{68}Ga-FAPI-46 PET/CT and ^{18}F-FDG PET/CT for restaging in patient with postoperative left breast cancer (36-y-old woman with large number of metastases). Several metastases to muscles were detectable only on ^{18}F-FDG PET/CT (red arrows). At same axillary level (right side of body), there were 1 and 3 detectable nodal metastases on ^{68}Ga-FAPI-46 PET/CT (SUV_{max}, 3.47; other 2 distal lymph nodes not measurable) and on ^{18}F-FDG PET/CT (SUV_{max}, 26.28, 18.54, and 29.60 from proximal to distal lymph nodes), respectively (blue arrows). In liver region (lower part of images), 2 liver metastases were detectable on ^{18}F-FDG PET/CT (SUV_{max}, 6.65 in segment 4 and 4.50 in segment 5); however, no liver metastases were detectable on ^{68}Ga-FAPI-46 PET/CT (blue arrows). SUV_{bw} = SUV based on body weight.

prostate cancer. Other therapies consisted of radiopharmaceutical therapy with [^{177}Lu]Lu-PSMA-617 (n = 4), radioembolization (n = 3), [^{223}Ra]Ra-chloride (n = 1), hormone therapy (for breast cancer and prostate cancer, n = 11), radiofrequency ablation (n = 2), and external-beam radiotherapy (n = 38). Information on the treatment is summarized in Table 1.

Prognostic Analysis

In the univariate analysis for ^{68}Ga-FAPI-46 PET/CT, total lesion number; the presence of nodal, visceral, and bone metastases; and the highest SUV_{max} of all lesions were significant predictors of short OS (hazard ratio [HR], 1.06, 2.18, 1.69, 2.05, and 1.03, respectively; 95% CI, 1.03–1.08, 1.32–3.60, 1.03–2.77, 1.12–3.77, and 1.00–1.07, respectively; $P < 0.01$, < 0.01, $= 0.04$, $= 0.02$, and $= 0.03$, respectively; Table 2). In the multivariate analysis (Table 2), total lesion number was significantly associated with OS (HR, 1.05; 95% CI, 1.01–1.10; $P = 0.02$), whereas the presence of nodal, visceral, and bone metastases and the highest SUV_{max} of all lesions were not (HR, 1.12, 1.10, 2.21, and 1.02, respectively; 95% CI, 0.57–2.19, 0.56–2.16, 0.93–5.26, and 0.98–1.07, respectively; $P = 0.75$, 0.78, 0.07, and 0.29, respectively). Kaplan–Meier curves for OS based on the total lesion number are shown in Figure 4 using the median total lesion number (n = 4) as the cutoff. The median survival of patients with at least 4 lesions (73 patients) versus less than 4 lesions (72 patients) was 17 and 25 mo, respectively ($P < 0.001$).

Regarding ^{18}F-FDG PET/CT (Table 2), total lesion number and the presence of nodal, visceral, and bone metastases were significantly associated with shorter OS (HR, 1.05, 2.31, 1.76, and 2.30, respectively; 95% CI, 1.03–1.08, 1.41–3.80, 1.07–2.92, and 1.27–4.17, respectively; $P < 0.01$, < 0.01, $= 0.03$, and < 0.01, respectively). In the multivariate analysis (Table 2), the presence of bone metastases was a predictor of shorter OS (HR, 3.46; 95% CI, 1.49–8.03; $P < 0.01$), whereas total lesion number and the presence of nodal and visceral metastases were not (HR, 1.04, 1.53, and 1.20, respectively; 95% CI, 0.999–1.08, 0.81–2.88, and 0.60–2.39, respectively; $P = 0.055$, 0.19, and 0.61, respectively). Kaplan–Meier curves for OS in the group with positive bone metastases (25 patients) and those with negative bone metastases (120 patients) are shown in Figure 4. The median survival was 13 and 23 mo, respectively ($P < 0.005$).

Regarding ^{68}Ga-FAPI-46 PET/CT in the patients with pancreatic cancer, total lesion number was significantly associated with shorter OS in the univariate analysis (HR, 1.09; 95% CI, 1.03–1.15; $P < 0.01$) and in the multivariate analysis (HR, 1.07; 95% CI, 1.004–1.13; $P = 0.04$). For ^{18}F-FDG PET/CT, bone metastases were a significant prognostic indicator for shorter OS in the univariate analysis (HR, 31.39; 95% CI, 4.33–227.36; $P < 0.01$). In the multivariate analysis, bone metastases were borderline-significant (HR, 8.67; 95% CI, 0.91–82.78; $P = 0.06$). These results are summarized in Table 3.

As for the patients with breast cancer using ^{68}Ga-FAPI-46 PET/CT, total lesion number was significantly associated with shorter OS in the univariate analysis (HR, 1.07; 95% CI, 1.01–1.13; $P = 0.02$) but was not significant in the multivariate analysis (HR, 1.03; 95% CI, 0.95–1.11; $P = 0.47$). For ^{18}F-FDG PET/CT, bone metastases were a significant prognostic indicator for OS in the univariate analysis (HR, 9.64; 95% CI, 1.12–83.30; $P = 0.04$) but was not significant in the multivariate analysis (HR, 5.58; 95% CI, 0.38–81.50; $P = 0.21$). These results are summarized in Table 4.

Concerning the subanalysis for patients with thoracic cancer, including lung cancer and pleural mesothelioma, no PET-derived prognostic factors were not associated with OS in the uni- and multivariate analyses. These results are summarized in Table 5.

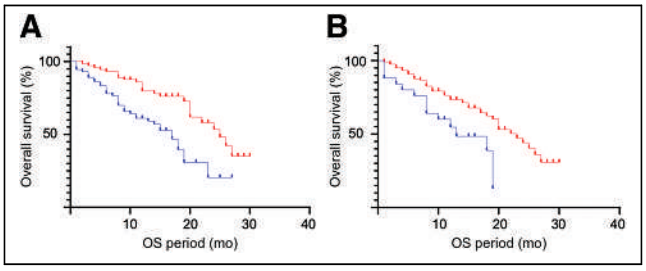

FIGURE 4. Kaplan–Meier analyses for OS regarding total lesion number on ^{68}Ga-FAPI-46 PET/CT (A) and presence of bone metastases on ^{18}F-FDG PET/CT (B). Blue and red lines are groups with ≥4 total lesions (median value of all patients) and those with ≤3 total lesions in A ($P <$ 0.001) and group with positive bone metastases and those with negative bone metastases in B ($P < 0.005$), respectively.

DISCUSSION

The results of our study reveal that ^{68}Ga-FAPI-46 PET/CT–based parameters have prognostic value in a mixed population of cancer patients. The presence of bone metastases on ^{18}F-FDG PET/CT, and lesion number on ^{68}Ga-FAPI-46 PET/CT (HR, 1.05), were independent risk factors for shorter OS in the multivariate analysis. Although the HR of the latter may appear small, continuous variables with a wide range (0–53) often display lower

TABLE 2
Uni- and Multivariate Analyses of OS Using Cox Proportional Hazards Regression Analysis
(Death Events, $n = 64$; Censored, $n = 81$)

	Univariate		Multivariate	
Parameter	HR	*P*	HR	*P*
^{68}Ga-FAPI-46 PET/CT				
Sex	1.25 (0.75–2.08)	0.40		
Age	1.01 (0.99–1.03)	0.31		
Restaging vs. initial staging	1.70 (0.98–2.93)	0.06		
Tumor entity*				
Mesothelioma ($n = 20$)	0.77 (0.37–1.59)	0.48	0.62 (0.28–1.34)	0.22
Breast cancer ($n = 17$)	0.67 (0.27–1.64)	0.38	0.30 (0.10–0.90)	0.03
Cholangiocarcinoma ($n = 15$)	0.56 (0.23–1.36)	0.20	0.43 (0.17–1.06)	0.07
Renal cell carcinoma ($n = 15$)	0.33 (0.10–1.10)	0.07	0.22 (0.06–0.84)	0.03
Colorectal cancer ($n = 15$)	0.44 (0.15–1.26)	0.13	0.39 (0.13–1.18)	0.10
Lung cancer ($n = 12$)	0.27 (0.06–1.14)	0.08	0.19 (0.04–0.85)	0.03
Prostate cancer ($n = 11$)	0.53 (0.20–1.38)	0.19	0.27 (0.08–0.91)	0.03
Total lesion number	1.06 (1.03–1.08)	<0.01	1.05 (1.01–1.10)	0.02
Nodal metastases	2.18 (1.32–3.60)	<0.01	1.12 (0.57–2.19)	0.75
Visceral metastases	1.69 (1.03–2.77)	0.04	1.10 (0.56–2.16)	0.78
Bone metastases	2.05 (1.12–3.77)	0.02	2.21 (0.93–5.26)	0.07
Highest SUV_{max}	1.03 (1.00–1.07)	0.03	1.02 (0.98–1.07)	0.29
^{18}F-FDG PET/CT				
Tumor entity*				
Mesothelioma ($n = 20$)	0.77 (0.37–1.59)	0.48	0.50 (0.23–1.06)	0.07
Breast cancer ($n = 17$)	0.67 (0.27–1.64)	0.38	0.20 (0.06–0.62)	<0.01
Cholangiocarcinoma ($n = 15$)	0.56 (0.23–1.36)	0.20	0.39 (0.16–0.97)	0.04
Renal cell carcinoma ($n = 15$)	0.33 (0.10–1.10)	0.07	0.16 (0.04–0.60)	<0.01
Colorectal cancer ($n = 15$)	0.44 (0.15–1.26)	0.13	0.30 (0.10–0.92)	0.03
Lung cancer ($n = 12$)	0.27 (0.06–1.14)	0.08	0.17 (0.04–0.75)	0.02
Prostate cancer ($n = 11$)	0.53 (0.20–1.38)	0.19	0.20 (0.06–0.69)	0.01
Total lesion number	1.05 (1.03–1.08)	<0.01	1.04 (0.999–1.08)	0.055
Nodal metastases	2.31 (1.41–3.80)	<0.01	1.53 (0.81–2.88)	0.19
Visceral metastases	1.76 (1.07–2.92)	0.03	1.20 (0.60–2.39)	0.61
Bone metastases	2.30 (1.27–4.17)	<0.01	3.46 (1.49–8.03)	<0.01
Highest SUV_{max}	1.02 (0.995–1.05)	0.11		

*Compared with pancreatic cancer.
Data are mean followed by 95% CI in parentheses.

HRs. Yet the effect of lesion number on the extreme ends of the spectrum is not negligible, as shown in the context of Ki-67, an established prognostic parameter in a multitude of malignancies, where HRs in the similar range are commonly observed (e.g., 1.05 in patients with adrenocortical carcinoma regarding OS (*18*)). In addition, the univariate analysis identified metastases to nodes, visceral organs, and bone and the highest SUV_{max} of all lesions on ^{68}Ga-FAPI-46 PET/CT as significant prognostic indicators for shorter OS. ^{68}Ga-FAPI-46 PET/CT–based parameters such as total lesion number, and ^{18}F-FDG PET/CT–based parameters such as the presence of hypermetabolic bone metastases, may aide risk stratification alongside other, already-established, prognostic markers (*19*). ^{18}F-FDG PET/CT as a prognostic marker is well established in a multitude of malignancies, underpinned by an extensive body of research, and is well understood, especially with regard to its associations with dedifferentiation and proliferation. ^{18}F-FDG PET/CT–derived markers that have been well studied in their association with OS are, among others, metabolic tumor volume and total lesion glycolysis, such as in patients with lung, pancreatic, and breast cancer (*19–21*).

On the basis of our results, it appears unlikely that ^{68}Ga-FAPI-46 PET/CT–derived markers will generally replace ^{18}F-FDG PET/CT,

TABLE 3
Uni- and Multivariate Subanalyses of OS for Patients with Pancreatic Cancer Using Cox Proportional Hazards Regression Analysis (Death Events, $n = 28$; Censored, $n = 12$)

	Univariate		Multivariate	
Parameter	HR	*P*	HR	*P*
^{68}Ga-FAPI-46 PET/CT				
Total lesion number	1.09 (1.03–1.15)	<0.01	1.07 (1.004–1.13)	0.04
^{18}F-FDG PET/CT				
Bone metastases	31.39 (4.33–227.36)	<0.01	8.67 (0.91–82.78)	0.06

Data are mean followed by 95% CI in parentheses.

yet they may serve as complementary markers, with lesion number being particularly promising. The latter may be the consequence of a better diagnostic performance in some tumor entities (*2*,*4*,*11*). Additionally, the identification of PET biomarkers derived from ^{68}Ga-FAPI-46 PET/CT can be of particular interest in tumor entities, where it could eventually become the gold standard for PET imaging (*22*).

^{68}Ga-FAPI-46 PET/CT may therefore aid treatment decisions not just by providing accurate staging but also by providing prognostic information. The impact on patient prognosis has previously been shown in the context of patients with colorectal cancer, where FAP expression on ^{68}Ga-FAPI-46 PET/CT was associated with a significantly shorter relapse-free survival (*9*).

In our subanalysis of patients with pancreatic cancer, bone metastases (HR, 31.39; 95% CI, 4.33–227.36; $P < 0.01$) in ^{18}F-FDG PET/CT were significantly associated with shorter OS in the univariate analysis and showed borderline significance (HR, 8.67; 95% CI, 0.91–82.78; $P = 0.06$) in the multivariate analysis. On the other hand, with regard to ^{68}Ga-FAPI-46 PET/CT–derived parameters, only total lesion number reached statistical significance in the univariate analysis (HR, 1.09; 95% CI, 1.03–1.15; $P < 0.01$) and multivariate analysis (HR, 1.07; 95% CI, 1.004–1.13; $P = 0.04$).

A prior study on pancreatic cancer has shown that SUV_{max} in ^{68}Ga-FAPI-04 PET/CT had a significant independent prognostic value for recurrence-free survival and that total pancreatic FAP expression (the sum of the multiplication of SUV_{mean} and total FAPI-avid volume) was a significant prognostic indicator for OS (*10*). Similarly, in a published metaanalysis, tumor SUV_{max} on ^{18}F-FDG PET/CT has been shown to be a significant prognostic factor for OS (*19*). Furthermore, a high glycolytic activity in pancreatic cancer has been linked with subtypes that commonly exhibit a poor prognosis (e.g., basal subtype) and is associated with metastatic spread (*23*). In our study, we additionally found that total lesion number on ^{68}Ga-FAPI-46 PET/CT could be a useful prognostic factor for OS in patients with pancreatic cancer. Importantly, the presence of bone metastases on PET/CT correlated more strongly with OS for ^{18}F-FDG than for ^{68}Ga-FAPI-46 in our study. This may be partly attributable to the fact that of the 4 of 39 patients with bone metastases secondary to pancreatic cancer, bone metastases were detected by ^{18}F-FDG PET/CT, by ^{68}Ga-FAPI-46 PET/CT, and by both modalities in 2, 3, and 1 cases, respectively. The large discrepancy in HR between the 2 modalities may therefore be caused by the low number of positive cases in the subgroup with pancreatic cancer.

To our knowledge, this was the first study to report on the prognostic implications of FAPI PET/CT in patients with breast cancer:

In our cohort, total lesion number on ^{68}Ga-FAPI-46 PET/CT, and bone metastases on ^{18}F-FDG PET/CT, were significant prognostic indicators for shorter OS in the univariate analysis; however, total lesion number on ^{68}Ga-FAPI-46 PET/CT and bone metastases on ^{18}F-FDG PET/CT were not significant in the

TABLE 4
Uni- and Multivariate Subanalyses of OS for Patients with Breast Cancer Using Cox Proportional Hazards Regression Analysis (Death Events, $n = 6$; Censored, $n = 11$)

	Univariate		Multivariate	
Parameter	HR	*P*	HR	*P*
^{68}Ga-FAPI-46 PET/CT				
Total lesion number	1.07 (1.01–1.13)	0.02	1.03 (0.95–1.11)	0.47
^{18}F-FDG PET/CT				
Bone metastases	9.64 (1.12–83.30)	0.04	5.58 (0.38–81.50)	0.21

Data are mean followed by 95% CI in parentheses.

TABLE 5
Uni- and Multivariate Subanalyses of OS for Patients with Thoracic Cancer Using Cox Proportional Hazards Regression Analysis (Death Events, $n = 11$; Censored, $n = 19$)

	Univariate	
Parameter	HR	*P*
^{68}Ga-FAPI-46 PET/CT		
Total lesion number	1.01 (0.93–1.10)	0.78
^{18}F-FDG PET/CT		
Bone metastases	1.62 (0.20–13.01)	0.65

Data are mean followed by 95% CI in parentheses.

multivariate analysis. The prognostic value of ^{18}F-FDG PET/CT has been shown by an expansive body of evidence, for which a correlation between glycolytic activity on the one hand and tumor aggressiveness and poor prognosis on the other hand could be established (*20*,*24*). The lack of statistically significant results in the multivariate analysis may at least partially be attributable to insufficient statistical power due to the sample size.

A central limitation of this study is the low number of patients for each tumor entity, potentially affecting statistical power and calling for further prospective analyses on larger cohorts. Especially for the Cox subanalysis, there are few total events and few events per variable (*25*). Also, it has yet to be determined which PET-derived parameters can most accurately predict OS. Future multicenter prospective analyses with a larger sample size may be warranted to confirm the results. In addition, the 50 cases used to train the reader may be a limitation, since interobserver agreement has been shown to be moderate at this experience level; an experience level of at least 300 cases may be needed for substantial agreement (*26*). The prognostic parameters we assessed could complement risk stratification alongside already-established risk factors, such as resection status and neural invasion in the context of pancreatic cancer (*27*,*28*). Also, the absence of segmentation of PET-derived whole-body tumor volume and whole-body SUV_{mean} may be a major limitation.

CONCLUSION

Here, we demonstrate an association of disease extent (parametrized by total lesion number on ^{68}Ga-FAPI-46 PET/CT) on the one hand and OS on the other hand in various malignancies, such as pancreatic cancer. In line with prior publications, ^{18}F-FDG PET/CT allowed for stratification of prognosis, especially in the presence of bone metastases. Improved risk stratification may aid patient management in the future.

DISCLOSURE

Masao Watanabe obtained a postdoctoral fellowship from Humboldt Foundation. Wolfgang Fendler reports fees from SOFIE Biosciences (research funding), Janssen (consultant, speaker), Calyx (consultant, image review), Bayer (consultant, speaker, research funding), Novartis (speaker, consultant), Telix (speaker), GE Healthcare (speaker), Eczacıbaşı Monrol (speaker), Abx (speaker), Amgen (speaker), and Urotrials (speaker), outside the submitted work. Rainer Hamacher reports grants from the Clinician Science Program of the University Medicine Essen Clinician Scientist Academy. He also reports other support from Eli Lilly and Company, Novartis, and PharmaMar, as well as personal fees from PharmaMar and Eli Lilly and Company, outside the submitted work. Kim Pabst reports personal fees and research funds from Bayer Healthcare, outside the submitted work, as well as a Junior Clinician Scientist Stipend from the University Medicine Essen Clinician Scientist Academy and travel fees from IPSEN. Stefan Kasper received honoraria from Merck Serono, MSD, Novartis, BMS, Amgen, Roche, Sanofi-Aventis, Servier, Incyte, Pierre Fabre, and Lilly and research funding from Lilly, BMS, and Roche. Bastian von Tresckow is an advisor or consultant for Allogene, Amgen, BMS/Celgene, Cerus, Gilead Kite, Incyte, IQVIA, Lilly, Merck Sharp & Dohme, Miltenyi, Novartis, Noscendo, Pentixapharm, Pfizer, Pierre Fabre, Qualworld, Roche, Sobi, and Takeda; has received honoraria from AbbVie, AstraZeneca, BMS/Celgene, Gilead Kite, Incyte, Lilly, Merck Sharp & Dohme, Novartis, Roche Pharma AG, and Takeda; reports research funding from Esteve (to the institution), Merck Sharp & Dohme (to the institution), Novartis (to the institution), and Takeda (to the institution); and reports travel support from AbbVie, AstraZeneca, Gilead Kite, Lilly, Merck Sharp & Dohme, Pierre Fabre, Roche, Takeda, and Novartis, all outside the submitted work. Sherko Kümmel reports a consultant or advisory role with Roche/Genentech, Genomic Health, Novartis, AstraZeneca, Amgen, Celgene, SOMATEX, Daiichi Sankyo, pfm medical, Pfizer, MSD Oncology, Lilly, Sonoscape, Gilead Sciences, Seagen, and Agendia. He also reports travel support and expenses from Roche, Daiichi Sankyo, and Gilead Sciences and an uncompensated relationship with WSG. Boris Hadaschik declares grants to the institution from Novartis, BMS, and the German Research Foundation; consulting fees from ABX, Accord, Amgen, AstraZeneca, Bayer, BMS, Janssen, Lightpoint Medical, and Pfizer; payment for lectures from Accord, Astellas, Janssen, and Monrol; support for travel or attending meetings from Bayer, Ipsen, and Janssen; and participation on data safety monitoring boards for Janssen, all outside the submitted work. Viktor Grünwald has received honoraria from Bristol-Myers Squibb, Pfizer, Ipsen, Eisai, MSD Oncology, Merck HealthCare, EUSAPharm, Apogepha, and Ono Pharmaceutical; has an advisory role with Bristol-Myers Squibb, Pfizer, MSD Oncology, Merck HealthCare, Ipsen, Eisai, Debiopharm, PCI Biotech, Cureteq, and Oncorena; and receives travel funds from Pfizer, Ipsen, and Merck HealthCare. Jens Siveke reports honoraria from AstraZeneca, Bayer, Immunocore, Novartis, Roche/Genentech, and Servier, outside the submitted work. Work in his laboratory is supported by the German Cancer Consortium. His institution receives research funding from Bristol-Myers Squibb, Celgene, Eisbach, Bio, and Roch/Genentech. He holds ownership in and serves on the board of directors of Pharma15. Ken Herrmann reports personal fees from Bayer, SIRTEX, Adacap, Curium, Endocyte, IPSEN, Siemens Healthineers, GE Healthcare, Amgen, Novartis, ymabs, Aktis Oncology, Theragnostics, and Pharma 15; personal fees and other fees from SOFIE Biosciences; nonfinancial support from ABX; and grants and personal fees from BTG, outside the submitted work. Manuel Weber reports personal fees from Boston Scientific, Terumo, Advanced Accelerator Applications, IPSEN, and Eli Lilly, outside the submitted work. No other potential conflict of interest relevant to this article was reported.

KEY POINTS

QUESTION: Do findings from ^{68}Ga-FAPI-46 PET/CT have prognostic implications regarding OS?

PERTINENT FINDINGS: Disease extent derived from ^{68}Ga-FAPI-46 PET/CT is a predictor of OS and may enhance risk stratification in various solid tumors.

IMPLICATIONS FOR PATIENT CARE: Improved tumor detection and risk stratification may aide clinical decisions and the pursuit of personalized medicine.

REFERENCES

1. Meyer C, Dahlbom M, Lindner T, et al. Radiation dosimetry and biodistribution of ^{68}Ga-FAPI-46 PET imaging in cancer patients. *J Nucl Med.* 2020;61:1171–1177.
2. Lan L, Zhang S, Xu T, et al. Prospective comparison of ^{68}Ga-FAPI versus ^{18}F-FDG PET/CT for tumor staging in biliary tract cancers. *Radiology.* 2022;304:648–657.
3. Wang L, Tang G, Hu K, et al. Comparison of ^{68}Ga-FAPI and ^{18}F-FDG PET/CT in the evaluation of advanced lung cancer. *Radiology.* 2022;303:191–199.
4. Pang Y, Zhao L, Luo Z, et al. Comparison of ^{68}Ga-FAPI and ^{18}F-FDG uptake in gastric, duodenal, and colorectal cancers. *Radiology.* 2021;298:393–402.
5. Fitzgerald AA, Weiner LM. The role of fibroblast activation protein in health and malignancy. *Cancer Metastasis Rev.* 2020;39:783–803.
6. Wikberg ML, Edin S, Lundberg IV, et al. High intratumoral expression of fibroblast activation protein (FAP) in colon cancer is associated with poorer patient prognosis. *Tumour Biol.* 2013;34:1013–1020.
7. Cohen SJ, Alpaugh RK, Palazzo I, et al. Fibroblast activation protein and its relationship to clinical outcome in pancreatic adenocarcinoma. *Pancreas.* 2008;37:154–158.
8. Moreno-Ruiz P, Corvigno S, Grootenhuis NCT, et al. Stromal FAP is an independent poor prognosis marker in non-small cell lung adenocarcinoma and associated with p53 mutation. *Lung Cancer.* 2021;155:10–19.
9. Strating E, Wassenaar E, Verhagen M, et al. Fibroblast activation protein identifies consensus molecular subtype 4 in colorectal cancer and allows its detection by ^{68}Ga-FAPI-PET imaging. *Br J Cancer.* 2022;127:145–155.
10. Ding J, Qiu J, Hao Z, et al. Prognostic value of preoperative [^{68}Ga]Ga-FAPI-04 PET/CT in patients with resectable pancreatic ductal adenocarcinoma in correlation with immunohistological characteristics. *Eur J Nucl Med Mol Imaging.* 2023;50:1780–1791.
11. Liu Q, Shi S, Liu S, et al. The added value of [^{68}Ga]Ga-DOTA-FAPI-04 PET/CT in pancreatic cancer: a comparison to [^{18}F]F-FDG. *Eur Radiol.* 2023;33:5007–5016.
12. Kessler L, Ferdinandus J, Hirmas N, et al. ^{68}Ga-FAPI as a diagnostic tool in sarcoma: data from the ^{68}Ga-FAPI PET prospective observational trial. *J Nucl Med.* 2022;63:89–95.
13. Ferdinandus J, Kessler L, Hirmas N, et al. Equivalent tumor detection for early and late FAPI-46 PET acquisition. *Eur J Nucl Med Mol Imaging.* 2021;48:3221–3227.
14. Kessler L, Ferdinandus J, Hirmas N, et al. Pitfalls and common findings in ^{68}Ga-FAPI PET: a pictorial analysis. *J Nucl Med.* 2022;63:890–896.
15. Hirmas N, Hamacher R, Sraieb M, et al. Fibroblast activation protein positron emission tomography and histopathology in a single-center database of 324 patients and 21 tumor entities. *J Nucl Med.* 2023;64:711–716.
16. Pabst KM, Trajkovic-Arsic M, Cheung PFY, et al. Superior tumor detection for ^{68}Ga-FAPI-46 versus ^{18}F-FDG PET/CT and conventional CT in patients with cholangiocarcinoma. *J Nucl Med.* 2023;64:1049–1055.
17. Lan L, Liu H, Wang Y, et al. The potential utility of [^{68}Ga]Ga-DOTA-FAPI-04 as a novel broad-spectrum oncologic and non-oncologic imaging agent: comparison with [^{18}F]FDG. *Eur J Nucl Med Mol Imaging.* 2022;49:963–979.
18. Beuschlein F, Weigel J, Saeger W, et al. Major prognostic role of Ki-67 in localized adrenocortical carcinoma after complete resection. *J Clin Endocrinol Metab.* 2015;100:841–849.
19. Zhu D, Wang L, Zhang H, et al. Prognostic value of ^{18}F-FDG-PET/CT parameters in patients with pancreatic carcinoma: a systematic review and meta-analysis. *Medicine (Baltimore).* 2017;96:e7813.
20. Paydary K, Seraj SM, Zadeh MZ, et al. The evolving role of FDG-PET/CT in the diagnosis, staging and treatment of breast cancer. *Mol Imaging Biol.* 2019;21:1–10.
21. Liu J, Dong M, Sun X, Li W, Xing L, Yu J. Prognostic value of ^{18}F-FDG PET/CT in surgical non-small cell lung cancer: a meta-analysis. *PLoS One.* 2016;11:e0146195.
22. Calais J, Mona CE. Will FAPI PET/CT replace FDG PET/CT in the next decade? Point—an important diagnostic, phenotypic, and biomarker role. *AJR.* 2021;216:305–306.
23. Martens S, Lefesvre P, Nicolle R, et al. Different shades of pancreatic ductal adenocarcinoma, different paths towards precision therapeutic applications. *Ann Oncol.* 2019;30:1428–1436.
24. Groheux D, Cochet A, Humbert O, et al. ^{18}F-FDG PET/CT for staging and restaging of breast cancer. *J Nucl Med.* 2016;57(suppl 1):17S–26S.
25. Vittinghoff E, McCulloch CE. Relaxing the rule of ten events per variable in logistic and Cox regression. *Am J Epidemiol.* 2007;165:710–718.
26. Mei R, Kessler L, Pabst KM, et al. ^{68}Ga-FAPI PET/CT interobserver agreement on tumor assessment: an international multicenter prospective study. *J Nucl Med.* 2023;64:1043–1048.
27. Strobel O, Neoptolemos J, Jäger D, Büchler MW. Optimizing the outcomes of pancreatic cancer surgery. *Nat Rev Clin Oncol.* 2019;16:11–26.
28. Iwasaki T, Hiraoka N, Ino Y, et al. Reduction of intrapancreatic neural density in cancer tissue predicts poorer outcome in pancreatic ductal carcinoma. *Cancer Sci.* 2019;110:1491–1502.

In Vivo PET Imaging of ^{89}Zr-Labeled Natural Killer Cells and the Modulating Effects of a Therapeutic Antibody

Truc T. Pham[1], Alicia Chenoweth[2,3], Natasha Patel[1], Arshiya Banu[1], Gabriel Osborn[2], Philip J. Blower[1], Sophia N. Karagiannis[2,3], and Michelle T. Ma[1]

[1]*Department of Imaging Chemistry and Biology, School of Bioengineering and Imaging Sciences, King's College London, London, United Kingdom;* [2]*St. John's Institute of Dermatology, School of Basic and Medical Biosciences, King's College London, London, United Kingdom; and* [3]*Breast Cancer Now Research Unit, School of Cancer and Pharmaceutical Sciences, King's College London, Guy's Hospital, London, United Kingdom*

Natural killer (NK) cells can kill cancer cells via antibody-dependent cell-mediated cytotoxicity (ADCC): a tumor-associated IgG antibody binds to the Fcγ receptor CD16 on NK cells via the antibody Fc region and activates the cytotoxic functions of the NK cell. Here, we used PET imaging to assess NK cell migration to human epidermal growth factor receptor 2 (HER2)–positive HCC1954 breast tumors, examining the influence of HER2-targeted trastuzumab antibody treatment on NK cell tumor accumulation. **Methods:** Human NK cells from healthy donors were expanded ex vivo and labeled with [^{89}Zr]Zr-oxine. In vitro experiments compared the phenotypic markers, viability, proliferation, migration, degranulation, and ADCC behaviors of both labeled (^{89}Zr-NK) and unlabeled NK cells. Female mice bearing orthotopic human breast HCC1954 tumors were administered ^{89}Zr-NK cells alongside trastuzumab treatment or a sham treatment and then scanned using PET/CT imaging over 7 d. Flow cytometry and γ-counting were used to analyze the presence of ^{89}Zr-NK cells in liver and spleen tissues. **Results:** ^{89}Zr cell radiolabeling yields measured 42.2% ± 8.0%. At an average specific activity of 16.7 ± 4.7 kBq/10^6 cells, ^{89}Zr-NK cells retained phenotypic and functional characteristics including CD56 and CD16 expression, viability, migration, degranulation, and ADCC capabilities. In vivo PET/CT studies indicated predominant accumulation of ^{89}Zr-NK cells in the liver and spleen. Ex vivo analyses of liver and spleen tissues indicated that the administered human ^{89}Zr-NK cells retained their radioactivity in vivo and that ^{89}Zr did not transfer to cells of murine soft tissues, thus validating this ^{89}Zr PET method for NK cell tracking. Notably, ^{89}Zr-NK cells migrated to HER2-positive tumors, both with and without trastuzumab treatment. Trastuzumab treatment was associated with an increased ^{89}Zr-NK cell signal at days 1 and 3 after injection. **Conclusion:** In vitro, ^{89}Zr-NK cells maintained key cellular and cytotoxic functions. In vivo, ^{89}Zr-NK cells trafficked to HER2-postive tumors, with trastuzumab treatment correlating with enhanced ^{89}Zr-NK infiltration. This study demonstrates the feasibility of using PET to image ^{89}Zr-NK cell infiltration into solid tumors.

Key Words: natural killer cell; ADCC; trastuzumab; HER2 receptor; cell tracking

J Nucl Med 2024; 65:1035–1042
DOI: 10.2967/jnumed.124.267876

Monoclonal IgG antibodies used in clinical oncology exert therapeutic effects by inhibiting cancer cell receptors that drive tumor proliferation. In breast cancer treatment, trastuzumab targets human epidermal growth factor receptor 2 (HER2). By binding of the antibody Fab region to HER2, trastuzumab prevents HER2 dimerization, thus inhibiting the downstream proliferative signals that promote tumor growth. In addition, in combination with immune effector cells (most notably natural killer [NK] cells), trastuzumab can trigger antibody-dependent cell-mediated cytotoxicity (ADCC), resulting in immune-cell activation and cancer-cell lysis.

NK cells express the low-affinity yet potent FcγRIIIA (or CD16) activating receptor. In vivo, a specific IgG monoclonal antibody can engage via its Fab region with its target antigen on a cancer cell; simultaneously, the Fc region of the monoclonal antibody is recognized by CD16, facilitating the activation of cytotoxic NK cell functions. NK cells can also independently induce cytotoxic responses against cancer cells through lytic synapse formation or apoptotic pathways. NK cells also modulate other immune responses involving T cells, macrophages, and dendritic cells through cytokine or chemokine pathways.

ADCC can contribute to the efficacy of HER2-targeted immunotherapies. In patients administered HER2-targeted immunotherapies, improved responses are associated with higher tumor infiltration of NK cells (*1*–*3*) or lymphocytes (*4*,*5*) in HER2-positive breast cancer biopsies. Furthermore, analyses of surgical specimens from HER2-positive breast cancers have previously revealed an increase in NK cells in tumor tissue after trastuzumab treatment, relative to specimens collected either before treatment (*1*) or from case-matched controls who did not receive trastuzumab treatment (*2*). Similarly, in a murine model of HER2-positive breast cancer, an increase in NK cell numbers was observed in tumors after treatment with a trastuzumab-derived antibody–drug conjugate (*6*). Highlighting the clinical significance of ADCC effects mediated by NK cells, a phase 1 clinical trial in patients with HER2-positive tumors recently reported that a therapeutic regime of expanded autologous NK cells in combination with trastuzumab is safe, exhibits tumor engagement, and shows preliminary evidence of therapeutic efficacy (*7*). Compared with paired tumor biopsies obtained before treatment, increases in NK cells,

Received Apr. 2, 2024; revision accepted Apr. 13, 2024.
For correspondence or reprints, contact Truc T. Pham (truc.pham@kcl.ac.uk), Sophia N. Karagiannis (sophia.karagiannis@kcl.ac.uk), or Michelle T. Ma (michelle.ma@kcl.ac.uk).
Published online Jun. 6, 2024.

lymphocytes, and apoptosis activity were observed in biopsies after treatment.

The distribution and tumor infiltration of NK cells, and how this may be influenced by therapeutic antibody treatment, is therefore important in understanding the immunologic landscape of cancer at the cellular, tissue, and whole-body levels. Whole-body imaging can provide spatial and longitudinal insights into the distribution of NK cells in vivo. In direct cell-tracking methods, NK cells are labeled ex vivo with a contrast agent and then administered for in vivo tracking using whole-body imaging. This approach has been previously applied using optical imaging (*8*,*9*), MRI (*10*), SPECT imaging or γ-scintigraphy with [^{111}In]In-oxine (*11*–*13*), and PET imaging using [^{89}Zr]Zr-oxine (*14*). Optical imaging and MRI can provide high-resolution images but lack quantitative attributes. In contrast, PET and γ-scintigraphy/SPECT imaging can provide real-time and quantitative information, and both are highly sensitive.

A recently developed method enables the radiolabeling of cells using [^{89}Zr]Zr-oxine (^{89}Zr half-life, 78.41 h), facilitating longitudinal cell tracking over 1–2 wk with PET (*15*). The method has been applied to track NK cells (*14*), T cells (*16*,*17*), and bone marrow cells (*18*) in vivo, among others (*19*). Similar methods using [^{111}In]In-oxine are well established for ^{111}In cell tracking with γ-scintigraphy/SPECT imaging. In both cases, [^{89}Zr]Zr-oxine and [^{111}In]In-oxine diffuse into cells and release the radionuclide intracellularly, resulting in cell labeling. Previous in vivo studies have investigated the biodistribution of ^{89}Zr- and ^{111}In-labeled NK cells in healthy and cancer subjects without augmentation of therapeutic adjuvants (*11*–*14*). Here, we use PET/CT tracking to study the biodistribution of ^{89}Zr-labeled human NK (^{89}Zr-NK) cells in mice bearing HER2-positive solid orthotopic HCC1954 human breast tumors and to assess whether administration of HER2-targeted trastuzumab enhances NK cell infiltration into tumors.

MATERIALS AND METHODS

Human NK Cells, ^{89}Zr Radiolabeling, and Cell Assays

Experiments using human blood received approval from King's College London–Research Ethics Committee (study reference HR/DP-20/21-24483). All donors provided written informed consent. NK cells were isolated from the mononuclear cell layer of human peripheral blood, cultured, and expanded ex vivo (*20*). [^{89}Zr]Zr-oxine (~45 kBq/10^6 cells) was added to ex vivo–expanded NK cells suspended in phosphate-buffered saline (PBS) at 15×10^6 to 20×10^6 cells/mL, followed by incubation for 15 min at ambient temperature (*15*), as shown in the supplemental materials (supplemental materials are available at http://jnm.snmjournals.org).

Cell retention, viability and growth assays, chemotaxis assays, CD107a degranulation assays, and ADCC assays were performed on ^{89}Zr-NK and unlabeled NK cells (supplemental materials).

In Vivo Murine and PET/CT Biodistribution Studies

Animal experiments were ethically reviewed by the Animal Welfare and Ethical Review Board at King's College London and were performed in accordance with the Animals (Scientific Procedures) Act 1986 U.K. Home Office regulations governing animal experimentation. NSG mice (8-to-10-wk-old female NOD-scid-γ [NOD.Cg-Prkdc^{scid} Il2rg^{tm1Wjl}/SzJ]; Charles River) were inoculated with 1.5×10^6 HCC1954 cells in the left mammary fat pad between the fourth and fifth pairs of nipples. Experiments commenced when tumors reached 100–150 mm^3.

Tumor-bearing mice were randomized into 3 groups and intravenously administered 1×10^7 freshly radiolabeled NK cells (150–200 kBq),

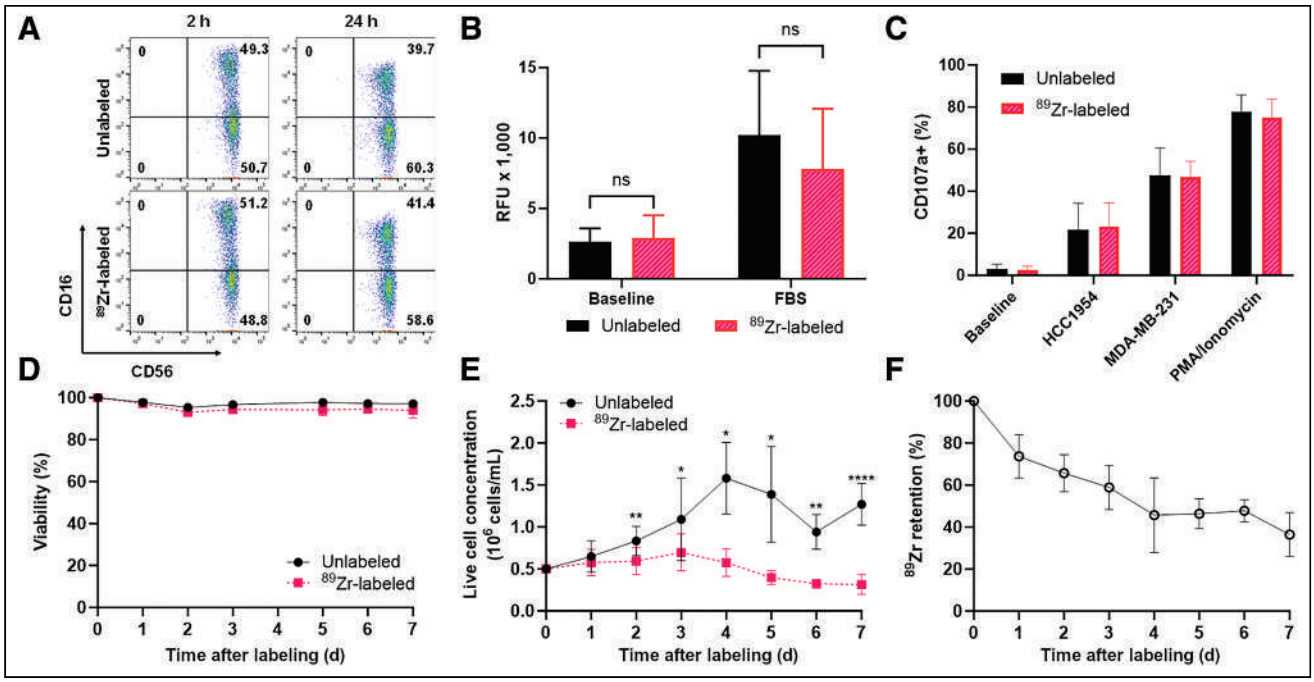

FIGURE 1. In vitro functional and phenotypic characteristics of ^{89}Zr-NK cells and ^{89}Zr-retention. (A) Flow cytometry shows comparable CD56 and CD16 expression in unlabeled and ^{89}Zr-NK cells. (B) Chemotaxis assays show that chemotactic responses to fetal bovine serum, in unlabeled and ^{89}Zr-NK cells, are similar (mean ± SD, $n = 5$). (C) Degranulation assays reveal similar degranulation levels in ^{89}Zr-NK and unlabeled NK cells under various conditions (mean ± SD, $n = 4$). (D and E) Viability (D) and proliferation profiles (E) indicate that both ^{89}Zr-NK and unlabeled NK cells remained viable for up to 7 d in culture without interleukins. Although unlabeled NK cells continued to proliferate, ^{89}Zr-NK cells did not (mean ± SD, $n = 7$). (F) ^{89}Zr retention in ^{89}Zr-NK cells gradually decreased over 7 d in culture, with 36.4% ± 10.5% of initial activity remaining on day 7 (mean ± SD, $n = 7$). *$P < 0.05$. **$P < 0.01$. ****$P < 0.0001$. FBS = fetal bovine serum; ns = nonsignificant; PMA = phorbol 12-myristate-13-acetate; RFU = relative fluorescence units.

rhIL-15 (2,500 IU), and either PBS, anti–normal immunosuppressive protein isotype control (5 mg/kg), or trastuzumab (5 mg/kg) (~200 μL of PBS). NK cells from 3 healthy human volunteers were used. Additional doses of rhIL-15 (2,500 IU/dose) were given on days 3 and 6 via intraperitoneal injection to support the in vivo survival and expansion of NK cells (*13*).

PET/CT imaging was conducted using a nanoScan PET/CT scanner (Mediso) on days 1, 3, and 7 after cell injection. The images were coregistered and analyzed using VivoQuant version 3.0 (Invicro). SPECT/CT imaging using [^{111}In]In-CHX-A″-DTPA-trastuzumab was performed to determine the antibody biodistribution (supplemental materials).

Ex Vivo Flow Cytometry Study

Single-cell suspensions, prepared from mouse liver and spleen collected 3 d after ^{89}Zr-NK cell administration, were stained with anti-human antibodies CD56-FITC, CD16-APC, and CD45-PE-Cy7. CD45-positive and CD45-negative populations were sorted on a BD FACSMelody cell sorter (BD Biosciences) and collected for γ-counting (supplemental materials).

Statistical Analysis

Independent experiments were conducted on separate days using NK cells from different donors. Statistical analysis was conducted using Prism 9.5.0 (GraphPad Software). Data are presented as mean ± SD. Statistical significance was determined using either an unpaired or paired 2-tailed Student *t* test. For tumor uptake analysis across the treatment groups, 1-way ANOVA followed by *t* tests with multiple comparison correction (Tukey method) was performed. A *P* value below 0.05 was considered statistically significant.

RESULTS

In Vitro–Labeled ^{89}Zr-NK Cells Show Comparable Phenotype and Functional Characteristics to Unlabeled NK Cells

Using a prefabricated oxine kit (*15*), [^{89}Zr]Zr-oxine was reproducibly synthesized, with a radiochemical yield of 90.0% ± 5.8%. Ex vivo–expanded human primary NK cells from peripheral blood were incubated with [^{89}Zr]Zr-oxine at room temperature for 15 min, with cell radiolabeling efficiencies of 42.2% ± 8.0%. The final specific activity measured 16.7 ± 4.7 kBq/10^6 cells.

To assess the effect of ^{89}Zr labeling on human NK cells, several NK cell markers and functions were measured in ^{89}Zr-NK cells, including phenotypic CD56 and CD16 expression and functional characteristics, namely, migratory ability, viability and proliferation, and cytotoxic degranulation and ADCC responses. Flow cytometry of both ^{89}Zr-NK (measured 2 and 24 h after radiolabeling) and unlabeled NK cells indicated that CD56 and CD16 expression was unaffected by ^{89}Zr labeling (Fig. 1A). The migration of ^{89}Zr-NK (24 h after radiolabeling) and unlabeled NK cells toward fetal bovine serum stimulus was similar, with migration toward fetal bovine serum for both cells shown to be 3- to 4-fold higher than background migration (Fig. 1B). The cytotoxic response of NK cells was measured in a degranulation assay by quantifying the levels of lysosome-associated membrane protein-1 (CD107a) (Fig. 1C). The percentages of CD107a-positive cells in both ^{89}Zr-NK cells and unlabeled NK cells were comparable across all conditions: high percentages in the phorbol 12-myristate-13-acetate/ionomycin–positive controls (74.9% ± 8.7% and 77.8% ± 8.0%), moderate percentages in the presence of either HCC1954 (23.4% ± 11.0% and 21.5% ± 12.7%) or MDA-MB-231 (46.7.4% ± 7.4% and 47.6% ± 13.0%) cocultures, and minimal baseline degranulation (2.4% ± 1.9% and 2.9% ± 2.4%).

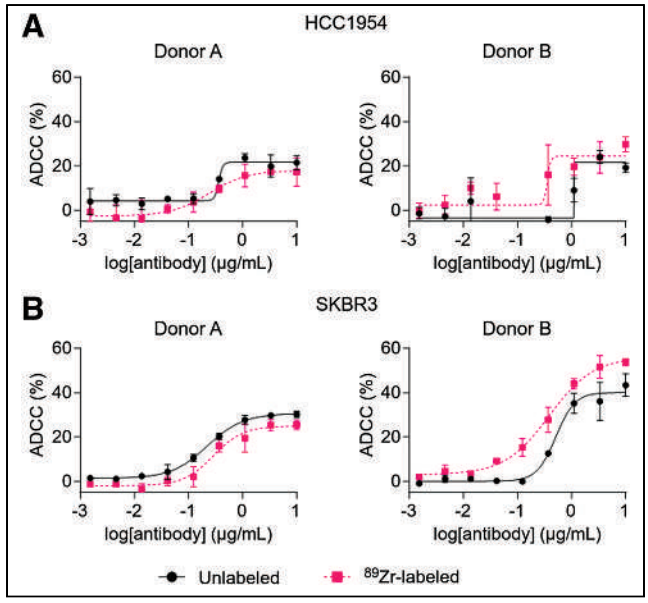

FIGURE 2. ADCC assays using ^{89}Zr-labeled and unlabeled NK cells against HER2-expressing breast cancer cell lines HCC1954 (A) and SKBR3 (B) (10:1 effector/target ratio) and various trastuzumab concentrations. ^{89}Zr-NK cells demonstrated similar ADCC response to unlabeled NK cells. ADCC response varied among human NK cells from different healthy volunteers (Supplemental Fig. 1). Data were fitted to 4-parameter logistic curve.

The viability of ^{89}Zr-NK cells in culture, determined by trypan blue assay, remained unaffected (>95%) over 7 d, as compared with unlabeled NK cells (Fig. 1D). However, in the absence of interleukins, ^{89}Zr-NK cells did not proliferate after radiolabeling, even at low levels of associated ^{89}Zr (~16 kBq/10^6 cells) (Fig. 1E), whereas unlabeled NK cells continued to proliferate; the difference became significant from day 2 in culture ($P < 0.05$). Lastly, ^{89}Zr-radioactivity slowly dissociated from NK cells, with the initial activity in the cells remaining at 73.7% ± 10.4% at day 1, 58.9% ± 10.5% at day 3, and 36.4% ± 10.5% at day 7 (Fig. 1F).

The cytolytic activity of ^{89}Zr-NK cells (24 h after radiolabeling) and unlabeled NK cells, from 4 healthy human donors, was assessed in ADCC assays using trastuzumab and HER2-positive breast cancer cell lines SKBR3 and HCC1954 (Fig. 2). For each donor, ^{89}Zr-NK cells displayed ADCC effects highly similar to those with unlabeled NK cells. Consistent with published literature, ADCC effects were donor-specific: trastuzumab boosted the cytolytic activity of NK cells from donors A and B against both cell lines in a concentration-dependent manner, whereas negligible ADCC effects were observed for donors C and D under our experimental conditions (Supplemental Fig. 1).

^{89}Zr-NK Cells in HCC1954 Tumor–Bearing Mice Demonstrate Enhanced Tumor Localization with Trastuzumab Treatment

Using PET/CT imaging, the migration and accumulation of human ^{89}Zr-NK cells were studied in female NSG immunodeficient mice (which lack T, B, and NK cells) bearing orthotopic human HCC1954 breast tumors. Despite expressing high levels of HER2, HCC1954 cells are resistant to the Fab-mediated HER2-binding downstream inhibitory (and associated therapeutic) effects of trastuzumab (*21*). Therefore, the HCC1954 model is useful in assessing trastuzumab treatment on NK cell tumor accumulation in a setting where the antibody can only exert Fc-mediated effector functions against these tumors.

Here, 1×10^7 ^{89}Zr-NK cells were coadministered to mice intravenously (tail vein) in combination with either a PBS sham ($n = 6$), HER2-targeted trastuzumab ($n = 6$), or a hapten-specific anti–normal immunosuppressive protein IgG1 isotype control antibody ($n = 4$) (which does not recognize mammalian antigens including HER2 but bears a human Fc region capable of binding to CD16 receptors of NK cells). NK cells from 3 different healthy volunteers were used, with 2 animals in each group receiving ^{89}Zr-NK cells from each volunteer. Additionally, mice received intraperitoneal doses of rhIL-15 to support the survival of NK cells in vivo (*13*). PET/CT scanning was performed 1, 3, and 7 d after injection of ^{89}Zr-NK cells.

In all mice, ^{89}Zr-NK cells migrated to the lungs, liver, and spleen within the first 24 h, with redistribution from the lungs to the liver and spleen over 7 d (Fig. 3A).

PET/CT imaging indicated that ^{89}Zr-NK cells accumulated in tumors but decreased from day 1 to day 7 after injection. ^{89}Zr-NK cell tumor distribution was highly heterogeneous in all groups of mice. A significant proportion of ^{89}Zr-NK cells localized at the periphery of tumors (Supplemental Video 1). Importantly, from PET quantification (Fig. 3B), mice in the trastuzumab-treated group demonstrated significantly higher ^{89}Zr-NK cell infiltration in tumors at 1 d after injection (0.66 ± 0.13 percentage of injected dose [%ID]·g^{-1}) compared with both the sham group (0.38 ± 0.16 %ID·g^{-1}, $P = 0.0063$) and the isotype group at 1 d after injection (0.37 ± 0.11 %ID·g^{-1}, $P = 0.0499$). Similarly, at 3 d after injection, the trastuzumab-treated group demonstrated higher ^{89}Zr-NK cell tumor infiltration (0.34 ± 0.12 %ID·g^{-1}) compared with both the sham group (0.21 ± 0.04 %ID·g^{-1}, $P = 0.0593$) and the isotype group (0.18 ± 0.03 %ID·g^{-1}, $P = 0.0268$). At the same time points, there was no significant difference in tumor activity between the isotype-treated group and the PBS sham–treated group. In concordance with the gradual loss of the ^{89}Zr label observed after culturing ^{89}Zr-NK cells for 7 d in vitro, in this in vivo study, only low amounts of ^{89}Zr were detected in tumors 7 d after injection (0.15 ± 0.04 %ID·g^{-1} in the trastuzumab group) and no differences between groups were found at this time point (Fig. 3B).

Ex vivo biodistribution and tissue γ-counting experiments at days 3 and 7 provided results similar to those of PET image quantification, demonstrating comparable radioactivity concentrations in major organs and tissues (Supplemental Fig. 2). However, no significant differences in tumor radioactivity between trastuzumab-treated, PBS sham, and isotype groups were found at day 3, likely because of the loss of NK cells during washing steps after dissection, given their predominant localization in the tumor periphery.

^{89}Zr-NK Cells Accumulate and Persist in Spleen and Liver Tissues

To validate this ^{89}Zr-NK PET imaging method, ex vivo flow cytometric phenotyping was undertaken. Liver and spleen tissues from mice administered ^{89}Zr-NK cells (3 d after injection) were processed to form single-cell suspensions, followed by staining. Flow cytometry (Fig. 4) revealed the presence of human CD45-positive cells, which were further identified as CD56-positive/CD16-positive NK cells. CD45-positive and CD45-negative cell populations were separated and counted for radioactivity: human CD45-positive cells from the liver measured an average of 1,899 counts per minute/10^3 cells, whereas CD45-negative cells measured 0.9 counts per minute/10^3 cells; CD45-positive cells from the spleen measured 1,230 counts per minute/10^3 cells, whereas CD45-negative cells measured 0.8 counts per minute/10^3 cells. This indicated that the ^{89}Zr signal was largely associated with human NK cells in soft tissue.

The accumulation of ^{89}Zr-NK cells was particularly high in the spleen across all groups, with ^{89}Zr radioactivity concentration the highest in animals coadministered trastuzumab at 3 and 7 d after injection (Fig. 3B). To investigate this further, ^{89}Zr-NK cells were coadministered with the [^{111}In]In-CHX-A″-DTPA-trastuzumab immunoconjugate. At 3 d after injection, PET/CT and SPECT/CT showed colocalization of the ^{89}Zr signal and ^{111}In signal (0.45 ± 0.001 %ID) in splenic tissue (Fig. 5A). SPECT/CT imaging also indicated that significant amounts of [^{111}In]In-CHX-A″-DTPA-trastuzumab accumulated in HER2-positive HCC1954 tumors (2.41 ± 0.006 %ID). Importantly, the heterogeneous PET signal, attributed to infiltration of ^{89}Zr-NK cells, was coincident with the SPECT signal of [^{111}In]In-CHX-A″-DTPA-trastuzumab in tumor tissue (Fig. 5B).

Lastly, to confirm the presence of human NK cells in spleen, liver, and tumors in this specific NSG orthotopic HCC1954 breast cancer murine model, NK cells were labeled ex vivo with fluorescent CMFDA (5-chloromethylfluorescein diacetate), before intravenous in vivo administration, both with and without trastuzumab. Confocal microscopy of tumor, lung, spleen, and liver sections obtained 3 d after injection and costained with DAPI (4′,6-diamidino-2-phenylindole) revealed the presence of CMFDA-labeled NK cells in these tissues (Fig. 6; Supplemental Fig. 3).

DISCUSSION

^{89}Zr-oxine (*19*) has been increasingly used for PET tracking of immune cells, including NK, chimeric antigen receptor T, γδ-T, and bone marrow cells (*16*,*17*). Here, the ^{89}Zr radiolabeling yields and in vitro cellular retention of NK cells were comparable to those of previous studies of NK cells (*14*) and other immune cells (*17*). Importantly, the average specific activity of ^{89}Zr-NK cells used here did not significantly alter crucial functional NK cell characteristics, including NK cellular viability, motility, activation, and cytolytic potency, and key phenotypic markers, consistent with prior reports (*14*). Although in vitro retention of ^{89}Zr radioactivity decreased over 7 d, retention at days 1 and 3 was sufficiently high to enable reliable in vivo ^{89}Zr-NK cell PET tracking.

PET/CT images revealed initial margination of ^{89}Zr-NK cells in lung—the first capillary bed encountered by intravenously injected cells—followed by redistribution to the liver and spleen. This is consistent with many prior cell-tracking reports (Supplemental Table 1) (*11*–*14*).

Additionally, ^{89}Zr activity accumulated in the mouse bones, most prominently in the joints, consistent with reports that dissociated oxyphilic Zr^{4+} is associated with regions of high bone mineralization (*22*). It is highly probable that a portion of this signal is a result of NK cell migration to the bone marrow (*11*). In addition, our ex vivo flow cytometric evaluations demonstrated that NK cells isolated from liver and spleen tissues showed 1,500-fold and 2,100-fold higher levels of ^{89}Zr radioactivity than did murine spleen and liver cells, respectively, indicating that in soft tissue, ^{89}Zr activity is largely associated with only the administered human NK cells.

Prior imaging studies in murine cancer models and cancer patients, showing the migration of prelabeled NK cells to tumors, are consistent with our data. Near-infrared optical imaging has indicated the in vivo migration of near-infrared-dye–labeled human NK cells to human MDA-MB-231 breast tumors in NSG mice (*8*). Whole-body SPECT imaging studies in patients with

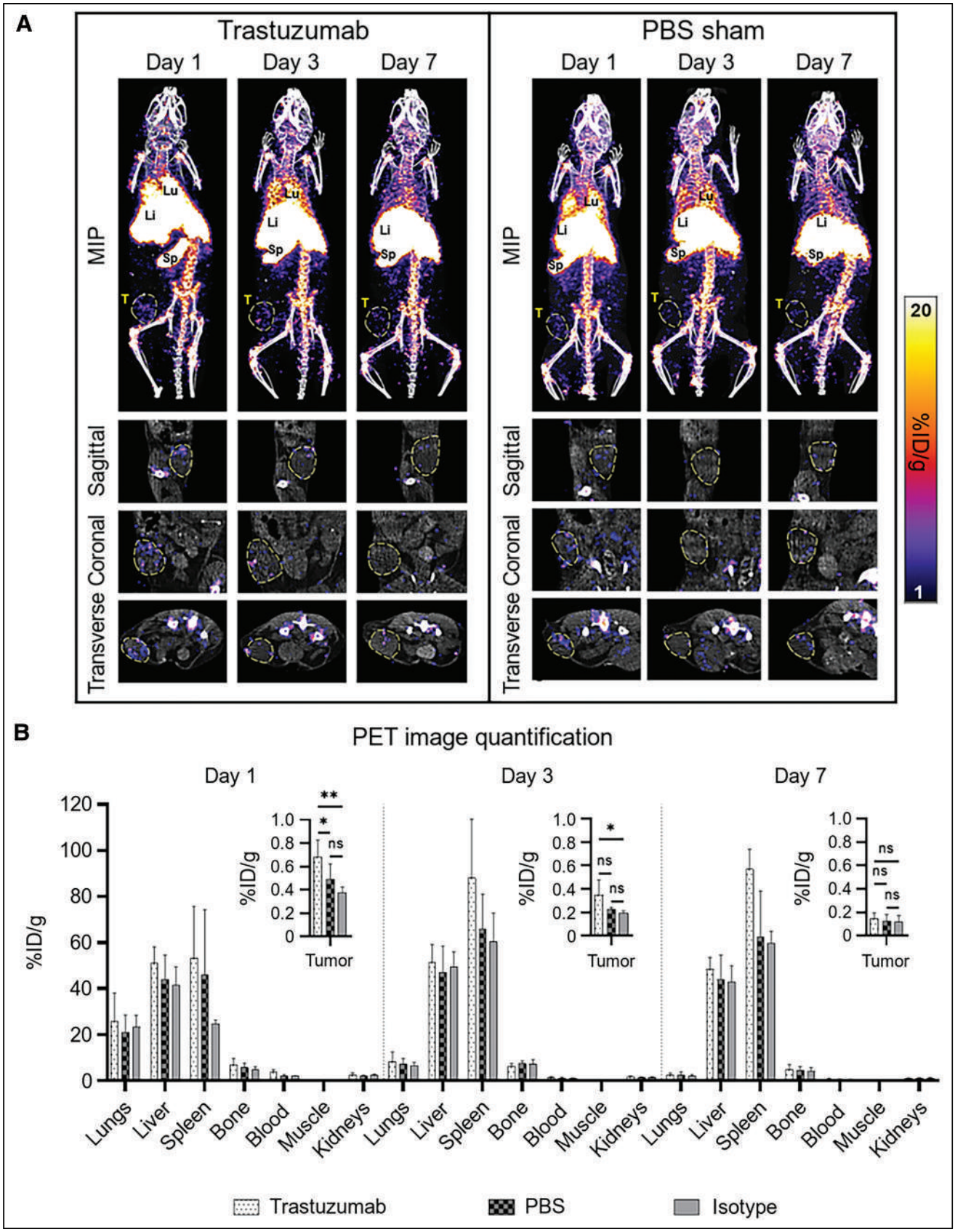

FIGURE 3. Biodistribution of ^{89}Zr-NK cells in female NSG mice bearing orthotopic HER2-expressing HCC1954 tumors. (A) Representative maximum-intensity projection (MIP) and tumor slice PET/CT images of mice administered ^{89}Zr-NK cells (10^7 cells, ~150–200 kBq) in combination with trastuzumab (5 mg/kg) or PBS only. Tumors are outlined for clarity. (B) PET image quantification of selected organs and tumors (mean ± SD, n = 4–6/group). *$P < 0.05$. **$P < 0.01$. Li = liver; Lu = lungs; MIP = maximum-intensity projection; ns = nonsignificant; Sp = spleen; T = tumor.

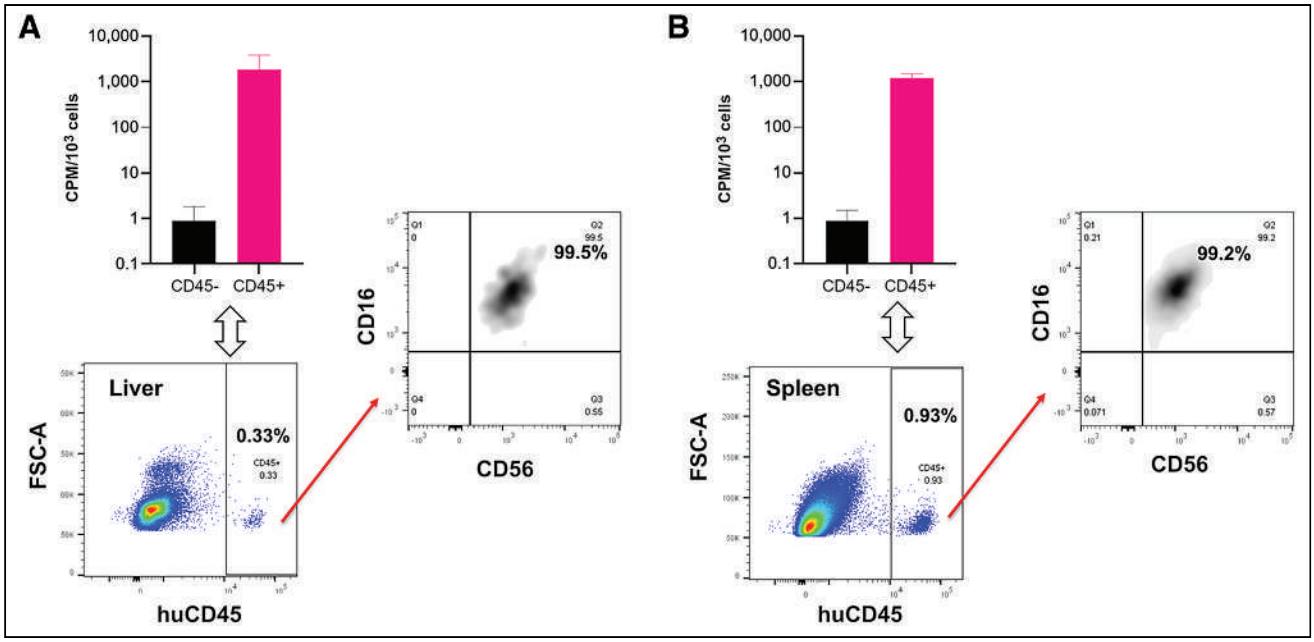

FIGURE 4. Flow cytometry and γ-counting of CD45-positive and CD45-negative cell populations from murine liver (A) and spleen (B) revealed that ^{89}Zr radioactivity was associated with human CD45-positive (huCD45) cells (n = 4, mean ± SD), which were confirmed as C56-positive/CD16-positive NK cells. CPM = counts per minute; FSC-A = forward scatter area.

renal cell carcinoma have evidenced that ^{111}In-labeled allogenic NK cells migrate to metastases (*11*).

We show that ^{89}Zr-NK cells migrate to HCC1954 breast cancer xenografts, with or without trastuzumab treatment. At 1 and 3 d after injection, enhanced NK cell infiltration in tumor tissue is associated with coadministration of trastuzumab, aligning with clinical evidence (*1*,*2*,*7*). However, although statistically significant, this enhancement remains relatively modest. Several mechanisms could restrict NK cell tumor infiltration. In solid tumors, such as ovarian carcinoma and lung cancer, NK cell activation by antitumor antibody therapy is limited (*23*–*25*). NK cells may be exhausted in the tumor microenvironment because of the downregulation of activation markers (*26*), leading to reduced infiltration and retention. Alternatively, on activation, CD16 can be shed or sequestered, thus modulating ADCC effects (*27*).

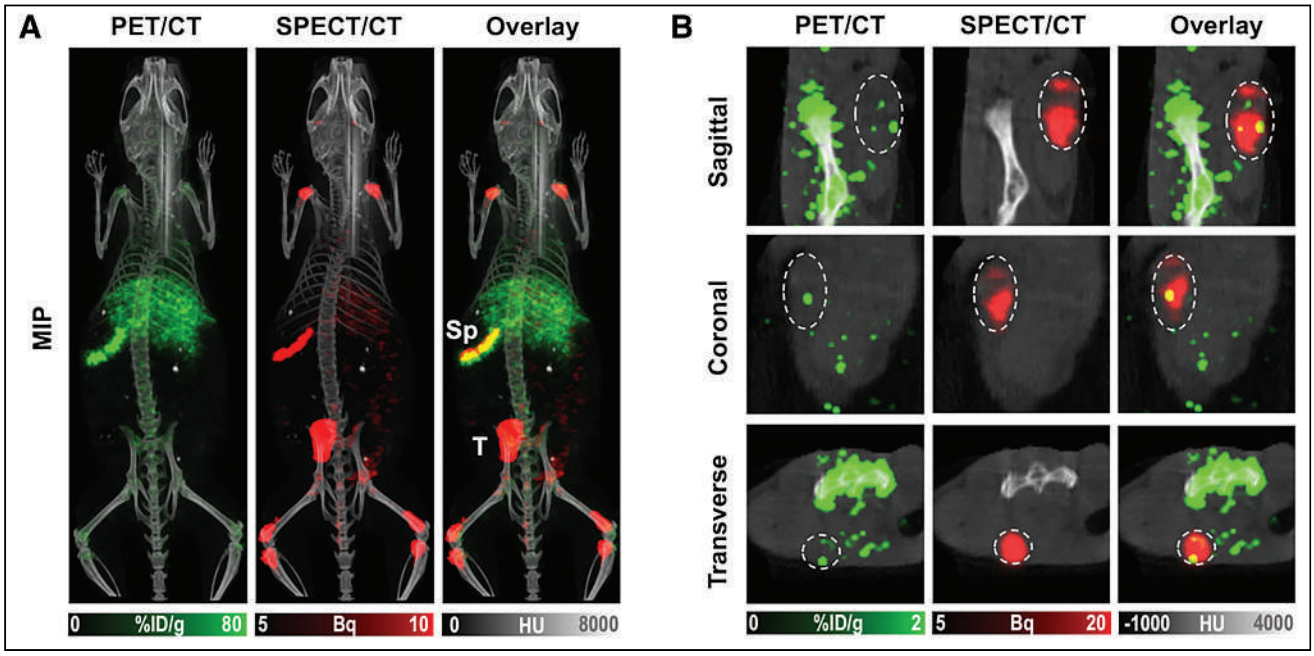

FIGURE 5. Maximum-intensity projection (MIP) (A) and tumor slice PET/CT and SPECT/CT (B) images of mice 3 d after injection of ^{89}Zr-NK cells in combination with [^{111}In]In-CHX-A″-DTPA-trastuzumab. HU = Hounsfield unit; Sp = spleen; T = tumor.

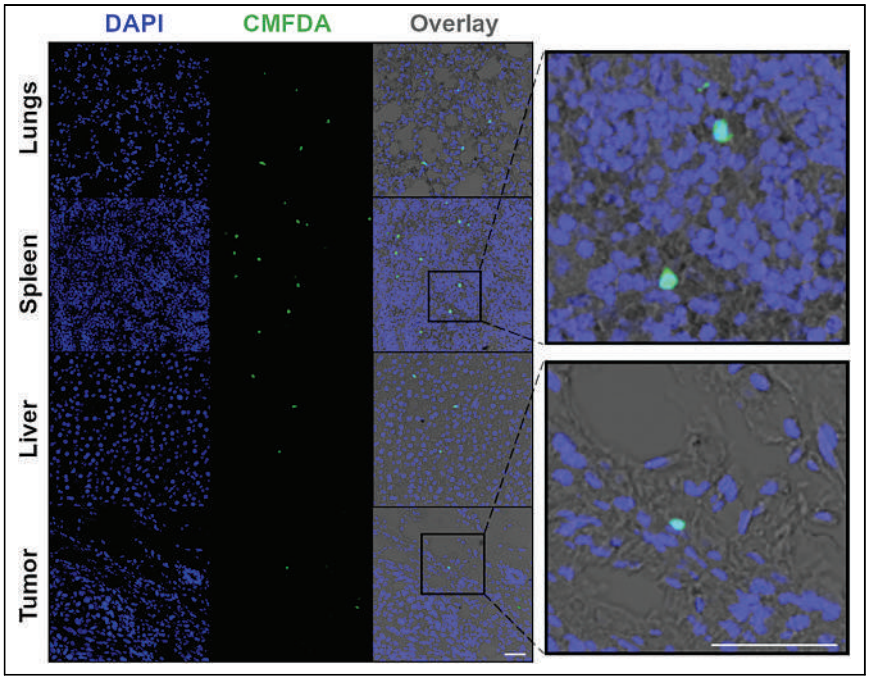

FIGURE 6. Confocal microscopy images (×40 magnification) of lung, spleen, liver, and tumor sections 3 d after injection of NK cells and trastuzumab. Sections stained with DAPI revealed presence of CMFDA–labeled NK cells. Scale bar is 50 μm. CMFDA = 5-chloromethylfluorescein diacetate; DAPI = 4′,6-diamidino-2-phenylindole.

Animals coadministered trastuzumab demonstrated higher splenic uptake of ^{89}Zr-NK cells than did animals coadministered a PBS sham at 3 and 7 d after injection. SPECT/CT indicated that significant amounts of [^{111}In]In-CHX-A″-DTPA-trastuzumab also localized to the spleen. Splenic vasculature is highly perfused and permeable to many blood-borne components: immune cells (*11–14*) and IgG antibodies (*28*) are well documented to accumulate in splenic tissue. In immune-deficient NSG mice that lack B cells and therefore normal endogenous levels of circulating immunoglobulins, exogenous human IgG antibodies exhibit particularly high uptake in the spleen. This has been attributed to antibody Fc binding to unoccupied murine Fc receptors expressed on spleen-residing monocytes, neutrophils, macrophages, and dendritic cells (*29*). In this study, it is possible that high residency of trastuzumab antibody in the spleen increases the accumulation of human ^{89}Zr-NK cells, which can compete with endogenous immune cells for binding to the humanized trastuzumab Fc region. However, we note that animals coadministered an IgG isotype control alongside ^{89}Zr-NK cells did not show the same levels of splenic ^{89}Zr activity as did animals coadministered trastuzumab.

Multiple doses of NK cells combined with antibody treatment can augment ADCC effects better than a single dose of NK cells or multiple doses of antibody alone (*27*). Future studies of different dosing regimens of ^{89}Zr-NK cells and antibody will allow more in-depth studies of cellular dynamics in the context of therapy.

CONCLUSION

We have shown the utility of [^{89}Zr]Zr-oxine for radiolabeling and tracking of human NK cells in a murine orthotopic human breast cancer model. This sensitive method enables quantitative assessment of changes in NK cell biodistribution in response to antibody therapies. Importantly, our findings reveal that NK cells migrate to orthotopic HER2-expressing HCC1954 tumors, with enhanced infiltration facilitated by HER2-targeted trastuzumab at early time points, aligning with clinical evidence. The use of ^{89}Zr and PET/CT can therefore aid the development and understanding of antibody therapies, in the context of the immune environment and Fc-mediated therapeutic effects.

DISCLOSURE

This research was supported by Cancer Research U.K. (C30122/A11527; C30122/A15774; C4278/A27066) including a Career Establishment Award (C63178/A24959), the EPSRC (EP/S032789/1), Wellcome Trust (WT212885/Z/18/Z; WT201959/Z/16/Z; WT088641/Z/09/Z), Breast Cancer Now (147; KCL-BCN-Q3), and the MRC (MR/L023091/1, MR/N013700/1). Philip Blower has submitted a patent application related to [^{89}Zr]Zr-oxine technology. Sophia Karagiannis is a founder and shareholder of Epsilogen Ltd. and declares patents on antibody technologies. No other potential conflict of interest relevant to this article was reported.

ACKNOWLEDGMENT

We thank Anthony Cheung for feedback on this article.

KEY POINTS

QUESTION: Can PET/CT assess [^{89}Zr]Zr-oxine–labeled human NK cell infiltration in HER2-positive breast tumors and quantify whether HER2-targeted trastuzumab therapy enhances this infiltration?

PERTINENT FINDINGS: ^{89}Zr-NK cells migrate to orthotopic HER2-expressing HCC1954 human tumors, with enhanced infiltration facilitated by HER2-targeted trastuzumab at early time points, aligning with clinical evidence.

IMPLICATIONS FOR PATIENT CARE: The use of ^{89}Zr and PET/CT can aid the development and understanding of antibody therapies, in the context of the immune environment and Fc-mediated therapeutic effects.

REFERENCES

1. Gennari R, Menard S, Fagnoni F, et al. Pilot study of the mechanism of action of preoperative trastuzumab in patients with primary operable breast tumors overexpressing HER2. *Clin Cancer Res.* 2004;10:5650–5655.
2. Arnould L, Gelly M, Penault-Llorca F, et al. Trastuzumab-based treatment of HER2-positive breast cancer: an antibody-dependent cellular cytotoxicity mechanism? *Br J Cancer.* 2006;94:259–267.
3. Muntasell A, Rojo F, Servitja S, et al. NK cell infiltrates and HLA class I expression in primary HER2 breast cancer predict and uncouple pathological response and disease-free survival. *Clin Cancer Res.* 2019;25:1535–1545.

4. Loi S, Michiels S, Salgado R, et al. Tumor infiltrating lymphocytes are prognostic in triple negative breast cancer and predictive for trastuzumab benefit in early breast cancer: results from the FinHER trial. *Ann Oncol.* 2014;25:1544–1550.
5. Denkert C, von Minckwitz G, Darb-Esfahani S, et al. Tumour-infiltrating lymphocytes and prognosis in different subtypes of breast cancer: a pooled analysis of 3771 patients treated with neoadjuvant therapy. *Lancet Oncol.* 2018;19:40–50.
6. Uong TNT, Lee K-H, Ahn S-J, et al. Real-time tracking of ex vivo-expanded natural killer cells toward human triple-negative breast cancers. *Front Immunol.* 2018; 9:825.
7. Uong TNT, Yoon MS, Lee K-H, et al. Live cell imaging of highly activated natural killer cells against human hepatocellular carcinoma in vivo. *Cytotherapy.* 2021;23: 799–809.
8. Hosahalli Vasanna S, Perera R, Jackson Z, Abenojar E, Exner A, Wald D. Non-invasive tracking of nanobubble tagged natural killer cells using clinical ultrasound. *Blood.* 2022;140(suppl 1):10283–10284.
9. Meller B, Frohn C, Brand JM, et al. Monitoring of a new approach of immunotherapy with allogenic ^{111}In-labelled NK cells in patients with renal cell carcinoma. *Eur J Nucl Med Mol Imaging.* 2004;31:403–407.
10. Matera L, Galetto A, Bello M, et al. In vivo migration of labeled autologous natural killer cells to liver metastases in patients with colon carcinoma. *J Transl Med.* 2006;4:49.
11. Cany J, van der Waart AB, Tordoir M, et al. Natural killer cells generated from cord blood hematopoietic progenitor cells efficiently target bone marrow-residing human leukemia cells in NOD/SCID/IL2Rgnull mice. *PLoS One.* 2013;8:e64384.
12. Sato N, Stringaris K, Davidson-Moncada JK, et al. In vivo tracking of adoptively transferred natural killer cells in rhesus macaques using ^{89}zirconium-oxine cell labeling and PET imaging. *Clin Cancer Res.* 2020;26:2573–2581.
13. Man F, Khan AA, Carrascal-Miniño A, Blower PJ, de Rosales RTM. A kit formulation for the preparation of [^{89}Zr]Zr(oxinate)$_4$ for PET cell tracking: white blood cell labelling and comparison with [^{111}In]In(oxinate)$_3$. *Nucl Med Biol.* 2020;90-91:31–40.
14. Weist MR, Starr R, Aguilar B, et al. PET of adoptively transferred chimeric antigen receptor T cells with ^{89}Zr-oxine. *J Nucl Med.* 2018;59:1531–1537.
15. Man F, Lim L, Volpe A, et al. In vivo PET tracking of ^{89}Zr-labeled Vγ9Vδ2 T cells to mouse xenograft breast tumors activated with liposomal alendronate. *Mol Ther.* 2019;27:219–229.
16. Asiedu KO, Koyasu S, Szajek LP, Choyke PL, Sato N. Bone marrow cell trafficking analyzed by ^{89}Zr-oxine positron emission tomography in a murine transplantation model. *Clin Cancer Res.* 2017;23:2759–2768.
17. Sato N, Wu H, Asiedu KO, Szajek LP, Griffiths GL, Choyke PL. ^{89}Zr-oxine complex PET cell imaging in monitoring cell-based therapies. *Radiology.* 2015;275: 490–500.
18. Charoenphun P, Meszaros LK, Chuamsaamarkkee K, et al. [^{89}Zr]oxinate$_4$ for long-term in vivo cell tracking by positron emission tomography. *Eur J Nucl Med Mol Imaging.* 2015;42:278–287.
19. NK cells expansion from human PBMCs or isolated NK cells. Miltenyi Biotec website. https://www.miltenyibiotec.com/GB-en/applications/all-protocols/nk-cell-expansion-from-human-pbmcs-or-isolated-nk-cells.html. Accessed May 2, 2024.
20. O'Brien NA, Browne BC, Chow L, et al. Activated phosphoinositide 3-kinase/AKT signaling confers resistance to trastuzumab but not lapatinib. *Mol Cancer Ther.* 2010;9:1489–1502.
21. Ma MT, Meszaros LK, Paterson BM, et al. Tripodal tris(hydroxypyridinone) ligands for immunoconjugate PET imaging with $^{89}Zr^{4+}$: comparison with desferrioxamine-B. *Dalton Trans.* 2015;44:4884–4900.
22. Lee SC, Shimasaki N, Lim JSJ, et al. Phase I trial of expanded, activated autologous NK-cell infusions with trastuzumab in patients with HER2-positive cancers. *Clin Cancer Res.* 2020;26:4494–4502.
23. Szmania S, Lapteva N, Garg T, et al. Ex vivo–expanded natural killer cells demonstrate robust proliferation in vivo in high-risk relapsed multiple myeloma patients. *J Immunother.* 2015;38:24–36.
24. Hu W, Wang G, Huang D, Sui M, Xu Y. Cancer immunotherapy based on natural killer cells: current progress and new opportunities. *Front Immunol.* 2019;10:1205.
25. Tong L, Jiménez-Cortegana C, Tay AHM, Wickström S, Galluzzi L, Lundqvist A. NK cells and solid tumors: therapeutic potential and persisting obstacles. *Mol Cancer.* 2022;21:206.
26. Ran GH, Lin YQ, Tian L, et al. Natural killer cell homing and trafficking in tissues and tumors: from biology to application. *Signal Transduct Target Ther.* 2022;7:205.
27. Zhu H, Blum RH, Bjordahl R, et al. Pluripotent stem cell-derived NK cells with high-affinity noncleavable CD16a mediate improved antitumor activity. *Blood.* 2020;135:399–410.
28. Cataldi M, Vigliotti C, Mosca T, Cammarota MR, Capone D. Emerging role of the spleen in the pharmacokinetics of monoclonal antibodies, nanoparticles and exosomes. *Int J Mol Sci.* 2017;18:1249.
29. Sharma SK, Chow A, Monette S, et al. Fc-mediated anomalous biodistribution of therapeutic antibodies in immunodeficient mouse models. *Cancer Res.* 2018;78: 1820–1832.

CEACAM5-Targeted Immuno-PET in Androgen Receptor–Negative Prostate Cancer

Cinzia Imberti*[1], Roberto De Gregorio*[1], Joshua A. Korsen[1,2], Tran T. Hoang[1,2], Samantha Khitrov[1], Teja Kalidindi[1], Subhiksha Nandakumar[3], Jooyoung Park[4], Samir Zaidi[5,6], Naga Vara Kishore Pillarsetty[1,7], and Jason S. Lewis[1,2,7,8]

[1]Department of Radiology, Memorial Sloan Kettering Cancer Center, New York, New York; [2]Department of Pharmacology, Weill Cornell Medicine, New York, New York; [3]Department of Epidemiology and Biostatistics, Memorial Sloan Kettering Cancer Center, New York, New York; [4]Department of Biomedical Sciences, Korea University College of Medicine, Seoul, Korea; [5]Department of Genitourinary Oncology, Memorial Sloan Kettering Cancer Center, New York, New York; [6]Human Oncology and Pathogenesis Program, Memorial Sloan Kettering Cancer Center, New York, New York; [7]Department of Radiology, Weill Cornell Medicine, New York, New York; and [8]Molecular Pharmacology Program, Memorial Sloan Kettering Cancer Center, New York, New York

The incidence of androgen receptor (AR)–negative (AR^-) prostate cancer, including aggressive neuroendocrine prostate cancer (NEPC), has more than doubled in the last decade, but its timely diagnosis is difficult as it lacks typical prostate cancer hallmarks. The carcinoembryonic antigen–related cell adhesion molecule 5 (CEACAM5) has recently been identified as an upregulated surface antigen in NEPC. We developed an immuno-PET agent targeting CEACAM5 and evaluated its ability to delineate AR^- prostate cancer in vivo. **Methods:** CEACAM5 expression was evaluated in a panel of prostate cancer cell lines by immunohistochemistry and Western blotting. The CEACAM5-targeting antibody labetuzumab was conjugated with the chelator desferrioxamine (DFO) and radiolabeled with ^{89}Zr. The in vivo distribution of the radiolabeled antibody was evaluated in xenograft prostate cancer models by PET imaging and ex vivo organ distribution. **Results:** The NEPC cell line H660 exhibited strong CEACAM5 expression, whereas expression was limited in the AR^- cell lines PC3 and DU145 and absent in the AR–positive cell line LNCaP. [^{89}Zr]Zr-DFO-labetuzumab imaging was able to clearly delineate both neuroendocrine H660 xenografts and AR^- DU145 in vivo but could not detect the AR–positive xenograft LNCaP. **Conclusion:** Immuno-PET imaging with [^{89}Zr]Zr-DFO-labetuzumab is a promising diagnostic tool for AR^- prostate cancer.

Key Words: CEACAM5; androgen receptor–negative prostate cancer; immuno-PET; molecular imaging

J Nucl Med 2024; 65:1043–1050
DOI: 10.2967/jnumed.123.267107

Prostate cancer is one of the most common types of cancer and the second leading cause of cancer-related deaths in men in the United States (*1*). Androgen receptor (AR)–dependent prostate cancer is the most frequent and most studied form of prostate cancer. Accordingly, AR–dependent prostate cancer management has seen significant improvement in recent years (*2*), with androgen deprivation therapy becoming the standard of care and several diagnostic biomarkers being identified, including prostate-specific antigen, prostate stem cell antigen, and prostate-specific membrane antigen (PSMA) (*3*). However, the incidence of AR–negative (AR^-) prostate cancer has greatly increased in the last few decades. This can be partly attributed to the selection pressure of androgen deprivation therapy, which can drive the emergence of AR^- cancer cells. Consequently, the percentage of patients with metastatic castration-resistant prostate cancer displaying an AR^- profile has increased from 11.7% in 1998–2011 to 36.6% in 2012–2016 (*2,4*). AR^- prostate cancers are not only hard to treat, being generally resistant to standard prostate cancer therapies, but also difficult to detect, since they lack typical AR–dependent prostate cancer diagnostic biomarkers such as PSMA and prostate stem cell antigen. Research into new diagnostic agents for AR^- prostate cancer is critical for timely diagnosis and treatment decisions, enabling earlier patient enrollment in clinical trials or initiation of chemotherapy as necessary.

A particularly aggressive form of treatment-related AR^- prostate cancer is neuroendocrine prostate cancer (NEPC), which arises because of the lineage plasticity of prostate cancer cells, resulting in neuroendocrine differentiation with loss of AR expression and acquisition of neuroendocrine markers such as chromogranin A, synaptophysin, and CD56 (also known as NCAM) (*5*). The δ-like ligand 3 has recently been recognized as an NEPC-specific biomarker, and we showed that ^{89}Zr-labeled δ-like ligand 3–targeting antibodies could selectively detect NEPC using PET (*6*) and that a ^{177}Lu-labeled version of the same antibody was effective in NEPC-targeted radiotherapy (*7*).

Recently, an integrated transcriptomic and cell-surface proteomic approach has identified the carcinoembryonic antigen–related cell adhesion molecule 5 (CEACAM5), also known as CEA or CD66e, as an upregulated antigen in a large subset of NEPC cell lines, patient-derived xenografts, and patient tumors (*8*). Elevated CEACAM5 serum levels in castration-resistant prostate cancer patients have previously been associated with aggressive disease and poor prognosis (*9*).

CEACAM5 is a member of the CEACAM family, a group of cell surface glycoproteins belonging to the superfamily of immunoglobulin cell adhesion molecules (*10,11*). It has 7 glycosylated extracellular immunoglobulin domains, including 1 variable-like domain (N domain) and 3 repeating units (A1B1, A2B2, and A3B3) comprising 6 constant C2-like domains. CEACAM5 is anchored to the cell membrane at the B3 domain through a

Received Jan. 3, 2024; revision accepted Apr. 13, 2024.
For correspondence or reprints, contact Naga Vara Kishore Pillarsetty (pillarsn@mskcc.org) or Jason S. Lewis (lewisj2@mskcc.org).
*Contributed equally to this work.
Published online May 23, 2024.

glycosylated phosphatidylinositol moiety. The most external domain is the N terminus, which plays a major role in cell–cell adhesion (*12*). CEACAM5 is overexpressed in several types of cancer, whereas distribution in normal tissue is limited mostly to the apical surface of the gastrointestinal epithelium and other mucosal epithelial cells. It was first recognized as a tumor-associated antigen in colorectal cancer (*13*) in the mid-1960s and was used both as a serum marker for this disease (because colon cancer cells continuously exfoliate membrane components into the bloodstream) and as a target for antibody-based imaging of colorectal cancer (*14*). A recently completed clinical trial (NCT00645060) investigated the use of a ^{90}Y humanized anti-CEACAM5 antibody, M5A, in patients with CEACAM5-producing cancers (including colorectal cancer, non–small cell lung cancer, breast cancer, and medullary thyroid cancer) (*15*). An ^{225}Ac version of the same antibody is currently in a clinical trial for α-radiotherapy of CEACAM5-expressing cancers (NCT05204147), whereas M5A antibodies labeled with ^{64}Cu and ^{124}I are being clinically investigated as PET diagnostic tools (NCT02293954 and NCT03993327). More recently, a CEACAM5-targeting ^{68}Ga single-domain antibody has been evaluated in colorectal cancer patients (*16*). Labetuzumab govitecan, an antibody–drug conjugate of a humanized anti-CEACAM5 antibody binding to CEACAM5 A3B3 epitope (labetuzumab) with the topoisomerase inhibitor SN-38, has been used for treatment-refractory metastatic colorectal cancer (*17*).

The recent identification of CEACAM5 as a potential marker for NEPC has paved the way for CEACAM5-targeted therapies to be investigated in prostate cancer. Labetuzumab govitecan was shown to eradicate CEACAM5-positive NEPC xenografts and patient-derived xenograft models (*18*). CEACAM5-targeting CAR-T cells encoding a single-chain variable fragment derived from either labetuzumab or the fully human monoclonal antibody 1G9 have also been developed and tested preclinically in NEPC models (*8,19*).

In this work, we explored the potential of CEACAM5 as an imaging biomarker for NEPC and other AR$^-$ prostate cancers to expand the diagnostic tools for early detection of these tumors. We investigated ^{89}Zr-labeled labetuzumab as a CEACAM5-targeted PET imaging agent, and we assessed its ability to detect AR$^-$ prostate cancers in vivo.

MATERIALS AND METHODS

Information on cell lines, xenograft establishment, immunohistochemistry, Western blotting, and matrix-assisted laser desorption/ionization determination of chelator-to-antibody ratio can be found in the supplemental materials (available at http://jnm.snmjournals.org). Methods for the analysis of CEACAM5 expression in organoids and metastatic biopsies are also reported in the supplemental materials.

Chemicals

The humanized monoclonal antibody labetuzumab was obtained from Genscript (purity > 99% as confirmed by size-exclusion chromatography–high-performance liquid chromatography; Supplemental Fig. 1). *p*-isothiocyanatobenzoyl DFO was obtained from Macrocyclics. ^{89}Zr was produced by proton bombardment of an ^{89}Y foil on a cyclotron (*20*) and supplied by the Radiochemistry and Molecular Imaging Probes Core at Memorial Sloan Kettering Cancer Center or by 3D Imaging. All aqueous solutions used for conjugation and radiolabeling were prepared with Chelex (Bio-Rad)-treated deionized water.

Conjugation

Conjugation was performed according to literature procedures (*21*). Labetuzumab (Genscript) or IgG1 (InVivoMab BE0297; Bio X Cell) solution in phosphate-buffered saline (PBS) was buffered to pH 8.5–9.0, followed by incubation with a 6-molar excess of the chelator *p*-isothiocyanatobenzoyl-DFO (8 mM in DMSO, <2% total volume) for 90 min on a thermomixer (37°C, 350 rpm). The immunoconjugates were then purified by size-exclusion chromatography on a PD-10 desalting column (GE Healthcare), eluted with PBS, and concentrated with a 50,000 molecular weight cut-off Amicon centrifugal filter.

Radiolabeling

The [^{89}Zr]Zr-oxalate solution (7.4 MBq) was adjusted to pH 6.8–7.2 by the addition of 1 M sodium carbonate (Na_2CO_3) and incubated at 37°C with the DFO-mAbs (labetuzumab-DFO or IgG-DFO isotype-matched control, 20 μg) for 1 h on a thermomixer (37°C, 350 rpm). Radiochemical purity was assessed by silica gel radio–instant thin-layer chromatography using 50 mM ethylenediaminetetraacetic acid as the eluent or by radio–high-performance liquid chromatography with a Yarra SEC-3000 column (Phenomenex) and an isocratic method (flow rate, 1 mL/min) using citrate buffer at pH 6.4 (100 mM sodium citrate, 100 mM sodium chloride) as the mobile phase. The product was purified on a PD-10 desalting column whenever radiochemical purity was inferior to 95%.

Stability to demetallation in serum was evaluated by incubating [^{89}Zr]Zr-DFO-labetuzumab in human serum at 37°C for 5 d. Radiochemical purity at different time points was determined by instant thin-layer chromatography in 50 mM ethylenediaminetetraacetic acid.

Bead-Binding Assay

To determine the CEACAM5 target-binding fraction of [^{89}Zr]Zr-DFO-labetuzumab, a bead-based binding assay was performed (*22*). Briefly, 20 μL of nickel–nitrilotriacetic acid beads (HisPur Beads; Thermo Fisher) were added to each microcentrifuge tube, washed with PBS with Tween (Croda Americas LLC) (PBST) (0.05% polysorbate-20 solution in PBS), and resuspended in 400 μL of PBST. One microgram of His-tagged CEACAM5 (10 μL, 0.1 mg/mL aqueous solution; Thermo Fisher Scientific) was added to each tube, and all tubes were placed on a rotating platform at 4°C for 15 min before centrifugation, removal of the supernatant, and washing with PBST. The beads were then resuspended in 400 μL of PBST, and 1 ng of [^{89}Zr]Zr-DFO-labetuzumab (1 μL of a 1 ng/μL solution in PBST) was added to all tubes. Tubes were left rotating at 4°C for 30 min. The supernatant was then collected, and the beads were washed 3 times with PBST. Beads, supernatant, and washing tubes were measured on a γ-counter, and the percentage of bead-bound activity was calculated. For the control, the procedure was the same except no His-tagged CEACAM5 was added to assess nonspecific binding of [^{89}Zr]Zr-DFO-labetuzumab to the naked beads. For the blocking group, the procedure was the same except for an excess of labetuzumab (5 μg, 5,000× excess), which was added to block specific binding of [^{89}Zr]Zr-DFO-labetuzumab to His-tagged CEACAM5.

Cell-Binding Assay

Cells were harvested, counted, placed in microcentrifuge tubes (10×10^6 cells in 0.2 mL of culture medium), and put on ice. Twenty microliters (3 ng) of a 0.15 μg/mL solution of [^{89}Zr]Zr-DFO-labetuzumab in PBS with 1% bovine serum albumin were added to each tube. For the blocking experiment, an excess of labetuzumab (5,000× excess) was added to the cells immediately before addition of the radiolabeled antibody. The cells were allowed to incubate for 1 h with gentle stirring in a vortex mixer every 15 min to resuspend the cells.

Then, the cells were centrifuged (600*g*, 5 min) and the supernatant collected. The cells were washed 3 times with 1 mL of ice-cold PBS followed by centrifugation (600*g*, 5 min) and removal of the supernatant in separate microcentrifuge tubes. Lastly, the cell pellet, the medium supernatant, and the 3 wash fractions were placed on a γ-counter to determine the percentage of cell-bound radioactivity of [^{89}Zr]Zr-DFO-labetuzumab.

Animal Studies

All animal experiments were approved by the Institutional Animal Care and Use Committee and Research Animal Resource Center at Memorial Sloan Kettering Cancer Center.

Ex Vivo Biodistribution Studies

Biodistribution studies were performed by euthanizing mice (4 per group) at 24, 48, or 120 h after injection with [^{89}Zr]Zr-DFO-labetuzumab (7.4 MBq, 20 μg, 100 μL in PBS) to evaluate the accumulation of the radiotracer in subcutaneous H660, DU145, or LNCaP xenografts.

Organs of interest and the tumor were harvested, weighed, and counted on a γ-counter to determine the accumulation of radioactivity. The percentage injected dose per gram was determined for each sample by normalizing the counts per sample to the total amount of activity injected.

Imaging Studies

PET imaging of mice bearing subcutaneous prostate cancer xenografts was performed. Mice bearing H660, DU145, or LNCaP tumors were intravenously injected with [^{89}Zr]Zr-DFO-labetuzumab or [^{89}Zr]Zr-DFO-IgG (7.4 MBq, 20 μg, 100 μL in PBS). For the blocking studies in H660 and DU145 models, the mice were preinjected with 20- or 10-fold unconjugated labetuzumab, respectively, 1 h before radiotracer administration. The mice were anesthetized with 1%–2% isoflurane, and images were acquired on an Inveon small-animal PET/CT instrument (Siemens) at different time points. After the final imaging time point, the mice were euthanized and ex vivo biodistribution was performed as described above.

Statistical Analysis

Statistical analysis was performed using GraphPad Prism 9.5.1. One-way ANOVA followed by Tukey multiple-comparison testing was used to identify statistically significant differences in organ accumulation between [^{89}Zr]Zr-DFO-labetuzumab at 120 h and the other groups (threshold for significance, $P = 0.05$).

RESULTS

Labetuzumab was conjugated with the DFO by non–site-specific conjugation to lysine residues according to literature procedures (Fig. 1A). Matrix-assisted laser desorption/ionization–time-of-flight

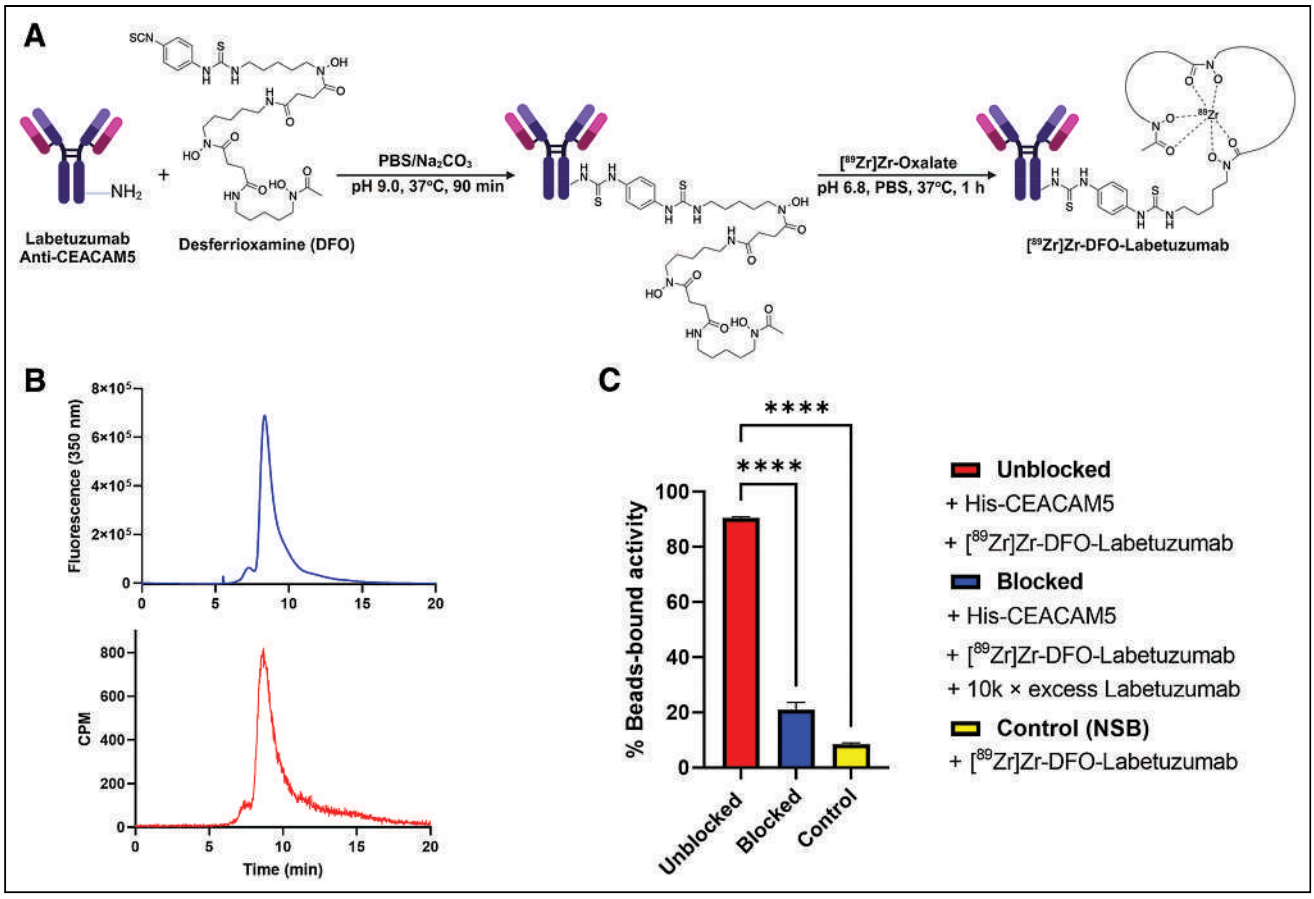

FIGURE 1. Labetuzumab radiolabeling and characterization. (A) Schematic representation of labetuzumab conjugation to DFO-NCS and radiolabeling with ^{89}Zr. (B) Size-exclusion chromatography–high-performance liquid chromatography trace showing quantitative radiolabeling of DFO-labetuzumab conjugate with 1 major peak in radiochromatogram (bottom) corresponding to immunoconjugate peak in fluorescence chromatogram (top, λ emission is 350 nm). The small shoulder at left of main peak is imputable to small amount of immunoconjugate aggregates. (C) Bead-based binding assay confirming CEACAM5-targeting capability of [^{89}Zr]Zr-DFO-labetuzumab, which could be blocked in presence of excess unconjugated antibody (demonstrating specificity) and low nonspecific binding (NSB). Values are expressed as average percentage uptake ± SEM. ****$P < 0.0001$.

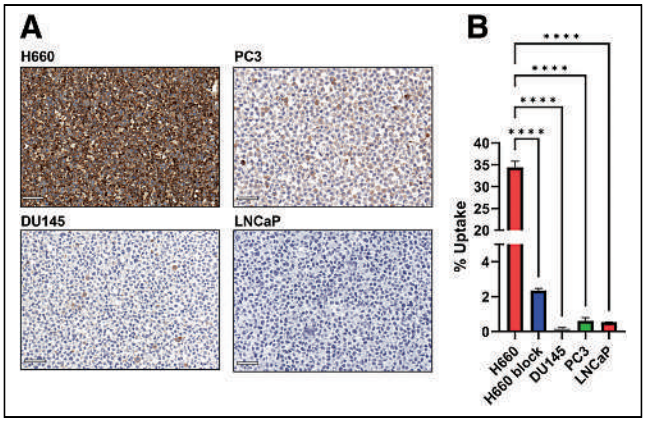

FIGURE 2. In vitro evaluation of prostate cancer cell lines. (A) Immunohistochemistry characterization of CEACAM5 expression in H660, PC3, DU145, and LNCaP cell lines; scale bar is 50 μm. (B) Uptake assay showing selective binding of [^{89}Zr]Zr-DFO-labetuzumab to H660 cells. Values are expressed as average percentage uptake ± SEM. ****$P < 0.0001$.

mass spectrometry analysis of the conjugate (Supplemental Fig. 2) revealed an average of 1.3 chelators per antibody.

Radiolabeling of the immunoconjugate with [^{89}Zr]Zr-oxalate at neutral pH consistently yielded [^{89}Zr]Zr-DFO-labetuzumab in quantitative radiochemical yield (>98%) and purity without the need for purification, as clearly indicated by radio–high-performance liquid chromatography analysis and instant thin-layer chromatography (Fig. 1B; Supplemental Fig. 3). The immunoconjugate remained stable in human serum for up to a week after incubation at 37°C (>98%, Supplemental Fig. 3).

To verify that the labetuzumab antibody maintained binding capacity to CEACAM5 after DFO conjugation and radiolabeling, a bead-binding assay was performed with His-tagged CEACAM5-covered nickel–nitrilotriacetic acid beads. [^{89}Zr]Zr-DFO-labetuzumab retained more than 90% binding to CEACAM5-bearing nickel–nitrilotriacetic acid beads, which could be blocked by an excess of unconjugated labetuzumab (Fig. 1C). These findings confirmed specificity of [^{89}Zr]Zr-DFO-labetuzumab binding to CEACAM5.

Expression of CEACAM5 was investigated in prostate cancer cell lines with a different AR and NEPC status, including hormone-sensitive prostate adenocarcinoma LNCaP (AR-positive [AR$^+$]/neuroendocrine [NE]-negative [NE$^-$]), NEPC H660 (AR$^-$/NE-positive [NE$^+$]), and double-negative prostate cancer (DNPC) DU145 and PC3 (AR$^-$/NE$^-$). Immunohistochemistry analysis of cell pellets showed extremely strong CEA expression in H660 (Fig. 2A). Milder expression was also observed in the DNPC cell lines PC3 and DU145, which are AR-null but do not display NEPC features, whereas AR$^+$ LNCaP cells did not show any CEACAM5 expression (Fig. 2A). On the other hand, when Western blotting was used to measure CEACAM5 protein expression in the same cell lines, only H660 showed visible CEACAM5 expression (Supplemental Fig. 4).

In agreement with these results, a cell-binding assay using [^{89}Zr]Zr-DFO-labetuzumab confirmed high binding to H660 cells (34.3% uptake, Fig. 2B). The binding could be blocked in the presence of excess unlabeled labetuzumab, confirming [^{89}Zr]Zr-DFO-labetuzumab binding specificity to the target antigen. Negligible binding was observed in all the other cell lines.

We then moved to in vivo PET imaging to evaluate the ability of [^{89}Zr]Zr-DFO-labetuzumab to delineate NEPC tumors in male nude mice bearing H660 xenografts. [^{89}Zr]Zr-DFO-labetuzumab showed excellent accumulation in H660 xenografts as early as 24 h and was able to reach remarkable uptake levels at 120 h, demonstrating the potential of anti-CEA imaging in NEPC tumors (Fig. 3A). This was also confirmed by [^{89}Zr]Zr-DFO-labetuzumab biodistribution studies at different time points (Fig. 3B; Supplemental Fig. 5). In contrast, when the [^{89}Zr]Zr-DFO-IgG was used, only low, nonspecific uptake was visible in the H660 tumors at all time points considered (Supplemental Fig. 6). Terminal ex vivo biodistribution (Fig. 3B) for [^{89}Zr]Zr-DFO-IgG similarly showed markedly reduced tumor accumulation compared with [^{89}Zr]Zr-DFO-labetuzumab, whereas uptake in other organs was largely identical, except for the liver, which showed increased uptake for the isotype-matched imaging group.

We further verified the specificity of our tracer in H660 tumors by performing a blocking experiment in which the administration of [^{89}Zr]Zr-DFO-labetuzumab was preceded by injection of excess unlabeled labetuzumab. Lower tumor uptake was observed at all time points, consistent with the specificity of the radioimmunoconjugate for the CEACAM5 receptor (Fig. 3A; Supplemental Fig. 7). Terminal biodistribution (120 h) for the blocking cohort revealed similar accumulation of [^{89}Zr]Zr-DFO-labetuzumab in all organs, with the only significant difference being tumor uptake (Fig. 3B; Supplemental Fig. 5).

On the basis of in vitro results, the AR$^-$/NE$^-$ prostate cancer model DU145 was initially chosen as the negative model for the in vivo study. However, PET imaging and ex vivo biodistribution showed unexpected tumor uptake, although lower than what observed in the H660 model (Figs. 4A and 4B; Supplemental Fig. 8). A blocking experiment with excess unlabeled labetuzumab confirmed that the observed uptake was specific (Fig. 4A; Supplemental Fig. 9). In contrast, when mice bearing subcutaneous AR$^+$/NE$^-$ LNCaP tumors were imaged with [^{89}Zr]Zr-DFO-labetuzumab, little tumor uptake was observed at any time point (Fig. 5; Supplemental Fig. 10).

Accordingly, when the biodistribution in the 3 models was compared (Fig. 6A), the AR$^-$/NE$^+$ H660 xenograft displayed the highest tumor-to-tissue ratios (tumor-to-blood ratio of 11 ± 1, tumor-to-muscle ratio of 98 ± 17), the AR$^-$/NE$^-$ DU145 displayed moderate but specific uptake, and no specific uptake was observed in the AR$^+$/NE$^-$ LNCaP tumors. Image quantification of tumor uptake from the PET study (Supplemental Fig. 11) also showed the same trend. Immunohistochemical analysis of resected tumor samples for each xenograft model (Fig. 6B, isotype-matched control in Supplemental Fig. 12) confirmed our in vivo findings, with H660 xenograft sections showing intense CEACAM5 expression throughout the tissue, DU145 showing heterogeneous CEACAM5 expression, and LNCaP xenografts completely lacking expression.

To check whether our unexpected observation of in vivo expression of CEACAM5 in both AR$^-$/NE$^+$ and AR$^-$/NE$^-$ prostate cancer xenografts is clinically valid and relevant, we analyzed CEACAM5 expression in a large cohort of human tumor organoids and metastatic biopsy samples of prostate cancer previously validated in the literature (*24,25*). In organoid samples (Fig. 7A), we found elevated CEACAM5 transcript levels in both NEPC organoids and a subset of DNPC organoids that the authors classified as stem cell-like prostate cancer, which express CD44 and other stem cell-like markers (*23*). In this classification, DU145 and PC3 are classified as stem cell-like prostate cancers. Generally, organoid expression of CEACAM5 showed a slightly negative correlation with the expression of PSMA, prostate-specific antigen, and AR (Supplemental Fig. 13). For the biopsy samples (Fig. 7B), all tissues displaying CEACAM5 expression (based on single-cell RNA

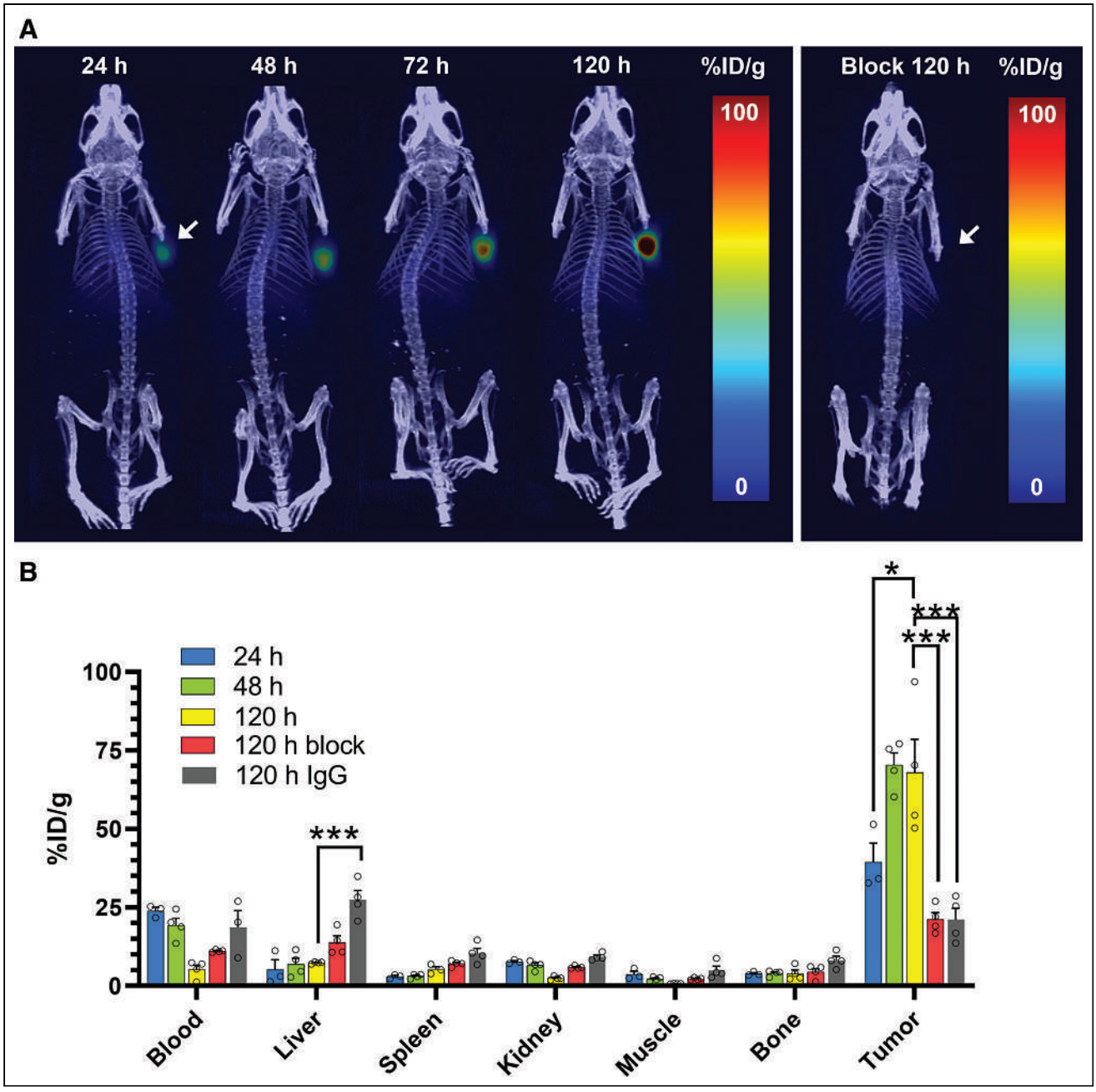

FIGURE 3. Evaluation of [^{89}Zr]Zr-DFO-labetuzumab in H660 xenografts. (A) Exemplar maximum-intensity projections obtained by dynamic PET imaging of mice injected with [^{89}Zr]Zr-DFO-labetuzumab at different time points after administration, showing remarkably high uptake of radioimmunoconjugate. This is compared (on right) with negligible uptake obtained at 120 h when excess of unconjugated labetuzumab was administered 1 h before [^{89}Zr]Zr-DFO-labetuzumab, confirming specific tumor uptake. (B) Ex vivo biodistribution in selected organs comparing accumulation of [^{89}Zr]Zr-DFO-labetuzumab at different time points, with the same tracer in presence of excess labetuzumab and [^{89}Zr]Zr-DFO-IgG. Values are expressed as average percentage injected dose per gram (%ID/g) ± SEM ($n = 4$, full biodistribution data in Supplemental Fig. 5). *$P < 0.05$. ***$P < 0.005$.

sequencing) were consistently located within the AR$^-$/NE$^+$ (NEPC) or the AR$^-$/NE$^-$ (DNPC) clusters, as classified according to the Uniform Manifold Approximation and Projection (Supplemental Fig. 14), but not in AR$^+$ castration-resistant prostate cancer cluster.

DISCUSSION

Receptor-targeted PET imaging provides a noninvasive tool to identify prostate cancer lesions, even when these are relatively inaccessible to biopsy, such as bone metastases. Compared with biopsy, imaging enables a better understanding of tumor and intratumor heterogeneity, by essentially illustrating the expression of a specific target receptor in the tumor tissue. Although PET imaging biomarkers have been identified and translated into the clinic for AR$^+$ prostate cancer (most notably ^{18}F-/^{68}Ga-PSMA), currently there are no clinical diagnostic tools for NEPC and DNPC.

The cell-adhesion molecule CEACAM5 has been investigated for imaging of colorectal cancer and, to a lesser extent, non–small cell

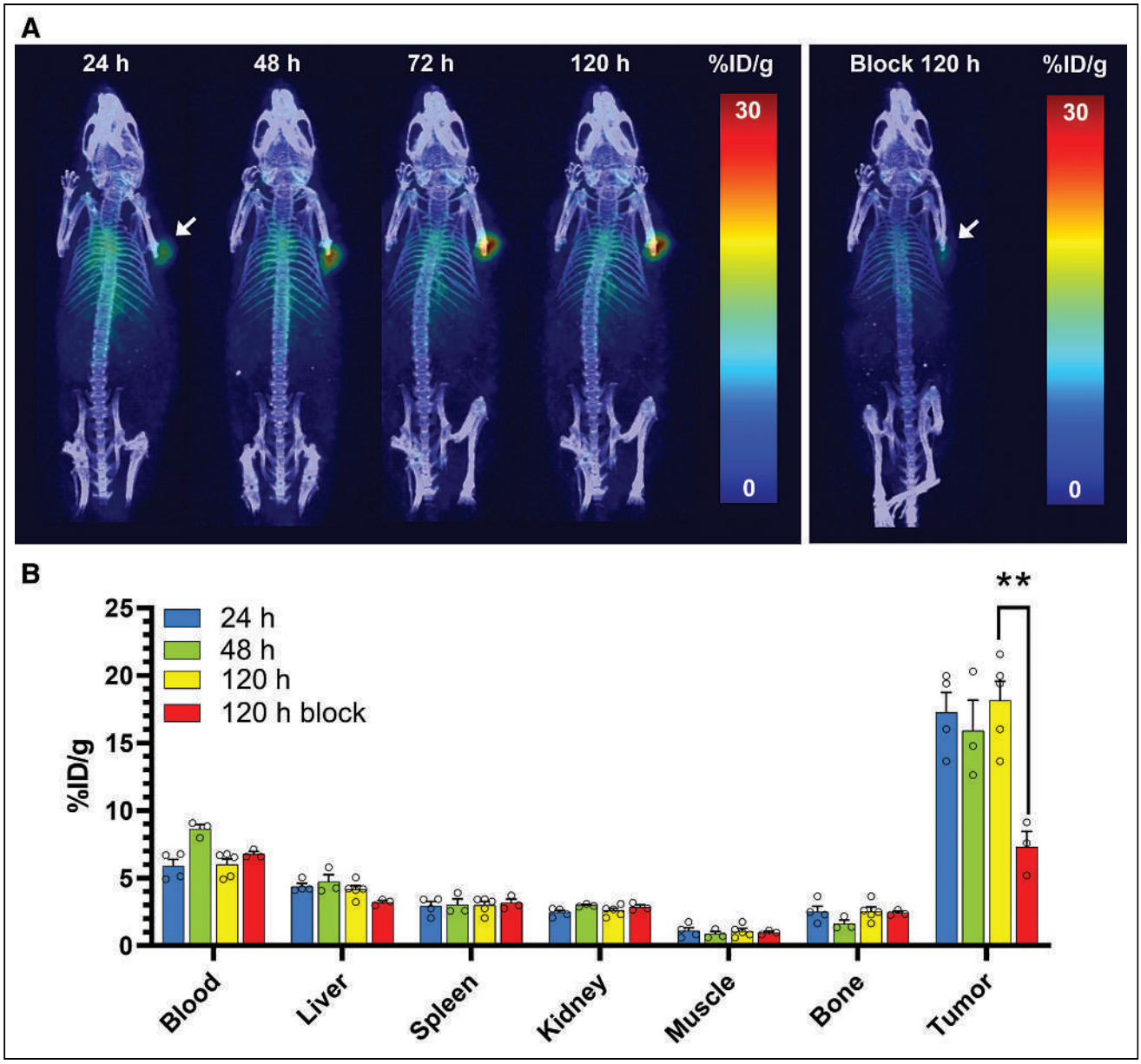

FIGURE 4. Evaluation of [^{89}Zr]Zr-DFO-labetuzumab in DU145 xenografts. (A) Exemplar maximum-intensity projections obtained by dynamic PET imaging of mice injected with [^{89}Zr]Zr-DFO-labetuzumab at different time points after administration, compared (on right) with negligible uptake obtained at 120 h for blocking study. (B) Ex vivo biodistribution in selected organs comparing accumulation of [^{89}Zr]Zr-DFO-labetuzumab at different time points with and without blocking. Values are expressed as average percentage injected dose per gram (%ID/g) ± SEM ($n = 4$, full biodistribution data in Supplemental Fig. 8). $^{**}P < 0.01$.

lung cancer. More recently, CEACAM5 was identified as a key receptor in NEPC, with the CEACAM5-targeting antibody–drug conjugate labetuzumab govitecan showing strong antitumor activity in preclinical studies with NEPC models (*18*).

Here, we have investigated the ability of [^{89}Zr]Zr-DFO-labetuzumab to effectively delineate NEPC in vivo using PET imaging in a H660 xenograft model, which we have previously shown to express the NEPC marker synaptophysin while lacking common prostate cancer biomarkers (AR, prostate-specific antigen, and PSMA) (*7*). The PET images obtained using [^{89}Zr]Zr-DFO-labetuzumab in this model demonstrated the remarkable ability of the radiotracer to accumulate in H660 xenografts. Specificity of the CEACAM5 targeting was confirmed by the ability of excess unlabeled labetuzumab to block tumor accumulation of the radiotracer and by the negligible tumor uptake of the ^{89}Zr-labeled isotype-matched control.

Intriguingly, the AR$^-$/NE$^-$ prostate cancer model DU145 could also be effectively delineated with [^{89}Zr]Zr-DFO-labetuzumab in vivo, and although much lower tumor accumulation was observed, contrast remained high because of low background signal. Immunohistochemical characterization of DU145 cells and xenograft showed that, although little expression of CEACAM5 was detected in cells, moderate levels of expression were measured in vivo. Previous reports by DeLucia et al. (*18*) and Lee et al. (*8*) have used the DU145 cells as a negative control but did not explore their behavior in vivo. Using PET imaging, we could gain unique

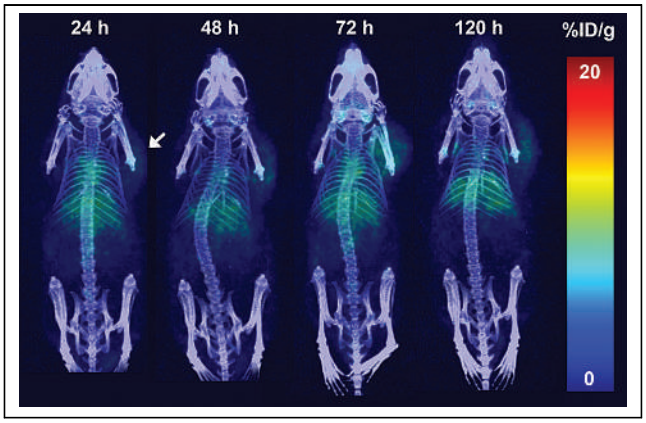

FIGURE 5. Evaluation of [^{89}Zr]Zr-DFO-labetuzumab in LNCaP xenografts. Exemplar maximum-intensity projections were obtained by dynamic PET imaging of LNCaP-bearing mice injected with [^{89}Zr]Zr-DFO-labetuzumab at different time points after administration (ex vivo biodistribution data in Supplemental Fig. 10).

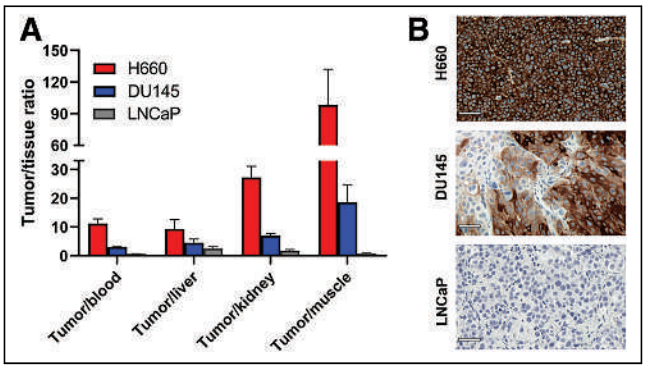

FIGURE 6. (A) Comparison of tumor-to-tissue ratios of [^{89}Zr]Zr-DFO-labetuzumab accumulation at 120 h after injection in 3 different xenograft models. (B) Ex vivo immunohistochemistry showing CEACAM5 expression in 3 models (scale bar, 50 μm).

insight suggesting that DU145 xenografts interact with the tumor microenvironment and start expressing CEACAM5.

Remarkably, analysis of CEACAM5 expression in human organoids and metastatic biopsy samples (Fig. 7) validated our experimental observation that CEACAM5 is expressed in both NEPC and a subset of DNPC prostate cancer. Our data and the literature reports suggest that CEACAM5 could serve as a biomarker for diagnosis of different types of AR$^-$ prostate cancer. This is particularly relevant because the increased use of potent AR signaling inhibitors in patients is resulting in a significantly increased proportion of patients with AR$^-$ prostate cancer of both NE$^-$ and NE$^+$ subtypes compared with the traditional AR$^+$ phenotype (*2*). For these patients, the development of an AR$^-$ diagnostic tool, such as CEACAM5-targeted immuno-PET, could enable early diagnosis and inform treatment decisions in the same way as PSMA PET does for AR-dependent prostate cancer.

One inherent limitation of our study, in view of a potential clinical translation, is the absence of CEACAM5 expression in mouse tissue, which prevents us from predicting specific accumulation of the radiotracer in nontarget organs. However, previous clinical imaging studies with anti-CEACAM5 antibodies have shown a relatively low background for this target (*25,26*). Another limitation of our study is that it is limited to subcutaneous xenograft tumors, which may not be representative of clinical AR$^-$ lesions. Further studies will include imaging in patient-derived xenograft models previously determined to be AR$^-$ by immunohistochemistry. Finally, to enable imaging at earlier time points than is possible with directly labeled anti-CEACAM5 full-length antibodies, pretargeting strategies (*27*) or smaller formats such as single-domain antibodies (*16*) could be explored in future studies.

Importantly, besides its potential as a diagnostic tool for AR$^-$ prostate cancer, PET imaging with [^{89}Zr]Zr-DFO-labetuzumab could also be used for patient stratification. Here, CEACAM5 immuno-PET imaging would serve as a biomarker to identify prostate cancer patients who could benefit from labetuzumab-govitecan and other CEACAM5-targeted therapies, including targeted radiotherapy approaches based on the same antibody carrying β- and α-emitting radiometals.

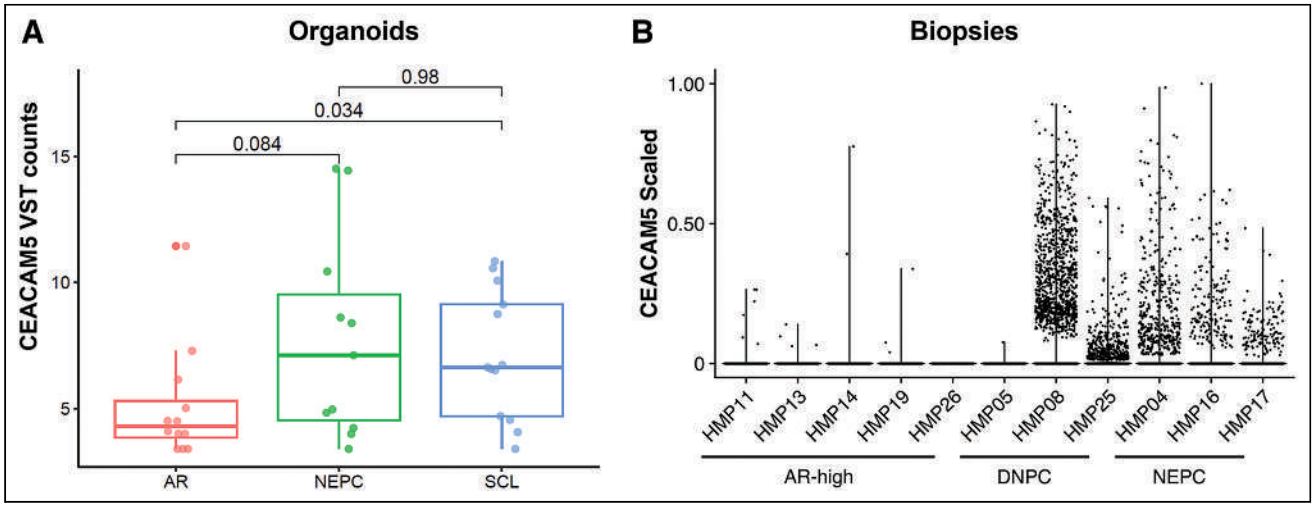

FIGURE 7. Evaluation of CEACAM5 expression in prostate cancer organoids and biopsies. (A) Box plots showing variance-stabilized transformed (VST) counts of CEACAM5 in AR$^+$, NEPC, and stem cell-like (SCL) organoid subtypes (significance analysis by Wilcox test). (B) Minimum to maximum scaled CECAM5 expression plotted by tumor biopsy and labeled by AR-high, DNPC, and NEPC biopsies.

CONCLUSION

Overall, these data show the ability of CEACAM5-targeted immuno-PET imaging to clearly delineate NEPC and other AR^- prostate cancers in vivo and pave the way to the development of an imaging-based diagnostic tool to enable early detection of these lesions and inform patient treatment.

DISCLOSURE

The study was supported by NCI R35 CA232130 (Jason Lewis), NIH T32 GM073546 (Joshua Korsen and Tran Hoang), and the Prostate Cancer Foundation (Jason Lewis). We acknowledge the Radiochemistry and Molecular Imaging Probes Core Facility, the Small Animal Imaging Facility, and the Molecular Cytology Core Facility at Memorial Sloan Kettering, which are supported by NIH grant P30 CA08748. No other potential conflict of interest relevant to this article was reported.

KEY POINTS

QUESTION: Can CEACAM5-targeted immuno-PET identify AR-null tumors, specifically NEPC, in vivo?

PERTINENT FINDINGS: [^{89}Zr]Zr-DFO-labetuzumab was able to clearly delineate the NE^+/AR^- model H660 in vivo but also, although to a lesser extent, the NE^-/AR^- model DU145. No uptake of the radiotracer was observed in NE^-/AR^+ LNCaP xenografts, suggesting its selectivity for AR^- prostate cancer.

IMPLICATIONS FOR PATIENT CARE: CEACAM5-targeted immuno-PET has the potential to be translated clinically as a noninvasive diagnostic tool to enable early detection of AR^- prostate cancer.

REFERENCES

1. Key statistics for prostate cancer. American Cancer Society website. https://www.cancer.org/cancer/types/prostate-cancer/about/key-statistics. Accessed April 24, 2024.
2. Bluemn EG, Coleman IM, Lucas JM, et al. Androgen receptor pathway-independent prostate cancer is sustained through FGF signaling. *Cancer Cell.* 2017;32:474–489.e6.
3. Roberts MJ, Maurer T, Perera M, et al. Using PSMA imaging for prognostication in localized and advanced prostate cancer. *Nat Rev Urol.* 2023;20:23–47.
4. Watson PA, Arora VK, Sawyers CL. Emerging mechanisms of resistance to androgen receptor inhibitors in prostate cancer. *Nat Rev Cancer.* 2015;15:701–711.
5. Merkens L, Sailer V, Lessel D. Aggressive variants of prostate cancer: underlying mechanisms of neuroendocrine transdifferentiation. *J Exp Clin Cancer Res.* 2022;41:46.
6. Korsen JA, Kalidindi TM, Khitrov S, et al. Molecular imaging of neuroendocrine prostate cancer by targeting Delta-like ligand 3. *J Nucl Med.* 2022;63:1401–1407.
7. Korsen JA, Gutierrez JA, Tully KM, et al. Delta-like ligand 3-targeted radioimmunotherapy for neuroendocrine prostate cancer. *Proc Natl Acad Sci USA.* 2022;119:e2203820119.
8. Lee JK, Bangayan NJ, Chai T, et al. Systemic surfaceome profiling identifies target antigens for immune-based therapy in subtypes of advanced prostate cancer. *Proc Natl Acad Sci USA.* 2018;115:E4473–E4482.
9. Aparicio AM, Harstark AL, Corn PG, et al. Platinum-based chemotherapy for variant castrate-resistant prostate cancer. *Clin Cancer Res.* 2013;19:3621–3630.
10. Kuespert K, Pils S, Hauck CR. CEACAMs: their role in physiology and pathophysiology. *Curr Opin Cell Biol.* 2006;18:565–571.
11. Paxton RJ, Mooser G, Pande H, et al. Sequence analysis of carcinoembryonic antigen: identification of glycosylation sites and homology with the immunoglobulin supergene family. *Proc Natl Acad Sci USA.* 1987;84:920–924.
12. Beauchemin N, Arabzadeh A. Carcinoembryonic antigen-related cell adhesion molecules (CEACAMs) in cancer progression and metastasis. *Cancer Metastasis Rev.* 2013;32:643–671.
13. Gold P, Freedman SO. Specific carcinoembryonic antigens of the human digestive system. *J Exp Med.* 1965;122:467–481.
14. Shively JE, Beatty JD. CEA-related antigens: molecular biology and clinical significance. *Crit Rev Oncol Hematol.* 1985;2:355–399.
15. Akhavan D, Yazaki P, Yamauchi D, et al. Phase I study of yttrium-90 radiolabeled M5A anti-carcinoembryonic antigen humanized antibody in patients with advanced carcinoembryonic antigen producing malignancies. *Cancer Biother Radiopharm.* 2020;35:10–15.
16. Li L, Lin XF, Wang L, et al. Immuno-PET of colorectal cancer with a CEA-targeted [^{68}Ga]Ga-nanobody: from bench to bedside. *Eur J Nucl Med Mol Imaging.* 2023;50:3735–3749.
17. Blumenthal RD, Leon E, Hansen HJ, Goldenberg DM. Expression patterns of CEACAM5 and CEACAM6 in primary and metastatic cancers. *BMC Cancer.* 2007;7:2.
18. DeLucia DC, Cardillo TM, Ang L, et al. Regulation of CEACAM5 and therapeutic efficacy of an anti-CEACAM5-SN38 antibody-drug conjugate in neuroendocrine prostate cancer. *Clin Cancer Res.* 2021;27:759–774.
19. Kim YJ, Li W, Zhelev DV, et al. Chimeric antigen receptor-T cells are effective against CEACAM5 expressing non-small cell lung cancer cells resistant to antibody-drug conjugates. *Front Oncol.* 2023;13:1124039.
20. Holland JP, Sheh YC, Lewis JS. Standardized methods for the production of high specific-activity zirconium-89. *Nucl Med Biol.* 2009;36:729–739.
21. Cooper MS, Sabbah E, Mather SJ. Conjugation of chelating agents to proteins and radiolabeling with trivalent metallic isotopes. *Nat Protoc.* 2006;1:314–317.
22. Sharma SK, Lyashchenko SK, Park HA, et al. A rapid bead-based radioligand binding assay for the determination of target-binding fraction and quality control of radiopharmaceuticals. *Nucl Med Biol.* 2019;71:32–38.
23. Tang FY, Xu D, Wang SQ, et al. Chromatin profiles classify castration-resistant prostate cancers suggesting therapeutic targets. *Science.* 2022;376:eabe1505.
24. Chan JM, Zaidi S, Love JR, et al. Lineage plasticity in prostate cancer depends on JAK/STAT inflammatory signaling. *Science.* 2022;377:1180–1191.
25. Wong JY, Yamauchi DM, Adhikarla V, et al. First-in-human pilot PET immunoimaging study of Cu-64-anti-carcinoembryonic antigen monoclonal antibody (hT84.66-M5A) in patients with carcinoembryonic antigen-producing cancers. *Cancer Biother Radiopharm.* 2023;38:26–37.
26. Wong JY, Thomas GE, Yamauchi D, et al. Clinical evaluation of indium-111-labeled chimeric antiCEA monoclonal antibody. *J Nucl Med.* 1997;38:1951–1959.
27. Bodet-Milin C, Bailly C, Touchefeu Y, et al. Clinical results in medullary thyroid carcinoma suggest high potential of pretargeted immuno-PET for tumor imaging and theranostic approaches. *Front Med (Lausanne).* 2019:6:124.

A Phase 0 Study to Assess the Biodistribution and Pharmacokinetics of a Radiolabeled Antibody Targeting Human Kallikrein 2 in Participants with Metastatic Castration-Resistant Prostate Cancer

Neeta Pandit-Taskar[1,2], Joseph A. O'Donoghue[3], Dushen Chetty[4], Steven Max[4], Danielle Wanik[5], Ohad Ilovich[5], Michael Russell[4], Tenzin Nyima[6], Chaitanya R. Divgi[4], Margaret Yu[4], and Michael J. Morris[7,8]

[1]Department of Radiology, Memorial Sloan Kettering Cancer Center, New York, New York; [2]Department of Radiology, Weill Cornell Medical Center, New York, New York; [3]Department of Medical Physics, Memorial Sloan Kettering Cancer Center, New York, New York; [4]Janssen Research & Development, LLC, Spring House, Pennsylvania; [5]Invicro, LLC, Boston, Massachusetts; [6]Memorial Sloan Kettering Cancer Center, New York, New York; [7]Genitourinary Oncology Service, Memorial Sloan Kettering Cancer Center, New York, New York; and [8]Department of Medicine, Weill Cornell Medicine, New York, New York

Despite the inclusion of multiple agents within the prostate cancer treatment landscape, new treatment options are needed to address the unmet need for patients with metastatic castration-resistant prostate cancer (mCRPC). Although prostate-specific membrane antigen is the only cell-surface target to yield clinical benefit in men with advanced prostate cancer, additional targets may further advance targeted immune, cytotoxic, radiopharmaceutical, and other tumor-directed therapies for these patients. Human kallikrein 2 (hK2) is a novel prostate-specific target with little to no expression in nonprostate tissues. This first-in-human phase 0 trial uses an ^{111}In-radiolabeled anti-hK2 monoclonal antibody, [^{111}In]-DOTA-h11B6, to credential hK2 as a potential target for prostate cancer treatment. **Methods:** Participants with progressive mCRPC received a single infusion of 2 mg of [^{111}In]-DOTA-h11B6 (185 MBq of ^{111}In), with or without 8 mg of unlabeled h11B6 to assess antibody mass effects. Sequential imaging and serial blood samples were collected to determine [^{111}In]-DOTA-h11B6 biodistribution, dosimetry, serum radioactivity, and pharmacokinetics. Safety was assessed within a 2-wk follow-up period from the time of [^{111}In]-DOTA-h11B6 administration. **Results:** Twenty-two participants received [^{111}In]-DOTA-h11B6 and are included in this analysis. Within 6–8 d of administration, [^{111}In]-DOTA-h11B6 visibly accumulated in known mCRPC lesions, with limited uptake in other organs. Two treatment-emergent adverse events unrelated to treatment occurred, including tumor-related bleeding in 1 patient, which led to early study discontinuation. Serum clearance, biodistribution, and tumor targeting were independent of total antibody mass (2 or 10 mg). **Conclusion:** This first-in-human study demonstrates that tumor-associated hK2 can be identified and targeted using h11B6 as a platform as the h11B6 antibody selectively accumulated in mCRPC metastases with mass-independent clearance kinetics. These data support the feasibility of hK2 as a target for imaging and hK2-directed agents as potential therapies in patients with mCRPC.

Key Words: mCRPC; hK2; KLK2; h11B6

J Nucl Med 2024; 65:1051–1056
DOI: 10.2967/jnumed.124.267416

Patients with metastatic castration-resistant prostate cancer (mCRPC) have limited treatment options as novel androgen receptor (AR) inhibitors and cytotoxic therapies move to the castration-sensitive setting (*1,2*). Recently, the mCRPC treatment landscape has expanded with the approval of the targeted radiopharmaceutical therapy ^{177}Lu-vipivotide tetraxetan (Pluvicto; Novartis), a systemic treatment that delivers radiation directly to the tumor cell, providing a novel mechanism for mCRPC treatment (*3*). Administration of such therapies requires a well-defined tumor-specific target to support effective payload delivery and minimal toxicity. In addition, other tumor-directed therapies, such as immunotherapies with chimeric antigen receptor T cells or T-cell–sequestering antibodies and antibody–drug conjugates, are promising avenues for drug development for mCRPC (*4,5*). Prostate-specific membrane antigen (PSMA) is the only cell surface target to be leveraged for clinical benefit in men with advanced prostate cancer; however, PSMA expression is heterogeneous among patients and even within patients on a lesion-to-lesion basis (*6*). PSMA is also putatively expressed in normal tissues such as the salivary and lacrimal glands, which can lead to off-tumor but on-target side effects in nonprostate tissue (*6*). Finally, patients who progress through PSMA-directed therapy may develop disease that does not express PSMA. New targets are therefore needed to address these shortcomings and to advance the treatment options for a disease as biologically dynamic and diverse as mCRPC.

Human kallikrein 2 (hK2; HUGO Gene Nomenclature Committee–approved gene symbol *KLK2*) is a trypsinlike antigen produced by columnar prostate epithelial cells with expression driven by AR signaling in a manner identical to that of the closely related gene encoding prostate-specific antigen (HUGO Gene Nomenclature Committee–approved gene symbol *KLK3*) (*7–10*). hK2 is both secreted and membrane-bound; however, unlike prostate-specific antigen, circulating hK2 is found at exceptionally low levels, where

Received Jan. 25, 2024; revision accepted Apr. 25, 2024.
For correspondence or reprints, contact Michael J. Morris (morrism@mskcc.org).
Published online May 23, 2024.

it can be bound by multiple protease inhibitor complexes (*7,8,11*). It has been shown that higher hK2 expression correlates with increased cell proliferation and lower apoptosis in castration-resistant prostate cancer specimens, thereby modulating the growth of castration-resistant disease (*12*). Additionally, a study reported 80% of mCRPC bone lesions to be AR-driven based on high expression of AR gene signatures, including both *KLK2* and *KLK3* (*13*). Increased AR signaling activity has demonstrated increased hK2 expression but decreased PSMA expression in multiple prostate cancer models (*8,14,15*). Specifically, treatment with the α-particle emitter ^{225}Ac generated a feed-forward mechanism with increased AR signaling and hK2 expression (*8*). This could impact therapeutic outcomes of targeting hK2 versus PSMA in mCRPC, because reactivation of AR signaling is commonly associated with mCRPC, despite castration serum levels of androgen. Indeed, preclinical observations in animal models showed improved survival after a single administration of hK2-targeting ^{225}Ac, suggesting a therapeutic benefit of targeting hK2 (*8*). Finally, hK2 expression shows prostate specificity and is relatively homogeneously expressed across disease stages, from localized to metastatic prostate cancer (*16*). Together, these data suggest hK2 to be a promising target for treatment.

In preclinical studies, reduction in tumor volume along with prolongation of survival were observed in mouse models of prostate cancer treated with the ^{225}Ac-radiolabeled humanized anti-hK2 monoclonal antibody, h11B6, where h11B6 bound only membrane-associated hK2 (*8,17*). This phase 0 first-in-human study evaluated the biodistribution, normal-tissue dosimetry, and tumor targeting of ^{111}In-radiolabeled h11B6 ([^{111}In]-DOTA-h11B6) to evaluate hK2 as a target in patients with mCRPC.

MATERIALS AND METHODS

Study Design and Participants

This was a phase 0 imaging study conducted to evaluate the biodistribution, normal-tissue dosimetry, and tumor targeting of [^{111}In]-DOTA-h11B6 (ClinicalTrials.gov identifier NCT04116164). After written informed consent for study participation was provided by the patients, screening of eligible participants was conducted 14 d before administration of the study agent. Participants at least 18 y of age with progressive measurable/evaluable mCRPC as defined by Prostate Cancer Working Group 3 criteria were prospectively enrolled in the study. Eligible participants had an Eastern Cooperative Oncology Group performance status of 1 or less, a Karnofsky performance scale score of 70 or greater, castrate testosterone levels less than 50 ng/dL, and metastatic disease documented by CT, PET/CT, MRI, or a radionuclide (^{99m}Tc-methylene diphosphonate or ^{18}F-NaF) bone scan. Participants with lesions identified by PSMA PET only and participants with pure small-cell or neuroendocrine prostate cancer were excluded. Participants could not have any condition that could impair the ability to comply with study procedures and could not have received radiotherapy or immunotherapy within 30 d, a therapeutic radioactive isotope within 28 d, or a single fraction of palliative radiotherapy within 14 d of administration of the study agent. Participants with a known allergy to antibodies were also excluded. The study was performed under a U.S. Food and Drug Administration–reviewed exploratory investigational new drug application and was approved by the Memorial Sloan Kettering Cancer Center Investigational Review Board, and all participants signed an informed consent form. Study data were collected and processed with adequate precautions to ensure confidentiality and compliance with data privacy protection laws and regulations.

The study enrolled participants in cohort 1, with the option to expand into an additional cohort at the discretion of the sponsor on the basis of findings from cohort 1. The focus of cohort 1 was to identify the optimal mass of [^{111}In]-DOTA-h11B6, which was defined as the mass at which there is minimal accumulation of radioactivity in parenchymal organs (liver, lung, spleen) and maximal accumulation in mCRPC lesions as assessed by imaging. Data collected from cohort 1 were used to estimate the serum clearance, the normal-tissue dosimetry, and the most favorable mass amount of [^{111}In]-DOTA-h11B6. Participants in cohort 1 received a single administration of [^{111}In]-DOTA-h11B6 (185 MBq) as a slow intravenous bolus over 1 min ± 30 s followed by a saline flush through an indwelling peripheral intravenous catheter.

Participants in cohort 1 were divided into 3 subcohorts (1A, 1B, and 1C). Participants in subcohort 1A received 2 mg of antibody ([^{111}In]-DOTA-h11B6 only) followed by imaging and biodistribution studies. Participants in subcohort 1B received 10 mg of antibody (8 mg of h11B6 and 2 mg of [^{111}In]-DOTA-h11B6) with subsequent imaging and biodistribution studies. Subcohort 1C was to receive 20 mg of antibody (18 mg of h11B6 and 2 mg of [^{111}In]-DOTA-h11B6) followed by imaging.

The primary endpoints of the study were safety and [^{111}In]-DOTA-h11B6 dosimetry, including serum clearance, optimal mass, and [^{111}In]-DOTA-h11B6 biodistribution. Secondary and exploratory endpoints included pharmacokinetic parameters and serum hK2 levels, respectively.

[^{111}In]-DOTA-h11B6 Imaging Agent

The macrocyclic chelator DOTA was conjugated to h11B6 (DiaProst AB) through incubation in a p-SCN-Bn-DOTA solution (MacroCyclics Inc.) at 25°C for 20 h. [^{111}In]-DOTA-h11B6 was prepared by incubating ^{111}In in acetate buffer for 2 h at 37°C with DOTA-h11B6. The reaction mixture was purified and tested for sterility, endotoxins, and radiochemical purity. Immunoreactivity was measured through a validated immunoassay. Preclinical testing of [^{111}In]-DOTA-h11B6 demonstrated radiochemical purity of more than 95% and immunoreactivity consistently greater than 80%. In vitro studies confirmed antigen-mediated antibody internalization as previously reported (*8*).

Assessments

Anterior and posterior planar ^{111}In whole-body images were obtained immediately after study agent administration (0–4 h) and on day 2 (24 ± 6 h), days 3–4 (42–78 h), and days 6–9 (114–198 h). A SPECT/CT scan from the inferior portion of the lungs to the kidneys was performed at one or more of these time points. For all time points except 0–4 h, participants were instructed to void urine before imaging. Imaging was performed on a dual-head hybrid γ-camera (Siemens Intevo SPECT/CT; Siemens Healthcare).

Blood samples were collected before treatment; 15, 30, 60, 120, and 240 min (±5 min) after study agent administration; at each imaging session; and at the 2-wk follow-up visit to measure the radioactivity and/or serum concentrations of h11B6. Vital signs (blood pressure, pulse, respiratory rate, temperature, and weight) were obtained before and up to 2 h after study agent administration as well as at imaging. Complete blood count and comprehensive metabolic panels were obtained at baseline and at follow-up.

Serum samples were measured in duplicate using an NaI (Tl) γ-well–type detector (Wallac Wizard 1480 automatic γ-counter; PerkinElmer) together with appropriate standards to assess radioactivity. The measured radioactivity concentrations were converted to a percentage of injected dose per liter, and serum volume of distribution was estimated as 100% per time-zero intercept of the percentage of injected dose per liter. Serum concentrations of h11B6 were determined using a validated immunoassay.

Absorbed radiation doses to normal tissues from [^{111}In]-DOTA-h11B6 were estimated on the basis of serum clearance of radioactivity and by image analysis of tissue uptake and retention of radioactivity over time. Data of the time-integrated activity coefficient derived from

this analysis were used with the U.S. Food and Drug Administration–approved software package application OLINDA/EXM version 2.0 (Hermes Medical Solutions) to estimate absorbed radiation doses to a panel of normal tissues using the MIRD method.

Accumulation of radioactivity was defined as an increasing ratio of tumor-to-nontumor signal over time in known sites of disease. The number of lesions that demonstrated accumulation of radioactivity was also measured.

Adverse events were assessed using the National Cancer Institute Common Terminology Criteria for Adverse Events version 5.0, and participants were monitored for side effects during infusion and at every follow-up visit for up to 2 wk after agent administration. Participants were contacted 1–2 d after study agent administration to ascertain occurrence of any treatment-emergent adverse events when symptoms were not assessed during an on-site visit.

Statistical Analysis

Descriptive statistics were calculated for key parameters, reported as the mean value and SD or SE.

RESULTS

Participant Population

Of the 22 participants included in this analysis, characteristics were comparable across the 2 subcohorts (16 in subcohort 1A and 6 in subcohort 1B; Table 1; Supplemental Table 1; supplemental materials are available at http://jnm.snmjournals.org). Since the optimum mass amount was determined in the first 2 subcohorts, the study did not accrue to subcohort 1C. SPECT/CT imaging identified tumors located in bone ($n = 14$), liver ($n = 3$), and lymph nodes ($n = 3$) (Table 1). ^{111}In-administered activities were similar between cohorts with a mean ± SD of 205 ± 16 MBq and 201 ± 7 MBq in subcohorts 1A and 1B, respectively.

Safety

All participants who received the study agent were included in the safety and tolerability analysis. [^{111}In]-DOTA-h11B6 was well tolerated. Of the 22 participants enrolled, 2 participants (9.1%) in

TABLE 1
Participant Characteristics Across Subcohorts

Subcohort	Patient	Age (y)	Weight (kg)	ECOG PS	Gleason score	Baseline PSA (ng/mL)	Primary metastatic tumor location*	Targeting location	Administered activity (MBq)
1A	001	84	92	0	9 (5 + 4)	19.7	Bone	Yes	218
	002	68	92	0	8 (3 + 5)	22.6	Liver	Yes	221
	003	70	85	0	7 (3 + 4)	40.5	Bone	Yes	202
	007	80	80	0	7 (4 + 3)	13.3	Bone	Yes	206
	009	70	111	0	6 (3 + 3)	43.5	Bone	Yes	213
	013	69	85	0	9 (5 + 4)	5.34	Nodes	Yes	210
	014	75	86	1		2.78	Bone	Yes	216
	016	75	60	1	9 (4 + 5)	1.34	Bone	Yes	199
	017	66	103	1	7 (3 + 4)	113	Bone	Yes	199
	018	61	100	1	10 (5 + 5)	73.8	Bone	Yes	196
	019	66	104	0	7 (3 + 4)	84.4	Bone	Yes	202
	020	72	90	0	9 (4 + 5)	2.44	Bone	Yes	203
	022	60	158	1	9 (4 + 5)	39.4	N/A†	N/A†	155
	023	81	92	0	7 (3 + 4)	10.5	Nodes	Yes	221
	025	62	111	0	7 (4 + 3)	9.38	Bone	Yes	197
	027	75	84	1	9 (4 + 5)	66.6	Liver	No	218
1B	004	68	85	0	9 (4 + 5)	4.96	Bone	Yes	206
	005	79	79	0	6 (3 + 3)	49.4	Bone	Yes	196
	006	82	56	1	7 (4 + 3)	124	Nodes	Yes	193
	008	56	91	0	9 (4 + 5)	507	Bone	Yes	201
	011	65	89	0	9 (4 + 5)	8.99	Liver	No	195
	015	72	109	0	9 (4 + 5)	1.33	None‡	None	213

*Tumor location is based on conventional imaging or PSMA PET.

†Participant was unable to complete remaining imaging per protocol because of noncompliance and discontinued study early. No results on tumor location or targeting are available.

‡Participant had no obvious disease on imaging.

ECOG PS = Eastern Cooperative Oncology Group performance status; PSA = prostate-specific antigen; N/A = not available.

Subcohort 1A received 2 mg of protein, and subcohort 1B received 10 mg of protein.

TABLE 2
Time-Integrated Activity Coefficients for Key Organs by Subcohort A (n = 15*) and Subcohort 1B (n = 6)

	Time (h)		
Subcohort	Kidney	Liver	Red marrow
1A	0.99 (0.05)	13.0 (0.6)	5.03 (0.19)
1B	0.87 (0.10)	12.8 (1.5)	4.69 (0.54)

*One participant was unable to complete remaining imaging per protocol because of noncompliance and discontinued study early.
Data are mean with SE in parentheses. Subcohort 1A received 2 mg of protein, and subcohort 1B received 10 mg of protein.

subcohort 1A experienced treatment-emergent adverse events, which were not treatment-related, including 1 case of grade 3 tumor-related bleeding and 1 case of grade 2 hypertension. The participant with tumor-related bleeding discontinued postinjection imaging. No infusion reactions or anaphylactoid reactions were reported.

Biodistribution, Pharmacokinetics, and Radioactivity Clearance

Serial whole-body images showed gradual clearance of radioactivity from the vascular compartment and gradual though normal accumulation in the liver at later time points. There was no evidence of increased physiologic [^{111}In]-DOTA-h11B6 accumulation in bones, salivary glands, or the thyroid at either antibody mass level. Time-integrated activity analyses confirmed predominant localization of [^{111}In]-DOTA-h11B6 in the vascular compartment rather than in critical normal organs (Table 2), and absorbed radiation doses of critical normal organs were low for both cohorts (Table 3). A complete list of absorbed radiation doses of normal organs is included in Supplemental Table 2. A relationship between administered antibody mass and biodistribution was not observed (Fig. 1A). Serum clearance kinetics showed a gradual decline in radioactivity over time (Fig. 1B), with no apparent difference between the 2-mg antibody mass (subcohort 1A) and 10-mg antibody mass (subcohort 1B), suggesting independence of antibody mass. The mean volume of [^{111}In]-DOTA-h11B6 distribution ± SE was 2.82 ± 0.13 L and 2.87 ± 0.26 L for subcohort 1A (n = 15) and subcohort 1B (n = 6), respectively.

Targeting of [^{111}In]-DOTA-h11B6 to known lesions was observed in 18 participants via SPECT/CT (Fig. 2) and was confirmed via ^{68}Ga-PSMA-11 PET/CT (data not presented). In the 4 participants with no evidence of lesion targeting, 1 participant had no evidence of disease by PSMA PET and 1 had incomplete imaging.

DISCUSSION

This first-in-human study demonstrated the favorable distribution of [^{111}In]-DOTA-h11B6 in participants with mCRPC and highlighted the feasibility of hK2-directed imaging. Tumor uptake was noted in 18 of 22 participants. Of the 4 participants with no evidence of tumor targeting, 1 had no evidence of disease by PSMA PET and 1 participant had incomplete imaging. Tumor accumulation of [^{111}In]-DOTA-h11B6 was visually observed approximately 4 d after agent administration and was more evident via imaging with increasing time after injection.

As with other monoclonal antibodies, serum clearance kinetics and time–activity analyses demonstrated antibody localization predominantly to the vascular compartment, with clearance characteristics comparable to those of other intact humanized IgGs (*18,19*). Imaging data further supported vascular compartment localization, with no evidence of significant parenchymal targeting or any extratumoral antigen sink. Importantly, the antibody mass amounts studied (2 and 10 mg) had no effect on serum clearance, volume of distribution, or tumor targeting.

[^{111}In]-DOTA-h11B6 was tolerated in participants with mCRPC. Two treatment-emergent adverse events were observed; however, these events were not related to the study treatment. The patient who experienced tumor-related bleeding discontinued the study early. Normal-organ and whole-body absorbed radiation doses were well within the limits of use for imaging radiopharmaceuticals. Unlike PSMA-targeted agents that are accompanied by an uptake in the lacrimal and salivary glands and in the renal tubules, which can lead to dose-limiting toxicity (*20*), targeting of hK2 with [^{111}In]-DOTA-h11B6 showed no significant uptake in the salivary glands and a modest renal uptake (0.22–0.23 mGy/MBq); therefore, low radiation doses to these organs is expected. Phase 1 studies assessing hK2-targeting therapies, including ^{225}Ac radioimmunotherapy, are currently ongoing and may further support hK2 as a therapeutic target in advanced prostate cancer (*21*). As off-target localization to parenchymal organs and bone marrow is a potential area of concern, especially for radioactive payloads, hK2-targeting radiolabeled agents will need careful monitoring. To this end, the risks of myelosuppression, renal and liver toxicity, and gastrointestinal effects have been identified with appropriate mitigation strategies in the ongoing phase 1 study assessing JNJ-6240 ([^{225}Ac]-DOTA-h11B6) (*21*).

The tumor-targeting specificity of [^{111}In]-DOTA-h11B6, its mass-independent biodistribution, and its tolerable safety profile together suggest a role for h11B6 as a carrier for targeted delivery of a conjugated payload for the treatment of mCRPC. Through

TABLE 3
Absorbed Radiation Doses for Key Organs by Subcohort 1A (n = 15*) and Subcohort 1B (n = 6)

	Absorbed dose/activity (mGy/MBq)			
Subcohort	Kidney	Liver	Red marrow	Total body
1A	0.23 (0.01)	0.45 (0.02)	0.17 (0.01)	0.12 (0.003)
1B	0.22 (0.02)	0.46 (0.05)	0.17 (0.01)	0.12 (0.01)

*One participant was unable to complete remaining imaging per protocol because of noncompliance and discontinued study early.
Data are mean with SE in parentheses. Subcohort 1A received 2 mg of protein, and subcohort 1B received 10 mg of protein.

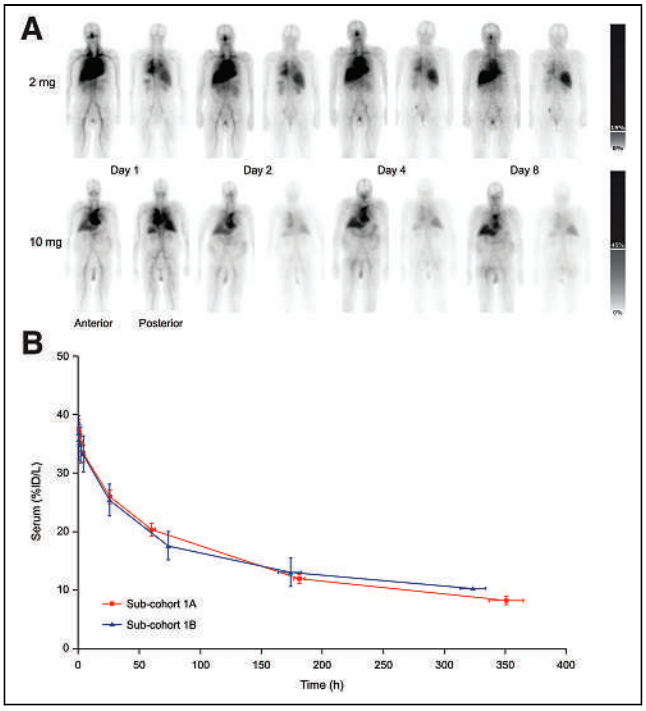

FIGURE 1. (A) Representative anterior and posterior whole-body images over time showing biodistribution after administration of 2 mg (top) or 10 mg (bottom) of [^{111}In]-DOTA-h11B6. Bars on right represent percentage of maximum pixel value over all images. (B) Average serum clearance kinetics are based on decay-corrected percentage of injected ^{111}In activity (percentage of injected dose per liter ± SE) across subcohort 1A (2 mg, n = 15) and subcohort 1B (10 mg, n = 6). %ID/L = percentage of injected dose per liter.

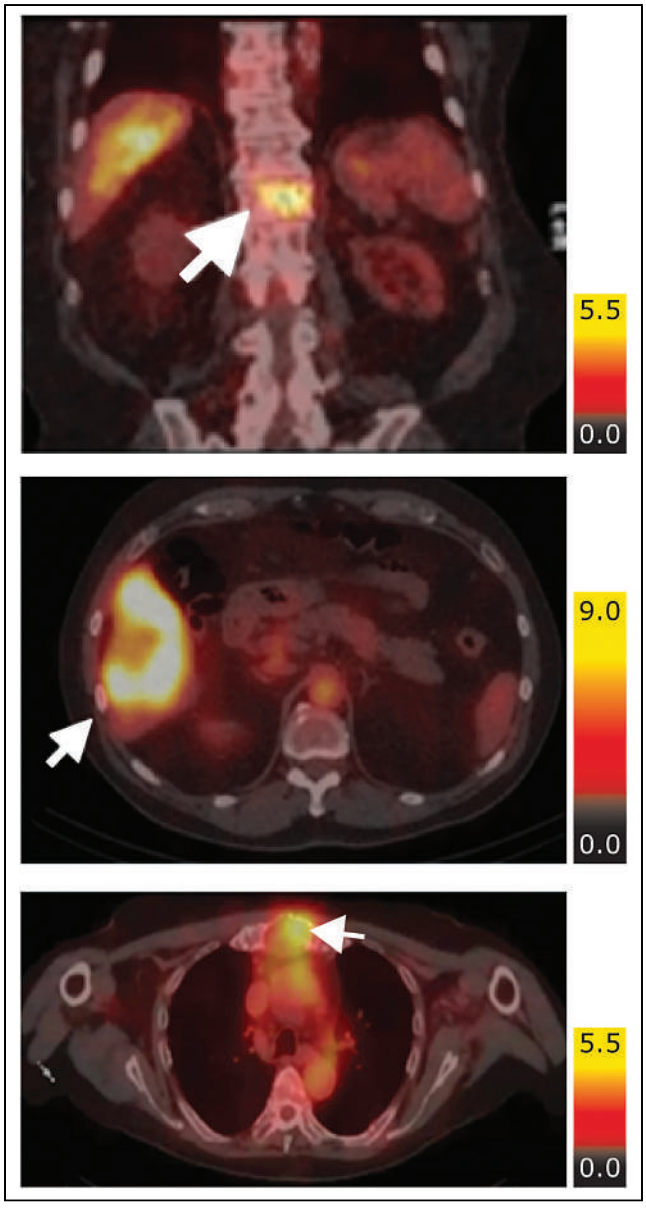

FIGURE 2. Representative images showing tumor uptake of [^{111}In]-DOTA-h11B6 administered at 2 mg (top 2 images) or 10 mg (lower image). Arrows denote lesions.

characterization of h11B6 biodistribution in human participants, this study further adds to previous preclinical prostate cancer studies (*8,22*) by validating the expression of hK2 in mCRPC, providing data to support the use of h11B6 in a clinical setting.

CONCLUSION

This phase 0 trial demonstrated that [^{111}In]-DOTA-h11B6 was well tolerated with mass-independent biodistribution and tumor targeting in mCRPC. These data not only confirm the validity of hK2 as both an imaging and a potential therapeutic target for mCRPC but also support the continued investigation of h11B6 for directed delivery of payloads such as therapeutic radionuclides to address an unmet need for additional mCRPC treatment options.

DISCLOSURE

This work was supported by Janssen Research & Development, LLC, and SpectronRX, Inc. Neeta Pandit-Taskar reports honoraria from Actinium Pharmaceuticals; a consulting or advisory role for Illumina, Progenics, Telix, and Lantheus; a Speakers Bureau association for Actinium Pharmaceuticals and Telix; research funding (institutional) from Bayer Health, Bristol Myers Squibb, Clarity Pharmaceuticals, Imaginab, Janssen Research & Development, LLC, Regeneron, Ymabs, and Innervate; and travel support from AstraZeneca and Bayer. Joseph O'Donoghue reports consulting for Janssen Research & Development, LLC; Invicro, LLC; and Curadh MTR. Dushen Chetty reports stock and other ownership interests for Novartis AG and is an employee of Janssen Research & Development, LLC. Steven Max, Margaret Yu, and Michael Russell report stock and other ownership interests for, and are employees of, Janssen Research & Development, LLC. Danielle Wanik reports research funding from Janssen Research & Development, LLC (institutional), and is an employee of Invicro LLC. Ohad Ilovich is an employee of Invicro LLC. Chaitanya Divgi reports a consulting or advisory role for Janssen Research & Development, LLC, and SpectronRX, Inc. Michael Morris reports stock and other ownership interests for Doximity; a consulting or advisory role for Lantheus Medical Imaging, AstraZeneca, Amgen, Daiichi, Convergent Therapeutics, Pfizer, ITM Isotope Technologies Munich, Clarity Pharmaceuticals, Blue Earth Diagnostics, POINT Biopharma, Telix Pharmaceuticals, Progenics, and Z-α; research funding from Bayer (institutional), Progenics (institutional), Corcept Therapeutics (institutional), Roche/Genentech (institutional), Janssen Research & Development, LLC (institutional), Celgene (institutional),

Novartis (institutional), and Astellas Pharma (institutional); and travel, accommodations, and expenses from AstraZeneca, APCCC, and Memorial Sloan Kettering Cancer Center. No other potential conflict of interest relevant to this article was reported.

ACKNOWLEDGMENTS

We thank the Prostate Cancer Clinical Trials Consortium (PCCTC LLC) for managing this clinical trial. Medical writing and editorial support was provided by Brittany Carson, PhD, and Amanda Hall, PhD, of MEDiSTRAVA.

KEY POINTS

QUESTION: Can hK2 expression be leveraged as a prostate cancer imaging and therapeutic target in humans?

PERTINENT FINDINGS: This first-in-human study demonstrated that the [^{111}In]-radiolabeled anti-hK2 antibody, [^{111}In]-DOTA-h11B6, selectively targeted mCRPC tumors without safety concerns.

IMPLICATIONS FOR PATIENT CARE: This study highlights the feasibility of hK2 as a prostate cancer target and supports continued investigation of h11B6 or other hK2-targeting agents in the treatment of mCRPC.

REFERENCES

1. NCCN Clinical Practice Guidelines in Oncology: Prostate Cancer. National Comprehensive Cancer Network website. https://www.nccn.org/professionals/physician_gls/pdf/prostate.pdf. Updated March 2024. Accessed May 2, 2024.
2. Marhold M, Kramer G, Krainer M, Le Magnen C. The prostate cancer landscape in Europe: current challenges, future opportunities. *Cancer Lett.* 2022;526:304–310.
3. Sartor O, de Bono J, Chi KN, et al. Lutetium-177-PSMA-617 for metastatic castration-resistant prostate cancer. *N Engl J Med.* 2021;385:1091–1103.
4. López-Campos F, Gajate P, Romero-Laorden N, et al. Immunotherapy in advanced prostate cancer: current knowledge and future directions. *Biomedicines.* 2022;10:537.
5. Shen J, Pachynski R, Nordquist LT, et al. 1804P APEX-01: first-in-human phase I/II study of ARX517 an anti-prostate-specific membrane antigen (PSMA) antibody-drug conjugate (ADC) in patients (pts) with metastatic castration-resistant prostate cancer (mCRPC). *Ann Oncol.* 2023;34(suppl 2):S974–S975.
6. Bostwick DG, Pacelli A, Blute M, Roche P, Murphy GP. Prostate specific membrane antigen expression in prostatic intraepithelial neoplasia and adenocarcinoma: a study of 184 cases. *Cancer.* 1998;82:2256–2261.
7. Saedi MS, Zhu Z, Marker K, et al. Human kallikrein 2 (hK2), but not prostate-specific antigen (PSA), rapidly complexes with protease inhibitor 6 (PI-6) released from prostate carcinoma cells. *Int J Cancer.* 2001;94:558–563.
8. McDevitt MR, Thorek DLJ, Hashimoto T, et al. Feed-forward alpha particle radiotherapy ablates androgen receptor-addicted prostate cancer. *Nat Commun.* 2018;9:1629.
9. Thorek DL, Evans MJ, Carlsson SV, Ulmert D, Lilja H. Prostate-specific kallikrein-related peptidases and their relation to prostate cancer biology and detection: established relevance and emerging roles. *Thromb Haemost.* 2013;110:484–492.
10. Becker C, Piironen T, Pettersson K, Hugosson J, Lilja H. Testing in serum for human glandular kallikrein 2, and free and total prostate specific antigen in biannual screening for prostate cancer. *J Urol.* 2003;170:1169–1174.
11. Piironen T, Lövgren J, Karp M, et al. Immunofluorometric assay for sensitive and specific measurement of human prostatic glandular kallikrein (hK2) in serum. *Clin Chem.* 1996;42:1034–1041.
12. Shang Z, Niu Y, Cai Q, et al. Human kallikrein 2 (KLK2) promotes prostate cancer cell growth via function as a modulator to promote the ARA70-enhanced androgen receptor transactivation. *Tumour Biol.* 2014;35:1881–1890.
13. Ylitalo EB, Thysell E, Jernberg E, et al. Subgroups of castration-resistant prostate cancer bone metastases defined through an inverse relationship between androgen receptor activity and immune response. *Eur Urol.* 2017;71:776–787.
14. Evans MJ, Smith-Jones PM, Wongvipat J, et al. Noninvasive measurement of androgen receptor signaling with a positron-emitting radiopharmaceutical that targets prostate-specific membrane antigen. *Proc Natl Acad Sci USA.* 2011;108:9578–9582.
15. Spratt DE, Evans MJ, Davis BJ, et al. Androgen receptor upregulation mediates radioresistance after ionizing radiation. *Cancer Res.* 2015;75:4688–4696.
16. Gene page. GTExPortal website. http://gtexportal.org/home/gene/KLK2. Updated April 11, 2024. Accessed May 2, 2024.
17. Timmermand OV, Ulmert D, Evans-Axelsson S, et al. Preclinical imaging of kallikrein-related peptidase 2 (hK2) in prostate cancer with a ^{111}In-radiolabelled monoclonal antibody, 11B6. *EJNMMI Res.* 2014;4:51.
18. Pandit-Taskar N, O'Donoghue JA, Durack JC, et al. A phase I/II study for analytic validation of ^{89}Zr-J591 immunoPET as a molecular imaging agent for metastatic prostate cancer. *Clin Cancer Res.* 2015;21:5277–5285.
19. Pandit-Taskar N, O'Donoghue JA, Divgi CR, et al. Indium 111-labeled J591 anti-PSMA antibody for vascular targeted imaging in progressive solid tumors. *EJNMMI Res.* 2015;5:28.
20. Ruigrok EAM, van Vliet N, Dalm SU, et al. Extensive preclinical evaluation of lutetium-177-labeled PSMA-specific tracers for prostate cancer radionuclide therapy. *Eur J Nucl Med Mol Imaging.* 2021;48:1339–1350.
21. Morris MJ, Sartor OA, Wong JYC, et al. A study of JNJ-69086420, an actinium-225-labeled antibody targeting human kallikrein-2 (hK2) for advanced prostate cancer [abstract]. *J Clin Oncol.* 2022;40(suppl 6):TPS206.
22. Thorek DL, Watson PA, Lee SG, et al. Internalization of secreted antigen-targeted antibodies by the neonatal Fc receptor for precision imaging of the androgen receptor axis. *Sci Transl Med.* 2016;8:367ra167.

Deescalated ^{225}Ac-PSMA-617 Versus ^{177}Lu/^{225}Ac-PSMA-617 Cocktail Therapy: A Single-Center Retrospective Analysis of 233 Patients

Hendrik Rathke[1,2], Erik Winter[1], Frank Bruchertseifer[3], Manuel Röhrich[1,4], Frederik Lars Giesel[5], Uwe Haberkorn[1], Alfred Morgenstern[3], and Clemens Kratochwil[1]

[1]*Department of Nuclear Medicine, Heidelberg University Hospital, Heidelberg, Germany;* [2]*Department of Nuclear Medicine, Bern University Hospital, Bern, Switzerland;* [3]*Joint Research Centre, European Commission, Karlsruhe, Germany;* [4]*Department of Nuclear Medicine, Mainz University Hospital, Mainz, Germany; and* [5]*Department of Nuclear Medicine, University Hospital Duesseldorf, Duesseldorf, Germany*

The aim of this work is to evaluate our clinical real-world data obtained with ^{225}Ac-PSMA-617 (AcPSMA), which were acquired under compassionate care regulations in patients with advanced-stage prostate cancer. The objective parameters that could be derived from this evaluation are compared with previous literature about AcPSMA and ^{177}Lu-PSMA-617 (LuPSMA). **Methods:** The medical files of all patients who had received AcPSMA on an individual patient basis at the Heidelberg University Hospital since January 2014 were analyzed retrospectively. Previously published patients were excluded. The remaining patients were tailored into 2 subgroups with different treatment strategies: group 1 received AcPSMA as a deescalated monotherapy, and group 2 received LuPSMA plus AcPSMA as a cocktail regimen. Baseline characteristics, serum prostate-specific antigen (PSA) response, and overall survival were compared with the most appropriate historical controls. **Results:** Of 287 patients treated, 54 were excluded because of previous publication and 233 were evaluated, 104 of whom received AcPSMA monotherapy (median, 6 MBq). In this group, 55 patients (53%) presented with a best PSA response of at least 50%. The other 129 patients received a cocktail therapy of AcPSMA (median, 4 MBq) plus LuPSMA (4 GBq). In this group, a best PSA response of at least 50% was observed in 74 patients (57%). The median overall survival in the monogroup was 9 mo and in the cocktail group was 15 mo. If adjusted for prognostic baseline characteristics, the efficacy of both regimens was not significantly different. **Conclusion:** Deescalated treatment activities of AcPSMA or AcPSMA and LuPSMA cocktail regimens present better tolerability with regard to xerostomia than previous regimens of at least 100 kBq/kg while retaining high antitumor activity in poor-prognosis prostate cancer patients.

Key Words: ^{225}Ac; ^{177}Lu; TAT; PSMA; mCRPC; cocktail

J Nucl Med 2024; 65:1057–1063
DOI: 10.2967/jnumed.123.267206

Prostate-specific membrane antigen (PSMA)–targeted α-therapy (TAT) for advanced-stage metastatic castration-resistant prostate cancer patients was introduced in 2014 (*1*). After a preliminary dosimetry estimate and brief empiric dose escalation (*2*), treatment activity of 100 kBq of ^{225}Ac-PSMA-617 (AcPSMA) per kilogram of body weight (kgBW) was proposed and applied to the next 40 patients (*3*). Using this protocol, promising efficacy with regard to duration of tumor control has been observed. However, salivary gland toxicity increased with cumulative treatment cycles and 10% of responding patients discontinued PSMA-TAT because of dose-limiting xerostomia.

In the following years and confirmative to one another, some research groups reported a relevant tumor sink effect for radiolabeled PSMA ligands in high-tumor-burden patients (*4–6*). Because our initial dose escalation was based on such advanced patients, it is likely that we overestimated the maximum tolerable dose with respect to low to intermediate tumor mass patients, including the ones who started PSMA-TAT with high tumor volume but achieved partial remission after the first treatment cycles. With growing acceptance of PSMA-targeted radiopharmaceutical therapy in general, an increasing number of patients with less advanced tumor spread were scheduled to our department to receive PSMA-TAT. Thus, the responsible nuclear medicine physicians often modified the regimen by reducing the treatment activity.

Some years ago, a pilot study introduced the concept of ^{177}Lu-PSMA-617 (LuPSMA) and AcPSMA combination therapy (*7*). One course of AcPSMA (median, 5.3 MBq; range, 1.5–7.9) combined with LuPSMA (median, 6.9 GBq; range, 5.0–11.6) was administered to 20 metastatic castration-resistant prostate cancer patients and followed by LuPSMA maintenance monotherapy. In a different publication from the same group, 2 cycles of LuPSMA (mean, 6.7 ± 1.8 GBq) were administered to 15 patients and augmented with 2.7 ± 1.1 MBq of AcPSMA in the first (n = 7), second (n = 3), or both (n = 5) cycles (*8*). In a third publication, 17 patients received a single cycle of 1.8–6.9 MBq of AcPSMA in combination with 3.8–8.2 GBq of LuPSMA (*9*). The salivary gland toxicity of these combination therapies was found to be favorable compared with 100 kBq of AcPSMA per kgBW and comparable to LuPSMA standard therapy. These preliminary reports have relevant limitations because of the variability in the numbers of performed treatment cycles, the range of administered activity of both LuPSMA and AcPSMA, short follow-up, low overall patient numbers, and major heterogeneity on how treatment was continued after the 1–2 cycles of combination therapy (i.e., some patients received a further combination and others received maintenance with LuPSMA only). Nevertheless, because of the low rate of reported xerostomia at promising antitumor activity, we

Received Dec. 17, 2023; revision accepted Apr. 25, 2024.
For correspondence or reprints, contact Hendrik Rathke (hendrik.rathke@ksgr.ch).
Published online Jun. 6, 2024.

considered the cocktail approach to be an encouraging strategy to refine the trade-off between tolerability and antitumor activity.

In this retrospective evaluation, we determined the tolerability, the prostate-specific antigen (PSA) response rate, and overall survival (OS) observed with patients receiving a regimen of less than 100 kBq of AcPSMA per kgBW or AcPSMA and LuPSMA cocktail therapy.

MATERIALS AND METHODS

Patients

We retrospectively analyzed all patients who started treatment with AcPSMA in the Department of Nuclear Medicine at Heidelberg University Hospital between January 2014 and July 2021. These patients were considered inappropriate for treatment or had already exhausted the approved treatments at that time. Experimental salvage therapies were offered on an individual patient basis under the conditions of the updated Declaration of Helsinki, paragraph 37 ("Unproven Interventions in Clinical Practice"), and national regulations. Patients were informed about the experimental nature of this therapy and gave written informed consent. Considering their own clinical experience with AcPSMA, general experience with PSMA-targeted radiopharmaceutical therapy, and patients' different clinical situations, physicians offered patients a dosing regimen that followed the best available knowledge at the time. Treatment with AcPSMA was offered only to patients with a positive PSMA baseline scan that was available under real-world conditions. For ^{68}Ga-PSMA-11, ^{18}F-DCFPyL, and ^{18}F-PSMA-1007, a SUV of more than 10 was defined as PSMA-positive. For ^{99m}Tc-PSMA tracers, tumor uptake equal to or higher than that of salivary glands in visual inspection in all measurable tumor lesions (in analogy to the VISION and TheraP clinical trials, only lesions $>$ 10 mm were considered measurable) was defined as PSMA-positive. This retrospective observational study was approved by the research ethics committee of the medical faculty of Heidelberg University (permit S-732/2018).

Patients who were previously published from our department were excluded from this analysis (*1*–*3*). Nevertheless, we cannot exclude partial overlap with pooled patient cohorts of patients treated in Germany that have been reported from a Dutch research group (*10*,*11*).

Radiopharmaceuticals, Patient Preparation, and Dosing Regimens

The PSMA-617 precursor was obtained from ABX. ^{225}Ac was produced by radiochemical extraction from ^{229}Th at the European Commission's Joint Research Centre (*12*). ^{177}Lu (EndolucinBeta) was obtained from ITM. The labeling conditions for AcPSMA and LuPSMA have been described previously (*1*,*13*). The treatment activity was determined on the basis of consensus of those authors who already had broad clinical experience with ^{131}I-MIP1095 (*14*), ^{90}Y-PSMA-617 (*15*), LuPSMA (*16*,*17*), AcPSMA (*2*), and ^{225}Ac-DOTATOC (*18*), considering the prognosis and progression velocity of each patient.

These individual treatment decisions can be assigned to 2 general concepts. The first concept, dynamic deescalation, means that the first cycle was performed with a fixed standard treatment activity of 8 MBq of AcPSMA (a simplification of the protocol of 100 kBq of AcPSMA per kgBW, considering an average body weight of 80 kg for male patients) in superscan-pattern patients and 6 MBq in normal biodistribution patients. Depending on PSA and clinical response, the treatment activity was reduced by 2 MBq for the subsequent cycles (i.e., 4–6 MBq for the second cycle and eventually 2–4 MBq for the third cycle).

The second approach was to administer a combination of approximately 4 GBq of LuPSMA together with 4 MBq of AcPSMA, which equals approximately 50% of the previously recommended LuPSMA and AcPSMA treatment doses, respectively.

In both concepts, the intention-to-treat protocol was a 3-cycle therapy, with cycles administered every 2 mo (8–9 wk). Standard androgen deprivation therapy and bone-protecting agents were continued during AcPSMA, but other therapies related to metastatic castration-resistant prostate cancer were discontinued (chemotherapies $>$ 6 wk in advance).

The treatment was administered as a slow (~30 s), intravenous free-hand injection from a lead-shielded syringe. Hydration with 2 L of physiologic electrolyte solution (Sterofundin; B. Braun Melsungen) was administered on the treatment day (starting 30 min before therapy with a flow of 250 mL/h; combination with oral or intravenous diuretics was clinically indicated) and the following day, respectively.

Follow-up and Statistical Data Analysis

Restaging per PSMA PET/CT or PSMA SPECT/CT was recommended 2 mo after the third treatment cycle (or earlier in cases of clinical and biochemical progression) at the location of the initial staging. In long-term follow-up, the urologist or oncologist chose imaging according to medical appropriateness. PSA was measured at week 8 and week 16 after the first treatment cycle and was evaluated with waterfall graphs for the week 8 PSA response or best PSA response obtained at either week 8 or week 16.

Statistical analysis was performed using SPSS version 28 (IBM). Median OS (mOS) was approximated with Kaplan–Meier curves using the data provided by local oncologists or national death record registers. Patients still alive were censored with their last available follow-up date (data freeze, May 2, 2022). The baseline characteristics of the cohorts were compared using (2-sided) Pearson correlation. OS was checked to determine whether it was related to the presence of bone marrow infiltration, and a significant difference was found between the groups (ANOVA). A propensity score matched-pair analysis (paired *t* test) was done for OS using the factors of age, Eastern Cooperative Oncology Group clinical performance status score, time to therapy, and presence of bone marrow infiltration.

RESULTS

From 287 patients who received AcPSMA between January 2014 and July 2021, 54 were previously published by our group and therefore excluded from this analysis. The medical files of the remaining 233 patients, who originated from several countries all over the globe (Supplemental Fig. 1 [supplemental materials are available at http://jnm.snmjournals.org]), were evaluated retrospectively. The analysis revealed that between 2014 and 2017, 104 patients received deescalated AcPSMA monotherapy and that between 2018 and 2021, 129 patients received a cocktail regimen.

The main characteristics of the patient cohorts receiving AcPSMA monotherapy and the AcPSMA and LuPSMA cocktail are provided in Table 1. The baseline profile of our patients is relatively similar to that of the patients who have been recruited to the VISION clinical trial (*19*). However, 5%–16% of our patients would not have been candidates for the VISION trial because of low platelet count and 12%–22% would not have been candidates because of low baseline hemoglobin. Our monotherapy and cocktail groups also included 37% and 32% of patients who had previously been treated with LuPSMA. Both of our groups included more patients with visceral metastases than did the VISION trial.

An itemwise comparison of our patients' baseline characteristics with the historical controls from the VISION trial is provided in Supplemental Table 1. In our patients, some other nonstandard treatments had been applied in advance of AcPSMA; in contrast, VISION patients received these treatments after LuPSMA (Supplemental Table 2). The baseline characteristics were well balanced between the monotherapy and the cocktail groups except for a significantly higher number of patients with bone marrow infiltration in the monotherapy group ($P < 0.001$).

TABLE 1
Patient Characteristics for AcPSMA Monotherapy Group and AcPSMA and LuPSMA Cocktail Group

Characteristic	AcPSMA	AcPSMA and LuPSMA
Patients (*n*)	104	129
Age (y)	62 (48–81)	62 (44–80)
ECOG score of 0–1 (%)	66.3	87.6
ECOG score ≥ 2 (%)	34.6	12.4
Time until PSMA therapy (mo)	85 (9–282)	76 (2–295)
Previous β-PSMA therapy (%)		
1 cycle	11	7
≥2 cycles	26	25
Site of disease (%)		
Lung	13	8
Liver	22	15
Lymph node	70	67
Bone	96	97
Bone marrow (superscan)	76	39
Brain	2	1
Other	21	15
PSA (ng/mL)	312 (0–4,843)	78 (0–6,557)
AP (IU/L)	203 (19–3,148)	128 (37–1,866)
LDH (IU/L)	403 (156–4,066)	245 (149–2,662)
Gleason score (%)		
6–7	30	28
8–10	53	61
Unknown	17	11
Previous therapy (%)		
Prostatectomy and lymph node dissection	53	51
Radiotherapy of primary tumor	32	19
Both local therapies	43	39
Previous NAAD therapy (%)	89	87
1 regimen	32	38
2 regimens	68	59
More than 2 regimens	0	3
No NAAD regimen	11	13
Previous taxane therapy (%)	70	71
1 regimen (%)	51	40
2 regimens (%)	32	41
3 regimens (%)	18	20
No chemotherapy regimen	30	29
PLT ≥ 100/nL (%)	84	95
PLT < 100/nL (%)	16	5
Hb ≥ 9 g/dL (%)	78	88
Hb < 9 g/dL (%)	22	12
Event death (%)	62.5	52
Event censored (%)	37.5	48

ECOG = Eastern Cooperative Oncology Group clinical performance status; AP = alkaline phosphatase (reference level, 40–130 U/L); LDH = lactate dehydrogenase (reference level, <342 U/L); NAAD = novel androgen axis drugs, i.e., abiraterone, enzalutamide, apalutamide, and darolutamide; PLT = platelet (reference level, 150–440/nL); Hb = hemoglobin.

Data are median and range.

Taxane retreatment with docetaxel and cabazitaxel in complete 6-cycle series was counted as additional treatment line.

Percentages may not total 100% because of rounding.

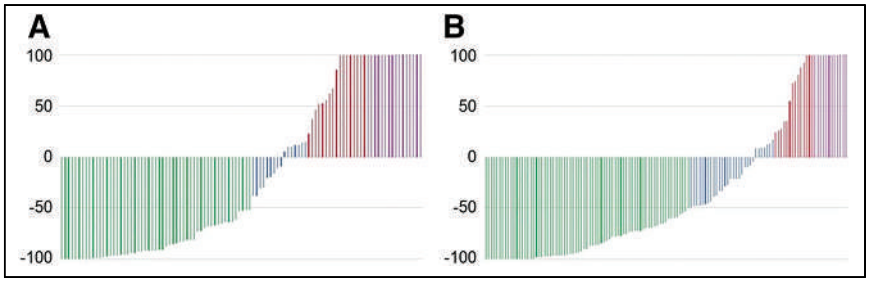

FIGURE 1. Waterfall graphs of best PSA response. (A) Of 104 patients receiving AcPSMA monotherapy, 55 had PSA decline of >50% (green); 16 had stable disease, defined by PSA decrease of <50% up to PSA increase of <20% (blue); 17 had PSA progression (red); and 16 were follow-up losses (purple). (B) Of 129 cocktail group patients, 74 had PSA decline of >50% (green), 36 had stable disease (blue), 17 had PSA progression (red), and 12 were follow-up losses (purple).

In total, 536 treatment cycles with cumulative treatment activity of 2,884 MBq of ^{225}Ac were administered to either 104 patients receiving AcPSMA monotherapy (250 cycles, 1,644 MBq of ^{225}Ac, and average of 6.6 MBq/cycle) or 129 patients receiving AcPSMA and LuPSMA cocktail therapy (286 cycles, 1,240 MBq of ^{225}Ac, and average of 4.3 MBq/cycle).

We did not observe acute adverse reactions during application and observed only moderate (numeric rating scale change of 2–4 compared with administration date) flare-up of pain in bone lesions in 37 of 536 treatments (7%) during the first 48-h observational phase after the injection. Mild xerostomia (Common Terminology Criteria for Adverse Events grade 1 or 2; National Cancer Institute) was reported from all patients. However, patients who discontinued PSMA-TAT did so because of insufficient PSA response, clinical nonresponse, or travel restrictions related to the coronavirus disease 2019 pandemic. In contrast to previous treatment regimens, none of the responding patients discontinued because of intolerable xerostomia.

After the first treatment cycle, of the 104 patients who received AcPSMA monotherapy, 46 (44%) achieved a decrease of more than 50% in the PSA level and 27 (26%) achieved a PSA decrease of more than 80% at week 8. Of the 129 patients who received AcPSMA and LuPSMA cocktail therapy, decreases in PSA of more than 50% and 80% were observed in 64 (50%) and 34 (26%), respectively, at week 8.

In the AcPSMA monogroup, the best PSA response, a PSA decline of more than 50%, was found in 55 of 104 patients (53%), and a PSA decline of more than 80% was found in 39 of 104 patients (38%; Fig. 1A). Best PSA responses of more than 50% were found in 74 of 129 patients (57%; Fig. 1B) and of more than 80% were found in 45 of 129 patients (35%) of the cocktail cohort. Consequently, there was no statistically significant difference in PSA response between the 2 groups (χ^2 test with Yates correction, $P = 0.49$, and without Yates correction, $P = 0.58$). The PSA response correlates well with the imaging response of the PET-positive volume. Positive radiologic responses of lymph nodal and visceral metastases were observed with both treatment schemes (Fig. 2).

The mOS of the AcPSMA monotherapy patients was 9.0 mo (95% CI, 7.2–10.8 mo), and the mOS of the cocktail therapy patients was 15.0 mo (95% CI, 11.0–19.0 mo). Kaplan–Meier curves are presented in Figure 3.

In ANOVA, OS was significantly ($P = 0.032$) dependent on the presence of bone marrow infiltration. Because the percentage of bone marrow–infiltrated patients was significantly ($P < 0.001$) higher in the monotherapy group, most likely the poor risk profile of this group is responsible for the shorter mOS observed. If a propensity score matched-pair analysis considering the Eastern Cooperative Oncology Group clinical performance status score, bone marrow infiltration, and time from diagnose to PSMA therapy is applied, the mOS between the 2 groups is not significantly different ($P = 0.174$).

DISCUSSION

In this work, we retrospectively compare 2 approaches to improve the tolerability of PSMA-TAT to salivary glands without losing too much antitumor activity. One group of patients received monotherapy with AcPSMA that was individually deescalated by considering baseline tumor burden and early PSA response, and another group received combination therapy of AcPSMA plus LuPSMA. PSA response and OS are not significantly different between the groups if propensity score matching for the Eastern Cooperative Oncology Group clinical performance status score and bone marrow infiltration is applied.

With our initially projected regimen of 100 kBq of AcPSMA per kgBW, a PSA response of more than 50% in 24 of 40 intention-to-treat patients (60%) was observed. However, 4 of 40 patients (10%) discontinued therapy because of xerostomia despite positive response (*3*). This dosing regimen has been used in other centers. Satapathy et al. (*20*) reported 11 patients (46%) with a PSA response of more than 50%; the follow-up was too short to assess mOS. Yadav et al. (*21*) reported 28 patients with a median follow-up of up to 22 mo

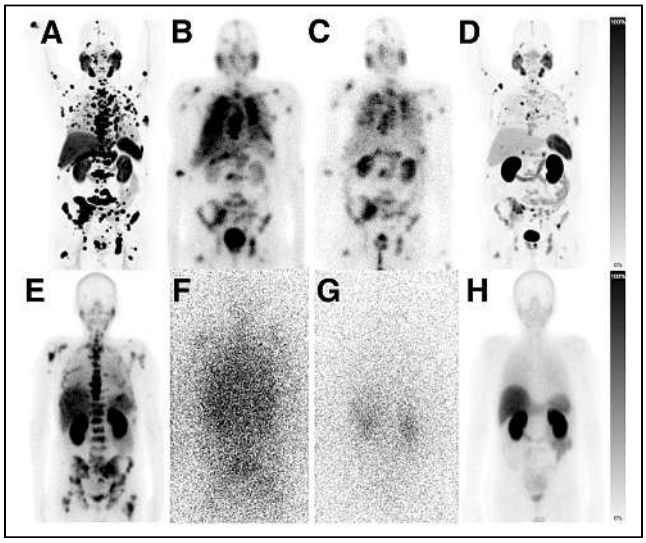

FIGURE 2. (A–D) Patient with meningeal, adrenal, pulmonary, lymph nodal, and osseous metastases. (A) Baseline staging per ^{18}F-PSMA-1007 PET/CT is demonstrated as maximum-intensity projection. (B and C) Two cycles of AcPSMA and LuPSMA cocktail therapy were documented per planar scan of 208-keV γ-line of ^{177}Lu. (D) PET/CT restaging presents partial remission. (E–H) Patient with adrenal, osseous, lymph nodal, and hepatic metastases. (E) Baseline imaging was done as planar ^{99m}Tc-PSMA scintigraphy. (F and G) AcPSMA monotherapy was documented per planar emission scans using 26% 440-keV and 12% 218-keV γ-coemissions of ^{213}Bi and ^{221}Fr. (H) Restaging per planar ^{99m}Tc-PSMA scintigraphy demonstrates near-total remission.

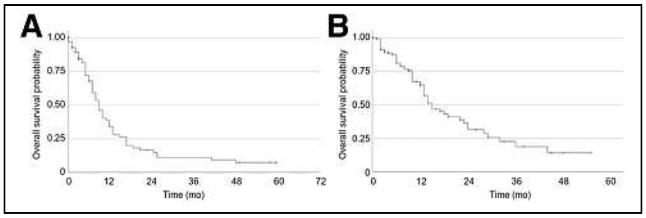

FIGURE 3. Kaplan–Meier curves for AcPSMA monotherapy group with mOS of 9 mo (95% CI, 7.18–10.82) (A) and for AcPSMA and LuPSMA cocktail group with mOS of 15 mo (95% CI, 10.93–19.02) (B).

and found that 39% of these patients had a PSA response of more than 50%, with a mOS of 17 mo. Previous chemotherapy in 82% (23/28) and the fraction of patients with previous LuPSMA (15/28) are comparable to our baseline characteristics (i.e., previous chemotherapy in 85% and 68% and previous LuPSMA in 37% and 32% of the AcPSMA monotherapy group and the cocktail group, respectively) (*21*). The fractions of cocktail group patients with lung, liver, and brain metastases were 10.7%, 10.7%, and 7%, respectively, versus 13%, 22%, and 2%, respectively, in our monotherapy group patients (*21*). Even higher treatment activities of 100–150 kBq/kg were used by Ballal et al. (*22*) and translated into a higher rate of treatment-related fatigue. Nevertheless, PSA response and mOS demonstrated no clear benefit from this additional treatment escalation. Neither the dynamic deescalation nor the cocktail regimen appear to be dramatically inferior to the AcPSMA regimen of at least 100 kBq/kg.

The dynamic deescalation approach has been reported previously by Sathekge et al. (*23*). In a cohort of 17 chemotherapy-naïve patients, a fixed dose of 8 MBq of AcPSMA for the first cycle was

TABLE 2
Overview of Available Literature About AcPSMA Monotherapy or Combination Therapy

Source	Patients (*n*)	Treatment activity	Cycles (*n*)	Ligand	PSA response > 50% (%)	mOS (mo)	Previous LuPSMA (%)
(*2*)	14	50, 100, 150, or 200 kBq/kg	31 (1–4) in study	PSMA-617	44	>12	21
(*3*)	40	100 kBq/kg	3–5/patient	PSMA-617	60	>12	20
(*23*)	17	7.4 MBq	59 in study	PSMA-617	82	NR	88
(*24*)	73	8, 7, 6, or 4 MBq, with deescalation of responders	210 in study	PSMA-617	70	18	70
(*21*)	28	100 kBq/kg	85 in study	PSMA-617	39	17	54
(*20*)	11	100 kBq/kg	25 in study	PSMA-617	45	NR	46
(*7*)	20	5.3 (1.5–7.9) MBq + 6.9 (5–11.6) GBq of ^{177}Lu	1/patient	PSMA-617	65	12	100
(*31*)	73	7.8/cycle mean	34 in study	PSMA-I&T	50	NR	79
(*8*)	15	2.7 ± 1.1 MBq + 6.7 ± 1.8 GBq of ^{177}Lu	2 (1–6)/ patient	PSMA-617	29	>20 PR; 8.3 SD, PD	100
(*10*)	13	8 MBq first cycle, 6 MBq subsequent cycles	3/patient	PSMA-617	69	8.5	15.4
(*28*)	12	7.4 MBq	25 in study	PSMA-617	50	10	58
(*29*)	38	100 kBq/kg	2 (2–5)/ patient	PSMA-617	66	12	23.6
(*30*)	13	100 kBq/kg, 7.6 (6–8.5) MBq	31 in study	PSMA-I&T	14.3	10	77
(*25*)	106	8 MBq first and second cycles, 6 MBq, and 4 MBq, with deescalation of responders	4 (1–9)/ patient	PSMA-617	80.2	15	6.6
(*27*)	23	7.6 (6.2–10) MBq mean	38 in study	PSMA-617	26	7.7	100
(*22*)	56	100–150 kBq/kg	204 in study	PSMA-617	67.8	15	48.2
This work	233		536 in study	PSMA-617			
Monotherapy	104	6 MBq, with deescalation of responders			53	9	37
Combination therapy	129	4 MBq + 4 GBq of ^{177}Lu			57	14	32

NR = not reported; PR = partial remission; SD = stable disease; PD = progression of disease.
Continuous data are median and range unless indicated otherwise.

administered, with consecutive deescalation in subsequent treatment cycles to 7, 6, or 4 MBq based on response to the previous treatment cycles. Grade 1 or 2 xerostomia was observed in all patients, but none was severe enough to lead to discontinuation of treatment. The week 8 PSA and best PSA responses of more than 50% were 76% (13/17) and 88% (15/17), respectively (*23*). The mOS could not be approximated because of the short follow-up of only 1 y (*23*). In a cohort of 73 men reported by the same group, xerostomia was seen in 85% of patients but never led to discontinuing treatment; a PSA response of more than 50% was observed in 70% of the patients, and mOS was 18 mo (*24*). Our results are similar with regard to tolerability, but only 53% of patients in the AcPSMA monotherapy group achieved a PSA response of more than 50%, which is inferior to the results from South Africa. However, this could be explained by the baseline characteristics. For example, lung, liver, and brain metastases were present in 3%, 5%, and 1% of the South African patients but 13%, 22%, and 2% of our patients (monotherapy group), respectively. Only 37% of the South African patients had previously received chemotherapy, but 85% of our patients had undergone such treatment.

So far, the largest study with dynamic deescalation of responding patients has been reported by Lawal et al. (*25*). Even though 32.1% of patients in this cohort presented with a superscan, hematologic tolerability was excellent and the superscan pattern was probably protective for salivary glands. Consequently, dose deescalation was done after 2 cycles of 8 MBq of AcPSMA. These results are confirmative to our experience that AcPSMA is well suited for patients with diffuse red marrow infiltration. It also supports the thesis that the initially proposed 100 kBq/kg tolerable dose might have been overestimated by the tumor sink effect.

A recent metaanalysis presented the most common side effects from AcPSMA with grade 1 or 2 xerostomia in 63.1% (89/141) of the evaluated patients (*26*). A complete overview of the available literature about AcPSMA monotherapy or combination therapy is provided in Table 2 (*2*,*3*,*7*–*10*,*20*–*25*,*27*–*31*).

The LuPSMA VISION trial (*19*) presents the best standard of comparison to evaluate the antitumor activity of our treatment protocols. This trial recruited patients between May 2018 and August 2019; thus, these patients are not historical controls but were treated contemporaneously with our patients and consequently received nearly identical standards of care (Supplemental Table 1). The mOS of VISION patients was 15.3 mo, which is remarkably similar to our AcPSMA and LuPSMA cocktail group, with a mOS of 15 mo. Prospective phase 3 results should not be compared with less reliable real-world data; however, the number of deaths observed versus patients censored, as an important quality criterion for Kaplan–Meier statistics, is almost equal (Supplemental Table 1), and the objective parameter OS is independent of the clinical follow-up protocol used. However, some discrepancies between the patient cohorts exist. Several other experimental, off-label, or antiquated treatments had already been applied in advance of PSMA-TAT to our patients but were offered to VISION patients as additional treatment lines with potential antitumor activity not before their progression under LuPSMA trial medication (Supplemental Table 2). Bone marrow superscan was an exclusion criterion in the VISION trial but was present in a large fraction of our patients and was found to be significantly correlated with OS. In addition, 5%–16% of our patients would not have been candidates for the VISION trial because of low platelet count, and 12%–22% would not have been candidates because of low baseline hemoglobin. A recent literature review found a decreased efficacy of PSMA-TAT if patients were previously exposed to LuPSMA (*32*). However, 11% of our AcPSMA monotherapy patients and 7% of our AcPSMA and LuPSMA cocktail patients received 1 cycle and 26% of the AcPSMA monotherapy patients and 25% of the AcPSMA and LuPSMA cocktail patients received at least 2 cycles of β-PSMA–targeted radiopharmaceutical therapy before TAT. Altogether, we observed similar antitumor activity despite prognostically worse patients. This observation is in line with preclinical research comparing ^{177}Lu- and ^{225}Ac-labeled PSMA ligands, which reported a favorable absorbed dose distribution to tumor cell nuclei from PSMA-TAT, especially in micrometastases (*33*–*35*).

This evaluation has mentionable limitations. Because PSMA-TAT was offered on an individual patient basis, there was no prospective randomization, but deescalation approaches were offered as the physician's choice. AcPSMA monotherapy was preferable and chosen in cases of diffuse-type organ infiltration, and the cocktail became standard once earlier-stage patients were scheduled by the referring urologists or oncologists. Real-world data are less stringent in the documentation of adverse events than pharmacovigilance monitoring in clinical trials; hence, they could not be evaluated systematically within this work. Because the urologist or oncologist chose the long-term follow-up (imaging and tumor markers) according to medical appropriateness, we were not able to obtain reliable radiologic progression-free survival data retrospectively.

CONCLUSION

Even deescalated treatment activities of the AcPSMA regimen or the AcPSMA and LuPSMA cocktail regimen present high antitumor activity in poor-prognosis prostate cancer. Considering the prognostic factors in the respective baseline profiles, the outcomes of both treatment regimens are well in line with previous AcPSMA studies. Treatment efficacy was similar to that reported for LuPSMA despite a worse initial situation. In contrast to previous high-dose regimens, none of the responding patients discontinued treatment because of xerostomia.

DISCLOSURE

Clemens Kratochwil and Uwe Haberkorn are coinventors of PSMA-617. Clemens Kratochwil, Uwe Haberkorn, Frederik Giesel, Frank Bruchertseifer, and Alfred Morgenstern are coinventors of an actinium-PSMA patent. Frederik Giesel and Uwe Haberkorn are coinventors of PSMA-1007. Frederik Giesel worked as scientific consultant for Telix. Clemens Kratochwil worked as scientific consultant for AAA/Novartis, Roche, and AdvanCell. Clemens Kratochwil, Uwe Haberkorn, and Frederik Giesel own shares of FAPI Holding. No other potential conflict of interest relevant to this article was reported.

KEY POINTS

QUESTION: Can the treatment activity of AcPSMA be reduced to improve tolerability compared with the current standard of 100 kBq/kgBW without losing too much antitumor activity?

PERTINENT FINDINGS: Despite worse prognostic baseline characteristics, mOS and PSA response rates are equivalent to VISION in patients with advanced-stage prostate cancer. None of the two tested approaches was obviously better than the other one.

IMPLICATIONS FOR PATIENT: Reduced-dose ^{225}Ac and ^{225}Ac/^{177}Lu cocktail PSMA-617 therapies have strong antitumor activity and a tolerable trade-off of side effects.

REFERENCES

1. Kratochwil C, Bruchertseifer F, Giesel FL, et al. ^{225}Ac-PSMA-617 for PSMA-targeted alpha-radiation therapy of metastatic castration-resistant prostate cancer. *J Nucl Med.* 2016;57:1941–1944.
2. Kratochwil C, Bruchertseifer F, Rathke H, et al. Targeted alpha-therapy of metastatic castration-resistant prostate cancer with ^{225}Ac-PSMA-617: dosimetry estimate and empiric dose finding. *J Nucl Med.* 2017;58:1624–1631.
3. Kratochwil C, Bruchertseifer F, Rathke H, et al. Targeted alpha-therapy of metastatic castration-resistant prostate cancer with ^{225}Ac-PSMA-617: swimmer-plot analysis suggests efficacy regarding duration of tumor control. *J Nucl Med.* 2018;59:795–802.
4. Gafita A, Wang H, Robertson A, et al. Tumor sink effect in ^{68}Ga-PSMA-11 PET: myth or reality? *J Nucl Med.* 2022;63:226–232.
5. Tuncel M, Telli T, Tuncali MC, Karabulut E. Predictive factors of tumor sink effect: insights from ^{177}Lu-prostate-specific membrane antigen therapy. *Ann Nucl Med.* 2021;35:529–539.
6. Filss C, Heinzel A, Miiller B, Vogg ATJ, Langen KJ, Mottaghy FM. Relevant tumor sink effect in prostate cancer patients receiving ^{177}Lu-PSMA-617 radioligand therapy. *Nuklearmedizin.* 2018;57:19–25.
7. Khreish F, Ebert N, Ries M, et al. ^{225}Ac-PSMA-617/^{177}Lu-PSMA-617 tandem therapy of metastatic castration-resistant prostate cancer: pilot experience. *Eur J Nucl Med Mol Imaging.* 2020;47:721–728.
8. Rosar F, Krause J, Bartholoma M, et al. Efficacy and safety of [^{225}Ac]Ac-PSMA-617 augmented [^{177}Lu]Lu-PSMA-617 radioligand therapy in patients with highly advanced mCRPC with poor prognosis. *Pharmaceutics.* 2021;13:722.
9. Rosar F, Hau F, Bartholoma M, et al. Molecular imaging and biochemical response assessment after a single cycle of [^{225}Ac]Ac-PSMA-617/[^{177}Lu]Lu-PSMA-617 tandem therapy in mCRPC patients who have progressed on [^{177}Lu]Lu-PSMA-617 monotherapy. *Theranostics.* 2021;11:4050–4060.
10. van der Doelen MJ, Mehra N, van Oort IM, et al. Clinical outcomes and molecular profiling of advanced metastatic castration-resistant prostate cancer patients treated with ^{225}Ac-PSMA-617 targeted alpha-radiation therapy. *Urol Oncol.* 2021;39:729.e7–729.e16.
11. Privé BM, Slootbeek PHJ, Laarhuis BI, et al. Impact of DNA damage repair defects on response to PSMA radioligand therapy in metastatic castration-resistant prostate cancer. *Prostate Cancer Prostatic Dis.* 2022;25:71–78.
12. Apostolidis C, Molinet R, Rasmussen G, Morgenstern A. Production of Ac-225 from Th-229 for targeted alpha therapy. *Anal Chem.* 2005;77:6288–6291.
13. Kratochwil C, Giesel FL, Stefanova M, et al. PSMA-targeted radionuclide therapy of metastatic castration-resistant prostate cancer with ^{177}Lu-labeled PSMA-617. *J Nucl Med.* 2016;57:1170–1176.
14. Afshar-Oromieh A, Haberkorn U, Zechmann C, et al. Repeated PSMA-targeting radioligand therapy of metastatic prostate cancer with ^{131}I-MIP-1095. *Eur J Nucl Med Mol Imaging.* 2017;44:950–959.
15. Rathke H, Flechsig P, Mier W, et al. Dosimetry estimate and initial clinical experience with ^{90}Y-PSMA-617. *J Nucl Med.* 2019;60:806–811.
16. Kratochwil C, Giesel FL, Eder M, et al. [^{177}Lu]Lutetium-labelled PSMA ligand-induced remission in a patient with metastatic prostate cancer. *Eur J Nucl Med Mol Imaging.* 2015;42:987–988.
17. Rathke H, Giesel FL, Flechsig P, et al. Repeated ^{177}Lu-labeled PSMA-617 radioligand therapy using treatment activities of up to 9.3 GBq. *J Nucl Med.* 2018;59:459–465.
18. Kratochwil C, Apostolidis L, Rathke H, et al. Dosing ^{225}Ac-DOTATOC in patients with somatostatin-receptor-positive solid tumors: 5-year follow-up of hematological and renal toxicity. *Eur J Nucl Med Mol Imaging.* 2021;49:54–63.
19. Sartor O, de Bono J, Chi KN, et al. Lutetium-177-PSMA-617 for metastatic castration-resistant prostate cancer. *N Engl J Med.* 2021;385:1091–1103.
20. Satapathy S, Mittal BR, Sood A, et al. Health-related quality-of-life outcomes with actinium-225-prostate-specific membrane antigen-617 therapy in patients with heavily pretreated metastatic castration-resistant prostate cancer. *Indian J Nucl Med.* 2020;35:299–304.
21. Yadav MP, Ballal S, Sahoo RK, Tripathi M, Seth A, Bal C. Efficacy and safety of ^{225}Ac-PSMA-617 targeted alpha therapy in metastatic castration-resistant prostate cancer patients. *Theranostics.* 2020;10:9364–9377.
22. Ballal S, Yadav MP, Satapathy S, et al. Long-term survival outcomes of salvage [^{225}Ac]Ac-PSMA-617 targeted alpha therapy in patients with PSMA-expressing end-stage metastatic castration-resistant prostate cancer: a real-world study. *Eur J Nucl Med Mol Imaging.* 2023;50:3777–3789.
23. Sathekge M, Bruchertseifer F, Knoesen O, et al. ^{225}Ac-PSMA-617 in chemotherapy-naive patients with advanced prostate cancer: a pilot study. *Eur J Nucl Med Mol Imaging.* 2019;46:129–138.
24. Sathekge M, Bruchertseifer F, Vorster M, et al. Predictors of overall and disease-free survival in metastatic castration-resistant prostate cancer patients receiving ^{225}Ac-PSMA-617 radioligand therapy. *J Nucl Med.* 2020;61:62–69.
25. Lawal IO, Morgenstern A, Vorster M, et al. Hematologic toxicity profile and efficacy of [^{225}Ac]Ac-PSMA-617 alpha-radioligand therapy of patients with extensive skeletal metastases of castration-resistant prostate cancer. *Eur J Nucl Med Mol Imaging.* 2022;49:3581–3592.
26. Ballal S, Yadav MP, Sahoo RK, Tripathi M, Dwivedi SN, Bal C. ^{225}Ac-PSMA-617-targeted alpha therapy for the treatment of metastatic castration-resistant prostate cancer: a systematic review and meta-analysis. *Prostate.* 2021;81:580–591.
27. Alan-Selcuk N, Beydagi G, Demirci E, et al. Clinical experience with [^{225}Ac]Ac-PSMA treatment in patients with [^{177}Lu]Lu-PSMA-refractory metastatic castration-resistant prostate cancer. *J Nucl Med.* 2023;64:1574–1580.
28. Sanli Y, Kuyumcu S, Simsek DH, et al. ^{225}Ac-prostate-specific membrane antigen therapy for castration-resistant prostate cancer: a single-center experience. *Clin Nucl Med.* 2021;46:943–951.
29. Sen I, Thakral P, Tiwari P, et al. Therapeutic efficacy of ^{225}Ac-PSMA-617 targeted alpha therapy in patients of metastatic castrate resistant prostate cancer after taxane-based chemotherapy. *Ann Nucl Med.* 2021;35:794–810.
30. Unterrainer LM, Beyer L, Zacherl MJ, et al. Total tumor volume on ^{18}F-PSMA-1007 PET as additional imaging biomarker in mCRPC patients undergoing PSMA-targeted alpha therapy with ^{225}Ac-PSMA-I&T. *Biomedicines.* 2022;10:946.
31. Zacherl MJ, Gildehaus FJ, Mittlmeier L, et al. First clinical results for PSMA-targeted alpha-therapy using ^{225}Ac-PSMA-I&T in advanced-mCRPC patients. *J Nucl Med.* 2021;62:669–674.
32. Stangl-Kremser J, Ricaurte-Fajardo A, Subramanian K, et al. Response to RL-^{225}Ac in prostate cancer: effect of prior treatment with RL-^{177}Lu—a systematic review of the literature. *Prostate.* 2023;83:901–911.
33. Lee H. Relative efficacy of ^{225}Ac-PSMA-617 and ^{177}Lu-PSMA-617 in prostate cancer based on subcellular dosimetry. *Mol Imaging Radionucl Ther.* 2022;31:1–6.
34. Ruigrok EAM, Tamborino G, de Blois E, et al. In vitro dose effect relationships of actinium-225- and lutetium-177-labeled PSMA-I&T. *Eur J Nucl Med Mol Imaging.* 2022;49:3627–3638.
35. Nava-Cabrera M, Azorin-Vega E, Oros-Pantoja R, Aranda-Lara L. Comparison between ^{177}Lu-iPSMA and ^{225}Ac-iPSMA dosimetry at a cellular level in an animal bone metastasis model. *Appl Radiat Isot.* 2021;176:109898.

Assessing Response to PSMA Radiopharmaceutical Therapies with Single SPECT Imaging at 24 Hours After Injection

Surekha Yadav[1], Fei Jiang[2], Sara Kurkowska[3,4], Rachelle Saelee[1], Amanda Morley[1], Felix Feng[5], Rahul Aggarwal[6], Courtney Lawhn-Heath[1], Carlos Uribe[3,7,8], and Thomas A. Hope[1,9,10]

[1]Department of Radiology and Biomedical Imaging, University of California San Francisco, San Francisco, California; [2]Department of Epidemiology and Biostatistics, University of California San Francisco, San Francisco, California; [3]Department of Integrative Oncology, BC Cancer Research Institute, Vancouver, British Columbia, Canada; [4]Department of Nuclear Medicine, Pomeranian Medical University, Szczecin, Poland; [5]Department of Radiation Oncology, University of California San Francisco, San Francisco, California; [6]Division of Hematology/Oncology, Department of Medicine, University of California San Francisco, San Francisco, California; [7]Department of Radiology, University of British Columbia, Vancouver, British Columbia, Canada; [8]Department of Molecular Imaging and Therapy, BC Cancer, Vancouver, British Columbia, Canada; [9]Department of Radiology, San Francisco VA Medical Center, San Francisco, California; and [10]Helen Diller Family Comprehensive Cancer Center, University of California San Francisco, San Francisco, California

Understanding the relationship between lesion-absorbed dose and tumor response in ^{177}Lu-PSMA-617 radiopharmaceutical therapies (RPTs) remains complex. We aimed to investigate whether baseline lesion-absorbed dose can predict lesion-based responses and to explore the connection between lesion-absorbed dose and prostate-specific antigen (PSA) response. **Methods:** In this retrospective study, we evaluated 50 patients with 335 index lesions undergoing ^{177}Lu-PSMA-617 RPT, who had dosimetry analysis performed on SPECT/CT at 24 h after cycles 1 and 2. First, we identified the index lesions for each patient and measured the lesion-based absorbed doses. Lesion-based response was calculated after cycle 2. Additionally, PSA50 response (a decline of 50% from baseline PSA) after cycle 2 was also calculated. The respective responses for mean and maximum absorbed doses and prostate-specific membrane antigen (PSMA) volumetric intensity product (VIP-PSMA) at cycles 1 and 2 were termed $SPECT_{mean}$, $SPECT_{maximum}$, and $SPECT_{VIP\text{-}PSMA}$, respectively. **Results:** Of the 50 patients reviewed, 46% achieved a PSA50 response after cycle 2. Of the 335 index lesions, 58% were osseous, 32% were lymph nodes, and 10% were soft-tissue metastatic lesions. The SPECT lesion-based responses were higher in PSA responders than in nonresponders ($SPECT_{mean}$ response of 46.8% ± 26.1% vs. 26.2% ± 24.5%, $P = 0.007$; $SPECT_{maximum}$ response of 45% ± 25.1% vs. 19% ± 27.0%, $P = 0.001$; $SPECT_{VIP\text{-}PSMA}$ response of 49.2% ± 30.3% vs. 14% ± 34.7%, $P = 0.0005$). An association was observed between PSA response and $SPECT_{VIP\text{-}PSMA}$ response ($R^2 = 0.40$ and $P < 0.0001$). A limited relationship was found between baseline absorbed dose measured with a 24-h single time point and SPECT lesion-based response ($R^2 = 0.05$, $P = 0.001$, and $R^2 = 0.03$, $P = 0.007$, for mean and maximum absorbed doses, respectively). **Conclusion:** In this retrospective study, quantitative lesion-based response correlated with patient-level PSA response. We observed a limited relationship between baseline absorbed dose and lesion-based responses. Most of the variance in response remains unexplained solely by baseline absorbed dose. Establishment of a dose–response relationship in RPT with a single time point at 24 h presented some limitations.

Key Words: SPECT/CT; dosimetry; prostate cancer; radiopharmaceutical therapy; response to RPT; theranostics

J Nucl Med 2024; 65:1064–1069
DOI: 10.2967/jnumed.123.267208

The relationship between lesion-absorbed dose and tumor response for radiopharmaceutical therapies (RPTs) is not well understood. As RPT fundamentally involves radiation delivery, knowledge of the absorbed dose versus the tumor response in external-beam radiotherapy serves as a useful starting point for evaluating this relationship for RPT. Dose–response relationships have been described in external-beam radiotherapy, aiding in predicting tumor response and potential tissue toxicity (*1–3*). Moreover, lesion dosimetry has been shown to optimize dose delivery for various cancers, playing a crucial role in treatment outcomes (*4–10*).

Unlike external-beam radiotherapy, where we have the ability to control and modify the absorbed dose to normal tissues and tumors, nonuniform dose delivery in systemic RPT renders the understanding of dose–response relationship considerably more challenging (*11–13*). There are preliminary data on dose response with ^{177}Lu-DOTATATE in pancreatic neuroendocrine tumors, demonstrating correlation between tumor-absorbed dose and tumor size reduction (*14*). The same group was, however, not able to establish a dose–response relationship in small-bowel neuroendocrine tumors (*15*). Most recently, in patients with gastroenteropancreatic neuroendocrine tumors who underwent ^{177}Lu-DOTATATE therapy, a study demonstrated that the tumor-absorbed dose was associated with radiologic response but not with overall survival (*16*).

Prostate-specific membrane antigen (PSMA)–targeting RPT using ^{177}Lu-PSMA-617 has demonstrated favorable prostate-specific antigen (PSA) response rates and longer progression-free survival and overall survival in patients with metastatic castration-resistant prostate cancer (*17*,*18*). Violet et al. performed whole-body tumor dosimetry and showed a correlation between absorbed tumor doses and PSA response after ^{177}Lu-PSMA-617 RPT at 12 wk (*19*). Another study looking into index lesion–based dosimetry

Received Dec. 7, 2023; revision accepted Apr. 8, 2024.
For correspondence or reprints, contact Thomas A. Hope (thomas.hope@ucsf.edu).
Published online May 9, 2024.

did not find a significant difference in mean absorbed dose and index lesion dose between PSA responders and nonresponders (*20*).

Overall, the relationship between lesion-absorbed dose and response in PSMA RPT remains unknown. Therefore, we aimed to analyze whether baseline lesion-absorbed dose, calculated with a single time point measured at 24 h, predicts lesion-based response in patients treated with ^{177}Lu-PSMA-617 RPT. Additionally, we analyzed the relationship between response based on lesion-absorbed dose and PSA response.

MATERIALS AND METHODS

Study Population

We conducted a retrospective review of patients with metastatic castration-resistant prostate cancer who received ^{177}Lu-PSMA-617 RPT between June 2022 and January 2023 at our institution. All patients who received a minimum of 2 cycles, with a treatment interval of 6–8 wk, and 24-h posttherapy SPECT/CT were included. The institutional review board approved this retrospective study, and the requirement to obtain informed consent was waived.

Posttherapy Scan Acquisition

Whole-body planar and SPECT/CT imaging were performed 1 d after each cycle in the context of routine clinical care using a dual-head γ-camera (Infinia Hawkeye; GE Healthcare) with the following acquisition parameters: 208% ± 10% keV photopeak, 170% ± 10% keV scatter window, 128 × 128 matrix, 20–30 s per projection, 60 projections in total using 2 detectors, medium-energy general-purpose collimators, and a low-dose CT scan for attenuation correction.

Lesion Selection

For each patient, lesions in each of 3 regions were included: lymph node, osseous, and soft tissue (e.g., liver, lung or adrenals). We included the highest- and lowest-expressing lesion based on visual assessment within each region, and the 3 largest remaining lesions, for up to a total of 5 lesions per region. To be included, soft-tissue lesions had to measure more than 10 mm along the long axis and lymph nodes had to measure more than 15 mm along the short axis on the CT component of the SPECT/CT scan. Osseous lesions had to measure more than 2 cm^3 in SPECT-segmented volume in order minimize the effect of partial-volume averaging (*21–24*). For liver and lung lesions, individual lesions were segmented individually, although if confluent, adjacent lesions were grouped.

Absorbed Dose Calculation

MIM SPECTRA Quant (MIM Software) was used for image reconstruction with an iterative ordered-subset expectation-maximization algorithm using 4 iterations and 10 subsets. Scatter correction, attenuation correction, and resolution recovery were applied (*25*). The kidneys were segmented using the autocontouring software from MIM with manual adjustment to region of interest as required. Quantitative dosimetry measurements were performed on the index lesions and kidneys at cycles 1 and 2. Lesion-based segmentation was done by a nuclear medicine physician using a standardized semiautomated workflow using SurePlan MRT (MIM software), which applies a single imaging time point for biokinetic evaluation based on the Hänscheid approach and performs dosimetry using voxel-based absorbed dose calculation using voxel S-value (*26*,*27*). To determine mean and maximum absorbed doses in grays, we performed segmentation on the dose map using a 42% threshold of the maximum (*26*,*28*). Additionally, similar to tumor lesion glycolysis and volumetric intensity product (VIP) used previously (*16*,*29*), we calculated the VIP-PSMA by multiplying the tumor volume and mean absorbed dose of the index lesions, excluding the least avid lesion.

Lesion-Based Response Evaluation

Mean and maximum absorbed doses and VIP-PSMA at cycles 1 and 2 were compared and their respective responses (termed $SPECT_{mean}$, $SPECT_{maximum}$, and $SPECT_{VIP\text{-}PSMA}$, respectively) were calculated using the following formula:

$$\text{Response} = 1 - \frac{\text{absorbed dose (cycle 1)} - \text{absorbed dose (cycle 2)}}{\text{absorbed dose (cycle 1)}}.$$

Biochemical Response Evaluation

Serum PSA levels served as the standard of reference for response assessment to therapy (*30*,*31*). Serum PSA from the day of the first cycle and 3 wk after the second cycle was used to calculate PSA response. A decline of 50% from baseline PSA was defined as a PSA50 response, and accordingly, patients were categorized as responders or nonresponders.

Radiographic Response Evaluation

Radiographic response was evaluated on the CT component of SPECT/CT scans for both cycle 1 and cycle 2. For lymph nodes, the maximum of the small-axis diameter was measured, whereas for other soft-tissue lesions, the maximum of the long-axis diameter was measured. Although lesion-level analysis was being performed, the relative change in the lesion size was calculated using the following equation, where D1 represents the lesion diameter at cycle 1 and D2 corresponds to the diameter at cycle 2:

$$\text{Response} = \frac{D1 - D2}{D1} \times 100.$$

Statistical Analysis

Descriptive statistics in the form of median with interquartile range and mean with SD for continuous variables and count with percentage for binary variables were used to describe quantitative variables from the clinical data. Lesion-level data were averaged for each patient to obtain patient-level data, and results were expressed as mean with SD. A Student *t* test was conducted to assess the relationship between lesion-based response and PSA response between responders and nonresponders. We used a linear regression model for patient-level analysis to assess the association between various predictors (baseline mean and maximum absorbed dose and VIP-PSMA) and PSA response. We used a linear mixed model for lesion-level analysis to explore the association between different parameters of absorbed dose and lesion-based response while considering that the data from the same subject share the same random component. Of the 5 lesions segmented for each patient, 4 lesions excluding the least avid lesions were termed index lesions and were analyzed collectively. The results for the least avid index lesions were analyzed separately. Because of lack of an established framework for SPECT lesion-based response, we extrapolated from the 30% decrease used in PERCIST and RECIP (*32*,*33*). A *P* value of less than 0.05 was considered significant.

RESULTS

Patient Characteristics

Fifty-seven sequential patients with metastatic castration-resistant prostate cancer received ^{177}Lu-PSMA RPT from June 2022 to January 2023. Seven patients did not meet the inclusion criteria. A patient flowchart and the demographic data are provided in Table 1 and Supplemental Figure 1. Of the 50 patients analyzed, 23 (46%) achieved a PSA50 response after cycle 2. Of the 335 index lesions analyzed, 58% (194) were osseous, 32% (107) were lymph nodes, and 10% (34) were soft-tissue lesions. Two patients were low PSA secretors and were excluded from the PSA response analysis. At the patient level, the average of the mean absorbed dose at cycle 1 was 7.5 ± 6.2 Gy. At the lesion

TABLE 1
Patient Demographics and Dosimetry Data

Parameter	Data
Total patients (*n*)	50
Age, median	72 (IQR, 67.2–78.7)
Gleason grade group,* median	5 (IQR, 4–5)
Prior treatments (*n*)	
ADT	50 (100%)
ARTT	50 (100%)
Chemotherapy	50 (100%)
Radical prostatectomy	18 (36%)
Radiation therapy	50 (100%)
Serum PSA before cycle 1, median	107.3 (IQR, 22.5–331.7)
Serum PSA after cycle 2, median	55.7 (IQR, 6.9–262.2)
Cycle 1, mean	
Administered activity (GBq)	7.1 (SD, 6.9–7.4)
Mean absorbed dose to index lesions (Gy)	7.54 (SD, 6.87)
Maximum absorbed dose to index lesions (Gy)	14.6 (SD, 14.8)
Mean absorbed dose to kidneys (Gy)	1.1 (SD, 0.2)
Cycle 2, mean	
Administered activity (GBq)	7.2 (SD, 7.1–7.4)
Mean absorbed dose to index lesions (Gy)	4.7 (SD, 5.1)
Maximum absorbed dose to index lesions (Gy)	9.8 (SD, 13.0)
Mean absorbed dose to kidneys (Gy)	1.1 (SD, 0.5)
Timing of posttreatment SPECT in relation to ^{177}Lu-PSMA RPT, median (h)	
Cycle 1	23. 9 (IQR, 21.3–25.9)
Cycle 2	24.6 (IQR, 21.3–26.2)

*Gleason grade – 4 = Gleason score (3 + 5); 5 = (4 + 4).
IQR = interquartile range; ADT = adrogen deprivation therapy; ARTT = androgen receptor–targeted therapy.

level, the average of the mean absorbed dose at cycle 1 was 6.7 ± 6.6 Gy (Fig. 1). The mean absorbed dose to kidneys during cycles 1 and 2 was 1.1 ± 0.2 Gy and 1.1 ± 0.5 Gy, respectively (Table 1).

Lesion-Based Response and PSA Response

The $SPECT_{mean}$ response from cycle 1 to cycle 2 was 46.8% ± 26.1% for responders and 26.2% ± 24.5% for nonresponders (P = 0.007). The $SPECT_{maximum}$ response from cycle 1 to cycle 2

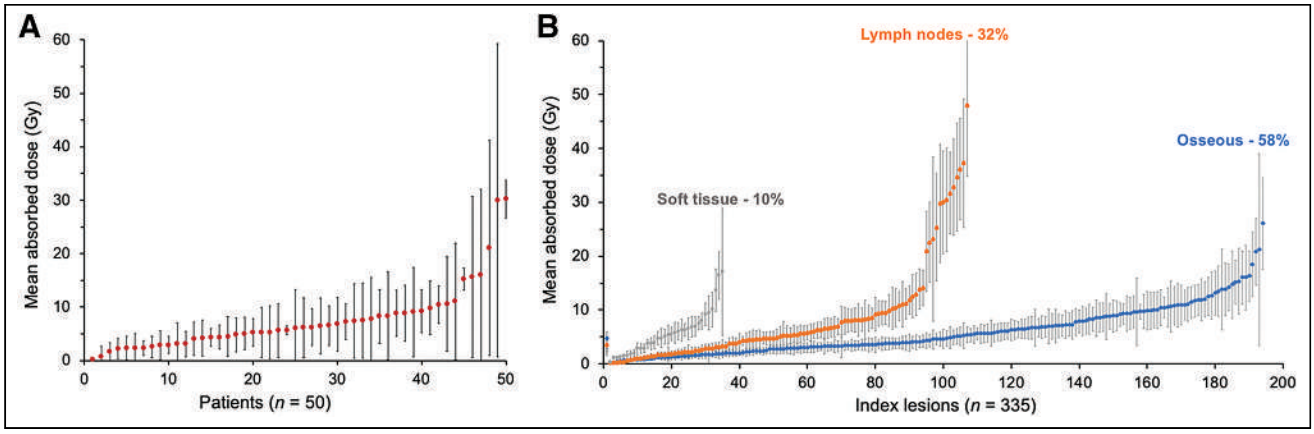

FIGURE 1. Scatterplots showing distribution of lesion-absorbed doses at cycle 1. (A) Mean of lesion mean absorbed dose within each individual patient, with whiskers representing SD. (B) Mean absorbed dose for each individual index lesion, with whiskers representing SD of dose within individual lesion.

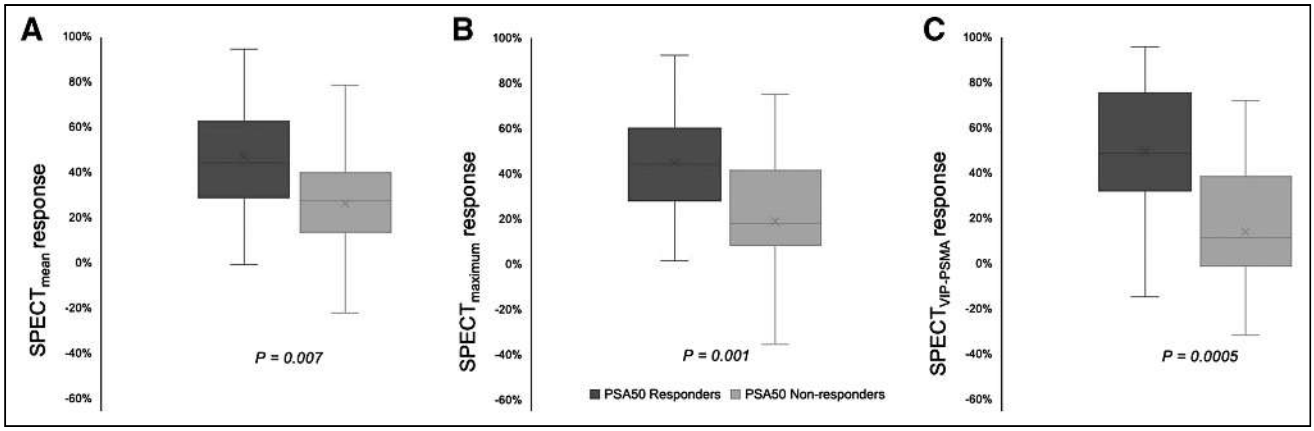

FIGURE 2. $SPECT_{mean}$ response (A), $SPECT_{maximum}$ response (B), and $SPECT_{VIP\text{-}PSMA}$ response (C) in PSA50 responders and nonresponders. Box plots display median and first and third quartiles. One outlier was observed at −100% for $SPECT_{VIP\text{-}PSMA}$ response.

was 45% ± 25.1% for responders and 19% ± 27.0% for nonresponders ($P = 0.001$). The $SPECT_{VIP\text{-}PSMA}$ response from cycle 1 to cycle 2 was 49.2% ± 30.3% for responders and 14% ± 34.7% for nonresponders ($P = 0.0005$, Fig. 2). There was an association between PSA response and $SPECT_{VIP\text{-}PSMA}$ response for the index lesions and for the single most avid lesion ($R^2 = 0.40$ and $P < 0.0001$ for index lesions and $R^2 = 0.35$ and $P < 0.0001$ for the single most avid lesion, respectively).

Lesion-Level Radiographic Response and SPECT-Based Response

For the lymph nodes, there was an association between radiographic response and SPECT-based response for the index lesions ($R^2 = 0.58$ and $P < 0.0001$ for $SPECT_{mean}$ response, $R^2 = 0.67$ and $P < 0.0001$ for $SPECT_{maximum}$ response, and $R^2 = 0.42$ and $P < 0.0001$ for $SPECT_{VIP\text{-}PSMA}$ response). For the soft tissues, among all the parameters, $SPECT_{VIP\text{-}PSMA}$ response for the index lesions had an association with the radiographic response ($R^2 = 0.34$ and $P < 0.005$). Additionally, for both the soft tissues and the lymph nodes, no association was observed between the baseline lesion-absorbed dose and the lesion-level radiographic response.

Baseline Lesion-Absorbed Dose and PSA Response

The mean lesion-absorbed dose at cycle 1 was 8.1 ± 6.7 Gy for responders and 7.3 ± 5.9 Gy for nonresponders ($P = 0.7$). The maximum lesion-absorbed dose during cycle 1 was 15.8 ± 13.0 Gy for responders and 14.0 ± 11.8 Gy for nonresponders ($P = 0.6$). The VIP-PSMA during cycle 1 was 104.9 ± 238.0 for responders and 61.0 ± 74.6 for nonresponders ($P = 0.3$). No association was observed between the baseline lesion-absorbed dose and PSA response (Supplemental Table 1).

Baseline Lesion-Absorbed Dose and Lesion-Based Response

With the 30% reduction response criterion, the mean absorbed dose during cycle 1 was 7.7 ± 8.3 Gy in responders ($n = 30$) and 7.3 ± 4.6 Gy in nonresponders ($n = 20$) ($P = 0.8$). The maximum absorbed dose during cycle 1 was 14.9 ± 10.6 Gy in responders and 14.1 ± 13.8 Gy in nonresponders ($P = 0.8$). The VIP-PSMA during cycle 1 was 113.4 ± 240.0 in responders and 59.1 ± 72.7 in nonresponders ($P = 0.2$). With a linear mixed-effects model at the lesion level, there was a minimal relationship between baseline absorbed dose and lesion-based response ($R^2 = 0.05$, $P = 0.001$, for mean absorbed dose and $SPECT_{mean}$ response; $R^2 = 0.03$, $P = 0.007$, for maximum absorbed dose and $SPECT_{maximum}$ response; Supplemental Table 1).

Location of Disease and Response

Lymph nodes had a higher mean absorbed dose than did osseous metastases during cycle 1 (8.3 Gy ± 9.4 Gy and 5.9 ± 4.5 Gy, respectively, $P = 0.001$). However, no significant difference was noted in the lesion-based response between lymph nodes and osseous metastases ($SPECT_{mean}$ response of 36.9% vs. 33.7%, $P > 0.05$). The mean absorbed dose during cycle 1 was the lowest for soft-tissue metastases (5.6 ± 4.1 Gy), and there was no significant difference between the lesion-based response in soft-tissue metastases and in the other 2 metastatic sites ($SPECT_{mean}$ response of 39%, $P > 0.05$, Supplemental Table 2).

Least Avid Lesions

There were 81 least avid lesions included. Although the mean absorbed dose during cycle 1 was significantly lower in the least avid lesions (3.68 ± 4.2 Gy, $P < 0.001$), there was no significant difference in lesion-based response between the least avid and other index lesions ($SPECT_{mean}$ of 30% vs. 36.5%, $P > 0.05$).

DISCUSSION

Our results suggest that patients with a PSA50 after 2 RPT cycles showed a significantly better SPECT/CT lesion-based response than did nonresponders. For the index lesions, neither the lesion-based response nor the PSA response strongly correlated with the baseline absorbed dose obtained using single SPECT imaging at 24 h.

In routine clinical practice, it is common to perform 24-h ^{177}Lu SPECT/CT scans because of their practicality. Since these were the only quantitative data available, we performed single-time-point dosimetry using the Hänscheid method despite its not being the optimal time point for dosimetric analysis as indicated by existing literature (*27*,*34*–*36*). The Hänscheid method, particularly when applied at the 24-h time point, underestimates absorbed doses to both the kidneys and the tumors (*35*–*37*). Consequently, our computed absorbed doses were comparatively lower than those reported in the literature (*19*,*20*). Although the reported doses are underestimated, the relative dose across patients and between patients at cycles 1 and 2 are reflective of the effect of the absorbed dose.

We did not observe a relationship between baseline lesion-absorbed dose and PSA response. Note that we looked at only 5 index lesions and not the total tumor burden. Violet et al. found higher whole-body tumor doses in patients with a PSA50, but index lesion dose did not correlate with PSA50 (*19*). Of note, they compared index lesion–absorbed dose with patient-level response

and not with individual lesion-level response. Similarly, our results did not show a relationship between baseline lesion-absorbed dose and PSA response. Völter et al. also failed to demonstrate a relationship between index lesion–absorbed dose and PSA response (*20*). Conversely, a study investigating RPT in patients with low-volume hormone-sensitive metastatic prostate cancer found a statistically significant correlation between the absorbed dose to the index lesion and PSA response, although in only 10 patients (*38*). We also observed an absorbed dose to the kidneys that would result in a lower absorbed dose than the 23 Gy to the kidneys extrapolated from external-beam radiation therapy. It could be that the lack of a dose–response relationship seen in our cohort is because the absorbed doses do not yet meet a threshold for tumor response; that is, we may be currently underdosing patients. Studies in the future that escalate the administered activity on the basis of the limits of target organs may result in more robust dose–response relationship. Dose escalation studies aiming to reach toxicity levels may establish a dose–response relationship in RPTs that has not yet been demonstrated in the literature.

Although we found a statistically significant relationship between baseline mean and maximum absorbed dose and their respective $SPECT_{mean}$ and $SPECT_{maximum}$ responses, the baseline absorbed dose is not sufficient to explain the variation in SPECT lesion-based response, suggesting that additional variables such as the tumor microenvironment should also be taken into account. Larger solid tumors with necrotic cores might have larger doses deposited in the necrotic region and would require a higher dose in the periphery (*39*). The tumor microenvironment, particularly the cancer-associated fibroblasts and the secretory factors, contribute to radiation resistance through signaling and immune modulation (*40*). Lastly, intrinsic radiation sensitivity is influenced by DNA repair, apoptosis, cellular proliferation, and hypoxia (*41–43*). Factors affecting tumor-absorbed dose and response in RPT are not fully understood, and ongoing analyses are aimed at shedding light on these aspects (*44*,*45*).

A recent study showed that 41.4% of the interviewed physicians made decisions to discontinue RPT based on clinical progression alone, signifying that the optimal measure for response assessment in RPT is still unclear (*46*). PSA as an early marker of response is not always accurate. Assessing measurable disease in radiographic response assessment on CT is hindered by bone metastases (*47*,*48*). PSMA PET–based parameters have been suggested (*33*,*49*,*50*), but their clinical implementation has yet to be seen.

Our results suggest that the $SPECT_{mean}$, $SPECT_{maximum}$, and $SPECT_{VIP\text{-}PSMA}$ responses were significantly higher in PSA responders than nonresponders. A 40% association between $SPECT_{VIP\text{-}PSMA}$ response and PSA response was noted in our study, whereas this association was less than 10% for baseline absorbed dose and lesion-based response. Additionally, we also demonstrated that $SPECT_{VIP\text{-}PSMA}$ response correlated with radiographic response for lymph nodes and soft-tissue metastases. Although baseline absorbed dose did not correlate with subsequent response, the relative change in the absorbed dose over cycles does match PSA and radiographic response well. The change in dose over cycles likely indicates the radiation sensitivity of the tumor. In parallel with our quantitative lesion-based dosimetric analysis, John et al. pursued a qualitative approach to assess response to RPT using SPECT/CT imaging assessment (*51*). SPECT/CT-based analysis, in terms of both qualitative and quantitative parameters, is an efficient and practical tool for response assessment to RPT.

One of the main limitations of this study is the use of single-time-point dosimetry at 24 h using the Hänscheid method. More accurate dosimetry with multiple time points or later time points may be helpful to understand the relationship between dose and response. Moreover, tumors usually present uptake and washout phases (i.e., a biexponential behavior) that is not correctly modeled by the Hänscheid simplification (*27*).

There are other limitations to our study as well. First, we did not perform radiographic or PSMA PET–based response evaluation to assess the dose–response relationship. Second, we did not perform whole-body tumor dosimetry analysis, which may have yielded different results; however, our goal was to understand relationships between dose and response at the lesion level. Third, the impact of additional treatment cycles and cumulative activity on the PSA outcomes for our patient group remains unclear because we focused on response with the first 2 cycles.

CONCLUSION

Establishing dose–response relationship in RPT remains challenging. Quantitative dosimetry lesion-based analysis of SPECT/CT imaging at cycles 1 and 2 of RPT predicted a better lesion-based response in PSA responders. Patient with higher lesion-based responses on cycle 2 dosimetry had a higher chance of PSA response. Although we observed a significant relationship between baseline absorbed dose and lesion-based responses, most of the variance in response remains unexplained by baseline absorbed dose alone. Lesion-based response on SPECT/CT in combination with PSA response may serve as an early response marker to ^{177}Lu-PSMA RPT.

DISCLOSURE

Thomas Hope has grant funding to the institution from Clovis Oncology, GE Healthcare, Lantheus, Janssen, the Prostate Cancer Foundation, Telix Pharmaceuticals, and the National Cancer Institute (R01CA235741 and R01CA212148). He received personal fees from Bayer, Cardinal Health, BlueEarth Diagnostics, and Lantheus and received fees from and has an equity interest in RayzeBio and Curium. No other potential conflict of interest relevant to this article was reported.

KEY POINTS

QUESTION: What is the relationship between baseline lesion-absorbed dose and lesion-based response in ^{177}Lu-PSMA-617 RPT, and how does this correlate with PSA response?

PERTINENT FINDINGS: PSA50 responders exhibited a significantly better lesion-based response on SPECT/CT after cycle 2 than did nonresponders. Although there was a relationship between baseline absorbed dose and lesion-based response, most of the variance cannot be attributed solely to baseline absorbed dose.

IMPLICATIONS FOR PATIENT CARE: Incorporating lesion-based response evaluation on SPECT/CT imaging with PSA response may be a valuable early response marker for ^{177}Lu-PSMA RPT.

REFERENCES

1. MacDougall ND, Graveling M, Hansen VN, Brownsword K, Morgan A. In vivo dosimetry in UK external beam radiotherapy: current and future usage. *Br J Radiol.* 2017;90:20160915.

2. Marks LB, Yorke ED, Jackson A, et al. Use of normal tissue complication probability models in the clinic. *Int J Radiat Oncol Biol Phys.* 2010;76(suppl):S10–S19.
3. Mijnheer B, Beddar S, Izewska J, Reft C. In vivo dosimetry in external beam radiotherapy: in vivo dosimetry in external beam radiotherapy. *Med Phys.* 2013;40:070903.
4. Wang S-L, Fang H, Hu C, et al. Hypofractionated versus conventional fractionated radiotherapy after breast-conserving surgery in the modern treatment era: a multicenter, randomized controlled trial from China. *J Clin Oncol.* 2020;38:3604–3614.
5. Emami B, Purdy JA, Manolis J, et al. Three-dimensional treatment planning for lung cancer. *Int J Radiat Oncol Biol Phys.* 1991;21:217–227.
6. Offersen BV, Alsner J, Nielsen HM, et al. Hypofractionated versus standard fractionated radiotherapy in patients with early breast cancer or ductal carcinoma in situ in a randomized phase III trial: the DBCG HYPO trial. *J Clin Oncol.* 2020;38: 3615–3625.
7. Nichols AC, Theurer J, Prisman E, et al. Radiotherapy versus transoral robotic surgery and neck dissection for oropharyngeal squamous cell carcinoma (ORATOR): an open-label, phase 2, randomised trial. *Lancet Oncol.* 2019;20:1349–1359.
8. Kim TH, Koh YH, Kim BH, et al. Proton beam radiotherapy vs. radiofrequency ablation for recurrent hepatocellular carcinoma: a randomized phase III trial. *J Hepatol.* 2021;74:603–612.
9. Palma DA, Olson R, Harrow S, et al. Stereotactic ablative radiotherapy versus standard of care palliative treatment in patients with oligometastatic cancers (SABR-COMET): a randomised, phase 2, open-label trial. *Lancet.* 2019;393:2051–2058.
10. Brady JL, Binkley MS, Hajj C, et al. Definitive radiotherapy for localized follicular lymphoma staged by ^{18}F-FDG PET-CT: a collaborative study by ILROG. *Blood.* 2019;133:237–245.
11. Wahl RL, Sgouros G, Iravani A, et al. Normal-tissue tolerance to radiopharmaceutical therapies, the knowns and the unknowns. *J Nucl Med.* 2021;62(suppl 3):23S–35S.
12. Sgouros G, Dewaraja YK, Escorcia F, et al. Tumor response to radiopharmaceutical therapies: the knowns and the unknowns. *J Nucl Med.* 2021;62(suppl 3): 12S–22S.
13. Strigari L, Konijnenberg M, Chiesa C, et al. The evidence base for the use of internal dosimetry in the clinical practice of molecular radiotherapy. *Eur J Nucl Med Mol Imaging.* 2014;41:1976–1988.
14. Ilan E, Sandström M, Wassberg C, et al. Dose response of pancreatic neuroendocrine tumors treated with peptide receptor radionuclide therapy using ^{177}Lu-DOTATATE. *J Nucl Med.* 2015;56:177–182.
15. Jahn U, Ilan E, Sandström M, Garske-Román U, Lubberink M, Sundin A. ^{177}Lu-DOTATATE peptide receptor radionuclide therapy: dose response in small intestinal neuroendocrine tumors. *Neuroendocrinology.* 2020;110:662–670.
16. Alipour R, Jackson P, Bressel M, et al. The relationship between tumour dosimetry, response, and overall survival in patients with unresectable neuroendocrine neoplasms (NEN) treated with ^{177}Lu DOTATATE (LuTate). *Eur J Nucl Med Mol Imaging.* 2023;50:2997–3010.
17. Hofman MS, Emmett L, Sandhu S, et al. [^{177}Lu]Lu-PSMA-617 versus cabazitaxel in patients with metastatic castration-resistant prostate cancer (TheraP): a randomised, open-label, phase 2 trial. *Lancet.* 2021;397:797–804.
18. Sartor O, De Bono J, Chi KN, et al. Lutetium-177–PSMA-617 for metastatic castration-resistant prostate cancer. *N Engl J Med.* 2021;385:1091–1103.
19. Violet J, Jackson P, Ferdinandus J, et al. Dosimetry of ^{177}Lu-PSMA-617 in metastatic castration-resistant prostate cancer: correlations between pretherapeutic imaging and whole-body tumor dosimetry with treatment outcomes. *J Nucl Med.* 2019;60:517–523.
20. Völter F, Mittlmeier L, Gosewisch A, et al. Correlation of an index-lesion-based SPECT dosimetry method with mean tumor dose and clinical outcome after ^{177}Lu-PSMA-617 radioligand therapy. *Diagnostics (Basel).* 2021;11:428.
21. Del Prete M, Buteau F-A, Arsenault F, et al. Personalized ^{177}Lu-octreotate peptide receptor radionuclide therapy of neuroendocrine tumours: initial results from the P-PRRT trial. *Eur J Nucl Med Mol Imaging.* 2019;46:728–742.
22. Staanum PF. Tumor dosimetry using ^{177}Lu: influence of background activity, measurement method and reconstruction algorithm. *EJNMMI Phys.* 2023;10:39.
23. Dewaraja YK, Frey EC, Sgouros G, et al. MIRD pamphlet no. 23: quantitative SPECT for patient-specific 3-dimensional dosimetry in internal radionuclide therapy. *J Nucl Med.* 2012;53:1310–1325.
24. Marquis H, Willowson KP, Bailey DL. Partial volume effect in SPECT & PET imaging and impact on radionuclide dosimetry estimates. *Asia Ocean J Nucl Med Biol.* 2023;11:44–54.
25. Nelson AS, Horstman BP. Quantitative SPECT/CT reconstruction with SPECTRA Quant®. MIM Software website. https://www.mimsoftware.com/portal/login?originalUrl=%2Fportal%2Ftraining%2Fradiology_nuc_med%2Fwhite_papers. Published February 7, 2022. Accessed October 23, 2023.
26. Cole NM, Mirando D, Nelson AS. Make it easy with single timepoint dosimetry. MIM Software website. https://go.mimsoftware.com/single-timepoint-dosimetry-white-paper. Published June 20, 2022. Accessed October 23, 2023.
27. Hänscheid H, Lapa C, Buck AK, Lassmann M, Werner RA. Dose mapping after endoradiotherapy with ^{177}Lu-DOTATATE/DOTATOC by a single measurement after 4 days. *J Nucl Med.* 2018;59:75–81.
28. Collarino A, Pereira Arias-Bouda LM, Valdés Olmos RA, et al. Experimental validation of absolute SPECT/CT quantification for response monitoring in breast cancer. *Med Phys.* 2018;45:2143–2153.
29. Larson SM. Tumor treatment response based on visual and quantitative changes in global tumor glycolysis using PET-FDG imaging. The visual response score and the change in total lesion glycolysis. *Clin Positron Imaging.* 1999;2:159–171.
30. Scher HI, Morris MJ, Stadler WM, et al. Trial design and objectives for castration-resistant prostate cancer: updated recommendations from the Prostate Cancer Clinical Trials Working Group 3. *J Clin Oncol.* 2016;34:1402–1418.
31. Gafita A, Heck MM, Rauscher I, et al. Early prostate-specific antigen changes and clinical outcome after ^{177}Lu-PSMA radionuclide treatment in patients with metastatic castration-resistant prostate cancer. *J Nucl Med.* 2020;61:1476–1483.
32. O JH, Lodge MA, Wahl RL. Practical PERCIST: a simplified guide to PET response criteria in solid tumors 1.0. *Radiology.* 2016;280:576–584.
33. Gafita A, Rauscher I, Weber M, et al. Novel framework for treatment response evaluation using PSMA-PET/CT in patients with metastatic castration-resistant prostate cancer (RECIP 1.0): an international multicenter study. *J Nucl Med.* 2022; 63:1651–1658.
34. Jackson PA, Hofman MS, Hicks RJ, Scalzo M, Violet J. Radiation dosimetry in ^{177}Lu-PSMA-617 therapy using a single posttreatment SPECT/CT scan: a novel methodology to generate time- and tissue-specific dose factors. *J Nucl Med.* 2020; 61:1030–1036.
35. Brosch-Lenz J, Delker A, Völter F, et al. Toward single-time-point image-based dosimetry of ^{177}Lu-PSMA-617 therapy. *J Nucl Med.* 2023;64:767–774.
36. Peterson AB, Mirando DM, Dewaraja YK. Accuracy and uncertainty analysis of reduced time point imaging effect on time-integrated activity for ^{177}Lu-DOTA-TATE PRRT in clinical patients and realistic simulations. PubMed website. https://pubmed.ncbi.nlm.nih.gov/37131738/. Published April 21, 2023. Accessed April 23, 2024.
37. Hou X, Brosch J, Uribe C, et al. Feasibility of single-time-point dosimetry for radiopharmaceutical therapies. *J Nucl Med.* 2021;62:1006–1011.
38. Peters SMB, Privé BM, De Bakker M, et al. Intra-therapeutic dosimetry of [^{177}Lu]Lu-PSMA-617 in low-volume hormone-sensitive metastatic prostate cancer patients and correlation with treatment outcome. *Eur J Nucl Med Mol Imaging.* 2022;49:460–469.
39. Une N, Takano-Kasuya M, Kitamura N, et al. The anti-angiogenic agent lenvatinib induces tumor vessel normalization and enhances radiosensitivity in hepatocellular tumors. *Med Oncol.* 2021;38:60.
40. Pereira PMR, Edwards KJ, Mandleywala K, et al. iNOS regulates the therapeutic response of pancreatic cancer cells to radiotherapy. *Cancer Res.* 2020;80: 1681–1692.
41. Tachibana I, Nishimura Y, Hanaoka K, et al. Tumor hypoxia detected by ^{18}F-fluoromisonidazole positron emission tomography (FMISO PET) as a prognostic indicator of radiotherapy (RT). *Anticancer Res.* 2018;38:1775–1781.
42. Scott JG, Sedor G, Ellsworth P, et al. Pan-cancer prediction of radiotherapy benefit using genomic-adjusted radiation dose (GARD): a cohort-based pooled analysis. *Lancet Oncol.* 2021;22:1221–1229.
43. Scott JG, Berglund A, Schell MJ, et al. A genome-based model for adjusting radiotherapy dose (GARD): a retrospective, cohort-based study. *Lancet Oncol.* 2017;18: 202–211.
44. Yard BD, Gopal P, Bannik K, Siemeister G, Hagemann UB, Abazeed ME. Cellular and genetic determinants of the sensitivity of cancer to α-particle irradiation. *Cancer Res.* 2019;79:5640–5651.
45. Sgouros G. α-particle–emitter radiopharmaceutical therapy: resistance is futile. *Cancer Res.* 2019;79:5479–5481.
46. Lorente D, Ravi P, Mehra N, et al. Interrogating metastatic prostate cancer treatment switch decisions: a multi-institutional survey. *Eur Urol Focus.* 2018;4: 235–244.
47. Zacho HD, Nielsen JB, Haberkorn U, Stenholt L, Petersen LJ. ^{68}Ga-PSMA PET/CT for the detection of bone metastases in prostate cancer: a systematic review of the published literature. *Clin Physiol Funct Imaging.* 2017;38:911–922.
48. Gupta M, Choudhury PS, Rawal S, Goel HC, Rao SA. Evaluation of RECIST, PERCIST, EORTC, and MDA criteria for assessing treatment response with Ga68-PSMA PET-CT in metastatic prostate cancer patient with biochemical progression: a comparative study. *Nucl Med Mol Imaging.* 2018;52:420–429.
49. Fanti S, Hadaschik B, Herrmann K. Proposal for systemic-therapy response-assessment criteria at the time of PSMA PET/CT imaging: the PSMA PET progression criteria. *J Nucl Med.* 2020;61:678–682.
50. Michalski K, Klein C, Brüggemann T, Meyer PT, Jilg CA, Ruf J. Assessing response to ^{177}Lu-PSMA radioligand therapy using modified PSMA PET progression criteria. *J Nucl Med.* 2021;62:1741–1746.
51. John N, Pathmanandavel S, Crumbaker M, et al. ^{177}Lu-PSMA SPECT quantitation at 6 weeks (dose 2) predicts short progression-free survival for patients undergoing ^{177}Lu-PSMA-I&T therapy. *J Nucl Med.* 2023;64:410–415.

Relationship Between Absorbed Dose and Response in Neuroendocrine Tumors Treated with [^{177}Lu]Lu-DOTATATE

Carl Fredrik Warfvinge[1,2], Johan Gustafsson[3], Daniel Roth[3], Jan Tennvall[2], Johanna Svensson[4], Peter Bernhardt[5,6], Anna Åkesson[7], Elinore Wieslander[1], Anna Sundlöv[2], and Katarina Sjögreen Gleisner[3]

[1]*Department of Hematology, Oncology, and Radiation Physics, Skåne University Hospital, Lund, Sweden;* [2]*Division of Oncology, Department of Clinical Sciences Lund, Lund University, Lund, Sweden;* [3]*Medical Radiation Physics, Lund University, Lund, Sweden;* [4]*Department of Oncology, Institute of Clinical Sciences, Sahlgrenska Academy, University of Gothenburg, Gothenburg, Sweden;* [5]*Department of Medical Physics and Biomedical Engineering, Sahlgrenska University Hospital, Gothenburg, Sweden;* [6]*Department of Medical Radiation Sciences, Institute of Clinical Sciences, Sahlgrenska Academy, University of Gothenburg, Gothenburg, Sweden; and* [7]*Clinical Studies Sweden, Forum South, Skåne University Hospital, Lund, Sweden*

Peptide receptor radionuclide therapy presents the possibility of tracing and quantifying the uptake of the drug in the body and performing dosimetry, potentially allowing individualization of treatment schemes. However, the details of how neuroendocrine tumors (NETs) respond to different absorbed doses are insufficiently known. Here, we investigated the relationship between tumor-absorbed dose and tumor response in a cohort of patients with NETs treated with [^{177}Lu]Lu-DOTATATE. **Methods:** This was a retrospective study based on 69 tumors in 32 patients treated within a clinical trial. Dosimetry was performed at each cycle of [^{177}Lu]Lu-DOTATATE, rendering 366 individual absorbed dose assessments. Hybrid planar–SPECT/CT imaging using [^{177}Lu]Lu-DOTATATE was used, including quantitative SPECT reconstruction, voxel-based absorbed dose rate calculation, semiautomatic image segmentation, and partial-volume correction. Changes in tumor volume were used to determine tumor response. The volume for each tumor was manually delineated on consecutive CT scans, giving a total of 712 individual tumor volume assessments. Tumors were stratified according to grade. The relationship between absorbed dose and response was investigated using mixed-effects models and logistic regression. Tumors smaller than 4 cm^3 were excluded. **Results:** In grade 2 NETs, a clear relationship between absorbed dose and volume reduction was observed. Our observations suggest a 90% probability of partial tumor response for an accumulated tumor-absorbed dose of at least 135 Gy. **Conclusion:** Our findings are in accordance with previous observations regarding the relationship between tumor shrinkage and absorbed dose. Moreover, our data suggest an absorbed dose threshold for partial response in grade 2 NETs. These observations provide valuable insights for the design of dosimetry-guided peptide receptor radionuclide therapy schemes.

Key Words: radionuclide therapy; neuroendocrine; dosimetry; tumor; [^{177}Lu]Lu-DOTATATE; dose response

J Nucl Med 2024; 65:1070–1075
DOI: 10.2967/jnumed.123.266991

For patients with metastatic somatostatin receptor–positive neuroendocrine tumors (NETs), [^{177}Lu]Lu-DOTATATE is an essential treatment. Results from the NETTER-1 clinical trial showed an improved median survival compared with treatment with high-dose somatostatin analogs in small-intestine NETs, with relatively modest side effects (*1*).

According to the established treatment scheme, all patients are given the same number of cycles (4), with a fixed activity per cycle (7.4 GBq). A radiobiologic perspective, however, suggests that the treatment effect of [^{177}Lu]Lu-DOTATATE could be improved through patient-specific dosimetry. Dosimetry takes advantage of the characteristics of the radioactive decay of ^{177}Lu, for which there is an intrinsic proportionality between the intensities of the cell-damaging β-radiation and the measurable γ-radiation, which provides a unique opportunity to quantify, and thus individualize, treatment.

A few groups have studied individualized dosimetry-guided [^{177}Lu]Lu-DOTATATE treatment, with the overarching goal of mitigating side effects and increasing the antitumor effect. In these studies, the cumulative administered activity was tailored to the patient, taking into consideration the absorbed dose to organs at risk, mainly the kidneys, rather than the absorbed dose to the tumors. The cumulative administered activity has been modified by either altering the number of treatment cycles (while keeping the activity per cycle fixed) or altering the activity per cycle (while keeping the number of treatment cycles fixed) (*2–4*). So far, these dosimetry-based [^{177}Lu]Lu-DOTATATE studies have not produced substantial survival benefits compared with the NETTER-1 results (*2*,*4–6*), although differences in patient populations preclude direct comparison of results.

The dosimetry-guided schedules adhere to an approach that maximizes the total administered activity within the constraints set by tissues at risk. Treatment optimization according to this approach assumes that a higher cumulative administered activity also results in a higher tumor-absorbed dose, leading to a higher likelihood of tumor response. However, in a previous study, a decreasing pattern in the tumor-absorbed dose over treatment cycles was observed, which was more pronounced for grade 2 (G2) NETs than for grade 1 (G1) NETs (*7*), suggesting that the timing of treatment intensification during the course of treatment could potentially also be of importance.

Still, fundamental pieces of knowledge are yet lacking in view of treatment optimization. Data supporting the relationship between tumor-absorbed dose and tumor response are still scarce for NETs treated with [^{177}Lu]Lu-DOTATATE. Existing observations suggest that tumor shrinkage becomes more pronounced with increasing absorbed doses in large pancreatic NETs (*8*). For small-intestine NETs, a similar observation has been made, although with an arguably weaker relationship (*9*,*10*). Nevertheless, data indicating which

Received Nov. 16, 2023; revision accepted Mar. 26, 2024.
For correspondence or reprints, contact Carl Fredrik Warfvinge (carl_fredrik.warfvinge@med.lu.se).
Published online May 9, 2024.

levels of absorbed doses are required to elicit tumor response do not yet exist, further limiting optimization of dosimetry-guided peptide receptor radionuclide therapy.

The aim of this study was to investigate parameters of importance for the response of NETs, including the total administered activity and the absorbed dose. Further aims included investigation of the existence of an absorbed dose–response relationship and the possibility of identifying a threshold absorbed dose required to elicit tumor response.

MATERIALS AND METHODS

Patient and Tumor Selection

Tumor data were derived from the Iluminet trial (NCT01456078) (*2*), a phase II nonrandomized clinical trial run at 2 sites in Sweden between 2011 and 2018. The study was approved by the institutional review board, and all subjects signed an informed consent form. In total, 103 patients with somatostatin receptor–expressing NETs were included. Tumors were allowed a Ki-67 index of no more than 20% (e.g., G1 and G2 tumors) based on the most recent biopsy before inclusion in the study. The included patients were given repeated cycles of [^{177}Lu]Lu-DOTATATE (7.4 GBq) at intervals ranging from 8 to 12 wk. Kidney dosimetry was performed after each cycle. On reaching an accumulated renal biologically effective dose of 27 ± 2 Gy, no further treatment cycles were given. Patients younger than 70 y with a good renal and hematologic tolerance and no signs of tumor progression were, however, allowed to continue up to a renal biologically effective dose of 40 ± 2 Gy. In the trial, follow-up of tumor response was done according to RECIST 1.1, based on contrast-enhanced CT (CECT) imaging and in a few cases MRI. Follow-up started at baseline (the first CECT before treatment began) and continued until the patient left the study. The intervals between CECT scans were initially fixed to every 3 mo, but with longer follow-up the intervals were prolonged and in practice ranged between 3 and 12 mo.

Data in this study were derived from the 48 patients in the ILUMINET study treated at the facility in Lund. For a tumor to be eligible for analysis, it needed to be quantifiable on both baseline CECT and hybrid planar–SPECT/CT using [^{177}Lu]Lu-DOTATATE images. Tumors with unsatisfactory dosimetry in any cycle or unsatisfactory visibility in subsequent CECT were excluded, as were skeletal tumors and tumors that progressed during treatment.

Tumor Volumetry from CT Images

Tumors were identified on all postbaseline CECT (or MRI) scans and were manually delineated using ARIA 15.6 (Varian Medical Systems, Inc.). When more than one CT contrast phase was available, the tumor was delineated in the phase where it was most readily visible throughout the range of scans. If the tumor was not sufficiently identifiable, it was excluded from the analyses, as were bone tumors. From defined volumes of interest (VOIs), tumor volumes were calculated by the software and extracted.

Tumor volumes were analyzed graphically as a function of time after baseline, and the times of the maximum (v_{max}) and minimum (v_{min}) tumor volumes were identified. The relative tumor volume reduction was calculated according to

$$\Delta v = (v_{max} - v_{min})/v_{max}. \quad \text{Eq. 1}$$

In most cases, v_{max} occurred at baseline. However, in some cases, v_{max} occurred at the next time of follow-up. Moreover, for a few tumors, the best response (v_{min}) occurred before the delivery of the last treatment cycle. For complementary analyses, the smallest tumor volume after treatment was then also scored.

Image-Based Dosimetry

Tumor dosimetry was based on a combination of SPECT/CT using [^{177}Lu]Lu-DOTATATE, performed at 1 d after administration, and planar image data, with nominal acquisition times at 1, 24, 96, and 168 h. Details of the image acquisition and of the methods for activity quantification and dosimetry have been presented earlier (*7*) and are summarized in Supplement 1 (supplemental materials are available at http://jnm.snmjournals.org) (*11–13*). Tumors were selected for analysis if deemed eligible, according to the criteria for planar images detailed previously (*14*). The absorbed dose to each tumor was determined for each cycle. The cumulative absorbed dose was determined both as the sum until the time of best response and as the sum over all delivered cycles. Likewise, the cumulative administered activity was determined until the time of best response and over all cycles. The uncertainty in absorbed dose for each cycle was assessed similarly as in Gear et al. (*15*). The uncertainty in cumulative absorbed dose over the cycles was then calculated assuming independence between cycles. Further details are provided in Supplement 2.

Statistical Analysis

Tumors with a volume reduction greater than or equal to 66% were defined as responders, whereas the remaining tumors were defined as nonresponders. The cutoff volume reduction was derived from RECIST 1.1, in which a reduction of more than 30% of the sum of diameters of predetermined lesions is classified a partial tumor response (*16*). Translated to volume for spheres, 30% corresponds to a volume reduction of 66%.

The potential association between tumor response and the cumulative absorbed dose, as well as the cumulative administered activity, was examined by analyzing the difference between the means for responders and nonresponders. To mitigate uncertainties in the tumor-absorbed doses, which become higher for smaller volumes (*15*,*17*), a volume cutoff was set such that tumors smaller than 4 cm^3 on the baseline CECT image were excluded from analysis. Since tumor grade has been previously found to affect the absorbed dose pattern over the cycles (*7*), separate analyses were made for grade 1 and 2 NETs. To take potential interaction between tumors in the same patient into account, a linear mixed-effects model was used to test the difference in means between responders and nonresponders, with patient identity included as a random effect. A P value of less than 0.05 was considered statistically significant. Supplement 3 provides details on the linear mixed-effects model.

For variables that exhibited a significant difference between responders and nonresponders, further analyses were made using nonlinear mixed models including both logistic regression for dichotomized response data and response-versus-dose modeling for continuous response data. Logistic regression was used to model the tumor control probability (TCP) by fitting of the logarithm of the odds ratio (Supplement 4). A patient-specific random effect was included for the intercept, and tumor grade was included as a factor. The SD in the modeled TCP was determined from the Jacobian and propagation of the covariance matrix obtained from model fitting. A 95% CI for the modeled TCP was obtained as 1.96 times the SD. Receiver operating characteristics were also analyzed to assess the consistency between observed and model-predicted probabilities for response, with a 95% CI estimated by bootstrapping with 10^4 bootstrap repetitions. Sensitivity and specificity were calculated for different absorbed doses. Response-versus-dose modeling was performed according to the asymptotic growth model using a nonlinear mixed model. A patient-specific random effect was included for the curve amplitude, and grade was included as a factor (Supplement 5). Normality of residuals was confirmed using a quantile–quantile plot and the Shapiro–Wilk test. Initial estimates for the model were obtained by making preliminary fits using a nonmixed model, and a 95% CI was determined in a manner corresponding to that for the logistic regression.

Statistical analyses were performed in R, version 4.2.2; mixed-effects models were implemented in package LME4 and NLME (*18*); significance tests were performed using emmeans, version 1.4.8-1; and receiver-operating-characteristic analyses were based on the package pROC (*19*).

RESULTS

Characteristics of Tumors

Initially, 275 tumors from 41 patients were included after an assessment of their visibility on baseline CECT scans and hybrid planar–SPECT/CT using [^{177}Lu]Lu-DOTATATE images acquired during therapy. Of these, 76 tumors were excluded because they were not deemed eligible for dosimetry, 81 tumors were excluded because of limited visibility on subsequent CECT scans, and 19 tumors were excluded because of immediate progression after inclusion in the study. After these exclusions, 118 tumors from 38 patients remained. These were identified on every subsequent CECT scan and delineated. After the exclusion of all tumors smaller than 4 cm^3, 69 tumors from 32 patients remained. Figure 1 demonstrates the selection process.

For the 32 patients, the time of follow-up ranged from 0.8 to 8.3 y, with a mean of 3.6 y and a median of 2.7 y. The number of cycles administered to the included patients ranged from 2 and 9, with a median of 5.5. The cumulative administered activity ranged from 15 to 67 GBq, with a median of 41 GBq.

The number of tumors per patient ranged from 1 to 9, with a median of 2. Table 1 summarizes the tumor origin and grade across patients. Of the 69 included tumors, 41 (59%) were G1 and 28 were G2 (41%). Forty-three (62%) tumors were of small-intestine origin, and 26 (38%) originated from other organs (17 from the pancreas, 5 from the lung, 1 from the right colon, and 1 from the ovaries; 2 were of unknown origin). Of the 43 tumors from the small intestine, 34 (79%) were G1 and 9 (21%) were G2. Of the 26 tumors from other organs, 7 (27%) were G1 and 19 (73%) were G2.

For all evaluated tumors, baseline volumes ranged from 4.0 to 630 cm^3, with a median of 17.1 cm^3. The tumor volume reduction ranged from 6.0% to 100%, with a median of 69.9%. For G1 tumors, the median tumor volume reduction was 63%, whereas for G2 it was 75%. The cumulative tumor-absorbed dose delivered until best response ranged from 22 to 368 Gy, with a median of 142 Gy. For G1, the median absorbed dose was 179 Gy (range, 35–368 Gy), and for G2 the corresponding values were 109 Gy and 22–226 Gy. The cumulative administered activity for G1 tumors was 22–67 GBq, with a median of 45 GBq. For G2 tumors, the median value was 30 GBq, with a range of 15–45 GBq.

Evaluation of Variables and Their Association with Response

Table 2 summarizes the results from analysis of the association between tumor response, cumulative administered activity, and tumor-absorbed dose, with means calculated using a linear mixed-effects model (Supplemental Eq. 1) and stratification according to tumor grade.

The cumulative administered activities did not significantly differ between responders and nonresponders for either G1 or G2 NETs. The mean absorbed doses were significantly higher for responding than for nonresponding G2 tumors ($P = 0.01$). For G1 tumors, there was a clear numeric difference, but statistical significance was not reached ($P = 0.08$). Figure 2 shows the absorbed dose data underlying Table 2 as box plots for G1 and G2 NETs, for responding and nonresponding tumors. For 5 tumors in 4 patients (2 G1 and 2 G2), the best response occurred before the delivery of all treatments. For this reason, complementary analyses were also performed on the association between the best response identified after treatment and the cumulative administered activity or tumor-absorbed dose over all cycles. The difference between this analysis and the results in Table 2 was thus the time when the tumor response and absorbed dose were evaluated for the 5 tumors.

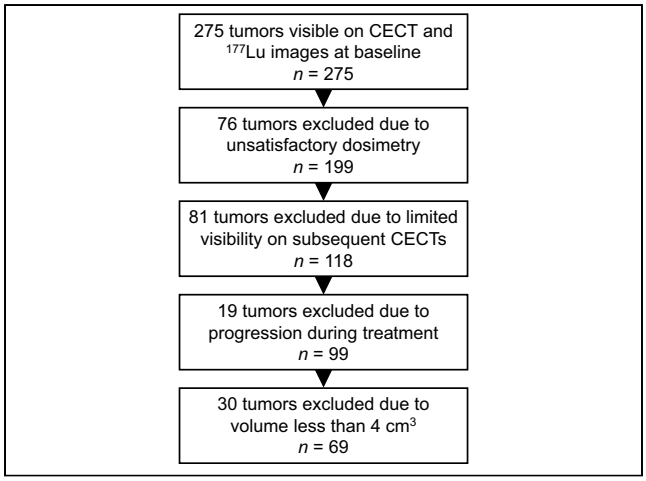

FIGURE 1. Schematic overview of selection of included tumors.

The results obtained were similar to those of Table 2 and Figure 3, with mean absorbed doses of 167 versus 203 Gy (G1) and 72 versus 129 Gy (G2) for nonresponders and responders, respectively. The results of the P values for differences between means were also similar, and results were thus consistent with Table 2.

Relationship Between Absorbed Dose and Response

Figure 3 shows the probability of tumor control as a function of absorbed dose for G2 NETs. As a significant difference in the absorbed doses between responders and nonresponders was not reached, corresponding analyses were not performed for G1 NETs.

Parameters describing the curve for G2 were obtained for the intercept (β_0 in Supplement 4) to -1.44 ± 0.78 (estimate $\pm$ SE) and rate constant for dose dependence $(\beta_1+\beta_2)$ of $0.027 \pm 0.01\ Gy^{-1}$. The receiver-operating-characteristic analysis yielded an area under the curve (AUC) of 0.89 (bootstrapped CI, 0.73–1). The optimal threshold (Youden J) TCP was obtained to 65%, corresponding to a sensitivity and specificity of 0.95 and 0.75, respectively, an odds ratio of 1.85 (95% CI, 0.71–4.85), and an absorbed dose of 76 Gy. From a clinical perspective, a TCP of, for example, 90% may be considered more relevant. For an absorbed dose of 135 Gy, a TCP of 90% (95% CI, 64%–98%) was obtained, corresponding to a sensitivity and specificity of 0.4 and 0.88, respectively. The continuous data underlying Figure 3 are presented in Figure 4.

Analysis of these data with the asymptotic growth model (Supplement 5) yielded a curve that leveled out at a volume reduction of 78%. The curve parameter determining the amplitude $(\beta_0+\beta_1)$ was obtained to 78% $\pm$ 7% (estimate $\pm$ SE), and the slope $(\beta_2+\beta_3)$ was obtained to 32 ± 12 Gy. The relative uncertainty in cumulative absorbed dose over cycles ranged from 4% to 10%, with a mean of 5%. The major uncertainty contribution was associated with estimation of tumor volume.

DISCUSSION

Our data provide empiric insights on parameters that govern the tumor response in G1 and G2 NETs. For both grades, the administered activity was found to be less informative as a predictor than the absorbed dose was, although significance in the difference between the absorbed doses for responders and responders was not reached for G1 NETs.

TABLE 1
Tumor Origin and Grade

Tumor			Patient		
	Tumor grade			Tumor grade	
Tumor origin	G1 (n = 41)	G2 (n = 28)	Tumor origin	G1 (n = 18)	G2 (n = 14)
Small-intestine NET (n = 43)	34	9	Small-intestine NET (n = 21)	14	7
Other NET (n = 26)	7	19	Other NET (n = 11)	4	7

Our data suggest that G2 tumors that respond well to peptide receptor radionuclide therapy generally have received a higher absorbed dose than G2 tumors that do not respond as well. In G1 tumors, similar results were observed, but without reaching significance. Although this particular observation is new, it also harmonizes well with previous data showing a dose–response relationship in the generally faster-growing pancreatic NETs but a less distinct dose–response relationship in the generally slower-growing small-intestine NETs (*9*,*10*). In our material, a majority of G1 tumors (83%) were small-intestine NETs whereas a minority of G2 tumors (32%) were small-intestine NETs. Taken together, the available data strongly suggest that there exists a relationship between response and increased absorbed doses in G2 tumors.

The cutoff in tumor volume on the baseline CECT was set to limit the influence of dosimetry uncertainties. The cutoff of 4 cm^3 was established as a compromise between loss of data and dosimetry uncertainties. Notably, the absorbed doses were determined for each cycle and then summed over cycles, and the relative uncertainty in the cumulative absorbed dose was thus expected to be lower than for a single cycle. However, as a consequence, approximately 40% of the analyzed tumor data were excluded. This is considered a major limitation to this study, as the relationship between absorbed dose and response for small tumors is left unanswered. In addition to the relatively sparse number of included tumors and patients, further limitations to this study are its retrospective and nonrandomized nature. Moreover, because of the time-consuming nature of tumor volume assessment, only one observer assessed the tumor volumes, possibly making CECT volumetry susceptible to operator bias.

To further elucidate the reasons behind the negative results obtained for G1 NETs, an exploratory analysis was performed of the impact of tumor volume at baseline. As the absorbed dose was not considered for this analysis, the 4 cm^3 volume cutoff was not required, and volume data on 118 tumors could be included. G1 and G2 tumors were separated into 2 groups based on their initial volume and the mean volume decrease estimated for the respective group using a linear mixed-effects model corresponding to Supplemental Equation 3.1, for different volume thresholds. Figure 5 shows box plots separated by tumor volumes below or above 30 cm^3 at baseline. For G1, there was a significant difference (P = 0.001) in the mean volume reduction between the 2 groups, with means of 70% versus 48% (medians, 70% vs. 47%). For G2, there was a similar tendency, although the difference was not significant (P = 0.07), with means of 73% versus 63% (medians, 86% vs. 59%). Although data did not allow for inclusion of baseline volume as a factor for the dose–response analyses, we find the observation interesting, in particular for G1 NETs. The expression of somatostatin 2 receptors has, in preclinical studies, been shown to vary across the tumor, implying that the activity uptake can be nonuniform (*20*,*21*). Most G1 tumors originate from small-intestine cells, known to excrete profibrotic substances, possibly then affecting the distribution of active tumor cells (*22*). In preclinical studies, the radiobiologic response has been observed to be nonuniform, protracted, and associated with cellular senescence (*20*). It is reasonable to assume that the nonuniformity is more pronounced for large than small tumors. In the perspective of the mean range of the β-particles emitted from ^{177}Lu, which is less than 0.5 mm in soft tissue, the absorbed dose distribution becomes nonuniform within the tumor, which together with a nonuniform distribution of active tumor cells may affect response. Possibly, therapy using ^{90}Y, with a longer electron range, could counteract the effects of nonuniformity (*23*).

To our knowledge, this was the first study to estimate the TCP in NETs treated with [^{177}Lu]Lu-DOTATATE. Because of the

TABLE 2
Cumulative Administered Activity and Absorbed Dose for G1 and G2 NETs

		Administered activity (GBq)		Absorbed dose (Gy)	
Grade	Response*	Mean	P	Mean	P
G1	Nonresponder	41	0.25	163	0.08
	Responder	43		203	
G2	Nonresponder	34	0.53	68	0.01
	Responder	35		128	

*Responders have ≥66% tumor volume reduction; nonresponders have <66% tumor volume reduction.
Means were estimated using linear mixed-effects models, and P values refer to difference between means.

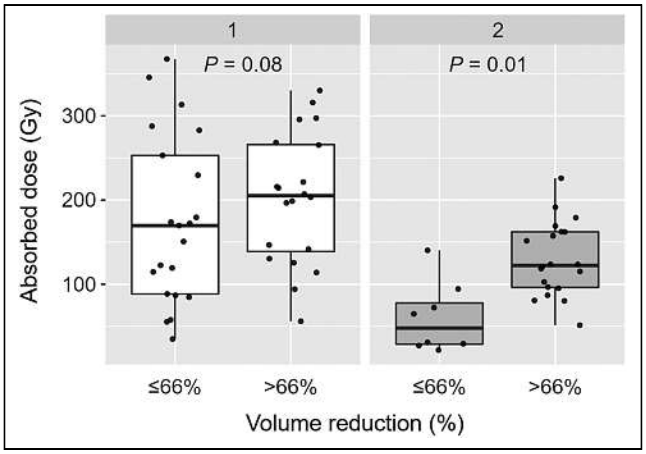

FIGURE 2. Cumulative absorbed dose until best response of G1 and G2 NETs, separated by volume reduction relative to baseline of 66%. Horizontal box-lines indicate median and 25th and 75th percentiles, and whiskers indicate 1.5 times interquartile range. Markers represent individual tumor data; horizontal dispersion within each box has been introduced for purpose of visibility.

small sample size, data did not allow for evaluation of the prediction capability, and the presented results would benefit from verification in an independent patient cohort. Nevertheless, our results appear to harmonize with 2 previous studies, exploring dose–response relationships in mixed populations of NET patients treated with ^{90}Y selective internal radiation therapy (*24*,*25*). In these studies, tumor-absorbed dose cutoffs of 191.3 and 200 Gy were found to be predictive of tumor response, with 93% and 80% sensitivity, respectively (*24*,*25*). Although these absorbed doses are slightly higher than those obtained in this study, the differences in treatment mode, radionuclide, and tumor characteristics, and the relatively small sample size in all 3 studies, make our results comparable and suggest that they may be clinically applicable.

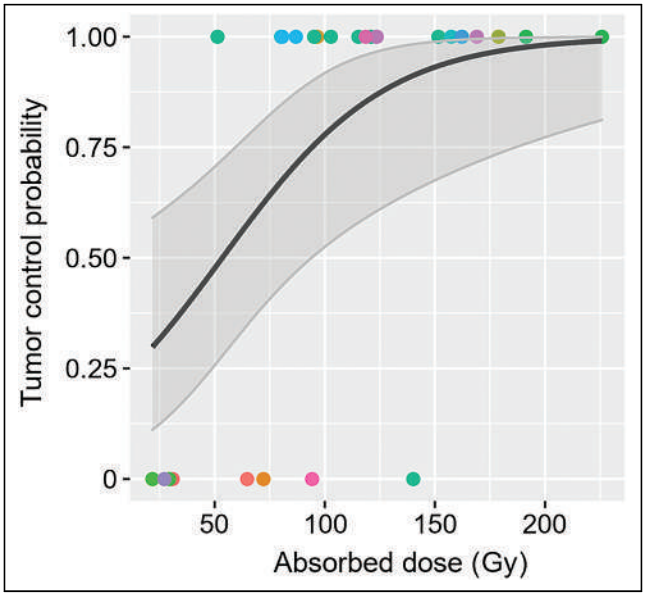

FIGURE 3. TCP for G2 NETs, as function of cumulative absorbed dose over all cycles. Tumor control was defined as 66% volumetric reduction after baseline. Colored points indicate data for individual tumors, where same color represents same patient. Black line shows result of logistic regression via mixed-effects model, and gray-shaded band indicates CI for fitted TCP curve.

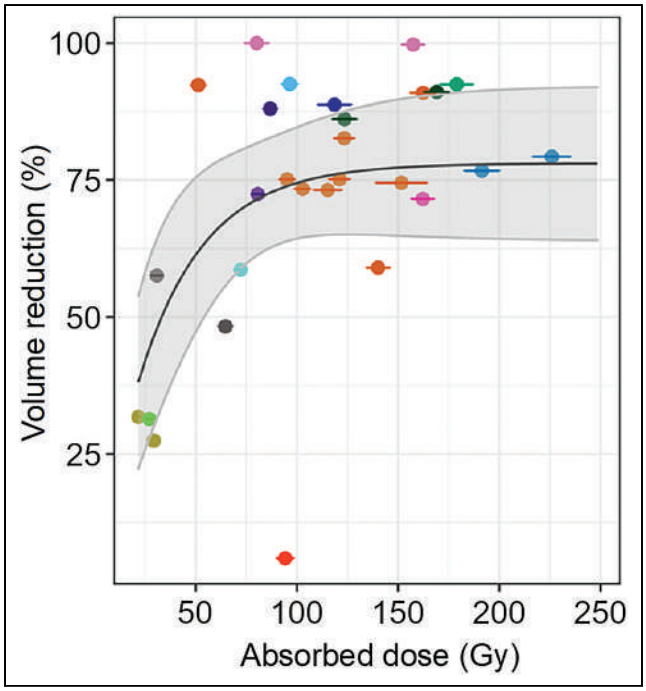

FIGURE 4. Tumor volume reduction as function of cumulative absorbed dose over all cycles to G2 NETs. Colored points indicate data for individual tumors, with same color representing same patient, and error bars indicate ±SD in cumulative absorbed dose. Black line shows result of modeling using mixed-effects asymptotic growth model, and gray-shaded band indicates CI for fitted curve.

In our clinical experience, some patients with a large tumor burden and distinct tumor-related symptoms may benefit from a swift reduction in tumor volume. In these cases, we believe it advisable to aim for a total tumor-absorbed dose of at least 150 Gy. It is, however, unclear whether tumor shrinkage is the ultimate goal in the treatment of NET patients in general. Low-grade NET is generally an indolent disease in which the patient lacks debilitating

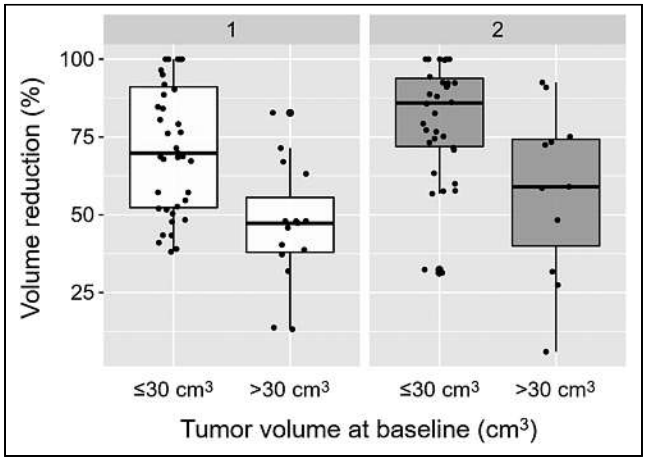

FIGURE 5. Volume reduction relative to baseline for G1 and G2 NETs, separated by 30 cm^3 tumor volume at baseline. Horizontal box-lines indicate median and 25th and 75th percentiles, and whiskers indicate 1.5 times interquartile range. Markers represent individual tumor data; horizontal dispersion within each box was introduced for purpose of visibility.

symptoms for long periods but in which the tumor eventually progresses. In these cases, time to tumor growth after peptide receptor radionuclide therapy might be a more relevant response metric than tumor shrinkage. This would also provide a response metric that may be more clinically attractive and possibly more suitable for response assessment of G1/small-intestine NETs. In our material, there were too few tumors that progressed during the observation period to enable such an analysis.

CONCLUSION

Our data are in accordance with previous observations that tumor response is dependent on tumor-absorbed dose in NETs treated with [^{177}Lu]Lu-DOTATATE. Moreover, our data suggest a TCP of 90% in tumors for an accumulated absorbed dose of at least 135 Gy. These observations provide valuable insights for the design of future dosimetry-guided peptide receptor radionuclide therapy schemes.

DISCLOSURE

Financial support was provided by the Swedish Cancer Society (211754Pj01H), Mrs. Berta Kamprad's Foundation (FBKS-2020-13 and FBKS-2020-8), the Southern Sweden Healthcare Region (Doktorand-2021-0901), and the Gunnar Nilsson Cancer Foundation (GN-2020-16-173). Peter Bernhardt and Johanna Svensson acknowledge support from the Swedish Cancer Society, the Jubilee Clinic Cancer Research Foundation, and the Swedish federal government under the ALF agreement. No other potential conflict of interest relevant to this article was reported.

ACKNOWLEDGMENTS

We thank our coworkers Jonas Scherman, Theo Sjögreen Gleisner, Fanny Mörnsjö Centofanti, and Paula Gluchowski, as well as all patients participating in the study.

KEY POINTS

QUESTION: Is tumor response dependent on the absorbed dose in NETs treated with[^{177}Lu]Lu-DOTATATE, and does a dose threshold for tumor response exist?

PERTINENT FINDINGS: In our retrospective study comparing dosimetry-derived tumor-absorbed doses and tumor response in NET G2 patients treated with [^{177}Lu]Lu-DOTATATE, a statistically significant correlation between tumor response and tumor-absorbed dose was found. Moreover, a tumor-absorbed dose of 135 Gy was suggested to provide a TCP of 90%.

IMPLICATIONS FOR PATIENT CARE: Our data suggest that future dosimetry-guided treatment schemes of [^{177}Lu]Lu-DOTATATE in NETs should aim for an accumulated tumor-absorbed dose of at least 135 Gy.

REFERENCES

1. Strosberg J, El-Haddad G, Wolin E, et al. Phase 3 trial of ^{177}Lu-Dotatate for midgut neuroendocrine tumors. *N Engl J Med.* 2017;376:125–135.
2. Sundlöv A, Gleisner KS, Tennvall J, et al. Phase II trial demonstrates the efficacy and safety of individualized, dosimetry-based ^{177}Lu-DOTATATE treatment of NET patients. *Eur J Nucl Med Mol Imaging.* 2022;49:3830–3840.
3. Sandström M, Garske-Román U, Granberg D, et al. Individualized dosimetry of kidney and bone marrow in patients undergoing ^{177}Lu-DOTA-octreotate treatment. *J Nucl Med.* 2013;54:33–41.
4. Del Prete M, Buteau F-A, Arsenault F, et al. Personalized ^{177}Lu-octreotate peptide receptor radionuclide therapy of neuroendocrine tumours: initial results from the P-PRRT trial. *Eur J Nucl Med Mol Imaging.* 2019;46:728–742.
5. Strosberg JR, Caplin ME, Kunz PL, et al. ^{177}Lu-Dotatate plus long-acting octreotide versus high-dose long-acting octreotide in patients with midgut neuroendocrine tumours (NETTER-1): final overall survival and long-term safety results from an open-label, randomised, controlled, phase 3 trial. *Lancet Oncol.* 2021;22:1752–1763.
6. Garske-Román U, Sandström M, Fröss Baron K, et al. Prospective observational study of ^{177}Lu-DOTA-octreotate therapy in 200 patients with advanced metastasized neuroendocrine tumours (NETs): feasibility and impact of a dosimetry-guided study protocol on outcome and toxicity. *Eur J Nucl Med Mol Imaging.* 2018;45:970–988.
7. Roth D, Gustafsson J, Warfvinge CF, et al. Dosimetric quantities in neuroendocrine tumors over treatment cycles with ^{177}Lu-DOTATATE. *J Nucl Med.* 2022;63:399–405.
8. Ilan E, Sandstrom M, Wassberg C, et al. Dose response of pancreatic neuroendocrine tumors treated with peptide receptor radionuclide therapy using ^{177}Lu-DOTATATE. *J Nucl Med.* 2015;56:177–182.
9. Jahn U, Ilan E, Sandstrom M, Lubberink M, Garske-Roman U, Sundin A. Peptide receptor radionuclide therapy (PRRT) with Lu-177-DOTATATE; differences in tumor dosimetry, vascularity and lesion metrics in pancreatic and small intestinal neuroendocrine neoplasms. *Cancers (Basel).* 2021;13:962
10. Jahn U, Ilan E, Sandström M, Garske-Roman U, Lubberink M, Sundin A. ^{177}Lu-DOTATATE peptide receptor radionuclide therapy: dose response in small intestinal neuroendocrine tumors. *Neuroendocrinology.* 2020;110:662–670.
11. Ljungberg M, Frey E, Sjogreen K, Liu X, Dewaraja Y, Strand SE. 3D absorbed dose calculations based on SPECT: evaluation for 111-In/90-Y therapy using Monte Carlo simulations. *Cancer Biother Radiopharm.* 2003;18:99–107.
12. Bielajew AF, Rogers DWO. PRESTA: the Parameter Reduced Electron-Step Transport Algorithm for electron Monte-Carlo transport. *Nucl Instrum Meth B.* 1987;18:165–181.
13. Ritz C, Baty F, Streibig JC, Gerhard D. Dose-response analysis using R. *PLoS One.* 2015;10:e0146021.
14. Roth D, Gustafsson J, Sundlöv A, Sjögreen Gleisner K. A method for tumor dosimetry based on hybrid planar-SPECT/CT images and semiautomatic segmentation. *Med Phys.* 2018;45:5004–5018.
15. Gear JI, Cox MG, Gustafsson J, et al. EANM practical guidance on uncertainty analysis for molecular radiotherapy absorbed dose calculations. *Eur J Nucl Med Mol Imaging.* 2018;45:2456–2474.
16. Eisenhauer EA, Therasse P, Bogaerts J, et al. New response evaluation criteria in solid tumours: revised RECIST guideline (version 1.1). *Eur J Cancer.* 2009;45:228–247.
17. Gustafsson J, Sundlov A, Sjogreen Gleisner K. SPECT image segmentation for estimation of tumour volume and activity concentration in ^{177}Lu-DOTATATE radionuclide therapy. *EJNMMI Res.* 2017;7:18.
18. Bates D, Maechler M, Bolker BM, Walker SC. Fitting linear mixed-effects models using lme4. *J Stat Softw.* 2015;67:1–48.
19. Robin X, Turck N, Hainard A, et al. pROC: an open-source package for R and S+ to analyze and compare ROC curves. *BMC Bioinformatics.* 2011;12:77.
20. O'Neill E, Mosley M, Cornelissen B. Imaging DNA damage response by gamma-H2AX in vivo predicts treatment response to lutetium-177 radioligand therapy and suggests senescence as a therapeutically desirable outcome. *Theranostics.* 2023;13:1302–1310.
21. O'Neill E, Kersemans V, Allen PD, et al. Imaging DNA damage repair in vivo after ^{177}Lu-DOTATATE therapy. *J Nucl Med.* 2020;61:743–750.
22. Cunningham JL, Tsolakis AV, Jacobson A, Janson ET. Connective tissue growth factor expression in endocrine tumors is associated with high stromal expression of alpha-smooth muscle actin. *Eur J Endocrinol.* 2010;163:691–697.
23. Kunikowska J, Zemczak A, Kolodziej M, et al. Tandem peptide receptor radionuclide therapy using ^{90}Y/^{177}Lu-DOTATATE for neuroendocrine tumors efficacy and side-effects: Polish multicenter experience. *Eur J Nucl Med Mol Imaging.* 2020;47:922–933.
24. Ebbers SC, van Roekel C, Braat MNGJA, Barentsz MW, Lam MGEH, Braat AJAT. Dose–response relationship after yttrium-90-radioembolization with glass microspheres in patients with neuroendocrine tumor liver metastases. *Eur J Nucl Med Mol Imaging.* 2022;49:1700–1710.
25. Chansanti O, Jahangiri Y, Matsui Y, et al. Tumor dose response in yttrium-90 resin microsphere embolization for neuroendocrine liver metastases: a tumor-specific analysis with dose estimation using SPECT-CT. *J Vasc Interv Radiol.* 2017;28:1528–1535.

Randomized Trial of Prostate-Specific Membrane Antigen PET/CT Before Definitive Radiotherapy for Unfavorable Intermediate- and High-Risk Prostate Cancer (PSMA-dRT Trial)

John Nikitas[1], Ethan Lam[2], Kiara Adame Booker[2], Wolfgang P. Fendler[3], Matthias Eiber[2], Boris Hadaschik[4], Ken Herrmann[3], Nader Hirmas[3], Helena Lanzafame[3], Martin Stuschke[5], Johannes Czernin[2], Michael L. Steinberg[1], Nicholas G. Nickols[1,6], Amar U. Kishan[1], and Jeremie Calais[2]

[1]Department of Radiation Oncology, UCLA, Los Angeles, California; [2]Ahmanson Translational Theranostics Division, Department of Molecular and Medical Pharmacology, UCLA, Los Angeles, California; [3]Department of Nuclear Medicine, University of Duisburg–Essen and German Cancer Consortium–University Hospital Essen, Essen, Germany; [4]Department of Urology, University of Duisburg–Essen and German Cancer Consortium–University Hospital Essen, Essen, Germany; [5]Department of Radiotherapy, University Hospital Essen, University of Duisburg–Essen, Essen, Germany; and [6]Radiation Oncology Service, Greater Los Angeles Veterans Affairs Healthcare System, Los Angeles, California

This multicenter randomized phase III trial (NCT04457245) evaluated the effect of performing prostate-specific membrane antigen (PSMA) PET/CT before definitive radiotherapy. **Methods:** Men with unfavorable intermediate- or high-risk prostate cancer were randomized 1.08:1 between receiving and not receiving a PSMA PET/CT scan before definitive radiotherapy. All other imaging modalities were allowed in the control arm. The primary endpoint was 5-y progression-free survival. **Results:** Fifty-four men were randomized between November 2020 and December 2021 (PSMA PET/CT, $n = 25$; control, $n = 29$). The trial closed early after approval and insurance coverage of PSMA PET/CT. In the PSMA PET/CT arm, 14 patients had localized disease (miT2b-cN0M0), 6 had locally advanced disease (miT3a-bN0M0), 3 had regional metastasis (miN1M0), and 1 had distant metastasis (miM1b). Four patients were upstaged. **Conclusion:** PSMA PET/CT upstaged 17% of patients, which allowed for more accurate radiotherapy planning. Unfortunately, this trial closed early before completion of target enrollment (54/316, 17%) and was underpowered to assess the effect of PSMA PET/CT on progression-free survival.

Key Words: PET; prostate cancer; prostate-specific membrane antigen; radiation therapy; randomized clinical trial

J Nucl Med 2024; 65:1076–1079
DOI: 10.2967/jnumed.123.267004

Prostate-specific membrane antigen (PSMA) is highly expressed in prostate cancer cells, making it an excellent target for PET radiotracers used to detect prostate cancer. PSMA PET/CT offers superior diagnostic accuracy for nodal and distant metastasis compared with both conventional imaging (CT, bone scanning, and MRI) (*1,2*) and non-PSMA radiotracer PET scans (*3–5*).

Received Nov. 3, 2023; revision accepted Mar. 28, 2024.
For correspondence or reprints, contact Jeremie Calais (jcalais@mednet.ucla.edu).
Published online Apr. 25, 2024.

Nonrandomized studies that used PSMA PET/CT for staging before definitive radiotherapy (dRT) reported distant metastasis in 6%–9% of patients and findings that led to either radiation dose escalation or pelvic lymph node irradiation in 13%–20% of patients (*6–9*). However, the effect of PSMA PET/CT staging before dRT on clinical outcomes has not been well studied in a randomized controlled trial. Here, we discuss the results of the PSMA-dRT phase III randomized controlled trial.

MATERIALS AND METHODS

Study Population

The PSMA-dRT trial was a multicenter phase III randomized controlled trial (ClinicalTrials.gov identifier NCT04457245). This was an investigator-initiated trial supported by Progenics Pharmaceuticals Inc., conducted under investigational new drug application 147591. The UCLA institutional review board approved this study (approval 20-000378) and all subjects gave written informed consent. The study protocol (supplemental material, available at http://jnm.snmjournals.org) was previously published (*10*).

This study was designed to randomize 312 men with unfavorable intermediate- or high-risk prostate cancer 1.08:1 between receiving and not receiving a PSMA PET/CT scan. This randomization was chosen to account for an estimated detection rate of 8% for extrapelvic metastasis on PSMA PET/CT. Patients in the intervention arm who were found to have extrapelvic metastasis were no longer eligible for dRT and were not included in the primary endpoint analysis. In the intervention arm, reports and DICOM images of the PSMA PET/CT were transferred to the treating radiation oncologist before radiotherapy planning. In the control arm, patients were staged per physician discretion (CT, MRI, bone scanning, or PET/CT with a non-PSMA radiotracer).

Radiotherapy Delivery

Radiotherapy was delivered at the treating radiation oncologist's facility. The treating radiation oncologist decided on the radiation modality (external-beam radiotherapy, low-dose-rate brachytherapy, high-dose-rate brachytherapy, or external-beam radiotherapy with a brachytherapy boost), radiation dose, fractionation (conventionally fractionated, moderately hypofractionated, or stereotactic body radiotherapy),

inclusion of elective pelvic lymph nodes, and inclusion of androgen deprivation therapy.

Patient Follow-up

Patients had follow-up visits with the treating radiation oncologist every 3–4 mo for the first year and every 6 mo thereafter. Patients underwent prostate-specific antigen testing around the time of each follow-up visit. Imaging follow-up was ordered per physician discretion if disease progression was suspected on the basis of a rising prostate-specific antigen level.

Study Endpoints

The primary endpoint was progression-free survival (PFS) at 5 y. Progression was defined as whichever of the following occurred first: prostate-specific antigen level more than 2 ng/mL above the postradiotherapy nadir, recurrence on imaging or biopsy, initiation of salvage therapy, or death. Progression was calculated starting from the time of randomization.

Statistical Analysis

Differences in patient and treatment characteristics between the 2 cohorts were compared using the Pearson χ^2 test for categoric variables and 2-tailed t tests for continuous variables. PFS was calculated using Kaplan–Meier survival analysis. Comparisons were made using log rank testing. All statistical analyses were performed using SPSS Statistics, version 28 (IBM Corp.).

RESULTS

Between November 2020 and December 2021, 54 patients were randomized (PSMA PET/CT, $n = 25$; control, $n = 29$). Two patients withdrew after randomization and were excluded (Fig. 1). Table 1 describes patient and treatment characteristics. There were no significant differences between the 2 groups.

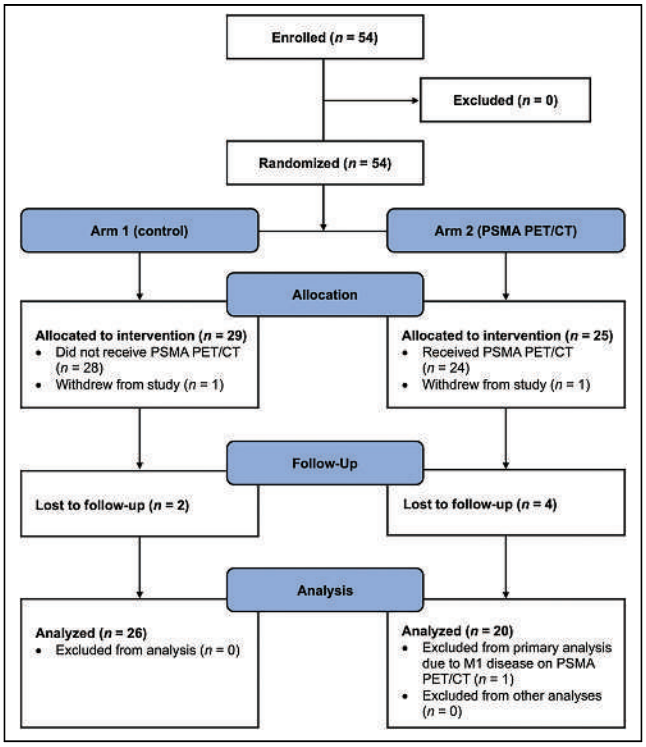

FIGURE 1. CONSORT (Consolidated Standards of Reporting Trials) flow diagram.

Among patients staged using PSMA PET/CT in the intervention arm ($n = 24$), 14 had localized disease (miT2b-cN0M0), 6 had locally advanced disease (miT3a-bN0M0), 3 had regional metastasis (miN1M0), and 1 had regional and distant metastasis (miN1M1b). Four were upstaged relative to baseline: 1 with locally advanced disease, 2 with regional metastasis, and 1 with distant metastasis.

All 3 patients with miN1M0 disease received pelvic lymph node irradiation. The patient with miN1M1b disease received upfront androgen deprivation therapy with abiraterone acetate and prednisone followed by consolidative radiotherapy to the prostate and pelvic lymph nodes.

After U.S. Food and Drug Administration approval of PSMA PET/CT radiotracers in 2021, patients gained access to PSMA PET/CT as a standard, medically reimbursed procedure. Consequently, the trial closed prematurely in February 2022 after the recruitment rate significantly decreased.

At the time of this analysis (August 2023), median follow-up was 21 mo (interquartile range, 17.6–26.3 mo). There were no cases of biochemical recurrence, disease recurrence, or prostate cancer–specific death in either arm. There were 2 nonprostate cancer deaths in the PSMA PET/CT arm. Two-year PFS was 93.8% for the PSMA PET/CT arm and 100% for the control arm. There were no significant differences between the 2 groups (Fig. 2, $P = 0.13$).

DISCUSSION

In this study of men with unfavorable intermediate- or high-risk prostate cancer, PSMA PET/CT upstaged 1 in 6 patients relative to baseline staging. This information guided target volume delineation, radiation dose, and hormone therapy intensification. This suggests that the adoption of PSMA PET/CT for primary staging in this patient population impacts management choices.

Unfortunately, this study was terminated prematurely after Food and Drug Administration approval of PSMA PET/CT radiotracers. Before Food and Drug Administration approval, there was significant interest in this trial among patients and enrolling physicians because of the otherwise significant hurdles to obtaining PSMA PET/CT. After Food and Drug Administration approval, most medical insurance companies in the United States covered PSMA PET/CT scans for primary staging of men with high-risk or unfavorable intermediate-risk prostate cancer, significantly reducing enrollment and the feasibility of the control arm.

As a result, this trial was closed after randomizing only 54 men, thus significantly reducing the statistical power of this study to detect a PFS difference. A second limitation is the low frequency of biochemical recurrence and disease progression in the first 2 y after dRT. Even in cohorts that include men with high-risk prostate cancer, reported 2-y rates are less than 5% (*11*). Thus, the only observed PFS events were 2 nonprostate cancer deaths in the PSMA PET/CT arm.

When examining upstaging rates of PSMA PET/CT compared with other imaging modalities, we found consistency with previously reported, prospective trials. The proPSMA study reported that PSMA PET/CT led to more frequent management changes than did conventional imaging (28% vs. 15%, $P = 0.008$) (*1*). A prospective, multicenter study in Australia by Roach et al. found that PSMA PET/CT changed management in 21% of cases (*9*). These are both similar to the 16.7% reported in our study.

Across multiple prospective studies, PSMA PET/CT has been shown to have superior accuracy and sensitivity for staging patients compared with conventional imaging. This information

TABLE 1
Patient and Treatment Characteristics

Characteristic	Control arm	PSMA PET/CT arm
All patients*		
Median age (y)	73.6	70.7
Race		
White	17 (58.6%)	16 (64.0%)
African American	2 (6.9%)	2 (8.0%)
Other	10 (34.5%)	7 (28.0%)
NCCN risk group		
Unfavorable intermediate risk	14 (48.3%)	11 (44.0%)
High risk	15 (51.7%)	14 (56.0%)
Median initial PSA (ng/mL)	8.4 (IQR, 4.9–20.5)	10.7 (IQR, 6.4–12.9)
Gleason score		
≤7	18 (62.1%)	13 (52.0%)
8	5 (17.2%)	4 (16.0%)
9–10	6 (20.7%)	8 (32.0%)
T stage by conventional imaging		
T1–2	25 (86.2%)	20 (80.0%)
T3–4	4 (13.8%)	5 (20.0%)
N stage by conventional imaging		
N0/Nx	27 (93.1%)	23 (92.0%)
N1	2 (6.9%)	2 (8.0%)
Conventional imaging performed		
CT	1 (3.4%)	1 (4.0%)
MRI	8 (27.6%)	7 (28.0%)
CT and MRI	3 (10.3%)	2 (8.0%)
Bone scan and CT	1 (3.4%)	1 (4.0%)
Bone scan and MRI	0 (0%)	3 (12.0%)
Bone scan, CT, and MRI	11 (37.9%)	10 (40.0%)
^{18}F-fluciclovine PET and MRI	4 (13.8%)	0 (0%)
^{18}F-fluciclovine PET, MRI, bone scan, and CT	1 (3.4%)	0 (0%)
^{18}F-fluciclovine PET, bone scan, and CT	0 (0%)	1 (4.0%)
Patients included in primary endpoint analysis†		
Concurrent ADT	21 (75.0%)	18 (75%)
Pelvic lymph node irradiation	7 (25.0%)	8 (33.3%)
PSMA PET/CT miTNM stage	—	
miT2bN0M0		10 (41.7%)
miT2cN0M0		4 (16.7%)
miT3aN0M0		4 (16.7%)
miT3bN0M0		2 (8.3%)
miT3aN1M0		3 (12.5%)
miT3bN1M1b		1 (4.2%)

*All patients in the study (n = 29 patients in the control arm and 25 patients in the PSMA PET/CT arm).
†Patients included in primary endpoint analysis (n = 28 patients in the control arm and 24 patients in the PSMA PET/CT arm).
NCCN = National Comprehensive Cancer Network; PSA = prostate-specific antigen; IQR = interquartile range; ADT = androgen deprivation therapy.
Data are number and percentage unless otherwise indicated.

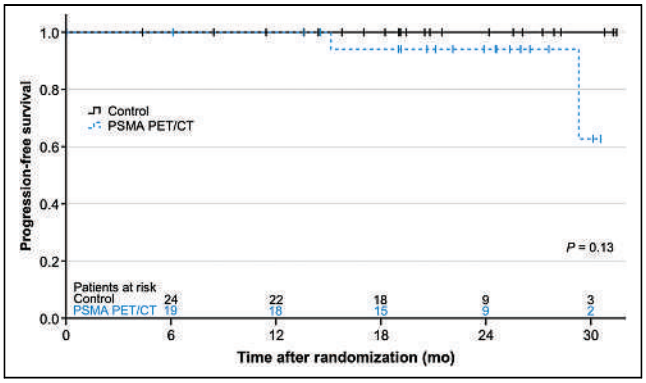

FIGURE 2. PFS: control and PSMA PET/CT cohorts were compared using log rank testing. Ticks represent censored cases. Patients with extrapelvic metastasis on PSMA PET/CT who were not eligible for dRT were excluded (1 patient).

can guide radiation volume delineation, radiation dose escalation, and hormone therapy intensification. The rapid adoption and availability of PSMA PET/CT staging has already changed prostate cancer treatment across the world. As a result of its success, the window to conduct prospective randomized controlled trials and show long-term clinical outcome benefits is closing. This raises questions about the expectations of the medical community to first demonstrate improved oncologic outcomes before widespread adoption. Including PSMA PET/CT staging in the design of future clinical trials is now warranted, and strong consideration must be given to how and whether PSMA PET/CT-based endpoints should be included as primary or secondary endpoints in clinical trials.

CONCLUSION

PSMA PET/CT upstaged 17% of patients, which allowed for more accurate radiotherapy planning. Unfortunately, this trial was underpowered to assess the effect of PSMA PET/CT on progression-free survival.

DISCLOSURE

This is an investigator-initiated trial with institutional funding (UCLA Ahmanson Translational Theranostics Division). This study is supported by Progenics Pharmaceuticals Inc., which supplies the study drug (^{18}F-DCFPyL) and financial support for the PET/CT technical costs associated with the study under the PyL Research Access Program (Progenics Pharmaceuticals, Inc.). John Nikitas received funding from the Christiaan W. Schiepers Theranostics Fellowship award. Jeremie Calais reported consulting fees from AAA, Astellas, Blue Earth Diagnostics, Curium Pharma, DS Pharma, EXINI, GE Healthcare, Isoray, IBA RadioPharma, Janssen, Lightpoint Medical, Lantheus, Monrol, Novartis, Progenics, POINT Biopharma, Radiomedix, Sanofi, and Telix Pharmaceuticals. Amar Kishan reported personal fees from ViewRay, Varian Medical Systems, and Janssen Pharmaceuticals and research funding from ViewRay. Boris Hadaschik reported serving on advisory boards for Janssen, Bayer, ABX, Lightpoint, Amgen, MSD, Pfizer, and Novartis; serving as an invited speaker for Accord, Astellas, and Janssen R&D; receiving honoraria from Uromed; receiving research support from AAA/Novartis, Bristol Myers Squibb, and the German Research Foundation; and having a leadership role with DKG, AUO, and DGU. Nicholas Nickols reported research grants from Janssen, Lantheus, and Bayer and personal fees from OncoLinea. Michael Steinberg reported receiving consulting fees from ViewRay. No other potential conflict of interest relevant to this article was reported.

KEY POINTS

QUESTION: What is the effect of performing PSMA PET/CT before dRT for prostate cancer?

PERTINENT FINDINGS: One in 6 patients was upstaged by PSMA PET/CT. This study closed early before completion of target enrollment (54/316, 17%) and was underpowered to assess the effect on PFS.

IMPLICATIONS FOR PATIENT CARE: Information from PSMA PET/CT can guide radiation volume delineation, radiation dose escalation, and hormone therapy intensification.

REFERENCES

1. Hofman MS, Lawrentschuk N, Francis RJ, et al. Prostate-specific membrane antigen PET-CT in patients with high-risk prostate cancer before curative-intent surgery or radiotherapy (proPSMA): a prospective, randomised, multicentre study. *Lancet.* 2020;395:1208–1216.
2. Hirmas N, Al-Ibraheem A, Herrmann K, et al. [^{68}Ga]PSMA PET/CT improves initial staging and management plan of patients with high-risk prostate cancer. *Mol Imaging Biol.* 2019;21:574–581.
3. Bluemel C, Krebs M, Polat B, et al. ^{68}Ga-PSMA-PET/CT in patients with biochemical prostate cancer recurrence and negative ^{18}F-choline-PET/CT. *Clin Nucl Med.* 2016;41:515–521.
4. Schwenck J, Rempp H, Reischl G, et al. Comparison of ^{68}Ga-labelled PSMA-11 and ^{11}C-choline in the detection of prostate cancer metastases by PET/CT. *Eur J Nucl Med Mol Imaging.* 2017;44:92–101.
5. Calais J, Ceci F, Eiber M, et al. ^{18}F-fluciclovine PET-CT and ^{68}Ga-PSMA-11 PET-CT in patients with early biochemical recurrence after prostatectomy: a prospective, single-centre, single-arm, comparative imaging trial. *Lancet Oncol.* 2019; 20:1286–1294.
6. Calais J, Kishan AU, Cao M, et al. Potential impact of ^{68}Ga-PSMA-11 PET/CT on the planning of definitive radiation therapy for prostate cancer. *J Nucl Med.* 2018; 59:1714–1721.
7. Frenzel T, Tienken M, Abel M, et al. The impact of [^{68}Ga]PSMA I&T PET/CT on radiotherapy planning in patients with prostate cancer. *Strahlenther Onkol.* 2018; 194:646–654.
8. Hruby G, Eade T, Emmett L, et al. ^{68}Ga-PSMA-PET/CT staging prior to definitive radiation treatment for prostate cancer. *Asia Pac J Clin Oncol.* 2018;14:343–346.
9. Roach PJ, Francis R, Emmett L, et al. The impact of ^{68}Ga-PSMSA PET/CT on management intent in prostate cancer: results of an Australian prospective multicenter study. *J Nucl Med.* 2018;59:82–88.
10. Calais J, Zhu S, Hirmas N, et al. Phase 3 multicenter randomized trial of PSMA PET/CT prior to definitive radiation therapy for unfavorable intermediate-risk or high-risk prostate cancer [PSMA dRT]: study protocol. *BMC Cancer.* 2021;21:512.
11. Ricco A, Barbera G, Lanciano R, et al. Favorable biochemical freedom from recurrence with stereotactic body radiation therapy for intermediate and high-risk prostate cancer: a single institutional experience with long-term follow-up. *Front Oncol.* 2020;10:1505.

True-Positive ^{18}F-Flotufolastat Lesions in Patients with Prostate Cancer Recurrence with Baseline-Negative Conventional Imaging: Results from the Prospective, Phase 3, Multicenter SPOTLIGHT Study

Mark T. Fleming[1], Rick Hermsen[2], Andrei S. Purysko[3], Albert Chau[4], Phillip Davis[5], Brian F. Chapin[6], David M. Schuster[7], and the SPOTLIGHT Study Group

[1]*Virginia Oncology Associates, US Oncology Network, Norfolk, Virginia;* [2]*Department of Nuclear Medicine, Canisius Wilhelmina Ziekenhuis, Nijmegen, The Netherlands;* [3]*Section of Abdominal Imaging and Nuclear Radiology Department, Cleveland Clinic, Cleveland, Ohio;* [4]*Blue Earth Diagnostics Ltd., Oxford, United Kingdom;* [5]*Blue Earth Diagnostics Inc., Monroe Township, New Jersey;* [6]*Department of Urology, University of Texas MD Anderson Cancer Center, Houston, Texas; and* [7]*Division of Nuclear Medicine and Molecular Imaging, Department of Radiology and Imaging Sciences, Emory University, Atlanta, Georgia*

^{18}F-rhPSMA-7.3 (^{18}F-flotufolastat) is a high-affinity prostate-specific membrane antigen–targeted diagnostic radiopharmaceutical for PET imaging in patients with prostate cancer. Here, we report findings from the SPOTLIGHT study (NCT04186845), assessing the performance of ^{18}F-flotufolastat PET/CT for identifying prostate-specific membrane antigen–positive lesions confirmed by standard of truth (SoT) in men with biochemical recurrence of prostate cancer and negative conventional imaging at baseline. **Methods:** Men with biochemical recurrence received 296 MBq of ^{18}F-flotufolastat intravenously and then underwent PET/CT 50–70 min later. ^{18}F-flotufolastat PET/CT findings were evaluated by 3 masked central readers and verified using histopathology or follow-up confirmatory imaging (CT, MRI, bone scan, or ^{18}F-fluciclovine PET/CT) as the SoT. The present analysis evaluated all patients who had negative conventional imaging at baseline, underwent ^{18}F-flotufolastat PET/CT, and had SoT verification by histopathology or follow-up confirmatory imaging to report detection rate (DR), which is the number of patients with at least 1 PET-positive lesion, divided by the number of evaluable patients, and verified DR (VDR), which is the proportion of patients with at least 1 true-positive lesion as verified by SoT, of all patients scanned (PET-positive and PET-negative scans). DR and VDR were calculated and stratified according to prior therapy. Majority read data (agreement between ≥2 readers) are reported. **Results:** In total, 171 patients with negative baseline conventional imaging and SoT by histopathology or post-PET confirmatory imaging were evaluated. By majority read, the overall ^{18}F-flotufolastat DR among these patients was 95% (163/171; 95% CI, 91.0%–98.0%), and 110 of 171 of these patients had at least 1 true-positive lesion identified (VDR, 64%; 95% CI, 56.7%–71.5%). In the postprostatectomy group (133/171), 8.3% of patients had at least 1 true-positive lesion in the prostate bed, 28% in pelvic lymph nodes, and 35% in other sites. Among those who had received radiotherapy (36/171), 50% of patients had true-positive detections in the prostate, 8.3% in pelvic lymph nodes, and 36% in other sites. **Conclusion:** ^{18}F-flotufolastat frequently identified true-positive prostate cancer lesions in patients with negative conventional imaging. ^{18}F-flotufolastat may help to better define sites of disease recurrence and inform salvage therapy decisions than does conventional imaging, potentially leading to improved outcomes.

Key Words: ^{18}F-flotufolastat; PSMA; rhPSMA; prostate cancer; biochemical recurrence

J Nucl Med 2024; 65:1080–1086
DOI: 10.2967/jnumed.123.267271

To effectively manage recurrent prostate cancer, it is essential to have accurate imaging techniques since the presence, volume, and distribution of disease will determine therapeutic choices (*1*). Prostate-specific membrane antigen (PSMA)–targeting radiopharmaceuticals have recently been included in the National Comprehensive Cancer Network, the American Society of Clinical Oncology guidelines, and the European guidelines for prostate cancer detection and selection for radiopharmaceutical therapy with PSMA-targeted agents, such as ^{177}Lu-PSMA-617 (*2–4*). PSMA-targeted PET radiopharmaceuticals such as ^{18}F-DCFPyL (^{18}F-piflufolastat; Pylarify; Lantheus) and ^{68}Ga-PSMA-11 offer improved sensitivity, specificity, and overall diagnostic accuracy compared with conventional imaging methods such as CT, MRI, and bone scintigraphy (*2,4*).

The PSMA-targeting radiopharmaceutical ^{18}F-flotufolastat (^{18}F-rhPSMA-7.3) has recently been approved by the U.S. Food and Drug Administration for diagnostic PET imaging of patients with unfavorable intermediate- and high-risk prostate cancer who are candidates for initial definitive therapy and for patients with suspected biochemical recurrence (BCR) based on elevated serum prostate-specific antigen (PSA) levels (*5*). ^{18}F-flotufolastat is a high-affinity PSMA-targeting PET radiopharmaceutical that is representative of a novel class of radiohybrid PSMA ligands that can be labeled with ^{18}F for diagnostic imaging or with α- or β-emitting radiometals for systemic radiation therapy (*6*). ^{18}F-flotufolastat is a single diastereoisomer of ^{18}F-rhPSMA-7 that shows high PSMA binding affinity and internalization by PSMA-expressing cells and

Received Dec. 21, 2023; revision accepted Mar. 26, 2024.
For correspondence or reprints, contact Mark T. Fleming (mark.fleming@usoncology.com).
Published online May 23, 2024.

a favorable diagnostic performance in patients with prostate cancer (*6–9*). ^{18}F-flotufolastat was selected for clinical development on the basis of preclinical assessments (*7*). Its favorable biodistribution profile in healthy volunteers and patients with prostate cancer (*10–12*) correlates with clinical data that show the low average urinary excretion of ^{18}F-flotufolastat does not impact image assessment for most patients (*13*). Primary data from the phase 3 SPOTLIGHT study (NCT04186845) show high detection rates (DRs) and standard-of-truth (SoT)–verified DRs (VDRs) with ^{18}F-flotufolastat for the accurate localization of recurrent prostate cancer across wide-ranging PSA values, alongside a favorable safety profile (*14–16*).

In this predefined exploratory analysis of the SPOTLIGHT study, we investigate the added clinical value of ^{18}F-flotufolastat PET/CT over conventional imaging and assess ^{18}F-flotufolastat PET/CT findings of local, nodal, and metastatic disease in patients with BCR and negative conventional imaging and patients who had SoT verification of PET/CT findings by histopathology or follow-up confirmatory imaging.

MATERIALS AND METHODS

Study Design and Patients

SPOTLIGHT was a phase 3, prospective, multicenter, open-label, single-arm study (*15*). As previously reported, the study protocol was approved by the independent ethics committee from each study site, and all patients provided written informed consent before enrollment (*15*). Men older than 18 y with previously treated and localized prostate cancer and a PSA level after radical prostatectomy (RP) (with or without radiotherapy) of at least 0.2 ng/mL (with confirmation), or nadir plus 2 ng/mL after radiotherapy, were eligible for inclusion if they were being considered for curative-intent salvage therapy (*15*).

Baseline Assessments

Recent conventional imaging was accepted if it had been collected 90 d or fewer before screening. If no conventional imaging was available, this was performed during the baseline assessments (primarily MRI, CT, bone scintigraphy, and ^{18}F-fluciclovine PET/CT) (*15*).

Imaging Procedures

^{18}F-flotufolastat PET/CT took place on day 1, as previously described (*15*). All PET/CT images were first read onsite to guide SoT verification activities before being sent for interpretation by 3 masked independent central readers. PET/CT findings were verified using histopathology or follow-up confirmatory imaging (CT, MRI, bone scan, or ^{18}F-fluciclovine PET/CT) as the SoT within 90 d after ^{18}F-flotufolastat PET/CT. When feasible, image-guided biopsies of suspected lesions identified by ^{18}F-flotufolastat PET/CT were performed within 60 d. A SoT consensus panel reviewed all available images using prespecified criteria (*15*).

Efficacy Endpoints

The overall patient-level DR was the number of patients with at least 1 PET-positive lesion divided by the number of patients with an evaluable PET scan. The VDR was the proportion of patients with at least 1 true-positive lesion verified by SoT, regardless of any coexisting false-positive lesions, of all patients scanned (including both PET-positive and PET-negative patients) (*15*). Any ^{18}F-flotufolastat PET-positive lesion not proven as a true-positive lesion by the SoT was categorized as a false-positive lesion by default. DR and VDR data were analyzed according to the patients' prior therapy and are presented at a patient level as well as by region: prostate or prostate bed, pelvic lymph nodes, or other (extrapelvic nodes, bone, viscera, and other soft tissues).

Statistical Analysis

The efficacy analysis population comprised all patients who underwent ^{18}F-flotufolastat imaging and had sufficient data for SoT determination (*15*). The present analysis focuses on patients in the efficacy analysis population who had negative conventional imaging at baseline and SoT confirmation through histopathology or follow-up confirmatory imaging. Imaging endpoints were summarized as point estimates (percentages) for the majority read (agreement between ≥2 readers), alongside 2-sided 95% CIs.

RESULTS

Patients

In total, 250 of 366 (68%) patients in the efficacy analysis population had negative conventional imaging at baseline. Of these patients, 171 of 250 (68%) had SoT determination based on histopathology (n = 46) or follow-up confirmatory imaging (n = 125) (Fig. 1). The baseline characteristics for these patients are provided in Table 1.

^{18}F-Flotufolastat–Positive Lesions in Patients with Negative Conventional Imaging

The overall ^{18}F-flotufolastat DR in patients with negative baseline imaging and post-PET SoT confirmation was 95% (163/171; 95% CI, 91.0%–98.0%) by majority read (Fig. 2; Supplemental Fig. 1; supplemental materials are available at http://jnm.snmjournals.org). The VDR was 64% (110/171; 95% CI, 56.7%–71.5%) (Fig. 2).

Regional ^{18}F-flotufolastat PET/CT DRs by majority read (Fig. 2; Supplemental Fig. 1) were 40% in the prostate or prostate bed, 39% in pelvic lymph nodes, and 47% in other sites. Verification of these lesions (predominantly by imaging) gave the following VDRs: 17%

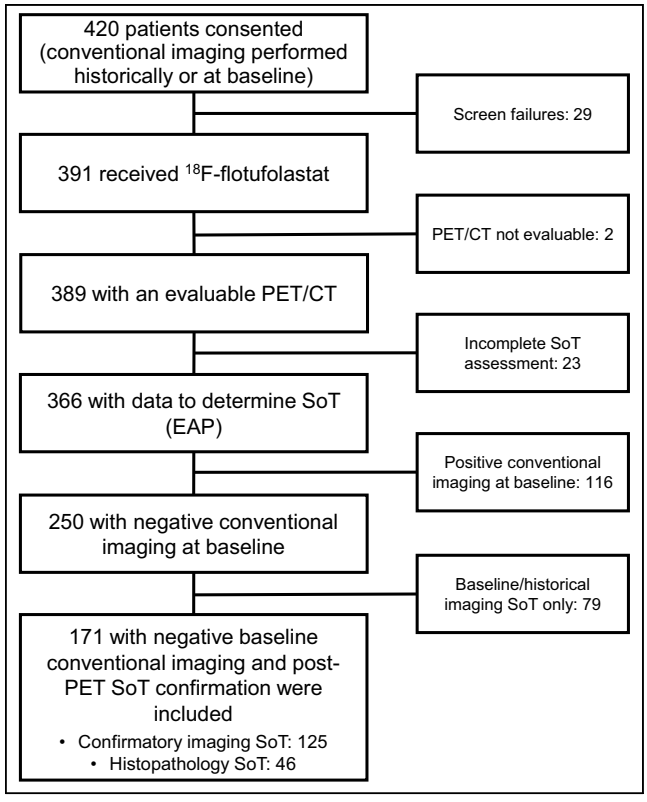

FIGURE 1. Standards for Reporting of Diagnostic Accuracy flow diagram of study participants. EAP = efficacy analysis population.

TABLE 1
Patient Baseline Characteristics and ^{18}F-Flotufolastat PET/CT and SoT Details

Parameter	Patients with negative baseline conventional imaging and post-PET SoT (n = 171)
Age (y)	69 (45–85)
Gleason score	
≤6	12 (7.0%)
7	101 (59%)
≥8	53 (31%)
Missing	5 (2.9%)
ISUP grade group	
1	12 (7.0%)
2	44 (26%)
3	52 (30%)
4	21 (12%)
5	32 (19%)
Missing	10 (5.8%)
Time from initial prostate cancer diagnosis (mo)	71 (2–409)
Prior therapy	
With prior prostatectomy	133 (78%)
With radiotherapy	67 (39%)
Without radiotherapy	66 (39%)
Without prior prostatectomy	38 (22%)
With radiotherapy	36 (21%)
With other therapy	2 (1.2%)
With no prior therapy	0 (0%)
Baseline PSA for all patients (ng/mL)	1.40 (0.20–48.70)
Patients with PSA <1 ng/mL	71 (42%)
Patients with PSA <2 ng/mL	95 (56%)
Baseline PSA for patients treated with prior prostatectomy with or without radiotherapy (ng/mL)*	0.85 (0.20–22.71)
Baseline PSA for patients treated with prior radiotherapy only (ng/mL)†	4.08 (1.11–48.70)‡
^{18}F-Flotufolastat	
Administered activity in MBq	306.3 (230.14–355.20)
Administered activity in mCi	8.28 (6.22–9.60)
SoT modality	
Histopathology	46 (27%)
Imaging only¶	125 (73%)
MRI	62 (36%)
CT	35 (20%)
Bone scan	5 (2.9%)
^{18}F-fluciclovine	37 (22%)

*Two patients received other therapies (n =133).
†Two patients received other therapies (n = 36).
‡One patient in SPOTLIGHT efficacy analysis population was found on reevaluation to have prescan PSA value that did not meet inclusion criterion. This patient was excluded from per-protocol population as previously reported (*15*).
¶Some patients were evaluated with more than 1 imaging technique.
ISUP = International Society of Urological Pathology.
Qualitative data are number and percentage. Continuous data are median and range.

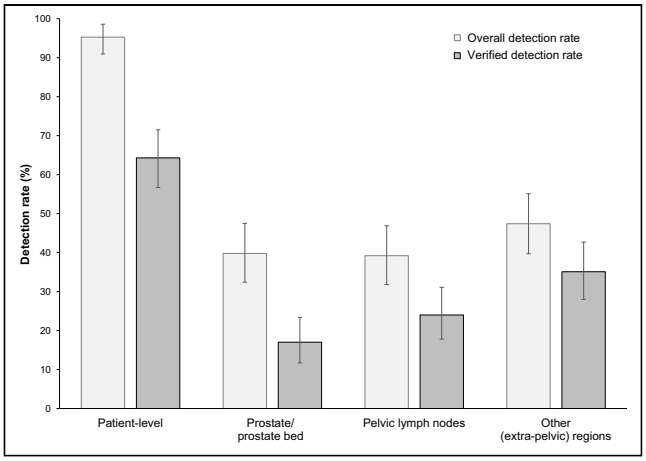

FIGURE 2. Patient- and region-level overall DRs and VDRs (majority read) for ^{18}F-flotufolastat PET/CT in patients with negative conventional imaging and post-PET SoT (n = 171).

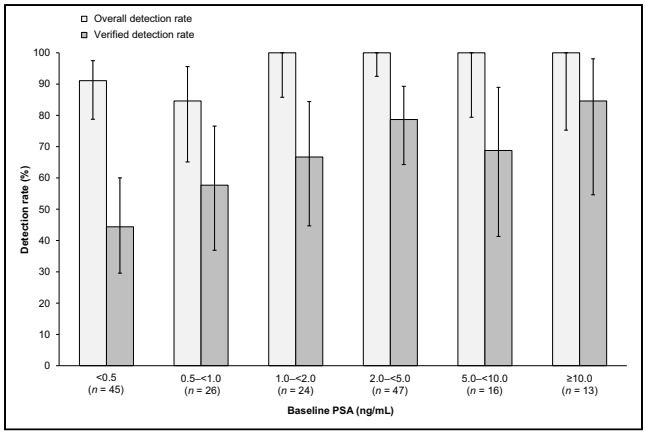

FIGURE 4. Patient- and region-level overall DRs and VDRs for ^{18}F-flotufolastat PET/CT (majority read) by baseline PSA category in patients with negative baseline conventional imaging and post-PET SoT.

in the prostate or prostate bed, 24% in pelvic lymph nodes, and 35% in other sites (Fig. 2).

^{18}F-Flotufolastat PET/CT DR by SoT Modality

In 46 of 171 patients (27%) who had histopathology data available for SoT, the overall DR and VDR were 98% and 80%, respectively. By region, the DR and VDR were 52% and 30% in the prostate or prostate bed, 39% and 28% in pelvic lymph nodes, and 52% and 41% in other sites, respectively (Fig. 3A).

In patients with post-PET confirmatory imaging SoT (125/171, 73%), the overall DR was 94% and the VDR was 58%. Regional DR and VDR were 35% and 12% in the prostate or prostate bed, 39% and 22% in pelvic lymph nodes, and 46% and 33% in other sites, respectively (Fig. 3B).

^{18}F-Flotufolastat PET/CT DR by Baseline PSA Category

Figure 4 shows the ^{18}F-flotufolastat PET/CT DR and VDR results by baseline PSA levels. Both DR and VDR broadly increased according to baseline PSA. DR ranged from 91% at a PSA of less than 0.5 ng/mL to 100% at a PSA of at least 1.0 ng/mL. VDR ranged from 44% to 85% across PSA categories, respectively.

^{18}F-Flotufolastat PET/CT DR by Prior Treatment

Overall DR and VDR were found to vary according to prior treatment (Figs. 5A and 5B). Among the patients treated with RP (n = 133), 33 (25%) had a histopathology SoT available and 100 (75%) had follow-up confirmatory imaging as the SoT. The patient-level DR among the patients with prior RP was 94%. The DR was 28% in the prostate bed, 44% in pelvic lymph nodes, and 47% in other sites (Fig. 5A). The patient-level VDR was 62%, and by region, the VDR was 8.3% in the prostate bed, 28% in pelvic lymph nodes, and 35% in other sites (Fig. 5A).

Among those patients who had received prior radiotherapy only (n = 36), 13 (36%) had a histopathology SoT and 23 (64%) had follow-up confirmatory imaging as the SoT. The overall DR for the patients with prior radiotherapy only was 100%. By region, the DR was 83% in the prostate, 22% in pelvic lymph nodes, and 47% in other sites (Fig. 5B). The overall VDR was 75%. The VDR was 50% in the prostate, 8.3% in pelvic lymph nodes, and 36% in other sites (Fig. 5B).

Very few patients had an alternative prior therapy (n = 2); therefore, no definitive conclusions could be drawn for them.

Figure 6 shows ^{18}F-flotufolastat PET/CT images from a patient in this cohort with BCR after radiotherapy (PSA, 1 ng/mL).

DISCUSSION

The prospective, phase 3, multicenter SPOTLIGHT study has reported the diagnostic utility of ^{18}F-flotufolastat PET/CT in men with BCR of prostate cancer (*15*). In this exploratory analysis, we assessed the ability of ^{18}F-flotufolastat PET/CT to identify true-positive (SoT-verified) lesions in the subgroup of SPOTLIGHT patients who had negative conventional imaging at baseline and sufficient data for SoT determination by histopathology or follow-up confirmatory imaging. Our data demonstrate a high likelihood of positive results from ^{18}F-flotufolastat PET/CT even when conventional imaging is negative.

Conventional imaging has limited utility for localizing recurrent disease, especially at low PSA levels. For instance, in patients with BCR after RP, only 11%–14% of patients have a positive CT scan (*4,17*), and previous studies have shown that the

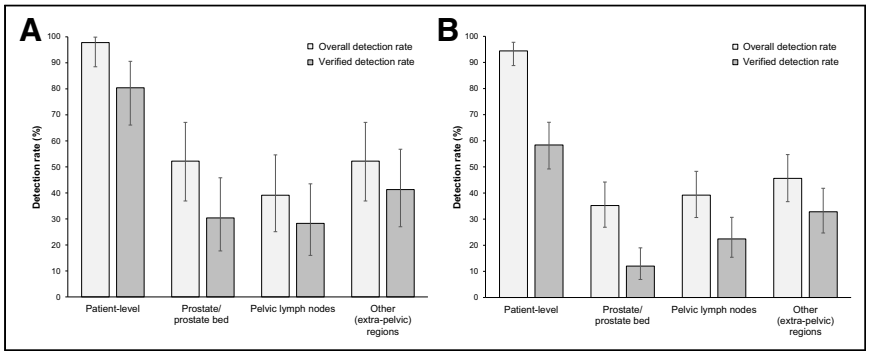

FIGURE 3. Patient- and region-level overall DRs and VDRs for ^{18}F-flotufolastat PET/CT (majority read) in patients with negative baseline conventional imaging and histopathology SoT (n = 46) (A) or post-PET imaging SoT (n = 125) (B).

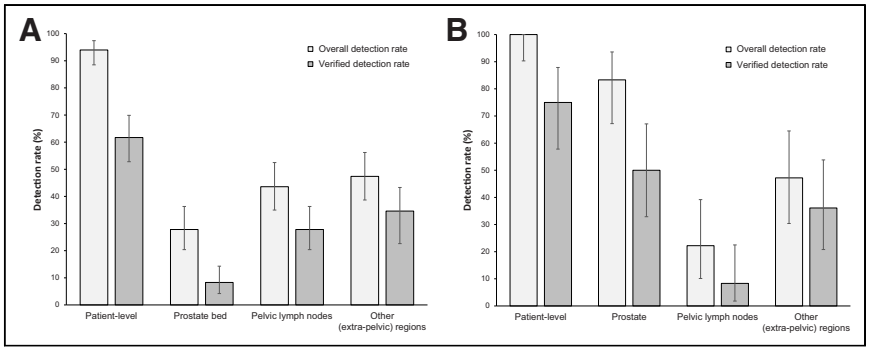

FIGURE 5. Patient- and region-level overall DRs and VDRs for ^{18}F-flotufolastat PET/CT (majority read) in patients with negative baseline conventional imaging and post-PET SoT treated with prior prostatectomy (n = 133) (A) or prior radiotherapy only (n = 36) (B).

mean PSA level associated with a positive CT scan can be as high as 27 ng/mL (*17,18*). Similarly, a positive bone scan is more likely at a PSA level of at least 20 ng/mL and unlikely at a PSA level of less than 7 ng/mL (*17,19*). PSMA-based PET offers sensitive imaging at low PSA levels (<0.5 ng/mL) and may help distinguish patients with local recurrence or locoregional spread from those with distant disease after RP, which may influence subsequent treatment choices, including salvage radiotherapy (*4*). In line with this, and because of the higher sensitivity and specificity of PSMA PET for the detection of micrometastatic disease, especially at low PSA levels, the current National Comprehensive Cancer Network and American Society of Clinical Oncology prostate cancer guidelines recommend PSMA PET (such as with ^{18}F-flotufolastat, ^{18}F-piflufolastat, or ^{68}Ga-PSMA-11-PET) as a front-line imaging tool for patients with BCR or during initial staging or as a work-up for progressive disease and patient selection for PSMA radiopharmaceutical therapy (*2,3*).

The SPOTLIGHT study reported an overall DR of 83% among 389 patients with BCR (PSA, 1.10 ng/mL; range, 0.03–134.6 ng/mL) (*15*). In our current analysis of patients with negative baseline imaging and post-PET SoT data (n = 171), the median baseline PSA value was 1.40 ng/mL, with 42% of patients having a PSA of less than 1.00 ng/mL. Our overall DR (95%) in these patients compares favorably with data for other PSMA PET radiopharmaceuticals. Data from the CONDOR study show an overall ^{18}F-piflufolastat DR of 59%–66% in patients with BCR and negative or equivocal standard-of-care imaging (*20*), and an overall DR of 75% has been reported for ^{68}Ga-PSMA-11 PET in patients with BCR (median PSA, 2.1 ng/mL), although these patients were included regardless of prior conventional imaging findings (*21*).

The overall DR in patients treated with prior radiotherapy (100%) was higher than that in patients who had prior RP (94%), and a similar pattern was observed in the prostate region. This is likely a reflection of higher baseline PSA levels in postradiotherapy patients (to meet the current criteria for BCR (*22*)). When DR and VDR for ^{18}F-flotufolastat PET/CT were analyzed by PSA category, the data indicated that both DR and VDR broadly increased according to baseline PSA (Fig. 4).

Although region-level DRs were moderate in some regions, likely because not every patient will have recurrent lesions in every region evaluated, the patient-level DR of 95% shows the high likelihood that ^{18}F-flotufolastat PET/CT will localize recurrent lesions among patients with suspected recurrence of prostate cancer, even in cases where conventional imaging is negative. Moreover, the use of the robust and new recommended metric by the U.S. Food and Drug Administration for BCR imaging trials, VDR, demonstrates how ^{18}F-flotufolastat PET/CT provides clinically meaningful information. The VDR of 64% observed across all patients with negative imaging at baseline indicates that ^{18}F-flotufolastat PET/CT enabled visualization of at least 1 true-positive lesion in nearly two thirds of patients that had been missed by conventional imaging. Accurate localization of these recurrent lesions can help inform patient management (*23,24*), which may result in improved outcomes (*25,26*).

It is worth noting that only follow-up conventional imaging (primarily MRI or bone and CT scans) was available as the SoT for most patients in this analysis (73%), rather than histopathology, which was available in only 27% of cases (at least partly due to the coronavirus disease 2019 pandemic); therefore, the VDR might partly be driven by false false-positive results due to a predominance of conventional imaging–only SoT; that is, a substantial proportion of false-positive lesions may have been proven to be true-positive lesions if histopathology had been available in a higher percentage of patients or if longer-term follow-up of these patients was available. In line with this, we show the VDR to be greater in patients with histopathology SoT than in patients with imaging SoT and closer to the overall DR, indicating that fewer PET-positive lesions are considered to be false-positive lesions

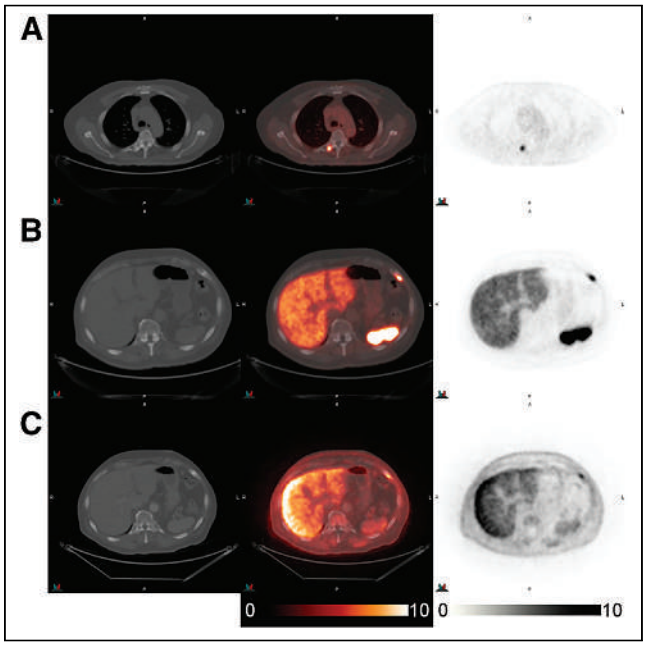

FIGURE 6. CT (left), fused ^{18}F-flotufolastat PET/CT (middle), and ^{18}F-flotufolastat PET (right) transverse images of 76-y-old patient initially presenting with high-risk prostate cancer (Gleason score, 4 + 5 = 9) and subsequently with BCR after radical prostatectomy (PSA, 1.0 ng/mL). ^{18}F-flotufolastat–avid focus was detected within mildly sclerotic right thoracic 5 transverse process (A) and was subsequently verified as true-positive by histopathology. In addition, ^{18}F-flotufolastat–avid lesion was detected in left seventh rib (B) and was also verified with ^{18}F-fluciclovine PET/CT (C).

when histopathology is used as the SoT. Currently, the National Comprehensive Cancer Network guidelines recommend histologic confirmation of any PET findings wherever possible to rule out false positives (*2*). Nonetheless, false positives are increasingly outweighed by the improved true-positive DR by PSMA PET imaging compared with conventional imaging (*2*), which has led to its recommendation over conventional imaging modalities for guiding treatment choices in patients with BCR (*2–4*).

CONCLUSION

The present findings from the SPOTLIGHT study show that ^{18}F-flotufolastat PET/CT frequently detects true-positive lesions among patients otherwise considered negative for recurrence by conventional imaging (particularly among patients with intact prostates). It may help to inform when to omit potentially toxic local treatment when finding multifocal metastatic disease. Such findings may help to better define sites of disease recurrence and inform salvage therapy decisions than is possible with conventional imaging alone.

DISCLOSURE

Mark Fleming has received travel expenses from Blue Earth Diagnostics. Rick Hermsen reports consultancy fees from Blue Earth Diagnostics and ABX GmbH. Andrei Purysko holds grants or contracts from the American College of Radiology, Blue Earth Diagnostics, and Koelis and has received consulting fees or honoraria from Blue Earth Diagnostics and Koelis. Albert Chau received consultancy fees from Blue Earth Diagnostics for data management and statistical services. Phillip Davis is an employee of Blue Earth Diagnostics. David Schuster has acted as a consultant for Global Medical Solutions Taiwan, Progenics Pharmaceuticals, Inc., Heidelberg University, and DuChemBio Co. Ltd.; participates through the Emory Office of Sponsored Projects in full compliance with Emory University sponsored research and conflict-of-interest regulations in sponsored grants including those funded or partially funded by Blue Earth Diagnostics, Nihon MediPhysics Co, Ltd., Telix Pharmaceuticals (US) Inc., Advanced Accelerator Applications, FUJIFILM Pharmaceuticals USA, Inc., Amgen Inc.; participates in educational initiatives with School of Breast Oncology and PrecisCa; and provides medicolegal consulting vetted through Emory SOM. This study was funded by Blue Earth Diagnostics Ltd., Oxford, U.K. No other potential conflict of interest relevant to this article was reported.

ACKNOWLEDGEMENTS

We gratefully acknowledge all participating institutions and their patients. Medical writing support was provided by Dr. Catriona Turnbull and Sandra Cusco (Blue Earth Diagnostics). The members of the SPOTLIGHT Study Group are Mohamad Allaf, Ryan J. Avery, Norbert Avril, Helen Barker, Laurence Belkoff, Peter Bostrom, Michael Cher, Diane Chisholm, Matthew F. Covington, Ian Cox, Giuseppe Esposito, Peter Gardiner, Benjamin A. Gartrell, David Gauden, Brian Helfand, Ashesh B. Jani, David Josephson, Matthew Kay, Bridget Koontz, Lale Kostakoglu, Phillip Kuo, William Lavely, Ing Han Liem, Mary Lokuta, Benjamin Lowentritt, Jeff Michalski, Matthew P. Miller, Karen Mourtzikos, Russell Pachynski, Ross Penny, Morand Piert, Soroush Rais-Bahrami, Gregory C. Ravizzini, Daniel Saltzstein, Bital Savir-Baruch, Barry A. Siegel, Rik Somford, Ashutosh Tewari, Przemyslaw Twardowski, Edward Uchio, Don Yoo, and Katherine Zukotynski.

KEY POINTS

QUESTION: Can ^{18}F-flotufolastat PET/CT detect lesions missed by conventional imaging in patients with suspected recurrence of prostate cancer?

PERTINENT FINDINGS: In patients with negative baseline conventional imaging, the overall ^{18}F-flotufolastat PET/CT DR was 95%, and 110 of 171 of these patients had at least 1 true-positive lesion verified by histopathology or follow-up confirmatory imaging (VDR, 64%). Overall DR and VDR varied according to the SoT modality and by prior therapy, with higher VDRs in patients with histopathology and in men treated with prior radiotherapy only. ^{18}F-flotufolastat PET/CT showed high levels of detection across a range of PSA values, including in patients with PSA levels less than 0.5 ng/mL.

IMPLICATIONS FOR PATIENT CARE: As ^{18}F-flotufolastat PET/CT frequently identifies true-positive lesions in patients with negative conventional imaging, it is a useful tool to accurately identify sites of disease recurrence and inform subsequent treatment decisions, potentially improving patient outcomes.

REFERENCES

1. Padhani AR, Lecouvet FE, Tunariu N, et al. Rationale for modernising imaging in advanced prostate cancer. *Eur Urol Focus.* 2017;3:223–239.
2. Schaeffer EM, Srinivas S, Adra N, et al. Prostate cancer, version 4.2023, NCCN clinical practice guidelines in oncology. *J Natl Compr Canc Netw.* 2023;21:1067–1096.
3. Garje R, Rumble RB, Parikh RA, et al. Systemic therapy update on ^{177}lutetium-PSMA-617 for metastatic castration-resistant prostate cancer: ASCO guideline rapid recommendation update. *J Clin Oncol.* 2023;11:JCO2302128.
4. Mottet N, Cornford P, van den Bergh RCN, et al. EAU-EANM-ESTRO-ESUR-ISUP-SIOG guidelines on prostate cancer. EAU website. https://d56bochluxqnz.cloudfront.net/documents/full-guideline/EAU-EANM-ESTRO-ESUR-ISUP-SIOG-Guidelines-on-Prostate-Cancer-2023_2023-06-13-141145_owmj.pdf. Updated 2023. Accessed April 19, 2024.
5. Highlights of prescribing information: POSLUMA (flotufolastat F 18) injection. U.S. Food and Drug Administration website. https://www.accessdata.fda.gov/drugsatfda_docs/label/2023/216023s000lbl.pdf. Revised May 2023. Accessed April 19, 2024.
6. Wurzer A, DiCarlo D, Schmidt A, et al. Radiohybrid ligands: a novel tracer concept exemplified by ^{18}F- or ^{68}Ga-labeled rhPSMA inhibitors. *J Nucl Med.* 2020;61:735–742.
7. Wurzer A, Parzinger M, Konrad M, et al. Preclinical comparison of four [^{18}F,^{nat}Ga]rhPSMA-7 isomers: influence of the stereoconfiguration on pharmacokinetics. *EJNMMI Res.* 2020;10:149.
8. Eiber M, Kronke M, Wurzer A, et al. ^{18}F-rhPSMA-7 positron emission tomography for the detection of biochemical recurrence of prostate cancer following radical prostatectomy. *J Nucl Med.* 2020;61:696–701.
9. Chantadisai M, Buschner G, Kronke M, et al. Positive predictive value and correct detection rate of ^{18}F-rhPSMA-7 PET in biochemically recurrent prostate cancer validated by composite reference standard. *J Nucl Med.* 2021;62:968–974.
10. Tolvanen T, Kalliokoski KK, Malaspina S, et al. Safety, biodistribution, and radiation dosimetry of ^{18}F-rhPSMA-7.3 in healthy adult volunteers. *J Nucl Med.* 2021;62:679–684.
11. Malaspina S, Oikonen V, Kuisma A, et al. Kinetic analysis and optimisation of ^{18}F-rhPSMA-7.3 PET imaging of prostate cancer. *Eur J Nucl Med Mol Imaging.* 2021;48:3723–3731.
12. Malaspina S, Taimen P, Kallajoki M, et al. Uptake of ^{18}F-rhPSMA-7.3 in PET imaging of prostate cancer: a phase 1 proof-of-concept study. *Cancer Biother Radiopharm.* 2022;37:205–213.
13. Kuo PH, Hermsen R, Penny R, Postema EJ. Quantitative and qualitative assessment of urinary activity of ^{18}F-flotufolastat-PET/CT in patients with prostate

cancer: a post hoc analysis of the LIGHTHOUSE and SPOTLIGHT studies. *Mol Imaging Biol.* 2024;26:53–60.
14. Lowentritt B. Impact of clinical factors on ^{18}F-rhPSMA-7.3 detection rates in men with recurrent prostate cancer: findings from the phase 3 SPOTLIGHT study [abstract]. *Int J Radiat Oncol Biol Phys.* 2022;114(suppl 3):S130–S131.
15. Jani AB, Ravizzini G, Gartrell BA, et al. Diagnostic performance and safety of ^{18}F-rhPSMA-7.3 PET in men with suspected prostate cancer recurrence: results from a phase 3, prospective, multicenter study (SPOTLIGHT). *J Urol.* 2023;210: 299–311.
16. Jani AB, Michalski JM, Chapin B, Schuster DM. Detection rate of ^{18}F-rhPSMA-7.3 PET in patients with suspected prostate cancer recurrence at PSA levels <1 ng/mL: data from the phase 3 SPOTLIGHT study [abstract]. *Int J Radiat Oncol Biol Phys.* 2023;40(suppl 6):S35–S36.
17. Beresford MJ, Gillatt D, Benson RJ, Ajithkumar T. A systematic review of the role of imaging before salvage radiotherapy for post-prostatectomy biochemical recurrence. *Clin Oncol (R Coll Radiol).* 2010;22:46–55.
18. Kane CJ, Amling CL, Johnstone PA, et al. Limited value of bone scintigraphy and computed tomography in assessing biochemical failure after radical prostatectomy. *Urology.* 2003;61:607–611.
19. Gomez P, Manoharan M, Kim SS, Soloway MS. Radionuclide bone scintigraphy in patients with biochemical recurrence after radical prostatectomy: when is it indicated? *BJU Int.* 2004;94:299–302.
20. Morris MJ, Rowe SP, Gorin MA, et al. Diagnostic performance of ^{18}F-DCFPyL-PET/CT in men with biochemically recurrent prostate cancer: results from the CONDOR phase III, multicenter study. *Clin Cancer Res.* 2021;27:3674–3682.
21. Fendler WP, Calais J, Eiber M, et al. Assessment of ^{68}Ga-PSMA-11 PET accuracy in localizing recurrent prostate cancer: a prospective single-arm clinical trial. *JAMA Oncol.* 2019;5:856–863.
22. Roach M, Hanks G, Thames H, et al. Defining biochemical failure following radiotherapy with or without hormonal therapy in men with clinically localized prostate cancer: recommendations of the RTOG-ASTRO Phoenix Consensus Conference. *Int J Radiat Oncol Biol Phys.* 2006;65:965–974.
23. Gulhane A, Lin D, Dash A, et al. [^{68}Ga]-PSMA-11 can clarify equivocal lesions on conventional imaging and change management decisions among men with previously treated prostate cancer [abstract]. *J Nucl Med.* 2022;63(suppl 2):3065.
24. Pozdnyakov A, Kulanthaivelu R, Bauman G, Ortega C, Veit-Haibach P, Metser U. The impact of PSMA PET on the treatment and outcomes of men with biochemical recurrence of prostate cancer: a systematic review and meta-analysis. *Prostate Cancer Prostatic Dis.* 2023;26:240–248.
25. Bianchi L, Ceci F, Balestrazzi E, et al. PSMA-PET guided treatment in prostate cancer patients with oligorecurrent progression after previous salvage treatment. *Cancers (Basel).* 2023;15:2027.
26. Mohan R, Kneebone A, Eade T, et al. Long-term outcomes of SBRT for PSMA PET detected oligometastatic prostate cancer. *Radiat Oncol.* 2023;18:127.

Receptor-Targeted Peptide Conjugates Based on Diphosphines Enable Preparation of ^{99m}Tc and ^{188}Re Theranostic Agents for Prostate Cancer

Truc T. Pham*[1], Ingebjørg N. Hungnes*[1], Charlotte Rivas[1], Julie Cleaver[2], George Firth[1], Philip J. Blower[1], Jane Sosabowski[2], Gary J.R. Cook[1], Lefteris Livieratos[1,3], Jennifer D. Young[1,2], Paul G. Pringle[4], and Michelle T. Ma[1]

[1]*School of Bioengineering and Imaging Sciences, St. Thomas' Hospital, King's College London, London, United Kingdom;* [2]*Centre for Cancer Biomarkers and Biotherapeutics, Barts Cancer Institute, John Vane Science Centre, Queen Mary University of London, London, United Kingdom;* [3]*Department of Nuclear Medicine, Guy's and St. Thomas' Hospitals NHS Foundation Trust, Guy's Hospital, London, United Kingdom; and* [4]*School of Chemistry, University of Bristol, Bristol, United Kingdom*

Benchtop ^{99}Mo/^{99m}Tc and ^{188}W/^{188}Re generators enable economical production of molecular theranostic ^{99m}Tc and ^{188}Re radiopharmaceuticals, provided that simple, kit-based chemistry exists to radiolabel targeting vectors with these radionuclides. We have previously described a diphosphine platform that efficiently incorporates ^{99m}Tc into receptor-targeted peptides. Here, we report its application to label a prostate-specific membrane antigen (PSMA)–targeted peptide with ^{99m}Tc and ^{188}Re for diagnostic imaging and systemic radiotherapy of prostate cancer. **Methods:** Two diphosphine-dipeptide bioconjugates, DP1-PSMAt and DP2-PSMAt, were formulated into kits for radiolabeling with ^{99m}Tc and ^{188}Re. The resulting radiotracers were studied in vitro, in prostate cancer cells, and in vivo in mouse xenograft models, to assess similarity of uptake and biodistribution for each ^{99m}Tc/^{188}Re pair of agents. **Results:** Both DP1-PSMAt and DP2-PSMAt could be efficiently radiolabeled with ^{99m}Tc and ^{188}Re using kit-based methods to furnish the isostructural compounds M-DP1-PSMAt and M-DP2-PSMAt (M = [^{99m}Tc]Tc, [^{188}Re]Re). All ^{99m}Tc/^{188}Re radiotracers demonstrated specific uptake in PSMA-expressing prostate cancer cells, with negligible uptake in prostate cancer cells that did not express PSMA or in which PSMA uptake was blocked. M-DP1-PSMAt and M-DP2-PSMAt also exhibited high tumor uptake (18–30 percentage injected dose per gram at 2 h after injection), low retention in nontarget organs, fast blood clearance, and excretion predominantly via a renal pathway. Importantly, each pair of ^{99m}Tc/^{188}Re radiotracers showed near-identical biologic behavior in these experiments. **Conclusion:** We have prepared and developed novel pairs of isostructural PSMA-targeting ^{99m}Tc/^{188}Re theranostic agents. These generator-based theranostic agents have potential to provide access to the benefits of PSMA-targeted diagnostic imaging and systemic radiotherapy in health care settings that do not routinely have access to either reactor-produced ^{177}Lu radiopharmaceuticals or PET/CT infrastructure.

Key Words: ^{99m}Tc; ^{188}Re; SPECT; phosphine; PSMA

J Nucl Med 2024; 65:1087–1094
DOI: 10.2967/jnumed.124.267450

The PSMAt peptide, which targets the prostate-specific membrane antigen (PSMA), has had clinical impact as a vector for delivering radionuclides to prostate cancer for diagnostic imaging and systemic peptide receptor radionuclide therapy (PRRT). The radiopharmaceutical [^{177}Lu]Lu-PSMA-617 (*1*,*2*) has recently been approved by the Food and Drug Administration for PRRT of metastatic castration-resistant prostate cancer. Diagnostic PET imaging with [^{68}Ga]Ga-PSMA-11 can inform clinical decision-making for treatment of prostate cancer, and [^{68}Ga]Ga-PSMA-11 is widely used as a diagnostic companion to [^{177}Lu]Lu-PSMA-617 (*3*). PSMA-targeted radiopharmaceuticals for SPECT/γ-scintigraphy imaging, such as [^{99m}Tc]Tc-MIP-1404 (*4*,*5*), [^{99m}Tc]Tc-PSMA-I&S (*6*,*7*), and [^{99m}Tc]Tc-EDDA/HYNIC-iPSMA (*8*,*9*), have been developed as alternatives to ^{68}Ga to enhance access to PSMA scanning when ^{68}Ga and PET are less accessible but generator-based ^{99m}Tc and SPECT/γ-scintigraphy cameras are available. Although these ^{99m}Tc (half-life of 6 h, 90% γ, 140 keV) radiotracers exhibit lower sensitivity than PSMA-targeted PET radiotracer alternatives, particularly in the case of biochemical recurrence of prostate cancer at low PSA levels or low tumor volumes, they have potential utility in providing useful diagnostic information at high tumor volumes, assessing suitability for and response to PRRT and radioguided surgery for which detection of every site of small volume of disease is less critical (*4*,*7*,*8*).

A range of radiometal ions with therapeutically efficacious emission profiles (e.g.,^{225}Ac, ^{227}Th, ^{212}Pb, and ^{161}Tb) has been used as alternatives to ^{177}Lu. However, in lower- and middle-income countries (LMICs), the availability of PRRT is limited by cost. The batch-produced radiopharmaceuticals that prevail in high-income countries are prohibitively expensive and are available only to the wealthiest patients in LMICs. Additionally, the availability of PET infrastructure, including cyclotrons and scanners, in LMICs is limited (*10*).

The chemistry of rhenium is closely similar to that of its lighter congener technetium. Importantly, β^--emitting ^{188}Re (half-life of 17 h, 100% β^-, 2.12 MeV, 15% γ, 155 keV) is available from a benchtop ^{188}W/^{188}Re generator, offering hospitals an economical and routinely accessible source of a therapeutic radionuclide. Radiopharmaceuticals based on the theranostic ^{99m}Tc/^{188}Re pair offer

Received Jan. 22, 2024; revision accepted Apr. 29, 2024.
For correspondence or reprints, contact Truc T. Pham (truc.pham@kcl.ac.uk) or Michelle T. Ma (michelle.ma@kcl.ac.uk).
*Contributed equally to this work.
Published online Jun. 6, 2024.

a potentially viable solution to economic and geographic barriers posed by existing theranostic PRRT (*11*–*13*). Traditional ^{99m}Tc-radiopharmaceuticals are used in 30 million scans worldwide per year, including in LMICs, in combination with γ-scintigraphy (*10*,*14*). Additionally, international consortia have identified ^{188}Re as a highly promising basis for systemic radiotherapy in LMICs: recognizing the affordability of ^{188}Re, the International Atomic Energy Agency has sponsored multinational clinical trials of ^{188}Re-labeled Lipiodol for treatment of inoperable liver cancer in LMICs (*11*). ^{188}Re-labeled Lipiodol proved effective and inexpensive. ^{188}Re-labeled bisphosphonates have also been extremely beneficial in palliative treatment of bone metastases in LMICs (*15*). There is high potential for the combination of ^{99m}Tc with ^{188}Re to provide economical, population-wide access to stratified molecular imaging and PRRT in LMICs, provided that suitable chemical platforms are available to enable radiochemical production of well-defined pairs of theranostic ^{99m}Tc/^{188}Re agents.

A new theranostic pair of ^{99m}Tc/^{188}Re-labeled peptide radiotracers has recently demonstrated preclinical and clinical PSMA-targeting efficacy in prostate cancer (*16*), highlighting the potential utility of this theranostic approach. We have contemporaneously developed 2 kit-based ^{99m}Tc-radiolabeled agents, [^{99m}Tc]Tc-DP1-PSMAt and [^{99m}Tc]Tc-DP2-PSMAt (Fig. 1; Supplemental Chart 1; supplemental materials are available at http://jnm.snmjournals.org.), targeting PSMA and reported their chemical properties (*17*). These compounds are based on a diphosphine chelator (*18*), which also coordinates Re^V: we have used analogous nonradioactive Re^V derivatives to chemically characterize the radioactive Tc^V compounds (*17*–*19*). Here, we report the preparation of isostructural and isoelectronic ^{188}Re-labeled derivatives ([^{188}Re]Re-DP1-PSMAt and [^{188}Re]Re-DP2-PSMAt), the biologic behavior of the novel ^{99m}Tc radiotracers in prostate cancer models, and the comparative biologic behavior of ^{188}Re compounds.

MATERIALS AND METHODS

^{188}Re Radiolabeling

[^{188}Re]Re^V-citrate was prepared from a saline solution of preconcentrated (*13*) [^{188}Re]ReO_4^- in more than 95% yield (*20*,*21*). An aliquot of this solution (75 μL) was added to a DP1-PSMAt kit or DP2-PSMAt kit (Supplemental Table 1), which was heated at 90°C for 30 min. The reaction solution was then analyzed by C18 radio–high-performance liquid chromatography (HPLC). [^{188}Re]Re-DP1-PSMAt eluted at 12.7 min, and [^{188}Re]Re-DP2-PSMAt eluted at 17.5 min (Supplemental Fig. 1). The reaction mixtures, containing either [^{188}Re]Re-DP1-PSMAt or [^{188}Re]Re-DP2-PSMAt, were purified and reformulated for biologic experiments.

^{99m}Tc and ^{188}Re Radiotracer Uptake in Prostate Cancer Cells

Solutions containing radiotracer (100 kBq in 8–12 μL of phosphate-buffered saline, >95% radiochemical purity) were added to DU145-PSMA+ or LNCaP prostate cancer cells (*22*), and the cells were incubated at 37°C for 1 h. Nonspecific uptake was determined using non–PSMA-expressing cells (DU145, PC3) or by blocking PSMA-expressing cells (DU145-PSMA+, LNCaP) with 2-phosphonomethyl pentanedioic acid (PMPA). After incubation, the cells were washed and samples collected for radioactivity counting. Uptake and localization of ^{99m}Tc radiotracers were measured over time (15, 30, 60, and 120 min) in DU145-PSMA+ or LNCaP cells (supplemental materials).

SPECT/CT Scanning and Biodistribution Studies in Mice

All animal experiments were ethically reviewed by an Animal Welfare and Ethical Review Board at either King's College London or Barts Cancer Institute and were performed in accordance with the Animals (Scientific Procedures) Act 1986 U.K. Home Office regulations governing animal experimentation. Subcutaneous prostate cancer DU145-PSMA+ or DU145 xenografts were produced in SCID/beige mice (male, 7–12 wk old). Subcutaneous LNCaP prostate cancer xenografts were produced in athymic nude mice (Crl:NU(NCr)-*Foxn1*^{nu}, male, 6–7 wk old). SPECT/CT and biodistribution studies using ^{99m}Tc and ^{188}Re radiotracers were performed once a tumor had reached an appropriate size (supplemental materials).

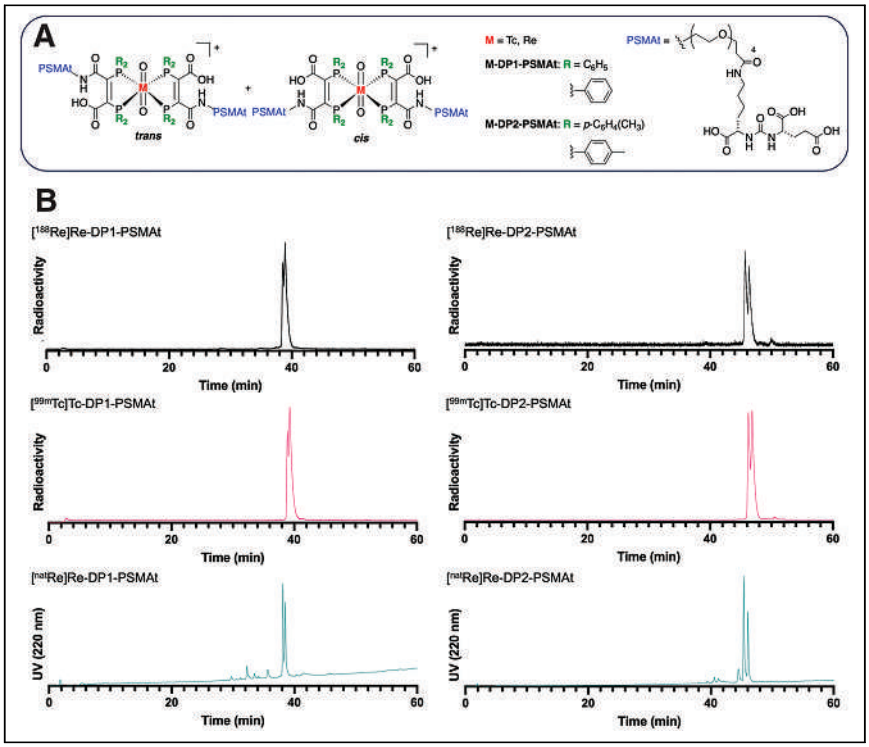

FIGURE 1. (A) Chemical structures of M-DP1-PSMAt and M-DP2-PSMAt, M = Tc (^{99m}Tc or ^{99g}Tc) and Re (^{nat}Re or ^{188}Re). (B) Reverse-phase C18-HPLC radiochromatograms showing coelution of [^{188}Re]Re-DP1-PSMAt, [^{99m}Tc]Tc-DP1-PSMAt, and [^{nat}Re]Re-DP1-PSMAt and coelution of [^{188}Re]Re-DP2-PSMAt, [^{99m}Tc]Tc-DP2-PSMAt, and [^{nat}Re]Re-DP2-PSMAt. UV = ultraviolet.

RESULTS

Preparation of [^{188}Re]Re-DP1-PSMAt and [^{188}Re]Re-DP2-PSMAt

We have previously prepared [^{99m}Tc]Tc-DP1-PSMAt and [^{99m}Tc]Tc-DP2-PSMAt using a single-step radiolabeling kit (*17*). Here, the analogous ^{188}Re agents were prepared in 2 steps from a saline solution containing [^{188}Re]ReO_4^-, obtained from a ^{188}W/^{188}Re OncoBeta generator. In the first step, [^{188}Re]ReO_4^- was reduced to a [^{188}Re]Re^V-citrate precursor: an aqueous solution containing [^{188}Re]ReO_4^- (~300–500 MBq), sodium citrate, and stannous chloride ($SnCl_2$), at pH 5.5, was heated at 90°C for 30 min, to give [^{188}Re]Re^V-citrate in more than 95% yield, as previously

described (*20,21*). After this, [^{188}Re]Re^{V}-citrate (~130–210 MBq) was added to a prefabricated, lyophilized kit (Supplemental Table 1) containing sodium carbonate, sodium tartrate, $SnCl_2$, and either DP1-PSMAt or DP2-PSMAt. The resulting radiolabeling solution (pH 8.0–8.5) was heated at 90°C for 30 min to form [^{188}Re]Re-DP1-PSMAt in 20%–70% radiochemical yield and [^{188}Re]Re-DP2-PSMAt in 20%–50% radiochemical yield (as determined by radio-HPLC): whereas formation of the desired products was reproducible, yields were not.

[^{188}Re]Re-DP1-PSMAt and [^{188}Re]Re-DP2-PSMAt were subsequently isolated using reverse-phase HPLC, lyophilized, and then reconstituted in phosphate-buffered saline to yield the radiotracers in more than 95% radiochemical purity. The purified ^{188}Re compounds were analyzed by reverse-phase radio-HPLC. Each ^{188}Re compound coeluted with its nonradioactive ^{nat}Re isotopolog and radioactive ^{99m}Tc analog (*17*), confirming not only the chemical identity of these new ^{188}Re agents but also that they are isostructural and isoelectronic with their ^{99m}Tc analogs (Fig. 1). Each rhenium and technetium compound consists of 2 closely eluting isomers, *cis*- and *trans*-$[M^{V}O_2(DPX\text{-}PSMAt)_2]^{+}$ (M = Re or Tc, X = 1 or 2) (*17*). The *cis* and *trans* designations denote the relative positions of the PSMAt moieties.

Solutions of each new ^{188}Re radiotracer were added to human serum and incubated at 37°C for 24 h followed by analysis by reverse-phase analytic radio-HPLC, which demonstrated that [^{188}Re]Re-DP1-PSMAt and [^{188}Re]Re-DP2-PSMAt are stable, with more than 95% each radiotracer, respectively, observed intact in human serum over this time frame (Supplemental Fig. 2).

Uptake of ^{99m}Tc and ^{188}Re Agents in Prostate Cancer Cells

To assess the specificity of the new radiotracers for PSMA, [^{99m}Tc]Tc-DP1-PSMAt and [^{99m}Tc]Tc-DP2-PSMAt (100 kBq) were each incubated with DU145-PSMA+ prostate cancer cells (DU145 cells transfected to express PSMA receptor) (*22*). After 1 h of incubation, uptake of each radiotracer was quantified. To assess specificity, each radiotracer was also coincubated with the PSMA inhibitor PMPA with DU145-PSMA+ cells and incubated with parental DU145 cells that do not express PSMA. [^{99m}Tc]Tc-DP1-PSMAt and [^{99m}Tc]Tc-DP2-PSMAt exhibited uptake in DU145-PSMA+ cells (12.4 ± 2.8 percentage added radioactivity [%AR] and 7.8 ± 1.3 %AR, respectively). This uptake was specific: DU145-PSMA+ cell uptake of [^{99m}Tc]Tc-DP1-PSMAt and [^{99m}Tc]Tc-DP2-PSMAt could be blocked with PMPA, and there was negligible uptake in parental DU145 cells (Fig. 2). The uptake of [^{99m}Tc]Tc-DP1-PSMAt and [^{99m}Tc]Tc-DP2-PSMAt was also studied in LNCaP prostate cancer cells, which natively express PSMA, and PC3 cells, which, like parental DU145 cells, do not express PSMA. In LNCaP cells, uptake of [^{99m}Tc]Tc-DP1-PSMAt and [^{99m}Tc]Tc-DP2-PSMAt measured 3.7 ± 1.2 %AR and 3.0 ± 0.8 %AR, respectively, whereas uptake of both radiotracers in PC3 cells measured less than 0.3 %AR. Uptake in LNCaP cells could also be blocked with PMPA.

The cellular localization of [^{99m}Tc]Tc-DP1-PSMAt and [^{99m}Tc]Tc-DP2-PSMAt was also evaluated in DU145-PSMA+ and LNCaP cells over time (Fig. 2). Uptake of both radiotracers increased over 2 h, and most cell-associated radioactivity was found in the internalized cell fraction at all measured time points for both PSMA-expressing cell lines. Uptake of [^{99m}Tc]Tc-DP1-PSMAt (both surface-bound and internalized radioactivity) was slightly higher than that of [^{99m}Tc]Tc-DP2-PSMAt.

Additionally, the uptake of [^{188}Re]Re-DP1-PSMAt and [^{188}Re] Re-DP2-PSMAt (100 kBq) was also assessed in the above-mentioned prostate cancer cell lines: both radiotracers exhibited uptake in DU145-PSMA+ cells (13.5 ± 2.7 %AR and 8.3 ± 0.7 %AR, respectively) and LNCaP cells (2.8 ± 1.6 %AR and 2.6 ± 1.6 %AR, respectively). This uptake was also specific: uptake of [^{188}Re]Re-DP1-PSMAt and [^{188}Re]Re-DP2-PSMAt could be blocked with PMPA, and there was negligible uptake in parental DU145 cells and PC3 cells (Fig. 2).

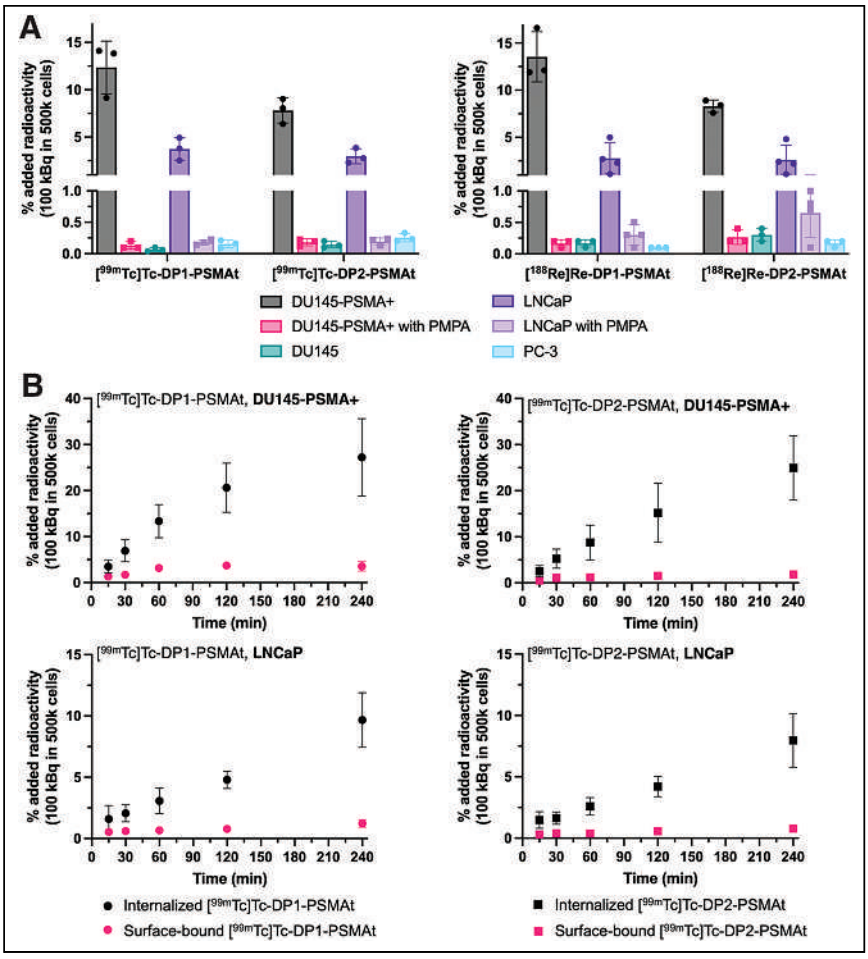

FIGURE 2. (A) Uptake of radiotracers in PSMA-positive and PSMA-negative prostate cancer cells. (B) Time course uptake and localization of ^{99m}Tc radiotracers in DU145-PSMA cells and LNCaP cells. Data are presented as mean ± SD; n = 3–4 biologic repeats performed in triplicate.

Biodistribution and SPECT/CT Imaging of ^{99m}Tc Radiotracers in Mice Bearing Prostate Cancer Tumors

The biodistributions of [^{99m}Tc]Tc-DP1-PSMAt and [^{99m}Tc]Tc-DP2-PSMAt were assessed in male SCID/beige mice bearing

DU145-PSMA+ xenograft tumors (Fig. 3). Each mouse was administered either [^{99m}Tc]Tc-DP1-PSMAt or [^{99m}Tc]Tc-DP2-PSMAt and euthanized at 2 h after injection ($n = 5$), followed by organ harvesting for ex vivo radioactivity counting. High amounts of each tracer were observed in tumors 2 h after injection; for [^{99m}Tc]Tc-DP1-PSMAt, the [^{99m}Tc]Tc concentration measured 18.0 ± 3.5 percentage injected dose per gram (%ID/g), and for [^{99m}Tc]Tc-DP2-PSMAt, the [^{99m}Tc]Tc concentration measured 29.4 ± 6.3 %ID/g.

To assess the specificity of each radiotracer, separate groups of animals, also bearing DU145-PSMA+ tumors, were coadministered either [^{99m}Tc]Tc-DP1-PSMAt and PMPA or [^{99m}Tc]Tc-DP2-PSMAt and PMPA to inhibit PSMA-mediated uptake of radiotracer ($n = 5$). In mice bearing DU145-PSMA+ tumors, coadministration of PMPA substantially decreased uptake of both [^{99m}Tc]Tc-DP1-PSMAt and [^{99m}Tc]Tc-DP2-PSMAt in tumors. For [^{99m}Tc]Tc-DP1-PSMAt, coadministration decreased uptake to 0.91 ± 0.29 %ID/g in tumors (compared with administration of [^{99m}Tc]Tc-DP1-PSMAt only: mean difference of 17.12 %ID/g, $P = 4 \times 10^{-4}$). For [^{99m}Tc]Tc-DP2-PSMAt, coadministration decreased uptake to 0.76 ± 0.45 %ID/g in tumors (compared with administration of [^{99m}Tc]Tc-DP2-PSMAt only: mean difference of 28.62 %ID/g, $P = 5 \times 10^{-4}$).

For both radiotracers, the concentration of ^{99m}Tc radioactivity in the kidneys 2 h after injection was high (Fig. 3). Increased amounts of [^{99m}Tc]Tc-DP2-PSMAt were measured in the kidneys 2 h after injection (183.3 ± 23.8 %ID/g,) compared with [^{99m}Tc]Tc-DP1-PSMAt (115.9 ± 27.3 %ID/g, mean difference of 67.4 %ID/g, $P = 0.003$). Notably, for animals administered [^{99m}Tc]Tc-DP1-PSMAt, coadministration of PMPA significantly decreased retention of ^{99m}Tc radioactivity in the kidneys. In contrast, although coadministration of PMPA also decreased the radioactivity concentration in the kidneys for animals injected with [^{99m}Tc]Tc-DP2-PSMAt, this effect was much less pronounced. There were also significant amounts of both radiotracers ([^{99m}Tc]Tc-DP1-PSMAt: 12.0 ± 5.3 %ID/g; [^{99m}Tc]Tc-DP2-PSMAt: 7.7 ± 3.4 %ID/g) that residualized in the spleen, which is known to express low levels of PSMA and accumulate PSMA-targeted radiotracers (*5*,*6*,*9*). As expected, coadministration of PMPA significantly decreased retention of ^{99m}Tc radioactivity in the spleen for both radiotracers ([^{99m}Tc]Tc-DP1-PSMAt: 0.2 ± 0.06 %ID/g, mean difference of 11.8 %ID/g, $P = 0.008$; [^{99m}Tc]Tc-DP2-PSMAt: 0.3 ± 0.18 %ID/g, mean difference of 7.4 %ID/g, $P = 0.008$).

Additionally, groups of mice bearing non–PSMA-expressing parental DU145 tumors were also administered these ^{99m}Tc radiotracers. For these groups, tumor uptake of [^{99m}Tc]Tc-DP1-PSMAt decreased to 0.24 ± 0.07 %ID/g, and tumor uptake of [^{99m}Tc]Tc-DP2-PSMAt decreased to 0.18 ± 0.07 %ID/g (Supplemental Fig. 3).

In SPECT/CT scans of animals administered either [^{99m}Tc]Tc-DP1-PSMAt or [^{99m}Tc]Tc-DP2-PSMAt only, tumors could be clearly delineated at both 2 h (Fig. 3) and 24 h (Supplemental Fig. 4) after injection. The kidneys and bladder were also clearly visible across these time points, consistent with ex vivo biodistribution data. SPECT/CT also showed negligible tumor uptake for animals either coadministered PMPA or bearing DU145 tumors that do not express PSMA receptor (Fig. 3). For all animals administered either [^{99m}Tc]Tc-DP1-PSMAt only or [^{99m}Tc]Tc-DP2-PSMAt only, the spleen was also identified in SPECT/CT scans acquired at 2 h after injection. Coadministration of PMPA decreased spleen uptake of both radiotracers.

Biodistribution of ^{188}Re Radiotracers in Mice Bearing Prostate Cancer Tumors

The biodistributions of the ^{188}Re radiotracers, [^{188}Re]Re-DP1-PSMAt and [^{188}Re]Re-DP2-PSMAt, were first assessed in SCID/beige mice bearing DU145-PSMA+ tumors (Fig. 3). Radioactivity concentration in the tumors of animals administered [^{188}Re]Re-DP1-PSMAt measured 27.7 ± 6.4 %ID/g at 2 h after injection, whereas that of animals given [^{188}Re]Re-DP2-PSMAt measured 19.2 ± 8.6 %ID/g. Both compounds cleared the circulation via a renal pathway, as evidenced by high concentrations of radioactivity measured in the kidneys ([^{188}Re]Re-DP1-PSMAt measured 88.3 ± 18.8 %ID/g, [^{188}Re]Re-DP2-PSMAt measured 96.8 ± 16.3 %ID/g). Biodistribution data also indicated that both compounds had low retention in nontarget, healthy organs and tissues, except for the spleen. In this experiment, there were no notable significant differences between the biodistribution profiles of [^{188}Re]Re-DP1-PSMAt and [^{188}Re]Re-DP2-PSMAt at 2 h after injection. As expected, coadministration of PMPA significantly inhibited uptake of both ^{188}Re radiotracers in the tumor and spleen.

Urine was collected from mice administered either [^{188}Re]Re-DP1-PSMAt or [^{188}Re]Re-DP2-PSMAt at 2 h after injection and was analyzed by reverse-phase radio-HPLC. Radiochromatograms showed that both [^{188}Re]Re-DP1-PSMAt and [^{188}Re]Re-DP2-PSMAt were highly stable and were cleared from the blood pool and excreted chemically intact (Supplemental Fig. 5).

With a view to developing a molecular [^{188}Re]Re-labeled agent for PSMA PRRT, we further characterized the biodistribution profiles of [^{188}Re]Re-DP1-PSMAt and [^{188}Re]Re-DP2-PSMAt in male athymic nude mice bearing LNCaP xenografts (Fig. 4), which recapitulate clinical metastatic prostate cancer more closely than DU145-PSMA+ xenografts. Importantly, the ^{188}Re agents exhibited significant retention in tumors up to at least 1 d after administration. In mice administered [^{188}Re]Re-DP1-PSMAt, LNCaP tumor uptake measured 7.0 ± 2.3 %ID/g at 2 h after injection and 2.9 ± 0.8 %ID/g at 24 h after injection. For [^{188}Re]Re-DP2-PSMAt, LNCaP tumor uptake measured 9.8 ± 2.8 %ID/g at 2 h after injection and 7.6 ± 4.4 %ID/g at 24 h after injection. With the exception of the kidneys, radioactivity concentrations in other organs were similar to what was observed in prior experiments with male SCID/beige mice.

The concentration of ^{188}Re agents in the kidneys was relatively high at 2 h after injection: [^{188}Re]Re-DP1-PSMAt measured 137.1 ± 34.6 %ID/g, and [^{188}Re]Re-DP2-PSMAt measured 162.8 ± 31.8 %ID/g. These decreased to 29.4 ± 4.9 %ID/g and 37.0 ± 12.2 %ID/g, respectively, at 24 h after injection. Separate groups of animals were coadministered the plasma expander Gelofusine, which has previously been used to reduce kidney retention of PRRT agents and minimize potential nephrotoxicity. For animals coadministered [^{188}Re]Re-DP1-PSMAt and Gelofusine, kidney retention decreased to 108.8 ± 13.3 %ID/g at 2 h after injection ($P = 0.11$); for [^{188}Re]Re-DP2-PSMAt, kidney retention decreased to 127.6 ± 17.7 %ID/g ($P = 0.046$).

Last, to further assess the biologic equivalence of pairs of ^{99m}Tc and ^{188}Re agents, the biodistributions of [^{99m}Tc]Tc-DP1-PSMAt and [^{99m}Tc]Tc-DP2-PSMAt were also assessed in athymic nude mice bearing LNCaP prostate cancer tumors. Importantly, the biodistribution patterns and clearance pathways of [^{99m}Tc]Tc-DP1-PSMAt and [^{188}Re]Re-DP1-PSMAt were highly similar when compared in the same mouse model (either male athymic nude mice bearing LNCaP xenografts or male SCID/beige mice bearing DU145-PSMA+ xenograft tumors). The same near-equivalent

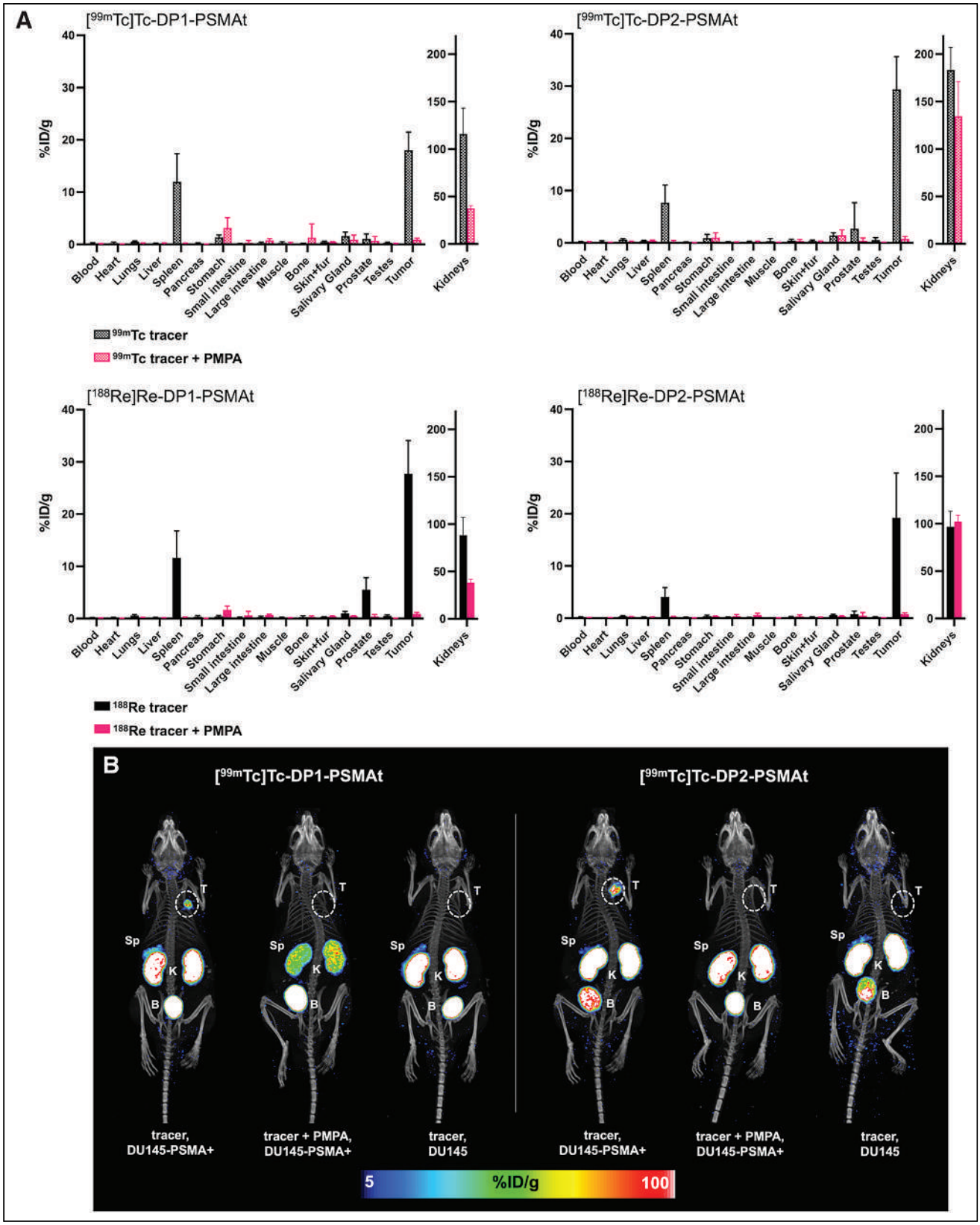

FIGURE 3. (A) Biodistribution (2 h after injection) of SCID/beige mice bearing DU145-PSMA+ prostate cancer tumors, administered either ^{99m}Tc or ^{188}Re radiotracers intravenously. To assess specificity of radiotracer uptake, additional groups of mice were also coadministered radiotracer and PMPA (Supplemental Tables 3 and 4). (B) Whole-body SPECT/CT maximum-intensity projections of SCID/beige mice bearing either DU145-PSMA+ tumors or DU145 tumors, administered either [^{99m}Tc]Tc-DP1-PSMAt or [^{99m}Tc]Tc-DP2-PSMAt, 2 h after injection. To inhibit uptake in DU145-PSMA+ tumors, animals were also coadministered PMPA.

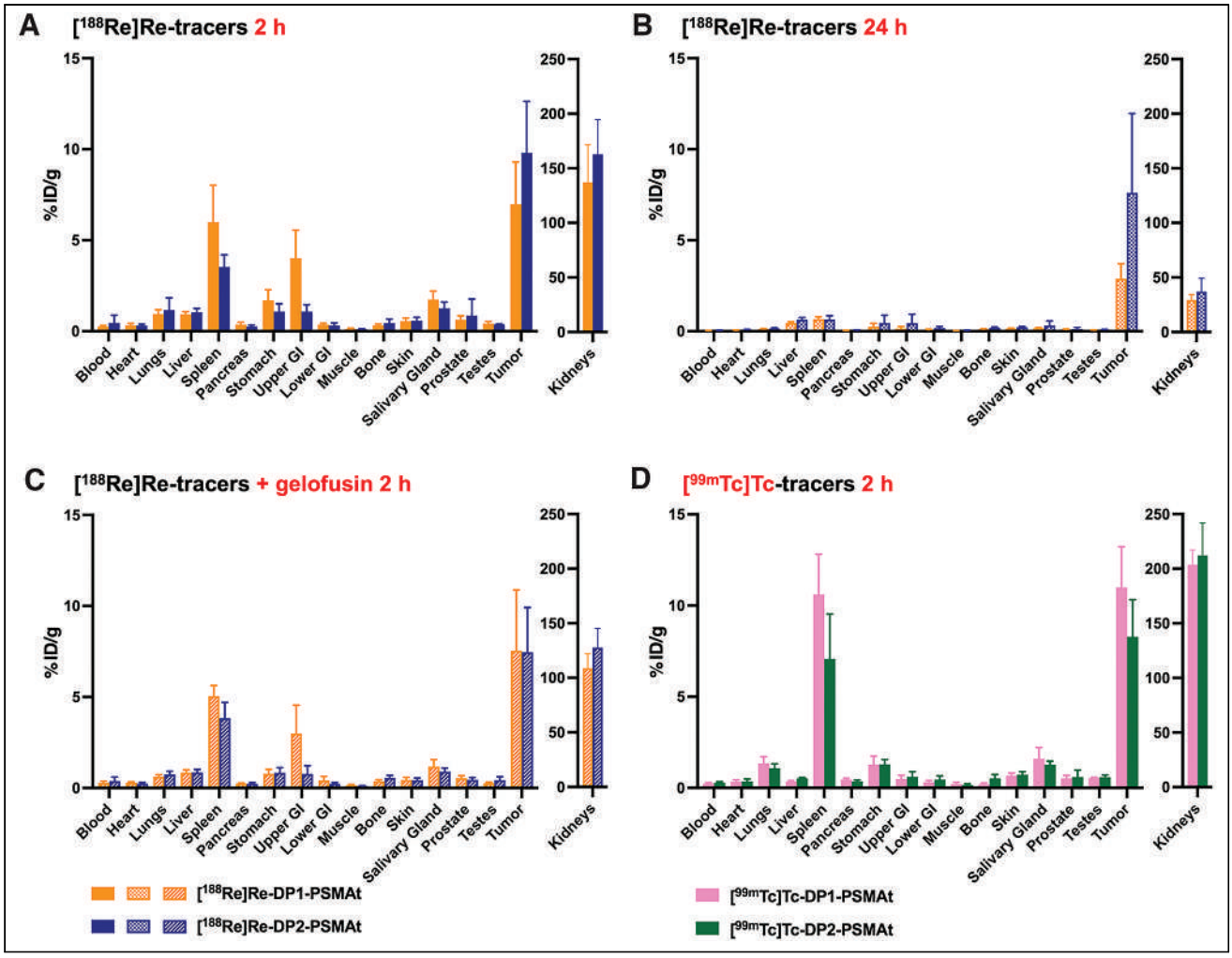

FIGURE 4. (A–C) Biodistribution of ^{188}Re in athymic nude mice bearing LNCaP prostate cancer tumors, administered either [^{188}Re]Re-DP1-PSMAt or [^{188}Re]Re-DP2-PSMAt at 2 h after injection (A), at 24 h after injection (B), and at 2 h after injection (C) with coadministration of Gelofusine. (D) Additionally, biodistributions of [^{99m}Tc]Tc-DP1-PSMAt and [^{99m}Tc]Tc-DP2-PSMAt at 2 h after injection were measured (Supplemental Tables 5–8). GI = gastrointestinal tract.

biodistribution patterns were observed for [^{99m}Tc]Tc-DP2-PSMAt and [^{188}Re]Re-DP2-PSMAt. Between analogous ^{99m}Tc and ^{188}Re radiotracers, the most notable difference in biodistribution behavior was that ^{99m}Tc radiotracers demonstrated consistently higher kidney residualization than did ^{188}Re radiotracers.

DISCUSSION

Theranostic PSMA-targeted radiopharmaceuticals have had an extraordinary impact on prostate cancer care in health care settings where they are available. We have developed 2 pairs of chemically analogous theranostic agents based on the generator-produced radionuclides ^{99m}Tc and ^{188}Re. Radio-HPLC alongside careful chemical characterization of nonradioactive or long-lived isotopologs (*17*) demonstrates that technetium and rhenium pairs are chemical analogs and isostructural. Consequently, each pair exhibits highly similar biologic behavior in in vitro and in vivo models of prostate cancer. Importantly, both ^{188}Re- and ^{99m}Tc-labeled complexes of DP1-PSMAt and DP2-PSMAt show a high accumulation in PSMA-expressing tumors and prostate cancer cells and, in vivo, rapidly clear from the circulation via a renal pathway, with minimal retention in healthy tissues. Furthermore, in vivo, these 4 radiotracers all demonstrate significant retention in prostate cancer tumors up to 24 h after injection.

In a clinical context, the favorable and near-identical biologic behaviors of chemically analogous ^{99m}Tc and ^{188}Re radiotracers bring about the possibility of using ^{99m}Tc molecular imaging to predict the biodistribution, accumulation, and dosimetry of a complementary ^{188}Re PRRT agent. Our novel theranostic pairs, M-DP1-PSMAt and M-DP2-PSMAt (M = [^{99m}Tc]Tc, [^{188}Re]Re), which use economical generator-produced isotopes, have strong potential utility for this purpose in prostate cancer treatment, particularly in LMICs. Additionally, the DP chemical platform underpinning these theranostic radiotracers is an excellent candidate for development of other peptide-based radiotracers: this technology could increase clinical use of receptor-targeted ^{99m}Tc and ^{188}Re radiopharmaceuticals and widen patient access to the benefits of molecular theranostic agents.

In this work, [^{99m}Tc]Tc-DP1-PSMAt, [^{99m}Tc]Tc-DP2-PSMAt, [^{188}Re]Re-DP1-PSMAt, and [^{188}Re]Re-DP2-PSMAt are all subject to postsynthetic HPLC purification and isolation procedures. Using HPLC, all these compounds can be easily separated from unreacted ligand and from unreacted ^{99m}Tc/^{188}Re-labeled precursors,

yielding radiotracers of extremely high specific activity; that is, with the exception of decay products, there is minimal unlabeled DP1-PSMAt or DP2-PSMAt present in final radiotracer formulations. This culminates in an extremely high accumulation in PSMA-expressing prostate cancer cells in vitro and tissue in vivo (tumors, spleen, and in the case of DP1-PSMAt derivatives, kidneys).

In some in vivo experiments, there were statistically significant differences in tumor uptake between DP1 and DP2 bioconjugate derivatives; however, these differences were not recapitulated in alternative experiments. For example, in experiments using SCID/beige mice bearing DU145-PSMA+ tumors at 2 h after injection, tumors had significantly higher [^{99m}Tc]Tc-DP2-PSMAt (29.4 ± 6.3 %ID/g) than [^{99m}Tc]Tc-DP1-PSMAt (18.0 ± 3.5 %ID/g; mean difference, 11.4 %ID/g; $P = 0.01$). However, in experiments using athymic nude mice bearing LNCaP tumors, no statistically significant difference in tumor uptake was observed between these 2 ^{99m}Tc radiotracers at 2 h after injection. Between homologous DP1 and DP2 radiotracers, the most notable difference was that M-DP1-PSMAt (M = [^{99m}Tc]Tc or [^{188}Re]Re) exhibited significantly higher spleen retention than did M-DP2-PSMAt at 2 h after injection (for comparisons of [^{99m}Tc]Tc DP1-PSMAt vs. [^{99m}Tc]Tc DP2-PSMAt or of [^{188}Re]Re-DP1-PSMAt vs. [^{188}Re]Re-DP2-PSMAt in SCID/beige or athymic nude mice, $P \leq 0.05$).

All 4 radiotracers exhibited high kidney residualization. In the case of DP1-PSMAt derivatives, it is likely that this retention is in part mediated by PSMA (in SCID/beige mice, [^{99m}Tc]Tc-DP1-PSMAt: 116 ± 27 %ID/g, with PMPA: 38 ± 2.9 %ID/g, $P = 2.88 \times 10^{-3}$; [^{188}Re]Re-DP1-PSMAt: 88 ± 19 %ID/g, with PMPA: 38 ± 3.4 %ID/g, $P = 1.16 \times 10^{-2}$). Murine kidney tissues, specifically proximal renal tubules and Bowman capsule, express PSMA (*23*). DP2 radiotracers consistently demonstrated higher kidney retention than DP1 radiotracers. We attribute this to the comparatively higher lipophilicity of DP2 derivatives (*17*). Prior comparative in vivo murine studies have observed that increases in the lipophilicity of PSMAt-derived compounds increase their kidney retention (*24*). Although coadministration of Gelofusine decreased kidney retention of ^{188}Re agents at 2 h after administration, this observed decrease was not statistically significant. In light of the comparatively similar tumor uptake of DP1 and DP2 radiotracers but the higher kidney retention of DP2 radiotracers, we postulate that DP1-based radiotracers are better clinical theranostic candidates.

Compared with the existing ^{99m}Tc- and ^{188}Re-radiolabeled tracers—[^{99m}Tc]Tc-MIP-1404 (*5*), [^{99m}Tc]Tc-PSMA-I&S (*6*), [^{99m}Tc] Tc-EDDA/HYNIC-iPSMA (*9*), and [^{188}Re]Re-PSMA-GCK01 (*16*)—the new DP-based radiotracers demonstrate either decreased or comparable residualization in murine liver and either increased or comparable blood clearance at 1–2 h after administration (Supplemental Table 2).

Like existing PSMA-targeted ^{99m}Tc radiotracers, both [^{99m}Tc]Tc-DP1-PSMAt and [^{99m}Tc]Tc-DP2-PSMAt can be formulated using a kit: our existing protocols and prototype kit radiosynthetic methods enable high radiochemical yields of desired radiotracer (80%–90%) by heating a saline solution of generator-produced [^{99m}Tc]TcO_4^- with kit components at 100°C for 5 min (*17–19*). We elected to use a 2-step protocol to prepare ^{188}Re-radiolabeled agents, in which a [^{188}Re]Re^V-citrate precursor is reacted with either DP1-PSMAt or DP2-PSMAt to yield the desired ^{188}Re radiotracers. This procedure is similar to prior radiosyntheses of [^{188}Re][Re^VO_2]$^+$-labeled phosphine-containing P_2S_2 and P_2N_2 tetradentate chelator derivatives (*20,21*). However, complexes of the latter chelators were obtained in more than 90% radiochemical yield; the highest radiochemical yields obtained for [^{188}Re]Re-DP1-PSMAt and [^{188}Re]Re-DP2-PSMAt were about 70% and 50%, respectively. We also note that the [^{188}Re][ReO^V]$^{3+}$-based complex, [^{188}Re]Re-PSMA-GCK01, can be obtained in 78% radiochemical yield and 96% radiochemical purity, using a one-pot radiochemical procedure (*16*). This procedure involves heating an aqueous solution of precursor GCK01, [^{188}Re]ReO_4^-, citrate, and ascorbic acid at pH 2.0–3.5 at high temperature for 1 h, followed by neutralization, further heating for 5 min, and final C18 Sep-Pak purification. We are currently optimizing kit-based formulations to increase the radiochemical yields of DP-based ^{99m}Tc and ^{188}Re radiotracers and to obviate postsynthetic purification procedures to remove unreacted ^{99m}Tc and ^{188}Re precursors.

CONCLUSION

We have developed new PSMA-targeting ^{99m}Tc/^{188}Re theranostic agents, using versatile diphosphine chemical platforms. These radiotracers can be prepared using eluate from bench-top ^{99m}Tc and ^{188}Re generators and chemical kits. The resulting isostructural ^{99m}Tc and ^{188}Re pairs show near-equivalent biologic behaviors in models of prostate cancer. We are further developing optimized kit-based formulations to enable near-quantitative radiochemical yields to obviate purification steps after radiolabeling. Our new, generator-based theranostic agents have potential to provide access to the benefits of PSMA-targeted diagnostic imaging and systemic radiotherapy in health care settings that do not routinely have access to either reactor-produced ^{177}Lu radiopharmaceuticals or PET/CT infrastructure.

DISCLOSURE

This research was supported by a Cancer Research UK. Career Establishment Award (C63178/A24959), an EPSRC program grant (EP/S032789/1), the Cancer Research UK. National Cancer Imaging Translational Accelerator Award (C4278/A27066), and the Wellcome Trust (212885/Z/18/Z). The authors have submitted a patent application describing the intellectual property described in this article. No other potential conflict of interest relevant to this article was reported.

ACKNOWLEDGMENTS

We are grateful for research assistance with animal work from James Cormack, Harmony Blythin, and Hagen Schmidt.

KEY POINTS

QUESTION: Are molecular theranostic radiotracers based on ^{99m}Tc and ^{188}Re feasible for diagnostic imaging and systemic radiotherapy of prostate cancer?

PERTINENT FINDINGS: Pairs of chemically analogous ^{99m}Tc/^{188}Re radiotracers show equivalent uptake in PSMA-expressing prostate cancer cells and favorable, highly similar biodistribution profiles in mouse models of prostate cancer.

IMPLICATIONS FOR PATIENT CARE: These generator-based theranostic agents have potential to provide access to the benefits of PSMA-targeted diagnostic imaging and systemic radiotherapy in health care settings that do not routinely have access to either cyclotron- or reactor-produced radionuclides.

REFERENCES

1. Sartor O, de Bono J, Chi KN, et al. Lutetium-177–PSMA-617 for metastatic castration-resistant prostate cancer. *N Engl J Med.* 2021;385:1091–1103.
2. Hofman MS, Violet J, Hicks RJ, et al. [^{177}Lu]-PSMA-617 radionuclide treatment in patients with metastatic castration-resistant prostate cancer (LuPSMA trial): a single-centre, single-arm, phase 2 study. *Lancet Oncol.* 2018;19:825–833.
3. Hofman MS, Lawrentschuk N, Francis RJ, et al. Prostate-specific membrane antigen PET-CT in patients with high-risk prostate cancer before curative-intent surgery or radiotherapy (proPSMA): a prospective, randomised, multicentre study. *Lancet.* 2020;395:1208–1216.
4. Schmidkonz C, Hollweg C, Beck M, et al. ^{99m}Tc-MIP-1404-SPECT/CT for the detection of PSMA-positive lesions in 225 patients with biochemical recurrence of prostate cancer. *Prostate.* 2018;78:54–63.
5. Hillier SM, Maresca KP, Lu G, et al. ^{99m}Tc-labeled small-molecule inhibitors of prostate-specific membrane antigen for molecular imaging of prostate cancer. *J Nucl Med.* 2013;54:1369–1376.
6. Robu S, Schottelius M, Eiber M, et al. Preclinical evaluation and first patient application of ^{99m}Tc-PSMA-I&S for SPECT imaging and radioguided surgery in prostate cancer. *J Nucl Med.* 2017;58:235–242.
7. Maurer T, Robu S, Schottelius M, et al. ^{99m}Technetium-based prostate-specific membrane antigen–radioguided surgery in recurrent prostate cancer. *Eur Urol.* 2019;75:659–666.
8. Lawal IO, Ankrah AO, Mokgoro NP, Vorster M, Maes A, Sathekge MM. Diagnostic sensitivity of Tc-99m HYNIC PSMA SPECT/CT in prostate carcinoma: a comparative analysis with Ga-68 PSMA PET/CT. *Prostate.* 2017;77:1205–1212.
9. Ferro-Flores G, Luna-Gutiérrez M, Ocampo-García B, et al. Clinical translation of a PSMA inhibitor for ^{99m}Tc-based SPECT. *Nucl Med Biol.* 2017;48:36–44.
10. Shinto A. An overview of nuclear medicine and PET CT in India. *Curr Trends Clin Med Imaging.* 2017;1:91–94.
11. Bernal P, Raoul J-L, Stare J, et al. International Atomic Energy Agency-sponsored multination study of intra-arterial rhenium-188-labeled lipiodol in the treatment of inoperable hepatocellular carcinoma: results with special emphasis on prognostic value of dosimetric study. *Semin Nucl Med.* 2008;38:S40–S45.
12. Shinto A. Rhenium-188: the poor man's yttrium. *World J Nucl Med.* 2017;16:1–2.
13. Blower PJ, Kettle AG, O'Doherty MJ, Coakley AJ, Knapp FF. ^{99m}Tc(V)DMSA quantitatively predicts ^{188}Re(V)DMSA distribution in patients with prostate cancer metastatic to bone. *Eur J Nucl Med.* 2000;27:1405–1409.
14. Jackson JA, Hungnes IN, Ma MT, Rivas C. Bioconjugates of chelators with peptides and proteins in nuclear medicine: historical importance, current innovations, and future challenges. *Bioconjug Chem.* 2020;31:483–491.
15. Shinto AS, Kameswaran M, Kamaleshwaran K, et al. Clinical utility of ^{188}rhenium-hydroxyethylidene-1,1-diphosphonate as a bone pain palliative in multiple malignancies. *World J Nucl Med.* 2018;17:228–235.
16. Cardinale J, Giesel FL, Wensky C, Rathke HG, Haberkorn U, Kratochwil C. PSMA-GCK01: a generator-based ^{99m}Tc-/^{188}Re-theranostic ligand for the prostate-specific membrane antigen. *J Nucl Med.* 2023;64:1069–1075.
17. Hungnes IN, Pham TT, Rivas C, et al. Versatile diphosphine chelators for radiolabeling peptides with ^{99m}Tc and ^{64}Cu. *Inorg Chem.* 2023;62:20608–20620.
18. Hungnes IN, Al-Salemee F, Gawne PJ, et al. One-step, kit-based radiopharmaceuticals for molecular SPECT imaging: a versatile diphosphine chelator for ^{99m}Tc radiolabelling of peptides. *Dalton Trans.* 2021;50:16156–16165.
19. Nuttall RE, Pham TT, Chadwick AC, et al. Diphosphine bioconjugates via Pt(0)-catalyzed hydrophosphination. A versatile chelator platform for technetium-99m and rhenium-188 radiolabeling of biomolecules. *Inorg Chem.* 2023;62:20582–20592.
20. Gali H, Hoffman TJ, Sieckman GL, Owen NK, Katti KV, Volkert WA. Synthesis, characterization, and labeling with ^{99m}Tc/^{188}Re of peptide conjugates containing a dithia-bisphosphine chelating agent. *Bioconjug Chem.* 2001;12:354–363.
21. Kothari KK, Gali H, Prabhu KR, et al. Synthesis and characterization of ^{99m}Tc- and ^{188}Re-complexes with a diamido-dihydroxymethylenephosphine-based bifunctional chelating agent (N_2P_2-BFCA). *Nucl Med Biol.* 2002;29:83–89.
22. Kampmeier F, Williams JD, Maher J, Mullen GE, Blower PJ. Design and preclinical evaluation of a ^{99m}Tc-labelled diabody of mAb J591 for SPECT imaging of prostate-specific membrane antigen (PSMA). *EJNMMI Res.* 2014;4:13.
23. Simons BW, Turtle NF, Ulmert DH, Abou DS, Thorek DLJ. PSMA expression in the Hi-Myc model; extended utility of a representative model of prostate adenocarcinoma for biological insight and as a drug discovery tool. *Prostate.* 2019;79:678–685.
24. Benešová M, Bauder-Wüst U, Schäfer M, et al. Linker modification strategies to control the prostate-specific membrane antigen (PSMA)-targeting and pharmacokinetic properties of DOTA-conjugated PSMA inhibitors. *J Med Chem.* 2016;59:1761–1775.

Safety and Efficacy of Radiosynoviorthesis: A Prospective Canadian Multicenter Study

Mélanie Desaulniers[1,2], Michel Paquette[1,2], Stéphanie Dubreuil[1,2], Helena Senta[1,2], Éric Lavallée[1,2], J. Carter Thorne[3–5], and Éric Turcotte[1,2]

[1]Department of Nuclear Medicine and Radiobiology, Université de Sherbrooke, Sherbrooke, Quebec, Canada; [2]Research Center of CHUS, CIUSSSE–CHUS, Sherbrooke, Quebec, Canada; [3]Arthritis Program Research Group Inc., Newmarket, Ontario, Canada; [4]Division of Rheumatology, University of Toronto, Toronto, Ontario, Canada; and [5]Division of Rheumatology, Southlake Regional Health Center, Newmarket, Ontario, Canada

Radiosynoviorthesis is approved in several European countries and the United States to treat refractory synovitis in many inflammatory joint diseases, such as rheumatoid arthritis, spondyloarthropathies, and other arthritic joint diseases. No radiopharmaceuticals for radiosynoviorthesis are currently approved in Canada. The aim of this Health Canada–approved trial was to demonstrate the safety and efficacy of radiosynoviorthesis. **Methods:** Between July 2012 and November 2017, we conducted a multicenter, prospective, interventional Canadian trial. Patients ($n = 360$) with synovitis refractory to standard treatments after failing 2 intraarticular glucocorticoid injections were included. They were followed up at 3, 6, and 12 mo. Outcome measures included adverse events (AEs) and clinical signs of synovitis (pain, swelling, and joint effusion) measured with the Health Assessment Questionnaire Disability Index, the Disease Activity Score, and the Visual Analog Scale. **Results:** In total, 392 joints were treated, including those reinjected after 6 mo ($n = 34$). Of these, 83.4% (327/392) were injected with [^{90}Y]Y-citrate for the knees and 9.9% (39/392) with [^{186}Re]Re-sulfide for medium-sized joints. Of the joints treated, 82.7% (324/392) were knees. Fifty-five AEs, most of them of mild grade, occurred and resolved without sequelae and were not life-threatening. The incidence of radiosynoviorthesis-related AEs was 9.4% (34/360). The proportion of patients showing an improvement in synovitis symptoms after radiosynoviorthesis was significant at 3 mo and was maintained up to 12 mo ($P < 0.001$). **Conclusion:** This study confirmed the safety of radiosynoviorthesis in the treatment of patients with synovitis refractory to standard treatments. There is evidence of sustained clinical efficacy at 12 mo, suggesting that radiosynoviorthesis is an effective treatment for improving synovitis symptoms.

Key Words: efficacy; radiosynoviorthesis; rhenium; safety; yttrium

J Nucl Med 2024; 65:1095–1100
DOI: 10.2967/jnumed.123.267297

Radiosynoviorthesis is an intraarticular radionuclide treatment used since 1952 to treat inflammatory joint diseases (*1*). Radiosynoviorthesis is approved in many European countries and the United States for the treatment of rheumatoid arthritis (RA), spondyloarthropathies, and other arthritic joint diseases (*2*). The aim of radiosynoviorthesis is to reduce synovitis symptoms after failure or incomplete response to systemic therapy and intraarticular glucocorticoid injections (*1*). When standard treatment fails, surgical synovectomy may be recommended to remove the inflamed synovial membrane (*3,4*). Radiosynoviorthesis is an outpatient alternative that delivers equivalent clinical results, is repeatable, reduces the rate of joint effusion after arthroplasty, and is less expensive than surgical synovectomy (*5–8*).

Previous studies have demonstrated that radiosynoviorthesis is safe. Between 1976 and 2001, 2,412 patients showed no increase in cancer risk, and there was no dose–response relationship with the number of treatments (*9*). In Europe, of 900,000 joints treated between 1990 and 2011, only 30 severe complications were reported (*10*). Moreover, radiosynoviorthesis is effective for refractory synovitis. Most studies report an improvement in symptoms during the first 6 mo after the procedure and good symptom control at 12 mo in 70% of patients (*11–13*). As previously described (*14*), [^{90}Y]Y-citrate and [^{186}Re]Re-sulfide were available in Canada through a Special Access Program authorization between 1999 and 2010. In 2011, further scientific evidence of the safety and efficacy of radiosynoviorthesis was needed, and to provide such evidence was the aim of this study.

MATERIALS AND METHODS

Patient Population

The enrollment flowchart is shown in Figure 1. Between July 2012 and November 2017, all screened patients ($n = 360$) from 12 hospitals in 5 Canadian provinces were included in this prospective, multicenter, open-label Canadian interventional trial (NCT01615991) approved by Health Canada (approval 9427-C2049-41C) and received radiosynoviorthesis with [^{90}Y]Y-citrate or [^{186}Re]Re-sulfide (IBA-CIS Bio International). There was no minimum or maximum age for inclusion. Patients had to be referred by a specialist physician (rheumatology, internal medicine, or orthopedics) and present clinical signs (pain, swelling, and joint effusion) of active mono- or oligosynovitis. The inflammatory joint diseases included are presented in Table 1. Patients had to have failed medical treatment, defined as the absence of clinical improvement of synovitis symptoms, after 6 mo or 2 intraarticular long-acting glucocorticoid injections. The pain had to limit daily activities or require large doses of analgesics. Patients who had undergone arthroscopic removal of the synovium were eligible. Joint imaging had to show maximally moderate destruction of cartilage or bone (Kellgren–Lawrence class ≤ 3).

Exclusion criteria were a joint puncture within the last 2 wk, surgery or arthroscopy within the last 6 wk, radiosynoviorthesis within

Received Dec. 18, 2023; revision accepted Apr. 22, 2024.
For correspondence or reprints, contact Mélanie Desaulniers (melanie.desaulniers2@usherbrooke.ca).
Published online May 16, 2024.

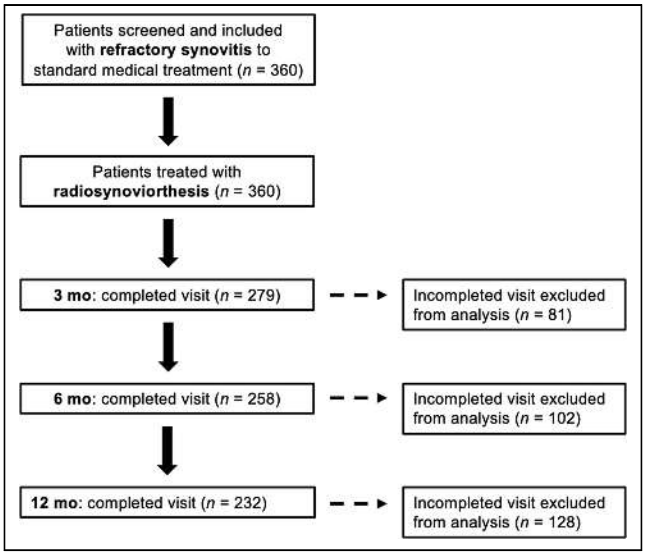

FIGURE 1. Enrollment flowchart.

the last 3 mo, and surgical synovectomy within the last 6 mo in this joint. After a sufficient waiting period, an initially ineligible patient could receive radiosynoviorthesis. Other exclusion criteria included intraarticular fracture, painful prosthesis, massive hemarthrosis, infection, synovial cyst rupture, pregnancy or breastfeeding, bone metastases, allergies to radiopharmaceuticals, and concurrent participation in another clinical trial related to the underlying condition. Data on excluded patients are unknown, as only results from included and treated patients were obtained.

The institutional Research Ethics Board approved this clinical trial (approval CIMS-2011-03), and all subjects gave written informed consent. Each participating site used its own funds to purchase radiopharmaceuticals from the manufacturer, who did not fund the present trial.

Radiosynoviorthesis Procedure

The skin was sterilized with an antiseptic pad saturated with 2% chlorhexidine gluconate and 70% isopropyl alcohol. Sterile drapes and gloves were used. The position of the needle in the synovial space was confirmed by aspiration of synovial fluid from the knee. For other joints, positioning was confirmed by contrast injection under fluoroscopy. [^{90}Y]Y-citrate or [^{186}Re]Re-sulfide was injected for the radiosynoviorthesis. The choice of radiopharmaceutical depended on the size of the joint, and administration was in accordance with the activities and volumes proposed for each radiopharmaceutical in Supplemental Table 1 (supplemental materials are available at http://jnm.snmjournals.org). The [^{90}Y]Y-citrate was used for the knees, and the [^{186}Re]Re-sulfide was used for the hips, shoulders, elbows, wrists, and ankles. On request and under certain circumstances, medium-sized joints could be injected with [^{90}Y]Y-citrate after approval by the steering committee, with the exception of the wrist. Several radiosynoviortheses in different joints during the same visit were possible, but the maximum total activity authorized per visit was 555 MBq with [^{90}Y]Y-citrate and 370 MBq with [^{186}Re]Re-sulfide. The needle was rinsed with methylprednisolone acetate, 40 mg/mL. The volume injected per joint is available in Supplemental Table 2. During needle removal, soft-tissue massage and pressure were applied to the puncture site. The joint had to be immobilized for 48 h. For knees, bed rest without splinting was recommended. If immobilization was not possible, a splint was used to limit movement, as for other joints. Joint scintigraphy was performed within 5 d of the procedure. Patients were followed up at 3, 6, and 12 mo.

TABLE 1
Patient Characteristics

Characteristic	Data
Age (y)	
Mean	50.5 (SD, 16.9)
Median	51.0 (range, 5.0–87.0)
Sex	
Female	185 (51.4%)
Male	173 (48.1%)
Unknown	2 (0.5%)
Joint inflammatory disease	
Spondyloarthropathies	110 (30.6%)
RA	89 (24.7%)
Osteoarthritis	43 (11.9%)
Pigmented villonodular synovitis	28 (7.8%)
Hemophilic arthropathy	23 (6.4%)
Undifferentiated arthritis	22 (6.1%)
Juvenile idiopathic arthritis	19 (5.3%)
Other inflammatory arthritis	15 (4.2%)
Recurrent joint effusion after surgery	9 (2.5%)
Unknown	2 (0.5%)
Concurrent medication	
nbDMARD	323 (89.7%)
bDMARD	21 (5.8%)
Unknown	16 (4.5%)
Joint treated	
Knee	324 (82.7%)
Ankle	24 (6.1%)
Elbow	18 (4.6%)
Wrist	13 (3.3%)
Shoulder	9 (2.3%)
Hip	4 (1.0%)
Radiopharmaceutical	
[^{90}Y]Y-citrate	327 (83.4%)
[^{186}Re]Re-sulfide	39 (10.0%)
Unknown	26 (6.6%)
Radiologic class of joint destruction	
0	218 (55.6%)
1	36 (9.2%)
2	35 (8.9%)
3	36 (9.2%)
Unknown	67 (17.1%)

nbDMARD = nonbiologic disease-modifying antirheumatic drug; bDMARD = biologic disease-modifying antirheumatic drug.

Data are number followed by percentage in parentheses, except for age. Total patients = 360, and total joints = 392.

Safety

All adverse events (AEs) after radiosynoviorthesis, regardless of grade or relationship to radiosynoviorthesis, were systematically reported by

the physician. AEs were graded as mild (no interference with the patient's usual activities), moderate (disruption of the patient's usual activities without the need for medical intervention), or severe (disruption of the patient's usual activities and requiring medical intervention). Moreover, AEs could be definitely related to the treatment, could be probably related (defined as a plausible chronology but potentially attributable to another underlying medical problem), or could be unrelated (defined as a cause-and-effect relationship that is not biologically plausible because of chronology). The safety profile was assessed on the basis of the incidence of AEs described per patient, category, and grades. A joint reaction requiring intraarticular glucocorticoid injection within 14 d of radiosynoviorthesis was considered an AE.

Efficacy

Without clinical improvement in synovitis symptoms (pain, swelling, and joint effusion), treatment failure was defined as the need for an intraarticular glucocorticoid injection more than 14 d after radiosynoviorthesis. A partial response was defined as the need for a second radiosynoviorthesis within the same joint after 6 mo, and steering committee approval was required.

At baseline and at 3, 6, and 12 mo, the patient's functional disability using the Health Assessment Questionnaire Disability Index (HAQ-DI) (*15*), the disease activity using the Disease Activity Score (DAS28) (*16*), and the patient's global assessment of disease activity using the Visual Analog Scale (VAS 100 mm) (*17*) were assessed. To be significant, HAQ-DI was to be reduced by 0.25, DAS28 by 1.2, and VAS 100 mm by 20 mm. The proportion of patients with improvement in pain, swelling, and joint effusion at 3, 6, and 12 mo was recorded.

Statistical Analysis

Patients were not excluded from the trial on the basis of missing data; on the contrary, for each variable or multivariate analysis, the maximum number of evaluable patients was used and reported. On the basis of 2009–2010 data available for radiosynoviorthesis performed in Canada under the Special Access Program, the initial target sample size was 1,500 joints. The trial was interrupted before reaching the predetermined number of joints because of a lack of financial resources and time to maintain the steering committee.

Descriptive statistics included mean, median, range, SD, or proportion with a 95% CI, as appropriate. For the incidence of patients with radiosynoviorthesis-related AEs, a 95% Clopper–Pearson CI is provided. The generalized estimating equation model was used to consider the repeated measurements for the main outcomes. If a specific time point was relevant, the McNemar test was used to compare evolution over time. All tests were 2-sided, with a significant probability threshold of 5% ($P < 0.05$). Analyses were performed using SPSS version 26.0 (IBM).

RESULTS

Patient Characteristics

Table 1 shows the patient characteristics at baseline, when the class of radiologic joint destruction was measured using the Kellgren and Lawrence system (*18*). A total of 360 patients and 392 joints, including those reinjected after 6 mo ($n = 34$), underwent radiosynoviorthesis. Before radiosynoviorthesis, 93.6% (337/360) of patients had failed 2 intraarticular glucocorticoid injections. The mean number ± SD of intraarticular glucocorticoid injections received in the past 12 mo was 2.5 ± 0.2. Radiosynoviorthesis was preferable to surgery in 87.2% (314/360) of patients.

Safety

The median patient follow-up time was 12 mo (range, 0–12 mo). The total number of AEs was 55 (Supplemental Table 3). The incidence of patients with radiosynoviorthesis-related AEs was 9.4% (34/360; 95% CI, 6.6%–13.0%). The categories and grades according to the frequency of AEs are presented in Table 2; 14.5% (8/55) of the AEs were severe, 51% (28/55) were mild, 23.6% (13/55) were moderate, and 10.9% (6/55) were of unknown severity. Only 23.6% (13/55) of AEs were definitely related to radiosynoviorthesis, 38.2% (21/55) were possibly related, 27.3% (15/55) were unrelated, and 10.9% (6/55) were of unknown relation. Among the 8 severe AEs, there were 3 cases of radiosynoviorthesis-related radiation synovitis, only one of which resolved with minor sequelae. The other two resolved without sequelae. There was one case of radiation skin necrosis that was severe, occurring at 7 mo and possibly related to radiosynoviorthesis, and a second case that was mild. A single case each of knee synovitis, septic arthritis, lymphadenopathy, and medication error was severe but not related to radiosynoviorthesis as reported by the physician. Systemic reactions (40.0%, 22/55) were attributable to intraarticular glucocorticoid injection. Additional subgroup analyses between spondyloarthropathies, RA, osteoarthritis, pigmented villonodular synovitis, hemophilic arthropathy, and juvenile idiopathic arthritis showed no significant differences in the incidence of AEs or treatment failure reported below.

Efficacy

A total of 16.8% (66/392; 95% CI, 13.3%–20.9%) of joints received an intraarticular glucocorticoid injection after 14 d, corresponding to therapeutic failure. Reinjection after 6 mo was needed in 8.7% of joints (34/392; 95% CI, 6.1%–11.9%), corresponding to a partial response. Among them, 17.6% (6/34) had RA, 14.7% (5/34) had osteoarthritis, and 67.6% (23/34) had diseases of other categories.

Figure 2 shows the proportion of patients who, after 3 mo, showed a significant improvement ($P < 0.001$) in synovitis symptoms (pain:

TABLE 2
Categories and Grades of AEs

AE category	All grades	Severe
Joint reaction		
Pain	9 (16.4%)	0 (0.0%)
Inflammation	7 (12.7%)	3 (5.5%)
Swelling	6 (10.9%)	0 (0.0%)
Effusion	4 (7.3%)	1 (1.8%)
Stiffness	1 (1.8%)	0 (0.0%)
Septic arthritis	1 (1.8%)	1 (1.8%)
Skin reaction		
Cutaneous necrosis	2 (0.6%)	1 (1.8%)
Skin hematoma	2 (0.6%)	0 (0.0%)
Systemic reaction		
Flushing	16 (4.4%)	0 (0.0%)
Fever and chills	2 (0.6%)	0 (0.0%)
Lymphadenopathy	2 (0.6%)	1 (1.8%)
Nausea	1 (0.3%)	0 (0.0%)
Palpitations	1 (0.3%)	0 (0.0%)
Medication error	1 (0.3%)	1 (1.8%)

Data are number followed by percentage in parentheses. Total AEs = 55.

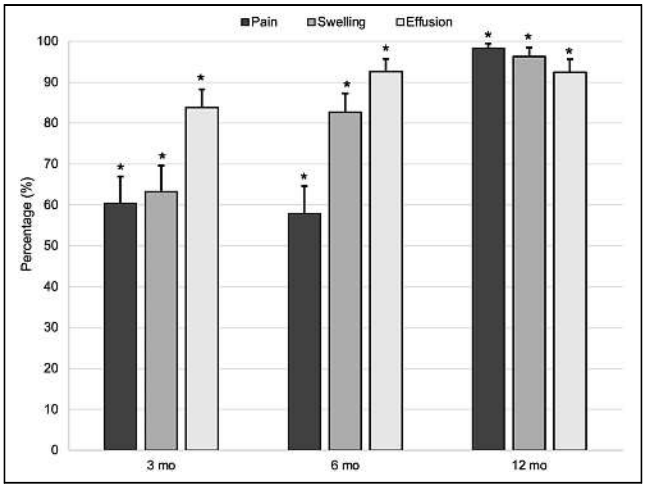

FIGURE 2. Percentage of patients with reduction in pain, swelling, and joint effusion at 3, 6, and 12 mo after radiosynoviorthesis. Upper brackets indicate 95% CI. Number of evaluable patients is 225 at 3 mo, 211 at 6 mo, and 188 at 12 mo for pain; 229 at 3 mo, 213 at 6 mo, and 189 at 12 mo for swelling; and 207 at 3 mo, 200 at 6 mo, and 178 at 12 mo for joint effusion. *Significant improvement in synovitis symptoms compared with baseline ($P < 0.001$).

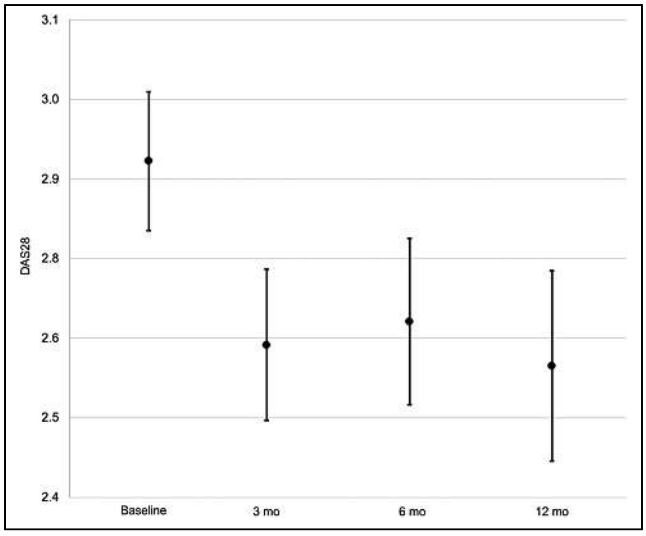

FIGURE 4. Decrease in disease activity based on DAS28 at baseline and during follow-up (3, 6, and 12 mo). Data are mean; brackets represent SD. No significant reduction in disease activity was observed at follow-up compared with baseline ($P = 0.1$). Smallest clinically significant difference in DAS28 is 1.2. Number of evaluable patients is 299 at baseline, 265 at 3 mo, 240 at 6 mo, and 200 at 12 mo.

60.4% [95% CI, 53.7%–66.9%] at 3 mo, 57.9% [95% CI, 50.8%–64.6%] at 6 mo, and 98.3% [95% CI, 95.4%–99.5%] at 12 mo; swelling: 63.2% [95% CI, 56.7%–69.6%] at 3 mo, 83.7% [95% CI, 77.9%–88.3%] at 6 mo, and 96.3% [95% CI, 92.5%–98.5%] at 12 mo; and joint effusion: 83.8% [95% CI, 77.8%–88.3%] at 3 mo, 92.6% [95% CI, 87.9%–95.7%] at 6 mo, and 92.4% [95% CI, 87.2%–95.6%] at 12 mo). Figure 3 shows a nonsignificant reduction in the patient's functional disability (mean HAQ-DI ± SD: 0.85 ± 0.07 at baseline, 0.69 ± 0.07 at 3 mo, 0.66 ± 0.07 at 6 mo, and 0.63 ± 0.08 at 12 mo; $P = 0.3$). On the other hand, the probability of HAQ-DI improvement decreased statistically significantly at 6 and 12 mo (generalized estimating equation odds ratio: 0.55 [95% CI, 0.35–0.86] at 6 mo [$P < 0.01$] and 0.42 [95% CI, 0.26–0.66] at 12 mo [$P < 0.01$]). DAS28 showed a nonsignificant reduction in disease activity (mean DAS28 ± SD: 2.9 ± 0.1 at baseline, 2.6 ± 0.1 at 3 mo, 2.7 ± 0.1 at 6 mo, and 2.6 ± 0.1 at 12 mo [$P = 0.1$]; generalized estimating equation odds ratio: 0.81 [95% CI, 0.42–1.54] at 6 mo [$P = 0.52$] and 0.95 [95% CI, 0.52–1.73] at 12 mo [$P = 0.86$]) (Fig. 4). Figure 5 shows the stability of global assessment of disease activity based on VAS 100 mm (mean VAS ± SD: 39.7 ± 3.1 at baseline, 40.0 ± 3.1 at 3 mo, 38.9 ± 3.5 at 6 mo, and

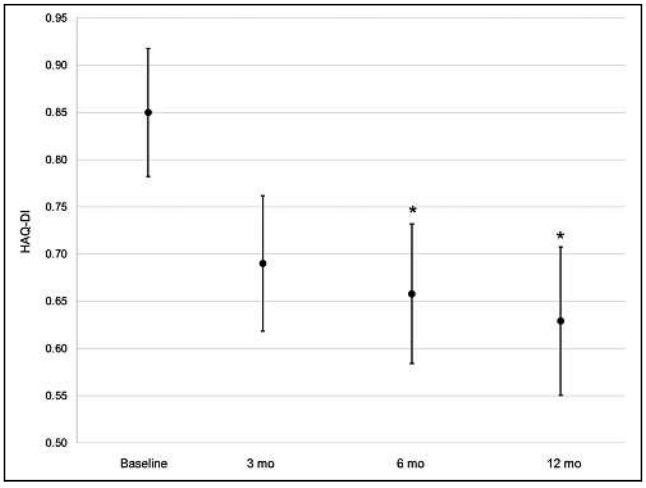

FIGURE 3. Improvement in patient's functional disability based on HAQ-DI at baseline and during follow-up (3, 6, and 12 mo). Data are mean; brackets represent SD. Nonsignificant reduction in patient's functional disability was observed at follow-up compared with baseline ($P = 0.3$). Smallest clinically significant difference in HAQ-DI is 0.25. Number of evaluable patients is 360 at baseline, 325 at 3 mo, 303 at 6 mo, and 251 at 12 mo. *Probability of HAQ-DI improvement decreases statistically significantly at 6 and 12 mo ($P < 0.01$).

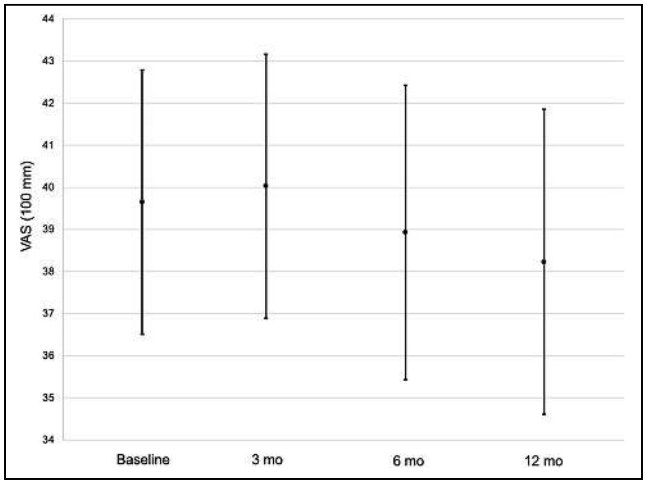

FIGURE 5. Stability of patient's global assessment of disease activity based on VAS at baseline and during follow-up (3, 6, and 12 mo). Data are mean; brackets represent SD. No significant change in patient's global assessment of disease activity was observed at follow-up compared with baseline ($P = 0.5$). Smallest clinically significant difference in VAS 100 mm is reduction of 20 mm. Number of evaluable patients is 286 at baseline, 255 at 3 mo, 238 at 6 mo, and 202 at 12 mo.

38.2 ± 3.6 at 12 mo [$P = 0.5$]; generalized estimating equation odds ratio: 1.14 [95% CI, 0.54–2.39] at 6 mo [$P = 0.74$] and 1.20 [95% CI, 0.68–2.13] at 12 mo [$P = 0.53$]). Additional subgroup analyses to compare the efficacy of radiosynoviorthesis between spondyloarthropathies, RA, osteoarthritis, pigmented villonodular synovitis, hemophilic arthropathy, and juvenile idiopathic arthritis showed no significant differences. No progression of the joint destruction initially present was observed, this joint destruction being observed in 32.7% (128/392; 95% CI, 28.0%–37.5%) of joints between baseline and 12 mo. Improvement in joint function at 12 mo was noted by physicians in 74.6% (91/122; 95% CI, 65.9%–82.0%) of patients.

DISCUSSION

In this study, mild and severe AEs occurred in 5.8% (21/360; 95% CI, 3.6%–8.8%) of patients. Most AEs were mild and resolved spontaneously. Other studies have also shown that radiosynoviorthesis using [^{90}Y]Y-citrate and [^{186}Re]Re-sulfide is safe and well tolerated (*11,19–21*), with no evidence of radiation-induced cancers at the long-term follow-up (*9,22,23*). In this trial, one of the severe complications requiring surgical and multidisciplinary management was radiation skin necrosis at the wrist injection site at 7 mo (*14*). The second case of radiation skin necrosis was mild, and both cutaneous complications resolved without sequelae. This serious complication occurred in only 0.6% of cases in our trial. In the literature, radiation skin necrosis is a complication occurring in 1.2% of patients (*24,25*). The choice of radioisotope is decisive in preventing this complication. Indeed, the extent of energy deposition in soft tissue by the chosen radioisotope is crucial, which explains why wrists with a thinner synovium benefit more from medium-energy radioisotopes, such as [^{186}Re]Re-sulfide (mean range, 1.2 mm), than from [^{90}Y]Y-citrate (mean range, 3.6 mm) (*2*). For this reason, even on request, treatment of a wrist with [^{90}Y]Y-citrate was not permitted in this trial.

Only one case of severe septic arthritis of the knee occurred, representing an incidence of 0.3%. This is in line with the 0.1% incidence of septic arthritis reported in the literature (*26*). Septic arthritis after radiosynoviorthesis is attributable to the procedure itself, not the radiopharmaceuticals, and is most often secondary to skin bacteria (*2,27*). A few studies have shown that certain risk factors, including diabetes, a prosthesis, and glucocorticoid coadministration during radiosynoviorthesis, were more likely to increase the risk of infection (*27,28*). Here, because of the lengthy interval between the procedure and the AE (12 mo), septic arthritis of the knee is explained by the patient's multiple underlying comorbidities rather than the radiosynoviorthesis.

In our study, the significant and maintained improvement in synovitis symptoms supports the efficacy of radiosynoviorthesis for the treatment of refractory synovitis. A systematic review with metaanalyses also demonstrated the efficacy of radiosynoviorthesis (*29*). For [^{186}Re]Re-sulfide radiosynoviorthesis, the success rate was 69%–100% at 6 mo and 54%–100% at more than 12 mo, compared with [^{90}Y]Y-citrate, for which the success rate was 24%–100% at 6 mo and 29%–94% at 12 mo. In our study, clinical improvement in joint function was seen in 73.3% of patients at 6 mo and in 74.6% at 12 mo. Our results are in line with a metaanalysis of 2,190 joints for which the overall response rate was 72.5% (*30*). There was also a significant early reduction in synovitis symptoms at 3 mo that was sustained at 12 mo. Some studies have also shown an early clinical response as early as 6 wk and a significant sustained response 10 y after radiosynoviorthesis (*11,12,19,26*). In addition, there was no progression of the joint destruction initially present. A 9-y study of 153 joints showed no structural progression in 80% of joints treated (*31*). Only 16.8% of treated joints required one or more intraarticular glucocorticoid injections after more than 14 d, confirming the therapeutic efficacy of radiosynoviorthesis. RA and osteoarthritis were the main underlying inflammatory conditions in the reinjected joints, but there was no significant difference between these groups for efficacy. This can be explained by the small cohort in our study and the presence of missing data. A study including 38 joints mainly affected by RA showed that a second attempt had a certain advantage (*11*). Other studies have reported better results for RA than for osteoarthritis (*26,30*). Finally, all joints in our study received a therapeutic dose of methylprednisolone acetate, 40 mg/mL, during radiosynoviorthesis for needle flushing. A 3-arm, double-blind study comparing [^{90}Y]Y-citrate with [^{90}Y]Y-citrate and glucocorticoids, and with glucocorticoids alone, demonstrated superior efficacy of [^{90}Y]Y-citrate versus glucocorticoids at 12 mo (*32*). This procedure probably did not influence the efficacy of radiosynoviorthesis.

Our study had a few limitations. Several variables, including blood tests, bone scans, and medical questionnaires, were not collected at the main site, resulting in several missing data. For example, response assessment by bone scintigraphy at 6 and 12 mo was not performed for this reason. Only 38.8% of bone scans were collected at the initial assessment, compared with 26.6% at 12 mo. However, one study involving 89 joints showed an improvement of over 68% in synovitis symptoms when followed up with 2-phase bone scans (*31*). Another limitation of the study is the absence of a comparator arm. However, our study demonstrated efficacy of 74.6% at 12 mo; this efficacy is superimposed on the success rates found in the literature, which range from 60% to 80% for radiosynoviorthesis and surgical synovectomy (*6,26*). As all patients received intraarticular glucocorticoid injections during radiosynoviorthesis, there may be a favorable or synergistic response to this combination therapy. Other studies have used the same approach and obtained results similar to ours (*25,26*).

CONCLUSION

The results of this Canadian cohort confirm the safety of radiosynoviorthesis with [^{90}Y]Y-citrate and [^{186}Re]Re-sulfide while showing this treatment to be efficacious for patients with refractory synovitis. The results also demonstrate that radiosynoviorthesis is a safe alternative to surgical synovectomy, for example—particularly in candidates with multiple comorbidities for whom surgery is undesirable—and significantly reduces synovitis symptoms in a majority of patients.

DISCLOSURE

No potential conflict of interest relevant to this article was reported.

ACKNOWLEDGMENTS

Special thanks are due to the Canadian coinvestigators of this research for their active participation in data collection, synoviorthesis, and participant follow-up: Dr. Joël Desroches (CHRTR, Quebec), Dr. Marcel Dumont (CHUQ–CHUL, Quebec), Dr. Michel Picard (CHUM, Quebec), Dr. J. Carter Thorne (Southlake Regional Health Centre, Ontario), Dr. Andrew Ross (QEII Hospital, Nova Scotia), Dr. Daniel Dionne (CSSS de Rimouski Neigette, Quebec), Dr. Jean-Mathieu Beauregard (CHUQ–Hôtel-Dieu and Hôpital

Maisonneuve, Quebec), Dr. Grégoire Blais (CH Granby, Quebec), Dr. Raymond Taillefer (CH Ste-Croix, Quebec), Dr. Lucie Carrier (Hôpital Pierre-Boucher, Quebec), Dr. François Raymond (CSSS de Gatineau, Quebec), Dr. Eugene Leung (Ottawa Hospital, Ontario), Dr. Rachel Shupack (St. Michael's Hospital, Ontario), Dr. Bohdan Bybel (Winnipeg Health Science Centre, Manitoba), Dr. Elaine Joughin (Alberta Children's Hospital, Alberta), Dr. Philip Cohen (Lions Gate Hospital, British Columbia), and Dr. Jonathan Romsa (Victoria Hospital LHSC, British Columbia). We thank the biostatistics department of the Research Center of CHUS (CRCHUS) for its support in the statistical analysis.

KEY POINTS

QUESTION: Is radiosynoviorthesis safe and effective?

PERTINENT FINDINGS: In this prospective, multicenter, open-label Canadian interventional trial of 360 patients and 392 joints treated with [^{90}Y]Y-citrate or [^{186}Re]Re-sulfide radiosynoviorthesis, the incidence of patients with radiosynoviorthesis-related AEs was 9.4%, the majority being mild and without sequelae. A significant and prolonged improvement in synovitis symptoms was also observed at 12 mo.

IMPLICATIONS FOR PATIENT CARE: Health Canada's official approval of radiopharmaceuticals for radiosynoviorthesis, a safe and effective treatment, would improve the quality of life of patients with synovitis refractory to standard treatments.

REFERENCES

1. Fellinger K, Schmid J. Local therapy of rheumatic diseases [in German]. *Wien Z Inn Med.* 1952;33:351–363.
2. Kampen WU, Boddenberg-Pätzold B, Fischer M, et al. The EANM guideline for radiosynoviorthesis. *Eur J Nucl Med Mol Imaging.* 2022;49:681–708.
3. Foster O, Brown N, Malik N, Akhtar Z, Thakur Z. A comprehensive review on surgical implications of rheumatoid arthritis. *Gen Surg Open A Open J.* 2020;1:28–34.
4. Wong Y, Cherk MH, Powell A, Cicuttini F, Bailey M, Kalff V. Efficacy of yttrium-90 synovectomy across a spectrum of arthropathies in an era of improved disease modifying drugs and treatment protocols. *Int J Rheum Dis.* 2014;17:78–83.
5. Schneider P, Farahati J, Reiners C. Radiosynovectomy in rheumatology, orthopedics, and hemophilia. *J Nucl Med.* 2005;46(suppl 1):48S–54S.
6. Karaman I, Guney A, Dogar F, et al. Comparison of arthroscopic, radioactive and combined synovectomy in the treatment of chronic non-specific knee synovitis. *Med Princ Pract.* 2014;23:551–555.
7. Deutsch E, Brodack JW, Deutsch KF. Radiation synovectomy revisited. *Eur J Nucl Med.* 1993;20:1113–1127.
8. Siegel ME, Siegel HJ, Luck JV Jr. Radiosynovectomy's clinical applications and cost effectiveness: a review. *Semin Nucl Med.* 1997;27:364–371.
9. Infante-Rivard C, Rivard GE, Derome F, et al. A retrospective cohort study of cancer incidence among patients treated with radiosynoviorthesis. *Haemophilia.* 2012; 18:805–809.
10. Fischer M, Brinker A, Sickmüller B. Safety of medicines: detection and reporting adverse reactions. In: Kampen UK, Fischer M. eds. *Local Treatment of Inflammatory Joint Diseases: Benefits and Risks.* Springer; 2015:1–30.
11. Jacob R, Smith T, Prakasha B, Joannides T. Yttrium90 synovectomy in the management of chronic knee arthritis: a single institution experience. *Rheumatol Int.* 2003;23:216–220.
12. Will R, Laing B, Edelman J, Lovegrove F, Surveyor I. Comparison of two yttrium-90 regimens in inflammatory and osteoarthropathies. *Ann Rheum Dis.* 1992;51: 262–265.
13. Zalewska J, Węgierska M, Barczyńska T, Waszczak M, Żuchowski P, Jeka S. Efficacy of radiation synovectomy (radiosynovectomy or radiosynoviorthesis) with yttrium-90 in exudative inflammation of synovial membrane of knee joints in patients with rheumatic diseases: preliminary report. *Reumatologia.* 2016;54:3–9.
14. Zeiadin N, Rampakakis E, Turcotte E, Senta H, Sampalis JS, Thorne C. Safety and therapeutic value of radiosynoviorthesis with yttrium-90: a Canadian single-centre experience. *Rheumatology (Oxford).* 2021;60:2434–2439.
15. van Groen MM, ten Klooster PM, Taal E, van de Laar MA, Glas CA. Application of the health assessment questionnaire disability index to various rheumatic diseases. *Qual Life Res.* 2010;19:1255–1263.
16. Wells G, Becker JC, Teng J, et al. Validation of the 28-joint Disease Activity Score (DAS28) and European League Against Rheumatism response criteria based on C-reactive protein against disease progression in patients with rheumatoid arthritis, and comparison with the DAS28 based on erythrocyte sedimentation rate. *Ann Rheum Dis.* 2009;68:954–960.
17. Boonstra AM, Schiphorst Preuper HR, Reneman MF, Posthumus JB, Stewart RE. Reliability and validity of the visual analogue scale for disability in patients with chronic musculoskeletal pain. *Int J Rehabil Res.* 2008;31:165–169.
18. Kellgren JH, Lawrence JS. Radiological assessment of osteo-arthrosis. *Ann Rheum Dis.* 1957;16:494–502.
19. Szentesi M, Nagy Z, Géher P, Papp I, Kampen WU. A prospective observational study on the long-term results of ^{90}yttrium citrate radiosynoviorthesis of synovitis in osteoarthritis of the knee joint. *Eur J Nucl Med Mol Imaging.* 2019;46:1633–1641.
20. Göbel D, Gratz S, von Rothkirch T, Becker W, Willert HG. Radiosynoviorthesis with rhenium-186 in rheumatoid arthritis: a prospective study of three treatment regimens. *Rheumatol Int.* 1997;17:105–108.
21. Liepe K. Efficacy of radiosynovectomy in rheumatoid arthritis. *Rheumatol Int.* 2012;32:3219–3224.
22. Vuorela J, Sokka T, Pukkala E, Hannonen P. Does yttrium radiosynovectomy increase the risk of cancer in patients with rheumatoid arthritis? *Ann Rheum Dis.* 2003;62:251–253.
23. Fernandez-Palazzi F, Caviglia H. On the safety of synoviorthesis in haemophilia. *Haemophilia.* 2001;7:50–53.
24. Kampen WU, Matis E, Czech N, Soti Z, Gratz S, Henze E. Serious complications after radiosynoviorthesis. Survey on frequency and treatment modalities. *Nuklearmedizin.* 2006;45:262–268.
25. Jahangier ZN, Jacobs JW, van Isselt JW, Bijlsma JW. Persistent synovitis treated with radiation synovectomy using yttrium-90: a retrospective evaluation of 83 procedures for 45 patients. *Br J Rheumatol.* 1997;36:861–869.
26. Szentesi M, van den Wyngaert T, Géher P, et al. Long-term clinical results from 10 years follow-up after radiosynoviorthesis: a prospective observational study. *Q J Nucl Med Mol Imaging.* 2022;66:324–333.
27. Kisielinski K, Bremer D, Knutsen A, Röttger P, Fitzek JG. Complications following radiosynoviorthesis in osteoarthritis and arthroplasty: osteonecrosis and intra-articular infection. *Joint Bone Spine.* 2010;77:252–257.
28. Armstrong RW, Bolding F. Septic arthritis after arthroscopy: the contributing roles of intraarticular steroids and environmental factors. *Am J Infect Control.* 1994;22: 16–18.
29. van der Zant FM, Boer RO, Moolenburgh JD, Jahangier ZN, Bijlsma JW, Jacobs JW. Radiation synovectomy with ^{90}yttrium, ^{186}rhenium and ^{169}erbium: a systematic literature review with meta-analyses. *Clin Exp Rheumatol.* 2009;27:130–139.
30. Kresnik E, Mikosch P, Gallowitsch HJ, et al. Clinical outcome of radiosynoviorthesis: a meta-analysis including 2190 treated joints. *Nucl Med Commun.* 2002;23: 683–688.
31. Szerb I, Gál T, Kiss D, Nagy V, Hangody L. Efficacy assessment of radiosynoviorthesis on the progression of radiological osteoarthritic features of hip and ankle joint in patients with osteoarthritis and rheumatoid arthritis. *Nuklearmedizin.* 2020; 59:269–275.
32. Rau R, Schütte H. Results of radiosynoviorthesis with yttrium 90 in chronic synovitis: a long-term prospective study. I. Total results and effect of local factors [in German]. *Z Rheumatol.* 1983;42:265–270.

Dose Reduction in Pediatric Oncology Patients with Delayed Total-Body [^{18}F]FDG PET/CT

Clemens Mingels[1,2], Benjamin A. Spencer[1], Hande Nalbant[1], Negar Omidvari[3], Mehrad Rokni[1], Axel Rominger[2], Fatma Sen[1], Simon R. Cherry[1,3], Ramsey D. Badawi[1,3], Yasser G. Abdelhafez[1,4], and Lorenzo Nardo[1]

[1]Department of Radiology, University of California Davis, Sacramento, California; [2]Department of Nuclear Medicine, Inselspital, Bern University Hospital, University of Bern, Bern, Switzerland; [3]Department of Biomedical Engineering, University of California Davis, Davis, California; and [4]Nuclear Medicine Unit, South Egypt Cancer Institute, Assiut University, Assiut, Egypt

Our aim was to define a lower limit of reduced injected activity in delayed [^{18}F]FDG total-body (TB) PET/CT in pediatric oncology patients. **Methods:** In this single-center prospective study, children were scanned for 20 min with TB PET/CT, 120 min after intravenous administration of a 4.07 ± 0.49 MBq/kg dose of [^{18}F]FDG. Five randomly subsampled low-count reconstructions were generated using $^1/_4$, $^1/_8$, $^1/_{16}$, and $^1/_{32}$ of the counts in the full-dose list-mode reference standard acquisition (20 min), to simulate dose reduction. For the 2 lowest-count reconstructions, smoothing was applied. Background uptake was measured with volumes of interest placed on the ascending aorta, right liver lobe, and third lumbar vertebra body (L3). Tumor lesions were segmented using a 40% isocontour volume-of-interest approach. Signal-to-noise ratio, tumor-to-background ratio, and contrast-to-noise ratio were calculated. Three physicians identified malignant lesions independently and assessed the image quality using a 5-point Likert scale. **Results:** In total, 113 malignant lesions were identified in 18 patients, who met the inclusion criteria. Of these lesions, 87.6% were quantifiable. Liver SUV_{mean} did not change significantly, whereas a lower signal-to-noise ratio was observed in all low-count reconstructions compared with the reference standard ($P < 0.0001$) because of higher noise rates. Tumor uptake (SUV_{max}), tumor-to-background ratio, and total lesion count were significantly lower in the reconstructions with $^1/_{16}$ and $^1/_{32}$ of the counts of the reference standard ($P < 0.001$). Contrast-to-noise ratio and clinical image quality were significantly lower in all low-count reconstructions than with the reference standard. **Conclusion:** Dose reduction for delayed [^{18}F]FDG TB PET/CT imaging in children is possible without loss of image quality or lesion conspicuity. However, our results indicate that to maintain comparable tumor uptake and lesion conspicuity, PET centers should not reduce the injected [^{18}F]FDG activity below 0.5 MBq/kg when using TB PET/CT in pediatric imaging at 120 min after injection.

Key Words: total-body PET/CT; dose reduction; pediatric oncology; long-axial-field-of-view PET/CT; [^{18}F]FDG

J Nucl Med 2024; 65:1101–1106
DOI: 10.2967/jnumed.124.267521

PET/CT has undergone rapid development since its first introduction (*1*). The latest paradigm shift was achieved by the introduction of long-axial-field-of-view and total-body (TB) PET/CT systems (*2–5*). The increased signal collection efficiency of these novel systems enables significant reduction of the injected radiopharmaceutical activity (dose reduction). In addition, delayed imaging time points (e.g., 120 min after injection) are possible, allowing further clearance of the radiotracer (*4,6–11*). With short-axial-field-of-view PET/CT, it has been shown that some tumors demonstrated higher [^{18}F]FDG uptake on delayed images (*12,13*) whereas benign lesions showed reduced tracer uptake over time (*14*). Therefore, delayed imaging was routinely established with the introduction of TB PET/CT to increase the image quality, which is of particular interest in pediatric patients (*10*).

Children with oncologic diseases such as lymphoma, sarcoma, and other soft-tissue malignancies are frequently referred to PET centers for staging or restaging (*15*). Accurate imaging is crucial because the therapy regime often relies on the PET/CT result (*16*). However, the scanning of children—compared with adults—harbors specific challenges. Accurate coregistration of PET and CT is needed to provide the high image quality necessary for interpretation. Because of patient motion, accurate coregistration is often not possible, especially in younger children. Moreover, children are more vulnerable to radiation, with an increased risk of developing secondary malignancies (*17*). It has been reported that the risk of developing childhood leukemia increases by 12%/mSv of cumulative bone marrow dose (*18*) and that 9% of all thyroid cancer cases are related to ionizing radiation (*19*). Therefore, many attempts have been made to reduce the radiation exposure of children undergoing frequent diagnostic procedures involving ionizing radiation (*20–22*).

First experiences with TB PET/CT have proven efficient in dose reduction (*4*). Chen et al. reported that half-dose imaging with [^{18}F]FDG TB PET/CT was sufficient in a cohort of 100 children, even with an acquisition of only 60 s, when 600 s was the reference standard (*22*). Consequently, ultra-low-dose [^{18}F]FDG PET/CT is theoretically possible with only $^1/_{20}$ of the clinical reference injected activity, which would reduce the effective dose of a pediatric PET scan to 0.18–0.26 mSv (*22–24*).

However, in late imaging protocols, which help reduce background and blood-pool activity but also diminish the overall count rate because of a higher amount of decayed activity, the feasibility of dose reduction has not yet been evaluated (*25*). The first aim of this study was to provide the methodology to evaluate the best reconstruction parameters for reduced injected activity in delayed imaging of pediatric oncology patients with TB PET/CT. The second aim was to assess the full potential of dose reduction clinically. The primary endpoint was to determine the lower limit of

Received Jan. 29, 2024; revision accepted Mar. 25, 2024.
For correspondence or reprints, contact Clemens Mingels (clemens.mingels@insel.ch).
Published online Apr. 25, 2024.

dose reduction with an image reconstruction protocol optimized for late [^{18}F]FDG TB PET/CT imaging.

MATERIALS AND METHODS

This study was approved by the University of California Davis institutional review board (approval 1470016). The study was performed in accordance with the Declaration of Helsinki.

Patient Population, Radiopharmaceutical, and Imaging

This was a retrospective analysis of prospectively collected registry-type data. Nineteen pediatric subjects' data were available for this study after written informed consent was obtained by the parents or guardian, providing access to the subjects' primary staging and follow-up examinations. From this cohort of 19, the initial staging examination was used for image evaluation, whereas the follow-up TB PET/CT scans from a subcohort of 12 of the 19 patients were used to optimize the reconstruction parameters. All patients underwent clinical routine [^{18}F]FDG PET/CT on a TB PET/CT scanner (uEXPLORER; United Imaging Healthcare). Subjects fasted for at least 6 h before a 4.07 ± 0.49 MBq/kg intravenous injection of [^{18}F]FDG. All patients underwent TB PET/CT scans 120 min after injection. A 20-min list-mode acquisition was recorded for all scans.

Inclusion criteria for the analysis were an age of less than 18 y, biopsy-proven oncologic disease, and the ability to successfully complete the clinical 20-min TB PET/CT scan without significant intrascan motion or use of anesthesia.

Data Preparation Using List-Mode Subsampling

Using short-frame reconstructions of a PET dataset for simulating low-count imaging will result in inherent interframe differences in the count distribution because of motion, physiologic uptake changes, and radioactive decay. To overcome this issue for a quantitative evaluation of low-count imaging scenarios, randomly subsampled low-count reconstructions were generated from the originally acquired raw list-mode data to simulate 4 reduced-dose datasets with approximately $^1/_4$, $^1/_8$, $^1/_{16}$, and $^1/_{32}$ of the total counts. The subsampling was performed by, first, randomly shuffling the list-mode coincidence events in the PET raw data and, subsequently, running a 4-frame dynamic reconstruction on the randomly shuffled dataset consisting of $^1/_4$, $^1/_8$, $^1/_{16}$, and $^1/_{32}$ of the reference standard. The dynamic frames had no overlap (i.e., a unique set of events used within each frame), to avoid interframe noise correlation in the quantitative comparison. The methodology is displayed in Figure 1. All standard data corrections were included in all reconstructions.

Reconstruction Parameter Optimization Study

The reconstruction parameter optimization study was performed by subsampling low-count reconstructions on the follow-up examinations of 12 pediatric subjects, with 4 reconstruction parameter sets for each subsampled dose, to provide a designated optimized reconstruction parameter set to be used in the image evaluation study of the 18 pediatric subjects. The 4 tested reconstruction parameter sets were chosen by the TB PET imaging team. This led to a dataset with 12 subjects, each with 4 subsampled acquisitions and 4 reconstruction parameter sets (12 × 4 × 4). For each subject and each subsampled acquisition, 3 nuclear medicine physicians reviewed the 4 image volumes side by side in randomized order and ranked them from best to worst. The preferred reconstruction parameter set was selected by consensus by 3 nuclear medicine physicians and was subsequently used for each reduced dose of the 18 initial staging examinations, providing a total of 18 × 4 subsampled low-count reconstructions (Table 1).

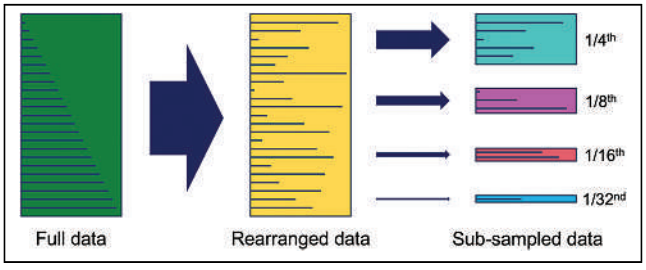

FIGURE 1. Graphical visualization of data shuffling method. Available full data were rearranged and consecutively subsampled into portions of total injected activity.

Semiquantitative Image Analysis

Tumor lesion uptake was quantified using a 40% isocontour volume of interest placed on the lesion as previously described (*4,26*). SUV_{max} and SUV_{peak} were used to assess the target lesion uptake. The background activity concentration was measured by placing a 30-mm-diameter spheric volume of interest in the right lobe of healthy liver tissue (*27*). An additional 10-mm-diameter sphere was placed on the ascending aorta and on the third lumbar vertebral body (L3) to characterize healthy organ uptake. In all cases, volumes of interest were initially placed on the reference standard image and then copied to the same anatomic locations in different reconstructions to avoid errors.

The signal-to-noise ratio (SNR) was defined as the reciprocal coefficient of variation of the liver background as follows:

$$\mathrm{SNR} = \frac{1}{\mathrm{COV}} = \left(\frac{\mu}{\sigma}\right),$$

where σ is the SD of the background volume of interest and μ is the SUV_{mean} of the background volume of interest (*4*). Tumor-to-background ratio (TBR) was defined from the ratio of tumor uptake (SUV_{max}) to liver uptake (SUV_{mean}) as follows:

$$\mathrm{TBR} = \frac{\mathrm{SUV_{max}(tumor)}}{\mathrm{SUV_{mean}\ (liver)}}.$$

Contrast-to-noise ratio (CNR) was calculated as follows:

$$\mathrm{CNR} = \frac{\mathrm{SUV_{mean}\ (lesion)} - \mathrm{SUV_{mean}(background\ liver)}}{\mathrm{SD(background\ liver)}},$$

as previously published (*28*). For semiquantitative image analysis, OsiriX version 13.0 (Pixmeo SARL) was used.

Visual Assessments of Lesion Detectability and Image Quality

Three nuclear medicine physicians evaluated lesion detectability. The number of malignant lesions per patient was counted to a maximum of 10 lesions. Image quality was rated on a 5-point Likert scale: 1 was classified as nondiagnostic and 5 as the state of the art (*29*). To minimize bias, reconstructions were anonymized and displayed randomly during the clinical evaluation.

Statistical Analysis

Statistical analysis was performed using Excel (Microsoft) and GraphPad Prism version 10 (*30*). Semiquantitative data are presented as mean ± SD or as median and range. Reconstructions were analyzed using paired *t* testing after checking for a normal distribution. *P* values of less than 0.05 were considered statistically significant.

RESULTS

Eighteen of the participants met the inclusion criteria. One patient was excluded because a 20-min acquisition was not possible in the clinical setting. From the total of 18 pediatric oncology patients included, 13 were male and 5 female, with a median age of 12 y (range, 5–17 y) and an average body mass index of 22.33 ± 4.93 kg/m^2. Patient characteristics are outlined in the

TABLE 1
Selected Reconstruction Parameters for Each Reduced Dose by Consensus from 3 Nuclear Medicine Physicians During Reconstruction Parameter Optimization

Protocol	Equivalent duration (s)	Reconstruction parameters					
		Isotropic voxel size (mm)	Iterations (*n*)	Subsets (*n*)	Point-spread function modeling	Smoothing	Filter FWHM (mm)
Reference standard	1,200	2.344	4	20	Yes	None	—
1/4 dose	300	2.344	4	20	Yes	None	—
1/8 dose	150	2.344	4	20	Yes	None	—
1/16 dose	75	2.344	4	20	Yes	Gaussian	4
1/32 dose	37	2.344	6	20	Yes	Gaussian + nonlocal means	4

FWHM = full width at half maximum.

supplemental materials (available at http://jnm.snmjournals.org). In the reference standard images, 113 malignant lesions were identified. Of these, 99 (87.6%) could be analyzed with the 40% isocontour approach in all reconstructions. The study flowchart is shown in the supplemental materials.

Reconstruction Parameter Optimization Study

Table 1 presents the optimized reconstruction parameters selected by the 3 nuclear medicine physicians. Increased smoothing was preferred for the reduced-dose reconstructions, specifically for 1/16- and 1/32-count levels. For the 1/4 and 1/8 reductions, the nuclear medicine physicians preferred the standard clinical reconstruction parameters except with the incorporation of point-spread function modeling.

Physiologic Uptake and SNR

Although liver SUV_{mean} did not significantly differ between the low-count reconstructions and the 20-min reference standard acquisition, liver SUV_{max} and SD were significantly higher in all low-count reconstructions ($P < 0.001$). Furthermore, liver SNR was significantly lower in all low-count reconstructions than with the reference standard ($P < 0.0001$) (Fig. 2). There was no significant difference in liver SNR among the low-count reconstructions. Blood pool and bone (L3) uptake and SNRs are outlined in the supplemental materials.

Tumor Uptake and Contrast

In total, 99 lesions were analyzed. Tumor uptake quantification was significantly affected in the 2 lowest-count reconstructions, showing a significantly lower ($P < 0.001$) tumor SUV_{max} in the 1/16 and 1/32 images than with the reference standard (Fig. 3). Tumor-to-background ratio was also significantly lower in these reconstructions (1/16 and 1/32, $P < 0.0001$), whereas the tumor-to-background ratio of the images with 1/4 and 1/8 of the counts of the reference standard showed no significant change from the full-dose image ($P = 0.46$ and 0.16) (Fig. 3). However, contrast-to-noise ratio was significantly lower in all low-count reconstructions than with the full-dose reference standard ($P < 0.0001$) (Fig. 3).

Clinical Image Evaluation and Number of Identified Lesions

The visual image quality assessments of all low-count reconstructions showed significantly lower Likert scale ratings than with the clinical reference standard (Fig. 4). The median rating of the full-dose reference image was 5 and was not affected in the 1/4-dose image. The median rating decreased to 4 for the 1/8-dose image, and the most impaired images ($P < 0.0001$) were found at 1/16 (median, 3) and 1/32 (median, 3) of the counts, as expected.

The visual lesion detectability evaluation revealed differences in the number of identified lesions throughout the different low-count reconstructions. Although a maximum of 113 lesions was identified in the clinical reference standard images by the 3 different readers independently, a maximum of 107 and 105 lesions was identified in the 1/4- and 1/8-dose reconstructions, respectively. These differences in lesion count were not significantly different from the reference standard ($P = 0.17$ and $P = 0.11$, respectively). However, we found significant differences in the number of identified lesions in the reconstructions with 1/16 and 1/32 of the

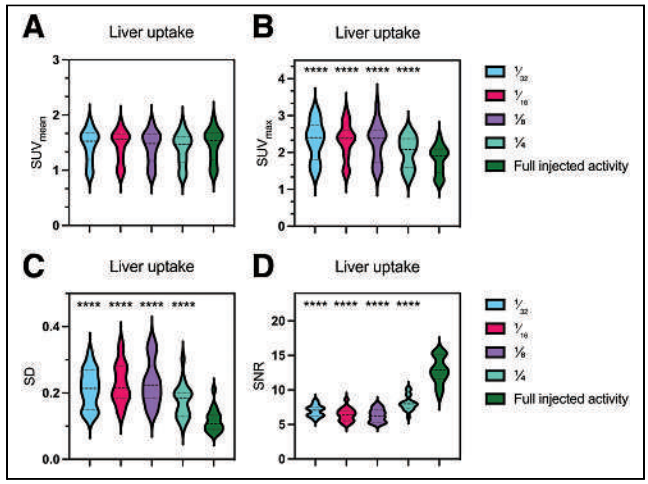

FIGURE 2. Liver SUV_{mean} (A) and SUV_{max} (B) in all low-count reconstructions, compared with full injected activity images, and SD (C) and SNR (D) in liver volumes of interest. *$P < 0.05$. **$P < 0.01$. ***$P < 0.001$. ****$P < 0.0001$.

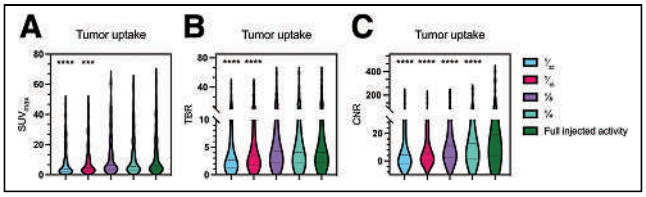

FIGURE 3. (A) Tumor SUV_{max} in all reconstructions, compared with full-injected-activity images. (B) Tumor-to-background ratio (TBR) in all reconstructions, compared with full-injected-activity images. (C) Contrast-to-noise ratio (CNR) in all reconstructions, compared with full-injected-activity images. *$P < 0.05$. **$P < 0.01$. ***$P < 0.001$. ****$P < 0.0001$.

counts of the reference standard. In the $^1/_{16}$-count reconstruction, a total of 102 lesions was identified ($P = 0.04$), and in the $^1/_{32}$-count reconstruction, readers identified only 88 lesions ($P < 0.0001$). Figure 4 shows the number of lesions identified by the 3 readers per patient, in which the medians were 8, 5.5, 5, 5, and 3.5 lesions per patient for the reference standard and for $^1/_4$, $^1/_8$, $^1/_{16}$, and $^1/_{32}$ of the reference standard, respectively.

Figure 5 illustrates an example of a 9-y-old patient for whom the detectability of the axillary lymphoma lesions was impaired by the increased noise level in the 2 lowest-count reconstructions, resulting in an inability to detect the lesion visually.

DISCUSSION

In this study investigating the lower limit for injected [^{18}F]FDG activity reduction in pediatric oncology patients, we evaluated the first data for delayed TB PET/CT in a prospective cohort. Showing that reduced injected activities are possible even in delayed imaging protocols may have the advantage of reducing absorbed doses in children, may reduce costs for the PET center, and may reduce diagnostic error due to higher tracer uptake in some malignant lesions and less uptake in some benign ones (*13*).

In our new method, we randomly shuffled the list-mode clinical reference standard acquisition of 20 min after injection to simulate reduction of injected activity. Clinical evaluation concluded that after a limit of $^1/_8$ of the reference standard, additional smoothing is required to compensate for the increased noise level (Table 1). This finding could be verified in the semiquantitative and qualitative image analysis of this study.

Liver SNR significantly decreased in the low-count reconstructions compared with the reference standard acquisition. However, we found no significant difference in the liver SNR among the reduced low-count reconstructions ($^1/_8$, $^1/_{16}$, and $^1/_{32}$), indicating that the reconstruction parameter optimization was mitigating this SNR degradation, as intended. The stable SNR was achieved by completing the first goal of the study to establish the methodology for reconstruction parameter optimization. We note that past studies missed this approach of reconstruction optimization (*24,31–33*). Therefore, this study ensured that these low-count datasets are a realistic representation of how dose reduction would be seen clinically.

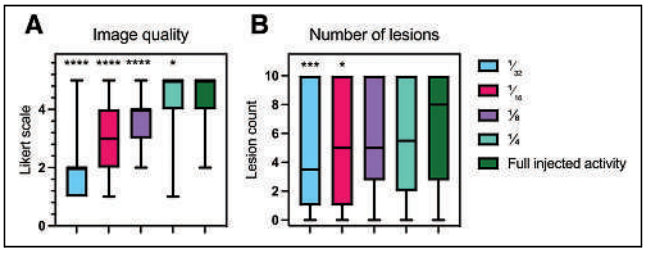

FIGURE 4. (A) Image quality on Likert scale (1–5) identified by 3 independent readers for all reconstructions, compared with full-injected-activity images. (B) Number of lesions identified by 3 independent readers for all reconstructions, compared with full-injected-activity images. *$P < 0.05$. **$P < 0.01$. ***$P < 0.001$. ****$P < 0.0001$.

This optimization was necessary because reducing the counts in any PET imaging protocol directly leads to increased noise (*34*). Furthermore, it is not expected that the reconstruction parameters suitable for a full-dose 20-min acquisition are also suitable for an acquisition with far lower count statistics (e.g., with $^1/_{16}$ or $^1/_{32}$ of the reference standard). However, previous approaches toward determining a lower limit for imaging pediatric oncology patients have not implemented image reconstruction optimization and, therefore, did not exploit the full potential of TB PET/CT in pediatric oncology (*24,35*).

Thus, even with the optimization of especially the low-count reconstructions ($^1/_{16}$ and $^1/_{32}$), we noted significantly decreased tumor uptake ($P < 0.001$), whereas the tumor uptake of $^1/_4$ or $^1/_8$ of the reference standard was not significantly reduced (Fig. 3). This finding sets the lower limit of count reduction to $^1/_8$ (i.e., 0.5 MBq/kg) of our clinical reference standard.

In agreement with the limit of injecting a 0.5 MBq/kg dose of [^{18}F]FDG in delayed TB PET/CT, the lesion conspicuity in the 2 lowest-count reconstructions was impaired, resulting in a significantly lower lesion count by the 3 independent readers ($^1/_{16}$, 90.3% of lesions identified [$P = 0.04$]; $^1/_{32}$, 77.9% of lesions identified [$P < 0.0001$]). Moreover, these reconstructions ($^1/_{16}$ and $^1/_{32}$) were found to be barely diagnostic, with ill-defined lesion conspicuity and impairment of diagnostic confidence. The subjective image noise was rated as increased to excessive and was found to be worse than average, according to the applied 5-point Likert scale (*29*). The clinical benefit of these 2 reconstructions is—despite the applied reconstruction optimization protocol—doubtful.

Our findings on the lower limits of count reduction for pediatric oncologic imaging agree well with the current [^{18}F]FDG PET/CT oncologic examination guideline published by the European Association of Nuclear Medicine, which suggests a time–activity product of at least 7 MBq·min·bed^{-1}·kg^{-1} for tumor imaging at 60 min after injection with short-axial-field-of-view PET/CT scanners (*36*). We showed that image quality is still acceptable, without significant changes in tumor uptake, tumor-to-background ratio, or lesion count, with an injected activity of 0.5 MBq/kg for delayed TB PET/CT scans in pediatric patients. A 0.5 MBq/kg injected activity translates to a time–activity product of 10 MBq·min·kg^{-1} for our delayed imaging protocol. Notably, this would correspond to 7 MBq·min·kg^{-1} for an [^{18}F]FDG TB PET/CT scan at 60 min after injection (*36*), showing even more potential to reduce the injected [^{18}F]FDG activity with TB PET/CT both at 60 min after injection and in the delayed protocols.

Some limitations of our study should be acknowledged. First, the sample size of 18 patients who met the inclusion criteria was small. However, our lesion-based analysis detected 113 malignant lesions and 99 analyzed lesions, strengthening our findings. Moreover, the study was not designed as a lesion detectability study. Nevertheless, our approach was sufficient to discriminate differences among the 4 subsampled datasets. Second, our study investigated potential use of lower injected activities using the subsampled list-mode data from a 20-min acquisition. Given that the subsampled list-mode data contain the same randoms rate and dead-time losses as the reference standard injected activity (4.07 MBq/kg), our method is an approximation. On the basis of Spencer et al., we estimate that this would equate to approximately a

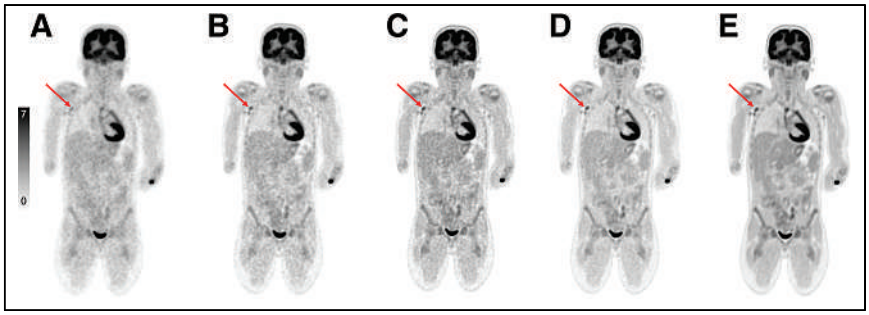

FIGURE 5. Different reconstructions for 9-y-old lymphoma patient: $^1/_{32}$ dose (A), $^1/_{16}$ dose (B) $^1/_8$ dose (C), $^1/_4$ dose (D), full dose (E). A–E show coronal slices in middle of body. Arrows indicate axillary lymphoma lesions.

4% improvement in true count rates (*37*). Therefore, in a real clinical setting we expect slightly better image quality than in our subsampled images because of a lower randoms rate and less dead time. The conclusions regarding reduced dose may be underestimated, and in a real clinical setting even lower injected activities might still yield diagnostic quality. Further studies may focus on true reduction of injected activities and compare the data with early PET/CT scans or scans from an adult patient.

In this preliminary study, only 4 low-count scans were investigated. This enabled us to define a limit of possible dose reductions at $^1/_8$ of the reference standard. However, there might still be a possibility to reduce the injected activity between the limit of $^1/_8$ and the next lower-count reconstruction ($^1/_{16}$) further. It is noteworthy that the patient cohort, with a median age of 12 y (range, 5–17 y) and an average body mass index of $22.33 \pm 4.93\ kg/m^2$, was relatively mature. This patient cohort was selected because of the inclusion criteria and clinical imaging settings, which did not allow sedation during the examination.

CONCLUSION

Injected activity reduction with delayed [^{18}F]FDG TB PET/CT imaging in children is possible without loss of image quality or lesion conspicuity. This study supported the reduction of injected radiotracer activity, especially in children who may undergo multiple follow-up studies. Our results indicate that the lower limit for delayed [^{18}F]FDG TB PET/CT imaging in pediatric oncology patients is 0.5 MBq/kg. Dose reduction can be generalized to other long-axial-field-of-view scanners; however, the precise magnitude of the reduced injected activity may be scanner-specific.

DISCLOSURE

Research reported in this publication was supported by the National Institutes of Health under award R01CA249422. The work was also supported by the In Vivo Translational Imaging Shared Resources with funds from NCI P30CA093373 and by the Fred and Julia Rusch Foundation for Nuclear Medicine Research and Education. Hande Nalbant's funding is partially provided by United Imaging Healthcare's UIH Fellowship Gift. Axel Rominger has received research support and speaker honoraria from Siemens. Lorenzo Nardo is the principal investigator of a service agreement with United Imaging Healthcare. Lorenzo Nardo is the site principal investigator of clinical trials supported by Novartis Pharmaceuticals Corp. Lorenzo Nardo is the principal investigator of clinical trials supported by Telix Pharmaceuticals, Lantheus Medical Imaging, and GE Healthcare. Lorenzo Nardo is coprincipal investigator of a clinical trial supported by Lilly. Ramsey Badawi is the principal investigator of a clinical trial supported by Lilly. Simon Cherry and Ramsey Badawi received research support from United Imaging Healthcare during the course of this work. The University of California Davis has a revenue sharing agreement with United Imaging Healthcare. Fatma Sen is the principal investigator of clinical research sponsored by Biogen. No other potential conflict of interest relevant to this article was reported.

ACKNOWLEDGMENTS

We thank the EXPLORER Molecular Imaging Center clinical research and compliance team, especially Phu Huynh, Dana Little, Ofilio Vigil, Lynda Painting, and Anh Nguyen.

KEY POINTS

QUESTIONS: Can we reduce the injected activity in delayed imaging protocols scanning pediatric oncology patients with [^{18}F]FDG TB PET/CT?

PERTINENT FINDINGS: In this prospective single-center study, delayed [^{18}F]FDG TB PET/CT in pediatric oncology patients enabled a reduction in the injected radioactivity (0.5 MBq/kg with a 20-min acquisition).

IMPLICATIONS FOR PATIENT CARE: [^{18}F]FDG TB PET/CT with delayed imaging protocols in pediatric oncology patients can decrease ionized radiation exposure.

REFERENCES

1. Beyer T, Townsend DW, Brun T, et al. A combined PET/CT scanner for clinical oncology. *J Nucl Med.* 2000;41:1369–1379.
2. Karp JS, Viswanath V, Geagan MJ, et al. PennPET Explorer: design and preliminary performance of a whole-body imager. *J Nucl Med.* 2020;61:136–143.
3. Badawi RD, Shi H, Hu P, et al. First human imaging studies with the EXPLORER total-body PET scanner. *J Nucl Med.* 2019;60:299–303.
4. Alberts I, Hünermund J-N, Prenosil G, et al. Clinical performance of long axial field of view PET/CT: a head-to-head intra-individual comparison of the Biograph Vision Quadra with the Biograph Vision PET/CT. *Eur J Nucl Med Mol Imaging.* 2021;48:2395–2404.
5. Mingels C, Caobelli F, Alavi A, et al. Total-body PET/CT or LAFOV PET/CT? Axial field-of-view clinical classification. *Eur J Nucl Med Mol Imaging.* 2024;51:951–953.
6. Alberts I, Sari H, Mingels C, et al. Long-axial field-of-view PET/CT: perspectives and review of a revolutionary development in nuclear medicine based on clinical experience in over 7000 patients. *Cancer Imaging.* 2023;23:28.
7. Alberts I, Prenosil G, Mingels C, et al. Feasibility of late acquisition [^{68}Ga]Ga-PSMA-11 PET/CT using a long axial field-of-view PET/CT scanner for the diagnosis of recurrent prostate cancer: first clinical experiences. *Eur J Nucl Med Mol Imaging.* 2021;48:4456–4462.
8. Mingels C, Weidner S, Sari H, et al. Impact of the new ultra-high sensitivity mode in a long axial field-of-view PET/CT. *Ann Nucl Med.* 2023;37:310–315.
9. Alberts I, Sachpekidis C, Prenosil G, et al. Digital PET/CT allows for shorter acquisition protocols or reduced radiopharmaceutical dose in [^{18}F]-FDG PET/CT. *Ann Nucl Med.* 2021;35:485–492.
10. Nardo L, Abdelhafez YG, Spencer BA, Badawi RD. Clinical implementation of total-body PET/CT at University of California, Davis. *PET Clin.* 2021;16:1–7.
11. Zhang Q, Hu Y, Zhou C, et al. Reducing pediatric total-body PET/CT imaging scan time with multimodal artificial intelligence technology. *EJNMMI Phys.* 2024;11:1.

12. Cheng G, Torigian DA, Zhuang H, Alavi A. When should we recommend use of dual time-point and delayed time-point imaging techniques in FDG PET? *Eur J Nucl Med Mol Imaging.* 2013;40:779–787.
13. Kubota K, Itoh M, Ozaki K, et al. Advantage of delayed whole-body FDG-PET imaging for tumour detection. *Eur J Nucl Med.* 2001;28:696–703.
14. Basu S, Kung J, Houseni M, Zhuang H, Tidmarsh GF, Alavi A. Temporal profile of fluorodeoxyglucose uptake in malignant lesions and normal organs over extended time periods in patients with lung carcinoma: implications for its utilization in assessing malignant lesions. *Q J Nucl Med Mol Imaging.* 2009;53:9–19.
15. McCarville MB. PET-CT imaging in pediatric oncology. *Cancer Imaging.* 2009;9: 35–43.
16. Vali R, Alessio A, Balza R, et al. SNMMI procedure standard/EANM practice guideline on pediatric ^{18}F-FDG PET/CT for oncology 1.0. *J Nucl Med.* 2021;62: 99–110.
17. Kutanzi KR, Lumen A, Koturbash I, Miousse IR. Pediatric exposures to ionizing radiation: carcinogenic considerations. *Int J Environ Res Public Health.* 2016; 13:1057.
18. Kendall GM, Little MP, Wakeford R, et al. A record-based case-control study of natural background radiation and the incidence of childhood leukaemia and other cancers in Great Britain during 1980-2006. *Leukemia.* 2013;27:3–9.
19. Ron E, Kleinerman RA, Boice JD. LiVolsi VA, Flannery JT, Fraumeni JF. A population-based case-control study of thyroid cancer. *J Natl Cancer Inst.* 1987; 79:1–12.
20. Tang S, Hu Y, Zeng J, et al. Significant CT dose reduction of 2-[^{18}F]FDG PET/CT in pretreatment pediatric lymphoma without compromising the diagnostic and staging efficacy. *Eur Radiol.* 2023;33:2248–2257.
21. Waelti S, Skawran S, Sartoretti T, et al. A third of the radiotracer dose: two decades of progress in pediatric [^{18}F]fluorodeoxyglucose PET/CT and PET/MR imaging. *Eur Radiol.* October 19, 2023 [Epub ahead of print].
22. Chen W, Liu L, Li Y, et al. Evaluation of pediatric malignancies using total-body PET/CT with half-dose [^{18}F]-FDG. *Eur J Nucl Med Mol Imaging.* 2022;49: 4145–4155.
23. Tan H, Qi C, Cao Y, et al. Ultralow-dose [^{18}F]FDG PET/CT imaging: demonstration of feasibility in dynamic and static images. *Eur Radiol.* 2023;33:5017–5027.
24. Zhao Y-M, Li Y-H, Chen T, et al. Image quality and lesion detectability in low-dose pediatric ^{18}F-FDG scans using total-body PET/CT. *Eur J Nucl Med Mol Imaging.* 2021;48:3378–3385.
25. Costantini DL, Vali R, Chan J, McQuattie S, Charron M. Dual-time-point FDG PET/CT for the evaluation of pediatric tumors. *AJR.* 2013;200:408–413.
26. Lee H, Paeng JC, Hong SH, et al. Appropriate margin thresholds for isocontour metabolic volumetry of fluorine-18 fluorodeoxyglucose PET in sarcoma: a hybrid PET/MRI study. *Nucl Med Commun.* 2016;37:1088–1094.
27. Wahl RL, Jacene H, Kasamon Y, Lodge MA. From RECIST to PERCIST: evolving considerations for PET response criteria in solid tumors. *J Nucl Med.* 2009;50(suppl 1): 122S–150S.
28. Yan J, Schaefferkoetter J, Conti M, Townsend D. A method to assess image quality for low-dose PET: analysis of SNR, CNR, bias and image noise. *Cancer Imaging.* 2016;16:26.
29. Calderón E, Schmidt FP, Lan W, et al. Image quality and quantitative PET parameters of low-dose [^{18}F]FDG PET in a long axial field-of-view PET/CT scanner. *Diagnostics (Basel).* 2023;13:3240.
30. Mingels C, Sachpekidis C, Bohn KP, et al. The influence of colour scale in lesion detection and patient-based sensitivity in [^{68}Ga]Ga-PSMA-PET/CT. *Nucl Med Commun.* 2021;42:495–502.
31. Li Y, Wang J, Hu J, et al. PET/CT scan without sedation: how to use total-body PET/CT to salvage child's involuntary movement? *Eur J Nucl Med Mol Imaging.* 2023;50:2912–2913.
32. Chen W, Liu L, Li Y, et al. Evaluation of pediatric malignancies using total-body PET/CT with half-dose [^{18}F]-FDG. *Eur J Nucl Med Mol Imaging.* 2022;49:4145–4155.
33. Dickson J, Eberlein U, Lassmann M. The effect of modern PET technology and techniques on the EANM paediatric dosage card. *Eur J Nucl Med Mol Imaging.* 2022;49:1964–1969.
34. MacDonald LR, Harrison RL, Alessio AM, Hunter WCJ, Lewellen TK, Kinahan PE. Effective count rates for PET scanners with reduced and extended axial field of view. *Phys Med Biol.* 2011;56:3629–3643.
35. Mohammadi N, Akhlaghi P. Evaluation of radiation dose to pediatric models from whole body PET/CT imaging. *J Appl Clin Med Phys.* 2022;23:e13545.
36. Boellaard R, Delgado-Bolton R, Oyen WJG, et al. FDG PET/CT: EANM procedure guidelines for tumour imaging: version 2.0. *Eur J Nucl Med Mol Imaging.* 2015;42:328–354.
37. Spencer BA, Berg E, Schmall JP, et al. Performance evaluation of the uEXPLORER total-body PET/CT scanner based on NEMA NU 2-2018 with additional tests to characterize PET scanners with a long axial field of view. *J Nucl Med.* 2021;62:861–870.

Natural History of Myocardial $\alpha_v\beta_3$ Integrin Expression After Acute Myocardial Infarction: Correlation with Changes in Myocardial Blood Flow

Matthieu Dietz[1–3], Christel H. Kamani[1,4], Colin Bousige[5], Vincent Dunet[1,6], Judith Delage[6,7], Vladimir Rubimbura[4,8], Marie Nicod Lalonde[1,6], Giorgio Treglia[1,6,9,10], Niklaus Schaefer[1,6], Wail Nammas[11,12], Antti Saraste[11,12], Juhani Knuuti[12], Nathan Mewton[2], and John O. Prior[1,6]

[1]Nuclear Medicine and Molecular Imaging Department, Lausanne University Hospital, Lausanne, Switzerland; [2]Institut de Cardiologie des Hospices Civils de Lyon, CarMeN Laboratory INSERM 1060, Université Claude Bernard Lyon 1, Lyon, France; [3]Service de Médecine Nucléaire, Hospices Civils de Lyon, Lyon, France; [4]Department of Cardiology, University Hospital of Lausanne, Lausanne, Switzerland; [5]Laboratoire des Multimatériaux et Interfaces, UMR CNRS 5615, Université Claude Bernard Lyon 1, Villeurbanne, France; [6]University of Lausanne, Lausanne, Switzerland; [7]Radiopharmacy Unit, Department of Pharmacy, University Hospital of Lausanne, Lausanne, Switzerland; [8]Department of Cardiology, Ensemble Hospitalier de la Côte, Morges, Switzerland; [9]Imaging Institute of Southern Switzerland, Ente Ospedaliero Cantonale, Bellinzona, Switzerland; [10]Faculty of Biomedical Sciences, Università della Svizzera Italiana, Lugano, Switzerland; [11]Heart Center, Turku University Hospital, Turku, Finland; and [12]Turku PET Centre, Turku University Hospital and University of Turku, Turku, Finland

Angiogenesis is an essential part of the cardiac repair process after myocardial infarction, but its spatiotemporal dynamics remain to be fully deciphered.^{68}Ga-NODAGA-Arg-Gly-Asp (RGD) is a PET tracer targeting $\alpha_v\beta_3$ integrin expression, which is a marker of angiogenesis. **Methods:** In this prospective single-center trial, we aimed to monitor angiogenesis through myocardial integrin $\alpha_v\beta_3$ expression in 20 patients with ST-segment elevation myocardial infarction (STEMI). In addition, the correlations between the expression levels of myocardial $\alpha_v\beta_3$ integrin and the subsequent changes in ^{82}Rb PET/CT parameters, including rest and stress myocardial blood flow (MBF), myocardial flow reserve (MFR), and wall motion abnormalities, were assessed. The patients underwent ^{68}Ga-NODAGA-RGD PET/CT and rest and stress ^{82}Rb-PET/CT at 1 wk, 1 mo, and 3 mo after STEMI. To assess ^{68}Ga-NODAGA-RGD uptake, the summed rest ^{82}Rb and ^{68}Ga-NODAGA-RGD images were coregistered, and segmental SUVs were calculated (RGD SUV). **Results:** At 1 wk after STEMI, 19 participants (95%) presented increased ^{68}Ga-NODAGA-RGD uptake in the infarcted myocardium. Seventeen participants completed the full imaging series. The values of the RGD SUV in the infarcted myocardium were stable 1 mo after STEMI (1 wk vs. 1 mo, 1.47 g/mL [interquartile range (IQR), 1.37–1.64 g/mL] vs. 1.47 g/mL [IQR, 1.30–1.66 g/mL]; $P = 0.9$), followed by a significant partial decrease at 3 mo (1.32 g/mL [IQR, 1.12–1.71 g/mL]; $P = 0.011$ vs. 1 wk and 0.018 vs. 1 mo). In segment-based analysis, positive correlations were found between RGD SUV at 1 wk and the subsequent changes in stress MBF (Spearman ρ: $r = 0.17$, $P = 0.0033$) and MFR (Spearman ρ: $r = 0.31$, $P < 0.0001$) at 1 mo. A negative correlation was found between RGD SUV at 1 wk and the subsequent changes in wall motion abnormalities at 3 mo (Spearman ρ: $r = -0.12$, $P = 0.035$). **Conclusion:** The present study found that $\alpha_v\beta_3$ integrin expression is significantly increased in the infarcted myocardium 1 wk after STEMI. This expression remains stable after 1 mo and partially decreases after 3 mo. Initial $\alpha_v\beta_3$ integrin expression at 1 wk is significantly weakly correlated with subsequent improvements in stress MBF, MFR, and wall motion analysis.

Key Words: integrin $\alpha_v\beta_3$; PET; myocardial infarction; angiogenesis; RGD

J Nucl Med 2024; 65:1107–1112
DOI: 10.2967/jnumed.124.267514

The initiation of cardiac repair after a myocardial infarction (MI) requires a complex series of processes. In the first few days after reperfusion, an inflammatory phase with intense inflammation and immune cell infiltration enables the infarct to be cleared of damaged cells. This phase is followed by a reparative and proliferative phase over the next several days, with a believed peak around day 7; it includes the resolution of inflammation, cardiac fibroblast proliferation, scar formation, and angiogenesis, which are essential parts of the repair process (*1,2*). However, the spatiotemporal dynamics of angiogenesis after an MI remain to be fully deciphered (*2*). To prevent heart failure after MI, an improved understanding of myocardial angiogenesis is essential for the future development of effective and targeted treatments.

The transmembrane glycoprotein $\alpha_v\beta_3$ integrin is involved in cell interaction with the extracellular matrix, migration, and proliferation. Integrin $\alpha_v\beta_3$ is expressed on activated endothelial cells, where it plays a critical role in the angiogenic process within the myocardium after injury (*3–6*). Expression of integrin $\alpha_v\beta_3$ has also been reported in other various cell types, such as fibroblasts and activated macrophages (*7–10*). This diversity in expression may introduce some confounding effects. However, $\alpha_v\beta_3$ imaging holds promise for assessment of cardiac wound healing and repair after MI (*11,12*). In 2015, in a publication summarizing advanced techniques to evaluate angiogenesis, the American Heart Association cited the use of radiotracers to assess integrin expression (*13*).

Received Jan. 24, 2024; revision accepted Apr. 13, 2024.
For correspondence or reprints, contact John O. Prior (john.prior@chuv.ch).
Published online May 9, 2024.

^{68}Ga-NODAGA-Arg-Gly-Asp (RGD) is a PET tracer having a high binding affinity for $\alpha_v\beta_3$ and favorable biokinetics (*14,15*). A widely used PET perfusion tracer in clinical practice is ^{82}Rb, allowing for accurate measurement of rest and stress myocardial perfusion in absolute units, with a test–retest methodologic precision of around 20% (*16*).

We hypothesized that myocardial ^{68}Ga-NODAGA-RGD uptake is increased during the peak of the proliferative phase after acute ST-segment elevation MI (STEMI) and is reduced during later stages of infarct healing. The objective of the present study was to assess the expression levels of myocardial $\alpha_v\beta_3$ integrin at 1 wk after STEMI and their potential evolution at 1 and 3 mo. In addition, the correlations between the expression levels of myocardial $\alpha_v\beta_3$ integrin and the subsequent changes in ^{82}Rb-PET/CT parameters, including rest and stress myocardial blood flow (MBF), myocardial flow reserve (MFR), and wall motion abnormalities, were assessed.

MATERIALS AND METHODS

Study Design

This was a prospective single-center trial conducted in the Centre Hospitalier Universitaire Vaudois (Lausanne, Switzerland). All participants were included within the first 12 h after symptom onset and underwent reperfusion (supplemental materials; available at http://jnm.snmjournals.org). The study was approved by the ethics committee of the canton of Vaud (protocol CER-VD 429/14) and registered at ClinicalTrials.gov (NCT03809689). All patients gave written informed consent.

PET/CT Imaging

All participants underwent ^{68}Ga-NODAGA-RGD PET/CT and rest and stress ^{82}Rb-PET/CT at 1 wk (4–10 d) after STEMI. Then, the participants underwent repeated ^{68}Ga-NODAGA-RGD PET/CT and rest and stress ^{82}Rb-PET/CT at 1 and 3 mo after STEMI (Fig. 1). The ^{82}Rb-PET/CT imaging was performed as previously described (*17*), with the complete imaging acquisition protocol reported in the supplemental materials. Briefly, a 5 MBq/kg dose of ^{82}Rb (Ruby-Fill generator and ^{82}Rb elution system; Jubilant DraxImage) was administered through an automated infusion system for 15–25 s, and 3-dimensional dynamic PET images were acquired for 6.1 min (12 × 8, 5 × 12, 1 × 30, 1 × 60, and 1 × 120 s). Stress acquisitions were then performed using the same protocol. Then, a median of 159 MBq of ^{68}Ga-NODAGA-RGD was injected as an intravenous bolus and was followed by a PET acquisition of 10 min after a median of 60 min. Images were reconstructed using ordered-subsets expectation maximization algorithms.

PET Image Analysis

Image analyses were performed using PMOD (version 4.3; PMOD Technologies).

^{82}Rb-PET/CT Analysis. Perfusion was assessed quantitatively, measuring MBF in mL/min/g at rest and stress using a 1-tissue-compartment model with a flow-dependent extraction correction (supplemental materials). Perfusion was also assessed visually and semiquantitatively. A segmental wall motion analysis was performed on rest-gated ^{82}Rb-PET images using a 5-point scoring scale, and the summed rest score for wall motion was derived. Rest left ventricular end-diastolic and end-systolic volumes, as well as ejection fraction, were computed.

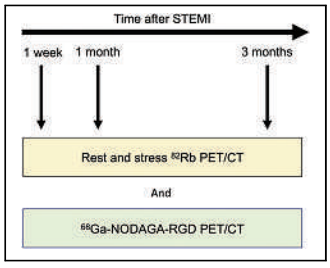

FIGURE 1. Experimental timeline.

^{68}Ga-NODAGA-RGD PET/CT Analysis. ^{68}Ga-NODAGA-RGD images were assessed visually and quantitatively. To assess the RGD uptake, the summed rest ^{82}Rb images and the ^{68}Ga-NODAGA-RGD images were coregistered (Supplemental Fig. 1). Polar maps of ^{68}Ga-NODAGA-RGD uptake expressed as SUVs (SUV; measured activity concentration [Bq/mL] × body weight [g]/injected dose at the time of image decay correction [Bq]) were generated, and mean segmental SUVs were calculated (RGD SUV). The characterization of the infarcted myocardium and the remote myocardium is detailed in the supplemental materials.

Statistical Analysis

No statistical methods were used to predetermine sample size. All statistical analyses were performed using R software (version 4.2.2, R Project). A P value of less than 0.05 was considered statistically significant. Continuous variables were expressed as median and interquartile range (IQR) or as mean ± SEM. The comparisons were performed using a Wilcoxon signed-ranks test. Categoric data were expressed as count and percentage. The Friedman test was used to compare continuous variables across multiple time points. When statistical significance was reached, post hoc Dunn multiple-comparison tests were used for pairwise comparisons. The correlations between RGD SUV and the subsequent changes in rest MBF, stress MBF, MFR, and wall motion analysis were assessed on all segments using the Spearman correlation analysis. The tests were selected because of the nonnormal distribution of the data, as determined by the Shapiro–Wilk test.

RESULTS

Participants

In total, 20 participants were included in the study (20% female; age, 63 y [IQR, 58–69 y]; Supplemental Table 1). Among the participants, 19 (95%) had no previous history of cardiovascular disease before the onset of acute STEMI. Only one participant had a history of prior coronary revascularization, with percutaneous coronary intervention (PCI) and coronary artery bypass graft surgery.

PCI was performed on all the participants 3.8 h (IQR, 2.3–6.3 h) after symptoms onset. Invasive angiography found single-vessel obstructive disease in 7 (35%) participants and multivessel obstructive coronary artery disease in 13 (65%). All participants underwent stenting using drug-eluting stents of the culprit lesion. One participant (5%) had unsuccessful reperfusion with a post-PCI thrombolysis in MI flow grade 1.

The 20 participants underwent rest and stress ^{82}Rb-PET/CT and ^{68}Ga-NODAGA-RGD PET/CT imaging 9 d (IQR, 7–10 d) after STEMI. A total of 18 participants underwent a second ^{82}Rb-PET/CT and ^{68}Ga-NODAGA-RGD PET/CT study 32 d (IQR, 30–37 d) after STEMI, and 17 participants underwent a third ^{82}Rb-PET/CT and ^{68}Ga-NODAGA-RGD PET/CT study 89 d (IQR, 83–96 d) after STEMI and completed the full imaging series. In segment-based analysis, rest and stress MBF, MFR, wall motion analysis, and RGD SUV were assessed for the full imaging series in 289 segments (17 × 17 participants).

Imaging Findings 1 Week After STEMI

Complete reperfusion, as indicated by absence of a significant perfusion defect (summed stress score < 4), was observed in 6 participants (33%). The rest MBF was 0.50 mL/min/g (IQR, 0.42–0.58 mL/min/g) across the entire myocardium, 0.58 mL/min/g (IQR, 0.48–0.60 mL/min/g) in the remote myocardium, and 0.38 mL/min/g (IQR, 0.34–0.52 mL/min/g) in the infarcted myocardium. Rest left ventricular ejection fraction was less than 50% in 12 participants

(60%). A total of 14 participants (70%) demonstrated segmental wall motion abnormalities (summed rest score for wall motion > 0).

A total of 19 participants (95%) presented RGD-positive segments ($n = 66$); those segments were always included in myocardial tissue perfused by the culprit coronary artery. Among those 66 positive segments, 55 were obtained from the 17 participants who completed the full imaging series and were selected to represent the infarcted myocardium. Among the 6 participants who experienced a complete reperfusion and had no significant ^{82}Rb PET perfusion defect (summed stress score < 4), RGD-positive segments were detected in 5 (83%).

Temporal Changes

The values of the RGD SUV in the infarcted myocardium were stable 1 mo after STEMI ($P = 0.9$ for post hoc comparison of 1 wk vs. 1 mo; Table 1), followed by a significant decrease at 3 mo ($P = 0.011$ for post hoc comparison with 1 wk, $P = 0.018$ for post hoc comparison with 1 mo; Table 1; Figs. 2 and 3). There was no significant change in RGD SUV in the remote myocardium throughout the follow-up (Friedman test $P = 0.59$). At all time points, the RGD SUVs of the infarcted myocardium and the remote myocardium were significantly different (all $P < 0.001$).

In participants with significant ^{82}Rb-PET/CT perfusion defects, areas of positive RGD uptake matched the extent of perfusion defects, with some slight extensions in border zones. In the 2 participants with the most severe infarcts (rest MBF in the infarcted myocardium at 1 wk of 0.30 mL/min/g and 0.26 mL/min/g), the RGD SUVs of the infarcted myocardium increased by at least 20% at 1 mo, without a change in clinical status or occurrence of events (Fig. 4; Supplemental Fig. 2). In these 2 participants, the RGD uptake started in the border zone and extended into the necrotic infarct core (Fig. 4). The RGD uptake was relatively homogeneous in all the other participants with smaller infarcts.

In participant-based analysis, global ^{82}Rb-PET/CT parameters and hemodynamics during ^{82}Rb-PET/CT imaging did not significantly change between initial and follow-up imaging (Supplemental Tables 2 and 3). Left ventricular ejection fraction improved by at least 5% in 8 (12%) of the 17 participants who completed the full imaging series. In segment-based analysis, rest MBF improved by at least 20% in 163 segments (56%), stress MBF improved by at least 20% in 164 segments (57%), MFR improved by at least 20% in 151 segments (52%), and wall motion abnormalities improved (difference score for wall motion ≥ 1) in 61 segments (21%).

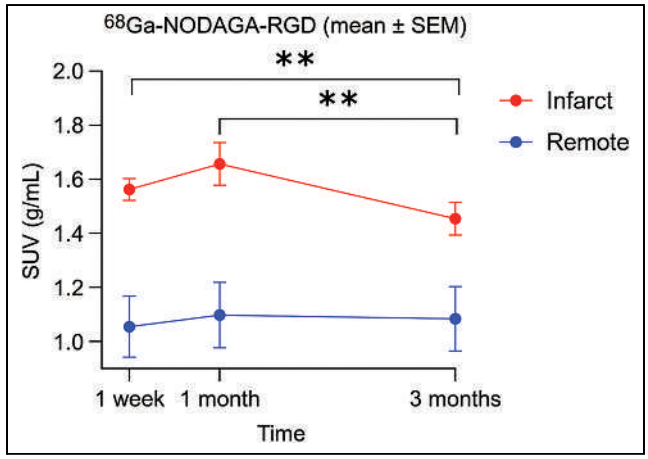

FIGURE 2. $\alpha_v\beta_3$ integrin expression in infarcted myocardium remained stable 1 mo after STEMI, followed by significant partial decrease at 3 mo. $^{**}P \leq 0.01$.

Correlations Between RGD SUV and Subsequent Changes in ^{82}Rb-PET Parameters

In segment-based analysis, positive correlations were found between initial RGD SUV at 1 wk and the subsequent changes at 3 mo in stress MBF (Spearman ρ: $r = 0.13$, $P = 0.026$) and MFR (Spearman ρ: $r = 0.18$, $P = 0.003$). There was no correlation between RGD SUV at 1 wk and the subsequent changes in rest MBF at 3 mo (Spearman ρ: $r = –0.08$, $P = 0.19$). A negative correlation was found between RGD SUV at 1 wk and the subsequent changes in wall motion abnormalities at 3 mo (Spearman ρ: $r = –0.12$, $P = 0.035$).

TABLE 1
Temporal Changes in Infarcted and Remote Myocardium

Parameter	1 wk	1 mo	3 mo
Infarcted myocardium			
RGD SUV (g/mL)	1.47 (1.37–1.64)	1.47 (1.30–1.66)	1.32 (1.12–1.71)*
Rest MBF (mL/min/g)	0.38 (0.34–0.52)	0.44 (0.31–0.58)	0.44 (0.37–0.52)
Stress MBF (mL/min/g)	1.16 (0.71–1.61)	1.49 (0.77–1.96)	1.51 (0.92–2.18)†
MFR (1)	3.04 (1.96–3.90)	2.94 (2.42–3.62)	3.50 (2.32–4.65)
Remote myocardium			
RGD SUV (g/mL)	1.05 (0.92–1.11)	1.01 (0.99–1.11)	1.05 (0.94–1.15)
Rest MBF (mL/min/g)	0.58 (0.48–0.60)	0.57 (0.46–0.75)	0.50 (0.49–0.69)
Stress MBF (mL/min/g)	1.88 (1.30–2.19)	1.99 (1.24–2.16)	1.92 (1.22–2.39)
MFR (1)	3.35 (2.67–4.16)	3.19 (2.28–3.51)	2.98 (2.27–4.75)

*$P = 0.011$ vs. 1 wk and $P = 0.018$ vs. 1 mo.
†$P = 0.035$ vs. 1 wk.
Variables are expressed as median and IQR. Number 1 after MFR indicates unitless dimension.

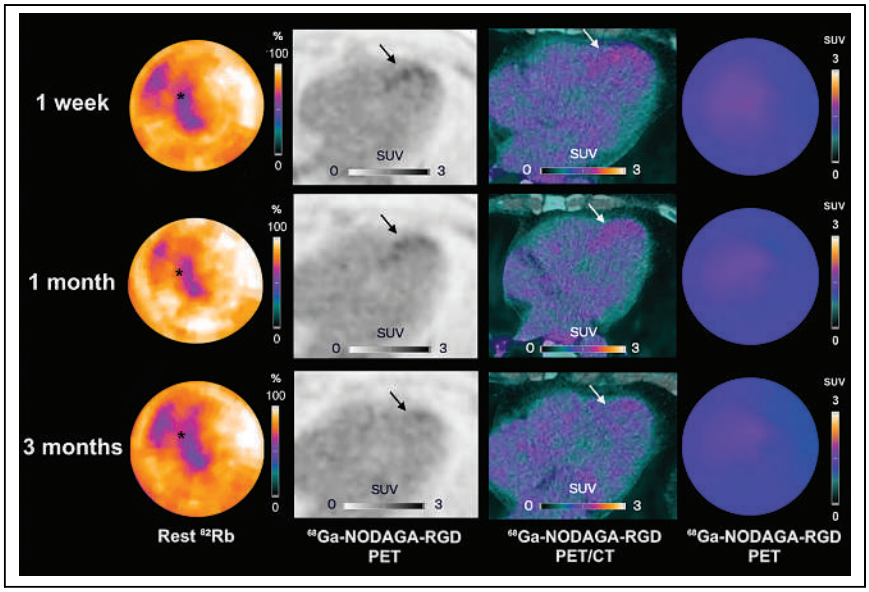

FIGURE 3. Participant example with decrease in $\alpha_v\beta_3$ integrin expression levels (arrows) in infarcted myocardium (asterisks) after 1 wk to follow-up at 3 mo. Shown are rest ^{82}Rb, ^{68}Ga-NODAGA-RGD PET, and ^{68}Ga-NODAGA-RGD PET/CT images at 1 wk (first row), 1 mo (second row), and 3 mo (third row) after STEMI.

In further analysis, positive significant correlations were found between RGD SUV and the subsequent changes in stress MBF and MFR in the 1-wk to 1-mo period (Spearman ρ: $r = 0.17$, $P = 0.0033$, and Spearman ρ: $r = 0.31$, $P < 0.0001$, respectively; Fig. 5). No correlation was found between RGD SUV at 1 mo and the subsequent changes at 3 mo in stress MBF (Spearman ρ: $r = 0.05$, $P = 0.44$) or in MFR (Spearman ρ: $r = -0.02$, $P = 0.72$). No correlation was found during these shorter periods between RGD SUV and the subsequent changes in wall motion abnormalities (1-wk to 1-mo period, Spearman ρ: $r = 0.02$, $P = 0.7$; 1-mo to 3-mo period, Spearman ρ: $r = 0.06$, $P = 0.33$).

DISCUSSION

The present study reported in vivo, in humans, an increased $\alpha_v\beta_3$ integrin expression in the infarcted myocardium 1 wk after STEMI. The levels of $\alpha_v\beta_3$ integrin expression remained stable at 1 mo after STEMI and partially decreased at 3 mo, suggesting that angiogenesis remains active 3 mo after the infarct. Moreover, there were significant weak correlations between the segmental levels of $\alpha_v\beta_3$ integrin expression at 1 wk and the subsequent improvements in stress MBF, MFR, and wall motion analysis.

The kinetics of angiogenesis after MI in humans remain poorly understood (*2*). The results reported here on myocardial $\alpha_v\beta_3$ integrin expression in vivo in the human infarcted myocardium found persistent activity at 1 mo, followed by a partial decline at 3 mo. The present results are consistent with the serial changes in vascular endothelial growth factor levels observed in several studies within the peripheral blood of patients with acute MI. These levels were reported to peak at 6 wk and subsequently decline to baseline levels at 5 mo (*18*). Another study found a progressive increase in vascular endothelial growth factor levels that started on the first day after acute MI, peaked at 2 wk, and then subsequently declined (*19*). Hence, it can be thought that this prolonged increase is necessary to preserve the remaining myocardium and limit hypoxic cellular destruction.

The prolonged $\alpha_v\beta_3$ integrin upregulation found here agrees with previous studies using radiolabeled RGD peptides after MI (*4,11,20,21*). In a rat model, the uptake of the ^{18}F-galacto-RGD tracer was detected only 3 d after MI and reached its highest levels between 1 and 3 wk; the levels were still detectable after 6 mo. Moreover, the evolution of ^{18}F-galacto-RGD tracer uptake correlated well with neovascularization as assessed by immunohistochemical CD31 staining (*4*). Similarly, the uptake pattern of ^{18}F-AlF-NOTA-PRGD2, in the infarcted area at various time points after MI, also started after only 3 d and peaked between 1 and 3 wk; a subsequent partial decrease was reported 4 mo after MI (*20*). In humans, Jenkins et al. (*11*) found that ^{18}F-labeled RGD uptake was increased within 2 wk in the infarcted myocardium. It persisted but was reduced after approximately 10 wk. There was no uptake found at sites of established old infarctions. It is of note that in the present

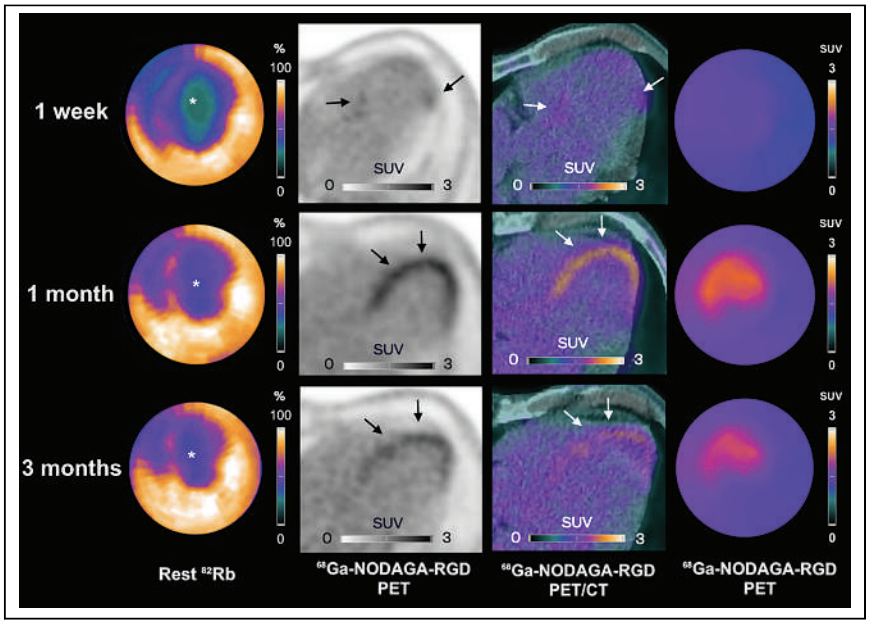

FIGURE 4. Participant example with increase in $\alpha_v\beta_3$ integrin expression levels (arrows) throughout follow-up within infarcted myocardium (asterisks). Shown are rest ^{82}Rb, ^{68}Ga-NODAGA-RGD PET, and ^{68}Ga-NODAGA-RGD PET/CT images at 1 wk (first row), 1 mo (second row), and 3 mo (third row) after STEMI. ^{68}Ga-NODAGA-RGD uptake started in border zone at 1 mo and subsequently extended into necrotic infarct core at both 1 and 3 mo.

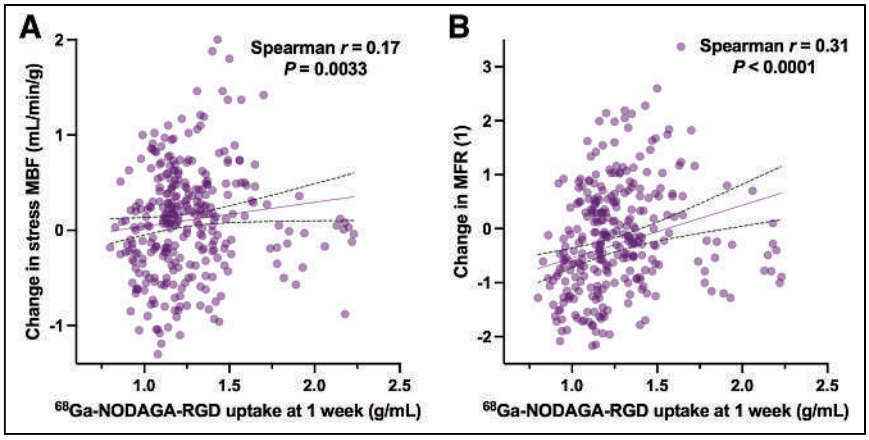

FIGURE 5. Correlations of ^{68}Ga-NODAGA-RGD uptake at 1 wk after STEMI with subsequent changes in stress MBF (A) and MFR (B) at 1 mo. Data points represent mean segmental values.

study, an examination of established old infarction sites was not conducted since none of the participants had an MI history before acute STEMI. Nevertheless, in our trial evaluating tumoral angiogenesis (NCT02666547), which includes some patients with a prior history of MI, we do not observe any visually positive uptake of ^{68}Ga-NODAGA-RGD in the myocardium.

The present study reported significant correlations between the segmental levels of $\alpha_v\beta_3$ integrin at 1 wk and the subsequent improvements in clinically relevant physiologic parameters, such as stress MBF, MFR, and wall motion analysis. Although the correlations were weak, they were determined using the Spearman rank correlation coefficient, which is insensitive to outliers. Additionally, the alignment of PET findings could have been more accurate, since distinct radiotracers (with high-energy positrons) and acquisitions were used. A stronger effect of these correlations can be assumed, which means that the correlations are likely relevant. Notably, a slightly stronger correlation was observed between $\alpha_v\beta_3$ integrin expression levels and improvements in MFR, which is considered a more robust independent prognostic factor than is stress MBF (*22*). Furthermore, no correlation was found between $\alpha_v\beta_3$ integrin expression levels and subsequent changes in rest MBF, a parameter unrelated to clinical outcomes and unaffected by post-MI recovery (*23,24*). The significant but weak correlation between $\alpha_v\beta_3$ integrin expression levels at 1 wk and functional outcomes aligns with previous challenges to translate microscopic levels of angiogenesis into functional improvements. For example, Wu et al. reported only trends toward lower perfusion defects and metabolism deficits in vascular endothelial growth factor–treated animal models, without statistically significant changes (*25*). Nevertheless, as here, several studies suggested that elevated $\alpha_v\beta_3$ integrin expression after ischemic myocardial injury is associated with subsequent improvement in regional left ventricular function (*6,11,12,26,27*). Recently, using the same PET tracer with ^{68}Ga-NODAGA-RGD, Nammas et al. reported in humans that $\alpha_v\beta_3$ integrin expression levels 1 wk after MI were linked to regional and global systolic dysfunction, as well as elevated left ventricular filling pressure, and predicted improved global left ventricular function 6 mo after MI (*12*). Despite these insights, further studies are warranted to better understand whether the angiogenic response is associated with functional recovery.

Variability was observed in the temporal pattern of ^{68}Ga-NODAGA-RGD uptake, with a notable increase found at 1 mo in 2 participants. Interestingly, the 2 participants affected were those experiencing the most severe infarcts. On the basis of these findings, it remains uncertain whether this increase in ^{68}Ga-NODAGA-RGD uptake is related to intensified reendothelialization and angiogenesis or indicates a shift toward myofibroblast cell types, suggesting an intensified fibrotic response. This delayed phase of repair is characterized by a reduction in inflammation and angiogenesis and a reorganization of the extracellular matrix through myofibroblast-driven type I and III collagen production (*1*). This more intense uptake during follow-up in infarcted areas where perfusion is most profoundly reduced, with a trend toward a delayed 1-mo peak, may reflect the need for a more intense healing process in those tissues.

The present trial had several limitations. Inflammatory cells and fibroblasts can express integrins such as $\alpha_v\beta_3$ (*7–10*), which can lead to reduced specificity. This may explain the weak correlations found between the 1-wk ^{68}Ga-NODAGA-RGD uptake and the subsequent improvements in flow, as well as the absence of correlation found from 1 mo onward. The positron range is higher for ^{68}Ga than for ^{18}F, which may affect image quality, especially in relatively small moving structures. Nevertheless, ^{68}Ga-NODAGA-RGD has the advantage of straightforward synthesis at room temperature with high radiochemical yield and purity. It can be radiolabeled rapidly (<30 min) and in a fully automated good-manufacturing-practice–compliant manner. Furthermore, the on-site availability of ^{68}Ge/^{68}Ga generators for centers without access to a cyclotron makes it a good alternative for ^{18}F-labeled compounds. Moreover, a higher uptake of multimeric RGD tracers than of monomeric tracers was reported (*28*). A multimodal imaging strategy, such as PET/MRI, could precisely delineate the area at risk and its border zone. The study would have been strengthened by an independent measure of regional function using echocardiography or MRI. Furthermore, the contribution of nonspecific uptake to ^{68}Ga-NODAGA-RGD accumulation cannot be excluded. However, positive uptake was found in segments with preserved perfusion and in segments with low perfusion, and as radiolabeled RGD-based peptides have shown rapid clearance from the circulation (*4,14*), it seems unlikely that nonspecific uptake related to changes in vascular permeability played a major role. Finally, the potential impact of standard medication regimens for coronary artery disease (e.g., statins, antihypertensives) on the uptake of ^{82}Rb or ^{68}Ga-NODAGA-RGD remains uncertain.

CONCLUSION

The present study found that $\alpha_v\beta_3$ integrin expression is significantly increased in the infarcted myocardium 1 wk after STEMI. This expression remained stable after 1 mo and partially decreased after 3 mo. Initial $\alpha_v\beta_3$ integrin expression at 1 wk was significantly weakly correlated with subsequent improvements in stress MBF, MFR, and wall motion analysis. An enhanced

comprehension of the mechanistic aspects of infarct $\alpha_v\beta_3$ integrin expression could provide multiple therapeutic options.

DISCLOSURE

The Swiss Heart Foundation (Bern, Switzerland) provided financial support in developing the ^{68}Ga-RGD radiopharmaceutical. Matthieu Dietz was a PhD student partially supported by research fellowship awards from the Société Française de Radiologie, Paris, France, and from the Agence Régionale de Santé Auvergne-Rhone-Alpes, Lyon, France. Antti Saraste discloses grants from the Research Council of Finland and Finnish Foundation for Cardiovascular Research and speaker or consultancy fees from Abbott, AstraZeneca, BMS, Janssen, Novartis, and Pfizer, outside the submitted work. Juhani Knuuti received consultancy fees from GE Healthcare and Synektik Pharma and speaker fees from Bayer, Lundbeck, Boehringer Ingelheim, Pfizer, and Siemens, outside the submitted work. No other potential conflict of interest relevant to this article was reported.

ACKNOWLEDGMENTS

We thank Christine Geldhof (Lausanne University Hospital, Lausanne, Switzerland) for her invaluable help. Additionally, we thank Shanez Haouari (DRS, Hospices Civils de Lyon) for her help in manuscript preparation. Lastly, we express our deep appreciation to all participating patients and their families.

KEY POINTS

QUESTION: What are the spatiotemporal dynamics of $\alpha_v\beta_3$ integrin expression after MI, and its correlation with changes in MBF, using ^{68}Ga-NODAGA-RGD PET/CT and rest and stress ^{82}Rb-PET/CT at 1 wk, 1 mo, and 3 mo after STEMI?

PERTINENT FINDINGS: This prospective clinical study showed that $\alpha_v\beta_3$ integrin expression was significantly increased in the infarcted myocardium 1 wk after STEMI. This expression remained stable after 1 mo and partially decreased after 3 mo. Initial $\alpha_v\beta_3$ integrin expression at 1 wk was significantly weakly correlated with subsequent improvements in stress MBF, MFR, and wall motion analysis.

IMPLICATIONS FOR PATIENT CARE: An enhanced comprehension of the mechanistic aspects of infarct $\alpha_v\beta_3$ integrin expression could provide multiple therapeutic options.

REFERENCES

1. Prabhu SD, Frangogiannis NG. The biological basis for cardiac repair after myocardial infarction: from inflammation to fibrosis. *Circ Res.* 2016;119:91–112.
2. Wu X, Reboll MR, Korf-Klingebiel M, Wollert KC. Angiogenesis after acute myocardial infarction. *Cardiovasc Res.* 2021;117:1257–1273.
3. Meoli DF, Sadeghi MM, Krassilnikova S, et al. Noninvasive imaging of myocardial angiogenesis following experimental myocardial infarction. *J Clin Invest.* 2004;113:1684–1691.
4. Higuchi T, Bengel FM, Seidl S, et al. Assessment of $\alpha_v\beta_3$ integrin expression after myocardial infarction by positron emission tomography. *Cardiovasc Res.* 2008;78:395–403.
5. Brooks PC, Clark RA, Cheresh DA. Requirement of vascular integrin $\alpha_v\beta_3$ for angiogenesis. *Science.* 1994;264:569–571.
6. Sherif HM, Saraste A, Nekolla SG, et al. Molecular imaging of early $\alpha_v\beta_3$ integrin expression predicts long-term left-ventricle remodeling after myocardial infarction in rats. *J Nucl Med.* 2012;53:318–323.
7. Antonov AS, Kolodgie FD, Munn DH, Gerrity RG. Regulation of macrophage foam cell formation by αVβ3 integrin. *Am J Pathol.* 2004;165:247–258.
8. van den Borne SWM, Isobe S, Verjans JW, et al. Molecular imaging of interstitial alterations in remodeling myocardium after myocardial infarction. *J Am Coll Cardiol.* 2008;52:2017–2028.
9. Asano Y, Ihn H, Yamane K, Jinnin M, Mimura Y, Tamaki K. Increased expression of integrin $\alpha_v\beta_3$ contributes to the establishment of autocrine TGF-beta signaling in scleroderma fibroblasts. *J Immunol.* 2005;175:7708–7718.
10. de Haas HJ, Arbustini E, Fuster V, Kramer CM, Narula J. Molecular imaging of the cardiac extracellular matrix. *Circ Res.* 2014;114:903–915.
11. Jenkins WSA, Vesey AT, Stirrat C, et al. Cardiac $\alpha_V\beta_3$ integrin expression following acute myocardial infarction in humans. *Heart.* 2017;103:607–615.
12. Nammas W, Paunonen C, Teuho J, et al. Imaging of myocardial $\alpha_v\beta_3$ integrin expression for evaluation of myocardial injury after acute myocardial infarction. *J Nucl Med.* 2024;65:132–138.
13. Simons M, Alitalo K, Annex BH, et al. American Heart Association Council on Basic Cardiovascular Sciences and Council on Cardiovascular Surgery and Anesthesia. State-of-the-art methods for evaluation of angiogenesis and tissue vascularization: a scientific statement from the American Heart Association. *Circ Res.* 2015;116:e99–e132.
14. Knetsch PA, Petrik M, Griessinger CM, et al. [^{68}Ga]NODAGA-RGD for imaging $\alpha_v\beta_3$ integrin expression. *Eur J Nucl Med Mol Imaging.* 2011;38:1303–1312.
15. Pohle K, Notni J, Bussemer J, Kessler H, Schwaiger M, Beer AJ. ^{68}Ga-NODAGA-RGD is a suitable substitute for ^{18}F-galacto-RGD and can be produced with high specific activity in a cGMP/GRP compliant automated process. *Nucl Med Biol.* 2012;39:777–784.
16. Kitkungvan D, Johnson NP, Roby AE, Patel MB, Kirkeeide R, Gould KL. Routine clinical quantitative rest stress myocardial perfusion for managing coronary artery disease: clinical relevance of test-retest variability. *JACC Cardiovasc Imaging.* 2017;10:565–577.
17. Dietz M, Kamani CH, Allenbach G, et al. Comparison of the prognostic value of impaired stress myocardial blood flow, myocardial flow reserve, and myocardial flow capacity on low-dose rubidium-82 SiPM PET/CT. *J Nucl Cardiol.* 2023;30:1385–1395.
18. Lee KW, Lip GYH, Blann AD. Plasma angiopoietin-1, angiopoietin-2, angiopoietin receptor tie-2, and vascular endothelial growth factor levels in acute coronary syndromes. *Circulation.* 2004;110:2355–2360.
19. Hojo Y, Ikeda U, Zhu Y, et al. Expression of vascular endothelial growth factor in patients with acute myocardial infarction. *J Am Coll Cardiol.* 2000;35:968–973.
20. Gao H, Lang L, Guo N, et al. PET imaging of angiogenesis after myocardial infarction/reperfusion using a one-step labeled integrin-targeted tracer ^{18}F-AlF-NOTA-PRGD2. *Eur J Nucl Med Mol Imaging.* 2012;39:683–692.
21. Makowski MR, Rischpler C, Ebersberger U, et al. Multiparametric PET and MRI of myocardial damage after myocardial infarction: correlation of integrin αvβ3 expression and myocardial blood flow. *Eur J Nucl Med Mol Imaging.* 2021;48:1070–1080.
22. Juárez-Orozco LE, Tio RA, Alexanderson E, et al. Quantitative myocardial perfusion evaluation with positron emission tomography and the risk of cardiovascular events in patients with coronary artery disease: a systematic review of prognostic studies. *Eur Heart J Cardiovasc Imaging.* 2018;19:1179–1187.
23. Johnson NP, Gould KL, De Bruyne B. Autoregulation of coronary blood supply in response to demand: JACC review topic of the week. *J Am Coll Cardiol.* 2021;77:2335–2345.
24. Cuculi F, De Maria GL, Meier P, et al. Impact of microvascular obstruction on the assessment of coronary flow reserve, index of microcirculatory resistance, and fractional flow reserve after ST-segment elevation myocardial infarction. *J Am Coll Cardiol.* 2014;64:1894–1904.
25. Wu JC, Chen IY, Wang Y, et al. Molecular imaging of the kinetics of vascular endothelial growth factor gene expression in ischemic myocardium. *Circulation.* 2004;110:685–691.
26. Bentsen S, Jensen JK, Christensen E, et al. [^{68}Ga]Ga-NODAGA-E[(cRGDyK)]2 angiogenesis PET following myocardial infarction in an experimental rat model predicts cardiac functional parameters and development of heart failure. *J Nucl Cardiol.* 2023;30:2073–2084.
27. Follin B, Hoeeg C, Hunter I, et al. [^{68}Ga]Ga-NODAGA-E[(cRGDyK)]2 and [^{64}Cu]Cu-DOTATATE PET predict improvement in ischemic cardiomyopathy. *Diagnostics (Basel).* 2023;13:268.
28. Notni J, Pohle K, Wester HJ. Be spoilt for choice with radiolabelled RGD peptides: preclinical evaluation of ^{68}Ga-TRAP(RGD)$_3$. *Nucl Med Biol.* 2013;40:33–41.

Determining Hemodynamically Significant Coronary Artery Disease: Patient-Specific Cutoffs in Quantitative Myocardial Blood Flow Using [^{15}O]H_2O PET Imaging

Roel Hoek[1], Pepijn A. van Diemen[1], Pieter G. Raijmakers[2], Roel S. Driessen[1], Yvemarie B.O. Somsen[1], Ruben W. de Winter[1], Ruurt A. Jukema[1], Jos W.R. Twisk[3], Lourens F.H.J. Robbers[1], Pim van der Harst[4], Antti Saraste[5,6], Mark Lubberink[7], Jens Sörensen[7], Paul Knaapen[1], Juhani Knuuti[5], and Ibrahim Danad[1,4]

[1]*Department of Cardiology, Amsterdam University Medical Center, Vrije Universiteit Amsterdam, Amsterdam, The Netherlands;* [2]*Department of Radiology and Nuclear Medicine, Amsterdam University Medical Center, Vrije Universiteit Amsterdam, Amsterdam, The Netherlands;* [3]*Department of Epidemiology and Data Science, Amsterdam University Medical Center, Vrije Universiteit Amsterdam, Amsterdam, The Netherlands;* [4]*Department of Cardiology, University Medical Center Utrecht, Utrecht, The Netherlands;* [5]*Turku PET Centre, Turku University Hospital and University of Turku, Turku, Finland;* [6]*Heart Center, Turku University Hospital and University of Turku, Turku, Finland; and* [7]*Nuclear Medicine and PET, Department of Surgical Sciences, Uppsala University, Uppsala, Sweden*

Currently, cutoffs of quantitative [^{15}O]H_2O PET to detect fractional flow reserve (FFR)–defined coronary artery disease (CAD) were derived from a single cohort that included patients without prior CAD. However, prior CAD, sex, and age can influence myocardial blood flow (MBF). Therefore, the present study determined the influence of prior CAD, sex, and age on optimal cutoffs of hyperemic MBF (hMBF) and coronary flow reserve (CFR) and evaluated whether cutoff optimization enhanced diagnostic performance of quantitative [^{15}O]H_2O PET against an FFR reference standard. **Methods:** Patients with chronic coronary symptoms underwent [^{15}O]H_2O PET and invasive coronary angiography with FFR. Optimal cutoffs for patients with and without prior CAD and subpopulations based on sex and age were determined. **Results:** This multicenter study included 560 patients. Optimal cutoffs were similar for patients with (n = 186) and without prior CAD (hMBF, 2.3 vs. 2.3 mL·min^{-1}·g^{-1}; CFR, 2.7 vs. 2.6). Females (n = 190) had higher hMBF cutoffs than males (2.8 vs. 2.3 mL·min^{-1}·g^{-1}), whereas CFRs were comparable (2.6 vs. 2.7). However, female sex–specific hMBF cutoff implementation decreased diagnostic accuracy as compared with the cutoff of 2.3 mL·min^{-1}·g^{-1} (72% vs. 82%, $P < 0.001$). Patients aged more than 70 y (n = 79) had lower hMBF (1.7 mL·min^{-1}·g^{-1}) and CFR (2.3) cutoffs than did patients aged 50 y or less, 51–60 y, and 61–70 y (hMBF, 2.3–2.4 mL·min^{-1}·g^{-1}; CFR, 2.7). Age-specific cutoffs in patients aged more than 70 y yielded comparable accuracy to the previously established cutoffs (hMBF, 72% vs. 76%, P = 0.664; CFR, 80% vs. 75%, P = 0.289). **Conclusion:** Patients with and without prior CAD had similar [^{15}O]H_2O PET cutoffs for detecting FFR-defined significant CAD. Stratifying patients according to sex and age led to different optimal cutoffs; however, these values did not translate into an increased overall accuracy as compared with previously established thresholds for MBF.

Key Words: PET; fractional flow reserve; cutoff values; hyperemic myocardial blood flow; coronary flow reserve; coronary artery disease

J Nucl Med 2024; 65:1113–1121
DOI: 10.2967/jnumed.123.267195

Received Jan. 2, 2024; revision accepted Apr. 8, 2024.
For correspondence or reprints, contact Ibrahim Danad (i.danad@umcutrecht.nl) or Roel Hoek (roel.hoek@amsterdamumc.nl).
Published online May 9, 2024.

A wide array of diagnostic modalities is available to evaluate the presence and functional repercussion of coronary artery disease (CAD). Among these diagnostic tools, [^{15}O]H_2O PET is considered the gold standard for noninvasive quantification of myocardial blood flow (MBF) and has well-established diagnostic and prognostic value (*1–3*). PET serves as a gatekeeper for invasive coronary angiography (ICA), where fractional flow reserve (FFR) is used to guide revascularization, considering its prognostic importance (*4*,*5*). One of the challenges of quantitative MBF interpretation to guide revascularization decision-making is the definition of normal and abnormal MBF, paralleling significant and nonsignificant FFR measurements. Currently used [^{15}O]H_2O PET cutoffs were derived from a collaborative study that found a cutoff of 2.3 mL·min^{-1}·g^{-1} for optimal hyperemic MBF (hMBF) and 2.5 for coronary flow reserve (CFR) to detect FFR-defined CAD (*6*). These cutoffs were established in a population without prior CAD, whereas contemporary guidelines endorse myocardial perfusion imaging for patients with a substantial clinical likelihood of obstructive CAD, including those with a prior CAD history (*7*,*8*). Patients with prior CAD and recurrence of symptoms have more advanced atherosclerotic disease and a higher prevalence of microvascular dysfunction, which can cause diminished MBF even in the absence of obstructive epicardial lesions (*9*,*10*). Moreover, prior studies revealed that both sex and age can affect myocardial perfusion values, irrespective of the presence of obstructive CAD (*6*,*11–16*). Conceivably, recalibrating [^{15}O]H_2O PET thresholds for the presence of prior CAD, sex, and age could enhance diagnostic performance in these distinct subpopulations. Therefore, the aim of this study was to assess how prior CAD, sex, and age impact the optimal cutoffs of quantitative [^{15}O]H_2O PET in detecting FFR-defined hemodynamically significant CAD. We further sought to compare the diagnostic performance of [^{15}O]H_2O PET using both general and patient-specific cutoffs.

MATERIALS AND METHODS

Patient Population

This was a multicenter study that included patients suspected of having obstructive CAD who underwent [^{15}O]H_2O PET perfusion

imaging and ICA in conjunction with FFR measurements. The patient population was derived from 3 participating centers: Amsterdam University Medical Center (n = 439), Turku University Hospital (n = 116), and Uppsala University Hospital (n = 5). Patients from the Amsterdam University Medical Center were derived from a clinical registry (n = 49), from the PACIFIC-1 trial (n = 204), or from the PACIFIC-2 trial (n = 186) (*9*,*10*). Patients from Turku University Hospital and Uppsala University Hospital were derived from clinical registries. General exclusion criteria were atrial fibrillation, contraindications for adenosine, pregnancy, and a history of coronary artery bypass graft surgery. Additional specific exclusion criteria of the PACIFIC trials are described elsewhere (*9*,*10*). Patients from the PACIFIC-2 trial had a documented cardiac history of myocardial infarction (MI) and/or percutaneous coronary intervention (PCI), whereas these patients were excluded from the PACIFIC-1 trial and clinical registries. Furthermore, patients from the PACIFIC-1 trial and clinical registries had a left ventricular ejection fraction of more than 50% on echocardiography. The maximum allowed interval between PET and ICA was 3 mo, and no cardiac events were documented within this period. Each center had the approval of a local institutional ethical review board, and all patients provided written informed consent.

[^{15}O]H_2O PET Perfusion Imaging, Quantification of MBF, and Interpretation of Perfusion Defect

All patients underwent [^{15}O]H_2O PET perfusion imaging using a hybrid PET/CT scanner with site-specific protocols. These protocols and quantification of MBF are described in the supplemental materials (available at http://jnm.snmjournals.org) (*6*,*17*–*21*). PET perfusion imaging polar maps were visually assessed for presence of a perfusion defect, defined as a defect of 2 or more adjacent segments within the right coronary artery territory and circumflex artery territory, and 4 or more adjacent segments within the left anterior descending artery territory. In the absence of a visual perfusion defect, the mean vascular hMBF/CFR was used for further analysis. If a visual perfusion defect was present, the mean hMBF/CFR of the involved segments was used for further analysis. Overlapping segments of a perfusion defect were not included in the mean perfusion value of the adjacent vascular territory. An example of the interpretation of a visual perfusion defect is shown in Supplemental Figure 1. Parametric segmental MBF values were allocated to their corresponding vascular territory according to the American Heart Association 17-segment model after correction for coronary dominance based on information obtained from ICA (*21*).

Scar Detection

In the context of the PACIFIC-2 trial, all patients with prior CAD included in our study received cardiac MRI besides PET perfusion imaging. For these individuals, the cardiac MRI data served to detect vascular areas with significant scarring. The extent of late gadolinium enhancement was visually analyzed according to the American Heart Association 17-segment model (excluding the apex) using a 5-point scale (0%, 1%–25%, 26%–50%, 51%–75%, >75%) (*21*). Significant scarring was defined as a vascular late gadolinium enhancement score of 2 or more. An additional description of the cardiac MRI acquisition protocol has been previously published (*10*).

ICA and FFR

ICA was performed using standard protocols. FFR was calculated by dividing the mean distal intracoronary pressure by the mean arterial pressure after inducing maximal hyperemia by infusion of intracoronary (150 μg) or intravenous (140 $\mu g \cdot kg^{-1} \cdot min^{-1}$) adenosine. In the context of the PACIFIC-1 and -2 trials, FFR measurements were performed in all major coronary arteries and side branches larger than 2.0 mm. For all other patients, FFR was measured in intermediate lesions (diameter stenosis, 30%–90%). Hemodynamically significant CAD was defined as an FFR of 0.80 or less or as coronary lesions with a diameter stenosis of more than 90% if FFR measurements were not performed. Conversely, vessels without an FFR of 0.80 or less or coronary lesions with a diameter stenosis of less than 30% were considered non-obstructive. Vessels with intermediate stenosis and no FFR measurement were excluded from further analysis, as were right coronary arteries functioning as a right ventricular branch or coronary anomalies.

Statistical Analysis

Univariable and multivariable regression analysis was performed to identify patient characteristics and traditional CAD risk factors that influence hMBF. The regression analysis was conducted using a linear mixed-effects model to account for multiple vessels deriving from the same patient. Interactions between prior MI, prior PCI, sex, and age were explored. Optimal cutoffs for hMBF and CFR were calculated for specific subpopulations stratified by the presence of prior CAD (defined as a prior MI and/or PCI), sex, and age (≤50, 51–60, 61–70, and >70 y), using the Youden index. Areas under the receiver-operating characteristic curve (AUC) were constructed using hMBF and CFR on both a per-patient (lowest vascular value of a patient) and per-vessel level and were compared using the DeLong method. The diagnostic performance of [^{15}O]H_2O PET–derived hMBF and CFR was assessed using both the previously established general cutoffs (hMBF, 2.3 $mL \cdot min^{-1} \cdot g^{-1}$; CFR, 2.5 (*6*)) and patient-specific optimal cutoffs for subpopulations in which hMBF cutoffs differed by more than 0.1 $mL \cdot min^{-1} \cdot g^{-1}$ from the general cutoff. The diagnostic performance of hMBF and CFR using the general cutoffs was calculated as well for all patients from the Amsterdam University Medical Centers and for all other patients. Per-patient diagnostic performance measures (sensitivity, specificity, positive and negative predictive values, and accuracy) were compared using the McNemar or χ^2 test (sensitivity, specificity, and accuracy) or using generalized estimation equations with an independent correlation structure (positive and negative predictive values). Per-vessel diagnostic performance measures were compared using generalized estimation equations with an exchangeable (sensitivity, specificity, and accuracy) or independent (positive and negative predictive values) correlation structure, to correct for multiple vessels deriving from the same patient. A 2-sided P value of less than 0.05 was considered statistically significant. Statistical analyses were performed using the SPSS software package (version 28.0; IBM) and MedCalc Statistical Software (version 20.006; MedCalc Software Ltd.).

RESULTS

Study Population

In total, 560 patients were eligible for inclusion in this study. Among their 1,680 vessels, 73 (4%) were excluded from further analysis: 56 (3%) because of the absence of FFR in an intermediate stenosis, 16 (1%) because the right coronary artery was a right ventricular branch, and 1 (<1%) because it was a coronary anomaly. As a result, 560 patients and 1,607 vessels were included (Fig. 1). Baseline characteristics are presented in Table 1. Mean age was 61 ± 9.1 y, and 370 (66%) patients were male. A total of 186 (33%) patients had prior CAD (98 [18%] prior MI and 168 [30%] prior PCI). Supplemental Table 1 presents the baseline characteristics stratified by patients with prior CAD, sex, and age. Of patients with prior CAD, cardiac MRI-defined left ventricular ejection fraction was less than 35% in 5 patients and 35%–54% in 44 patients. All other patients had a normal left ventricular ejection fraction.

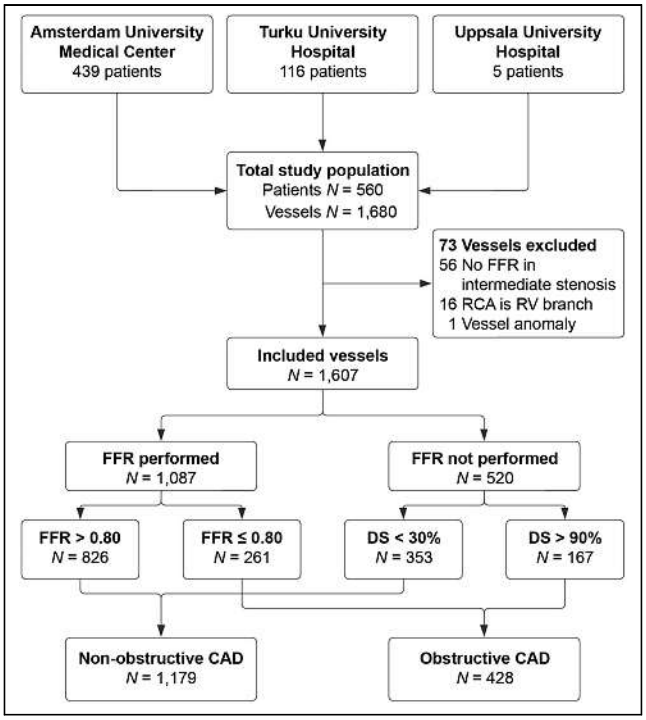

FIGURE 1. Study flowchart of included patients and vessels, with corresponding presence of FFR interrogation. DS = diameter stenosis; RCA = right coronary artery; RV = right ventricular.

MBF in Relationship to Prior CAD, Sex, and Age

The relationship between myocardial perfusion and prior CAD, sex, and age in vessels with and without obstructive CAD is depicted in Figure 2. In patients with a prior CAD, hMBF and CFR were lower in non-obstructive vessels but higher in obstructive vessels, when compared to patients without prior CAD. hMBF was higher in females than males for both non-obstructive and obstructive vessels, whereas CFR was comparable between the sexes. Among the age groups 50 y or less, 51–60 y, and 61–70 y, hMBF and CFR exhibited no significant differences. However, patients aged more than 70 y had lower hMBF in non-obstructive vessels than did patients aged 50 y or less or patients aged 51–60 y. Furthermore, CFR in patients aged more than 70 y was lower in both non-obstructive vessels (as compared with all other groups) and obstructive vessels (as compared with patients aged 51–60 y and patients aged 61–70 y). Resting MBF measures are presented in Supplemental Table 2. Table 2 shows the result of a regression analysis describing the influence of patient-specific characteristics and traditional CAD risk factors on hMBF. In a multivariable regression analysis, female sex, age, smoking, diabetes, and hypertension were significantly and independently associated with hMBF. There was a significant interaction between prior MI and the female sex ($P = 0.030$) and between prior PCI and the male sex ($P = 0.006$) (Supplemental Table 3).

Optimal Cutoffs and Diagnostic Performance of $[^{15}O]H_2O$ PET

The vessel-specific optimal cutoffs and corresponding AUC analysis of $[^{15}O]H_2O$ PET for predicting obstructive CAD in the patient-specific subpopulations are shown in Table 3 and Supplemental Figure 2. Patients without prior CAD had an optimal cutoff of 2.3 $mL \cdot min^{-1} \cdot g^{-1}$ for hMBF and 2.6 for CFR. The overall presence of prior CAD, prior MI, and prior PCI did not influence cutoffs.

TABLE 1
Baseline Characteristics of Total Study Population ($n = 560$)

Characteristic	Data
Age (y)	61 ± 9.1
Male sex	370 (66)
Body mass index ($kg \cdot m^{-2}$)	27 ± 4.0
Cardiac history	186 (33)
Prior MI	98 (18)
Prior PCI	168 (30)
Cardiovascular risk factors	
Family history of CAD	235 (42)
Smoking (current or history)	250 (45)
Diabetes mellitus	97 (17)
Hypertension	292 (52)
Hypercholesterolemia	300 (54)
Symptoms	
Typical angina	212 (38)
Atypical angina	217 (39)
Nonspecific chest discomfort	131 (24)
Medication	
Single antiplatelet therapy	428 (76)
Dual antiplatelet therapy	66 (12)
β-blocker	354 (63)
ACE inhibitor or AR blocker	240 (43)
Calcium channel blocker	150 (27)
Statin	424 (76)
Obstructive CAD	273 (49)

Data are presented as mean ± SD or as absolute number followed by percentage in parentheses.

ACE = angiotensin-converting enzyme; AR = angiotensin receptor.

However, in vascular territories with late gadolinium enhancement–defined scarring, CFR showed a cutoff of 2.0. Males showed similar thresholds of hMBF (2.3 $mL \cdot min^{-1} \cdot g^{-1}$) and CFR (2.7), whereas females exhibited a higher threshold for hMBF, at 2.8 $mL \cdot min^{-1} \cdot g^{-1}$, with a corresponding cutoff of 2.6 for CFR. Regarding age, only patients aged more than 70 y displayed disparate thresholds: 1.7 $mL \cdot min^{-1} \cdot g^{-1}$ for hMBF and 2.3 for CFR. Cutoffs based on different FFR and angiographic thresholds are shown in Supplemental Tables 4 and 5.

Figure 3 shows the AUC analyses with corresponding 95% CIs of the patient-specific subpopulations on a per-patient level. The diagnostic performance of hMBF in patients without prior CAD was significantly higher than in patients with prior CAD (AUC, 0.87 [95% CI, 0.85–0.92] vs. 0.80 [95% CI, 0.74–0.86]; $P = 0.021$), whereas the diagnostic performance of CFR was comparable between these groups ($P = 0.069$). For the subpopulations based on sex and age, AUC analysis revealed no significant differences between groups for either hMBF or CFR.

The per-patient diagnostic performance of hMBF and CFR for patients from the Amsterdam University Medical Center ($n = 439$)

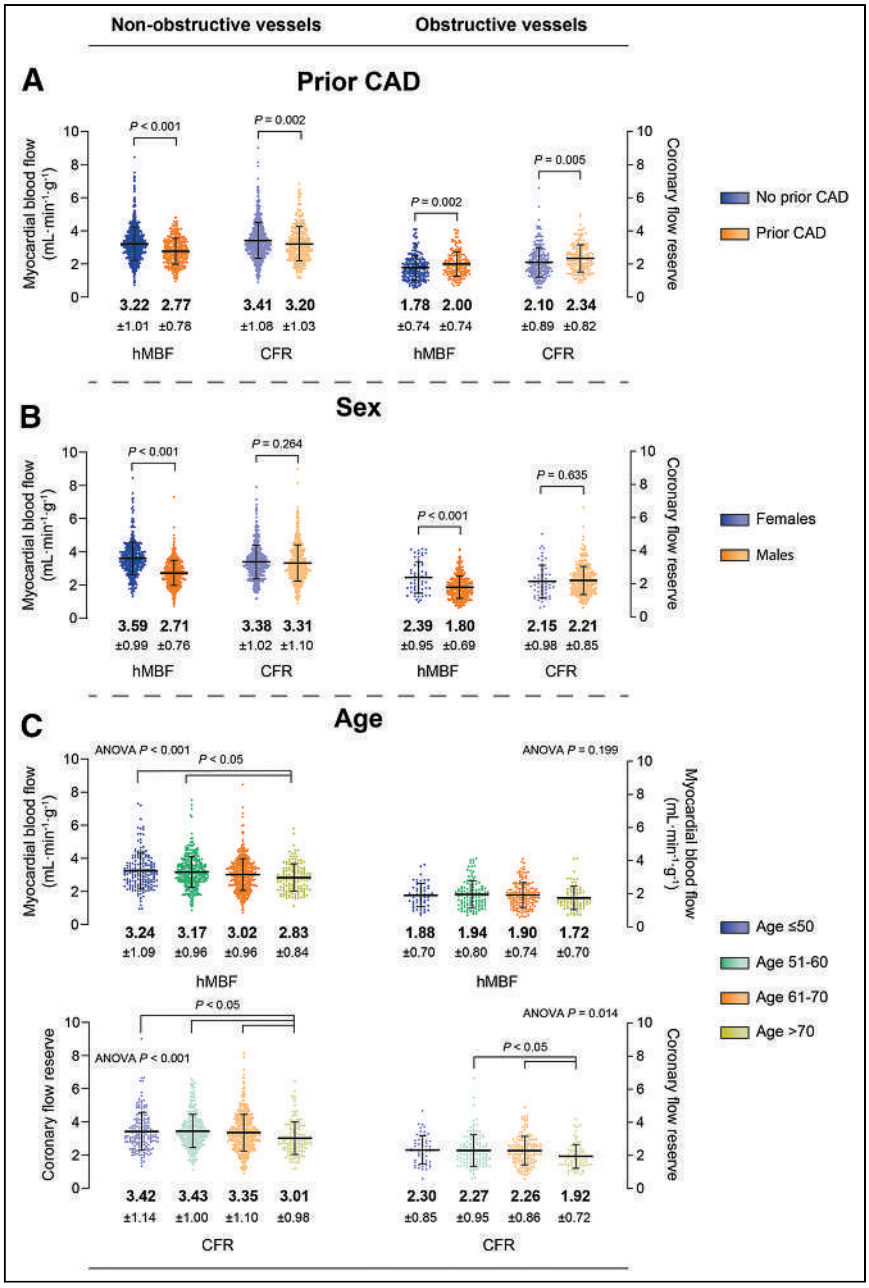

FIGURE 2. Relationship between myocardial perfusion and patient characteristics in vessels with and without obstructive CAD. Patients are divided into subpopulations, stratified by prior CAD (defined as prior MI and/or PCI) (A), sex (B), and age (C).

compared with those from Turku University Hospital and Uppsala University Hospital ($n = 121$) is shown in Supplemental Table 6.

Influence of Cutoff Optimization on Diagnostic Performance of [^{15}O]H_2O PET in Females and Patients Aged More Than 70 Years

The implementation of optimized cutoffs in females resulted in a decreased per-patient specificity, positive predictive value, and accuracy for hMBF (all $P < 0.001$), whereas for CFR only specificity decreased ($P = 0.031$) (Fig. 4A). Per-patient accuracy was highest for hMBF using the general cutoff (82%)—superior to the accuracy of CFR using both the general (76%, $P = 0.015$) and the specific (73%, $P = 0.001$) cutoffs. Per-vessel diagnostic performance is shown in Supplemental Table 7. The per-vessel accuracy of hMBF using the general cutoff (87%) was superior to that of hMBF using the specific cutoff (80%, $P < 0.001$) and to that of CFR using either the general (81%, $P < 0.001$) or the specific (79%, $P < 0.001$) cutoff.

In patients aged more than 70 y, cutoff optimization led to a reduced per-patient sensitivity for hMBF ($P < 0.001$), whereas specificity and positive predictive value increased for both hMBF and CFR (all $P \leq 0.031$) (Fig. 4B). The highest per-patient accuracy was observed for CFR using the specific cutoff (80%), but there was no statistically significant improvement over the accuracy of hMBF using either the general (76%, $P = 0.581$) or the specific (72%, $P = 0.263$) cutoff. Per-vessel diagnostic performance is shown in Supplemental Table 7. Per-vessel accuracy was highest for hMBF using the specific cutoff (83%), outperforming the accuracy of hMBF and CFR using the general cutoffs (both 73%, $P = 0.003$) and comparable to the accuracy of CFR using the specific cutoff (79%, $P = 0.081$).

DISCUSSION

This study examined how prior CAD, sex, and age affect the optimal cutoffs of quantitative [^{15}O]H_2O PET in identifying FFR-defined hemodynamically significant CAD. Previous efforts have not optimized hMBF and CFR thresholds using [^{15}O]H_2O PET for these subgroups. The key findings of this study are that prior MI and/or PCI did not require specific hMBF and CFR thresholds for predicting hemodynamically significant CAD; that females presented a higher hMBF cutoff than did males; that elderly patients (>70 y) exhibited lower thresholds for hMBF and CFR than did younger patients; and that the optimized cutoffs did not improve overall accuracy for these specific subpopulations.

Influence of Prior CAD

Diffuse atherosclerosis and coronary microvascular dysfunction impair myocardial perfusion in patients with prior CAD, resulting in a potential disparity between FFR and MBF when PET is used as a guide for coronary revascularizations (*22*,*23*). Moreover, the presence of myocardial scarring influences the amount of viable tissue in a vascular territory, with a subsequent impact on FFR, whereas MBF alterations might occur due to diminished tracer extraction in viable portions of scarred regions (*24*,*25*). As a result, the optimal hMBF to distinguish between normal and ischemic MBF as defined by FFR may differ from that of patients without

TABLE 2
Uni- and Multivariable Regression Analysis of Influence of Patient-Specific Characteristics and Risk Factors on hMBF

	Univariable		Multivariable	
Characteristic	β	*P*	β	*P*
Obstructive CAD	−0.642	<0.001	−0.608	<0.001
Prior MI	−0.328	0.003	−0.077	0.430
Prior PCI	−0.235	0.010	0.143	0.090
Sex (female)	1.065	<0.001	0.884	<0.001
Age	−0.019	<0.001	−0.016	<0.001
Body mass index ($kg \cdot m^{-2}$)	−0.030	0.004	−0.008	0.381
Family history of CAD	0.005	0.952	−0.044	0.497
Smoking	−0.300	<0.001	−0.133	0.043
Diabetes mellitus	−0.435	<0.001	−0.188	0.035
Hypertension	−0.335	<0.001	−0.163	0.016
Hypercholesterolemia	−0.253	0.002	−0.041	0.531

prior CAD. In our study, although perfusion was lower in patients with prior CAD than in their counterparts without prior CAD in non-obstructive vessels, the independent presence of prior MI or PCI did not influence hMBF. Consequently, the optimal cutoffs for hMBF and CFR were consistent with those of patients without prior CAD. Notably, even when vascular territories with the presence of late gadolinium enhancement–defined scarring were considered, optimal hMBF thresholds remained unchanged, although CFR displayed a remarkable decrease in these regions. Prior studies assessing the diagnostic performance of $[^{15}O]H_2O$ PET using thresholds similar to those established in our study indicated reduced diagnostic performance in patients with prior CAD compared with those without, which is confirmed by the lower AUC of hMBF in patients with prior CAD than in those without in our study (*9*,*10*). Our findings emphasize that these disparities in diagnostic performance are likely related to diffuse and microvascular atherosclerotic disease rather than being the result of suboptimal PET thresholds in either group.

Impact of Sex

Risk factors impact myocardial perfusion irrespective of epicardial atherosclerotic burden by increasing microvascular resistance (*26*). Sex, however, has been demonstrated to exert the largest influence on stress perfusion values. This apparent phenomenon has been attributed to sex differences in the hormonal milieu and the subsequent protective effects of estrogens in preserving the

TABLE 3
Vessel-Specific Optimal Cutoffs and AUC Analysis of $[^{15}O]H_2O$ PET

	hMBF		CFR			
Parameter	Cutoff ($mL \cdot min^{-1} \cdot g^{-1}$)	AUC	Cutoff	AUC	Vessels (*n*)	Disease (%)
No prior CAD	2.3	0.88 (0.86–0.90)	2.6	0.84 (0.82–0.86)	1058	23
Prior CAD	2.3	0.76 (0.73–0.80)	2.7	0.75 (0.71–0.78)	549	33
Prior MI*	2.3	0.76 (0.71–0.81)	2.7	0.72 (0.66–0.77)	289	36
Prior PCI*	2.3	0.74 (0.70–0.78)	2.7	0.73 (0.68–0.76)	497	31
LGE-defined scar	2.3	0.76 (0.68–0.83)	2.0	0.75 (0.67–0.82)	149	41
Males	2.3	0.82 (0.79–0.84)	2.7	0.80 (0.77–0.82)	1053	35
Females	2.8	0.80 (0.77–0.84)	2.6	0.82 (0.78–0.85)	554	10
Age ≤ 50 y	2.4	0.87 (0.82–0.91)	2.7	0.79 (0.73–0.84)	227	26
Age 51–60 y	2.4	0.85 (0.81–0.88)	2.7	0.82 (0.79–0.86)	507	25
Age 61–70 y	2.3	0.83 (0.80–0.86)	2.7	0.79 (0.76–0.82)	648	25
Age > 70 y	1.7	0.86 (0.81–0.91)	2.3	0.84 (0.78–0.88)	225	35

*Not vessel-specific, as documented by per-patient cardiac history.
LGE = late gadolinium enhancement.
Data in parentheses are 95% CI.

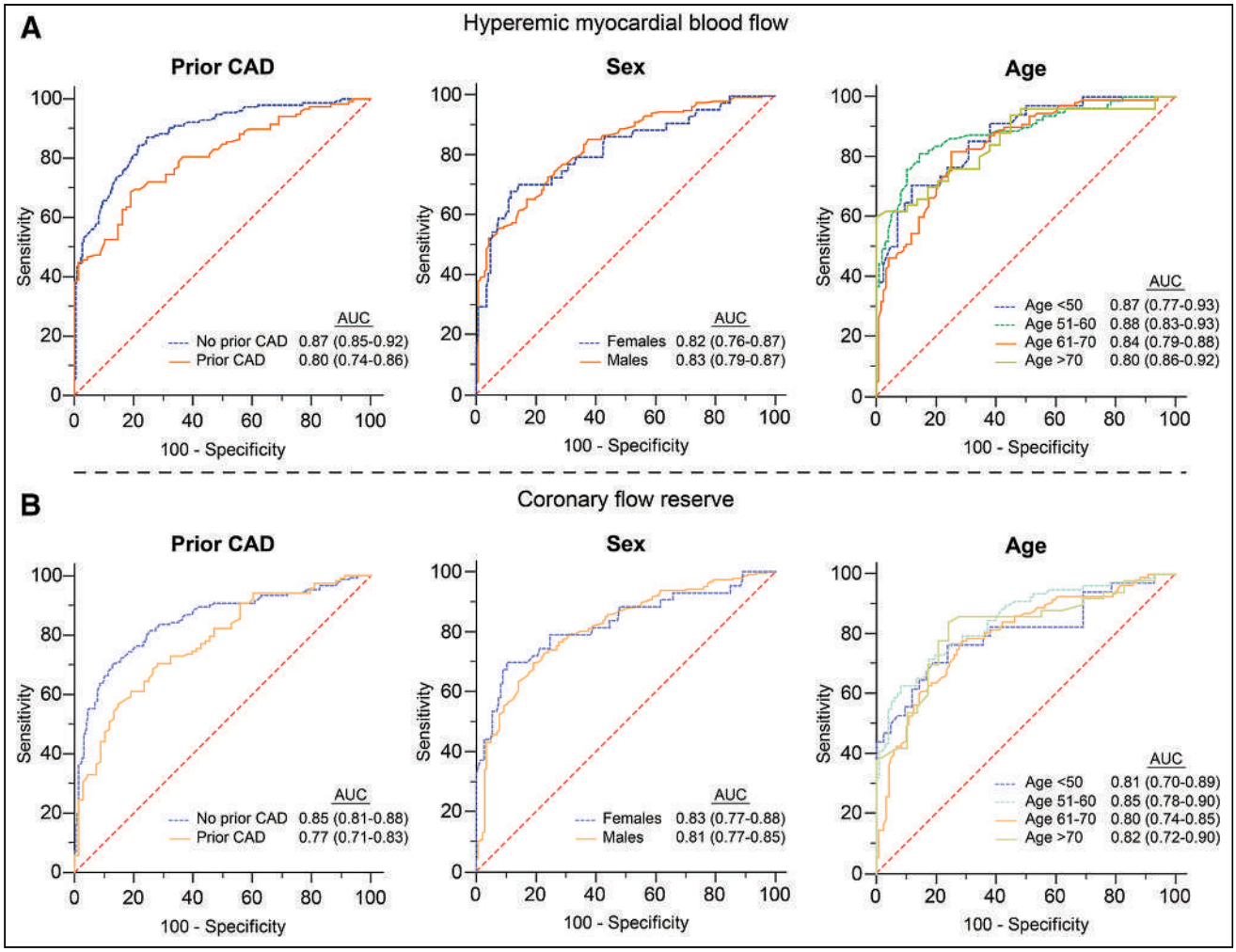

FIGURE 3. AUC analysis and corresponding 95% CI of [^{15}O]H_2O PET–derived hMBF and CFR to detect FFR-defined hemodynamically significant CAD for specific subpopulations on per-patient level.

function of the coronary microvasculature. Indeed, estrogen replacement therapy has been shown to reduce minimal coronary microvascular resistance and thus preserve the functional integrity of the microvasculature (*27*). An experimental study on animal models, however, has linked blunted resting MBF to testosterone levels, whereas stress perfusion levels remained unchanged (*11*). Indeed, in a study by Duvernoy et al., hMBF remained significantly higher in females than in their male counterparts despite the fact that the females were postmenopausal (*28*). Irrespective of the underlying mechanism, one may postulate that a different threshold for myocardial perfusion values should be established to account for the differences in vasomotor function, to optimize the diagnostic value of quantitative PET, and to facilitate its role as a guide for coronary revascularizations. Therefore, females might benefit from a different cutoff for the detection of hemodynamic significant CAD as refereed by FFR, giving an impetus to personalize PET-guided management. In our study, AUCs between sexes were comparable, and specific cutoffs for males did not differ from the prior established thresholds (*6*). Females, on the other hand, demonstrated higher hMBF cutoffs than did males (2.8 vs. 2.3 $mL \cdot min^{-1} \cdot g^{-1}$), whereas thresholds for CFR remained comparable between the sexes (2.7 vs. 2.6). Prior studies have shown similar results, although lower CFRs in females have been described as well (*6*,*14*,*28*–*30*). The threshold for CFR is similar for both males and females, and thus, CFR is preferably used instead of hMBF for large datasets attenuating the bias in flow values introduced by sex on, for example, prediction of adverse events. However, reliance on a higher ischemic threshold in females would result in an overestimation of abnormal stress perfusion scans were it to serve as a gatekeeper test for the catheterization laboratory. Because of the relatively low disease prevalence in females, the increased sensitivity of a higher hMBF cutoff came at the expense of a loss of specificity resulting in an overall reduced accuracy on both a per-vessel and a per-patient level. From a clinical per-patient perspective, the increase in sensitivity was not deemed sufficient to recommend the use of this specific cutoff for minimizing false deferrals to the catheterization laboratory. For CFR, the diagnostic performance of optimized thresholds followed the same trend, albeit not as pronounced given the minimal sex difference for this flow parameter. Accordingly, the accuracy of hMBF surpassed that of CFR despite the implementation of specific CFR thresholds, in line with previous studies

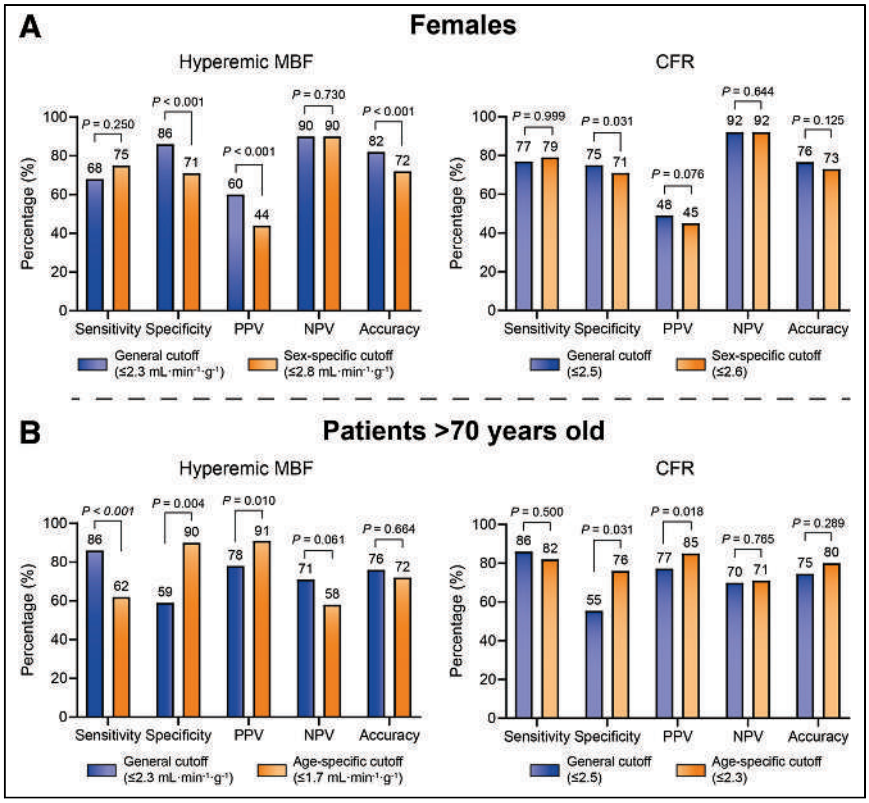

FIGURE 4. Per-patient diagnostic performance of hMBF and CFR with general and patient-specific optimal cutoffs in females (A) and patients > 70 y old (B). NPV = negative predictive value; PPV = positive predictive value.

(*6*,*31*,*32*). All in all, our results do not support the use of sex-specific cutoffs and indicate that hMBF is the most reliable marker for hemodynamic significant epicardial disease in this specific population.

Effect of Age

As age advances, several factors have been reported to influence myocardial perfusion. Diffuse atherosclerosis causes endothelial dysfunction by prohibiting endothelium-dependent vasodilatation of the coronary arteries. In a study by Egashira et al., an increase in peak coronary blood flow using an endothelium-dependent vasodilator correlated negatively with age, whereas the response to an endothelium-independent vasodilator was only slightly affected by age (*33*). Moreover, age-related morphologic changes in smooth muscle cells can increase arterial impedance (*34*). These factors can equally be attributed to the microvasculature, increasing microvascular resistance and subsequently decreasing stress perfusion and flow reserve (*15*,*35*). With multiple factors other than epicardial disease reducing myocardial perfusion in elderly patients, correcting perfusion for age might, arguably, optimize diagnosis establishment. In our study, like a study by Uren et al. (*15*), hMBF and CFR were similar for age groups up to 70 y but declined afterward, whereas AUCs between the groups were comparable. These findings are mirrored by the optimal cutoffs identified for different age groups in our study, where, as age exceeded 70 y, cutoffs decreased to 1.7 $mL \cdot min^{-1} \cdot g^{-1}$ for hMBF and 2.3 for CFR. With a relative high disease prevalence in older patients, the increase in specificity with age-specific cutoffs outweighed the concomitant fall in sensitivity on a per-vessel level, suggesting a potential benefit from the use of age-specific thresholds. Nevertheless, this difference between the use of cutoffs did not extend to the clinical applicability of perfusion imaging, as reflected by the per-patient analysis. The reduced rate of false positives by lowering the cutoff in the elderly was counterbalanced by the increase in false negatives, resulting in equal diagnostic accuracy. In fact, the conventional cutoff is superior in preventing these patients from a false deferral from the catheterization laboratory. All in all, our findings suggest that the general cutoffs remain applicable even for patients aged more than 70 y.

Role of Cutoffs in Clinical Practice

The use of binary cutoffs seems insurmountable in daily clinical practice, especially when cardiac PET perfusion imaging is being used as a guide for coronary revascularization compared with having a mere gatekeeper function. The difficulty of cutoffs is underscored by a study of Vester et al., in which cutoffs for predicting revascularization and for predicting relief of angina after PCI in patients after coronary artery bypass graft surgery substantially differed from 1.36 to 1.99 $mL \cdot min^{-1} \cdot g^{-1}$ for hMBF and from 1.20 to 2.35 for CFR (*36*). Moreover, cutoffs in our study slightly changed when different FFR or angiographic references were applied, further implying that cutoffs depend on the intended clinical purpose. Indeed, any measure of myocardial perfusion is continuous by its biologic nature and cannot merely be confined to a binary threshold. This oversimplification, although sometimes helpful for clinical decision-making and interpretation of test results, implies that there is a myocardial perfusion threshold at which the benefit of a treatment suddenly appears or disappears. Instead, a more comprehensive evaluation using both PET-derived MBF and FFR will likely allow tailoring of medical therapy and interventions based on their individual disease phenotype, giving an impetus to personalized medicine. This will presumably improve patient satisfaction, temper expectations of invasive procedures, and improve adherence to medical therapy. However, there have not yet been any prospective studies evaluating PET-guided clinical decision-making based on stratification of myocardial perfusion, such as using the concept of coronary flow capacity, ischemic burden, or relative flow ratio.

Limitations

Several limitations need to be acknowledged. First, the Youden index was used to calculate optimal cutoffs. Although the Youden index seeks the optimal balance between sensitivity and specificity, diagnostic accuracy calculations derived from these cutoffs may not consistently translate to the highest attainable diagnostic accuracy given that accuracy is affected by disease prevalence, which differs between specific subpopulations. Second, the present study included a relatively small number of patients aged more

than 70 y, which limits the statistical power for accuracy assessment in this subpopulation. Third, we used $[^{15}O]H_2O$ as the PET tracer. Consequently, the generalizability of our findings to other PET tracers, such as $[^{13}N]NH_3$, ^{82}Rb, or ^{18}F-flurpiridaz, should be considered with caution. This is the case especially in patients with scarring, as $[^{15}O]H_2O$ measures perfusion predominantly in the viable tissue fraction, whereas other PET tracers measure average perfusion in the myocardium. Fourth, the patient groups with reduced global left ventricular ejection fraction or heart failure were mostly excluded. In these patients, the flow capacity is typically reduced because of global myocardial damage, and the same cutoffs may not be valid. Finally, attention was paid to matching visual perfusion defects with their corresponding subtended coronary artery by accounting for coronary dominance. Nevertheless, when a visual defect exceeded more than one coronary territory, following the American Heart Association 17-segment model, mismatches between coronary arteries and their respective vascular regions might have occurred.

CONCLUSION

Optimal cutoffs of quantitative $[^{15}O]H_2O$ PET–derived hMBF and CFR to detect FFR-defined significant CAD were similar between patients with prior CAD (prior MI and/or PCI) and patients without prior CAD. Moreover, optimal cutoffs for hMBF were higher in females than males, whereas optimal cutoffs for both hMBF and CFR were lower in patients 70 y or older than in their younger counterparts. Nevertheless, the application of optimized cutoffs within these specific subpopulations did not enhance diagnostic performance. Our findings advocate the use of previously established general cutoffs for detection of FFR-defined significant CAD in the interpretation of myocardial perfusion parameters.

DISCLOSURE

No potential conflict of interest relevant to this article was reported.

KEY POINTS

QUESTION: What is the influence of prior CAD, sex, and age on optimal cutoffs of myocardial perfusion parameters, and does cutoff optimization enhance the diagnostic performance of quantitative $[^{15}O]H_2O$ PET for detecting hemodynamically significant CAD?

PERTINENT FINDINGS: The presence of prior CAD did not influence optimal cutoffs of quantitative $[^{15}O]H_2O$ PET for detecting FFR-defined hemodynamically significant CAD. For females, however, optimal myocardial perfusion cutoffs were higher than in males. Patients aged more than 70 y had a lower threshold of perfusion parameters than did their younger counterparts. These differences in cutoffs in respective subpopulations pave the way for personalized medicine. Nonetheless, optimizing cutoffs did not exert a positive influence on the diagnostic performance of quantitative $[^{15}O]H_2O$ PET for detecting FFR-defined hemodynamically significant disease.

IMPLICATIONS FOR PATIENT CARE: Clinicians can confidently interpret the results of myocardial perfusion imaging based on general nonspecific cutoffs.

REFERENCES

1. Bergmann SR, Fox KA, Rand AL, et al. Quantification of regional myocardial blood flow in vivo with $H_2{}^{15}O$. *Circulation.* 1984;70:724–733.
2. Maaniitty T, Knuuti J, Saraste A. ^{15}O-water PET MPI: current status and future perspectives. *Semin Nucl Med.* 2020;50:238–247.
3. Bom MJ, van Diemen PA, Driessen RS, et al. Prognostic value of $[^{15}O]H_2O$ positron emission tomography-derived global and regional myocardial perfusion. *Eur Heart J Cardiovasc Imaging.* 2020;21:777–786.
4. Xaplanteris P, Fournier S, Pijls NHJ, et al. Five-year outcomes with PCI guided by fractional flow reserve. *N Engl J Med.* 2018;379:250–259.
5. Zimmermann FM, Ferrara A, Johnson NP, et al. Deferral vs. performance of percutaneous coronary intervention of functionally non-significant coronary stenosis: 15-year follow-up of the DEFER trial. *Eur Heart J.* 2015;36:3182–3188.
6. Danad I, Uusitalo V, Kero T, et al. Quantitative assessment of myocardial perfusion in the detection of significant coronary artery disease: cutoff values and diagnostic accuracy of quantitative $[^{15}O]H_2O$ PET imaging. *J Am Coll Cardiol.* 2014; 64:1464–1475.
7. Knuuti J, Wijns W, Saraste A, et al. 2019 ESC guidelines for the diagnosis and management of chronic coronary syndromes. *Eur Heart J.* 2020;41:407–477.
8. Virani SS, Newby LK, Arnold SV, et al. AHA/ACC/ACCP/ASPC/NLA/PCNA guideline for the management of patients with chronic coronary disease: a report of the American Heart Association/American College of Cardiology Joint Committee on Clinical Practice Guidelines. *J Am Coll Cardiol.* 2023;82:833–955.
9. Danad I, Raijmakers PG, Driessen RS, et al. Comparison of coronary CT angiography, SPECT, PET, and hybrid imaging for diagnosis of ischemic heart disease determined by fractional flow reserve. *JAMA Cardiol.* 2017;2:1100–1107.
10. Driessen RS, van Diemen PA, Raijmakers PG, et al. Functional stress imaging to predict abnormal coronary fractional flow reserve: the PACIFIC 2 study. *Eur Heart J.* 2022;43:3118–3128.
11. Haider A, Bengs S, Portmann A, et al. Role of sex hormones in modulating myocardial perfusion and coronary flow reserve. *Eur J Nucl Med Mol Imaging.* 2022; 49:2209–2218.
12. Han SH, Bae JH, Holmes DR Jr, et al. Sex differences in atheroma burden and endothelial function in patients with early coronary atherosclerosis. *Eur Heart J.* 2008;29:1359–1369.
13. Kobayashi Y, Fearon WF, Honda Y, et al. Effect of sex differences on invasive measures of coronary microvascular dysfunction in patients with angina in the absence of obstructive coronary artery disease. *JACC Cardiovasc Interv.* 2015;8: 1433–1441.
14. Danad I, Raijmakers PG, Appelman YE, et al. Coronary risk factors and myocardial blood flow in patients evaluated for coronary artery disease: a quantitative $[^{15}O]$H2O PET/CT study. *Eur J Nucl Med Mol Imaging.* 2012;39:102–112.
15. Uren NG, Camici PG, Melin JA, et al. Effect of aging on myocardial perfusion reserve. *J Nucl Med.* 1995;36:2032–2036.
16. Patel MB, Bui LP, Kirkeeide RL, Gould KL. Imaging microvascular dysfunction and mechanisms for female-male differences in CAD. *JACC Cardiovasc Imaging.* 2016;9:465–482.
17. Danad I, Raijmakers PG, Harms HJ, et al. Impact of anatomical and functional severity of coronary atherosclerotic plaques on the transmural perfusion gradient: a $[^{15}O]H_2O$ PET study. *Eur Heart J.* 2014;35:2094–2105.
18. Kajander S, Joutsiniemi E, Saraste M, et al. Cardiac positron emission tomography/computed tomography imaging accurately detects anatomically and functionally significant coronary artery disease. *Circulation.* 2010;122:603–613.
19. Harms HJ, Knaapen P, de Haan S, Halbmeijer R, Lammertsma AA, Lubberink M. Automatic generation of absolute myocardial blood flow images using $[^{15}O]H_2O$ and a clinical PET/CT scanner. *Eur J Nucl Med Mol Imaging.* 2011;38:930–939.
20. Nesterov SV, Han C, Mäki M, et al. Myocardial perfusion quantitation with ^{15}O-labelled water PET: high reproducibility of the new cardiac analysis software (Carimas). *Eur J Nucl Med Mol Imaging.* 2009;36:1594–1602.
21. Cerqueira MD, Weissman NJ, Dilsizian V, et al. Standardized myocardial segmentation and nomenclature for tomographic imaging of the heart. A statement for healthcare professionals from the Cardiac Imaging Committee of the Council on Clinical Cardiology of the American Heart Association. *Circulation.* 2002;105:539–542.
22. Cox DA, Vita JA, Treasure CB, et al. Atherosclerosis impairs flow-mediated dilation of coronary arteries in humans. *Circulation.* 1989;80:458–465.
23. Schindler TH, Schelbert HR, Quercioli A, Dilsizian V. Cardiac PET imaging for the detection and monitoring of coronary artery disease and microvascular health. *JACC Cardiovasc Imaging.* 2010;3:623–640.
24. Pijls NH. Fractional flow reserve after previous myocardial infarction. *Eur Heart J.* 2007;28:2301–2302.
25. Kim HY, Lim HS, Doh JH, et al. Physiological severity of coronary artery stenosis depends on the amount of myocardial mass subtended by the coronary artery. *JACC Cardiovasc Interv.* 2016;9:1548–1560.

26. Kaufmann PA, Camici PG. Myocardial blood flow measurement by PET: technical aspects and clinical applications. *J Nucl Med.* 2005;46:75–88.
27. Campisi R, Nathan L, Pampaloni MH, et al. Noninvasive assessment of coronary microcirculatory function in postmenopausal women and effects of short-term and long-term estrogen administration. *Circulation.* 2002;105:425–430.
28. Duvernoy CS, Meyer C, Seifert-Klauss V, et al. Gender differences in myocardial blood flow dynamics: lipid profile and hemodynamic effects. *J Am Coll Cardiol.* 1999;33:463–470.
29. Chareonthaitawee P, Kaufmann PA, Rimoldi O, Camici PG. Heterogeneity of resting and hyperemic myocardial blood flow in healthy humans. *Cardiovasc Res.* 2001;50:151–161.
30. Chung JH, Lee KE, Lee JM, et al. Effect of sex difference of coronary microvascular dysfunction on long-term outcomes in deferred lesions. *JACC Cardiovasc Interv.* 2020;13:1669–1679.
31. Danad I, Raijmakers PG, Appelman YE, et al. Hybrid imaging using quantitative $H_2{}^{15}O$ PET and CT-based coronary angiography for the detection of coronary artery disease. *J Nucl Med.* 2013;54:55–63.
32. Joutsiniemi E, Saraste A, Pietila M, et al. Absolute flow or myocardial flow reserve for the detection of significant coronary artery disease? *Eur Heart J Cardiovasc Imaging.* 2014;15:659–665.
33. Egashira K, Inou T, Hirooka Y, et al. Effects of age on endothelium-dependent vasodilation of resistance coronary artery by acetylcholine in humans. *Circulation.* 1993;88:77–81.
34. Scioli MG, Bielli A, Arcuri G, Ferlosio A, Orlandi A. Ageing and microvasculature. *Vasc Cell.* 2014;6:19.
35. van de Hoef TP, Echavarria-Pinto M, Meuwissen M, Stegehuis VE, Escaned J, Piek JJ. Contribution of age-related microvascular dysfunction to abnormal coronary: hemodynamics in patients with ischemic heart disease. *JACC Cardiovasc Interv.* 2020;13:20–29.
36. Vester M, Madsen S, Kjærulff MLG, et al. Myocardial perfusion imaging by ^{15}O-H_2O positron emission tomography predicts clinical revascularization procedures in symptomatic patients with previous coronary artery bypass graft. *Eur Heart J Open.* 2023;3:oead044.

Patterns of Early Neocortical Amyloid-β Accumulation: A PET Population-Based Study

Emily E. Lecy*[1,2], Hoon-Ki Min*[1], Christopher J. Apgar[1,2], Daniela D. Maltais[1], Emily S. Lundt[3], Sabrina M. Albertson[3], Matthew L. Senjem[4], Christopher G. Schwarz[1], Hugo Botha[5], Jonathan Graff-Radford[5], David T. Jones[5], Prashanthi Vemuri[1], Kejal Kantarci[1], David S. Knopman[5], Ronald C. Petersen[5], Clifford R. Jack Jr.[1], Jeyeon Lee[1,6], and Val J. Lowe[1]

[1]Department of Radiology, Mayo Clinic, Rochester, Minnesota; [2]Department of Neuroscience, University of Minnesota, Minneapolis, Minnesota; [3]Division of Biostatistics, Department of Health Sciences Research, Mayo Clinic, Rochester, Minnesota; [4]Department of Technology, Mayo Clinic, Rochester, Minnesota; [5]Department of Neurology, Mayo Clinic, Rochester, Minnesota; and [6]Department of Biomedical Engineering, College of Medicine, Hanyang University, Seoul, South Korea

The widespread deposition of amyloid-β (Aβ) plaques in late-stage Alzheimer disease is well defined and confirmed by in vivo PET. However, there are discrepancies between which regions contribute to the earliest topographic Aβ deposition within the neocortex. **Methods:** This study investigated Aβ signals in the perithreshold SUV ratio range using Pittsburgh compound B (PiB) PET in a population-based study cross-sectionally and longitudinally. PiB PET scans from 1,088 participants determined the early patterns of PiB loading in the neocortex. **Results:** Early-stage Aβ loading is seen first in the temporal, cingulate, and occipital regions. Regional early deposition patterns are similar in both apolipoprotein ε4 carriers and noncarriers. Clustering analysis shows groups with different patterns of early amyloid deposition. **Conclusion:** These findings of initial Aβ deposition patterns may be of significance for diagnostics and understanding the development of Alzheimer disease phenotypes.

Key Words: amyloid-β; Pittsburgh compound B; PiB; PET; early stage

J Nucl Med 2024; 65:1122–1128
DOI: 10.2967/jnumed.123.267150

The neuropathology of Alzheimer disease (AD) is characterized by the deposition of amyloid-β (Aβ) plaques (*1*). PET using Aβ tracers has added to our understanding of Aβ deposition and AD progression. The first Aβ radiotracer, ^{11}C-labeled Pittsburgh compound B ([^{11}C]C-PiB), has been used in AD studies for more than a decade (*2*) and aligns with histologic findings of Aβ localization (*3*). Other Aβ PET biomarkers show similar diagnostic accuracy to [^{11}C]C-PiB, further establishing its efficacy (*4,5*). Currently, the widespread aggregation of Aβ plaques in late-stage AD is well established (*6*); however, there are discrepancies in how and where Aβ deposition begins (*5,7*).

Neuropathologic studies describe the progression of Aβ deposition in 5 ordered stages termed Thal phases (*8*). The first Thal phase of isocortical Aβ deposition is defined as occurring exclusively in the neocortex, with the exception of the paracentral lobule, and as being diffusely distributed and without a specific neocortical regional pattern (*8*). Although these postmortem histologic studies provide conclusive results on the location of Aβ proteins (*9*), it remains difficult to observe Aβ early progression because of small sample sizes and because most of the samples are from patients whose Aβ onset was likely years before (*8*).

PET imaging provides an in vivo picture of neocortical deposition and longitudinal development. Past PET studies suggest areas of Aβ origination; however, these studies show inconsistencies in the regions where early Aβ aggregation begins—describing early Aβ aggregation as occurring in many areas, including the frontotemporal association cortices (*10*), frontomedial areas (*11*), large-scale brain networks such as the default mode network (*12*), parietal regions such as the precuneus (*11,13*), cingulate (*13*), and medial orbitofrontal areas (*11,13*). There are also discrepancies in the role of the temporal lobe in initial accumulation, with some claiming it to be a later aggregation point (*11*) and others deeming it an early accumulation site (*10*). These studies are limited by using preselected cohorts, which limit the ability to generalize their results, and by lacking assessment of risk factors on Aβ aggregation patterns, such as apolipoprotein-ε4 (APOE) status or familial history (*14*). These inconsistencies in study design and conclusions on early aggregation of Aβ demonstrate a need to revisit the earliest patterns of Aβ in a population-based study.

Here, [^{11}C]C-PiB PET was used in an epidemiologic community-based population study to assess the prevalence of focal early Aβ signal changes across brain regions in the neocortex both cross-sectionally and longitudinally. To see subtle differences in Aβ deposition, we selected participants who had an amyloid signal near the global [^{11}C]C-PiB cutoff (*15*), we determined elevated Aβ status for each region of interest (ROI) independently compared with younger cognitively unimpaired (CU) individuals (*16*), and we analyzed the elevated [^{11}C]C-PiB data by ROI-wise analysis. Patterns of early regional Aβ deposition were assessed, and cluster analysis was used to determine subgroups with different Aβ deposition patterns within the population.

MATERIALS AND METHODS

Participants

All participants were enrolled in the Mayo Clinic Study of Aging (MCSA), a population-based randomized aging study from Olmsted

Received Nov. 27, 2023; revision accepted Apr. 29, 2024.
For correspondence or reprints, contact Val J. Lowe (vlowe@mayo.edu) or Jeyeon Lee (jeyeonlee@hanyang.ac.kr).
*Contributed equally to this work.
Published online May 23, 2024.

County, Minnesota (*17*). Participants provided written informed consent to participate in the study, with the approval of the Mayo Clinic and Olmsted Medical Center Institutional Review Boards. At enrollment and at all subsequent visits, the participants were clinically diagnosed as being CU, as having mild cognitive impairment, or as having dementia, via a consensus conference process (Supplemental Table 1; supplemental materials are available at http://jnm.snmjournals.org).

Neuroimaging and Image Analysis

Participants received a [^{11}C]C-PiB dose (range, 293.8–746.3 MBq), followed by a 33.5- to 64.5-min postinjection period before imaging began. The PET acquisition took 20 min, as previously described (*18*). Cortical ROIs were defined by the Mayo Clinic Adult Lifespan Template and ADIR122 atlas (*19*). An SUV ratio (SUVr) image was calculated by dividing the median uptake in the cerebellar crus gray matter. Regional SUVr was defined as the median uptake across all gray matter voxels in an ROI. Two-component partial-volume correction was used (*20*). Global SUVr was computed from a meta-ROI.

Early PiB Group and Subgroups

A population was created by selecting those who had amyloid signal near the global [^{11}C]C-PiB cutoff (SUVr of 1.42) (*15*). Specifically, participants of this study, deemed the early PiB group, were 50 y of age or older with a global SUVr of 1.29–1.64 (Fig. 1; Supplemental Fig. 1). The lower cutoff (1.29) represents the lower tertile boundary of those CU 50 y or older in the MCSA. The upper limit (1.64) is the lower tertile boundary for those 50 y or older in the MCSA with elevated amyloid levels. The early PiB group (n = 1,088) comprised 89.6% CU individuals, 9.9% patients with mild cognitive impairment, and 0.6% patients with dementia (Supplemental Table 1). The ethnic distribution of the early PiB group is summarized in Supplemental Table 2.

The early PiB group was then further distributed into subgroups based on each individual's number of ROIs with elevated [^{11}C]C-PiB levels (i.e., the greater the number of elevated ROIs, the higher the participant group assignment). The regional elevated [^{11}C]C-PiB level was determined by using region-specific cutoffs as being above the 95th percentile of younger CU MCSA individuals (30–49 y, n = 146; Supplemental Table 3) (*18*). Six equitably participant-sized subgroupings were made: very low (n = 170), low (n = 180), low-moderate (n = 185), moderate (n = 186), moderate-high (n = 190), and high (n = 177) (Table 1; Fig. 1).

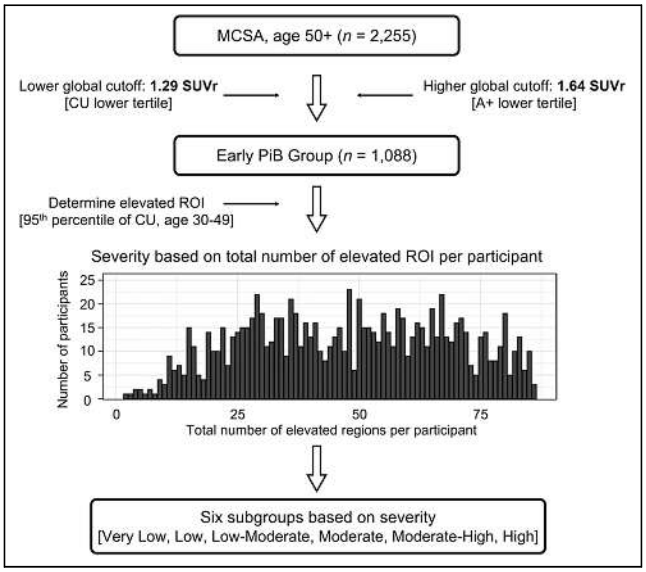

FIGURE 1. Participant selection criteria for early PiB group from MCSA and distribution into subgroups based on regions with elevated amyloid signals. Subgroups range from very low to high based on number of affected regions. A+ = amyloid-positive.

Clustering and Statistical Analysis

Agglomerative hierarchic clustering analysis (*21*) with the Ward linkage method was performed using regional SUVr values (averaged over the hemisphere). The number of clusters was fixed to 3 (k = 3) a priori. The algorithm does not guarantee finding the optimal solution, and thus we also performed a k-means clustering analysis to compare the results (*22*). Squared Euclidean distance was used as the similarity measure. Analyses were performed using R Statistical Software (version 3.6.2). More details are provided in the supplemental materials.

RESULTS

Cross-Sectional Staging of Regional Amyloid Deposition

Elevated [^{11}C]C-PiB PET determined by region-specific cutoffs was observed in over 80% of participants within the fusiform gyrus, angular gyrus, inferior and middle temporal region, middle occipital region, and calcarine region (Fig. 2A). The amygdala and superior temporal pole had minimal [^{11}C]C-PiB PET SUVr elevation, being present in under 25% of the population. The overall frequency pattern of amyloid positivity was not visually different when applying the hemisphere-specific cutoff (left or right) or the global hemispheric cutoff (voxel-weighted median of left and right).

Estimation of regional Aβ progression by subgrouping using regional frequencies of amyloid positivity revealed unique early patterns of amyloid burden (Fig. 2B; Supplemental Fig. 2). The temporal cortex, posterior cingulate cortex, occipital cortex, and angular gyrus showed an early elevated [^{11}C]C-PiB SUVr in the very low subgroup. Unique regional patterns appeared throughout the subgroups and eventually saturated all regions in the high subgroup. Additionally, the fusiform, inferior, and middle temporal regions; middle temporal pole; posterior cingulate cortex; angular gyrus; calcarine region; and inferior and middle occipital lobes showed consistently elevated [^{11}C]C-PiB PET signals higher than the mean or regional percentage of other regions in the subgroups until all regions became saturated. Relationships between APOE genotype and early [^{11}C]C-PiB SUVr were considered; however, both APOE genotypes showed similar patterns visually (APOE-ε4 carriers in red and noncarriers in blue; Supplemental Fig. 3), implying little effect of genotypes on regional Aβ burden. The median regional SUVr values for subgroups are shown on surface renderings (Supplemental Fig. 3).

Hierarchic Clustering

Hierarchic cluster analysis of the moderate, moderate-high, and high subgroups was performed to investigate heterogeneity of regional trends in early Aβ deposition. Each cluster revealed distinct spatial patterns of Aβ deposition in the brain: the frontal cluster showed a higher [^{11}C]C-PiB PET signal in the frontal lobe and a lower signal in the occipital lobe, the occipitoparietal cluster showed a higher [^{11}C]C-PiB PET signal in both the parietal and the occipital lobes and a lower signal in the frontal lobe, and the global cluster showed a generally lower [^{11}C]C-PiB PET signal and diffuse patterns (Fig. 3). Pairwise statistical comparisons of the mean regional SUVr between clusters are shown in Supplemental Figure 4 (2-sample t test). The t-distributed stochastic neighbor embedding projection also showed distinct grouping between the clusters (Fig. 3C). Particularly, the global [^{11}C]C-PiB SUVr did not significantly differ between the frontal and occipitoparietal clusters; however, the clusters showed convincingly

TABLE 1
Subgroup Demographics of Early PiB Subgroups and Younger CU Group

Demographic	Younger CU (n = 164)	Very low (n = 170)	Low (n = 180)	Low-moderate (n = 185)	Moderate (n = 186)	Moderate-high (n = 190)	High (n = 177)	P
Age (y)								<0.001*
Mean ± SD	41 ± 6	67 ± 10	71 ± 10	72 ± 9	74 ± 9	75 ± 9	75 ± 8	
Range	31–50	51–92	50–94	52–93	52–91	54–93	53–93	
Sex (n)								0.597†
Female	73 (44.5%)	85 (50.0%)	80 (44.4%)	87 (47.0%)	99 (53.2%)	95 (50.0%)	82 (46.3%)	
Male	91 (55.5%)	85 (50.0%)	100 (55.6%)	98 (53.0%)	87 (46.8%)	95 (50.0%)	95 (53.7%)	
Education (y)								<0.001*
N-Miss	0	0	1	0	0	0	0	
Mean ± SD	15.76 ± 2.24	15.25 ± 2.62	14.84 ± 2.73	14.55 ± 2.55	14.30 ± 2.56	14.33 ± 2.74	14.37 ± 2.68	
Range	11.00–20.00	9.00–20.00	7.00–20.00	8.00–20.00	7.00–20.00	0.00–20.00	6.00–20.00	
Diagnosis (n)								
N-Miss	0	1	1	1	0	1	2	
CU	164 (100.0%)	159 (94.1%)	162 (90.5%)	168 (91.3%)	165 (88.7%)	165 (87.3%)	150 (85.7%)	
MCI	0 (0.0%)	10 (5.9%)	17 (9.5%)	15 (8.2%)	20 (10.8%)	22 (11.6%)	23 (13.1%)	
Dementia	0 (0.0%)	0 (0.0%)	0 (0.0%)	1 (0.5%)	1 (0.5%)	2 (1.1%)	2 (1.1%)	
Other	0 (0.0%)	0 (0.0%)	0 (0.0%)	0 (0.0%)	0 (0.0%)	0 (0.0%)	0 (0.0%)	
APOE-ε4 (n)								0.040†
N-Miss	19	15	10	10	12	10	12	
Noncarrier	112 (77.2%)	121 (78.1%)	137 (80.6%)	127 (72.6%)	141 (81.0%)	133 (73.9%)	111 (67.3%)	
Carrier	33 (22.8%)	34 (21.9%)	33 (19.4%)	48 (27.4%)	33 (19.0%)	47 (26.1%)	54 (32.7%)	
PVC GM SUVr								<0.001*
Mean ± SD	1.23 ± 0.05	1.31 ± 0.01	1.33 ± 0.02	1.35 ± 0.02	1.38 ± 0.04	1.42 ± 0.05	1.49 ± 0.07	
Range	1.10–1.40	1.30–1.35	1.30–1.44	1.31–1.46	1.33–1.58	1.36–1.62	1.39–1.62	

*ANOVA.
†Pearson χ^2 test.
N-Miss = number of participants missing this particular variable; MCI = mild cognitive impairment; PVC GM SUVr = partial-volume–corrected gray matter [^{11}C]C-PiB SUVr.

different [^{11}C]C-PiB uptake levels between the frontal and occipitoparietal regions (Fig. 3C; Supplemental Fig. 4).

The clusters had unequal sizes but were similar in diagnosis and age (Table 2). APOE-ε4 carriers were associated with the frontal and occipitoparietal cluster groups, whereas noncarriers were associated with the global cluster. In comparisons of k-means and hierarchic cluster analysis, both methods provided similar results (Supplemental Fig. 5). Additional clustering was estimated by using the same hyperparameters but leaving regions separated by hemispheres. However, we did not discern any clear asymmetric patterns between hemispheres (Supplemental Fig. 6). The hierarchic clustering was performed using regional [^{11}C]C-PiB SUVr within subgroups. Starting from the low-moderate and moderate subgroups, a similar pattern of group separations (i.e., frontal, occipitoparietal, and global) showing differences in the parietal, frontal, and occipital lobes was observed (Supplemental Fig. 7).

Longitudinal Changes in [^{11}C]C-PiB PET Signals by Clusters

To investigate the difference in Aβ progression between clusters, annual [^{11}C]C-PiB SUVr changes with serial data in each cluster subgroup were analyzed (n = 33, 64, and 186 for the frontal, occipitoparietal, and global groups, respectively; Fig. 4). The

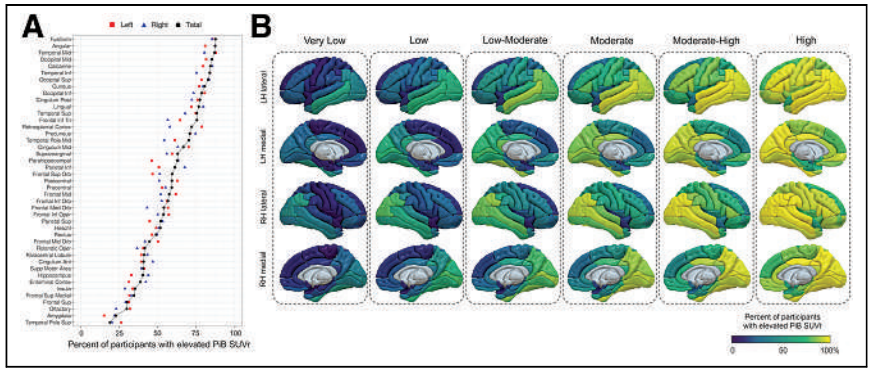

FIGURE 2. Regional elevated PiB PET signals across subgroups. (A) Percentage of participants with elevated [^{11}C]C-PiB signals in specific brain regions, indicating prevalent early amyloid positivity. (B) Surface renderings showing percentage of elevated [^{11}C]C-PiB signals by brain region and subgroup, highlighting unique early amyloid patterns. LH = left hemisphere; RH = right hemisphere.

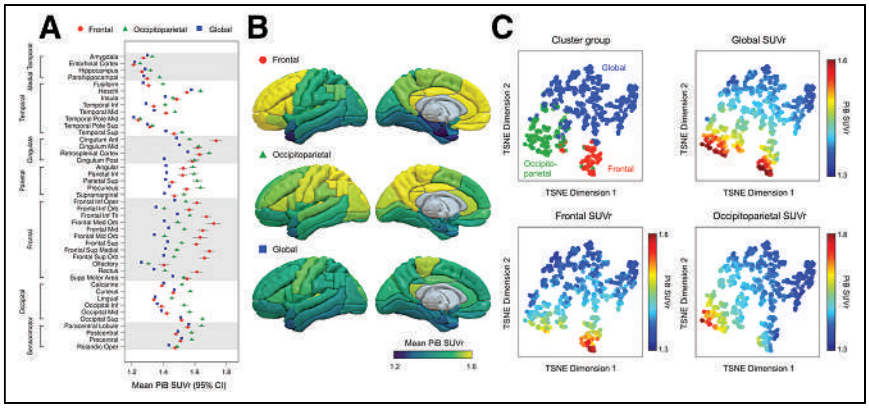

FIGURE 3. Hierarchic clustering of PiB PET signals in advanced subgroups. (A) Mean regional [^{11}C]C-PiB PET SUVr for identified clusters with varying patterns of amyloid deposition. (B) Three-dimensional visualizations of average SUVr maps for each cluster. (C) *t*-distributed stochastic neighbor embedding (TSNE) projection illustrating distinctiveness of clusters based on SUVr values.

frontal group showed the highest Aβ accumulation rates across cortices, followed by the occipitoparietal group. Comparing the frontal and occipitoparietal groups, we found that the frontal cluster showed a significantly higher accumulation rate in the frontal lobe and cingulate cortex ($P < 0.05$, 2-sample *t* test; Supplemental Fig. 8). The occipitoparietal group also showed a higher progression than the global group ($P < 0.05$, 2-sample *t* test; Supplemental Fig. 8). The changes in cognitive test score were also considered, and a few comparisons showed statistical significance ($P = 0.02$ and $P = 0.03$ for attention and Clinical Dementia Rating–global, respectively; linear model ANOVA; Supplemental Table 4). In pairwise post hoc comparisons, the occipitoparietal group showed a higher decline than the global group ($P = 0.02$ and $P = 0.049$ for attention and Clinical Dementia Rating–global, respectively; *t* test). No significant differences were found in the changes in clinical diagnosis (Supplemental Table 5).

DISCUSSION

This study revealed regional patterns of initial Aβ deposition within the neocortex to be in the temporal, cingulate, and occipital

TABLE 2
Demographics of Cluster Populations from Figure 3

Demographic	Frontal (n = 60)	Occipitoparietal (n = 131)	Global (n = 362)	P
Age (y)				<0.001*
Mean ± SD	75 ± 7	78 ± 8	73 ± 8	
Range	61–90	53–93	52–93	
Sex (n)				0.035†
Female	29 (48.3%)	53 (40.5%)	194 (53.6%)	
Male	31 (51.7%)	78 (59.5%)	168 (46.4%)	
Education (y)				0.476*
Mean ± SD	14.27 ± 2.98	14.58 ± 2.60	14.25 ± 2.62	
Range	6.00–20.00	7.00–20.00	0.00–20.00	
Diagnosis (n)				0.761†
N-Miss	0	1	2	
CU	53 (88.3%)	111 (85.4%)	316 (87.8%)	
MCI	6 (10.0%)	17 (13.1%)	42 (11.7%)	
Dementia	1 (1.7%)	2 (1.5%)	2 (0.6%)	
APOE-ε4 (n)				<0.001†
N-Miss	3	12	19	
Noncarrier	30 (52.6%)	83 (69.7%)	272 (79.3%)	
Carrier	27 (47.4%)	36 (30.3%)	71 (20.7%)	
PVC GM SUVr				<0.001*
Mean ± SD	1.52 ± 0.06	1.50 ± 0.06	1.39 ± 0.03	
Range	1.42–1.62	1.37–1.62	1.33–1.49	

*ANOVA.
†Pearson χ^2 test.
N-Miss = number of participants missing this particular variable; MCI = mild cognitive impairment; PVC GM SUVr = partial-volume–corrected gray matter [^{11}C]C-PiB SUVr.

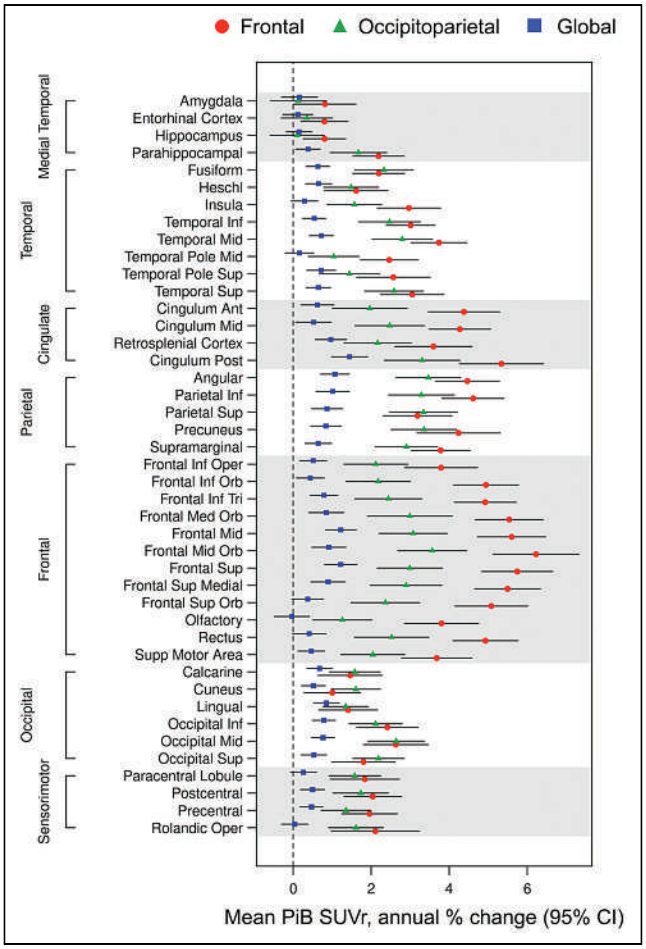

FIGURE 4. Annual change in [^{11}C]C-PiB PET SUVr across clusters with available serial data (n = 283), comparing amyloid accumulation rates and highlighting differences between clusters.

regions. The percentage of patients in each subgroup with elevated Aβ in these specific regions increased sequentially with increasing global SUVr even when below typical global cutoffs. We found that early regional Aβ patterns can be seen in both APOE carriers and noncarriers. The use of region-specific cutoffs as determined in the young CU group allowed us to survey distinct areas that showed early Aβ distributions that may otherwise go unseen using traditional global meta-ROI analysis.

The initial areas of Aβ deposition included the temporal, cingulate, and occipital lobes—namely, the fusiform gyrus, inferior temporal lobe, middle temporal region, middle temporal pole, superior temporal lobe, posterior cingulum, angular gyrus, calcarine region, cuneus, lingual gyrus, inferior occipital lobe, middle occipital lobe, and superior occipital lobe. Areas with the greatest elevated [^{11}C]C-PiB SUVr levels in early patterns of deposition include the fusiform gyrus, angular gyrus, inferior temporal region, and middle temporal region. Studies analyzing early Aβ deposition have found differing results, with some stating that initial aggregation sites are found across the frontal lobe (*11–13*) and the parietal (*12,13*) and temporal areas (*10*) and other claiming that temporal areas are the later points of aggregation (*11*). Our data suggest that in the earliest subgroups of Aβ accumulation, the initial rise is seen in the temporal lobe, posterior cingulate region, and occipital lobe.

These findings are supported by theories of the functional connectivity and activity within the brain (*12*). Both high neuronal connectivity and activity have been linked to the release and deposition of Aβ (*23,24*). The high neuronal connectivity of the posterior cingulate (*25*) and occipital lobe (*26*) appears to make these regions more vulnerable to Aβ deposition, as seen in our results and others (*23,27*). Our results showing an early Aβ load in the middle prefrontal cortex, posterior cingulate, precuneus, and angular gyrus supports the idea that the default mode network may relate to Aβ deposition (*12*). The default mode network includes brain regions with high connectivity, particularly in a spontaneous resting state (*28*), and has been shown to be vulnerable to Aβ deposition (*26,29*).

Aβ load in the sensorimotor cortex has shown conflicting results, with some claiming there is deposition in the sensorimotor cortex (*30*). We found that deposition rates across subgroups are slower in this region than in other regions (Fig. 3) but that SUVr values increase steadily across the subgroups (Supplemental Fig. 3). Because the sensorimotor cortex is hyperexcitable (*24*), it may have higher susceptibility to Aβ deposition late in the disease but possibly not at early stages (*27*). However, there is a lack of explanation as to why this area has the lowest Aβ deposition (*30*).

Clustering analysis defined several subgroups with distinct patterns of early regional [^{11}C]C-PiB PET signal: high in the frontal lobe and low in the parietal and occipital lobes (frontal cluster), high in the parietal and occipital lobes and low in the frontal lobe (occipitoparietal cluster), and low in the temporal, parietal, frontal, and occipital lobes (global cluster). This observation aligns with a recent study that reported 3 subtypes of spatial–temporal amyloid accumulation (i.e., frontal, parietal, and occipital) (*31*). The cingulate and sensorimotor cortices had similar levels of deposition between clusters. The parahippocampal gyrus, fusiform gyrus, inferior and middle temporal region, and sensorimotor cortices showed a higher Aβ load in the occipitoparietal cluster, and the anterior cingulate cortex had a higher Aβ deposition in the frontal cluster. Interestingly, the global cluster group showed similar regional frequencies of amyloid positivity to other participants included in the analysis, but the global SUVr was significantly lower than for other clusters (Fig. 3C; Table 2). There is limited information about the heterogeneities in initial Aβ regional deposition, but it has been seen that the regional prevalence of cerebral amyloid deposition differs across individuals—even for those with cognitive impairment (*32*). The clinical implications of these heterogeneities are not understood; however, their appearance suggests early development of different subgroup-related phenotypes. The findings of this study could serve as a basis for designing a power analysis to assess theoretic drug effects and determine the sample sizes necessary to ensure confidence in the findings. Future analysis and correlation with tau deposition patterns and clinical outcome are needed.

APOE-ε4 carriers made up 30.3%, 47.4%, and 20.7% of participants in the frontal, occipitoparietal, and global clusters, respectively. In the frontal and occipitoparietal clusters, which had a higher percentage of APOE-ε4 carriers, the parietal and frontal lobes had a relatively higher [^{11}C]C-PiB SUVr. Others have shown that APOE-ε4 carriers have heightened levels of Aβ deposition in the frontal parietal regions, validating these patterns (*14*). There were fewer APOE-ε4 carriers in the global cluster, where deposition was low across multiple areas of the brain, again suggesting that APOE carriers may have specific patterns of Aβ deposition that differ from noncarriers.

In the longitudinal analysis, the brain regions with a higher relative Aβ progression include the frontal, cingulate, temporal, parietal,

and occipital lobes, consistent with past studies (*11,13*). Subgroup comparison showed that the frontal cluster had a higher Aβ longitudinal deposition. The occipitoparietal group also showed higher rates of accumulation than the global cluster; however, a lower annual percentage change was seen in the frontal and cingulate cortices than in the frontal cluster. This result aligns with the fact that being an APOE-ε4 carrier heightens the risk of Aβ deposition (*33*) and causes deposition earlier in life, given the high proportion of APOE-ε4 carriers in the frontal and occipitoparietal clusters.

This study was limited by the difficulty of confirming PET findings. Studies suggest that cerebrospinal fluid can detect abnormal Aβ before PET can, but autopsy confirmation is needed (*34*). Because lowered β-amyloid 42 in cerebrospinal fluid correlates strongly with the presentation of an early amyloid load in preclinical AD stages (*34*) and correlates with APOE carriers (*35*), a comparison of early PET findings and cerebrospinal fluid could be helpful. Because our study had few AD dementia participants (n = 0.6%), we cannot confirm that the patterns we observed are associated with eventual AD, even though this is a possible outcome. Despite this limitation, it is important to study Aβ deposition early, within CU individuals, given that Aβ deposition may begin about 20 y before dementia occurs (*8*).

CONCLUSION

Initial Aβ deposition occurs in specific brain regions, and some subgroups have distinct patterns of deposition that may represent different clinical phenotypes linked to APOE status. Inconsistencies in past studies describing early aggregation areas may be only a demonstration of the presence of different subgroups. We suggest that when larger cohorts are considered, the earliest patterns of Aβ are seen as a heterogeneous mix of pattern subtypes representing different paths of Aβ deposition that may eventually predispose to distinct AD phenotypes. Identifying these regions of early aggregation and examining their properties in a population study may best elucidate how Aβ aggregation starts in sporadic AD. This knowledge is crucial in advancing both diagnostic techniques, understanding the development of AD phenotypes, and developing disease-modifying drugs.

DISCLOSURE

Funding support was provided through NIH grants R01 AG073282, P30 AG62677, R01 AG068206, U01 AG006786, P50 AG016574, R01 AG034676, R37 AG011378, R01 AG041851, R01 NS097495, R01 AG056366, and U01 NS100620; Hanyang University (HY-202300000003038); the GHR Foundation; the Elsie and Marvin Dekelboum Family Foundation; the Alexander Family Alzheimer's Disease Research Professorship of the Mayo Clinic; the Liston Award Family Foundation; the Robert H. and Clarice Smith and Abigail van Buren Alzheimer's Disease Research Program; the Schuler Foundation; and the Mayo Foundation for Medical Education and Research. Matthew Senjem has held stock in Align Technology, Inc., Inovio Pharmaceuticals, Inc., Mesa Laboratories, Inc., Johnson and Johnson, LHC Group, Inc., Natus Medical Inc., and Varex Imaging Corp., unrelated to this work. Christopher Schwarz receives National Institutes of Health (NIH) support. Jonathan Graff-Radford is on the editorial board for Neurology and receives NIH support. Prashanthi Vemuri received speaker fees from Miller Medical Communications, Inc., and NIH support. Kejal Kantarci consults for Biogen, receives research support from Avid Radiopharmaceuticals and Eli Lilly, and is funded by NIH and the Alzheimer Drug Discovery Foundation. David Knopman serves on a data safety monitoring board for the DIAN study and a tau therapeutic for Biogen (no personal compensation); is a site investigator for Biogen aducanumab trials; participates in clinical trials sponsored by Lilly Pharmaceuticals and the University of Southern California; consults for Samus Therapeutics, Roche, Magellan Health, and Alzeca Biosciences (no personal compensation); and receives NIH support. Ronald Petersen consults for Roche, Inc., Merck, Inc., Biogen, Inc., Eisai, Inc., Genentech, Inc., and Nestle, Inc.; served on a data safety monitoring board for Genentech; receives royalties from Oxford University Press and UpToDate; and receives NIH support. Clifford Jack, Jr., consulted for Lily, serves on an independent data safety monitoring board for Roche, speaks for Eisai (no personal compensation), and is supported by NIH and the Alexander Family Alzheimer Disease Research Professorship of the Mayo Clinic. Val Lowe consults for Bayer Schering Pharma, Piramal Life Sciences, Life Molecular Imaging, Eisai Inc., AVID Radiopharmaceuticals, Eli Lilly and Co., and Merck Research and receives research support from GE Healthcare, Siemens Molecular Imaging, AVID Radiopharmaceuticals, and the NIH (NIA, NCI). No other potential conflict of interest relevant to this article was reported.

ACKNOWLEDGMENTS

We thank all volunteers, participants, and coordinators for their invaluable contributions to this research.

KEY POINTS

QUESTION: Which neocortical region shows the earliest topographic Aβ deposition?

PERTINENT FINDINGS: Early-stage Aβ loading is seen in the temporal, cingulate, and occipital regions. Clustering analysis shows groups with different patterns of early amyloid deposition.

IMPLICATIONS FOR PATIENT CARE: This population-based study provides generalizable data about amyloid load.

REFERENCES

1. Terry RD, Masliah E, Salmon DP, et al. Physical basis of cognitive alterations in Alzheimer's disease: synapse loss is the major correlate of cognitive impairment. *Ann Neurol.* 1991;30:572–580.
2. Klunk WE, Engler H, Nordberg A, et al. Imaging brain amyloid in Alzheimer's disease with Pittsburgh compound-B. *Ann Neurol.* 2004;55:306–319.
3. Zhang S, Han D, Tan X, Feng J, Guo Y, Ding Y. Diagnostic accuracy of ^{18}F-FDG and ^{11}C-PIB-PET for prediction of short-term conversion to Alzheimer's disease in subjects with mild cognitive impairment. *Int J Clin Pract.* 2012;66:185–198.
4. Lowe VJ, Lundt E, Knopman D, et al. Comparison of [^{18}F]flutemetamol and [^{11}C]Pittsburgh compound-B in cognitively normal young, cognitively normal elderly, and Alzheimer's disease dementia individuals. *Neuroimage Clin.* 2017;16:295–302.
5. Wolk DA, Grachev ID, Buckley C, et al. Association between in vivo fluorine 18-labeled flutemetamol amyloid positron emission tomography imaging and in vivo cerebral cortical histopathology. *Arch Neurol.* 2011;68:1398–1403.
6. Engler H, Forsberg A, Almkvist O, et al. Two-year follow-up of amyloid deposition in patients with Alzheimer's disease. *Brain.* 2006;129:2856–2866.
7. Villemagne VL, Pike KE, Chetelat G, et al. Longitudinal assessment of Aβ and cognition in aging and Alzheimer disease. *Ann Neurol.* 2011;69:181–192.
8. Thal DR, Rub U, Orantes M, Braak H. Phases of Aβ-deposition in the human brain and its relevance for the development of AD. *Neurology.* 2002;58:1791–1800.
9. Bharadwaj PR, Dubey AK, Masters CL, Martins RN, Macreadie IG. Aβ aggregation and possible implications in Alzheimer's disease pathogenesis. *J Cell Mol Med.* 2009;13:412–421.

10. Cho H, Choi JY, Hwang MS, et al. In vivo cortical spreading pattern of tau and amyloid in the Alzheimer disease spectrum. *Ann Neurol.* 2016;80:247–258.
11. Grothe MJ, Barthel H, Sepulcre J, et al. In vivo staging of regional amyloid deposition. *Neurology.* 2017;89:2031–2038.
12. Palmqvist S, Scholl M, Strandberg O, et al. Earliest accumulation of β-amyloid occurs within the default-mode network and concurrently affects brain connectivity. *Nat Commun.* 2017;8:1214.
13. Mattsson N, Palmqvist S, Stomrud E, Vogel J, Hansson O. Staging β-amyloid pathology with amyloid positron emission tomography. *JAMA Neurol.* 2019;76:1319–1329.
14. Pletnikova O, Kageyama Y, Rudow G, et al. The spectrum of preclinical Alzheimer's disease pathology and its modulation by ApoE genotype. *Neurobiol Aging.* 2018;71:72–80.
15. Jack CR Jr, Wiste HJ, Weigand SD, et al. Defining imaging biomarker cut points for brain aging and Alzheimer's disease. *Alzheimers Dement.* 2017;13:205–216.
16. Lowe VJ, Bruinsma TJ, Min HK, et al. Elevated medial temporal lobe and pervasive brain tau-PET signal in normal participants. *Alzheimers Dement (Amst).* 2018;10:210–216.
17. Roberts RO, Geda YE, Knopman DS, et al. The Mayo Clinic Study of Aging: design and sampling, participation, baseline measures and sample characteristics. *Neuroepidemiology.* 2008;30:58–69.
18. Lowe VJ, Lundt ES, Senjem ML, et al. White matter reference region in PET studies of ^{11}C-Pittsburgh compound B uptake: effects of age and amyloid-β deposition. *J Nucl Med.* 2018;59:1583–1589.
19. Tzourio-Mazoyer N, Landeau B, Papathanassiou D, et al. Automated anatomical labeling of activations in SPM using a macroscopic anatomical parcellation of the MNI MRI single-subject brain. *Neuroimage.* 2002;15:273–289.
20. Meltzer CC, Leal JP, Mayberg HS, Wagner HN Jr, Frost JJ. Correction of PET data for partial volume effects in human cerebral cortex by MR imaging. *J Comput Assist Tomogr.* 1990;14:561–570.
21. Everitt BS, Landau S, Leese M, Stahl D. An introduction to classification and clustering. In: Shewhart WA, Wilks SS, eds. *Cluster Analysis.* John Wiley & Sons, Ltd; 2011:1–13.
22. Lloyd S. Least squares quantization in PCM. *IEEE Trans Inf Theory.* 1982;28:129–137.
23. Li X, Uemura K, Hashimoto T, et al. Neuronal activity and secreted amyloid β lead to altered amyloid β precursor protein and presenilin 1 interactions. *Neurobiol Dis.* 2013;50:127–134.
24. Ferreri F, Vecchio F, Vollero L, et al. Sensorimotor cortex excitability and connectivity in Alzheimer's disease: a TMS-EEG co-registration study. *Hum Brain Mapp.* 2016;37:2083–2096.
25. Buckner RL, Sepulcre J, Talukdar T, et al. Cortical hubs revealed by intrinsic functional connectivity: mapping, assessment of stability, and relation to Alzheimer's disease. *J Neurosci.* 2009;29:1860–1873.
26. Hafkemeijer A, van der Grond J, Rombouts SA. Imaging the default mode network in aging and dementia. *Biochim Biophys Acta.* 2012;1822:431–441.
27. Cirrito JR, Kang J-E, Lee J, et al. Endocytosis is required for synaptic activity-dependent release of amyloid-beta in vivo. *Neuron.* 2008;58:42–51.
28. Mohan A, Roberto AJ, Mohan A, et al. The significance of the default mode network (DMN) in neurological and neuropsychiatric disorders: a review. *Yale J Biol Med.* 2016;89:49–57.
29. Bero AW, Yan P, Roh JH, et al. Neuronal activity regulates the regional vulnerability to amyloid-β deposition. *Nat Neurosci.* 2011;14:750–756.
30. Fantoni E, Collij L, Lopes Alves I, Buckley C, Farrar G; AMYPAD consortium. The spatial-temporal ordering of amyloid pathology and opportunities for PET imaging. *J Nucl Med.* 2020;61:166–171.
31. Collij LE, Salvado G, Wottschel V, et al. Spatial-temporal patterns of beta-amyloid accumulation: a subtype and stage inference model analysis. *Neurology.* 2022;98:e1692–e1703.
32. Byun MS, Kim SE, Park J, et al. Heterogeneity of regional brain atrophy patterns associated with distinct progression rates in Alzheimer's disease. *PLoS One.* 2015;10:e0142756.
33. Rodrigue KM, Kennedy KM, Park DC. Beta-amyloid deposition and the aging brain. *Neuropsychol Rev.* 2009;19:436–450.
34. Palmqvist S, Mattsson N, Hansson O. Cerebrospinal fluid analysis detects cerebral amyloid-β accumulation earlier than positron emission tomography. *Brain.* 2016;139:1226–1236.
35. Mattsson N, Insel PS, Donohue M, et al. Independent information from cerebrospinal fluid amyloid-beta and florbetapir imaging in Alzheimer's disease. *Brain.* 2015;138:772–783.

Cerebral ^{18}F-FDG PET/CT Metabolism as Diagnostic Signature for Central Nervous System Toxicity After Immune Checkpoint Blockade Cancer Treatment

Yifei Ma*[1], Jiling Zeng*[2,3], Fadian Ding*[1], Yiwei Xu[4], Youlong Wang[5], Guanqing Zhong[6], Nianqi Liu[7], Yanqi Wang[8,9], Yiming Li[10], Shuqin Chen[11], Xiaolong Wei[11], Pengfei Zhu[12], Guangmin Jian[12], Yu Si Niu[13], Guangzhen Fu[14], Cantong Liu[4], Guiqiang Li[8], Xiaotong Zhou[15], Ao Zhang[3,6], and Shangeng Weng[1]

*[1]Department of Hepatobiliary and Pancreatic Surgery, Institute of Abdominal Surgery, Fujian Provincial Key Laboratory of Precision Medicine for Cancer, and Department of Hepatobiliary and Pancreatic Surgery, National Regional Medical Center Binhai Campus, First Affiliated Hospital of Fujian Medical University, Fuzhou, China; [2]Department of Nuclear Medicine, State Key Laboratory of Oncology in South China, Collaborative Innovation Center for Cancer Medicine, Guangzhou, China; [3]State Key Laboratory of Oncology in South China, Guangdong Key Laboratory of Nasopharyngeal Carcinoma Diagnosis and Therapy, Guangdong Provincial Clinical Research Center for Cancer, Guangzhou, China; [4]Department of Clinical Laboratory Medicine, Cancer Hospital of Shantou University Medical College, Shantou, China; [5]Department of General Surgery, Hainan Hospital of People's Liberation Army General Hospital, Sanya, China; [6]Department of Clinical Laboratory, State Key Laboratory of Oncology in South China, Collaborative Innovation Center for Cancer Medicine, Guangdong Key Laboratory of Nasopharyngeal Carcinoma Diagnosis and Therapy, Sun Yat-Sen University Cancer Center, Guangzhou, China; [7]Faculty of Psychology, Institute of Educational Science, Huazhong University of Science and Technology, Wuhan, China; [8]Department of Orthopedics and Spine Surgery, Second Affiliated Hospital of Shantou University Medical College, Shantou, China; [9]School of Public Health, Shantou University, Shantou, China; [10]Department of Neurosurgery, Beijing Tiantan Hospital Capital Medical University, Beijing, China; [11]Department of Pathology, Cancer Hospital of Shantou University Medical College, Shantou, China; [12]Department of Clinical Laboratory, First Affiliated Hospital of Zhengzhou University, Zhengzhou, China; [13]Acute Communicable Disease Epidemiology Division, Dallas County Health and Human Services, Dallas, Texas; [14]Key Clinical Laboratory of Henan Province, First Affiliated Hospital of Zhengzhou University, Zhengzhou, China; and [15]Department of Bone and Soft Tissue Oncology, Cancer Hospital of Shantou University Medical College, Shantou, China

Our aim was to investigate probable biomarkers specific to immune-related central nervous system toxicity (CNST) in cancer patients treated with immune checkpoint inhibitors (ICI) by analysis of ^{18}F-FDG PET/CT images. **Methods:** Cancer patients receiving ICI treatment were enrolled in a multicenter observational study that analyzed regional metabolic changes before and during CNST onset from January 2020 to February 2022. In 1:1 propensity score–matched pairs, the regional SUV_{mean} of each bilateral brain lobe of CNST patients (CNST+) was compared with that of patients who had central nervous system infections (CNSIs) and patients without CNST or CNSI (CNST−). In a validation cohort, patients were recruited from February 2022 to July 2023 and followed up for 24 wk after the start of ICI. Early changes in regional SUV_{mean} at 5–6 wk after therapy initiation were evaluated for ability to predict later CNST onset. **Results:** Of 6,395 ICI-treated patients, 2,387 underwent prognostic ^{18}F-FDG PET/CT and 125 of the scanned patients had CNST (median time from ICI treatment to onset, 9 wk; quartile range, 2–23 wk). Regional ^{18}F-FDG PET/CT SUV_{mean} changes were higher in CNST+ than in CNST− patients (117 patient pairs) but were lower than in CNSI patients (50 pairs). Differentiating analysis reached an area under the curve (AUC) of 0.83 (95% CI, 0.78–0.88) for CNST+ versus CNST− and of 0.80 (95% CI, 0.72–0.89) for CNST+ versus CNSI. Changes in SUV_{mean} were also higher before CNST onset than for CNST− (60 pairs; AUC, 0.74; 95% CI, 0.66–0.83). In a validation cohort of 2,878 patients, preonset changes in SUV_{mean} reached an AUC of 0.86 (95% CI, 0.79–0.94) in predicting later CNST incidence. **Conclusion:** Brain regional hypermetabolism could be detected during and before CNST clinical onset. CNST may be a distinct pathologic entity versus brain infections defined by ^{18}F-FDG PET/CT brain scans. Regional SUV differences may be translated into early diagnostic tools based on moderate differentiating accuracy in our study.

Key Words: ^{18}F-FDG PET/CT brain imaging; immunotherapy; immune-related CNS toxicity; regional metabolism; differential diagnosis

J Nucl Med 2024; 65:1129–1136
DOI: 10.2967/jnumed.123.267025

Immune checkpoint inhibitors (ICIs) have revolutionized the therapeutic landscape and significantly prolonged survival during the past decade, making ICI one of the primary therapies in nearly all types of cancer (*1*). ICIs inflict immune-related adverse events due to systemic T-cell activation, which can happen in any organ and have been reported to have an incidence of 10%–90% for any grade (*2–4*). However, immune-related adverse events in the central nervous system, or central nervous system toxicity (CNST), are less prevalent than in other organs, with an incidence of 1%–8% reported previously and fewer than 1% of cases being fatal (*5*,*6*). CNST has varieties of pathology types, including but not limited to immune-related meningitis, encephalitis, demyelinating encephalopathy, and central nervous system vasculitis (*7*). Although the exact pathoetiology is not thoroughly known, CNST

Received Nov. 16, 2023; revision accepted Mar. 25, 2024.
For correspondence or reprints, contact Shangeng Weng (shangeng@sina.com) or Ao Zhang (zhangao@sysucc.org.cn).
*Contributed equally to this work.
Published online May 2, 2024.

is currently suggested to be induced by local inflammation from deranged immune attack (*8*).

CNST presents mostly with unspecific symptoms, including headaches (>50%), confusion, partial seizures, limb pain, and the meningeal irritation sign (*9*). Given the higher incidence of central nervous system infection (CNSI) in cancer patients and significant overlapping symptoms, CNST is usually diagnosed when other causes are excluded, including infection, brain hemorrhage, stroke, metabolic encephalopathy, and brain metastasis (*10*). Methods applied in clinical diagnosis involve traditional imaging protocols, cerebral spinal fluid analysis, and neurologic work-ups (*10*). According to the Consensus Statement of Neurologic Adverse Events, most suspected cases are given a possible diagnosis for further trial therapies because of the difficulty of making a definite diagnosis (*8*). Because of the unpredictable incidence of this severe complication during ICI treatment, which many patients may receive for years, the development of biomarkers for early diagnosis is crucial (*11*). However, efficient methods and predictable biomarkers for differential diagnosis are presently lacking, hindering subsequent management options.

^{18}F-FDG PET/CT is a noninvasive imaging tool applied in diagnostic and prognostic protocols for cancer patients. Besides its utility in cancer management, the high sensitivity of ^{18}F-FDG PET/CT imaging has long been well established for identifying inflammatory processes involving higher local metabolism (*12*). Anecdotal case reports of ^{18}F-FDG PET/CT imaging analysis in evaluations of immune-related adverse events are being reported, but the characteristics of CNST have not been extensively reviewed (*13*). A pilot retrospective study of 58 melanoma patients identified metabolic biomarkers to delineate patients with or without immune-related adverse events in the lung, colon, and thyroid gland (*14*). Furthermore, ^{18}F-FDG PET/CT imaging is capable of sensitively detecting local autoimmune attacks in cerebral regions and has been established as an alternative tool to diagnose autoimmune or paraneoplastic encephalitis (*15*,*16*). More direct evidence was found in a recent ^{18}F-FDG PET/CT study of anti-LG1 protein autoimmune encephalitis, which is pathologically similar to CNST; biomarkers were identified that can signify disease course (*17*). Thus, we hypothesize that brain metabolism may be characteristic in patients with CNST (*18*,*19*).

Because of the low incidence of CNST, pivotal research on diagnostic biomarker identification for CNST has been statistically difficult to perform in underpowered sample sizes (*20*). Nevertheless, as ICIs are becoming more available in real-world settings, pilot multicenter analysis is encouraged to identify markers in the growing number of CNST cases. In the current study, we retrospectively reviewed cerebral metabolism in ICI-treated cancer patients, with the aim of obtaining preliminary evidence of diagnostic biomarkers for subclinical or syndromal CNST.

MATERIALS AND METHODS

Participants and Eligibility Criteria

We performed a multicenter, retrospective, case-control study to analyze early CNST-related metabolic changes in cerebral ^{18}F-FDG PET/CT images of ICI-treated cancer patients, who were divided into a discovery cohort and a validation cohort. In the discovery cohort, cancer patients receiving ICI treatment were enrolled from January 2020 to February 2022, and in the validation cohort, patients were enrolled from February 2022 to July 2023. Demographic and clinical variables were recorded from chart review. The research setting was the nuclear medicine departments of 4 academic hospitals in China (supplemental materials, available at http://jnm.snmjournals.org) (*21*–*28*). The retrospective protocol of the study was approved by the institutional review board of the Affiliated Cancer Hospital of Shantou University Medical College. All procedure was performed according to the Helsinki Declaration. The participants had given written informed consent to use of clinical information for medical research. Reporting adhered to the Strengthening the Reporting of Observational Studies in Epidemiology checklist for cohort studies.

Chart review divided ICI-treated cancer patients into 3 groups: patients with CNST (CNST+ group), with CNSI (CNSI group), and without CNST or CNSI (CNST− group, defined as no CNST or CNSI for ≥5 mo after ICI treatment, as most patients developed CNST before 20 wk as previously described) (*29*). The diagnostic protocols for CNST were according to the Consensus Statement of Neurologic Adverse Events (the supplemental materials provide detailed criteria) (*8*). All symptoms related to diagnosis and excluding CNST followed Common Terminology Criteria for Adverse Events (version 5.0). The date of CNST diagnosis was identified by review of outpatient and inpatient charts.

Research Goals and Statistics

The research goals are illustrated in Figure 1A. We did 2 independent comparison analyses (between the CNST+ and CNST− groups and between the CNST+ and CNSI groups) to investigate the specificity of cerebral regional SUV_{mean} in CNST+ patients. First, regional SUV_{mean} changes was calculated and compared between the CNST+ group (calculated as the SUV_{mean} difference between baseline and CNST onset) and the CNST− group (serving as a negative control comparison). Second, the SUV_{mean} of subtype CNST was compared with the SUV_{mean} of subtype CNSI (serving as a positive control comparison). For each step, a principal-component analysis and a neural network computation model were adopted to evaluate the differentiating ability of regional SUV_{mean} in ^{18}F-FDG PET/CT scans.

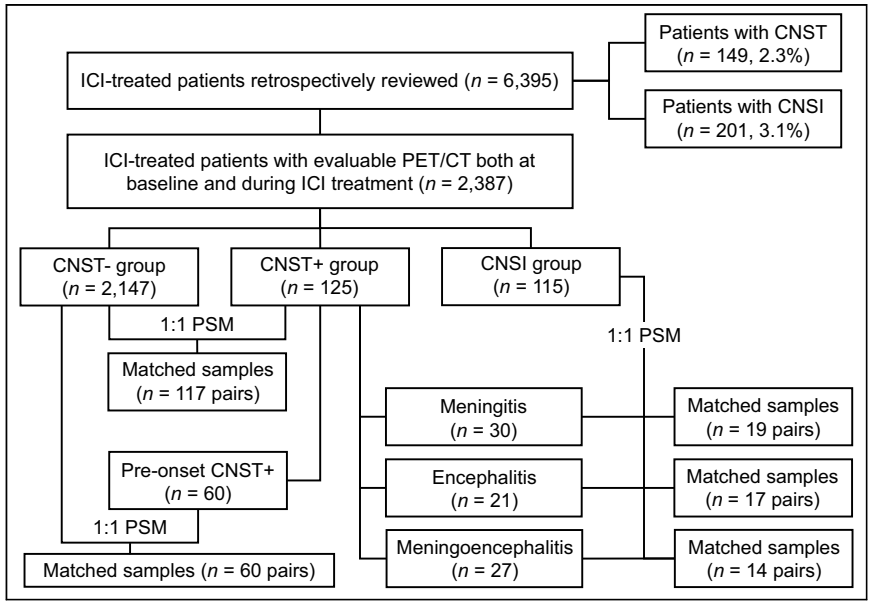

FIGURE 1. Research flowchart.

TABLE 1
Baseline Variables Before and After Propensity Score Matching for CNST+ and CNST− Subtypes

Variable	Before matching (n = 2,272)			After matching (n = 117 pairs)			
	CNST+ (n = 125)	CNST− (n = 2,147)	P*	CNST+	CNST−	SMD	P†
Age	59.71 (10.21)	57.82 (12.28)	0.05	59.25 (10.07)	59.84 (11.28)	0.06	0.76
Body mass index	22.90 (3.20)	23.23 (3.00)	0.24	22.80 (3.20)	23.18 (3.04)	0.12	0.23
Male sex	82 (65.6)	1169 (54.4)	0.02	75 (64.1)	77 (65.8)	0.04	0.88
Positive smoking history	38 (30.4)	510 (23.8)	0.09	38 (32.5)	33 (28.2)	0.09	0.54
Abnormal CRP	10 (8.0)	214 (10.0)	0.47	10 (8.5)	13 (11.1)	0.09	0.66
Concurrent target therapy	29 (23.2)	531 (24.7)	0.70	28 (23.9)	21 (17.9)	0.14	0.35
Concurrent chemotherapy	63 (50.4)	875 (40.8)	0.03	56 (47.9)	56 (47.9)	<0.01	1.00
Radiotherapy history	5 (4.0)	153 (7.1)	0.18	5 (4.3)	5 (4.3)	<0.01	1.00
Primary surgery	108 (86.4)	1609 (74.9)	<0.01	100 (85.5)	95 (81.2)	0.12	0.44
Stage of I and II	53 (42.4)	894 (41.6)	0.82	49 (41.9)	50 (42.8)	0.03	0.59
Comorbid neurologic disease	8 (6.4)	127 (5.9)	0.82	8 (6.8)	5 (4.3)	0.10	0.58
Comorbid CHF	7 (5.6)	123 (5.7)	0.95	4 (3.4)	4 (3.4)	<0.01	1.00
ECOG score	2 (1.06)	2.19 (1.09)	0.06	2.01 (1.03)	2.04 (1.20)	0.03	0.98
Positive mental problem	31 (24.8)	609 (28.4)	0.39	30 (25.6)	33 (28.2)	0.06	0.67
Treatment							
Atezolizumab	13 (7.0)	264 (12.3)	<0.01	12 (10.3)	15 (12.8)	0.02	0.83
Camrelizumab	7 (5.6)	274 (12.8)		7 (6.0)	7 (6.0)	<0.01	
Durvalumab	8 (6.4)	113 (5.3)		7 (6.0)	5 (4.3)	0.07	
Nivolumab	24 (19.2)	540 (25.2)		24 (20.5)	31 (26.5)	0.15	
Pembrolizumab	22 (17.6)	235 (10.9)		20 (17.1)	22 (18.8)	0.04	
Sintilimab	35 (28.0)	610 (28.4)		33 (28.2)	26 (22.2)	0.13	
Toripalimab	16 (12.8)	111 (5.2)		14 (12.0)	11 (9.4)	0.08	
Cancer type							
Nasopharyngeal carcinoma	8 (6.4)	175 (8.2)	0.06	8 (6.8)	6 (5.1)	0.07	0.96
Non–small cell lung cancer	41 (31.8)	555 (25.9)		39 (33.3)	42 (35.9)	0.05	
Colorectal carcinoma	19 (15.2)	187 (8.7)		15 (12.8)	16 (13.7)	0.02	
Gastric cancers	3 (2.4)	78 (3.6)		0 (0.0)	3 (2.6)	0.17	
Hepatocellular carcinoma	5 (4.0)	92 (4.3)		5 (4.3)	7 (6.0)	0.09	
Oral carcinoma	2 (1.6)	96 (4.5)		2 (1.7)	2 (1.7)	<0.01	
Biliary and pancreatic cancers	3 (2.4)	101 (4.7)		3 (2.6)	2 (1.7)	0.06	
Sarcoma	2 (1.6)	86 (4.0)		5 (4.3)	2 (1.7)	0.07	
Renal cell carcinoma	6 (4.8)	128 (6.0)		6 (5.1)	7 (6.0)	0.03	
Urogenital cancers	3 (2.4)	103 (4.8)		3 (2.6)	3 (2.6)	<0.01	
Mesothelioma	4 (3.2)	136 (6.3)		4 (3.4)	4 (3.4)	0.04	
Lymphoma	11 (8.8)	173 (8.1)		10 (8.5)	9 (7.7)	<0.01	
Other cancer types	8 (6.4)	147 (6.8)		8 (6.8)	6 (5.1)	0.2	
Unknown cancer types	10 (8.0)	90 (4.2)		9 (7.7)	8 (6.8)	0.03	
Whole-brain SUV_{mean}	4.40 (1.35)	5.75 (1.39)	<0.01	4.57 (1.21)	4.48 (1.26)	0.07	0.27

*Independent t test (continuous) or χ^2 test (categoric).

†Wilcoxon signed-rank test (continuous), McNemar nonparametric test (binary), and χ^2 test (multiple categories).

SMD = standardized mean difference to show imbalance levels of variables after matching (variable with SMD > 0.25 is considered poorly matched); CRP = C-reactive protein; CHF = congestive heart failure; ECOG = Eastern Cooperative Oncology Group.

Data are number followed by percentage in parentheses, except for whole-brain SUV_{mean}, for which SD is given in parentheses.

Third, for the CNST+ subgroup analysis, we queried whether there were early changes in brain metabolism before CNST symptoms started. To minimize the false-positive rate, subgroup analysis in the CNST+ group included only patients who underwent ^{18}F-FDG PET/CT at least 4 wk before CNST onset (i.e., preonset). Changes in SUV_{mean} from the baseline ^{18}F-FDG PET/CT images to the preonset images in CNST+ patients were calculated and compared with changes in SUV_{mean} in the CNST− group. If multiple images were present, only the earliest image was analyzed. A neural network computation model was adopted to evaluate the differentiating ability of regional SUV_{mean} in ^{18}F-FDG PET/CT scans. Last, in an independent validation cohort, preonset regional SUV_{mean} changes at 5–6 wk after ICI initiation were evaluated in a real-world setting to determine whether they may predict the later incidence of CNST, and a nomogram was built to quantify the disease-free (CNST-free) survival probability. Statistical comparison, propensity score matching, and modeling details of the neural network computation are shown in the supplemental materials (*22*,*23*,*27*).

RESULTS

Demographics

The study on the discovery cohort included 6,395 patients who had ever received ICI therapy and 2,387 patients who had evaluable ^{18}F-FDG PET/CT scans both at baseline and during ICI treatment. One hundred forty-nine patients had CNST (incidence, 2.3%), and 125 patients had evaluable ^{18}F-FDG PET/CT scans (Fig. 1A). Briefly, there were 125 CNST+ patients in the imaging study (69.3% male), with a mean age of 59.71 y (SD, 10.21 y), spanning nearly all known cancer types and ICI types. Baseline information was substantially different from that in the CNST− group, and 1:1 propensity score matching (PSM) was performed for balancing. Of the 125 CNST+ patients, 117 were matched with 117 CNST− patients. Baseline information before and after propensity score matching is shown in Table 1. Additional details on CNST characteristics are shown in Supplemental Table 1. Blood glucose levels in comparable groups are shown in Supplemental Figure 1, and representative images are shown in Supplemental Figure 2.

Regional Uptake Values of CNST+ Compared with CNST− Patients

We first investigated metabolic changes in patients experiencing CNST in each brain region. By the Wilcoxon signed-rank test, there was a significant increase ($P < 0.01$) in SUV_{mean} from baseline to CNST onset in all regions except the brain stem, occipital lobe, and cerebellum (Supplemental Fig. 3A, power of statistical tests reached >0.90 assuming a 2-sided α of 0.05). The median value of whole-brain SUV_{mean} in the CNST− group did not significantly differ from baseline, but this statistical test was underpowered ($P = 0.06$; power, 0.31). We then compared changes in both groups in PSM pairs. Compared with CNST− patients, there were significantly more increases in SUV_{mean} in each region of CNST+ patients except in the brain stem, occipital lobe, and cerebellum (Fig. 2A). Principal-component analysis indicated a relatively poor differentiating ability between the CNST+ and CNST− groups ($R = 0.14$, Supplemental Fig. 4A). However, the calculated differentiating ability from the neural network computation-based model showed an area under the curve (AUC) of 0.83 (95% CI, 0.78–0.88; Supplemental Fig. 4B). Principal-component analysis of CNST subtypes indicated an R of 0.64 (Fig. 2B).

Regional Uptake Values of CNST+ Subtypes Compared with CNSI Subtypes

Clinical symptoms and imaging studies of CNST may mimic CNSI, and thus we tested the specificity of CNST regional uptake values by comparing CNST+ with PSM samples of CNSI subtypes: immune-related versus infectious meningitis, meningoencephalitis, and encephalitis. In total, 201 patients who had a diagnosis of CNSI were reviewed, 115 of whom had available ^{18}F-FDG PET/CT images during CNSI onset. We adopted optimal matching for 3 subtypes between CNST+ and CNSI. Nearest-neighbor matching was adopted for other baseline variables. Finally, 50 pairs were matched from 3 subtypes of CNST+ and CNSI patients, including 19 pairs of meningitis, 17 pairs of meningoencephalitis, and 14 pairs of encephalitis, with baseline demographic details before and after PSM shown in Table 2. The regional SUV_{mean} of the immune-related meningitis subtype was significantly lower than that of infectious meningitis in all regions of interest (Fig. 3A). In the meningoencephalitis subtype, regional values were also lower in CNST+ patients in nearly all regions, except for the brain stem and cerebellum (Fig. 3B). In the encephalitis subtype, a significantly lower SUV_{mean} was seen in the whole brain and in the limbic area in CNST+ patients, although a higher SUV_{mean} was seen in the parietal region of CNST+ patients (Fig. 3C). Principal-component analysis indicated a moderate to high ability to differentiate the 3 subtypes between CNST+ and CNSI (Figs. 3D–3F). Differential diagnostic tests of the neural network computation-based radiomic model indicated relatively good accuracy (AUC, 0.80; 95% CI, 0.72–0.89; Supplemental Fig. 5A).

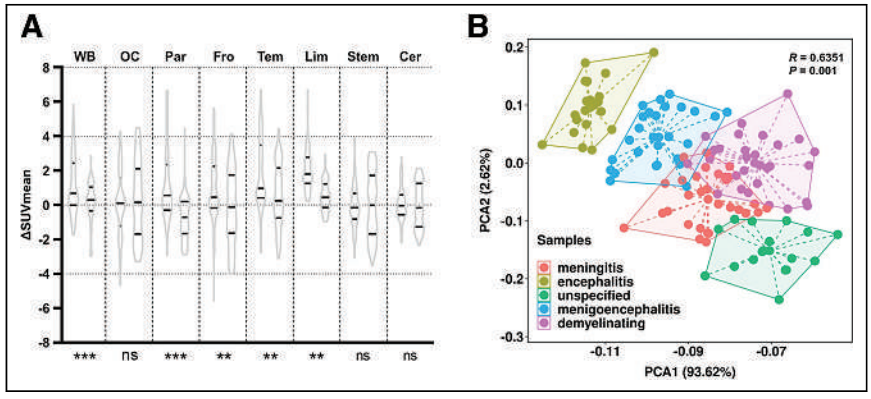

FIGURE 2. Comparison analysis of regional uptake value changes with negative control. (A) Negative control comparison: changes in SUV_{mean} from baseline to disease onset in CNST+ patients (left side of plot for each region) and changes in SUV_{mean} from baseline to >5 mo after treatment in negative control (right side of plot for each region), matched by propensity scores. Black lines indicate median and range (first to third quartiles). Nonparametric Wilcoxon signed-rank test was performed to compare distribution. Significant difference in changes in SUV_{mean} was seen between 2 groups in whole-brain area and in parietal, frontal, temporal, and limbic regions. (B) Principal-component analysis of ^{18}F-FDG PET/CT radiomic uptake values to differentiate CNST subtypes in CNST+ patients ($R = 0.64$). Cer = cerebellum; fro = frontal lobe; lim = limbic area; ns = nonsignificant; OC = occipital lobe; par = parietal lobe; PCA = principal-component analysis; stem = brain stem; tem = temporal lobe; WB = whole brain. *$P < 0.05$. **$P < 0.01$. ***$P < 0.001$.

TABLE 2
Baseline Variables Before and After Propensity Score Matching for CNST+ and CNSI Subtypes

Variable	Before matching (n = 193)			After matching (n = 50 pairs)			
	CNST+ (n = 78)	CNSI (n = 115)	P*	CNST+	CNSI	SMD	P†
Age	59.15 (10.85)	53.63 (14.25)	<0.01	56.66 (11.37)	59.12 (9.43)	0.23	0.50
Body mass index	23.23 (3.33)	22.97 (1.12)	0.43	22.76 (3.27)	22.92 (1.14)	0.05	0.81
Male sex	50 (64.1)	68 (59.1)	0.49	31 (62.0)	31 (62.0)	<0.01	1.00
Positive smoking history	22 (28.2)	28 (24.3)	0.55	14 (28.0)	13 (26.0)	0.04	1.00
Meningitis	30 (38.5)	38 (33.0)	0.70	19 (38.0)	19 (38.0)	<0.01	1.00
Encephalitis	21 (26.9)	36 (31.3)		17 (34.0)	17 (34.0)	<0.01	
Meningoencephalitis	27 (34.6)	41 (35.7)		14 (28.0)	14 (28.0)	<0.01	
Concurrent target therapy	22 (28.2)	32 (27.8)	0.95	11 (22.0)	10 (20.0)	0.04	1.00
Concurrent chemotherapy	39 (50.0)	57 (49.6)	0.95	27 (54.0)	30 (60.0)	0.12	0.68
Radiotherapy history	3 (3.8)	6 (5.2)	0.66	2 (4.0)	3 (6.0)	0.10	1.00
Primary surgery	66 (84.6)	91 (79.1)	0.34	44 (88.0)	43 (86.0)	0.06	1.00
Stage of I and II	28 (35.9)	47 (50.9)	0.91	18 (36.0)	20 (40.0)	0.11	0.80
Comorbid neurologic disease	4 (5.1)	9 (7.8)	0.46	3 (6.0)	3 (6.0)	<0.01	1.00
Comorbid CHF	3 (3.8)	7 (6.1)	0.49	1 (2.0)	1 (2.0)	<0.01	1.00
ECOG score	1.94 (1.15)	2.28 (1.20)	0.05	2.08 (1.10)	2.06 (1.19)	0.02	0.95
Positive mental problem	23 (29.5)	33 (28.7)	0.91	15 (30.0)	13 (26.0)	0.09	0.83
Treatment							
Atezolizumab	9 (11.5)	8 (7.0)	0.37	6 (12.0)	4 (8.0)	0.12	0.92
Camrelizumab	5 (6.4)	7 (6.1)		3 (6.0)	2 (4.0)	0.08	
Durvalumab	7 (9.0)	10 (8.7)		6 (12.0)	5 (10.0)	0.07	
Nivolumab	15 (19.2)	17 (14.8)		12 (24.0)	9 (18.0)	0.15	
Pembrolizumab	12 (15.4)	15 (13.0)		6 (12.0)	8 (16.0)	−0.11	
Sintilimab	21 (26.9)	34 (29.6)		11 (22.0)	14 (28.0)	−0.13	
Tislelizumab	0 (0.0)	8 (7.0)		0 (0.0)	0 (0.0)	NA	
Toripalimab	9 (11.5)	16 (13.9)		6 (12.0)	8 (16.0)	−0.12	
Cancer type							
Nasopharyngeal carcinoma	2 (2.6)	15 (13.0)	0.07	2 (4.0)	4 (8.0)	0.18	0.90
Non–small cell lung cancer	25 (32.1)	23 (20.0)		15 (30.0)	13 (26.0)	0.09	
Colorectal carcinoma	14 (17.9)	19 (16.5)		10 (20.0)	10 (20.0)	0.00	
Gastric cancers	1 (1.3)	2 (1.7)		0 (0.0)	1 (2.0)	0.18	
Esophageal cancers	0 (0.0)	11 (9.6)		0 (0.0)	0 (0.0)	NA	
Hepatocellular carcinoma	3 (3.8)	2 (1.7)		1 (2.0)	2 (4.0)	0.10	
Oral carcinoma	2 (2.6)	3 (2.6)		0 (0.0)	1 (2.0)	0.13	
Biliary and pancreatic cancers	0 (0.0)	1 (0.9)		0 (0.0)	0 (0.0)	NA	
Other cancer types	6 (7.7)	6 (5.2)		3 (6.0)	4 (8.0)	0.07	
Lymphoma	8 (10.3)	6 (5.2)		5 (10.0)	5 (10.0)	0.00	
Mesothelioma	1 (1.3)	2 (1.7)		1 (2.0)	1 (2.0)	0.00	
Renal cell carcinoma	3 (3.8)	1 (0.9)		2 (4.0)	1 (2.0)	0.10	
Urogenital cancers	1 (1.3)	3 (2.6)		1 (2.0)	2 (4.0)	0.18	
Sarcoma	2 (2.6)	4 (3.5)		2 (4.0)	0 (0.0)	0.25	
Unknown types	10 (12.8)	17 (14.8)		8 (16.0)	6 (12.0)	0.12	
Whole-brain SUV_{mean}	4.61 (1.25)	4.63 (1.49)	0.92	4.72 (1.16)	4.54 (1.50)	0.15	0.45

*Independent t test (continuous) or χ^2 test (categoric).

†Wilcoxon signed-rank test (continuous), McNemar nonparametric test (binary), and χ^2 test (multiple categories).

SMD = standardized mean difference to show imbalance levels of variables after matching (variable with SMD > 0.25 is considered poorly matched); CHF = congestive heart failure; ECOG = Eastern Cooperative Oncology Group.

Data are number followed by percentage in parentheses, except for whole-brain SUV_{mean}, for which SD is given in parentheses.

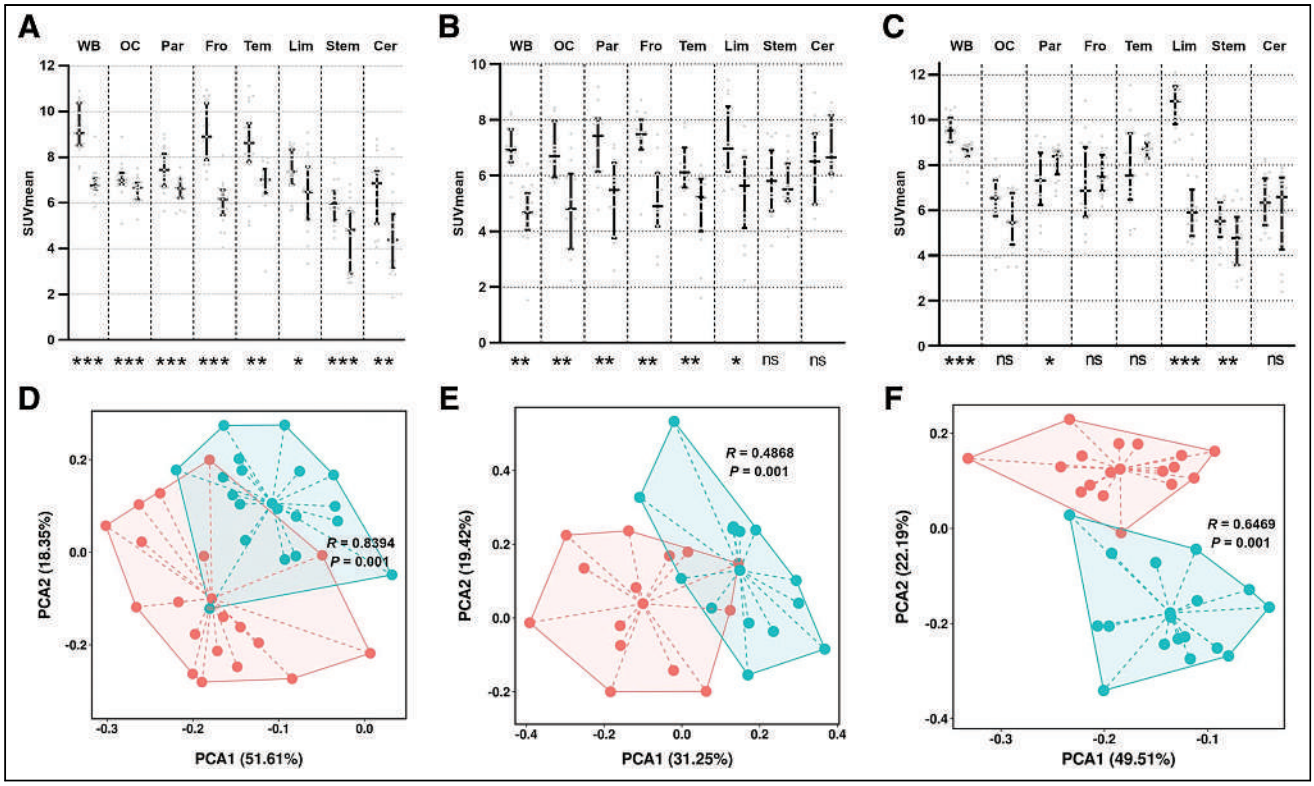

FIGURE 3. Comparison of regional uptake between CNSI and CNST subtypes. For each region, left side of plot is patients with infectious disease and right side is patients with immune-related disease. (A) SUV_{mean} distribution plot in infectious meningitis patients and immune-related meningitis patients in each brain lobe. Black lines indicate median and range (first to third quartiles). Wilcoxon signed rank was performed to compare distribution of SUV_{mean} between 2 subtypes. Significant difference in SUV_{mean} was seen in all regions of interest. (B) SUV_{mean} distribution plot in infectious meningoencephalitis patients and immune-related meningoencephalitis patients in each brain lobe. Black lines indicate median and range (first to third quartiles). Wilcoxon signed rank test was performed to compare distribution of SUV_{mean} between 2 subtypes. Significant difference in SUV_{mean} was seen in whole-brain area and in occipital, parietal, frontal, temporal, and limbic regions. (C) SUV_{mean} distribution plot in infectious encephalitis patients and immune-related encephalitis patients in each brain lobe. Black lines indicate median and range (first to third quartiles). Wilcoxon signed rank test was performed to compare distribution of SUV_{mean} between 2 subtypes. Significant difference in SUV_{mean} was seen in whole-brain area and in parietal, brain stein, and limbic regions. Intergroup difference was seen in meningitis diagnosis ($R = 0.84$) and in encephalitis ($R = 0.65$). (D–F) PCA of ^{18}F-FDG PET/CT radiomic uptake values to differentiate subtypes of meningitis (D), meningoencephalitis (E), and encephalitis (F). Intergroup difference in meningitis diagnosis ($R = 0.84$) and in encephalitis ($R = 0.65$). Cer = cerebellum; fro = frontal lobe; lim = limbic area; ns = nonsignificant; OC = occipital lobe; par = parietal lobe; PCA = principal-component analysis; stem = brain stem; tem = temporal lobe; WB = whole brain. $^{*}P < 0.05$. $^{**}P < 0.01$. $^{***}P < 0.001$.

Evaluating and Validating Preonset SUV_{mean} Changes as Marker to Predict Later CNST Incidence

We next investigated whether changes in brain regional metabolism were present before CNST onset. Sixty patients with available preonset ^{18}F-FDG PET/CT images were identified. The median time from ICI treatment to the earliest scanning was 12 wk (quartile range, 5.75–15.25 wk). The median time from the earliest scanning to CNST onset was 10 wk (quartile range, 8.75–14 wk).

Each regional SUV_{mean} was compared with the baseline value in CNST+ patients. There was a significant increase ($P < 0.01$) in SUV_{mean} as compared with baseline in all regions except the occipital lobe, brain stem, and cerebellum (Fig. 4A). The median SUV_{mean} increased from 4.83 to 4.88 in the whole brain, from 3.81 to 4.48 in the parietal lobe, from 4.30 to 4.44 in the frontal lobe, from 4.31 to 4.81 in the temporal lobe, from 3.84 to 4.52 in the limbic area, and from 4.92 to 5.04 in the cerebellum. These changes were validated in PSM samples (60 pairs) between CNST+ and CNST− patients. Changes in SUV_{mean} were significantly higher in CNST+ patients than in CNST− patients in the whole brain, frontal lobe, temporal lobe, and limbic area (Fig. 4B). The differentiating ability between CNST+ and CNST− patients was evaluated using ROC curve analysis, with an AUC of 0.74 (Supplemental Fig. 6B), and a nomogram was drawn to quantify the risk of future CNST (Supplemental Fig. 6A).

In the independent validation cohort, we aimed to evaluate whether early regional changes in SUV_{mean} may predict the later incidence of CNST. We recruited 2,881 patients to undergo prognostic scanning and followed them up for 24 wk. Three patients were excluded because CNST occurred before prognostic scanning, and thus early changes of SUV_{mean} in ^{18}F-FDG PET/CT were evaluable in 2,878 patients (1,540 male and 1,338 female; mean age, 64.2 ± 5.79 y) for predictive ability. In total, 38 patients (24-wk incidence rate, 1.3%) were diagnosed with CNST, at a mean of 14.79 ± 6.66 wk after ICI initiation. A nomogram to quantify disease-free survival was thus drawn, with an AUC of 0.86 (95% CI, 0.79–0.94; Figs. 4C and 4D).

DISCUSSION

This pilot case-control study of multicenter samples investigated regional metabolism specific to CNST and evaluated the accuracy of preonset regional metabolic changes in predicting the future onset of CNST. CNST was also identified in ^{18}F-FDG PET/CT images as a

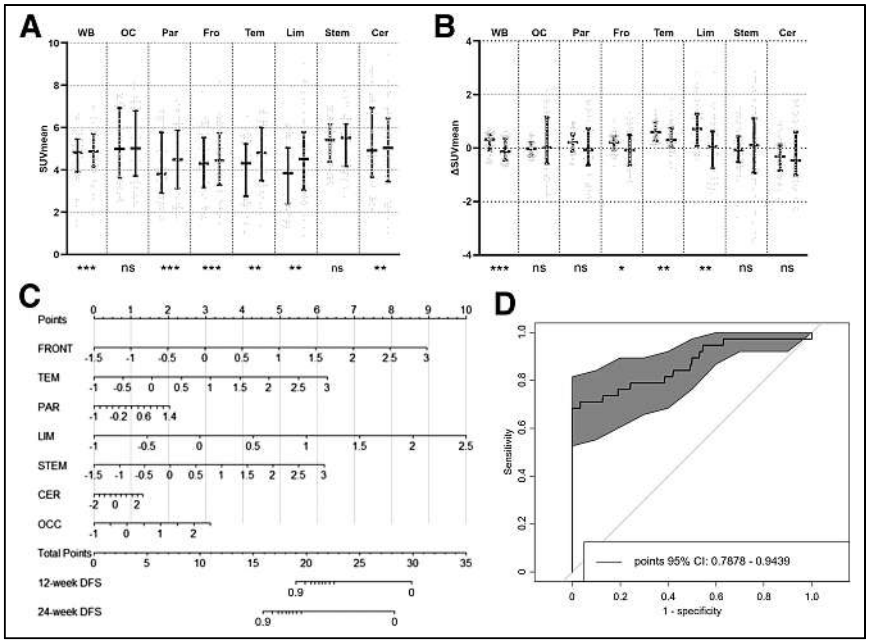

FIGURE 4. Comparison of regional uptake value changes before CNST onset. (A) Self-control comparison: SUV_{mean} distribution plot in CNST+ patients at baseline (before treatment, left side of plot for each region) and before CNST onset (right side of plot for each region) in each lobe. Black lines indicate median and range (first to third quartiles). SUV_{mean} in each region did not conform to normal distribution, and nonparametric Wilcoxon signed-rank test was performed to compare distribution at baseline and after CNST. Significant increases were seen in whole-brain area and in parietal, frontal, temporal, and limbic regions, and significant decreases were seen in cerebellum ($z = -3.50$, -0.49, -3.51, -3.59, -6.73, -5.54, -0.45, and -3.72, respectively, for rank differences in each comparison). (B) Negative control comparison: changes in SUV_{mean} from baseline to preonset scan in CNST+ patients (left side of plot for each region) and changes in SUV_{mean} from baseline to <5 mo after treatment in negative control (right side of plot for each region), matched by propensity scores. Black lines indicate median and range (first to third quartiles). Values did not conform to normal distribution, and nonparametric Wilcoxon signed-rank test was performed to compare distribution of changes in SUV_{mean} between 2 groups. Significant difference in changes in SUV_{mean} was seen in whole-brain area and in temporal, frontal, and limbic regions ($z = -3.69$, -0.75, -1.39, -2.41, -6.61, -4.42, -0.25, and -0.36, respectively, for rank differences in each comparison). (C) ^{18}F-FDG PET/CT radiomic monogram in validation cohort using early changes (5–6 wk after treatment initiation) of regional uptake values. Specifically, changes in SUV_{mean}, as compared with baseline SUV_{mean}, can be projected to point ruler. Total scores were added to obtain 24-wk disease-free survival probability. (D) Predicted future CNST risk vs. actual CNST risk in validation cohort, plotted as receiver-operating-characteristic curves. Cer = cerebellum; DFS = disease-free survival; fro and front = frontal lobe; lim = limbic area; ns = nonsignificant; OC and OCC = occipital lobe; par = parietal lobe; stem = brain stem; tem = temporal lobe; WB = whole brain. *$P < 0.05$. **$P < 0.01$. ***$P < 0.001$.

pathologic entity with specific regional hypermetabolism as compared with brain infection or CNST− patients. Prior case reports showed that the limbic area may be a prominent area of immune attack, and our results showed that hypermetabolism was seen in the whole brain and in the occipital, frontal, and temporal lobes. SUV_{mean} differed between CNST+ and CNSI in several regions—a positive control in terms of inflammation hypermetabolism (*29*). To our knowledge, our study was the first to analyze metabolism changes in brain immune-related adverse events after ICI treatment and the first to demonstrate that brain hypermetabolism, as a biomarker, may be present well before CNST symptoms exist. These regional metabolism differences were subsequently analyzed by radiomic methods, which showed moderate differentiating abilities. Early metabolism changes can be translated into a suggestive diagnostic tool. Considering the wide application of ^{18}F-FDG PET/CT in prognostic indexing of ICI-based treatment regimens, our pilot study may give initial evidence about quantitative biomarkers to assist CNST diagnosis. Given the extremely low incidence of CNST in ICI-treated cancer patients, with clinical characteristics similar to those of brain infection, use as a noninvasive, quantitative tool to suggest levels of neuroinflammation during active ICI treatment may be a possibility.

Interestingly, early changes in cerebral metabolism were detected 10 wk (quartile range 8.75–14 wk) before CNST onset in a subgroup of patients ($n = 60$). Although the study recruited a relatively large sample size in terms of CNST incidence, subgroup statistical tests of differences in early changes as compared with CNST− patients may be underpowered to yield conclusive evidence and must be interpreted cautiously. However, the results may support an accumulative immune attack that may happen early before onset, as pointed out by radiologic evidence in other organs (*14*). Preclinical models also support autoimmunity before symptom onset (*30*). In our study, the earliest onset time for CNST+ patients with preonset ^{18}F-FDG PET/CT scans happened in the 12 wk after ICI treatment, suggesting a rather late onset. It should be noted that most cases of previously reported CNST had an early-onset symptom, usually beginning at the first month of ICI treatment. Thus, our preonset ^{18}F-FDG PET/CT scans may not be useful as a monitoring tool but rather suggest that immune attacks may occur even before clinical signs.

The ICIs used in our cohorts are all directed toward the programmed cell death protein 1 and programmed death ligand 1 pathways. However, currently, most immune-related reactions occur when ipilimumab, alone or in combination, is directed toward cytotoxic T-lymphocyte–associated protein 4. As such, what we report here may represent only one aspect, or a partial population, of CNST, and future research is encouraged to investigate immune-related adverse events inflicted by other types of immunotherapy (*7–9*). Also, ICIs may unmask, rather than induce, a preexisting inflammatory condition. As some patients may have an unreported history of mild autoimmune or rheumatic conditions, they may have an increased risk of CNST; this topic may require further investigation (*31*).

This study had some limitations. First, it had a retrospective design with uncontrolled recall bias in chart review. Second, the ^{18}F-FDG PET/CT scanning time, which was based on oncologist preference and tumor prognostic functions, could not be precisely matched between comparable groups. We chose ^{18}F-FDG PET/CT scanning after 5 mo of ICI therapy in CNST− patients to match the time period in CNST+ patients. Third, there are many confounders that can trigger regional metabolism changes. The SUV in our study was based on activity, weight, and injected dose, without further use of single-subject statistical parametric mapping analysis to normalize intensity. Lack of standardization in intensity normalization, with the correspondingly unknown effect on quantification output, may make the use of SUV in brain ^{18}F-FDG PET/CT quantification less accurate. The population was quite heterogeneous, as it

comprised patients with very different neoplasms in which ICI is often used in various combinations with chemotherapy—a potential cause of uncontrolled confounders during comparison (*10*). Also, age and sex were dictating factors in cerebral metabolism (*32*). Baseline factors were compared statistically, and several factors were significantly different as shown in Table 1. However, the PSM method, which included multiple baseline confounders in this study, partially salvaged the selection bias. Last, although the sample size was relatively large in the context of the extreme low incidence of CNST, statistical power remained low in matched comparisons, especially in the comparison statistics of matched subtypes of CNST versus CNSI. Future metaanalyses or large-sample research is encouraged to augment the statistical power.

CONCLUSION

Cerebral metabolism seemed increased in CNST+ patients on active ICI therapy as compared with CNST− patients but seemed lower than in CNSI patients in certain brain regions. Early regional changes that were present before CNST seemed to suggest a preonset immune attack, and such early regional changes may be translated into a diagnostic tool based on moderate accuracy in the observational study.

DISCLOSURE

This work was supported by a Fujian Province science and technology innovation joint fund project (2020Y9130 to Shangeng Weng) and by National Natural Science Foundation of China youth science fund projects (82102687 to Yifei Ma and 82201922 to Ao Zhang). The funders had no role in the design or conduct of the study. No other potential conflict of interest relevant to this article was reported.

ACKNOWLEDGMENT

We acknowledge the volunteers who participated in the study.

KEY POINTS

QUESTION: What are the probable biomarkers specific to immune-related CNST in cancer patients treated with ICI by imaging analysis of ^{18}F-FDG PET/CT?

PERTINENT FINDINGS: In a validation cohort of 2,878 patients, preonset changes in SUV_{mean} reached an AUC of 0.86 (95% CI, 0.79–0.94) in predicting the later incidence of CNST.

IMPLICATIONS FOR PATIENT CARE: Regional SUV differences may be translated into early diagnostic tools based on moderate differentiating accuracy in our study.

REFERENCES

1. Kruger S, Ilmer M, Kobold S, et al. Advances in cancer immunotherapy 2019: latest trends. *J Exp Clin Cancer Res.* 2019;38:268.
2. Horvat T, Adel N, Dang T, et al. Immune-related adverse events, need for systemic immunosuppression, and effects on survival and time to treatment failure in patients with melanoma treated with ipilimumab at Memorial Sloan Kettering Cancer Center. *J Clin Oncol.* 2015;33:3193–3198.
3. Postow MA, Sidlow R, Hellmann M. Immune-related adverse events associated with immune checkpoint blockade. *N Engl J Med.* 2018;378:158–168.
4. Jing Y, Liu J, Ye Y, et al. Multi-omics prediction of immune-related adverse events during checkpoint immunotherapy. *Nat Commun.* 2020;11:4946.
5. Wick W, Hertenstein A, Platten M. Neurological sequelae of cancer immunotherapies and targeted therapies. *Lancet Oncol.* 2016;17:e529–e541.
6. Perrinjaquet C, Desbaillets N, Hottinger AF. Neurotoxicity associated with cancer immunotherapy: immune checkpoint inhibitors and chimeric antigen receptor T-cell therapy. *Curr Opin Neurol.* 2019;32:500–510.
7. Johnson DB, Manouchehri A, Haugh AM, et al. Neurologic toxicity associated with immune checkpoint inhibitors: a pharmacovigilance study. *J Immunother Cancer.* 2019;7:134.
8. Guidon AC, Burton LB, Chwalisz BK, et al. Consensus disease definitions for neurologic immune-related adverse events of immune checkpoint inhibitors. *J Immunother Cancer.* 2021;9:e002890.
9. Winter SF, Vaios EJ, Dietrich J. Central nervous system injury from novel cancer immunotherapies. *Curr Opin Neurol.* 2020;33:723–735.
10. Vogrig A, Muñiz-Castrillo S, Farina A, Honnorat J, Joubert B. How to diagnose and manage neurological toxicities of immune checkpoint inhibitors: an update. *J Neurol.* 2022;269:1701–1714.
11. Spain L, Diem S, Larkin J. Management of toxicities of immune checkpoint inhibitors. *Cancer Treat Rev.* 2016;44:51–60.
12. Larson SM. Cancer or inflammation? A holy grail for nuclear medicine. *J Nucl Med.* 1994;35:1653–1655.
13. Dimitrakopoulou-Strauss A. Monitoring of patients with metastatic melanoma treated with immune checkpoint inhibitors using PET-CT. *Cancer Immunol Immunother.* 2019;68:813–822.
14. Hribernik N, Huff DT, Studen A, et al. Quantitative imaging biomarkers of immune-related adverse events in immune-checkpoint blockade-treated metastatic melanoma patients: a pilot study. *Eur J Nucl Med Mol Imaging.* 2022;49:1857–1869.
15. Bordonne M, Chawki MB, Doyen M, et al. Brain ^{18}F-FDG PET for the diagnosis of autoimmune encephalitis: a systematic review and a meta-analysis. *Eur J Nucl Med Mol Imaging.* 2021;48:3847–3858.
16. Solnes LB, Jones KM, Rowe SP, et al. Diagnostic value of ^{18}F-FDG PET/CT versus MRI in the setting of antibody-specific autoimmune encephalitis. *J Nucl Med.* 2017;58:1307–1313.
17. Rissanen E, Carter K, Cicero S, et al. Cortical and subcortical dysmetabolism are dynamic markers of clinical disability and course in anti-LGI1 encephalitis. *Neurol Neuroimmunol Neuroinflamm.* 2022;9:e1136.
18. Yshii LM, Hohlfeld R, Liblau RS. Inflammatory CNS disease caused by immune checkpoint inhibitors: status and perspectives. *Nat Rev Neurol.* 2017;13:755–763.
19. Joly F, Castel H, Tron L, Lange M, Vardy J. Potential effect of immunotherapy agents on cognitive function in cancer patients. *J Natl Cancer Inst.* 2020;112:123–127.
20. Chow SC, Shao J, Wang H, Lokhnygina Y. *Sample Size Calculations in Clinical Research.* Chapman and Hall/CRC; 2017:373–383.
21. Tzourio-Mazoyer N, Landeau B, Papathanassiou D, et al. Automated anatomical labeling of activations in SPM using a macroscopic anatomical parcellation of the MNI MRI single-subject brain. *Neuroimage.* 2002;15:273–289.
22. Clarke KR. Non-parametric multivariate analyses of changes in community structure. *Austral Ecol.* 1993;18:117–143.
23. Warton DI, Wright ST, Wang Y. Distance-based multivariate analyses confound location and dispersion effects. *Methods Ecol Evol.* 2012;3:89–101.
24. Yun M, Nie B, Wen W, et al. Assessment of cerebral glucose metabolism in patients with heart failure by ^{18}F-FDG PET/CT imaging. *J Nucl Cardiol.* 2022;29:476–488.
25. Lyra V, Parissis J, Kallergi M, et al. ^{18}F-FDG PET/CT brain glucose metabolism as a marker of different types of depression comorbidity in chronic heart failure patients with impaired systolic function. *Eur J Heart Fail.* 2020;22:2138–2146.
26. Johnson NA, Jahng GH, Weiner MW, et al. Pattern of cerebral hypoperfusion in Alzheimer disease and mild cognitive impairment measured with arterial spin-labeling MR imaging: initial experience. *Radiology.* 2005;234:851–859.
27. Fleiss JL, Levin B, Paik MO. *Statistical Methods for Rates and Proportions.* 3rd ed. John Wiley & Sons, Inc. 2003:373–406.
28. Austin PC. Balance diagnostics for comparing the distribution of baseline covariates between treatment groups in propensity-score matched samples. *Stat Med.* 2009;28:3083–3107.
29. Müller-Jensen L, Zierold S, Versluis JM, et al. Characteristics of immune checkpoint inhibitor-induced encephalitis and comparison with HSV-1 and anti-LGI1 encephalitis: a retrospective multicentre cohort study. *Eur J Cancer.* 2022;175:224–235.
30. Iwama S, De Remigis A, Callahan MK, Slovin SF, Wolchok JD, Caturegli P. Pituitary expression of CTLA-4 mediates hypophysitis secondary to administration of CTLA-4 blocking antibody. *Sci Transl Med.* 2014;6:230ra45.
31. Lusa A, Alvarez C, Saxena Beem S, Schwartz TA, Ishizawar R. Immune-related adverse events in patients with pre-existing autoimmune rheumatologic disease on immune checkpoint inhibitor therapy. *BMC Rheumatol.* 2022;6:64.
32. Jones JS, Goldstein SJ, Wang J, et al. Evaluation of brain structure and metabolism in currently depressed adults with a history of childhood trauma. *Transl Psychiatry.* 2022;12:392.

Granzyme B PET Imaging for Assessment of Disease Activity in Inflammatory Bowel Disease

Pedram Heidari, Arvin Haj-Mirzaian, Suma Prabhu, Bahar Ataeinia, Shadi A. Esfahani, and Umar Mahmood

Center for Precision Imaging and Division of Nuclear Medicine and Molecular Imaging, Department of Radiology, Massachusetts General Hospital, Harvard Medical School, Boston, Massachusetts

Developing a noninvasive imaging method to detect immune system activation with a high temporal resolution is key to improving inflammatory bowel disease (IBD) management. In this study, granzyme B (GZMB), typically released from cytotoxic T and natural killer cells, was targeted using PET with ^{68}Ga-NOTA-GZP (where GZP is β-Ala–Gly–Gly–Ile–Glu–Phe–Asp–CHO) to detect early intestinal inflammation in murine models of colitis. **Methods:** Bioinformatic analysis was used to assess the potential of GZMB as a biomarker for detecting IBD and predicting response to treatment. Human active and quiescent Crohn disease and ulcerative colitis tissues were stained for GZMB. We used IL-10$^{-/-}$ mice treated with dextran sulfate sodium (DSS) as an IBD model, wild-type C57BL/6J mice as a control, and anti–tumor necrosis factor as therapy. We used a murine GZMB-binding peptide conjugated to a NOTA chelator (NOTA-GZP) labeled with ^{68}Ga as the PET tracer. PET imaging was conducted at 1, 3, and 4 wk after colitis induction to evaluate temporal changes. **Results:** Bioinformatic analysis showed that GZMB gene expression is significantly upregulated in human ulcerative colitis and Crohn disease compared with the noninflamed bowel by 2.98-fold and 1.92-fold, respectively; its expression is lower by 2.16-fold in treatment responders than in nonresponders. Immunofluorescence staining of human tissues demonstrated a significantly higher GZMB in patients with active than with quiescent IBD ($P = 0.032$).^{68}Ga-NOTA-GZP PET imaging showed significantly increased bowel uptake in IL-10$^{-/-}$ mice with DSS-induced colitis compared with vehicle-treated IL-10$^{-/-}$ mice (SUV_{mean}, 0.75 vs. 0.24; $P < 0.001$) and both vehicle- and DSS-treated wild-type mice (SUV_{mean}, 0.26 and 0.37; $P < 0.001$). In the IL-10$^{-/-}$ DSS-induced colitis model, the bowel PET probe uptake decreased in response to treatment with tumor necrosis factor–α (SUV_{mean}, 0.32; $P < 0.001$). There was a 4-fold increase in colonic uptake of ^{68}Ga-NOTA-GZP in the colitis model compared with the control 1 wk after colitis induction. The uptake gradually decreased to approximately 2-fold by 4 wk after IBD induction; however, the inflamed bowel uptake remained significantly higher than control at all time points (week 4 SUV_{mean}, 0.23 vs. 0.08; $P = 0.001$). **Conclusion:** GZMB is a promising biomarker to detect active IBD and predict response to treatment. This study provides compelling evidence to translate GZMB PET for imaging IBD activity in clinical settings.

Key Words: inflammatory bowel disease; PET imaging; granzyme B; ^{68}Ga-NOTA-GZP; colitis

J Nucl Med 2024; 65:1137–1143
DOI: 10.2967/jnumed.123.267344

Inflammatory bowel disease (IBD) is a chronic gastrointestinal inflammatory disorder and includes 2 major groups: Crohn disease (CD) and ulcerative colitis (UC) (*1*). Although there have been notable advancements in the clinical management of IBD, substantial challenges remain in enhancing diagnostic precision, overcoming issues with treatment intolerance, and addressing the recurrent cycle of remission and relapse (*2,3*). In addition, long-standing IBD is associated with an increased risk of cancer, which necessitates constant monitoring of disease activity (*4–6*). Although endoscopy is widely used for the diagnosis and management of IBD, it has limitations, such as invasiveness and lack of ability to capture the abnormalities in deep bowel wall layers (*7,8*). Leveraging multimodal imaging such as PET/CT and PET/MRI enhances IBD diagnosis accuracy beyond the reach of standard colonoscopy, allowing for detailed visualization in regions inaccessible to endoscopic evaluation and offering a comprehensive view of inflammatory activity and structural changes (*9*). Hence, noninvasive imaging techniques are urgently needed to provide real-time information on specific pathologic processes across the entire bowel and to offer a high temporal resolution for accurate detection, staging, and quantitative evaluation of response to treatment (*10*). Recent research has shown that molecular imaging with SPECT and PET may be more accurate for identifying gastrointestinal inflammation in both clinical and preclinical settings, with the added advantage of real-time information (*11–15*). Since IBD is an immune-mediated disease, imaging biomarkers that provide information on specific immune mediators could be valuable in early diagnosis and evaluation of treatment response (*16*).

The pathophysiology of IBD is believed to involve dysregulation of innate and adaptive immune systems. Therefore, tracking the activity of immune cells, particularly natural killer cells and CD8$^+$ cytotoxic T cells, which initiate the inflammatory cascade in the bowel, could indicate inflammation status in IBD (*17,18*). Granzyme B (GZMB) is a serine protease released by immune cells, mainly activated natural killer cells and CD8$^+$ cytotoxic T cells, that triggers apoptosis in infected, neoplastic, or malfunctioning cells (*19*). It has been suggested that GZMB is an early initiator of inflammation in IBD (*19*). Hence, PET imaging of GZMB could capture the inflammatory status of the mucosal immune layer of the gastrointestinal tract in the early stages of IBD. Our group has developed and used a GZMB-targeted peptide-based PET imaging probe, ^{68}Ga-NOTA-GZP, where GZP is β-Ala–Gly–Gly–Ile–Glu–Phe–Asp–CHO. We have shown that GZMB PET can noninvasively evaluate the effectiveness of immune checkpoint inhibitors and predict the immunotherapy response in preclinical cancer models and immune-related adverse events (*20–23*). These results built the foundation of our next-step

Received Dec. 26, 2023; revision accepted Apr. 18, 2024.
For correspondence or reprints, contact Pedram Heidari (pheidari@mgh.harvard.edu).
Published online May 16, 2024.

efforts to explore the application of GZMB PET in the setting of IBD.

This study aimed to establish GZMB PET as a noninvasive and accurate imaging technique for detecting bowel inflammation and monitoring response to treatment in IBD. We first evaluated GZMB gene expression in human CD, UC, and noninflamed bowel using bioinformatics data and assessed the GZMB gene expression and excretion level in human bowel tissues with active and quiescent inflammation. Next, we studied the ability of GZMB PET to quantify bowel inflammation compared with control conditions, the disease activity over time, and in response to antiinflammatory treatment in an established mouse model of colitis.

MATERIALS AND METHODS

Dataset Acquisition for Bioinformatics and Differential Gene Expression Analysis

The gene expression datasets were obtained from the Gene Expression Omnibus public platform under accession numbers GSE10191, GSE25220, GSE36807, GSE117993, GSE95437, GSE93624, GSE11831, GSE57945, GSE75214, GSE16879, and GSE100833. The study design and sample acquisition are detailed in Supplemental Table 1 (supplemental materials are available at http://jnm.snmjournals.org). A systematic search was performed on the Gene Expression Omnibus (*24*) using the following keywords: "inflammatory bowel disease," "ulcerative colitis," and "Crohn's disease," with "*Homo sapiens*" as the tissue donor species filter.

The datasets were classified into 3 subgroups based on study design and IBD conditions, including UC compared with non-IBD colon conditions (8 datasets), CD compared with non-IBD colon conditions (7 datasets), and treatment responder compared with nonresponder IBD patients (2 datasets) (Supplemental Table 1). The differential gene expression analysis was performed for each dataset, followed by gene intersection analysis to find the common genes in different datasets in each colon condition group. The common genes were then ranked on the basis of fold change among different groups.

We compared 2 sample groups using the "affy" and "limma" R packages after preprocessing and normalizing the microarray datasets to identify significant differential gene expression levels that varied depending on the experimental settings.

GZMB Quantification on Immunofluorescence Staining of Human Colon Tissues

Formalin-fixed paraffin-embedded tissue blocks from active and quiescent IBD patients and normal bowel tissue were obtained from OriGene. Immunofluorescence staining against GZMB was performed on cut samples using methods previously described (*23*); briefly, we incubated slides with rabbit antihuman GZMB (ab243879; Abcam) primary antibody at 1:100 dilution at 4°C overnight, followed by Alexa Fluor 647 (Life Technologies Corp.) conjugated goat antirabbit IgG (A32733; ThermoFisher) secondary antibody at 1:100 dilution and nuclear staining with 4′,6-diamidino-2-phenylindole at a 1 μg/mL concentration. Fluorescence images were acquired with a cell imaging multimode reader (Cytation 5; Agilent). Semiquantitative analysis was performed by measuring the cumulative total fluorescence signal in a gray-scale image related to GZMB expression divided by the cumulative total fluorescence signal in a gray-scale image related to 4′,6-diamidino-2-phenylindole (as a measure of the total number of cells) using Fiji software (version 2.9.0; National Institutes of Health).

Animals and Groups

Animal studies were conducted with the approval of the Institutional Animal Care and Use Committee, and all animal experiments were conducted following the "Animal Research: Reporting of In Vivo Experiments" guidelines. Six-week-old male wild-type C57BL/6J (n = 18) and IL-10$^{-/-}$ mice (with C57BL/6J background, n = 83) were used (Jackson Laboratories). After acclimatization, both IL-10$^{-/-}$ and C57BL/6J mice were divided into 2 major groups. The first group received only autoclaved water as a vehicle control (IL-10$^{-/-}$ vehicle, n = 13, and C57BL/6J vehicle, n = 7). In the second group, colitis was induced by supplementing 3% dextran sulfate sodium (DSS; Sigma) in the autoclaved drinking water for 7 d (IL-10$^{-/-}$ DSS, n = 22, and C57BL/6J DSS, n = 11), followed by restoring regular water on day 8 (*25*). IL-10$^{-/-}$ DSS-treated mice were divided into subgroups not treated (n = 9) or treated with anti–tumor necrosis factor (TNF) (n = 13, a single 100-μg dose of murine anti-TNF injection intraperitoneally [XT3.11, BE0058; Bio X Cell]) (*26*). Furthermore, we used an additional 48 IL-10$^{-/-}$ mice to assess temporal changes in ^{68}Ga-NOTA-GZP over 4 wk, dividing them into 2 groups: 24 mice treated with DSS and 24 treated with a vehicle. Supplemental Figure 1 provides a schematic representation of the study's timeline and the grouping methodology used. All animals were monitored 3 times a week for changes in behavior, weight loss, stool consistency, blood in the stool, and anal prolapse. At the end of the experiments, the animals were euthanized in a humane manner using CO_2 gas, according to the guidelines recommended by the American Veterinary Medical Association for the euthanasia of laboratory animals. The procedure was performed ensuring a gradual-fill method to minimize animal distress. In addition, since the UC mouse model is well established and responds effectively to anti-TNF treatment, we minimized the use of animals and addressed potential ethical concerns by not using IgG1 monoclonal antibody treatment as a control group to the anti-TNF group.

^{68}Ga-NOTA-GZP Probe Synthesis

^{68}Ga-NOTA-GZP was synthesized using ^{68}Ga eluted from a ^{68}Ge/^{68}Ga generator (Eckert & Ziegler) as previously described (*23*). Briefly, NOTA-GZP (50 μg) was mixed with ^{68}Ga (370 MBq) in 2 M 4-(2-hydroxyethyl)piperazine-1-ethanesulfonic acid buffer, and the pH was adjusted to 3.5–4.0. The reaction mixture was incubated for 10 min at room temperature. The product was then purified using a reverse-phase C18 Sep-Pak (Waters) solid-phase extraction cartridge and diluted with saline before administration to mice. The radiolabeling yield was measured by instant thin-layer chromatography as previously described (*27,28*). We exclusively used the ^{68}Ga-NOTA-GZP probe as our primary probe because of its well-established efficacy in our prior research, eliminating the need for a control peptide.

Animal ^{68}Ga-NOTA-GZP PET/CT Imaging and Biodistribution Analysis

Mice from all groups were imaged with a rodent PET/CT scanner (TriFoil Imaging) 7 d after treatment with DSS or vehicle. Approximately 7.4 MBq of ^{68}Ga-NOTA-GZP were intravenously injected, and PET/CT was performed 1 h after injection. Before imaging, the mice were anesthetized with 2% isoflurane, and 100 μL of diatrizoate meglumine and diatrizoate sodium solution (Gastrografin; Bracco) were administered intrarectally as a large-intestine contrast agent. PET images were acquired for 20 min at a single bed position, followed by CT acquisition for approximately 10 min. We used a heating system to keep the mice warm during the scans. Throughout the imaging process, we monitored vital signs, including core temperature, heart rate, and respiratory rate, using equipment from SA Instruments, Inc. The acquired images were reconstructed using a 3-dimensional maximum-likelihood expectation maximization algorithm with 4 iterations and 20 subsets. Under CT guidance, a 3-dimensional region of interest was drawn over the colon. The bowel's SUV_{mean} was calculated within the 3-dimensional region of interest using VivoQuant software (Invicro).

Immediately after the PET/CT acquisition, biodistribution analysis of the ^{68}Ga-NOTA-GZP images was conducted for a subset of animals (7–13 animals/group). The animals were euthanized, blood and organs were harvested and weighed, and the retained radioactivity was measured using a γ-counter (Wizard; Perkin Elmer). Raw mean counts of the tissue were corrected for background activity, decay, and tissue weight and reported as percentage injected dose per gram. Additionally, the colon and cecum of each animal were fixed or processed for further cytokine analyses.

Cytokine Analysis of Colon Samples

The extracted colon tissues from the colitis-induced mice, on day 7 after induction, were rinsed using ice-cold phosphate-buffered saline followed by cold complete RPMI 1640 medium. Tissues were then cut longitudinally, and a 5 mm^2 sample of each tissue was placed in a small petri dish and incubated at 37°C for 24 h with 1.5 mL of complete RPMI medium supplemented with 5% CO_2. The supernatant was aspirated, centrifuged at 4,100*g* for 10 min, and stored at −70°C until used for biomarker analyses. The cytokine analysis was performed using a ProcartaPlex mouse immune monitoring panel 48-plex kit (catalog no. EPX480-20834-901; Thermo Fisher Scientific). A panel of 48 inflammatory markers was analyzed using the Luminex 200 system (Thermo Fisher Scientific).

Statistical Analysis

Statistical analyses were performed using Prism software (GraphPad). Differences in variables were assessed by 2-tailed Student *t* tests, 2-way ANOVA, or 3-way ANOVA, depending on the comparison. After ANOVA, a post hoc Holm–Sidak multiple-comparisons test was applied. A *P* value of less than 0.05 was considered statistically significant. Values are reported as mean ± SD. We used the false-discovery rate or Benjamini–Hochberg method as a statistical correction method for differential gene expression analysis, to accurately identify significant differences between sample groups. The criteria for identifying differential gene expression were set as an adjusted *P* value of less than 0.05 and an absolute $\log_2$ fold change of more than 0.6, which provided a statistically significant and biologically meaningful threshold for identifying differentially expressed genes.

RESULTS

GZMB Is Biomarker of IBD

When comparing whole transcriptome profiling between UC and non-IBD bowel conditions, we observed significant alterations in 4328, 2985, 3993, 245, 1460, 2131, 2526, and 1896 genes in the bowel in GSE10191, GSE11831, GSE16879, GSE25220, GSE36807, GSE75214, GSE95437, and GSE117993 datasets, respectively (Supplemental Fig. 2; Supplemental Tables 2 and 3). Among these genes, we found 48 genes consistently altered in UC compared with non-IBD conditions, including 44 upregulated and 4 downregulated genes (Fig. 1A; Supplemental Table 4). The GZMB gene showed a significant upregulation of 2.98-fold in UC compared with non-IBD conditions (Fig. 1B).

In the analyses of GSE11831, GSE16879, GSE57945, GSE75214, GSE93624, GSE95437, and GSE117993 datasets, we observed significant alterations in 817, 1975, 1406, 1137, 1181, 2316, and 673 genes, respectively, in the colon for patients with CD compared with non-IBD conditions (Supplemental Fig. 2; Supplemental Tables 2 and 5). We identified 97 consistently altered genes across all databases, including 81 upregulated and 16 downregulated genes (Fig. 1C). The GZMB gene showed a significant upregulation of 1.92-fold in CD compared with non-IBD conditions (Fig. 1D). Heatmap analysis of all significantly altered genes in UC and CD samples compared with non-IBD conditions is shown in Figure 1E. These findings suggest that GZMB could be a potential diagnostic marker for IBD.

We investigated the expression of GZMB in the bowels of patients with IBD in response to treatment using the GSE16879 and GSE100833 databases and in active versus inactive IBD using the GSE75214 database. A reanalysis of GSE16879 demonstrated that GZMB was significantly upregulated in IBD at baseline in both treatment responders and nonresponders compared with

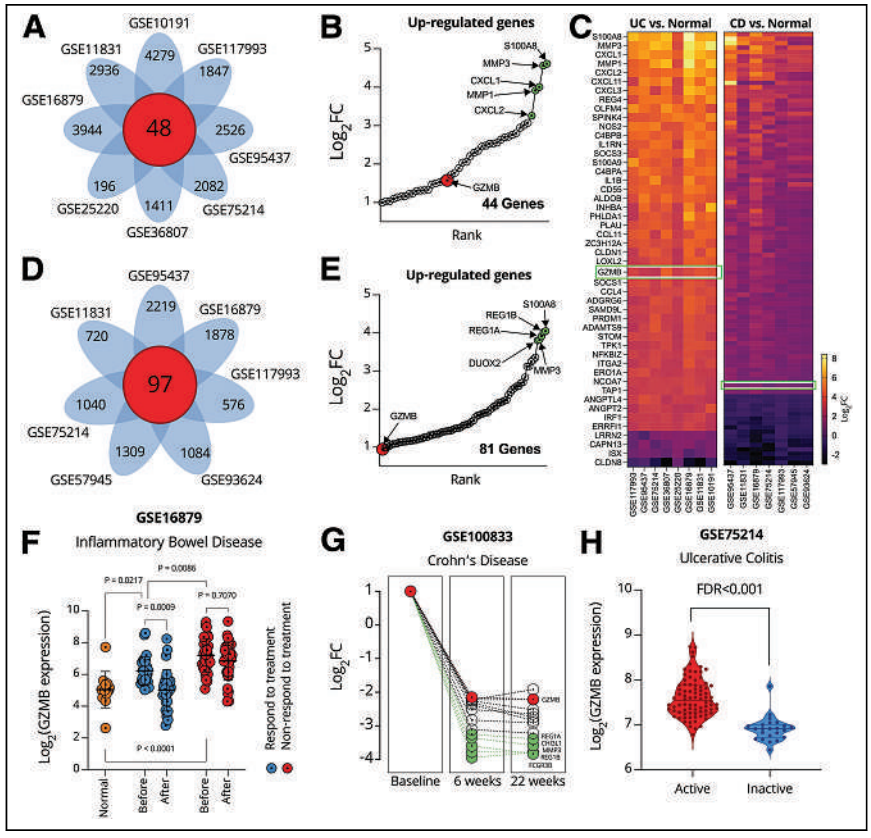

FIGURE 1. GZMB as biomarker in IBD for detecting active disease and evaluating treatment response using bioinformatic analysis. (A) Number of significantly altered genes in active UC vs. normal tissues. (B) Upregulated genes that were in common in UC 8 datasets ranked by $\log_2$ fold change. (C) Heat map of up- and downregulated genes in UC and CD tissues compared with normal tissue. (D) Number of altered genes in active CD vs. normal tissues. (E) Upregulated genes that were in common in CD 7 datasets ranked by $\log_2$ fold change. (F) Gene expression of GZMB in patients before and after treatment analyzed by 1-way ANOVA followed by adjusting *P* value using Benjamini–Hochberg method (data are mean ± SD). (G) Top 15 genes significantly decreased after treatment at different time points (green spots represent top 5 genes, which decreased after treatment, and red represents GZMB). (H) Evaluation of GZMB gene expression in active and inactive UC using *t* test analysis. FDR = false-discovery rate; $\log_2$FC = $\log_2$ fold change.

corresponding normal noninflamed bowel samples. The GZMB gene decreased by 2.16-fold in patients who responded to the first infliximab treatment but showed no significant change in patients who did not respond to the treatment (Fig. 1F). Additionally, in the reanalysis of the GSE100833 database, GZMB was among the top 15 downregulated genes, showing a decrease of 2.16-fold as early as 6 wk after ustekinumab treatment in IBD patients who responded to treatment, and remained low in remission (Fig. 1G). The downregulation of GZMB at 6 wk after treatment was observed in bowel samples regardless of their anatomic site, that is, taken from the rectum; sigmoid descending, transverse, or ascending colon; or terminal ileum (Supplemental Fig. 3). Furthermore, we investigated the differential gene expression of GZMB in IBD patients with active and inactive inflammation. Consistent with our previous findings, GSE75214 database analysis revealed that the expression of GZMB was significantly higher in patients with active IBD than in those with inactive disease (false-discovery rate $< 0.001\%$, Fig. 1H). Collectively, these findings from published online databases support the potential of GZMB as a diagnostic biomarker of IBD and its utility for monitoring treatment response early after initiation of treatment in patients with IBD.

GZMB Is Highly Excreted in Clinically Active IBD

Immunofluorescence staining of human intestinal specimens for GZMB was strong at the lamina propria in active CD samples (Fig. 2A), with significantly weaker staining in the quiescent or normal colon samples (0.32 ± 0.19 vs. 0.06 ± 0.03, $P = 0.032$) (Figs. 2B–2E). These findings confirm the potential of GZMB as a histologic and imaging biomarker for assessing disease activity in human subjects with IBD.

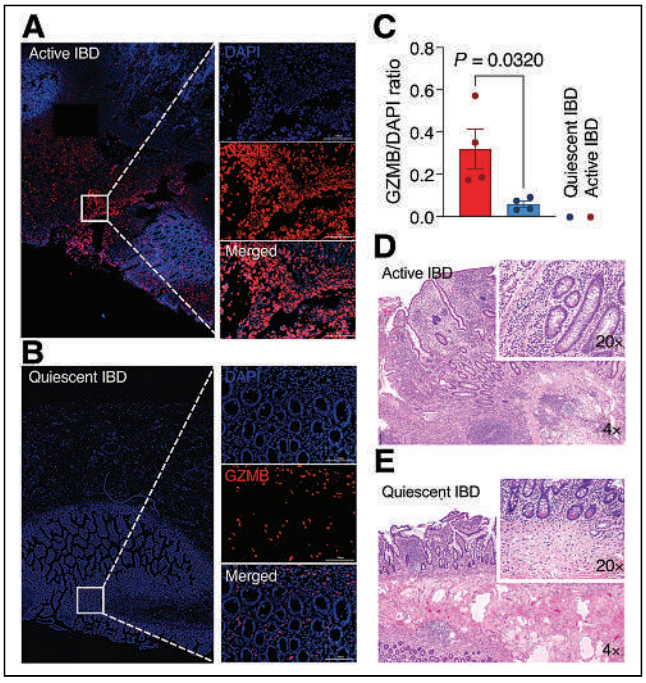

FIGURE 2. (A) Immunofluorescence evaluation of GZMB expression in active IBD. (B) Immunofluorescence evaluation of GZMB expression in quiescent IBD. (C) Quantitative analysis of GZMB to 4′,6-diamidino-2-phenylindole ratio in active IBD vs. quiescent IBD (data are mean ± SEM, 4/group). (D) Hematoxylin and eosin staining of corresponding active IBD samples at indicated magnification. (E) Hematoxylin and eosin staining of corresponding quiescent IBD samples at indicated magnification. Scale bars represent 100 μm. DAPI = 4′,6-diamidino-2-phenylindole.

^{68}Ga-NOTA-GZP Has Favorable Characteristics for Imaging Bowel Inflammation

We made ^{68}Ga-NOTA-GZP with a yield of 67% ± 11%, more than 95% radiochemical purity, and specific activity of 5,190 ± 1,100 MBq/mg. The biodistribution of ^{68}Ga-NOTA-GZP in normal mice (3/group) showed rapid renal elimination of the probe and low background uptake in the liver, blood pool, and other nontarget organs (Supplemental Fig. 4A). In vehicle-treated wild-type animals, probe uptake in the intestines and stomach remained below the level in the blood pool (0.29 ± 0.04, 0.25 ± 0.03, and 0.40 ± 0.05 percentage injected dose per gram, respectively), indicating a favorable biodistribution for imaging active inflammation in the gastrointestinal tract (Supplemental Fig. 4B).

GZMB PET Imaging Can Detect Active Bowel Inflammation

Representative axial and coronal ^{68}Ga-NOTA-GZP PET/CT images of the animal models at 7 d after treatment are shown in Figures 3A and 3B. Quantitative analyses of the PET images showed a low level of uptake in the bowel of wild-type mice treated with either vehicle or DSS (SUV_{mean}, 0.26 ± 0.05 vs. 0.37 ± 0.11, respectively; $P = 0.255$; Figs. 3A–3C). The IL-10$^{-/-}$ mice with DSS-induced colitis demonstrated significantly higher ^{68}Ga-NOTA-GZP uptake than that in IL-10$^{-/-}$ mice treated with vehicle (SUV_{mean}, 0.76 ± 0.10 vs. 0.24 ± 0.10, respectively; $P < 0.001$; Figs. 3A–3C). Anti-TNF treatment significantly decreased PET uptake in the IL-10$^{-/-}$ mice with colitis, compared with untreated mice with active colitis (SUV_{mean}, 0.32 ± 0.14 vs. 0.76 ± 0.10; $P < 0.001$; Figs. 3A–3C). The ex vivo measurement of the retained activity in the extracted intestinal specimens of the mice in all groups confirmed the results of PET studies, demonstrating that ^{68}Ga-NOTA-GZP uptake was significantly higher in intestinal specimens of IL-10$^{-/-}$ mice with DSS-induced colitis than in other groups (percentage injected dose per gram: 3.38 ± 0.39, 0.94 ± 0.57, 0.59 ± 0.29, 0.86 ± 0.25, and 0.59 ± 0.53 in IL-10$^{-/-}$ vehicle-treated, IL-10$^{-/-}$ DSS-induced colitis treated with anti-TNF, wild-type vehicle-treated, and wild-type DSS-treated, respectively; $P < 0.001$; Fig. 3D).

GZMB PET Has Favorable Temporal Resolution for Imaging IBD Activity

Serial ^{68}Ga-NOTA-GZP PET imaging over 4 wk after colitis induction showed a significant 4-fold increase in colonic uptake 1 wk after DSS colitis induction in the IL10$^{-/-}$ mice compared with vehicle-treated IL10$^{-/-}$ mice. Uptake in the former group gradually decreased by 4 wk to approximately 2-fold higher than in the vehicle-treated IL10$^{-/-}$ control (Fig. 3E). ^{68}Ga-NOTA-GZP uptake was significantly higher in the DSS-induced colitis group than in vehicle-treated IL10$^{-/-}$ mice at all time points (repeated-measure ANOVA, 8/group; Fig. 3E).

Cytokine Profile of Extracted Colon Samples Confirmed Dysregulated Cell-Mediated Immune Response in DSS-Induced IL10$^{-/-}$ Colitis Model

Quantification of the level of cytokines in extracted colon tissue from the DSS-induced IL10$^{-/-}$ colitis model (Fig. 4) demonstrated an increase in Th1 and Th22 cytokines (including interferon; interleukins 1β, 6, and 22; and TNF) and absence of Th2 and Th17 cytokines (including interleukins 4, 5, 10, 13, and 17) (Fig. 4). Moreover, there was a marked increase in multiple monocyte chemotactic factors such as macrophage inflammatory proteins 1 and 2, interleukin 18, and monocyte chemotactic proteins 1

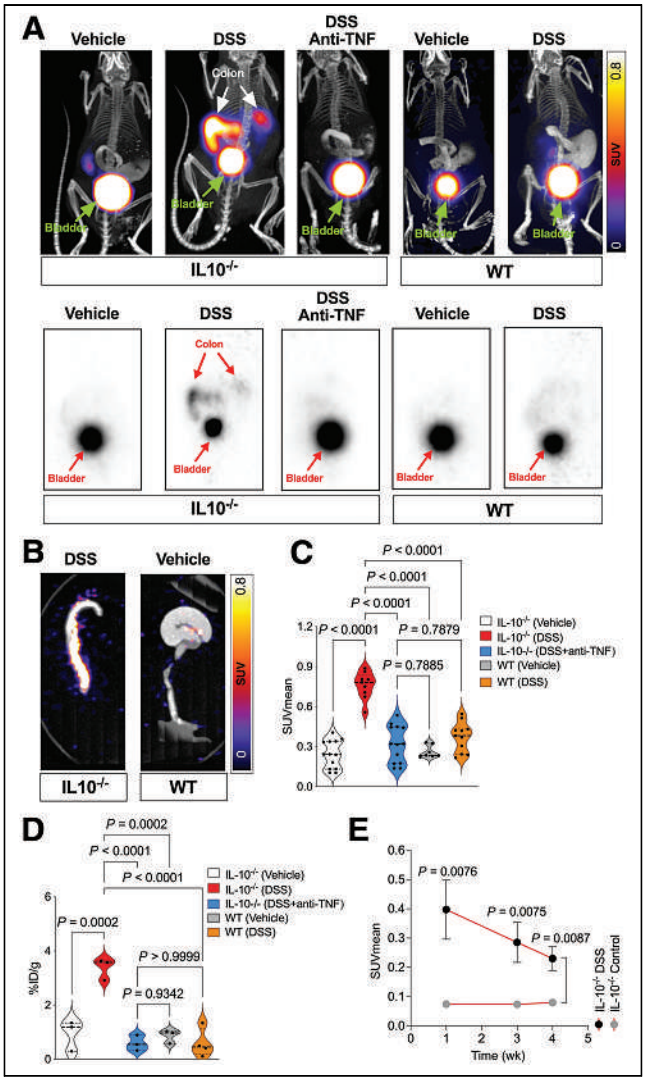

FIGURE 3. (A) Coronal representation of ^{68}Ga-NOTA-GZP PET imaging patterns alongside CT scans, encompassing both combined PET/CT and standalone PET views in IL10$^{-/-}$ mice treated with vehicle, DSS, or DSS plus anti-TNF, as well as wild-type animals treated with DSS or vehicle. (B) Representative axial view of ^{68}Ga-NOTA-GZP PET/CT uptake pattern in IL10$^{-/-}$ mice treated with DSS and wild-type mice treated with vehicle. (C) Quantitative analysis of ^{68}Ga-NOTA-GZP PET/CT SUV_{mean} in DSS-treated IL10$^{-/-}$ mice compared with other groups (7–13/group). (D) ^{68}Ga-NOTA-GZP uptake in ex vivo PET/CT imaging experiment of extracted colonic specimens (3/group). (E) Temporal change in ^{68}Ga-NOTA-GZP PET/CT uptake during 4 wk after DSS induction (data are mean ± SEM, 8/group). %ID = percentage injected dose; WT = wild-type.

and 3, which could be observed in a dysregulated immune condition, such as IBD (Fig. 4) (*29*).

DISCUSSION

Effective management of IBD requires close monitoring of disease activity. However, the lack of reliable, noninvasive techniques for assessing IBD activity remains a challenge (*30*). Commonly used endoscopic assessment and tissue sampling are invasive and do not offer adequate reach to assess the state of disease reliably. Anatomic imaging techniques such as CT or MR enterography show the sequelae of the prolonged inflammation

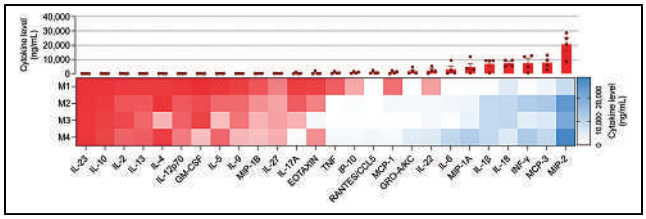

FIGURE 4. Evaluation of colonic cytokine levels in different groups (M1–M4 represent each mouse's data; red box represents cytokine levels < 250 ng/mL).

and often do not have the temporal resolution necessary for close disease monitoring. Molecular imaging techniques can potentially fill this gap because of their high sensitivity and time resolution. Different molecular imaging tracers have been tested in experimental IBD studies with variable results (*14,30–32*). Many of these techniques are indirect measures of active colonic inflammation and therefore may not be mechanistically linked to the pathophysiology of IBD (*34*). We believe GZMB PET imaging can potentially answer this unmet need as it mechanistically targets the early phase of disease activation in IBD and, because of the rapid turnover of the target, provides high temporal resolution for imaging IBD disease activity.

We hypothesized that GZMB PET imaging could be noninvasively used to evaluate IBD activity in vivo. GZMB directly induces intestinal epithelial cell damage, disrupts the integrity of the gut barrier, and contributes to the breakdown of the intestinal mucosa in IBD (*34*). In addition, GZMB can promote the production of proinflammatory cytokines, such as interleukin 1β, TNF, and interleukin 18, which are involved in the inflammatory cascade in IBD (*35*). It modulates the function of regulatory T cells (*36,37*), dysregulation of which leads to further propagation of inflammation in IBD. Moreover, GZMB excretion promotes tissue damage and fibrosis (*38*) by activating the fibroblasts, producing excessive collagen and fibrosis in the bowel (*39*). We have previously shown that GZMB PET imaging could be a predictive biomarker of immunotherapy response in cancer patients (*22,23*). Subsequently, we showed that GZMB PET imaging can detect immune-related adverse events mechanistically due to the imbalance between immune activation and self-tolerance, similar to IBD (*40*). To further investigate the potential of GZMB as a biomarker for IBD disease activity and treatment response assessment, we performed bioinformatic and ex vivo analyses of IBD human samples. Bioinformatic analyses of datasets showed high GZMB gene upregulation in both active CD and UC in comparison to inactive- or non-IBD conditions. In line with our study, a similar report revealed GZMB as a top potential biomarker associated with diagnosis of rheumatoid arthritis, as another condition with a similar dysregulated immune response (*41*). Immunofluorescence staining of human intestinal specimens confirmed our bioinformatic analysis results by showing strong GZMB staining in active CD samples compared with quiescent IBD or normal samples. Collectively, these findings supported our hypothesis that ^{68}Ga-NOTA-GZP PET imaging could be potentially used to assess disease activity in IBD.

Our experiments showed that intestinal uptake of ^{68}Ga-NOTA-GZP was significantly higher in our colitis mouse model than in the controls. We showed that ^{68}Ga-NOTA-GZP PET imaging can effectively detect GZMB in the intestinal tissue of mice with colitis, with low uptake in the normal gastrointestinal tract, which is

desirable for IBD imaging. Moreover, the significant dynamic change in ^{68}Ga-NOTA-GZP uptake over 4 wk suggests that this imaging technique could be a useful biomarker of disease activity in IBD patients, allowing for real-time assessment of active inflammation and more tailored treatment interventions. Additionally, we showed that ^{68}Ga-NOTA-GZP uptake was significantly reduced in the group that received therapy, showing the ability of this imaging to assess the treatment response rapidly. Unlike other PET imaging modalities for detecting IBD—such as immune-PET imaging methods that focus on membranous markers such as CD69 and OX40, ^{18}F-FDG PET/CT for inflammation (*42*), and ^{68}Ga-FAPI PET/CT for fibrosis (*43*)—GZMB PET imaging does not merely localize immune cells, inflammation, or fibrosis lesions. Rather, GZMB PET uniquely captures immune activity, which is particularly crucial in autoimmune diseases such as IBD, for which the dynamic nature of immune responses plays a pivotal role in disease progression and management. This new technique's ability to reflect the functional state of immune cells—specifically, their cytolytic activity—provides critical insights into the mechanisms driving inflammation and tissue damage. Unlike other imaging modalities that target membranous markers and highlight immune cell presence, GZMB imaging delves more deeply, offering a window into the effector functions of these cells. This distinction is vital for IBD, for which the spatial and temporal patterns of immune activity, rather than the mere accumulation of immune cells, dictate the course of the disease. By focusing on immune activity, GZMB PET imaging facilitates a more accurate assessment of the inflammatory status, enabling targeted interventions that can more effectively modulate the disease process.

This study had some limitations. The GZMB PET imaging was studied in only one mouse model of IBD and needs to be validated in other mouse models of IBD. However, the model was mechanistically chosen to imitate the early stages of IBD, in which a combination of mucosal barrier disruption and dysregulated response to gut antigens triggers intestinal inflammation. Therefore, we believe our findings are repeatable in other mouse models of IBD. We hope to validate these findings in human subjects with active IBD. Another limitation is that this study primarily focused on the early detection of IBD activity, and we did not explore the potential of GZMB PET imaging in monitoring acute flares of disease in the background of chronic bowel inflammation, long-term disease progression, or response to multiple treatment regimens. Future research should aim to replicate these results in clinical trials to establish the efficacy and practicality of GZMB PET imaging in routine IBD management.

CONCLUSION

GZMB PET imaging is a potentially promising approach for detecting IBD disease activity, monitoring intestinal inflammation, and assessing the treatment response to antiinflammatory medications. It might improve diagnosis certainty in difficult-to-biopsy regions of the intestine, monitor disease activity, and guide treatment regimens. These findings warrant further investigation in clinical trials to evaluate this imaging technique's feasibility and clinical utility in IBD patients.

DISCLOSURE

This study was funded by K08CA249047 (Pedram Heidari), R01DK123143 (Umar Mahmood), and K08CA259626 (Shadi Esfahani). Umar Mahmood is a cofounder, shareholder, and consultant (scientific advisory board) of CytoSite BioPharma. No other potential conflict of interest relevant to this article was reported.

KEY POINTS

QUESTION: Does targeting GZMB with ^{68}Ga-NOTA-GZP PET imaging provide a reliable, noninvasive method for detecting early intestinal inflammation in murine models of IBD, and can it predict treatment response?

PERTINENT FINDINGS: Bioinformatic analysis and immunofluorescence staining confirmed GZMB as a significant biomarker in IBD, showing upregulation in active human UC and CD. ^{68}Ga-NOTA-GZP PET imaging demonstrated significantly higher uptake in IL-10$^{-/-}$ mice with DSS-induced colitis than in controls, with a 4-fold increase in uptake 1 wk after induction. The uptake correlated with treatment response, decreasing significantly in anti-TNF–treated models.

IMPLICATIONS FOR PATIENT CARE: The successful application of ^{68}Ga-NOTA-GZP PET imaging to detect GZMB suggests a promising noninvasive method for early detection of IBD activity and monitoring of treatment efficacy, potentially guiding more personalized patient management strategies in clinical settings.

REFERENCES

1. Lamb CA, Kennedy NA, Raine T, et al. British Society of Gastroenterology consensus guidelines on the management of inflammatory bowel disease in adults. *Gut.* 2019;68(suppl 3):s1–s106.
2. Laass MW, Roggenbuck D, Conrad K. Diagnosis and classification of Crohn's disease. *Autoimmun Rev.* 2014;13:467–471.
3. Conrad K, Roggenbuck D, Laass MW. Diagnosis and classification of ulcerative colitis. *Autoimmun Rev.* 2014;13:463–466.
4. Lightner AL, Moncrief SB, Smyrk TC, et al. Long-standing Crohn's disease and its implication on anal squamous cell cancer management. *Int J Colorectal Dis.* 2017;32:661–666.
5. Kraus S, Arber N. Inflammation and colorectal cancer. *Curr Opin Pharmacol.* 2009;9:405–410.
6. Xie J, Itzkowitz SH. Cancer in inflammatory bowel disease. *World J Gastroenterol.* 2008;14:378–389.
7. Tanaka M, Riddell R. The pathological diagnosis and differential diagnosis of Crohn's disease. *Hepatogastroenterology.* 1990;37:18–31.
8. Seyedian SS, Nokhostin F, Malamir MD. A review of the diagnosis, prevention, and treatment methods of inflammatory bowel disease. *J Med Life.* 2019;12:113–122.
9. Noriega-Álvarez E, Martín-Comín J. Molecular imaging in inflammatory bowel disease. *Semin Nucl Med.* 2023;53:273–286.
10. Lovinfosse P, Hustinx R. The role of PET imaging in inflammatory bowel diseases: state-of-the-art review. *Q J Nucl Med Mol Imaging.* 2022;66:206–217.
11. Ahmad R, Ajlan AM, Eskander AA, et al. Magnetic resonance imaging in the management of Crohn's disease: a systematic review and meta-analysis. *Insights Imaging.* 2021;12:118.
12. Qiu Y, Mao R, Chen BL, et al. Systematic review with meta-analysis: magnetic resonance enterography vs. computed tomography enterography for evaluating disease activity in small bowel Crohn's disease. *Aliment Pharmacol Ther.* 2014;40:134–146.
13. Catalano O, Maccioni F, Lauri C, Auletta S, Dierckx R, Signore A. Hybrid imaging in Crohn's disease: from SPECT/CT to PET/MR and new image interpretation criteria. *Q J Nucl Med Mol Imaging.* 2017;62:40–55.
14. Freise AC, Zettlitz KA, Salazar FB, et al. Immuno-PET in inflammatory bowel disease: imaging CD4-positive T cells in a murine model of colitis. *J Nucl Med.* 2018;59:980–985.
15. Dmochowska N, Tieu W, Keller MD, et al. Immuno-PET of innate immune markers CD11b and IL-1β detects inflammation in murine colitis. *J Nucl Med.* 2019;60:858–863.

16. Dmochowska N, Wardill HR, Hughes PA. Advances in imaging specific mediators of inflammatory bowel disease. *Int J Mol Sci.* 2018;19:2471.
17. Roberts-Thomson IC, Fon J, Uylaki W, Cummins AG, Barry S. Cells, cytokines and inflammatory bowel disease: a clinical perspective. *Expert Rev Gastroenterol Hepatol.* 2011;5:703–716.
18. Shih DQ, Targan SR. Insights into IBD pathogenesis. *Curr Gastroenterol Rep.* 2009;11:473–480.
19. Kim TJ, Koo JS, Kim SJ, et al. Role of IL-1ra and granzyme B as biomarkers in active Crohn's disease patients. *Biomarkers.* 2018;23:161–166.
20. LaSalle T, Austin EE, Rigney G, et al. Granzyme B PET imaging of immune-mediated tumor killing as a tool for understanding immunotherapy response. *J Immunother Cancer.* 2020;8:e000291.
21. de Aguiar Ferreira C, Heidari P, Ataeinia B, et al. Immune checkpoint inhibitor-mediated cancer theranostics with radiolabeled anti-granzyme b peptide. *Pharmaceutics.* 2022;14:1460.
22. Larimer BM, Bloch E, Nesti S, et al. The effectiveness of checkpoint inhibitor combinations and administration timing can be measured by granzyme B PET imaging. *Clin Cancer Res.* 2019;25:1196–1205.
23. Larimer BM, Wehrenberg-Klee E, Dubois F, et al. Granzyme B PET imaging as a predictive biomarker of immunotherapy response. *Cancer Res.* 2017;77:2318–2327.
24. Barrett T, Wilhite SE, Ledoux P, et al. NCBI GEO: archive for functional genomics data sets—update. *Nucleic Acids Res.* 2013;41:D991–D995.
25. Okayasu I, Hatakeyama S, Yamada M, Ohkusa T, Inagaki Y, Nakaya R. A novel method in the induction of reliable experimental acute and chronic ulcerative colitis in mice. *Gastroenterology.* 1990;98:694–702.
26. Bloemendaal FM, Levin AD, Wildenberg ME, et al. Anti–tumor necrosis factor with a glyco-engineered Fc-region has increased efficacy in mice with colitis. *Gastroenterology.* 2017;153:1351–1362.e4.
27. Aslani A, Snowdon GM, Bailey DL, Schembri GP, Bailey EA, Roach PJ. Gallium-68 DOTATATE production with automated PET radiopharmaceutical synthesis system: a three year experience. *Asia Ocean J Nucl Med Biol.* 2014;2:75–86.
28. Mokaleng BB, Ebenhan T, Ramesh S, et al. Synthesis, ^{68}Ga-radiolabeling, and preliminary in vivo assessment of a depsipeptide-derived compound as a potential PET/CT infection imaging agent. *BioMed Res Int.* 2015;2015:284354.
29. Santamaria P. Cytokines and chemokines in autoimmune disease: an overview. *Adv Exp Med Biol.* 2003;520:1–7.
30. Caobelli F, Evangelista L, Quartuccio N, et al. Role of molecular imaging in the management of patients affected by inflammatory bowel disease: state-of-the-art. *World J Radiol.* 2016;8:829–845.
31. Saboury B, Salavati A, Brothers A, et al. FDG PET/CT in Crohn's disease: correlation of quantitative FDG PET/CT parameters with clinical and endoscopic surrogate markers of disease activity. *Eur J Nucl Med Mol Imaging.* 2014;41:605–614.
32. Kaaru E, Bianchi A, Wunder A, Rasche V, Stiller D. Molecular imaging in preclinical models of IBD with nuclear imaging techniques: state-of-the-art and perspectives. *Inflamm Bowel Dis.* 2016;22:2491–2498.
33. Catalano OA, Wu V, Mahmood U, et al. Diagnostic performance of PET/MR in the evaluation of active inflammation in Crohn disease. *Am J Nucl Med Mol Imaging.* 2018;8:62–69.
34. Geem D, Harusato A, Flannigan K, Denning TL. Harnessing regulatory T cells for the treatment of inflammatory bowel disease. *Inflamm Bowel Dis.* 2015;21:1409–1418.
35. Joeckel LT, Wallich R, Martin P, et al. Mouse granzyme K has pro-inflammatory potential. *Cell Death Differ.* 2011;18:1112–1119.
36. Hou J, Hsu J-M, Hung M-C. Molecular mechanisms and functions of pyroptosis in inflammation and antitumor immunity. *Mol Cell.* 2021;81:4579–4590.
37. Loebbermann J, Thornton H, Durant L, et al. Regulatory T cells expressing granzyme B play a critical role in controlling lung inflammation during acute viral infection. *Mucosal Immunol.* 2012;5:161–172.
38. Ramos GP, Papadakis KA. Mechanisms of disease: inflammatory bowel diseases. *Mayo Clin Proc.* 2019;94:155–165.
39. Hiebert PR, Granville DJ. Granzyme B in injury, inflammation, and repair. *Trends Mol Med.* 2012;18:732–741.
40. Ferreira CA, Heidari P, Ataeinia B, et al. Non-invasive detection of immunotherapy-induced adverse events. *Clin Cancer Res.* 2021;27:5353–5364.
41. Feng ZW, Tang YC, Sheng XY, et al. Screening and identification of potential hub genes and immune cell infiltration in the synovial tissue of rheumatoid arthritis by bioinformatic approach. *Heliyon.* 2023;9:e12799.
42. Louis E, Ancion G, Colard A, Spote V, Belaiche J, Hustinx R. Noninvasive assessment of Crohn's disease intestinal lesions with ^{18}F-FDG PET/CT. *J Nucl Med.* 2007;48:1053–1059.
43. Scharitzer M, Macher-Beer A, Mang T, et al. Evaluation of intestinal fibrosis with ^{68}Ga-FAPI PET/MR enterography in Crohn disease. *Radiology.* 2023;307:e222389.

Deep Learning–Enabled Quantification of ^{99m}Tc-Pyrophosphate SPECT/CT for Cardiac Amyloidosis

Robert J.H. Miller*[1], Aakash Shanbhag*[2,3], Anna M. Michalowska[2], Paul Kavanagh[2], Joanna X. Liang[2], Valerie Builoff[2], Nowell M. Fine[1], Damini Dey[2], Daniel S. Berman[2], and Piotr J. Slomka[2]

[1]*Department of Cardiac Sciences, University of Calgary, Calgary, Alberta, Canada;* [2]*Departments of Medicine (Division of Artificial Intelligence in Medicine), Imaging, and Biomedical Sciences, Cedars-Sinai Medical Center, Los Angeles, California; and* [3]*Signal and Image Processing Institute, Ming Hsieh Department of Electrical and Computer Engineering, University of Southern California, Los Angeles, California*

Transthyretin cardiac amyloidosis (ATTR CA) is increasingly recognized as a cause of heart failure in older patients, with ^{99m}Tc-pyrophosphate imaging frequently used to establish the diagnosis. Visual interpretation of SPECT images is the gold standard for interpretation but is inherently subjective. Manual quantitation of SPECT myocardial ^{99m}Tc-pyrophosphate activity is time-consuming and not performed clinically. We evaluated a deep learning approach for fully automated volumetric quantitation of ^{99m}Tc-pyrophosphate using segmentation of coregistered anatomic structures from CT attenuation maps. **Methods:** Patients who underwent SPECT/CT ^{99m}Tc-pyrophosphate imaging for suspected ATTR CA were included. Diagnosis of ATTR CA was determined using standard criteria. Cardiac chambers and myocardium were segmented from CT attenuation maps using a foundational deep learning model and then applied to attenuation-corrected SPECT images to quantify radiotracer activity. We evaluated the diagnostic accuracy of target-to-background ratio (TBR), cardiac pyrophosphate activity (CPA), and volume of involvement (VOI) using the area under the receiver operating characteristic curve (AUC). We then evaluated associations with the composite outcome of cardiovascular death or heart failure hospitalization. **Results:** In total, 299 patients were included (median age, 76 y), with ATTR CA diagnosed in 83 (27.8%) patients. CPA (AUC, 0.989; 95% CI, 0.974–1.00) and VOI (AUC, 0.988; 95% CI, 0.973–1.00) had the highest prediction performance for ATTR CA. The next highest AUC was for TBR (AUC, 0.979; 95% CI, 0.964–0.995). The AUC for CPA was significantly higher than that for heart-to-contralateral ratio (AUC, 0.975; 95% CI, 0.952–0.998; $P = 0.046$). Twenty-three patients with ATTR CA experienced cardiovascular death or heart failure hospitalization. All methods for establishing TBR, CPA, and VOI were associated with an increased risk of events after adjustment for age, with hazard ratios ranging from 1.41 to 1.84 per SD increase. **Conclusion:** Deep learning segmentation of coregistered CT attenuation maps is not affected by the pattern of radiotracer uptake and allows for fully automatic quantification of hot-spot SPECT imaging such as ^{99m}Tc-pyrophosphate. This approach can be used to accurately identify patients with ATTR CA and may play a role in risk prediction.

Key Words: cardiac amyloidosis; technetium pyrophosphate; quantification; diagnostic accuracy; biomarker

J Nucl Med 2024; 65:1144–1150
DOI: 10.2967/jnumed.124.267542

Transthyretin cardiac amyloidosis (ATTR CA) is an increasingly recognized cause of heart failure (*1*). Bone scintigraphy imaging with tracers such as ^{99m}Tc-pyrophosphate has been established as a highly accurate tool for diagnosing ATTR CA, with initial studies describing evaluation of planar images alone (*2*). However, subsequent studies have shown potential pitfalls from using this approach (*3*). Visual evaluation of SPECT images, in combination with screening for light chain amyloidosis, has now become the gold standard for noninvasive diagnosis (*4*). SPECT imaging improves diagnostic accuracy but is inherently subjective and requires expertise.

Hybrid SPECT/CT imaging facilitates more robust methods to quantify myocardial radiotracer activity. Scully et al. demonstrated high diagnostic accuracy for quantitation using SUVs from regions placed manually on SPECT/CT images (*5*). In our previous work, we demonstrated that quantitative measures have high diagnostic accuracy (*6*) and correlate with native myocardial T1 (*7*). However, these techniques have not translated into clinical practice, at least in part because they require time-consuming manual segmentation. Recent developments in foundational deep learning models have made it feasible to segment cardiac chambers and ventricular myocardium from noncontrast, ungated CT images (*8*). These algorithms can be leveraged to automate and objectify the manual processes involved in quantifying radiotracer uptake in the myocardium in a robust manner that is not affected by the tracer uptake pattern. We developed this automated workflow for ^{99m}Tc-pyrophosphate uptake quantification and then evaluated the potential clinical utility of different approaches to quantitation.

MATERIALS AND METHODS

Study Population

In this retrospective study, we identified patients who underwent ^{99m}Tc-pyrophosphate SPECT/CT imaging at the University of Calgary between March 2020 and October 2022. For each patient with more than one ^{99m}Tc-pyrophosphate study, only the first study was included. Additionally, we excluded 7 cases with significant registration errors identified during quality control processes. Significant offset in any direction between rib or spine uptake and anatomic landmarks was considered misregistration. This study was reviewed and approved by the Institutional Review Board at the University of Calgary (REB19-1448), and the requirement to obtain informed consent was waived.

Clinical Data

Demographics, past medical history, and red flags for ATTR CA at the time of imaging were determined through manual review of

Received Jan. 29, 2024; revision accepted Apr. 3, 2024.
For correspondence or reprints, contact Piotr J. Slomka (piotr.slomka@cshs.org).
*Contributed equally to this work.
Published online May 9, 2024.

electronic medical records. Diagnosis of ATTR CA was based on the presence of, first, an endomyocardial biopsy positive for ATTR; second, diffuse myocardial uptake on SPECT/CT imaging after exclusion of monoclonal protein; or third, evidence of infiltrative cardiomyopathy on echocardiography or cardiac MRI with either a documented pathologic gene variant or a noncardiac biopsy demonstrating ATTR amyloidosis (*4,9*). One patient was diagnosed on the basis of the third criterion; this patient had undergone carpal tunnel biopsy (*10*) and showed mildly reduced biventricular function on cardiac MRI (genetic testing pending). At our center, coverage criteria for tafamidis initially required pathologic confirmation of disease, but this requirement was eventually removed to allow for noninvasive confirmation of diagnosis. An outline of patient diagnosis adjudication is shown in Supplemental Figure 1 (supplemental materials are available at http://jnm.snmjournals.org). All ATTR CA adjudication was performed with masking of the quantitative image results.

Imaging Protocols

Imaging with ^{99m}Tc-pyrophosphate was performed according to 1 of 2 protocols. All subjects underwent imaging on either an NM Discovery 870 (GE Healthcare, $n = 233$) or an NM Discovery 670 (GE Healthcare, $n = 63$) scanner. Patients received 740 MBq (20 mCi) of ^{99m}Tc-pyrophosphate, with planar images obtained at 3 h after injection over a 5- to 8-min duration, with a heart-centered field of view. SPECT images were acquired at 3 h with a 10% energy window and a 128 × 128 matrix. Patients imaged with the NM Discovery 870 had a total acquisition time of 12 min using a wide-energy, high-resolution collimator. Patients imaged with the NM Discovery 670 had a total acquisition time of 15 min using a low-energy high-resolution collimator. For both scanner systems, CT attenuation correction imaging was performed during an end-expiratory breath hold with no gating, in helical mode, with a slice thickness of 5 mm, tube voltage of 120 kVp and 20 mA, and a 512 × 512 matrix.

Expert Image Interpretation

Planar myocardial radiotracer retention was quantified from the 3-h images using heart-to-contralateral ratio at the time of clinical interpretation (*4*). Planar images at 3 h were also graded visually using Perugini grading (*2*). SPECT images at 3 h were visually assessed to determine whether diffuse radiotracer activity was present or absent in the myocardium (*4*).

CT Attenuation Correction Segmentation

A previously validated foundational deep learning model (Total Segmentator) was used to segment all heart chambers and myocardium (*11*). The model uses a no-new-Net (nnU-Net) architecture to automatically segment a variety of anatomic structures from CT images (*11*). A key advantage of this approach is the automatic optimization of the various hyperparameters, including an ensemble of 2- and 3-dimensional U-Net networks at multiple resolutions. For cardiac structures, the model was trained using expert annotations from contrast images, which were transferred to registered noncontrast images. We recently demonstrated excellent correlations between estimates from noncontrast CT and volumes manually segmented from gated, contrast-enhanced CT (left ventricular [LV] myocardium Spearman $r = 0.947$, LA volume Spearman $r = 0.926$) (*12*). The left atrium (LA) and LV myocardium, right atrium, and aorta regions derived automatically from the CT attenuation correction scans were then used to quantify the tracer on coregistered attenuation-corrected ^{99m}Tc-pyrophosphate SPECT images.

CT-Guided Quantification

All ^{99m}Tc-pyrophosphate quantification was performed using attenuation-corrected images. We used CT-derived LV myocardial boundaries to determine maximum myocardial counts. Maximum myocardial counts, corrected for radiotracer delay and camera sensitivity (*13*), were used to calculate the SUV_{max} from injected dose and weight (*14*). We also evaluated target-to-background ratio (TBR), as well as cardiac pyrophosphate activity (CPA) and volume of involvement (VOI), on the basis of our previous work (*6*). TBR is calculated as the maximum activity in the target (myocardium) divided by the mean activity of the background. VOI is quantified as the total volume of activity above threshold (maximum activity of the background) (*6*). CPA is quantified as the total activity (integrating volume and intensity) above threshold, divided by mean background activity (*6*).

For TBR, VOI, and CPA, LV myocardium was used as the target region, but we evaluated 5 methods for determining background activity. The first 3 methods were based on LA activity. First, we used the full cardiac segments to quantify LA ^{99m}Tc-pyrophosphate activity and LV myocardial ^{99m}Tc-pyrophosphate activity. These segmentations were used to quantify TBR_{full}, VOI_{full}, and CPA_{full}. Next, we evaluated a reduced-size left atrial region (reduced by 50%) to measure LA background activity. The reduced LA region was used to quantify TBR_{small}, VOI_{small}, and CPA_{small}. Lastly, we considered 5 regions of interests (200 mm^3 each) randomly sampled within the LA volume. This method was used to define TBR_{roi}, VOI_{roi}, and CPA_{roi} measures. Similarly, we used maximal uptake in the right atrium to derive TBR_{ra}, VOI_{ra}, and CPA_{ra} and maximal uptake in the aorta derive TBR_{aorta}, VOI_{aorta}, and CPA_{aorta}. Examples of the segmentation methods and overall deep learning workflow are shown in Figure 1.

Outcomes

The primary outcome was diagnostic accuracy for ATTR CA. In the secondary analysis, we evaluated associations with the combined

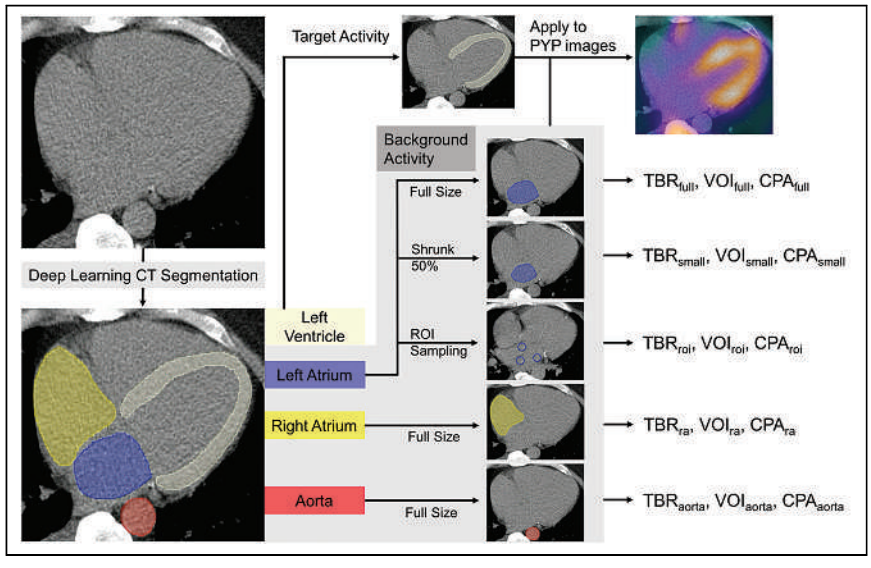

FIGURE 1. Overview of segmentation and image quantification. Deep learning was used to segment noncontrast CT scans. LV myocardium segmentation was used without modification. We evaluated 5 methods for determining background activity. LA was sampled with full region, reduced region (shrunk 50% but centered in LA), and random regions of interest. Right atrium and aorta were sampled with full-size volumes. These segmentations were used to calculate TBR, VOI, and CPA. PYP = ^{99m}Tc-pyrophosphate; ROI = region of interest.

clinical outcome of cardiovascular death or heart failure hospitalization. Admissions for heart failure were ascertained from electronic medical records based on a primary admitting diagnosis of heart failure using the standardized codes from the International Classification of Diseases, 10th revision (*15*). Cardiovascular mortality was ascertained from electronic medical records and included death related to heart failure, myocardial infarction, or sudden death (*16*). Follow-up was censored at the last time that follow-up status could be verified. Outcomes were adjudicated with masking of the ^{99m}Tc-pyrophosphate results.

Statistical Analysis

Categorical variables were summarized as numbers and percentages and compared with a χ^2 or Fisher exact test as appropriate. Continuous variables were summarized as mean and SD and compared using Student *t* test if normally distributed and summarized as median and interquartile range and compared using Wilcoxon rank sum test if not.

Prediction performance was evaluated using areas under the receiver operating characteristic curve (AUCs) and compared using the method of DeLong et al. (*17*). SPECT visual interpretation was not included in this analysis since it was used in part to adjudicate diagnosis. Unadjusted and age-adjusted associations with the combined outcome of cardiovascular death or heart failure hospitalization were assessed using Cox proportional hazards models. Multivariable models were limited to age-adjusted associations, given the low number of events (*18*). The proportional hazards assumption was assessed using Schoenfeld residuals, with no significant violations identified.

All statistical tests were 2-sided, with a *P* value of less than 0.05 considered statistically significant. All analyses were performed with STATA version 13 (StataCorp).

RESULTS

Patient Population

In total, 299 patients were included in the study, with a diagnosis of ATTR CA in 83 patients. The population characteristics are outlined in Table 1. Patients with ATTR CA were older (median age, 82 vs. 74 y; $P < 0.001$) and more likely to be male (81.9% vs. 56.5%; $P < 0.001$).

Cardiac chamber measurements took an average of 15.8 ± 0.2 s (including time for chamber segmentation and image quantification). Cases demonstrating chamber segmentation and image quantification are shown in Figure 2 for a patient with ATTR CA and in Figure 3 for a patient without ATTR CA. Imaging parameters are outlined in Table 2. The median SUV_{max}, TBR, VOI, and CPA, regardless of the quantification method, were significantly higher in patients with ATTR CA (all $P < 0.001$). Distributions of quantitative imaging variables are shown in Supplemental Figure 2.

Diagnostic Accuracy

Prediction performance for ATTR CA using clinical and quantitative measures, and using new automated measures with reduced LA volume as the background, is shown in Figure 4. CPA_{small} (AUC, 0.989; 95% CI, 0.974–1.00) and VOI_{small} (AUC, 0.988; 95% CI, 0.973–1.00) had the highest prediction performance for ATTR CA. The AUC for CPA_{small} was significantly higher than that for the heart-to-contralateral ratio (AUC, 0.975; 95% CI, 0.952–0.998; $P = 0.046$) and SUV_{max} (AUC, 0.944; 95% CI, 0.919–0.970; $P = 0.013$).

Prediction performance for ATTR CA using all automated methods for quantifying CPA is shown in Supplemental Figure 3. Of the quantification methods, CPA_{small} (AUC, 0.989; 95% CI, 0.974–1.00) and CPA_{ra} (AUC, 0.987; 95% CI, 0.970–1.00) had the highest prediction performance. Prediction performance for methods of quantifying TBR is shown in Supplemental Figure 4. Prediction performance using VOI, shown in Supplemental Figure 5, was similar to the results for CPA.

Clinical Outcomes

Among the 83 patients with ATTR CA, during a median follow-up of 1.6 y (interquartile range, 1.0–1.9 y), 15 patients experienced heart failure–related hospitalization and 8 patients experienced cardiovascular death as the first event. Unadjusted and age-adjusted associations with the combined outcome of cardiovascular death or heart failure hospitalization are shown in Figure 5. Most quantitative variables were associated with an

TABLE 1
Population Characteristics Stratified by Presence of ATTR CA

Characteristic	No ATTR CA ($n = 216$)	ATTR CA ($n = 83$)	*P*
Median age (y)	74 (IQR, 65–80)	82 (IQR, 72–86)	<0.001
Male (*n*)	122 (56.5%)	68 (81.9%)	<0.001
Medical history (*n*)			
Hypertension	152 (70.4%)	59 (71.1%)	0.900
Diabetes	56 (25.9%)	10 (12.0%)	0.010
Coronary artery disease	49 (22.7%)	20 (24.1%)	0.801
Atrial fibrillation	64 (29.6%)	37 (44.6%)	0.014
Amyloid red flags (*n*)			
Bilateral carpal tunnel syndrome	6 (2.8%)	41 (49.4%)	<0.001
Spinal stenosis	9 (4.2%)	15 (18.1%)	<0.001
Peripheral neuropathy	57 (26.4%)	46 (55.4%)	<0.001
Previous TAVI	6 (2.8%)	2 (2.4%)	0.852

IQR = interquartile range; TAVI = transcatheter aortic valve implantation.

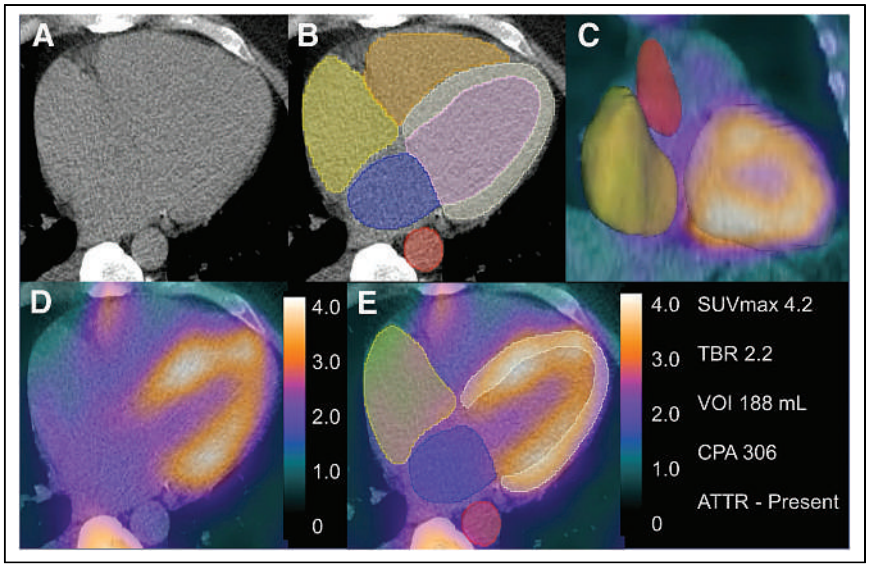

FIGURE 2. Example patient with ATTR CA. (A and B) Attenuation correction imaging (A) segmented using deep learning (B). (C) Three-dimensional segmentations for all chambers. (D) Hybrid SPECT/CT imaging, with scale in SUV. (E) Chamber segmentations applied to coregistered SPECT to quantify radiotracer activity.

increased risk of cardiovascular death or heart failure hospitalization in unadjusted analyses. After adjustment for age, all quantitative variables were associated with an increased risk of events, with hazard ratios ranging from 1.41 to 1.84 per SD increase.

DISCUSSION

We demonstrated the feasibility of fully automated quantification of ^{99m}Tc-pyrophosphate uptake using deep learning segmentation of coregistered CT attenuation maps. We leveraged CT anatomic information to identify structures that cannot be consistently identified using ^{99m}Tc-pyrophosphate imaging alone. The diagnostic accuracy for ^{99m}Tc-pyrophosphate quantification was consistently excellent, without the need for manual intervention. Quantification was independent of variability in ^{99m}Tc-pyrophosphate uptake, allowing quantification in cases with low uptake, where methods based on SPECT imaging alone may be subjective and unreliable. Lastly, we demonstrated the potential clinical importance of automated measures by evaluating associations with the combined outcome of cardiovascular mortality or hospitalization due to heart failure. Overall, our results suggest that fully automated quantitation of ^{99m}Tc-pyrophosphate is possible and could potentially be used to support physician interpretation or risk stratification.

There has been a significant increase in the use of ^{99m}Tc-pyrophosphate imaging in response to the high diagnostic accuracy of the test and increasing awareness regarding ATTR CA (*19*). As a result, ^{99m}Tc-pyrophosphate imaging is increasingly performed in community centers, where physicians may have less expertise in the technique. Although SPECT imaging is highly accurate when analyzed by experienced observers, experience is required to differentiate blood pool from myocardial radiotracer activity, particularly in cases with lower uptake. Dual-isotope imaging was proposed for quantifying myocardial uptake (*20*). However, this is currently impractical because of limited access to thallium, increased radiation exposure, and lack of a consistent definition of background activity. Hybrid SPECT/CT allows physicians to identify anatomic landmarks (*21*), so it is intuitive to use a similar approach for artificial intelligence approaches to image evaluation. We demonstrate the feasibility of this approach, using a deep learning model to segment CT attenuation imaging to facilitate automated quantification of SPECT tracer. A similar approach has been applied to whole-heart segmentation from CT attenuation correction imaging (*22*). Our method has the potential advantage of separating out regions of blood-pool activity from myocardial uptake and also providing the measures of overall disease burden such as CPA or VOI. Furthermore, the segmentation method for CT images was previously externally validated (*12*). Importantly, since the method is based on CT imaging, it does not rely on (or assume) any specific distribution of radiotracer. The model segments CT images rapidly (<16 s) and could be deployed as a preprocessing step, since the pipeline is fully automated. Therefore, it could be deployed in a clinical workflow without interruption to support physician interpretation, which may be particularly beneficial in centers without extensive ^{99m}Tc-pyrophosphate imaging expertise.

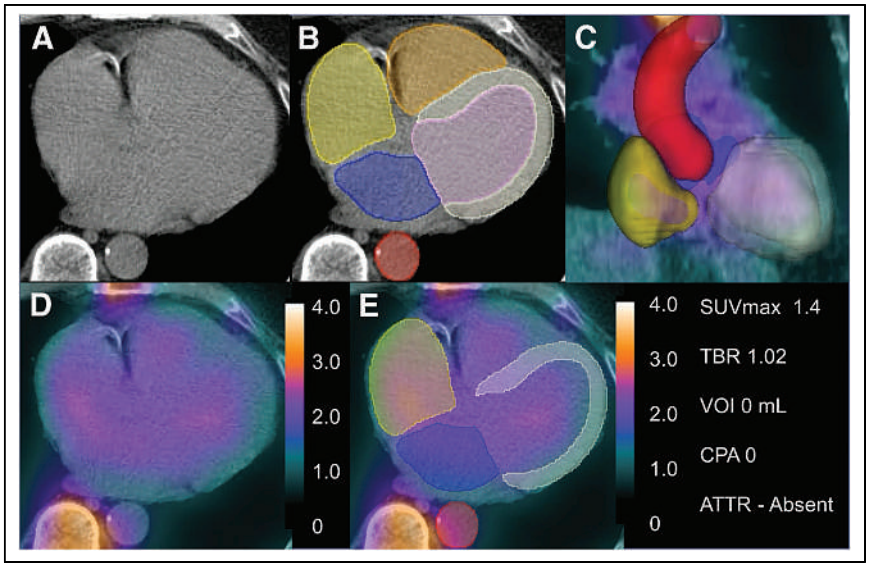

FIGURE 3. Example patient without ATTR CA. (A and B) Attenuation correction imaging (A) segmented using deep learning (B). (C) Three-dimensional segmentations for all chambers. (D) Hybrid SPECT/CT imaging, with scale in SUV. (E) Chamber segmentations applied to coregistered SPECT to quantify radiotracer activity.

Several different methods for quantifying radiotracer ^{99m}Tc-pyrophosphate activity have been proposed to date. Scully et al.

TABLE 2
Imaging Characteristics Stratified by Presence of ATTR CA

Characteristic	No ATTR CA (n = 216)	ATTR CA (n = 83)	P
Clinical analysis			
Perugini grade 2/3 (n)	10 (4.6%)	80 (96.4%)	<0.001
HCL ratio	1.1 (1.0–1.2)	1.7 (1.5–1.9)	<0.001
SPECT visual positive (n)	0 (0.0%)	82 (98.8%)	<0.001
Quantitative analysis			
SUV_{max}	1.4 (0.5–1.7)	3.9 (2.8–5.7)	<0.001
TBR_{full}	1.18 (1.1–1.3)	2.1 (1.8–2.4)	<0.001
VOI_{full}	0 (0–0)	46.5 (13.7–71.0)	<0.001
CPA_{full}	0 (0–0)	74.7 (22.6–112)	<0.001
TBR_{small}	1.1 (1.0–1.3)	2.1 (1.8–2.4)	<0.001
VOI_{small}	0 (0–0)	67.2 (31.8–105)	<0.001
CPA_{small}	0 (0–0)	105 (46.2–177)	<0.001
TBR_{roi}	1.2 (1.1–1.3)	2.17 (1.8–2.4)	<0.001
VOI_{roi}	10.4 (2.9–28.1)	129 (91.3–166)	<0.001
CPA_{roi}	10.1 (3.0–27.5)	181 (120–235)	<0.001
TBR_{ra}	1.3 (1.2–1.5)	2.4 (2.1–2.9)	<0.001
VOI_{ra}	0 (0–0.2)	93.5 (47.0–130)	<0.001
CPA_{ra}	0 (0–0.2)	162 (84.3–233)	<0.001
TBR_{ao}	1.3 (1.2–1.5)	2.6 (2.3–3.3)	<0.001
VOI_{ao}	0 (0–0)	31.2 (5.9–63.9)	<0.001
CPA_{ao}	0 (0–0)	73.5 (12.3–154)	<0.001

HCL = heart to contralateral.
Continuous data are median and interquartile range.

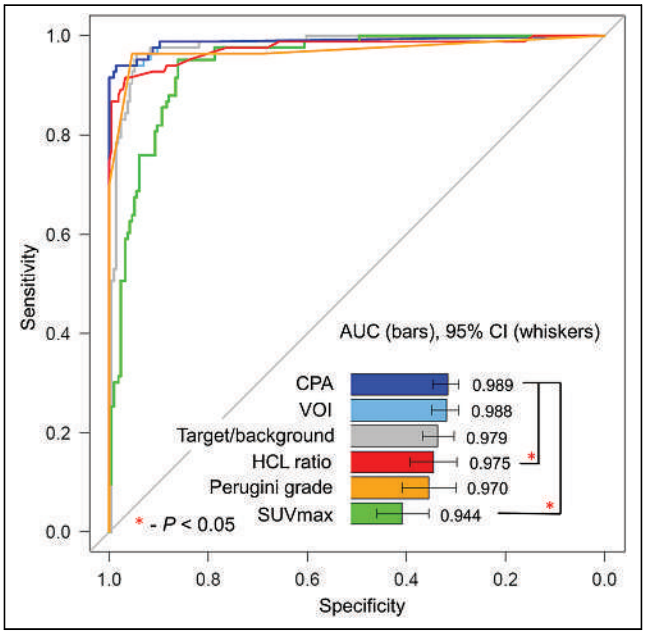

FIGURE 4. Prediction performance for diagnosis of ATTR CA using clinical and quantitative methods (n = 83/299). SUV_{max} was quantified from LV myocardium region. Background for TBR, CPA, and VOI was reduced-size region of interest in LA. HCL = heart to contralateral.

evaluated SUV_{peak} in myocardium as well as a retention index (*5*). Kessler et al. evaluated a method for whole-heart quantitation of radiotracer activity (*23*), which demonstrated high diagnostic accuracy. For quantifying cardiac amyloid activity, Dorbala et al. proposed a method that relied on manually defining myocardium on CT attenuation imaging and then transferring those contours to associated ^{99m}Tc-pyrophosphate imaging (*24*). Importantly, these measurements correlated strongly with cardiovascular MR markers of disease burden (*24*). In our previous work, we demonstrated that CPA and VOI (manually derived) have high diagnostic accuracy (*6*) and correlate with native myocardial T1 (*7*). However, all of those studies relied on tedious manual segmentation, which is a barrier to clinical translation.

We evaluated a large number of quantitation schemes facilitated by automated segmentation of CT structures. The diagnostic accuracy of most quantitative variables was excellent, with only a few significant differences identified. SUV_{max} had slightly lower diagnostic accuracy, which may be a reflection of inherent limitations in quantifying SUV from SPECT imaging (*25*) or of the fact that SUV_{max} is defined by a single pixel value. There was a trend toward higher prediction performance for methods using small LA volumes or RA volumes as background. All of the methods had diagnostic accuracy similar or superior to that of planar interpretation, which was informed by SPECT visual interpretation (since we relied on clinically reported planar interpretation). All of the methods for quantifying ^{99m}Tc-pyrophosphate activity from

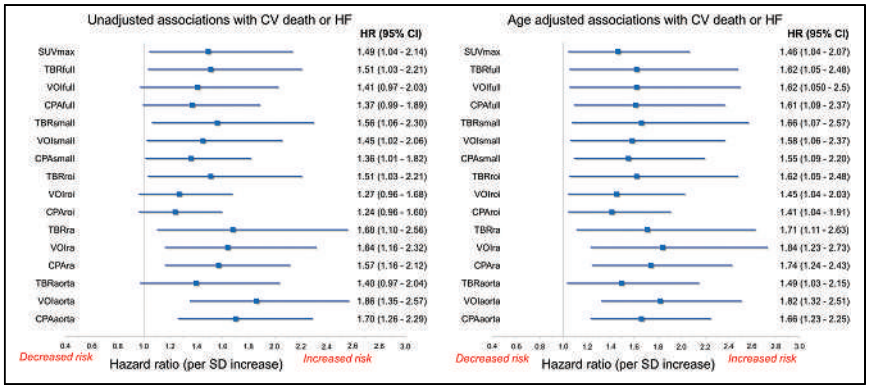

FIGURE 5. Associations (per SD increase) with incidence of cardiovascular (CV) death or heart failure (HF) hospitalization in patients with ATTR CA.

SPECT/CT were associated with the combined clinical outcome after adjustment for age. Further large-scale comparisons may be needed to differentiate more precisely between different methods of determining the background counts.

Identification of diffuse myocardial uptake on SPECT images is part of the diagnostic criteria for ATTR CA (*4*) but requires expertise to accurately differentiate blood pool from myocardium. Therefore, quantitative analysis of SPECT/CT may be particularly valuable in smaller centers, with less expertise, as a diagnostic tool. Furthermore, risk prediction remains an important clinical need, particularly with the emergence of additional therapies for ATTR CA (*26*). Objective and automated SPECT/CT quantification may identify patients at highest risk and also provide precise assessment of changes in radiotracer uptake in response to therapy (*27*). Artificial intelligence–based volumetric quantification of ^{99m}Tc-pyrophosphate activity, and potentially other bone-seeking radiotracers, may be a particularly precise way to follow changes in response to disease-modifying therapies (*28*). This could potentially be used to identify patients who are not responding to therapy and could be transitioned to other therapies.

Our study had a few important limitations. We quantified all SPECT/CT images at 3 h using ^{99m}Tc-pyrophosphate, and the results may not extrapolate to centers performing imaging only at 1 h (*3*) or using other radiotracers (*29*). Endomyocardial biopsy was not performed on most patients. Although a pathologic diagnosis would provide greater certainty regarding adjudication of ATTR CA, this is not reflective of clinical practice, which has shifted to increasingly noninvasive diagnosis (*3*). Additionally, we had a limited number of patients with serial studies and therefore were not able to assess changes over time or in response to therapy (*28*). However, this would be an important next step in evaluating this approach. Lastly, we relied on spatial registration between CT and ^{99m}Tc-pyrophosphate images. Expert oversight is needed to verify if the registration is correct, which may be difficult in cases with limited uptake. Nevertheless, correct SPECT/CT alignment is required for attenuation correction of the ^{99m}Tc-pyrophosphate counts, even if CT is not used for the region definition. Thus, any quantitative approach for attenuation-corrected ^{99m}Tc-pyrophosphate SPECT scans must ensure correct SPECT/CT registration.

CONCLUSION

The anatomic information available from CT attenuation correction imaging can be leveraged by deep learning to automatically segment and quantify ^{99m}Tc-pyrophosphate imaging regardless of the intensity or distribution of radiotracer uptake. This approach can be used to support physician interpretation of ^{99m}Tc-pyrophosphate images, which may be particularly beneficial in community centers, or to quantify radiotracer activity, which may potentially play a role in assessment of therapies or risk stratification.

DISCLOSURE

This research was supported in part by grant R35HL161195 from the National Heart, Lung, and Blood Institute/National Institutes of Health (NHLBI/NIH) (principal investigator, Piotr Slomka). The content is solely the responsibility of the authors and does not necessarily represent the official views of the National Institutes of Health. Robert Miller reports research and consulting support from Pfizer. Nowell Fine reports research and consulting support from Pfizer, Akcea, Alnylam, and Eidos. Paul Kavanagh, Daniel Berman, and Piotr Slomka participate in software royalties for QPS software at Cedars-Sinai Medical Center. Piotr Slomka has received research grant support from Siemens Medical Systems and consulting fees from Synektik. Daniel Berman has served as a consultant for GE Healthcare. No other potential conflict of interest relevant to this article was reported.

KEY POINTS

QUESTION: Can deep learning use anatomic information from CT attenuation maps to automatically quantify ^{99m}Tc-pyrophosphate imaging?

PERTINENT FINDINGS: Using 299 patients, we demonstrated the feasibility of a deep learning–based approach for quantifying ^{99m}Tc-pyrophosphate imaging, with a mean processing time of less than 16 s. Measures of ^{99m}Tc-pyrophosphate radiotracer uptake have high diagnostic accuracy for ATTR CA and were associated with the composite outcome of cardiovascular death or heart failure–related hospitalization.

IMPLICATIONS FOR PATIENT CARE: CT-guided quantification of ^{99m}Tc-pyrophosphate imaging can be used to automate analysis, support physician interpretation, and provide quantitative risk stratification.

REFERENCES

1. Ruberg FL, Grogan M, Hanna M, Kelly JW, Maurer MS. Transthyretin amyloid cardiomyopathy. *J Am Coll Cardiol.* 2019;73:2872–2891.
2. Perugini E, Guidalotti PL, Salvi F, et al. Noninvasive etiologic diagnosis of cardiac amyloidosis using ^{99m}Tc-3,3-diphosphono-1,2-propanodicarboxylic acid scintigraphy. *J Am Coll Cardiol.* 2005;46:1076–1084.
3. Masri A, Bukhari S, Ahmad S, et al. Efficient 1-hour technetium-99m pyrophosphate imaging protocol for the diagnosis of transthyretin cardiac amyloidosis. *Circ Cardiovasc Imaging.* 2020;13:e010249.
4. Dorbala S, Ando Y, Bokhari S, et al. ASNC/AHA/ASE/EANM/HFSA/ISA/SCMR/SNMMI expert consensus recommendations for multimodality imaging in cardiac amyloidosis. *J Nucl Cardiol.* 2020;27:659–673.
5. Scully PR, Morris E, Patel KP, et al. DPD quantification in cardiac amyloidosis. *JACC Cardiovasc Imaging.* 2020;13:1353–1363.
6. Miller RJH, Cadet S, Mah D, et al. Diagnostic and prognostic value of technetium-99m pyrophosphate uptake quantitation for transthyretin cardiac amyloidosis. *J Nucl Cardiol.* 2021;28:1835–1845.

7. Roshankar G, White GC, Cadet S, et al. Quantitative technetium pyrophosphate and cardiovascular magnetic resonance in patients with suspected cardiac amyloidosis. *J Nucl Cardiol.* 2022;29:2679–2690.
8. Han D, Shanbhag A, Miller RJH, et al. Artificial intelligence-based automated left ventricular mass quantification from non-contrast cardiac CT scans: correlation with contrast CT and cardiac MRI. medRxiv website. https://www.medrxiv.org/content/10.1101/2024.01.12.24301169v1. Published January 13, 2024. Accessed April 18, 2024.
9. Garcia-Pavia P, Rapezzi C, Adler Y, et al. Diagnosis and treatment of cardiac amyloidosis. A position statement of the European Society of Cardiology Working Group on Myocardial and Pericardial Diseases. *Eur J Heart Fail.* 2021;23:512–526.
10. Khayambashi S, Elzinga K, Hahn C, et al. Amyloidosis tissue confirmation for tafamidis eligibility using transverse carpal ligament and tenosynovium biopsy. *Can J Cardiol.* 2022;38:1643–1646.
11. Wasserthal J, Breit H-C, Meyer MT, et al. TotalSegmentator: robust segmentation of 104 anatomic structures in CT images. *Radiol Artif Intell.* 2023;5:e230024.
12. Miller RJ, Shanbhag A, Killekar A, et al. AI-defined cardiac anatomy improves risk stratification of hybrid perfusion imaging. *JACC Cardiovasc Imaging.* March 6, 2024 [Epub ahead of print].
13. Ito T, Matsusaka Y, Onoguchi M, et al. Experimental evaluation of the GE NM/CT 870 CZT clinical SPECT system. *J Appl Clin Med Phys.* 2021;22:165–177.
14. Kinahan PE, Fletcher JW. Positron emission tomography-computed tomography standardized uptake values in clinical practice and assessing response to therapy. *Semin Ultrasound CT MR.* 2010;31:496–505.
15. Southern DA, Norris CM, Quan H, et al. An administrative data merging solution for dealing with missing data in a clinical registry. *BMC Med Res Methodol.* 2008;8:1.
16. Hicks KA, Tcheng JE, Bozkurt B, et al. 2014 ACC/AHA key data elements and definitions for cardiovascular endpoint events in clinical trials. *J Am Coll Cardiol.* 2015;66:403–469.
17. DeLong ER, DeLong DM, Clarke-Pearson DL. Comparing the areas under two or more correlated receiver operating characteristic curves. *Biometrics.* 1988;44:837–845.
18. Austin PC, Steyerberg EW. Events per variable (EPV) and the relative performance of different strategies for estimating the out-of-sample validity of logistic regression models. *Stat Methods Med Res.* 2017;26:796–808.
19. Poterucha TJ, Elias P, Bokhari S, et al. Diagnosing transthyretin cardiac amyloidosis by technetium Tc 99m pyrophosphate: a test in evolution. *JACC Cardiovasc Imaging.* 2021;14:1221–1231.
20. Tamarappoo B, Otaki Y, Manabe O, et al. Simultaneous Tc-99m PYP/Tl-201 dual-isotope SPECT myocardial imaging in patients with suspected cardiac amyloidosis. *J Nucl Cardiol.* 2020;27:28–37.
21. Sperry BW, Bateman TM, Akin EA, et al. Hot spot imaging in cardiovascular diseases. *J Nucl Med.* 2022;63:1722–1740.
22. Bhattaru A, Rojulpote C, Vidula M, et al. Deep learning approach for automated segmentation of myocardium using bone scintigraphy SPECT/CT in patients with suspected cardiac amyloidosis. *J Nucl Cardiol.* 2024;33:101809.
23. Kessler L, Fragoso Costa P, Kersting D, et al. Quantitative ^{99m}Tc-DPD-SPECT/CT assessment of cardiac amyloidosis. *J Nucl Cardiol.* 2023;30:101–111.
24. Dorbala S, Park MA, Cuddy S, et al. Absolute quantitation of cardiac (99m)Tc-pyrophosphate using cadmium-zinc-telluride-based SPECT/CT. *J Nucl Med.* 2021;62:716–722.
25. Dickson JC, Armstrong IS, Gabiña PM, et al. EANM practice guideline for quantitative SPECT-CT. *Eur J Nucl Med Mol Imaging.* 2023;50:980–995.
26. Maurer MS, Kale P, Fontana M, et al. Patisiran treatment in patients with transthyretin cardiac amyloidosis. *N Engl J Med.* 2023;389:1553–1565.
27. Fontana M, Martinez-Naharro A, Chacko L, et al. Reduction in CMR derived extracellular volume with patisiran indicates cardiac amyloid regression. *JACC Cardiovasc Imaging.* 2021;14:189–199.
28. Papathanasiou M, Kessler L, Bengel FM, et al. Regression of myocardial ^{99m}Tc-DPD uptake after tafamidis treatment of cardiac transthyretin amyloidosis. *J Nucl Med.* 2023;64:1083–1086.
29. Hutt DF, Quigley AM, Page J, et al. Utility and limitations of 3,3-diphosphono-1,2-propanodicarboxylic acid scintigraphy in systemic amyloidosis. *Eur Heart J Cardiovasc Imaging.* 2014;15:1289–1298.

Histology-Based Radiomics for [^{18}F]FDG PET Identifies Tissue Heterogeneity in Pancreatic Cancer

Esther M.M. Smeets*[1], Marija Trajkovic-Arsic*[2,3], Daan Geijs[4], Sinan Karakaya[2,3], Monica van Zanten[5], Lodewijk A.A. Brosens[4], Benedikt Feuerecker[6–9], Martin Gotthardt[1], Jens T. Siveke[2,3,10], Rickmer Braren[7], Francesco Ciompi†[4], and Erik H.J.G. Aarntzen†[1]

[1]*Department of Medical Imaging, Radboud University Medical Center, Nijmegen, The Netherlands;* [2]*German Cancer Consortium, partner site Essen, a partnership between DKFZ and University Hospital Essen, Essen, Germany;* [3]*Bridge Institute of Experimental Tumor Therapy and Division of Solid Tumor Translational Oncology, West German Cancer Center, University Hospital Essen, University of Duisburg–Essen, Essen, Germany;* [4]*Department of Pathology, Radboud University Medical Center, Nijmegen, The Netherlands;* [5]*Department of Pathology, Canisius Wilhelmina Ziekenhuis, Nijmegen, The Netherlands;* [6]*Department of Nuclear Medicine, School of Medicine, Technical University of Munich, Munich, Germany;* [7]*Department of Radiology, School of Medicine, Technical University of Munich, Munich, Germany;* [8]*German Cancer Consortium, partner site Munich, a partnership between DKFZ and Technical University of Munich, Munich, Germany;* [9]*Department of Radiology, Ludwig Maximilians University, Munich, Germany; and* [10]*National Center for Tumor Diseases West, Campus Essen, Essen, Germany*

Radiomics features can reveal hidden patterns in a tumor but usually lack an underlying biologic rationale. In this work, we aimed to investigate whether there is a correlation between radiomics features extracted from [^{18}F]FDG PET images and histologic expression patterns of a glycolytic marker, monocarboxylate transporter-4 (MCT4), in pancreatic cancer. **Methods:** A cohort of pancreatic ductal adenocarcinoma patients (n = 29) for whom both tumor cross sections and [^{18}F]FDG PET/CT scans were available was used to develop an [^{18}F]FDG PET radiomics signature. By using immunohistochemistry for MCT4, we computed density maps of MCT4 expression and extracted pathomics features. Cluster analysis identified 2 subgroups with distinct MCT4 expression patterns. From corresponding [^{18}F]FDG PET scans, radiomics features that associate with the predefined MCT4 subgroups were identified. **Results:** Complex heat map visualization showed that the MCT4-high/heterogeneous subgroup was correlating with a higher MCT4 expression level and local variation. This pattern linked to a specific [^{18}F]FDG PET signature, characterized by a higher SUV_{mean} and SUV_{max} and second-order radiomics features, correlating with local variation. This MCT4-based [^{18}F]FDG PET signature of 7 radiomics features demonstrated prognostic value in an independent cohort of pancreatic cancer patients (n = 71) and identified patients with worse survival. **Conclusion:** Our cross-modal pipeline allows the development of PET scan signatures based on immunohistochemical analysis of markers of a particular biologic feature, here demonstrated on pancreatic cancer using intratumoral MCT4 expression levels to select [^{18}F]FDG PET radiomics features. This study demonstrated the potential of radiomics scores to noninvasively capture intratumoral marker heterogeneity and identify a subset of pancreatic ductal adenocarcinoma patients with a poor prognosis.

Key Words: machine learning; [^{18}F]FDG PET; immunohistochemistry; tumor metabolism; pancreatic cancer

J Nucl Med 2024; 65:1151–1159
DOI: 10.2967/jnumed.123.266262

Received Jul. 1, 2023; revision accepted Apr. 22, 2024.
For correspondence or reprints, contact Erik H.J.G. Aarntzen (erik.aarntzen@radboudumc.nl).
*Contributed equally to this work.
†Contributed equally to this work.
Published online May 23, 2024.

Pronounced tumor heterogeneity is one of the hallmarks of pancreatic ductal adenocarcinoma (PDAC) (*1–4*). Different molecular subtypes of PDAC coexist in the same patient (*5,6*), exploiting distinct metabolic pathways (*7*) and thus providing a survival advantage under metabolic challenges such as low oxygen and nutrient supply. Moreover, the high adaptive fitness and metabolic plasticity of PDAC allow and support treatment resistance (*8–14*).

Pronounced activation of glycolysis, the Warburg effect, is one of the oldest cancer features described (*15*). In PDAC, high expression of glycolytic genes indeed predicts worse survival, both in a resectable setting and in a metastatic setting (*7*). Monocarboxylate transporter 4 (MCT4) is a lactate exporter and the last player in the glycolytic set of reactions. Histopathologic analysis of MCT4 in PDAC showed that high MCT4 expression, both in cancer and in stromal cells, predicts substantially worse survival (*16*).

Clinically, glucose uptake into tumors is detected via PET imaging with the radiotracer [^{18}F]FDG (*17*). Metabolic activity readouts measured by [^{18}F]FDG PET, such as SUV_{max}, were reported to correlate with PDAC tumor grading (*18*) and to have prognostic value (*19,20*), generally showing that a higher [^{18}F]FDG uptake is associated with a poor outcome (*21*). However, these single readouts extracted from the [^{18}F]FDG PET images are assumed to represent the whole lesion, although it is well observed that PDAC tumors often present heterogeneous [^{18}F]FDG uptake patterns (*22,23*). The general failure of PDAC clinical trials is attributed mostly to tissue heterogeneity and the resulting difficulty in selecting patients who would benefit from a particular therapy. Thus, there is an urgent need for noninvasive methods that could be used for patient selection. Radiomics technology, by allowing extraction and quantification of medical image characteristics and investigation of their correlation with underlying biologic features, shows a predictive value that can guide optimal therapy planning.

In this work, we aimed to use a radiomics approach to identify and extract features from [^{18}F]FDG PET images that allow capture of glycolytic heterogeneity and, subsequently, patient stratification based on that heterogeneity. Current approaches to PDAC subtyping demand invasive (biopsy/resection) and labor-intensive (RNA/histopathologic analysis) procedures and suffer from sampling error since only a part

of the tumor is analyzed. Differently, whole-tumor PET images acknowledge the intratumoral heterogeneity, and radiomics allows extraction and quantification of multiple features from [^{18}F]FDG PET images, describing patterns of tracer distribution in the whole PDAC lesion (*24*). Although some studies show a radiomics score to have prognostic value (*25*), most studies lack a plausible link between tracer uptake and its biologic underpinnings. So far, some general histopathologic features such as tissue cellularity have been correlated with radiomics texture features derived from [^{18}F]FDG PET images in different tumors (*26,27*). However, to the best of our knowledge, correlating radiomics features with the expression of a defined histopathologic marker that underlies a specific biologic process, such as MCT4 here as a glycolysis marker, has not been explored yet. This caveat in the biologic rationale for a given radiomics score hampers further fine-tuning in the development of [^{18}F]FDG PET as a noninvasive biomarker for PDAC characterization (*28*).

To this end, we introduce 3 methodologies to the field of PDAC research. First, we extract so-called pathomics features via texture analysis of density maps based on the immunohistochemical expression patterns of different markers, also revealing expression heterogeneity for each marker independently. Second, we link 3-dimensional data from PET analyses one-to-one with 2-dimensional data from digital pathology by investigating the distribution of immunohistochemistry staining at a comparable resolution of PET images in an automated way.

Last, we apply the MCT4-based pathomics features to develop [^{18}F]FDG PET–based radiomics scores. Here, we offer a radiomics-based, automated approach to correlate histopathologic MCT4 expression analysis with [^{18}F]FDG PET image features, allowing development of radiomics scores that capture intratumoral glycolytic marker heterogeneity as a noninvasive means to identify a subset of PDAC patients with a poor prognosis.

MATERIALS AND METHODS

This study was performed in line with the principles of the Declaration of Helsinki. Approval was granted by the Medical Ethical Review Committee of region Arnhem-Nijmegen on June 18, 2018, under study number CMO2018-4420.

Patient Characteristics

A development cohort of 29 patients who underwent resection of PDAC, and from whom paired whole-tumor cross sections and PET scans were available, was used to develop an [^{18}F]FDG PET/CT signature that captures intratumoral marker (MCT4, MCT1, pan-cytokeratin, and collagen) expression patterns. The availability of whole-tumor tissue minimized sampling error and enabled acknowledgment of tumor heterogeneity. Details on the proposed pipeline can be found in the supplemental methods (supplemental materials are available at http://jnm.snmjournals.org) and in Figure 1, Supplemental Figures 1–6, and Supplemental Tables 1–3 (*29–39*). The prognostic value of this [^{18}F]FDG PET/CT signature was investigated in an independent validation cohort of 71 pancreatic cancer patients who underwent palliative treatment.

Algorithm Optimization for Immunohistochemistry Analyses

Resected PDAC tumors from the development cohort were processed in one block, and consecutive tissue sections were stained for monocarboxylate transporter 4 (MCT4), monocarboxylate transporter 1 (MCT1), pan-cytokeratin, and collagen marker (sirius red) (the supplemental materials provide details on the immunohistochemistry protocols). Pathomics features and texture features were extracted via texture analysis of density maps of the expression of each individual marker. Pathomics features (n = 74) were computed using an immunohistochemistry algorithm based on the output of an optimized color-unmixing method (Fig. 1; Supplemental Fig. 3). Color thresholds from the staining of interest and background staining were used to create density maps from which all pathomics features were then extracted. Of a total 74 pathomics features, 37 were robust to variations in density map parameters (kernel size, image discretization, and in silico cutting) and were selected for further comparison (Supplemental Table 2). The k-means clustering of the 37 pathomics features revealed 2 distinct clusters of patients.

Algorithm Optimization for PET Analyses

From the [^{18}F]FDG PET scans, 3-dimensional segmentation of the tumor was performed by SUV_{max} 40% isocontour and manual correction (supplemental materials), and 73 radiomics features were extracted. Features were tested for stability with respect to several imaging parameters (image discretization and optimal respiratory gating), and 16 robust features were selected (Supplemental Table 3). Next, the radiomics features (n = 7) from the PET scans that were most discriminative in identifying the patient clusters as defined by MCT4 pathomics features were selected. The predictability and clinical significance of the identified 7 radiomics features were assessed in an independent validation cohort.

Subgroup Identification. On the Uniform Manifold Approximation and Projection (UMAP) using all the robust MCT4 pathomics features, we observed different subgroups of patients. To identify these subgroups with different MCT4 expression patterns, the k-means unsupervised clustering algorithm (k = 2) was applied to all the robust MCT4 pathomics features. On the basis of these k-means labels, we selected the MCT4 pathomics features that were most discriminative for these subgroups (as described in the "Feature Selection" section). Hierarchic heat map clustering, also called Complex Heatmap Visualization (CHV) (*40*), of these selected features was used to investigate differences in the pathomics feature values of the different subgroups. This information was used to investigate and interpret biologic differences between subgroups. This process was repeated for MCT1, pan-cytokeratin, and stroma marker.

Next, we investigated the radiomics features extracted from the [^{18}F]FDG PET scan. On the basis of UMAPs, we identified different subgroups of patients using the k-means (k = 2). We observed a high overlap between one of the MCT4 subgroups and a subgroup based on the PET features. On the basis of the MCT4 k-means labels and the radiomics features, we selected radiomics features that were most discriminative for the MCT4 subgroups (as described in the "Feature Selection" section). On the basis of CHV with these MCT4-based selected radiomics features, we investigated differences in the radiomics feature values of the different subgroups and used this information for biologic interpretation.

Feature Selection. At different points in this study, we selected features (pathomics or radiomics features) that were most discriminative for a label that is generated by k-means (MCT4, MCT1, pan-cytokeratin, stroma). Every time, we used the same approach with a different set of features and a different set of labels. We used minimum redundancy maximum relevance (mRMR) (*41*) with a bootstrap approach to select features. For each bootstrap, 15 features were selected using the mRMR. Using majority voting, features were selected that occur in at least 75% of the bootstraps. Next, it was checked whether the selected features also occur in alternative feature selection methods using Kbest (χ^2, k = 15), linear support vector classification (k = 15, scoring f1, cv 2), and random forest (15 features, 10 times). Only features that were identified via the mRMR approach and by at least one of the other feature selection methods were finally taken into the final list of selected features.

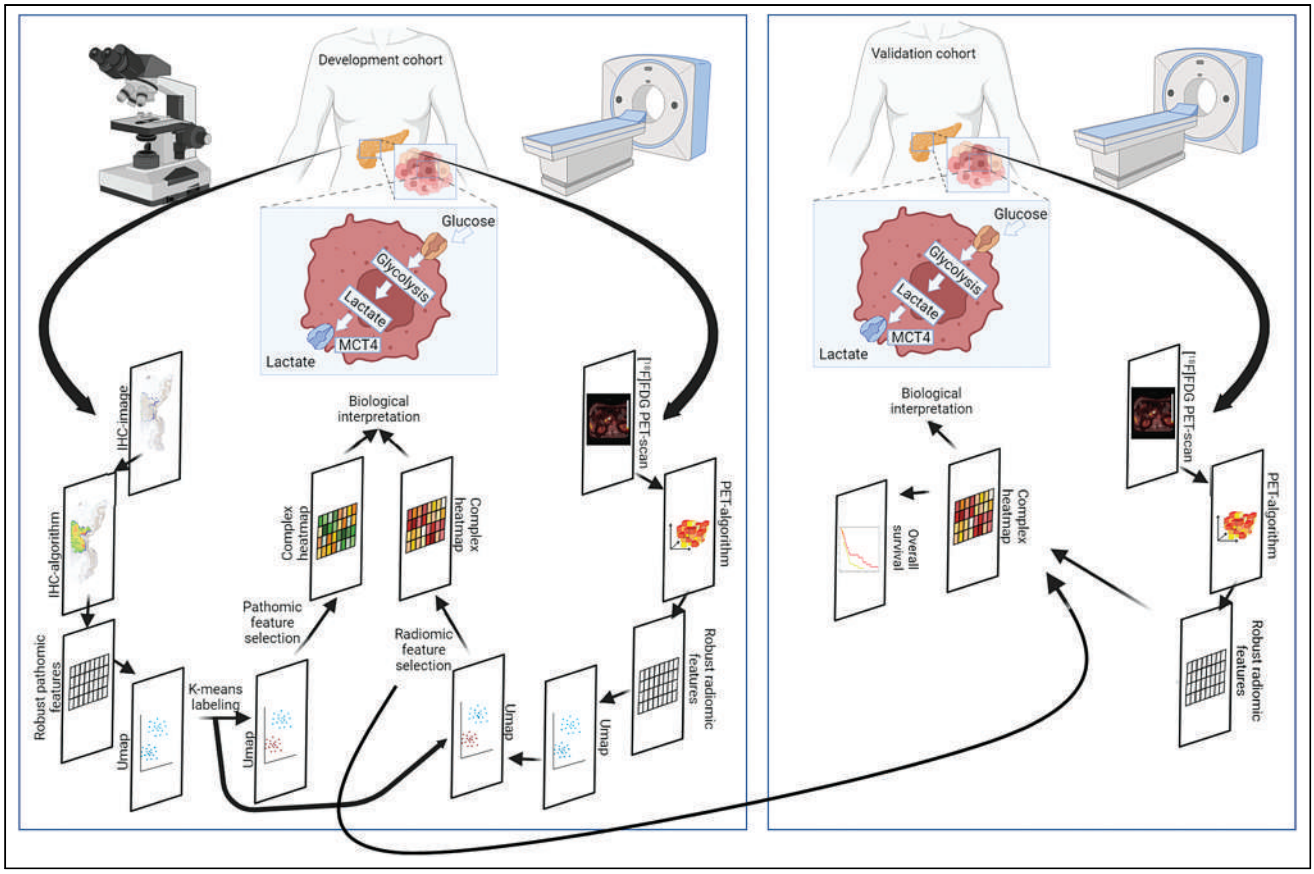

FIGURE 1. Overview of imaging analysis pipeline. In development cohort (29 patients), whole-tumor cross sections capturing intratumoral heterogeneity were stained for markers for glycolysis (MCT4, MCT1) and markers for cancer and stromal cells (pan-cytokeratin, sirius red) and processed into density maps. From these density maps, pathomics features were computed, which allowed identification of clusters of patients with similar spatial distributions of investigated markers. In parallel, [^{18}F]FDG PET images from same patients were analyzed to extract radiomics features, which were then selected to reflect pathomics scores. MCT4-based radiomics score of 7 selected features for [^{18}F]FDG PET was subsequently applied in validation cohort (71 patients) and identified subgroup of PDAC patients with poor prognosis. IHC = immunohistochemistry.

RESULTS

Pathomics Features Identify Distinct MCT4 Expression Patterns

Visual immunohistochemistry analysis revealed that MCT4 is expressed both on tumor cells and on stromal cells, with prominent expression on tumor cells. Visualization of the robust pathomics features (n = 37, Supplemental Table 2) in the feature space via UMAP revealed 2 clearly distinct clusters of MCT4 expression patterns (Fig. 2A). Therefore, we performed clustering analysis using the k-means algorithm (with k = 2 on a 37-dimensional pathomics feature space) to label the patients as MCT4-high/heterogeneous (n = 19) or MCT4-low/homogeneous (n = 10) (Fig. 2B).

We further selected the pathomics features most discriminative for the 2 identified k-means patient clusters, MCT4-high/heterogeneous and MCT4-low/homogeneous. For this purpose, we used feature selection techniques using MCT4-high/heterogeneous and MCT4-low/homogeneous as targets. A combination of 4 different feature selection methods (mRMR, Kbest, linear support vector classification, and random forest; supplemental methods) was used. Five pathomics features were identified as most discriminative for MCT4-high/heterogeneous versus MCT4-low/homogeneous: ratio (percentage of pixels stained for MCT4 compared with the total tumor region); 90 percentile, a first-order feature; inverse difference normalized from the gray level cooccurrence matrix; zone percentage from the gray level size zone

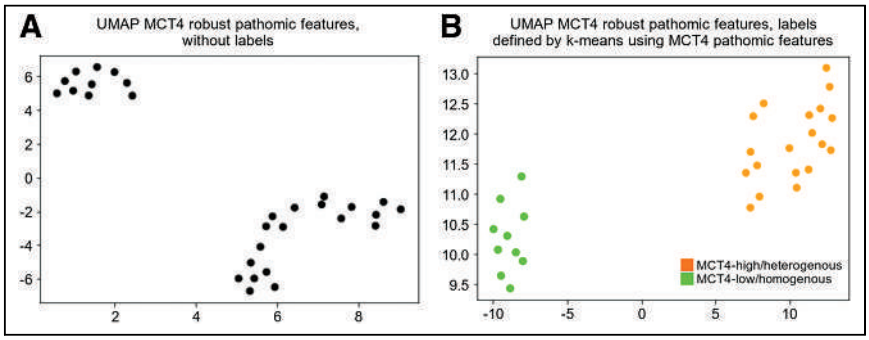

FIGURE 2. MCT4 expression patterns identify distinct MCT4 expression subtypes in PDAC patients using UMAP visualization. (A) Visualization of patient clusters with UMAP using all robust MCT4 pathomics features (n = 37) shows 2 clusters. (B) Use of k-means (k = 2) identifies 2 patient clusters: MCT4-high/heterogeneous and MCT4-low/homogeneous.

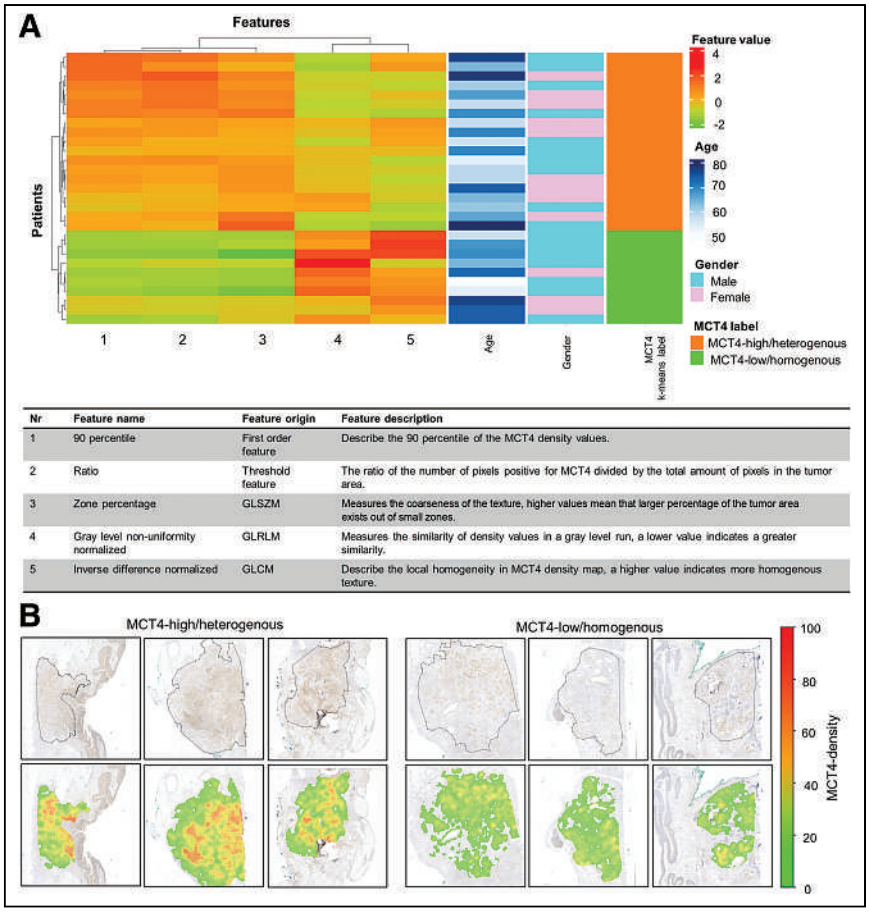

Nr	Feature name	Feature origin	Feature description
1	90 percentile	First order feature	Describe the 90 percentile of the MCT4 density values.
2	Ratio	Threshold feature	The ratio of the number of pixels positive for MCT4 divided by the total amount of pixels in the tumor area.
3	Zone percentage	GLSZM	Measures the coarseness of the texture, higher values mean that larger percentage of the tumor area exists out of small zones.
4	Gray level non-uniformity normalized	GLRLM	Measures the similarity of density values in a gray level run, a lower value indicates a greater similarity.
5	Inverse difference normalized	GLCM	Describe the local homogeneity in MCT4 density map, a higher value indicates more homogenous texture.

FIGURE 3. MCT4 expression patterns identify distinct MCT4 expression subtypes in PDAC. (A) CHV visualization of 2 patient clusters using MCT4 robust pathomics features. (B) Examples of representative density maps for MCT4-high/heterogeneous and MCT4-low/homogeneous patients. GLCM = gray level cooccurrence matrix; GLRLM = gray level run length matrix; GLSZM = gray level size zone matrix.

matrix; and gray level nonuniformity normalized from the gray level run length matrix (Supplemental Table 4).

After visual inspection of the CHV graph, where the 5 selected pathomics features were plotted, we observed a clear difference between MCT4-high/heterogeneous and MCT4-low/homogeneous clusters (Fig. 3A). The MCT4-high/heterogeneous patient cluster contained tumors with a high amount and density of MCT4 expression and a more heterogeneous and fine-grained texture, as opposed to the MCT4-low/homogeneous patient cluster, which contained a lower intensity and lower density of MCT4 expression with a more homogeneous and compact texture (Figs. 3A and 3B).

MCT4 Expression Patterns Link to [^{18}F]FDG Uptake Patterns

We further explored whether the clusters observed in MCT4 histologic images can be correlated with the glycolytic activity of the tumor captured via [^{18}F]FDG PET images. For this purpose, we used the data of the development cohort for whom both histology and PET scans were available (Fig. 1). On the basis of the segmented 3-dimensional volumes, a set of 73 radiomics texture features were computed (the supplemental materials provide details) (*31*), and 16 radiomics features, defined as robust, were selected (Supplemental Table 3). Using UMAP based on the 16 robust radiomics features, we observed 2 patient clusters (Fig. 4A).

As done for MCT4 pathomics features, we also analyzed the importance of PET radiomics features by clustering PET data into 2 subgroups defined by MCT4 k-means labels (i.e., MCT4-high/heterogeneous and MCT4-low/homogeneous) on a 16-dimensional radiomics feature space. We used the same feature selection techniques as were used for immunohistochemistry data (mRMR, Kbest, linear support vector classification, and random forest), which determined that 7 radiomics features were most discriminative: the 5 first-order features SUV_{mean}, SUV_{max}, uniformity, total lesion glycolysis (TLG), and interquartile range, as well as inverse difference and informational measure of correlation 1 from the gray level cooccurrence matrix (Supplemental Table 5 (*31*)). Using these 7 selected features, we obtained patient clustering similar to that when all radiomics features were used (Figs. 4B and 4C).

Visual inspection of the CHV confirmed that the cluster containing mostly MCT4-high/heterogeneous cases was associated with higher and heterogeneous [^{18}F]FDG uptake (Fig. 5A). This subgroup was also associated with more local variation in intratumoral [^{18}F]FDG uptake and with lower local homogeneity than was the other PET cluster, containing a mixture of MCT4-high/heterogeneous and MCT4-low/homogeneous (Figs. 5A and 5B). These results suggest that tumors with high [^{18}F]FDG uptake present higher and more heterogeneous expression patterns of the MCT4 lactate exporter and that biologically interpretable patterns may underlie the features of PET images.

Next, we challenged the ability of single features of the radiomics score, such as the commonly used SUV_{mean}, SUV_{max}, and TLG, to stratify patients according to

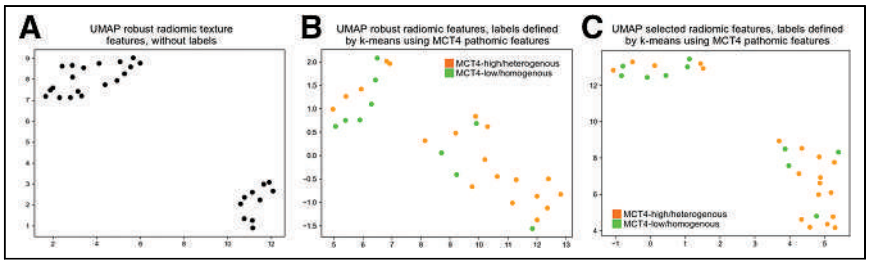

FIGURE 4. [^{18}F]FDG expression patterns identify distinct subtypes in PDAC patients that link to MCT4 expression. Two distinct patient clusters using [^{18}F]FDG PET radiomics features are visualized. (A) UMAP with 16 robust radiomics features showing 2 clusters. (B) UMAP with 16 robust radiomics features and based on MCT4-high/heterogeneous and MCT4-low/homogeneous. (C) UMAP with 7 selected radiomics features and based on MCT4-high/heterogeneous (n = 19) and MCT4-low/homogeneous (n = 10).

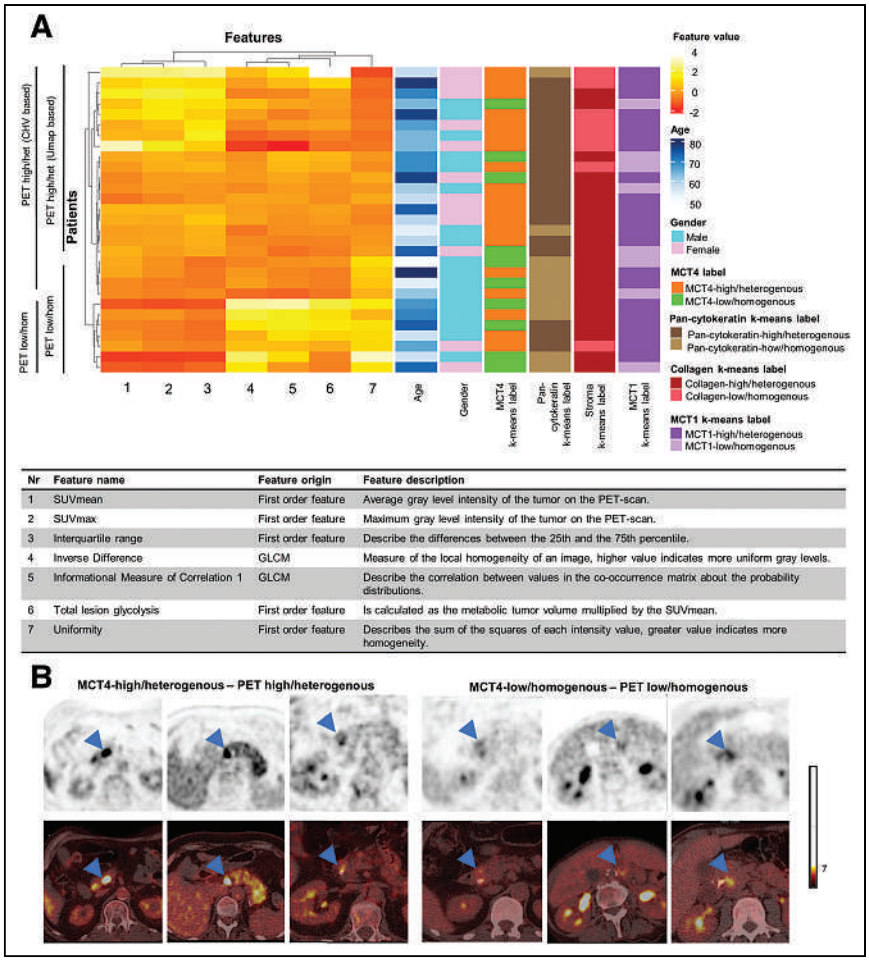

Nr	Feature name	Feature origin	Feature description
1	SUVmean	First order feature	Average gray level intensity of the tumor on the PET-scan.
2	SUVmax	First order feature	Maximum gray level intensity of the tumor on the PET-scan.
3	Interquartile range	First order feature	Describe the differences between the 25th and the 75th percentile.
4	Inverse Difference	GLCM	Measure of the local homogeneity of an image, higher value indicates more uniform gray levels.
5	Informational Measure of Correlation 1	GLCM	Describe the correlation between values in the co-occurrence matrix about the probability distributions.
6	Total lesion glycolysis	First order feature	Is calculated as the metabolic tumor volume multiplied by the SUVmean.
7	Uniformity	First order feature	Describes the sum of the squares of each intensity value, greater value indicates more homogeneity.

FIGURE 5. MCT4 expression profiles link to [^{18}F]FDG PET uptake patterns. (A) Visualization of PET feature values of selected radiomics features using CHV. (B) Visualization of [^{18}F]FDG uptake patterns (arrowheads) on representative examples of PET scans of MCT4-high/heterogeneous and MCT4-low/homogeneous. GLCM = gray level cooccurrence matrix; het = heterogeneous; hom = homogeneous.

MCT4 expression patterns. Single features in combinations of two also demonstrated good ability in discovering MCT4 expression patterns in the tissue, which could be further fine-tuned using the 7 selected features (Supplemental Figs. 7–9). To maximize the potential of this MCT4-based radiomics score for other PDAC cohorts with different frequencies of distinct MCT4 expression patterns and to minimize dependency on arbitrary choices, we opted to proceed with a signature of 7 PET features, allowing an unsupervised clustering approach.

[^{18}F]FDG Uptake Patterns Are Not Associated with MCT1 Expression Patterns

In addition to MCT4, we also stained consecutive tumor slides for lactate transporter MCT1. MCT1 was also found to be expressed on tumor and stromal cells, with prominent expression in stroma as well. Using the same setup as for the MCT4 analysis, MCT1 pathomics features were extracted. Since the results of the stability test on MCT4 features are based solely on technical aspects of whole-slide image processing, we also considered the same set of features as robust for density map parameters in MCT1.

These stable pathomics features identified 2 distinct patient clusters in our immunohistochemistry development cohort (Supplemental Fig. 10A). The k-means clustering (k = 2) on MCT1 robust pathomics features identified 2 patterns (MCT1-high/heterogeneous and MCT1-low/homogeneous) of MCT1 expression (Supplemental Fig. 10B). After feature selection based on the MCT1 k-means label, we observed that MCT1-high/heterogeneous was associated with features that showed higher MCT1 expression in smaller zones (Supplemental Figs. 10C and 10D; Supplemental Table 6) than was MCT1-low/homogeneous. However, MCT1 expression patterns had a mixed presence in the 2 clusters of PET-derived features, and we were not able to correlate MCT1 expression pattern to a particular [^{18}F]FDG uptake pattern on PET (Fig. 5A; Supplemental Fig. 11).

[^{18}F]FDG Uptake Patterns Are Associated with Pan-Cytokeratin Expression Patterns

To investigate whether [^{18}F]FDG PET signals can be attributed to PDAC tumor cells and not to other cells in the tumor microenvironment, pathomics scores of pan-cytokeratin (a cancer cell marker) staining performed on consecutive whole-tumor sections were calculated. Stable pathomics features identified 2 distinct clusters of patients based on pan-cytokeratin immunohistochemistry (Supplemental Fig. 12A). The k-means clustering (k = 2) on pan-cytokeratin robust pathomics features defined 2 patterns (pan-cytokeratin-high/heterogeneous and pan-cytokeratin-low/homogeneous) of pan-cytokeratin expression (Supplemental Fig. 12B). After feature selection based on the pan-cytokeratin k-means label, we observed that pan-cytokeratin–high/heterogeneous was associated with features that showed more variation in pan-cytokeratin expression (Supplemental Figs. 12C and 12D; Supplemental Table 7) than was pan-cytokeratin–low/homogeneous. Similar to what was observed for MCT4, pan-cytokeratin–high/heterogeneous expression showed a high overlap with the PET-high/heterogeneous expression pattern (Fig. 5A; Supplemental Figs. 13A and 13B). This suggests that [^{18}F]FDG PET radiomics could be correlated with MCT4-high/heterogeneous and pan-cytokeratin–high/heterogeneous expression patterns (Fig. 5A; Supplemental Figs. 13C and 13D), supporting the presence of MCT4-expressing PDAC cancer cells in PET-high/heterogeneous tumor regions.

[^{18}F]FDG Uptake Patterns Are Associated with Collagen Expression Patterns

The presence of stroma and collagen fibers in the stroma in PDAC is a known determinant of low oxygen and nutrient supply and thus one of the tissue characteristics underpinning metabolic heterogeneity. Therefore, we also investigated collagen expression patterns. Stable collagen pathomics features identified 2 distinct

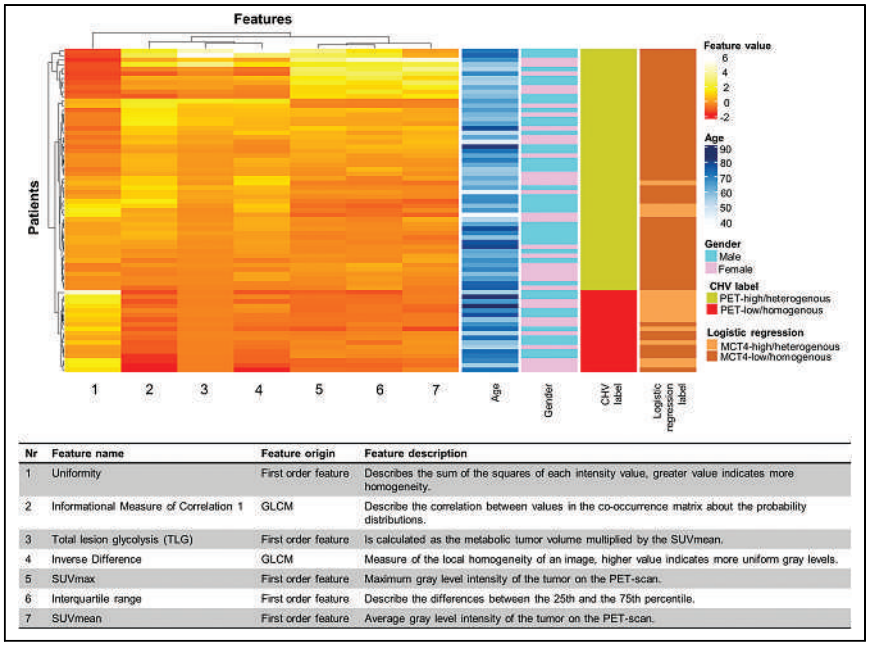

Nr	Feature name	Feature origin	Feature description
1	Uniformity	First order feature	Describes the sum of the squares of each intensity value, greater value indicates more homogeneity.
2	Informational Measure of Correlation 1	GLCM	Describe the correlation between values in the co-occurrence matrix about the probability distributions.
3	Total lesion glycolysis (TLG)	First order feature	Is calculated as the metabolic tumor volume multiplied by the SUVmean.
4	Inverse Difference	GLCM	Measure of the local homogeneity of an image, higher value indicates more uniform gray levels.
5	SUVmax	First order feature	Maximum gray level intensity of the tumor on the PET-scan.
6	Interquartile range	First order feature	Describe the differences between the 25th and the 75th percentile.
7	SUVmean	First order feature	Average gray level intensity of the tumor on the PET-scan.

FIGURE 6. MCT4-based [^{18}F]FDG PET radiomics features identify subgroups with different [^{18}F]FDG expression patterns. Shown is visualization of PET feature values with CHV using selected radiomics features in validation cohort (n = 71). GLCM = gray level cooccurrence matrix.

clusters of patients based on sirius red histologic staining (Supplemental Fig. 14A). The k-means clustering (k = 2) defined 2 patterns: collagen-high/heterogeneous and collagen-low/homogeneous expression (Supplemental Fig. 14B). After feature selection based on the collagen k-means label, it was observed that the collagen-high/heterogeneous cluster comprised features describing an increased variation in collagen expression (Supplemental Figs. 14C and 14D; Supplemental Table 8). Collagen-low/homogeneous expression showed a partial overlap with [^{18}F]FDG PET-high/heterogeneous expression (Fig. 5A; Supplemental Figs. 15A and 15B). This suggests that [^{18}F]FDG PET uptake patterns are, at least in part, correlated with collagen expression patterns (Fig. 5A; Supplemental Figs. 15C and 15D).

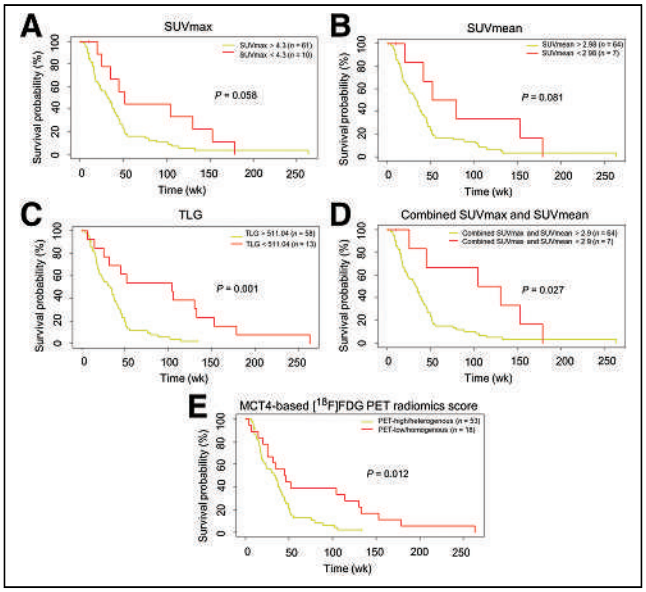

FIGURE 7. MCT4-based [^{18}F]FDG PET patterns can be associated with overall survival. (A–C) Survival curves based on optimal cutoff for SUV_{max}, SUV_{mean}, and TLG for validation cohort. High TLG predicts worse survival. (D) Survival curve based on optimal cutoff for combined SUV_{max} and SUV_{mean} (calculated by [SUV_{max} − SUV_{mean}] × SUV_{mean}) for validation cohort. (E) Correlation of MCT4-based [^{18}F]FDG PET–derived features with overall survival. Kaplan–Meier survival curves demonstrate impact of these PET-derived features on overall survival. PET-high/heterogeneous label predicts worse survival with statistical significance.

[^{18}F]FDG PET Patterns Associate with Overall Survival

High MCT4 expression was previously shown to predict worse survival in PDAC (*16*). Thus, the clinical impact of the MCT4-based [^{18}F]FDG PET radiomics score of the 7 selected radiomics features was investigated in an independent multicenter cohort of 71 PDAC patients (validation cohort) who received not surgical resection but systemic treatment in a palliative setting or best supportive care (Supplemental Table 1). [^{18}F]FDG PET was performed for all patients before the start of systemic treatment. Using this validation cohort, we generated a CHV of the 7 selected radiomics features (radiomics score). The analysis revealed 2 subgroups of patients (PET-high/heterogeneous and PET-low/homogeneous; Fig. 6), which were then used for survival analysis. The PET-high/heterogeneous subgroup presented a worse prognosis than the PET-low/homogeneous subgroup (median overall survival of 34.1 and 45.5 wk, respectively; P = 0.01; Fig. 7). In addition, we trained a logistic regression model to predict MCT4-based patterns with the radiomics score of the 7 selected features. For training, we used the 29 cases from the development cohort using the MCT4-label and the 7 radiomics features. We applied the trained model to the validation cohort, and for each patient we obtained the likelihood of belonging to the MCT4-high/heterogeneous or the MCT4-low/homogeneous subgroup based on radiomics features. Using these predictions, we observed a high concordance in the PET-high/heterogeneous subgroup; 49 of 53 (92.45%) patients were also labeled as MCT4-high/heterogeneous (Fig. 6; Supplemental Table 9). For the PET-low/homogeneous subgroup, the concordance with MCT4-low/homogeneous patterns was somewhat lower, at 11 of 18 (61.11%) (Fig. 6). Therefore, MCT4-based [^{18}F]FDG PET radiomics features allow noninvasive detection of a subset of patients with a poor prognosis.

Furthermore, we analyzed whether patient survival can be predicted by single radiomics features such as the traditionally used SUV_{max}, SUV_{mean}, and TLG, using the optimal cutoff algorithm for optimal separation of patients in survival groups with minimal P value (highest statistical power). The 7-feature radiomics score provides survival prediction with similar statistical power to SUV_{mean} and SUV_{max} as single features only or combined. However, as a sole feature, higher TLG better predicts worse survival in PDAC patients (Fig. 7) (*42*).

DISCUSSION

It is increasingly understood that PDAC intra- and intertumoral heterogeneity plays a pivotal role in treatment resistance. To effectively

treat PDAC, patient-tailored approaches based on subtype detection and patient stratification are mandatory. This generally requires invasive tissue extraction procedures for genomic or transcriptomic analyses (*43*). Therefore, noninvasive biomarkers that address and represent the tumor biology are highly needed.

Although the data on the existence of a glycolytic subtype of PDAC are convincing (*7,44,45*), and [^{18}F]FDG PET as a clinical glycolysis surrogate marker has stood for decades, a good interpretation of [^{18}F]FDG PET signals with a correlation to the underlying biology is missing in PDAC, as well as in many other tumor types. The utility of [^{18}F]FDG PET for PDAC detection and patient stratification has been challenging with different groups using different SUV_{max} cutoffs for optimal stratification (*46*). Furthermore, SUV_{max} is extrapolated as representative of the whole tumor, neglecting intratumoral heterogeneity.

To fill this gap, we aimed to compare the histologic expression of the metabolic markers MCT4 and MCT1 with the findings of [^{18}F]FDG PET scans in a cohort of patients ($n = 29$) for whom both [^{18}F]FDG PET data and histologic tumor samples were available.

We performed an immunohistochemistry analysis for the lactate transporters MCT4, MCT1, pan-cytokeratin, and sirius red and a consequent radiomics study in which we extracted the most discriminative pathomics features from the histologic staining and correlated these with [^{18}F]FDG PET images. On the basis of the histologic expression patterns of MCT4 and comparative analysis with the [^{18}F]FDG PET signals of the corresponding patients, we determined a set of 7 radiomics features that identify patients with MCT4-high/heterogeneous expression patterns. A good correlation between MCT4-high/heterogeneous histologic patterns and [^{18}F]FDG PET high/heterogeneous radiomics expression patterns was revealed, suggesting a connection between MCT4 positivity and a high [^{18}F]FDG PET signal in tumors.

Furthermore, our observation of a good positive correlation of the PET-high/heterogeneous radiomics feature expression pattern with the pan-cytokeratin–high/heterogeneous pathomics feature expression pattern and the collagen-low/homogeneous feature expression pattern supports the view that tumor regions that are rich in MCT4/pan-cytokeratin–positive cancer cells but poor in collagen-positive stroma are underlying those prominent [^{18}F]FDG PET signals. Stroma-rich PDAC submicroenvironments are generally less populated with cancer cells (*13*), and in addition, stromal fibers per se organize a barrier for delivery of nutrients (*47*), including glucose, thus supporting the lower glycolysis in those tumor areas and observed PET-low/homogeneous [^{18}F]FDG signals (Supplemental Fig. 16).

It should be noted that the selected 5 MCT4 pathomics features correlate well with each other and that the stratification power of single features may be high as well. This can in part be explained by the relatively small size of our developmental cohort ($n = 29$), with rather uniform sizes of smaller PDAC tumors. We anticipate that the 7-feature radiomics score is more robust to variation and less dependent on arbitrary choices than using single features. This will especially be relevant when applying this signature to larger tumors with more pronounced tissue heterogeneity or cohorts with different distributions of MCT4 expression patterns. Thus, to generate a model that can potentially be generalized, we opt for using scores of several features, as we did for all 5 selected pathomics features used here, rather than single features (*48*).

High expression of MCT4 is a well-described predictor of worse survival in PDAC patients (*16*). We thus challenged the prognostic power of the developed MCT4-based PET radiomics score on a larger set of PDAC patients ($n = 71$) in an independent multicenter validation cohort. The radiomics score successfully stratified patients into subgroups with prognostic relevance, where patients with PET-high/heterogeneous label had worse survival. Also, it should be noted that single features of the score, such as SUV_{mean}, SUV_{max}, or TLG, also performed well in the patient stratification and that the predictive power of the radiomics score is certainly a result of the synergism achieved by combining them. However, the good predictive power of high TLG in the validation cohort is notable and can potentially be attributed to 2 issues: the first is that TLG is a combination of 2 traits (tumor size and SUV_{mean}) that, additively, surpass the power of the single traits, and the second is that tumors with high TLG are larger tumors known to predict worse survival (*42*). It should also be noted that for generation of survival curves based on SUV_{mean}, SUV_{max}, and TLG, we used an algorithm for optimal separation of patients to obtain the minimal P value, which potentially introduces a forced positive bias into the result. The PET label, however, is a selected group of radiomics features based on histologic MCT4 expression patterns, with no presumption on potential prognostic value. To provide the ultimate evidence that high MCT4 expression indeed underlies the high [^{18}F]FDG signals, future studies with a larger, independent cohort of patients with available histologic material and [^{18}F]FDG PET scans are warranted.

In addition to direct correlations, we observed cases that did not match MCT4-based patterns in [^{18}F]FDG PET signatures, which urges us to consider some biologic and technical limitations of our approach. First, for the purpose of a histology-based imaging biomarker centered around glycolytic activity, we choose MCT4 expression, as MCT4 was previously shown to correlate with molecular subtypes and survival in PDAC (*16*). However, the roles and cellular allotment of MCT4 in the tumor microenvironment are complex, and other lactate transporters may also play a role in cancer (*49,50*) and contribute to glycolytic turnover. In PDAC, MCT1 expression has also been shown to have prognostic value (*45*), and it functions mainly as a lactate importer, expressed on oxidative cancer cells that potentially use lactate as fuel. Consequently, these oxidative cancer cells consume less glucose and hence present lower [^{18}F]FDG uptake (*49*). In our cohort, MCT1 expression did not correlate with [^{18}F]FDG uptake patterns. This also implies that glycolytic pancreatic cancer cells may outcompete oxidative pancreatic cancer cells. However, the initial selection of patients also included only patients with [^{18}F]FDG uptake above the background level to delineate the tumor on PET images. Inclusion of such patients may have resulted in a preselection of those who had molecular subtypes of PDAC with higher glycolytic activity.

Second, the observed local variation in [^{18}F]FDG uptake described in the PET-high/heterogeneous subgroup may illustrate the coexistence of PDAC cells that rely on both glycolysis and oxidative phosphorylation as a main energy source. Additionally, MCT4 not only may export lactate but also may be involved in transport of other metabolites, such as pyruvate and ketones (*49,50–52*). Therefore, MCT4 expression may reflect not only glycolysis but also, in part, activity of additional metabolic pathways present at the cellular level.

Last, when histology is linked to [^{18}F]FDG uptake on PET, it should be noted that neither of these is tumor-cell–specific per se. MCT4 expression was also observed in stroma and in other noncancer cells, indicating active glycolysis in other cells as well. Also, [^{18}F]FDG uptake along the pancreatic–biliary stent, which was present in 22 patients, or in obstructive pancreatitis distal from the tumor localization, demonstrates that [^{18}F]FDG uptake and glucose metabolism are a part of non–cancer-related inflammatory processes as well (Supplemental Fig. 17). Together, these additional

mechanisms may be present in patients whose [^{18}F]FDG uptake pattern did not match the identified MCT4 patterns. Cross-modal image analysis pipelines are intrinsically impacted by differences in the specifications of imaging hardware. In this study, when linking the molecular markers on a cellular level to tissue-based measurements by PET, we encountered the problem of the low PET spatial resolution that results in loss of information on [^{18}F]FDG PET and its extracted features. Variations in glucose metabolism in intratumoral subvoxel regions are averaged on PET but can be quantified on MCT4-based density maps. To match the PET images, we choose to compute features on MCT4 density maps at the lowest spatial resolution, which was 128 μm/pixel. Another consequence of the lower spatial resolution of PET is the challenging delineation of tumors, which may be located around organs with high background [^{18}F]FDG uptake (aorta, liver, intestines, kidneys) or may be hard to discriminate from [^{18}F]FDG uptake in adjacent abscesses, cysts, or lymph nodes. Although tumor delineation was based on 40% SUV_{max} isocontouring to maximize uniformity, it still required manual checking and correction before the final tumor volume was determined. Last, the developmental patient cohort consisted of tumors that were completely resected, thus being, in general, primary tumors of earlier T stage. For tumors with even smaller diameters, the spatial resolution of PET will be limiting and the presented MCT4-based [^{18}F]FDG PET radiomics score is difficult to apply. However, smaller tumors do undergo surgery more often, and tissue is then available for direct analyses on MCT4 expression. Despite the technical difficulties, developing a noninvasive imaging biomarker of intratumoral metabolic heterogeneity is increasingly relevant to predict treatment efficacy in cancers in general (*8–12*) and for PDAC in particular (*13,14*). For example, stereotactic body radiation therapy for locally advanced or irresectable PDAC is emerging (*53,54*), indicating that our findings could be of particular interest to optimize radiation treatment plans (*55,56*). Moreover, the strong dependency of most cancers on glycolysis, also in the presence of sufficient oxygen, is increasingly used as a target for therapeutic interference (*57*), including selective blockade of monocarboxylate lactate transporters (*58,59*).

The general failure of PDAC clinical trials so far is mostly due to tissue heterogeneity and the resulting difficulty in choosing patients who would benefit from a selected therapy. By combining multiple pathomics and radiomics features and a whole-tumor view on both a pathologic and a radiologic level, we avoid reducing the tumor metabolic activity to a single value output, typically using SUV_{max}, leading to a descriptive statement of a tumor as being glycolytic or nonglycolytic. We support a view that combines multiple pathomics and radiomics features and can thus provide a better overview of the tumor's heterogeneous appearance and biology.

We envisage that in the future the [^{18}F]FDG PET radiomics features will be used not only to better predict patient survival but also to stratify patients for, for example, antimetabolic or glycolytic therapies. Furthermore, observations that we make here are potentially applicable to other cancer entities, especially those with a known high dependency on glycolysis (e.g., renal cancer and glioblastoma).

CONCLUSION

We envision that our approach to developing pathomics-based PET radiomics scores facilitates the adoption and implementation of PET imaging as a noninvasive biomarker to interrogate relevant aspects of tumor biology (*28*). The cross-modal image analysis pipeline developed in this study is among the first to use quantitative immunohistochemistry to link protein expression patterns to PET radiomics obtained in routine clinical practice.

DISCLOSURE

This study was supported the Radboud Oncologie Fonds/Stichting Bergh in het Zadel, partner of the Dutch Cancer Society (grant KUN2015-8106 and an institutional junior researcher grant to Erik Aarntzen), the Deutsche Forschungsgemeinschaft (405344257 [SI1549/3-2] and 421166016 [SI1549/4-1]), the German Federal Ministry of Education and Research (01KD2206A/SATURN3), the CANTAR research network of the Ministry of Culture and Science of the State of North Rhine-Westphalia, and the European Union Seventh Framework Program for Research, Technologic Development, and Demonstration (CAM-PaC grant 602783). Jens Siveke and Marija Trajkovic-Arsic are supported by the German Cancer Consortium. Jens Siveke receives honoraria as a consultant or for continuing medical education presentations from AstraZeneca, Bayer, Boehringer Ingelheim, Bristol-Myers Squibb, Immunocore, Merck Sharp & Dohme, Novartis, Roche/Genentech, and Servier. His institution receives research funding from Abalos Therapeutics, AstraZeneca, Boehringer Ingelheim, Bristol-Myers Squibb, Celgene, Eisbach Bio, and Roche/Genentech; he holds ownership and serves on the Board of Directors of Pharma15, all outside the submitted work. Francesco Ciompi was chair of the Scientific and Medical Advisory Board of TRIBVN Healthcare, France, and received advisory board fees from TRIBVN Healthcare, France, in the last 5 y. He is a shareholder of Aiosyn BV, the Netherlands. This article reflects the views of the authors, and Aiosyn BV is not liable for any use that may be made of the information contained herein. No other potential conflict of interest relevant to this article was reported.

ACKNOWLEDGMENT

We thank Ine van Raaij for assisting with immunohistochemistry protocols.

KEY POINTS

QUESTION: Can quantitative immunohistochemistry provide ground to develop PET radiomics scores with a biologic rationale?

PERTINENT FINDINGS: We developed and validated a radiomics-based, automated approach to correlate histopathologic MCT4 expression analysis with [^{18}F]FDG PET image features, allowing development of tissue-based radiomics scores that capture intratumoral glycolytic heterogeneity as a noninvasive means to identify a subset of PDAC patients with a poor prognosis.

IMPLICATIONS FOR PATIENT CARE: This cross-modal image analysis pipeline facilitates the adoption and implementation of PET imaging as a noninvasive biomarker to interrogate relevant aspects of tumor biology based on quantitative immunohistochemistry.

REFERENCES

1. Meacham CE, Morrison SJ. Tumour heterogeneity and cancer cell plasticity. *Nature.* 2013;501:328–337.
2. Zhao Y, Murciano-Goroff YR, Xue JY, et al. Diverse alterations associated with resistance to KRAS(G12C) inhibition. *Nature.* 2021;599:679–683.
3. Bedard PL, Hansen AR, Ratain MJ, Siu LL. Tumour heterogeneity in the clinic. *Nature.* 2013;501:355–364.

4. Hanahan D, Weinberg RA. Hallmarks of cancer: the next generation. *Cell.* 2011; 144:646–674.
5. Collisson EA, Sadanandam A, Olson P, et al. Subtypes of pancreatic ductal adenocarcinoma and their differing responses to therapy. *Nat Med.* 2011;17:500–503.
6. Bailey P, Chang DK, Nones K, et al. Genomic analyses identify molecular subtypes of pancreatic cancer. *Nature.* 2016;531:47–52.
7. Karasinska JM, Topham JT, Kalloger SE, et al. Altered gene expression along the glycolysis-cholesterol synthesis axis is associated with outcome in pancreatic cancer. *Clin Cancer Res.* 2020;26:135–146.
8. Kim J, DeBerardinis RJ. Mechanisms and implications of metabolic heterogeneity in cancer. *Cell Metab.* 2019;30:434–446.
9. Lloyd MC, Cunningham JJ, Bui MM, Gillies RJ, Brown JS, Gatenby RA. Darwinian dynamics of intratumoral heterogeneity: not solely random mutations but also variable environmental selection forces. *Cancer Res.* 2016;76:3136–3144.
10. Rybinski B, Yun K. Addressing intra-tumoral heterogeneity and therapy resistance. *Oncotarget.* 2016;7:72322–72342.
11. Junttila MR, de Sauvage FJ. Influence of tumour micro-environment heterogeneity on therapeutic response. *Nature.* 2013;501:346–354.
12. Vasan N, Baselga J, Hyman DM. A view on drug resistance in cancer. *Nature.* 2019;575:299–309.
13. Grünwald BT, Devisme A, Andrieux G, et al. Spatially confined sub-tumor microenvironments in pancreatic cancer. *Cell.* 2021;184:5577–5592.e18.
14. Raghavan S, Winter PS, Navia AW, et al. Microenvironment drives cell state, plasticity, and drug response in pancreatic cancer. *Cell.* 2021;184:6119–6137.e26.
15. Chan AK, Bruce JI, Siriwardena AK. Glucose metabolic phenotype of pancreatic cancer. *World J Gastroenterol.* 2016;22:3471–3485.
16. Baek G, Tse YF, Hu Z, et al. MCT4 defines a glycolytic subtype of pancreatic cancer with poor prognosis and unique metabolic dependencies. *Cell Rep.* 2014;9: 2233–2249.
17. Yamamoto K, Brender JR, Seki T, et al. Molecular imaging of the tumor microenvironment reveals the relationship between tumor oxygenation, glucose uptake, and glycolysis in pancreatic ductal adenocarcinoma. *Cancer Res.* 2020;80:2087–2093.
18. Xing H, Hao Z, Zhu W, et al. Preoperative prediction of pathological grade in pancreatic ductal adenocarcinoma based on ^{18}F-FDG PET/CT radiomics. *EJNMMI Res.* 2021;11:19.
19. Sperti C, Friziero A, Serafini S, et al. Prognostic implications of 18-FDG positron emission tomography/computed tomography in resectable pancreatic cancer. *J Clin Med.* 2020;9:2169.
20. Mohamed E, Needham A, Psarelli E, et al. Prognostic value of ^{18}FDG PET/CT volumetric parameters in the survival prediction of patients with pancreatic cancer. *Eur J Surg Oncol.* 2020;46:1532–1538.
21. Wang L, Dong P, Shen G, et al. ^{18}F-fluorodeoxyglucose positron emission tomography predicts treatment efficacy and clinical outcome for patients with pancreatic carcinoma: a meta-analysis. *Pancreas.* 2019;48:996–1002.
22. Hyun SH, Kim HS, Choi SH, et al. Intratumoral heterogeneity of ^{18}F-FDG uptake predicts survival in patients with pancreatic ductal adenocarcinoma. *Eur J Nucl Med Mol Imaging.* 2016;43:1461–1468.
23. Lim CH, Cho YS, Choi JY, et al. Imaging phenotype using ^{18}F-fluorodeoxyglucose positron emission tomography-based radiomics and genetic alterations of pancreatic ductal adenocarcinoma. *Eur J Nucl Med Mol Imaging.* 2020;47:2113–2122.
24. O'Connor JP, Rose CJ, Waterton JC, Carano RA, Parker GJ, Jackson A. Imaging intratumor heterogeneity: role in therapy response, resistance, and clinical outcome. *Clin Cancer Res.* 2015;21:249–257.
25. Toyama Y, Hotta M, Motoi F, Takanami K, Minamimoto R, Takase K. Prognostic value of FDG-PET radiomics with machine learning in pancreatic cancer. *Sci Rep.* 2020;10:17024.
26. Orlhac F, Theze B, Soussan M, Boisgard R, Buvat I. Multiscale texture analysis: from ^{18}F-FDG PET images to histologic images. *J Nucl Med.* 2016;57:1823–1828.
27. Fanchon LM, Dogan S, Moreira AL, et al. Feasibility of in situ, high-resolution correlation of tracer uptake with histopathology by quantitative autoradiography of biopsy specimens obtained under ^{18}F-FDG PET/CT guidance. *J Nucl Med.* 2015; 56:538–544.
28. Tomaszewski MR, Gillies RJ. The biological meaning of radiomic features. *Radiology.* 2021;298:505–516.
29. Leijenaar RT, Carvalho S, Velazquez ER, et al. Stability of FDG-PET radiomics features: an integrated analysis of test-retest and inter-observer variability. *Acta Oncol.* 2013;52:1391–1397.
30. Boellaard R, Delgado-Bolton R, Oyen WJ, et al. FDG PET/CT: EANM procedure guidelines for tumour imaging: version 2.0. *Eur J Nucl Med Mol Imaging.* 2015; 42:328–354.
31. van Griethuysen JJM, Fedorov A, Parmar C, et al. Computational radiomics system to decode the radiographic phenotype. *Cancer Res.* 2017;77:e104–e107.
32. Smeets EMM, Withaar DS, Grootjans W, et al. Optimal respiratory-gated [^{18}F]FDG PET/CT significantly impacts the quantification of metabolic parameters and their correlation with overall survival in patients with pancreatic ductal adenocarcinoma. *EJNMMI Res.* 2019;9:24.
33. Grootjans W, Kok P, Butter J, Aarntzen E. Management of respiratory motion artefacts in ^{18}F-fluorodeoxyglucose positron emission tomography using an amplitude-based optimal respiratory gating algorithm. *J Vis Exp.* July 23, 2020.
34. Geijs DJ, Intezar M, van der Laak JAWM, Litjens GJS. Automatic color unmixing of IHC stained whole slide images. Paper presented at: SPIE Medical Imaging; March 6, 2018; Houston, TX.
35. Ruifrok AC, Johnston DA. Quantification of histochemical staining by color deconvolution. *Anal Quant Cytol Histol.* 2001;23:291–299.
36. Bándi P, Balkenhol M, van Ginneken B, van der Laak J, Litjens G. Resolution-agnostic tissue segmentation in whole-slide histopathology images with convolutional neural networks. *PeerJ.* 2019;7:e8242.
37. Leijenaar RT, Nalbantov G, Carvalho S, et al. The effect of SUV discretization in quantitative FDG-PET radiomics: the need for standardized methodology in tumor texture analysis. *Sci Rep.* 2015;5:11075.
38. Smeets EMM, Withaar DS, Grootjans W, et al. Optimal respiratory-gated [^{18}F]FDG PET/CT significantly impacts the quantification of metabolic parameters and their correlation with overall survival in patients with pancreatic ductal adenocarcinoma. *EJNMMI Res.* 2019;9:24.
39. Grootjans W, Tixier F, van der Vos CS, et al. The impact of optimal respiratory gating and image noise on evaluation of intratumor heterogeneity on ^{18}F-FDG PET imaging of lung cancer. *J Nucl Med.* 2016;57:1692–1698.
40. Gu Z, Eils R, Schlesner M. Complex heatmaps reveal patterns and correlations in multidimensional genomic data. *Bioinformatics.* 2016;32:2847–2849.
41. De Jay N, Papillon-Cavanagh S, Olsen C, El-Hachem N, Bontempi G, Haibe-Kains B. mRMRe: an R package for parallelized mRMR ensemble feature selection. *Bioinformatics.* 2013;29:2365–2368.
42. Takahashi C, Shridhar R, Huston J, Meredith K. Correlation of tumor size and survival in pancreatic cancer. *J Gastrointest Oncol.* 2018;9:910–921.
43. Ju J, Wismans LV, Mustafa DAM, et al. Robust deep learning model for prognostic stratification of pancreatic ductal adenocarcinoma patients. *iScience.* 2021;24:103415.
44. Daemen A, Peterson D, Sahu N, et al. Metabolite profiling stratifies pancreatic ductal adenocarcinomas into subtypes with distinct sensitivities to metabolic inhibitors. *Proc Natl Acad Sci USA.* 2015;112:E4410–E4417.
45. Heid I, Münch C, Karakaya S, et al. Functional noninvasive detection of glycolytic pancreatic ductal adenocarcinoma. *Cancer Metab.* 2022;10:24.
46. Arnone A, Laudicella R, Caobelli F, et al. Clinical impact of ^{18}F-FDG PET/CT in the diagnostic workup of pancreatic ductal adenocarcinoma: a systematic review. *Diagnostics (Basel).* 2020;10:1042.
47. Derle A, De Santis MC, Gozzelino L, Ratto E, Martini M. The role of metabolic adaptation to nutrient stress in pancreatic cancer. *Cell Stress.* 2018;2:332–339.
48. Li D, Hu B, Zhou Y, Wan T, Si X. Impact of tumor size on survival of patients with resected pancreatic ductal adenocarcinoma: a systematic review and meta-analysis. *BMC Cancer.* 2018;18:985.
49. Payen VL, Mina E, Van Hée VF, Porporato PE, Sonveaux P. Monocarboxylate transporters in cancer. *Mol Metab.* 2020;33:48–66.
50. Pinheiro C, Longatto-Filho A, Azevedo-Silva J, Casal M, Schmitt FC, Baltazar F. Role of monocarboxylate transporters in human cancers: state of the art. *J Bioenerg Biomembr.* 2012;44:127–139.
51. Halestrap AP. Monocarboxylic acid transport. *Compr Physiol.* 2013;3:1611–1643.
52. Sun X, Wang M, Wang M, et al. Role of proton-coupled monocarboxylate transporters in cancer: from metabolic crosstalk to therapeutic potential. *Front Cell Dev Biol.* 2020;8:651.
53. Ermongkonchai T, Khor R, Muralidharan V, et al. Stereotactic radiotherapy and the potential role of magnetic resonance-guided adaptive techniques for pancreatic cancer. *World J Gastroenterol.* 2022;28:745–754.
54. Spiliopoulos S, Zurlo MT, Casella A, et al. Current status of non-surgical treatment of locally advanced pancreatic cancer. *World J Gastrointest Oncol.* 2021; 13:2064–2075.
55. Su W, Ren S, Zhu X, Zhang H, Zuo C. Standardized thresholds of volume-based PET/CT parameters predicting survival of patients with pancreatic head cancer treated with stereotactic body radiation therapy. *Ann Nucl Med.* 2020;34:379–387.
56. Ren S, Zhu X, Zhang A, Li D, Zuo C, Zhang H. Prognostic value of ^{18}F-FDG PET/CT metabolic parameters in patients with locally advanced pancreatic cancer treated with stereotactic body radiation therapy. *Cancer Imaging.* 2020;20:22.
57. Wilde L, Roche M, Domingo-Vidal M, et al. Metabolic coupling and the reverse Warburg effect in cancer: implications for novel biomarker and anticancer agent development. *Semin Oncol.* 2017;44:198–203.
58. Halestrap AP. The monocarboxylate transporter family: structure and functional characterization. *IUBMB Life.* 2012;64:1–9.
59. Schneiderhan W, Scheler M, Holzmann KH, et al. CD147 silencing inhibits lactate transport and reduces malignant potential of pancreatic cancer cells in in vivo and in vitro models. *Gut.* 2009;58:1391–1398.

Example of Artificial Intelligence–Based Decision Support for Amino Acid PET: Early Prediction of Suspected Brain Tumor Foci for Patient Management

Philipp Lohmann[1,2], Robin Gutsche[1], Jan-Michael Werner[3], N. Jon Shah[1,4], Karl-Josef Langen[1,2,5], and Norbert Galldiks[1,3,5]

[1]*Institute of Neuroscience and Medicine (INM-3/-4), Forschungszentrum Juelich, Juelich, Germany;* [2]*Department of Nuclear Medicine, University Hospital RWTH Aachen, Aachen, Germany;* [3]*Department of Neurology, Medical Faculty and University Hospital of Cologne, University of Cologne, Cologne, Germany;* [4]*Department of Neurology, University Hospital RWTH Aachen, Aachen, Germany; and* [5]*Center for Integrated Oncology Aachen Bonn Cologne Duesseldorf (CIO ABCD), Germany*

A 43-y-old man with equivocal findings on anatomic MRI underwent additional *O*-(2-[^{18}F]fluoroethyl)-L-tyrosine (^{18}F-FET) PET for further diagnosis of a suspected glioma. MRI showed no contrast enhancement, but fluid-attenuated inversion recovery (FLAIR) hyperintensities were apparent in the left thalamus and frontoparietal region (Fig. 1A). In spatial correspondence with the FLAIR signal alterations, only the left thalamic region segmented by an experienced nuclear medicine physician showed a slightly increased ^{18}F-FET uptake (mean tumor-to-brain ratio, 1.5) (Fig. 1B).

The baseline ^{18}F-FET PET was subsequently analyzed using the artificial intelligence (AI)–based segmentation tool JuST_Brain-PET (*1*). Surprisingly, a second lesion in the frontoparietal region, not segmented by the expert, was identified by the AI algorithm (Fig. 1B).

Although the left thalamic lesion showed no progression in the follow-up imaging 4 mo later, the additional frontoparietal lesion, initially considered a false-positive, progressed to become a small contrast-enhancing and metabolically active lesion (mean tumor-to-brain ratio, 2.1) (Fig. 1C). Neuropathologic analysis of tissue obtained from stereotactic biopsy revealed a molecular glioblastoma (central nervous system World Health Organization grade 4, isocitric dehydrogenase wild type, telomerase reverse transcriptase promoter mutant) without typical histologic findings such as microvascular proliferation and necrosis (*2*).

Although neither the thalamic nor the frontoparietal lesion showed pathologically increased ^{18}F-FET uptake on the baseline scan, the AI tool correctly predicted a pathologic process at an early disease stage and could have potentially influenced diagnostic and treatment decisions, such as biopsy guidance and target volume definition for radiotherapy.

This incidental finding highlights the potential of AI-based decision support for patient management in terms of diagnostic and treatment planning based on amino acid PET.

The study was approved by the local ethics committees (EK 055/19), and the subject gave written informed consent.

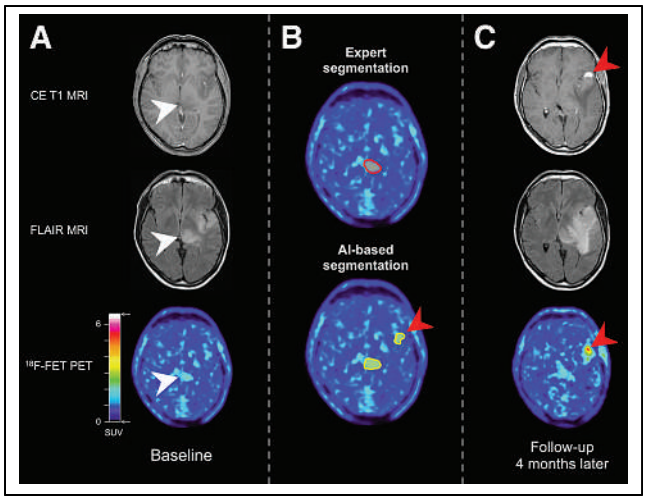

FIGURE 1. Baseline scan (A), segmentation results (B), and follow-up scan (C) from patient with molecular glioblastoma. Baseline MRI showed FLAIR hyperintensities in left thalamus and frontoparietal region (white arrowheads). In contrast to expert segmentation, in which only left thalamic region showed slightly increased uptake (red contour), AI algorithm identified additional frontoparietal lesion on baseline PET that subsequently progressed to contrast-enhancing and metabolically active lesion (red arrowheads). CE T1 = contrast-enhanced T1-weighted.

DISCLOSURE

This work was supported by the Deutsche Forschungsgemeinschaft (project 428090865/SPP 2177 [Robin Gutsche; Norbert Galldiks; Philipp Lohmann]). Norbert Galldiks and Philipp Lohmann received honoraria for lectures from Blue Earth Diagnostics. Norbert Galldiks received honoraria for advisory board participation from Telix Pharmaceuticals. No other potential conflict of interest relevant to this article was reported.

REFERENCES

1. Gutsche R, Lowis C, Ziemons K, et al. Automated brain tumor detection and segmentation for treatment response assessment using amino acid PET. *J Nucl Med.* 2023;64:1594–1602.
2. Louis DN, Perry A, Wesseling P, et al. The 2021 WHO classification of tumors of the central nervous system: a summary. *Neuro Oncol.* 2021;23:1231–1251.

Received Nov. 22, 2023; revision accepted Jan. 29, 2024.
For correspondence or reprints, contact Philipp Lohmann (p.lohmann@fz-juelich.de).
Published online Feb. 15, 2024.

DOI: 10.2967/jnumed.123.267112

Case Report: Pulmonary Actinomyces Infection Mimics Lung Cancer on [^{68}Ga]Ga-FAPI PET/CT

Giulia Cuzzani*[1], Emilia Fortunati*[2], Lucia Zanoni[2], Cristina Nanni[2], Filippo Antonacci[3], Francesca Giunchi[4], Gian Piero Bandelli[5], Irene Brusa[2], Piergiorgio Solli[3], and Stefano Fanti[1,2]

[1]*Nuclear Medicine, Alma Mater Studiorum University of Bologna, Bologna, Italy;* [2]*Nuclear Medicine, IRCCS, Azienda Ospedaliero–Universitaria di Bologna, Bologna, Italy;* [3]*Division of Thoracic Surgery, IRCCS, Azienda Ospedaliero–Universitaria di Bologna, Bologna, Italy;* [4]*Pathology, IRCCS, Azienda Ospedaliero–Universitaria di Bologna, Bologna, Italy; and* [5]*Interventional Pulmonology Unit, IRCCS, Azienda Ospedaliero–Universitaria di Bologna, Bologna, Italy*

Actinomycosis is a rare gram-positive infection, generally granulomatous. The diagnosis can be complex and sometimes can be achieved only at the chronic stage. *Actinomyces* normally colonize the mouth, urogenital tract, and gastrointestinal tract, whereas pulmonary infections occur primarily as a complication of secretion aspiration (*1*).

A 70-y-old patient who had undergone previous surgery for prostate cancer, was a former smoker, and had a family history of lung cancer presented with hemoptysis. A thoracic high-resolution CT scan detected a 45-mm heterogeneous pulmonary nodule (with surrounding ground-glass opacification) in the inferior right lobe, suggestive of malignancy and no significant adenopathies. Subsequent [^{18}F]F-FDG PET/CT showed significant uptake in the nodule, with SUV_{max} of 12.7 (Fig. 1A). For the suspected lung cancer, the patient was then enrolled in a prospective monocentric interventional study (EudraCT number 2021-006570-23 [CE AVEC: 51/2022/Farm/AOUBo]; the study protocol was approved by a Committee on Ethics, and all subjects signed a written informed-consent form). The patient underwent [^{68}Ga]Ga-fibroblast activation protein inhibitor (FAPI)-46 PET/CT 23 d later. The images showed only mild uptake (SUV_{max}, 5.9 at 60 min after injection; Fig. 1B) in the pulmonary nodule, slightly increasing on delayed scanning (SUV_{max}, 8.9 at 160 min). No lymph node uptake was detected.

Bronchoscopy was performed, and the frozen-section procedure showed reactive bronchial cells with granulocyte infiltration and lymphocytes; however, the results of microbiology and biochemical blood testing were negative. Subsequent CT confirmed the lung finding, with necrotic center features, not responding to antibiotic therapy. One month after [^{68}Ga]Ga-FAPI-46 PET/CT, the patient was hospitalized for recurrent hemoptysis, low hemoglobin level, and weight loss. After multidisciplinary evaluation, the patient was referred for right inferior lobectomy. The definitive histopathologic diagnosis excluded the presence of neoplastic cells; on the contrary, it showed acute bronchopneumonia and chronic abscess with gram-positive colonies, consistent with actinomycosis. Immunohistochemistry was also performed (Figs. 1C and 1D) with FAPI (53066; Abcam) and IRF-4 (EP190 [Ventana; Roche]) double staining: FAPI antibody reacts with fibroblasts and plasma cells, whereas IRF-4 is a specific immunostain for plasma cells.

Although actinomycosis is well known to mimic lung cancer on [^{18}F]F-FDG PET/CT (*2,3*), this is a clear example of how the new tracer [^{68}Ga]Ga-FAPI-46 can also be misleading in infection.

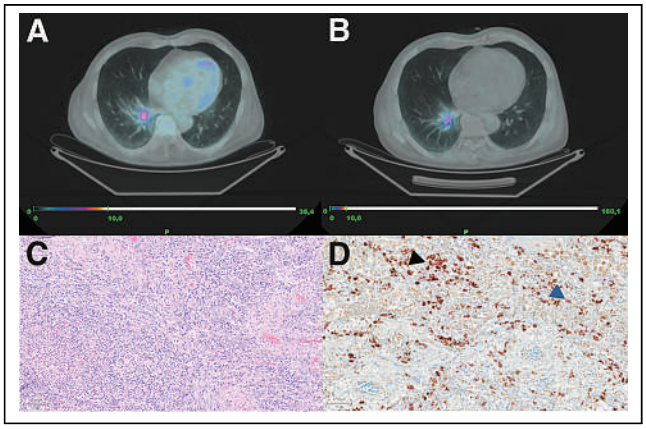

FIGURE 1. (A) Lung nodule on transaxial [^{18}F]F-FDG PET fused with attenuation-corrected CT. (B) Lung nodule on transaxial [^{68}Ga]Ga-FAPI-46 PET fused with attenuation-corrected CT (60-min uptake time). PET intensity scales are based on SUV body weight (g/mL). (C) Hematoxylin- and eosin-stained sections at ×4 magnification. Acute and chronic pneumonia with abscess formation is seen. Lesion is seen with rich acute and chronic inflammation, plasma cells, and fibroblasts. (D) Brown color represents fibroblast activation protein positivity in plasma cells and fibroblasts (black arrowhead), and red color represents IRTA1 nuclear immunoreactivity in plasma cells (blue arrowhead). Magnification is ×10.

However, [^{18}F]F-FDG and [^{68}Ga]Ga-FAPI-46 uptake proved to be different, with [^{68}Ga]Ga-FAPI-46 uptake being slightly milder.

Although a few other cases of granulomatous diseases mimicking malignancies on [^{68}Ga]Ga-FAPI PET/CT have been described (*4*), full knowledge of this promising tracer's features and pitfalls (*5*) has yet to be acquired.

DISCLOSURE

This research project was funded by FIN-RER 2020 Program of Emilia-Romagna Region. No other potential conflict of interest relevant to this article was reported.

REFERENCES

1. Valour F, Sénéchal A, Dupieux C, et al. Actinomycosis: etiology, clinical features, diagnosis, treatment, and management. *Infect Drug Resist.* 2014;7:183–197.
2. Aydin Y, Arslan R, Filik M. Pulmonary actinomycosis mimicks lung cancer. *Rev Soc Bras Med Trop.* 2022;55:e0195.
3. Kogure S, Yamamoto N, Watanabe F, Yuasa U, Tokui T, Shomura S. Pulmonary actinomycosis which was clinically suggested lung cancer;report of a case [in Japanese]. *Kyobu Geka.* 2011;64:254–257.
4. Meetschen M, Sandach P, Darwiche K, et al. Rabbit fever:granulomatous inflammation by *Francisella tularensis* mimics lung cancer in dual tracer ^{18}FDG and ^{68}Ga-FAPI PET/CT. *Eur J Nucl Med Mol Imaging.* 2023;50:2567–2569.
5. Hotta M, Rieger AC, Jafarvand MG, et al. Non-oncologic incidental uptake on FAPI PET/CT imaging. *Br J Radiol.* 2023;96:20220463.

Received Nov. 28, 2023; revision accepted Feb. 13, 2024.
For correspondence or reprints, contact Giulia Cuzzani (giulia.cuzzani2@studio.unibo.it).
*Contributed equally to this work.
Published online Mar. 7, 2024.

DOI: 10.2967/jnumed.123.267155

LBCA® Lobular Breast Cancer Alliance

Awareness Education Advocacy Research

Did you know?

Invasive lobular carcinoma (ILC) tumors often elude detection with standard breast imaging because they do not form in lumps.

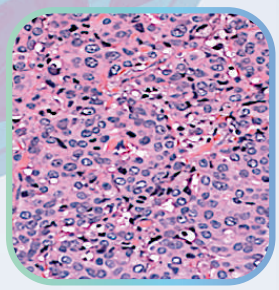

LOBULAR Breast Cancer

the 2nd most common Breast Cancer

- 15% of breast cancer diagnoses
- over 43,000 women diagnosed each year
- No targeted treatments

Learn about Lobular Breast Cancer and the ILC Patient Community

Check out our publications library

WWW.LOBULARBREASTCANCER.ORG

2024 ACNM/SNMMI **HOT TOPICS** Webinar Series

SNMMI and ACNM are excited to announce the lineup for the 2024 Hot Topics Webinar Series. **These informative webinars will take place at 12:00 pm ET on the second Tuesday of each month and are complimentary for ACNM and SNMMI members.**

- **History of Nuclear Medicine Technology**
  On Demand | *Fred Fahey*
- **AI in Nuclear Medicine: State of the Union**
  On Demand | *Katherine Zukotynski*
- **Prostate Radioligand Therapy Prior to Chemotherapy**
  On Demand | *Oliver Sartor*
- **PET/MR for Pediatrics**
  On Demand | *Helen Nadel*
- **Evolving Landscape of Prostate Cancer Imaging**
  On Demand | *François Bénard*
- **The Evolution of PRRT for NET–Y90, Lu177, Ac225**
  On Demand | *Lisa Bodei*
- **Advancing Precision Therapeutics in Dementia–How Does Imaging Fit In?**
  July 9 | *Sandra Black*
- **Contemporary Approach to PET Myocardial Perfusion Imaging**
  August 13 | *Panithaya Chareonthaitawee*
- **ER/PR/HER2-Targeted Imaging for Breast Cancer**
  September 10 | *Farrokh Dehdashti*
- **PET for Histiocytosis/ Erdheim Chester Disease**
  October 8 | *Sonia Mahajan*
- **What is New in Infection Imaging?**
  November 12 | *Ora Israel*
- **Prostate Cancer Imaging Agents–Is There a Difference?**
  December 10 | *Wolfgang Weber*

SNMMI SOCIETY OF NUCLEAR MEDICINE & MOLECULAR IMAGING

ACNM American College of Nuclear Medicine

Register today!

www.acnmonline.org/webinars

03202441

SPECTRUM
DYNAMICS MEDICAL

Breaking Barriers in SPECT Theranostics

VERITON-CT digital SPECT/CT, the system with the best sensitivity and energy resolution, enables you to image Lu177 PSMA and Lu177 Dotatate with speed and accuracy, and prepares you for future Theranostic agents.

VERITON-CT®
SERIES

Continuing to Break Barriers in SPECT Cardiac Imaging

D-SPECT continues to innovate with Dynamic SPECT, Advanced Planar Imaging, and AI Enhancements for tomorrow's Nuclear Cardiology.

D-SPECT®
SERIES

www.spectrum-dynamics.com

Scan to Learn More

7
24

The Journal of Nuclear Medicine

July 2024 ■ Vol. 65 ■ Pages 995–1161